Dioxygen reactivity of new models of copper oxygenases : electrochemical and spectroscopic studies

Federica Gennarini

THÈSE / UNIVERSITÉ DE BRETAGNE OCCIDENTALE
sous le sceau de l'Université Bretagne Loire

pour obtenir le titre de
DOCTEUR DE L'UNIVERSITÉ DE BRETAGNE OCCIDENTALE
Mention : Chimie fine
École Doctorale Matière, Molécules et Matériaux

présentée par
Federica GENNARINI
Préparée au CEMCA, UMR CNRS 6521

Dioxygen reactivity of new models of copper oxygenases: electrochemical and spectroscopic studies.

Thèse soutenue le 29 Novembre 2017
devant le jury composé de :

Anna COMPANY, Directeur de Recherche
Université de Girona / *Rapporteur*

Christophe BUCHER, Directeur de Recherche CNRS
Ecole normale supérieure de Lyon / Rapporteur

Frédéric BANSE, Professeur
Université de Paris-Sud / *Examinateur*

Paul-Alain JAFFRES, Professeur
Université de Bretagne Occidentale / *Examinateur*

Nicolas LE POUL, Chargé de Recherche CNRS
Université de Bretagne Occidentale / *Directeur de thèse*

Yves LE MEST, Directeur de Recherche CNRS
Université de Bretagne Occidentale / *Directeur de thèse*

Thèse de doctorat

Université de Bretagne Occidentale-UFR Sciences et Techniques

Ecole Doctorale Matière, Molécules et Matériaux (3M)

Pour l'obtention du grade de

DOCTEUR DE L'UNIVERSITE DE BRETAGNE OCCIDENTALE

Mention : Sciences de la matière

Spécialité : chimie

Présentée par :

Federica GENNARINI

Dioxygen reactivity of new models of copper oxygenases: electrochemical and spectroscopic studies

Soutenue le 29 novembre 2017 devant le jury composé de

Rapporteurs :

Anna COMPANY, Directeur de Recherche, Université de Girona

Christophe BUCHER, Directeur de Recherche CNRS, Ecole normale supérieure de Lyon

Examinateurs :

Frédéric BANSE, Professeur, Université de Paris-Sud

Paul-Alain JAFFRES, Professeur, Université de Bretagne Occidentale

Directeurs de thèse :

Dr. Nicolas LE POUL, Chargé de recherche CNRS, Université de Bretagne Occidentale

Dr. Yves LE MEST, Directeur de recherche CNRS, Université de Bretagne Occidentale

Acknowledgements

Thank you to the jury for agreeing to be members of this PhD examination. Thank you to Dr Anna Company from University of Girona, Dr Christophe Bucher from the Ecole Normale Supérieure of Lyon, Pr Frédéric Banse from University of Paris-Sud and Pr Paul-Alain Jaffrès from University of Western Brittany (Brest) for being my reporters and examiners.

Before proceeding to the body of this manuscript, I wanted to write some words of thanks to the people who have supported me along the way. Henceforth, I will write in the French language.

Tout d'abord, je voudrais remercier l'équipe d'électrochimie pour m'avoir accueillie dans son laboratoire, et aussi souligner la disponibilité, la gentillesse, la confiance et la patience de ses membres à mon égard. Je suis arrivée au laboratoire il y a trois ans comme biotechnologiste pour commencer mes travaux de recherche et je vais maintenant les terminer comme biotechnologiste et chimiste. Mes premiers remerciements vont à mon directeur de thèse et encadrant, Dr. Nicolas Le Poul, qui avec professionnalisme et compétence, a suivi mon travail de thèse jusqu'au bout. Il a toujours répondu à mes questions et à mes doutes, malgré tous ses nombreux engagements de travail. Je conserverai avec moi tous les schémas, les dessins et les notes de ses précieuses leçons sur la chimie et l'électrochimie, et aussi ceux des prototypes des cellules de spectro-électrochimie que nous avons inventés et que j'ai expérimentés. Grâce à tout cela je ne me suis pas ennuyée un seul instant ! Merci Nicolas pour tes conseils professionnels et pour avoir été mon coach mental quand cela s'est avéré nécessaire. Je voudrais remercier également le Dr. Yves Le Mest, aussi directeur de thèse, qui m'a montré son soutien et ses encouragements depuis mon arrivée en France, le 29 septembre 2014. Merci Yves pour être fier de mes progrès en français.

Eh voilà, trois ans à Brest, trois ans à l'UBO, trois ans au deuxième étage du laboratoire UMR 6521. Trois années pendant lesquelles j'ai considéré le laboratoire comme ma maison, et je ne pourrais pas être plus reconnaissante aux formidables personnes que j'ai rencontrées, et avec qui j'ai vécu de belles expériences. Formidables comme vous, Laurianne et Bénédicte. Laurianne, ingénieure d'étude dans l'équipe, mais bien plus que ça ! Elle est le soutien des manipulations vouées à l'échec avant même d'avoir commencées. Je me rappellerai toujours de ta bonne humeur, de ta disponibilité pour m'aider dans le laboratoire

lors des manipulations spécifiques, et aussi de toutes les électrodes que nous avons construites ensemble! Merci aussi de ton aide pour les mesures de RPE. Un remerciement pour Bénédicte, maître de conférences et responsable de la révision finale de tous mes rapports, présentations et exposés, pour être perfectionniste au travail ! Merci pour ton écoute et ton encouragement quand j'en avais besoin. Je n'oublierai pas non plus ton affection presque maternelle qui m'a aidée quand je me sentais seule et loin de ma famille. Et bien entendu, merci aussi pour ton aide dans tous mes nombreux déménagements ! Merci Isidoro – le génie (comme il aime se définir), chercheur postdoctorant espagnol, qui a partagé avec moi de longues journées au laboratoire lors de mes deux premières années de thèse. Il fut le premier à m'expliquer comment faire une bonne soudure et à connaitre les astuces de l'électrochimie à basse température. Merci pour m'avoir laissée utiliser ton matériel, jalousement gardé dans ton placard : « l'intouchable placard d'Isidoro ». Je me rappellerai toujours quand on se battait pour la réservation des potentiostats !

Merci à vous tous parce que sans vous je ne serai jamais arrivée à ce stade.

Ce projet de recherche a aussi été fructueux grâce aux collaborations avec les collègues chercheurs de Grenoble et de Marseille. Je suis vraiment heureuse de l'opportunité que j'ai eu de vous connaitre et de la possibilité d'avoir pu participer à des réunions si motivantes et intéressantes. Merci donc au Pr Marius Réglier, pour ses leçons au tableau qui m'ont à chaque fois motivée ; au Dr Catherine Belle pour toutes nos réunions téléphoniques; au Dr Jalila Simaan pour l'efficacité de ses programmes de travail ; au Dr Hélène Jamet pour tous les calculs et ses explications sur le vaste monde de la chimie théorique ; au Dr Aurore Thibon pour avoir partagé le travail délirant sur le complexe ATP144. Merci également au Dr Bruno Faure, au Dr Amélie Kochem, au Dr Marianthi Kafentzi et à James pour leur sympathie, collaboration et soutien … et à tous ceux qui ont été présents plus ou moins longtemps. Merci à vous tous pour avoir partagé des bons moments de science et de divertissement.

Je voudrais également remercier toutes les personnes du laboratoire UMR CNRS 6521. Avec vos sourires et vos « Bonjour, ça va ? », vous avez contribué à rendre mes journées meilleures. Je voudrais remercier le Pr Philippe Schollhammer, directeur de l'UMR, le Pr Paul-Alain Jaffrès, directeur du Département de Chimie grâce à qui j'ai pu effectuer ma mission d'enseignement, et tous les collègues enseignants pour leurs précieux conseils. Merci à Nelly Kervarec du service commun RMN-RPE pour sa disponibilité et sa bonne humeur, et

à Claude Calvarin, souffleur de verre, pour les fabuleux montages qu'il a réalisés. Merci aux secrétaires Maryline et Isabelle, toujours présentes pour m'aider dans les démarches administratives.

Merci aussi aux doctorants du laboratoire UMR CNRS 6521. En particulier Dany pour avoir partagé avec moi les responsabilités du deuxième étage. Merci Salma, Clé, Andrea pour votre sympathie, votre amitié et nos fous rires quand on se croisait dans les couloirs. A Massi, un remerciement particulier, pour ta bonne humeur, pour ton encouragement jusqu'à la fin parce que « It's not over until I win ».

Grâce à une bourse de financement de mobilité sortante proposée par l'Ecole Doctorale, j'ai eu la possibilité, durant ma thèse, d'effectuer un stage de recherche de trois mois au Canada. A cet égard, je voudrais remercier Dr. Xavier Ottenwaelder, professeur associé à l'Université Concordia (Montréal) pour m'avoir accueillie dans son laboratoire.

Si ces trois années se sont aussi bien passées c'est aussi grâce aux personnes que j'ai rencontrées en dehors du laboratoire et avec lesquelles j'ai partagé le quotidien et des amitiés sincères. Merci à vous, toutes et tous, camarades de la cité universitaire. Merci à ma chère amie Francesca, qui m'a encouragé et soutenue chaque fois ; grâce à nos appels et messages, l'Italie me paraissait moins loin….

Grazie agli amici e familiari che mi accolgono a braccia aperte al mio rientro in Italia. Grazie alla mia famiglia, perché é sempre presente nonostante io sia sempre più lontana, ma in particolar modo, grazie a mia sorella, per la complicità che ci rende l'una per l'altra.

Grazie a tutti, merci à tous, thank you all.

Federica

Abbreviations

ABNO	9-Azabicyclo[3.3.1]nonane N-Oxyl	ET	electron transfer
AcOH	acideacétique	Et_2O	diethyl ether
Asp	aspartic acid	EtOAc	ethyl acetate
BDE	bond dissociation energy	EXAFS	spectroscopy extended x-ray absorption fine structure
BESs	bioelectrochemical systems	Fc	ferrocene
BPEP	bis(2-pyridylethyl)amine	Fc^+	ferrocenium
bpman	2,7-bis(di-2-pyridylmethyl)amine-1,8-naphthyridine	glu	glutamate
BPMEP	bis(2-pyridylmethylethyl)amine	GO	galactose oxidase
BPMP	bis(2-pyridylmethyl)amine	HAT	hydrogen atom transfer
bpnp	2,7-bis(di-2pyridyl)-1,8-naphthyridine	Hc	hemocyanin
$BuNH_2$	butylamine	His	histidine
CA	chronoamperometry	LMCT	ligand metal charge transfer
CF_3	trifluoromethyl	MeCN	acetonitrile
CF_3Cl	chlorotrifluoromethane	met	methionine
CO	cathecol oxidase	MPA	3-mercaptopropionic acid
CuA	cytochrome c oxidase	NBu_4Cl	tetramethylammonium chloride
CuB	cytochrome c oxidase	NBu_4PF_6	tetrabutylammonium hexafluorophosphate
Cu-MOR	copper-exchanged zeolites	NHE	normal hydrogen electrode
CuZ	nitrous-oxide reductase	$NOBF_4$	nitrosonium tetrafluoroborate
CV	cyclic voltammetry	*np*	1,8-naphthyridine
CYP	cytochrome	OTf	o-triflate
D	diffusion coefficient	PC	propylene carbonate
DCM	dichloromethane	PCET	proton couplee electron transfer
DFT	density functional theory	PHM	peptidyl α-hydroxylating mono oxygenase
DHA	dihydroanthracene	pMMO	particulate Methane Mono Oxygenase
DNA	deoxyribonucleic acid	PPOs	phenoxidase
DPA	2,2'-dipicolylamine	PT	proton transfer
dpen	2,7-bis(di-2-pyridylethyl)-1,8-naphthyridine	RDEV	rotating disk electrode voltammetry
dpfn	2,7-bis(di-2-pyridylethyl)fluoromethyl)-1,8-naphthyridine	ROS	reactive oxygen species
DßM	dopamine ß-hydroxylase	sMMO	soluble Methane Mono Oxygenase
$E_{1/2}$	half-wave potential	LPMO	lytic polysaccharide mono oxygenase
E_{pa}	anodic peak potential	SOD	superoxide dismutase
E_{pc}	cathodic peak potential	TD-DFT	time dependent - density functional theory
$E^{0'}$	standard potential	THF	tetrahydrofuran
EPR	electron paramagnetic resonance	TLCV	thin layer cyclic voltammetry
TON	turnover number	$t_{1/2}$	half-life
Ty	tyrosinase	τ	Addison parameter

Summary

Chapter III

Dicopper complex with a naphthyridyne spacer

Chapter IV

Bisamide dicopper complexes with alkoxo or phenoxo spacers

CONCLUSION

APPENDIX

Résumé français

Principaux résultats des travaux de thèse

Foreword

In the context of the energy crisis combined with green house effects, the look for new energy sources, environmentally friendly, is one of the most important challenges currently in research. Methane (CH_4), the primary component in natural gas, is one of the major energy sources on Earth. Moreover methane is also a greenhouse gas that remains in the atmosphere for approximately 9-15 years. It is over 20 times more effective in greenhouse effect than carbon dioxide over a 100-year period. Hence an important objective for chemists, in terms of sustainable development, is the transformation of methane into a liquid form such as methanol, concurrently, to reduce its greenhouse gas effect and to increase its potential as a petroleum alternative for fuels and in the petrochemical industry. Currently, industrial methanol production is accomplished by steam reforming of methane, which requires high temperatures and pressures. Therefore, alternative processes such as the selective direct oxidation of methane to methanol are of considerable interest. However, methane has the strongest C-H bond of any hydrocarbon (104 kcal/mol), thus its selective oxidation to methanol without further oxidation is extremely challenging.

In Nature, methane monooxygenases (MMOs) accomplish the direct conversion of methane into methanol at ambient temperature and atmospheric pressure allowing the harnessing of methane as an energy source and for the synthesis of the life required molecules.

Among the family of MMOs, the particulate Methane Monooxygenase (pMMO) is a dicopper enzyme: its active site has been the subject of a controversy about the metal content and structure of the active site for catalytic oxidation. The most recent results propose a dinuclear copper center, which reacts with dioxygen to produce a Cu_2/O_2 as active species in methane oxidation such as (μ-η^2:η^2-peroxo)$Cu^{II}Cu^{II}$ or bis(μ-oxo)$Cu^{III}Cu^{III}$. However, DFT calculations suggest that a 1-electron reduced mixed-valent bis(μ-oxo)$Cu^{III}Cu^{II}$ species has greater oxidizing power to cleave the methane C-H bond rather than either the symmetric (μ-η^2:η^2-peroxo)$Cu^{II}Cu^{II}$ or bis(μ-oxo)$Cu^{III}Cu^{III}$.

Our group has been developing the electrochemical and spectroscopic studies of biomimetic copper complexes. Our objectives are to develop new insights into the knowledge of the redox processes of the copper centers associated with O_2 activation and catalytic reactions for organic substrates.

The objective of this thesis is the synthesis and characterization of new dicopper complexes able to model the active site of pMMO. More specifically our quest is the design of new ligands able to generate mixed valent $Cu^{III}Cu^{II}$ species as model the putative mixed valent $Cu_2^{III,II}O_2$ key intermediate in the pMMO catalytic cycle. The strategy consists in associating two coordinating biomimetic scaffolds in a short distance, close to that observed in the enzyme, by a rigid linker so as to control the coordination and tune the redox potential.

In **Chapter I**, a bibliographic survey about the function and active site of copper enzymes is proposed. It is specifically focused on pMMO, Catechol Oxidase, Tyrosinase and Galactose Oxidase. We also pay some attention on biomimetic models and to the intermediates species in the catalytic cycles. Recent results prove that the mixed valent bis(μ-oxo)$Cu_2^{III,II}$ or (μ-OH, μ-O)$Cu_2^{III,II}$ could be essential for the strong C-H bond activation. The design of the most advantageous scaffold of ligand to achieve this target is discussed.

Chapter II describes a series of complexes in which two DPA (dipyridylamine) coordinating scaffolds are linked by a phenoxo bridge. Symmetrical and unsymmetrical complexes are investigated. The oxidation pattern of the [(μ-O)-(μ-OH)] complexes is closely analyzed by electrochemistry, spectroscopy and spectroelectrochemistry. The localization of the redox site is discussed on the basis of TD-DFT calculations.

In **Chapter III**, the very short, rigid and redox-innocent naphthyridine spacer, associates two bis-pyridyne Cu sites, bridged through a bis(μ-OH) mode. In conjunction with classical techniques, low temperature spectroelectrochemical measurements have been carried out to analyze the formation of a mixed valent bis(μ-hydroxo)$Cu_2^{III,II}$ species. Its electronic structure is discussed on theoretical basis, as well as the relationship between structure and redox potential.

Chapter IV focuses the attention on a bisamide scaffold capable to lower the oxidation potential of the copper site. A bis-amide alkoxo linked complex and unsymmetrical DPA-amide phenoxo bridged complexes have been synthesized and characterized. In addition to our common electrochemical and spectroscopic techniques, cryo-spectroelectromichal measurements are carried to analyze the oxidation reactions.

Chapter I

Copper-oxygen adducts

in enzymes and biomimetic complexes

I. General aspects of copper enzymes and copper-oxygen adducts

Copper proteins are involved in numerous processes that impact life and environment.[1] In 1816 Meissner and Bucholz isolated for the first time copper in plants,[2],[3],[4] but the first evidence for an essential need of copper for living systems was obtained by McHargue in 1925.[5] This author showed that copper has an important function in the formation of hemoglobin and in the metabolism of animals having red blood. Since, many studies have emphasized the ubiquitous role of copper in biological events such as energy metabolism (cytochrome *c* oxidase), production of melanin pigment (tyrosinase) or catecholamine. Copper is also involved in inflammation processes linked to cancer, atherosclerosis and oxidative damage (superoxide dismutase). In plants, it is present in plastocyanin which performs electron transport for photosynthesis, in ceruloplasmin (for the iron and copper metabolism) or in more specialized enzymes like tryptophan oxygenase (to regulate the tryptophan metabolism), ascorbate oxidase (to produce dehydroascorbate and H_2O) and laccase (that it takes part in the formation of lignin).[6]

Active sites of copper proteins can be mainly classified in three types (I, II, III), according to their nuclearity and chemical composition (Table I.1).[6],[7] This classification was made originally on the basis of structural and spectroscopic properties, but also reflects a differentiation in functionality. Hence, type I copper proteins, such as azurin, are involved in electron transfer processes. Their particular structure makes them suitable for performing efficient electronic transfer with low reorganizational energy for a wide range of redox potentials (200 to 1000 mV vs NHE). Type II copper proteins display oxygenase and oxidase functionalities, at a single Cu site, with the help of a co-factor (tyrosyl radical for galactose oxidase) or a second electron reservoir [Cu center at 11 Å distance for Dopamine β-Monooxygenase (DβM) and Peptidyl α-hydroxylating monooxygenase (PHM) for example]. Type III copper proteins use dicopper centers to achieve catalytic oxidation of biomolecules (tyrosine for formation of melanin and pigments in tyrosinase), or dioxygen transport (hemocyanin). In these enzymes, the two copper centers are antiferromagnetically coupled. Other supplementary types of copper enzymes have been reported in the literature such as CuA (cytochrome *c* oxidase and nitrous-oxide reductase), CuB (cytochrome *c* oxidase), CuZ (nitrous-oxide reductase), Type 0 or Red copper proteins, obtained by mutation of amino-acid residues.[6] More generally, the rich chemistry of copper (Cu^I, Cu^{II}, Cu^{III} oxidation states) confers a broad range of activities allowing to act through one- or multiple electrons processes. Hence, copper is involved in electron transfer (ET) reactions, O_2 binding, activation and reduction, as well as NO_2^- and N_2O reduction.[7]

Table I.1. Classification and functionality of copper proteins with selected examples.

Type I	
Azurin	Electron transfer
Plastocyanin	Electron transfer
Stellacyanin	Electron transfer
Type II	
Amine oxidase	Primary amines oxidation
Galactose oxidase	Galactose oxidation
Glyoxal oxidase	Aldehyde oxidation
Cytochrome c oxidase	4 e- reduction of O_2 into H_2O
Dopamine β-monooxygenase (DβM)	Dopamine hydroxylation
Peptidyl α-hydroxylating monooxygenase (PHM)	Neuropeptide hydroxylation
Type III	
Hemocyanin (Hc)	O_2 dioxygen
Tyrosinase (Ty)	Tyrosine hydroxylation and catechol oxidation
Catechol oxidase (CO)	Catechol oxidation

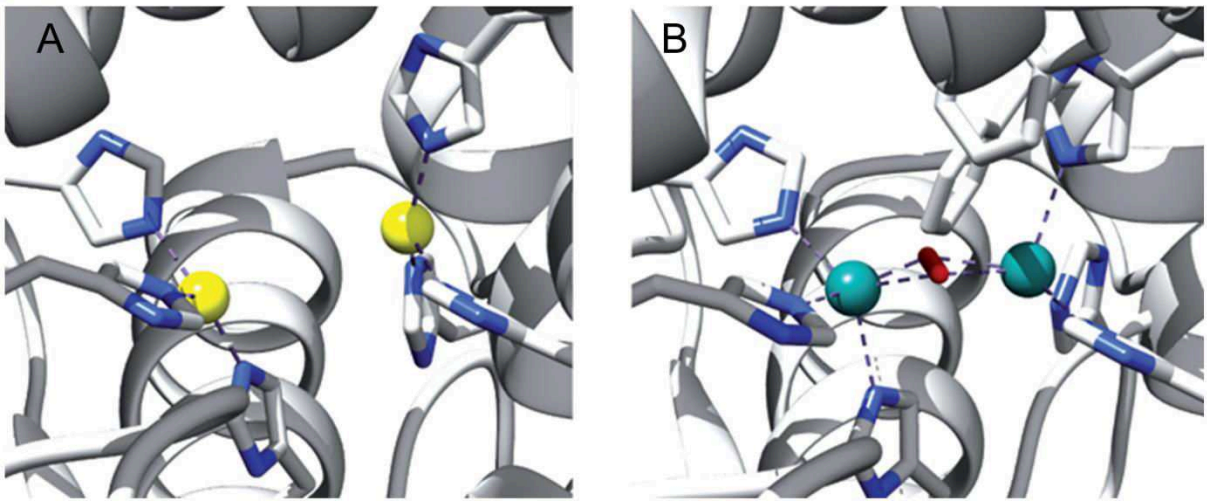

Figure I.1. View of the active site of the hemocyanin (Hc) of the Atlantic horseshoe crab, *Limulus polyphemus*, determined by X-ray diffraction. A) Deoxy-Hc at 2.2 Å resolution (PDB ID: 1LLA), B) Oxy-Hc at 2.4 Å resolution (PDB ID: 1OXY). Reproduced from Ref. [8].

Most of copper enzymes are involved in reactions that activate O_2 for its incorporation into biomolecules (oxygenase activity) and/or its reduction into water (oxidase activity). The role of these catalysts is essential since molecular oxygen is not a good oxidant (kinetically speaking) for organic substrates, because of its triplet configuration. The activation of dioxygen by active sites of copper enzymes occurs by reaction of O_2 with one or several Cu^I centers, leading to the formation of transient

superoxide, peroxide and related oxidizing species.[7] Copper enzymes which can activate O_2 can be classified into dioxygenase, monooxygenase or oxidase families. Oxygenases, which belong to the class of oxidoreductases, can transfer an oxygen atom from molecular oxygen to a substrate. This family includes: i) monoxygenases, also known as mixed function oxidases, that transfer one oxygen atom to the substrate, while the other is reduced to water, and ii) dioxygenases, or oxygen transferases, that incorporate both oxygen atoms of dioxygen into the initial substrate to obtain the product.

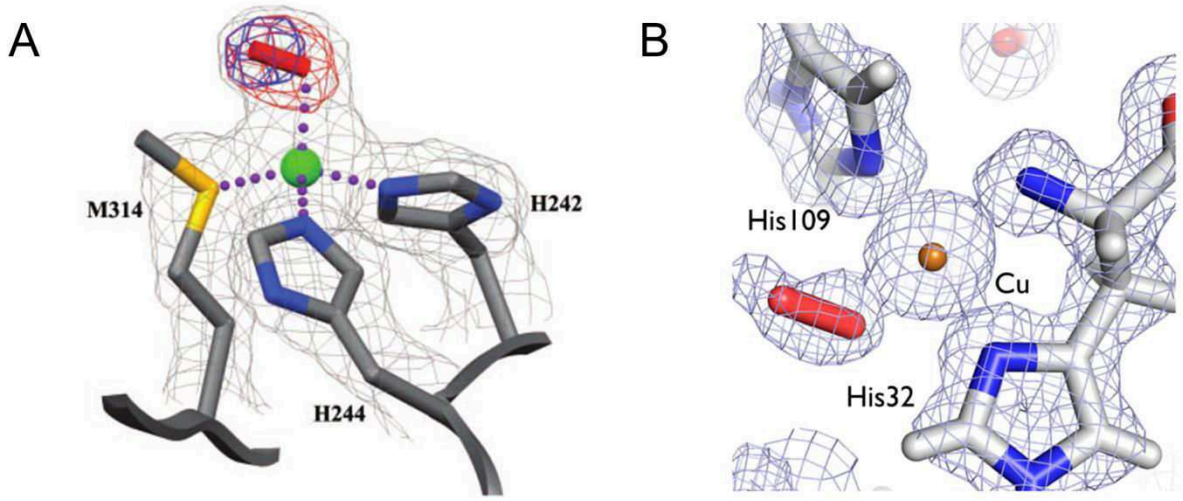

Figure I.2. View of the active site of A) oxy-PHM and B) oxy-LPMO. Reproduced from Refs. [9] and [10], respectively.

In the last three decades, bioinorganic chemists and biologists have focused their efforts on the identification of reactive intermediates involved in copper-based oxidation reactions. Hemocyanin, as oxygen carrier in arthropodal and molluscan hemolymph, was one of the first copper enzymes to be investigated. X-ray structure of the active site oxyhemocyanin could be resolved in 1994 by Magnus *et al.*.[11],[12] It displayed a side-on (μ-η^2:η^2-peroxo)dicopper(II) core (Figure I.1), as previously anticipated by Kitajima and co-workers with a sterically hindered hydrotris(pyrazolyl)borate synthetic model.[13] Since, few other structures of copper-oxygen adducts in enzymes have been resolved: an end-on superoxo CuO_2 moiety in PHM[9] (Figure I.2A), a reduced O_2-derived species bound to Cu in Lytic Polysaccharide MonoOxygenase (LPMO)[10] (Figure I.2B), and side-on peroxo species in oxygenated binuclear copper proteins (e.g., hemocyanin[11], tyrosinase,[14] and phenoloxidase[15]). More information about structural and spectroscopic features of metal-oxygen centers has been obtained from synthetic models of enzymatic active sites (Figure I.3).[16],[17],[18] Numerous solid-state structures of superoxo, peroxo and hydroxoperoxo have been reported for a wide range or N-ligands mononuclear and dinuclear complexes. Fast-time acquisition UV-Vis and Raman spectroscopies have been complementary used at low temperatures to discriminate between the different possible adducts

(Figure I.3). So far, the combination of these two techniques has probably become sufficient nowadays to guess the hypothetical structure on the basis of the large amount of data reported.[18]

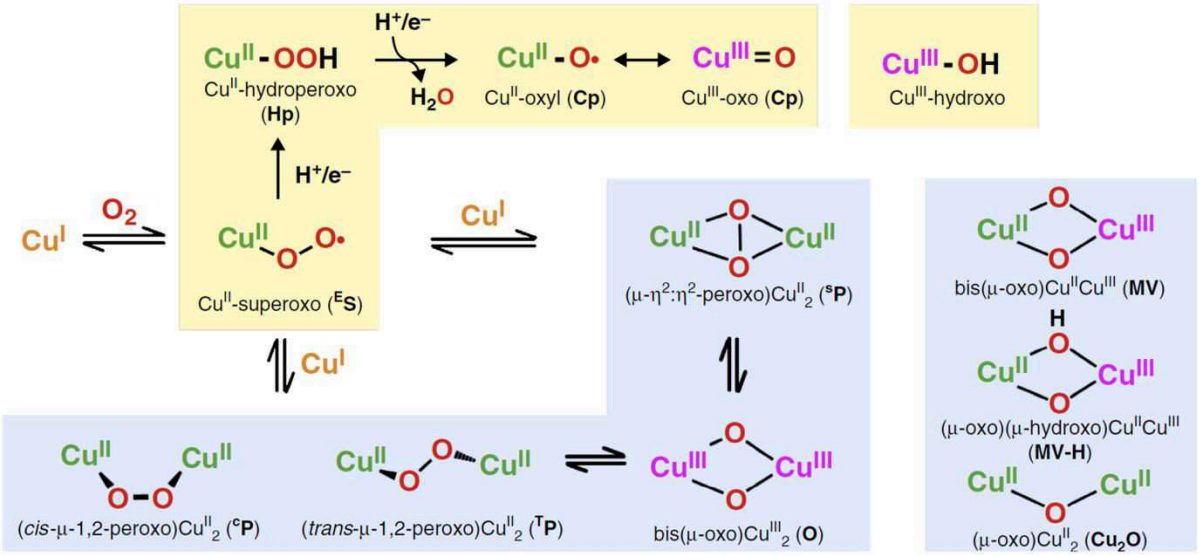

Figure I.3. Copper-oxygen adducts in copper enzymes and their models. Reproduced from Ref. [19].

Aside from the fundamental importance of elucidating the mechanisms at work in copper enzymes, research on copper-oxygen adducts has been motivated by the development of devices which integrate the specific properties of the enzymes, hence are bio-inspired. In particular, activation of dioxygen is of high interest in different research area (energy, synthetic chemistry, environmental chemistry…). Amongst them, one major challenge is the development of efficient devices which can perform catalytic oxidation of C-H bond under atmospheric pressure and at room temperature using dioxygen as O-source. Oxidation of methane into products of interests, such as methanol, by this approach is one of the most targeted objectives. Methane, which is emitted from a variety of natural and human influenced sources, is a greenhouse gas that remains in the atmosphere for approximately 9-15 years. It is over 20 times more effective in greenhouse effect than carbon dioxide over a 100 year period. On the other hand, methane is also a primary constituent of natural gas and an important energy source. To reduce its greenhouse gas effect and to increase its potential as a petroleum alternative for fuels and in the petrochemical industry, its transformation into a liquid form such as methanol is of current interest in chemistry. Currently, industrial methanol production from methane is accomplished by steam reforming of methane into a mixture of H_2 and CO, followed by methanol synthesis. These processes require high temperatures and pressures and alternatives such as the selective direct oxidation of methane into methanol are of considerable interest. However, methane has the strongest C-H bond of any hydrocarbon (104 kcal/mol), thus its selective oxidation to methanol without further oxidation is extremely challenging. It could indeed minimize losses in natural gas usage and produce feedstocks for fuels with little loss in transport from a storage site. Recently, the

catalytic efficiency of copper-based particulate methane monooxygenases (pMMO) for the *in vivo* oxidation of methane was investigated by Rosenzweig and co-workers.[20] Results showed a rather low turnover (2.5 s^{-1}), that could be overcome by highly expressing MMOs. One question raised concerned the cost of making such biosynthetic machinery as well as the remained activity of the biocatalysts for long periods of time under growth limiting conditions. As stated by the authors, the development of more efficient mutants of methane-oxidizing organisms would also require more convenient methods.

Another challenging reaction in synthetic chemistry is the oxidation of alcohol into ketones and aldehydes by using molecular oxygen and alcohol oxidases.[21] This reaction is of particular importance because it allows the introduction of carbonyl groups, which can further react with C-, N-, O- and S-nucleophiles and allows the extension of a given carbon backbone. Alcohol oxidases commonly use a metal cofactor which mediates the electron transfer. This is the case of the galactose oxidase (GO), a type II Cu enzyme, which displays a single copper ion in the active site.

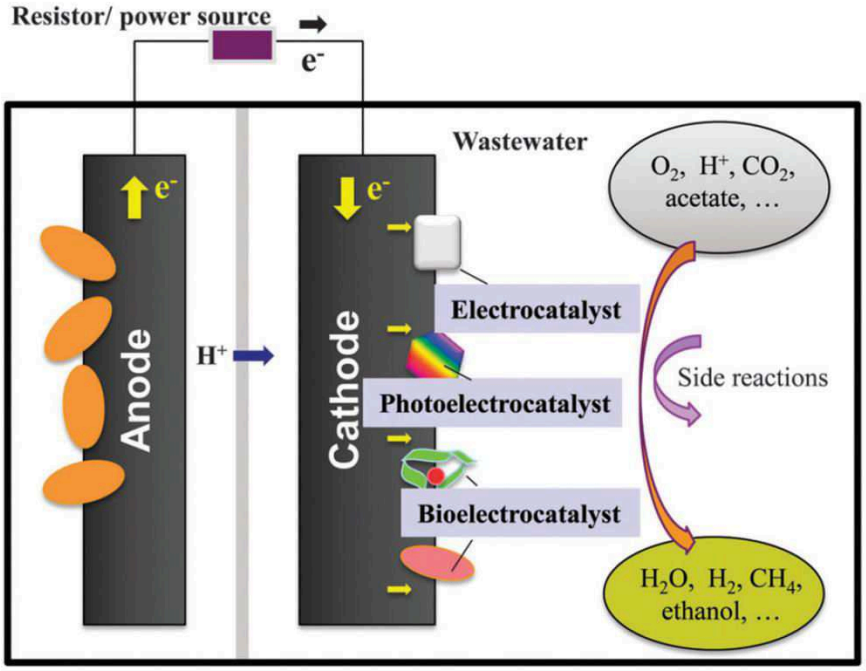

Figure I.4. Principle of a bioelectrochemical system (BES) using laccase for dioxygen reduction. Reproduced from Ref. [22].

Copper-enzymes properties have also been well exploited in environmental science. For example, Tyrosinase, a type III copper enzyme which performs the aerobic oxidation of o-monophenols into o-diphenols then o-quinones, has been employed as a biotechnological device for the detection / decomposition of phenols in containing wastewaters and contaminated soils.[23],[24] It has also been used in the detection of other molecules of interest such as dopamine or bisphenols A.[25],[26] The attachment of tyrosinase was performed on several support materials (biopolymer, carbon

nanotubes) to avoid a loss of catalytic properties.[26],[27] More generally, numerous bioelectrochemical devices based on copper enzymes have been developed during the last twenty years. An emerging domain concerns bioelectrochemical systems (BESs), for wastewater treatment or even for net energy generation.[22] For these devices (Figure I.4), microorganisms are used as catalysts at the anode of an electrochemical cell to directly extract electrical energy from organic matter by an oxidation process. The cathode process involves an electrocatalyst which mediates the reduction of dioxygen or other substrates which are present in solution. One main challenge is to find efficient electrocatalytic systems at the cathode. Laccase, a tricopper-based enzyme, was shown to be a good candidate for oxygen reduction, because the redox potential of its active site (0.78 V vs. SHE at neutral pH) is very close to that of the O_2/H_2O redox couple (0.81 V). Indeed, the use of a laccase cathode in BESs generated one order of magnitude higher power density than a Pt cathode control.[22]

Another research interest has been found with Cu,Zn superoxide-dismutase (SOD) enzymes, which can be used in biomedical application as bioelectrochemical sensors to quantitatively perform *in-vitro* measurements of superoxide ions in biologic fluids.[6] Cu,Zn superoxide dismutase plays an important role in cell protection mechanisms against oxidative damage from reactive oxygen species (ROS) by specifically catalyzing the disproportionation of $O_2^{\bullet-}$ to O_2 and H_2O_2. The practical determination of its concentration is of interest since an increase of activity in superoxide has been found to occur in response to traumatic brain injury, ischemia, reperfusion and hypoxia. $O_2^{\bullet-}$ is also involved progressive neurodegenerative diseases, such as Parkinson's disease. Several generations of Cu,Zn SOD biosensors have been developed, depending on the direct (superoxide) or indirect (resulting H_2O_2) type of substrate which is detected.[28] For example, direct electron transfer of bovine erythrocyte copper-zinc superoxide dismutase could be efficiently promoted by a self-assembled monolayer (SAM) of 3-mercaptopropionic acid (MPA) confined on a gold electrode (Figure I.5).[29] The SOD-based device displayed sensing properties in both anodic and cathodic polarizations. Other reported sensors have been developed, by varying the nature of the electrode material (Pt, Au and carbon fiber) and the immobilization techniques, such as entrapment within a membrane, cross-linking, covalent bonding and physical adsorption.[28],[30] One current challenge is to found optimal conditions for a selective detection of the superoxide ion against H_2O_2 and other biomolecules (ascorbic acid and uric acid). Recent works have shown the possibility to increase the sensitivity of the device towards superoxide ions by using porous Pt–Pd nanomaterials which increase the surface area and the number of active sites, and fasten the electron transfer.[31] So far, few reports exist for measuring $O_2^{\bullet-}$ levels *in-vivo* in freely-moving animals because of its low concentration, fleeting existence and high reactivity in the *in-vivo* environment.

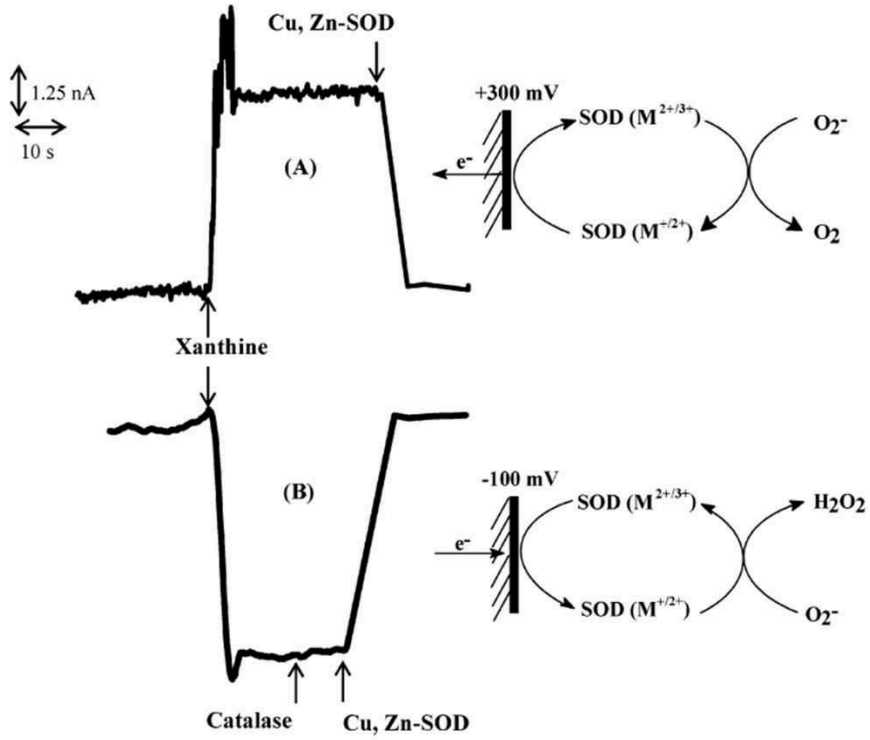

Figure I.5. Example of a direct sensing of the superoxide ion by a bipolarizable Cu,Zn-SOD electrochemical sensor. Reproduced from Ref. [29].

In conclusion, this short survey demonstrates that the specific properties of copper-enzymes, and particularly copper-oxygen adducts, can be exploited to develop efficient devices in many different domains ranging from energy to medical science. Alternatively, these properties can be reproduced in part in bio-inspired synthetic systems. Many biomimetic devices have been indeed developed from known mechanisms / key intermediates and resolved structures of active sites of enzymes. For all these reasons, understanding the formation, chemical-physical properties and reactivity of diverse biochemical or synthetic copper-oxygen adducts keeps being a field of great interest. In particular, if we can learn the manner in which biological system efficiently activate C-H bond oxidation under mild conditions, we have the potential to aid efforts to relieve our energy concerns by developing copper catalysts which can oxidatively activate strong C-H bonds, such as in methane.

In the following sections, we have focused on three specific copper-enzymes: the particulate methane monooxygenase (pMMO), the galactose-oxidase (GO) and the tyrosinase/catechol oxidase (Ty/CO). A short description of the recent advances on their structural and spectroscopic properties is provided, as well as their functionalities. This description is followed by recent investigations on their synthetic models (structure/reactivity).

II. O_2 activation in pMMO, CO/Ty and GO enzymes

II.1. The particulate Methane Monoxygenase

The particulate methane monooxygenase (pMMO) is a protein present in methanotrophic bacteria that catalyze the hydroxylation of methane. While iron-based soluble methane monoxygenase (sMMO) is present in cytoplasm of bacteria cells, copper-based pMMO can be found in membrane of bacteria cells. The structure and mechanism of these two enzymes are different although both of them catalyze the same reaction. Compared to sMMO, the knowledge on pMMO is less extensive. Its metal sites were only recently unveiled by the resolution of several crystal structures: pMMO from *Methylococcus capsulatus* (Bath),[32] from *Methylosinus trichosporium* OB3b,[33] and from *Methylocystis species* strain M.[34] The pMMO is a trimeric protein and each monomer is composed of three polypeptide subunits, α (pmoB) ~47 kDa, β (pmoA) ~24 kDa and γ (pmoC) ~22 kDa, in a $\alpha_3\beta_3\gamma_3$ polypeptide arrangement (Figure I.6). The trimer is ~105 Å in length and ~90 Å in diameter with a large hole at its center. The pmoB subunits form the soluble region, which consists of six β-barrels, two from each protomer, and extends ~45 Å from the membrane region (Figure I.6).

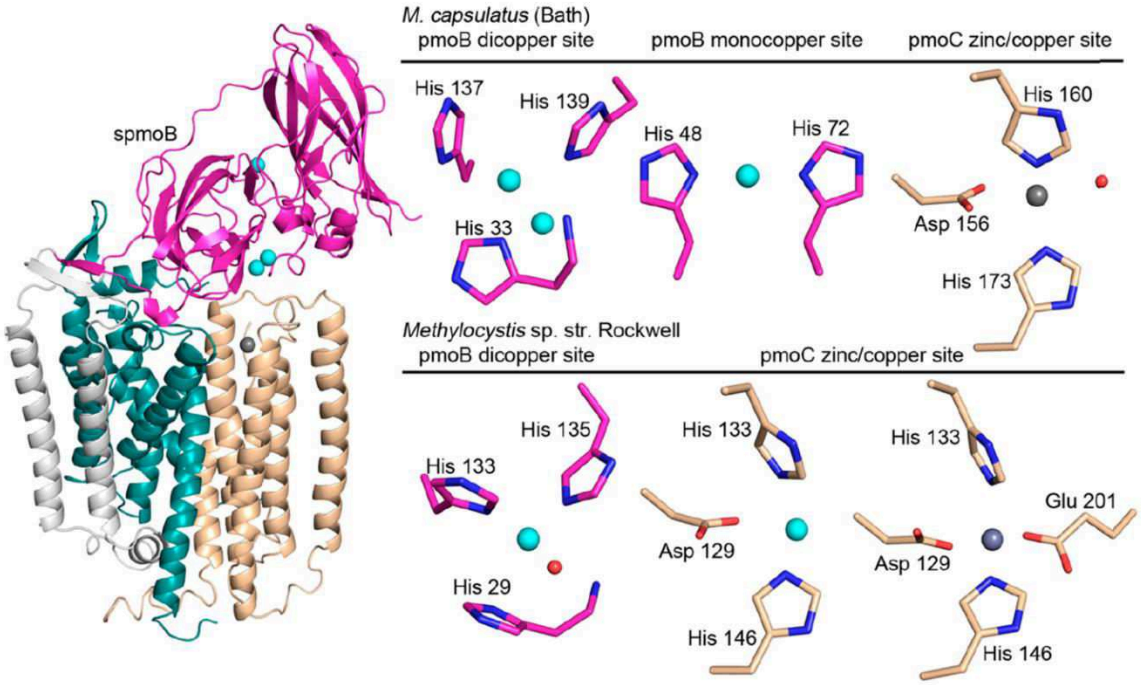

Figure I.6. pMMO crystal structures containing three polypeptide subunits (pmoB (magenta), pmoA (cyan), pmoC (brown)) and two transmembrane helices (gray). Dicopper, monocopper, and zinc/copper sites are shown as cyan and gray sphere. The *M. capsulatus* (Bath) pMMO structure contains dicopper, monocopper, and zinc sites (top right, PDB 3RGB). In the *Methylocystis sp.* strain Rockwell pMMO structure (bottom right), the dicopper site is modeled with a single copper ion and a solvent molecule, and the zinc/copper site is occupied by copper (PDB 4PHZ). Solvent ligands are shown as red spheres. Reproduced from Ref. [35].

The pmoA and pmoC subunits comprise the majority of the membrane region. Hydrophilic residues line the inside of the hole in the soluble region while hydrophobic residues line the hole in the membrane region. A single subunit of pmoB consists of two anti-parallel β-barrels (one seven stranded, the other eight) located at both the N-terminus and C-terminus. These β-barrels are roughly perpendicular to one another and are separated by a β-hairpin and two transmembrane helices. The pmoB was found to contain two distinct metal sites: one mononuclear copper center and one binuclear copper site as shown in Figure I.6 (top right) for *M. capsulatus* (Bath). Note that in the *Methylocystis sp*. structure (Figure I.6, bottom right), the dicopper site is modeled with a single copper ion and a solvent molecule, and is suggested to be due to the increased lability of copper.

The mononuclear copper center in *M. capsulatus* (Bath) is located ~25 Å above the membrane near the N-terminal β-barrel surface and is coordinated via δ-N atoms of His 48 and His 72 in a close to linear fashion (Figure I.6). Another residue, Gln 404, is within 3 Å of copper. This site is not conserved in pMMO from *M. trichosporium* OB3b.

The binuclear copper center in pmoB in *M. capsulatus* (Bath) is found ~10 Å from the lipid bilayer and is believed to be the active site for methane oxidation. The dicopper core is coordinated to His 33, His 137 and His 139 (Figure I.6). The Cu-Cu distance was refined to ~2.6 Å. The pmoC contains the third metal binding site in the crystal structure. This site, ~19 Å from the binuclear copper site, contains zinc. The Zn^{II} coordination environment is represented by a distorted tetrahedron made up by the conserved residues Asp 156, His 160, and His 173 from pmoC and Glu 195 from pmoA (Figure I.6).[36]

The particulate enzyme has been the subject of a controversy about the metal content and the structure of its active site.[7] The most recent results published by A. Rosenzweig and co-workers suggest that the dinuclear copper center is the site of oxidation of methane into methanol.[35] X-ray crystallography and spectroscopic (XAS) experiments performed on variants obtained by site-directed mutagenesis suggest that the binuclear copper site is in a localized mixed-valence $Cu^{I}Cu^{II}$ state.[7] Reduction of the dicopper core into $Cu^{I}Cu^{I}$ would increase the Cu-Cu distance from 2.51 to 2.65 Å. Alternatively, Chan an co-workers have proposed that methane oxidation would occur at a trinuclear copper site[37],[38] (Figure I.7, left), although X-ray structures of pMMOs from *M. capsulatus* (Bath) and *M. trichosporium* OB3b do not reveal evidence for a tricopper cluster. According to these authors, the oxidation process would occur in an empty hydrophilic cavity which has been identified in the transmembrane domain of these protein structures and can be modeled with a tricopper cluster into this site.[37],[38],[39] These authors argue that spectroscopic evidence for the tricopper cluster in pMMO has been reported for pMMO-enriched membranes as well as the protein purified from these membranes under anaerobic conditions.

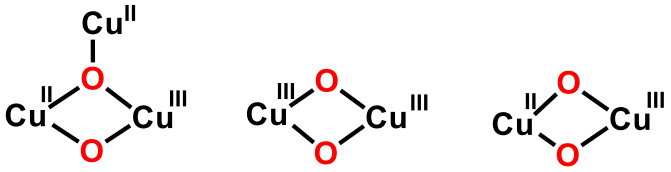

Figure I.7. Proposed copper-oxygen adducts for the catalytic oxidation of methane in pMMO by Chan and co-workers. Reproduced from Ref. [40].

The exact mechanism for this important reaction in pMMO still remains uncertain. Since no intermediates have been identified in pMMO to date, the current insight into the mechanism of pMMO has largely been derived from models, both experimental and computational. Several putative copper-oxygen intermediate species have been proposed for methane oxidation in pMMO: Cu-oxo, dicopper μ-oxo or peroxo, and trinuclear μ-oxo.[7],[40],[41] Chan and Chen have employed DFT calculations to compare the kinetics of the oxo-tranfer reaction to methane for three different copper-oxygen adducts: a trinuclear copper cluster bis(μ_3-oxo)trinuclear $Cu_3^{II,II,III}$ complex, (ii) a bis(μ-oxo) Cu_2^{III} complex, and (iii) a mixed-valence bis(μ-oxo)$Cu^{II}Cu^{III}$ complex (Figure I.7).[40] The results obtained indicate that the trinuclear copper cluster adduct displays the most facile pathway for methane hydroxylation amongst the three proposed systems.

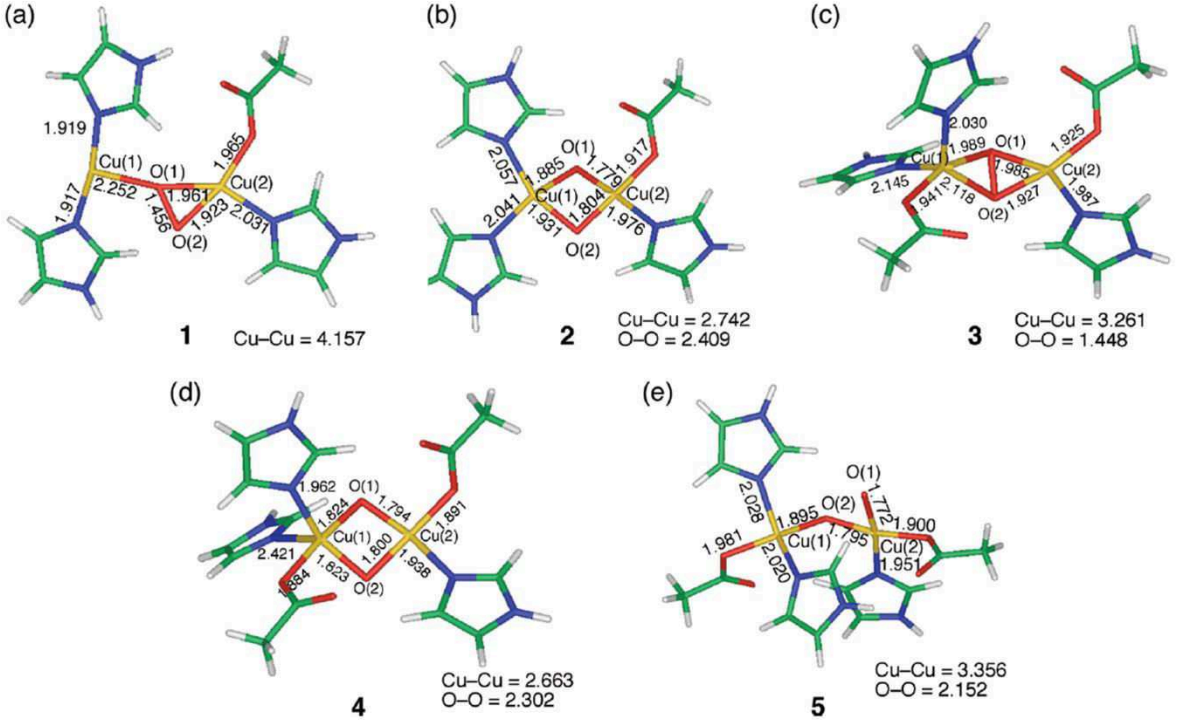

Figure I.8. Modeled structures of the active site of pMMo used by Yoshizawa *et al*: a) (μ-η^1:η^2-peroxo)Cu^ICu^{II} **1**; b) bis(μ-oxo)$Cu^{II}Cu^{III}$ **2**; c) (μ-η^2:η^2-peroxo)$Cu^{II}Cu^{II}$ **3**; d) bis(μ-oxo)$Cu^{III}Cu^{III}$ **4**; and e) (μ-oxo)$Cu^{III}Cu^{III}$ **5**. Reproduced from Ref. [41].

On the basis of X-ray experimental data which demonstrated the presence of a dinuclear site in pMMO, Yoshizawa and co-workers performed DFT calculations on the reactivity of the dicopper site towards methane.[41] The complexes considered are constituted of a dicopper core coordinated to imidazole units as a model of the histidine and to the acetate as a model of the Glu35 and Asp79 present in the active site of pMMO (Figure I.8). DFT calculations were focused on the mechanistic pathway and associated energetics for the conversion methane-methanol starting from (μ-η^1:η^2-peroxo)Cu^ICu^{II} **1** and (μ-η^2:η^2-peroxo)$Cu^{II}Cu^{II}$ **3** species, which are experimentally-evidenced copper-oxygen intermediates for pMMO. Calculations indicated clearly that peroxo species **1** and **3** have no ability to activate the C-H bond for the hydroxylation of methane. However, they can evolve towards specific copper-oxygen active adducts bis(μ-oxo)$Cu^{II}Cu^{III}$ **2**, a bis(μ-oxo)$Cu^{III}Cu^{III}$ **4** and (μ-oxo)$Cu^{III}Cu^{III}$ **5**). The energy diagrams in Figures I.9 and I.10 show the reaction pathway starting from **1** and **3**, respectively. Hence, the (μ-η^1:η^2-peroxo)Cu^ICu^{II} **1** can evolve towards a mixed-valent bis(μ-oxo)$Cu^{II}Cu^{III}$ species **2** (by O-O bond breaking), which can further forms a complex with methane (Figure I.9). The first transition state (**TS1**) is related to the important electronic process that leads to the C-H bond dissociation, resulting to the formation of the methyl intermediate. The second transition state **TS2** is connected to the formation of the C-O bond of methanol. This process requires a 24.3 kcal/mol activation energy, which is 8.2 kcal/mol above the **TS1** energy barrier (16.1 kcal/mol). This result shows that the rate-determining step is not the C-H bond dissociation step in the methane oxidation, but the C-O bond making. From the energy diagram using **3** as precursor (Figure I.10), the methane can be activated by copper-oxo complexes **4** and **5**. The activation energy for the reaction **3** to **4** or **5** is significantly high (14.1 kcal/mol and 21.0 kcal/mol respectively). Note also that energies of **4** and **5** are different, and consequently that the formation of **4** (vs **5**) is more energetically favored. As for the pathway starting from **1**, C-O bond making requires higher activation energy than C-H bond dissociation.

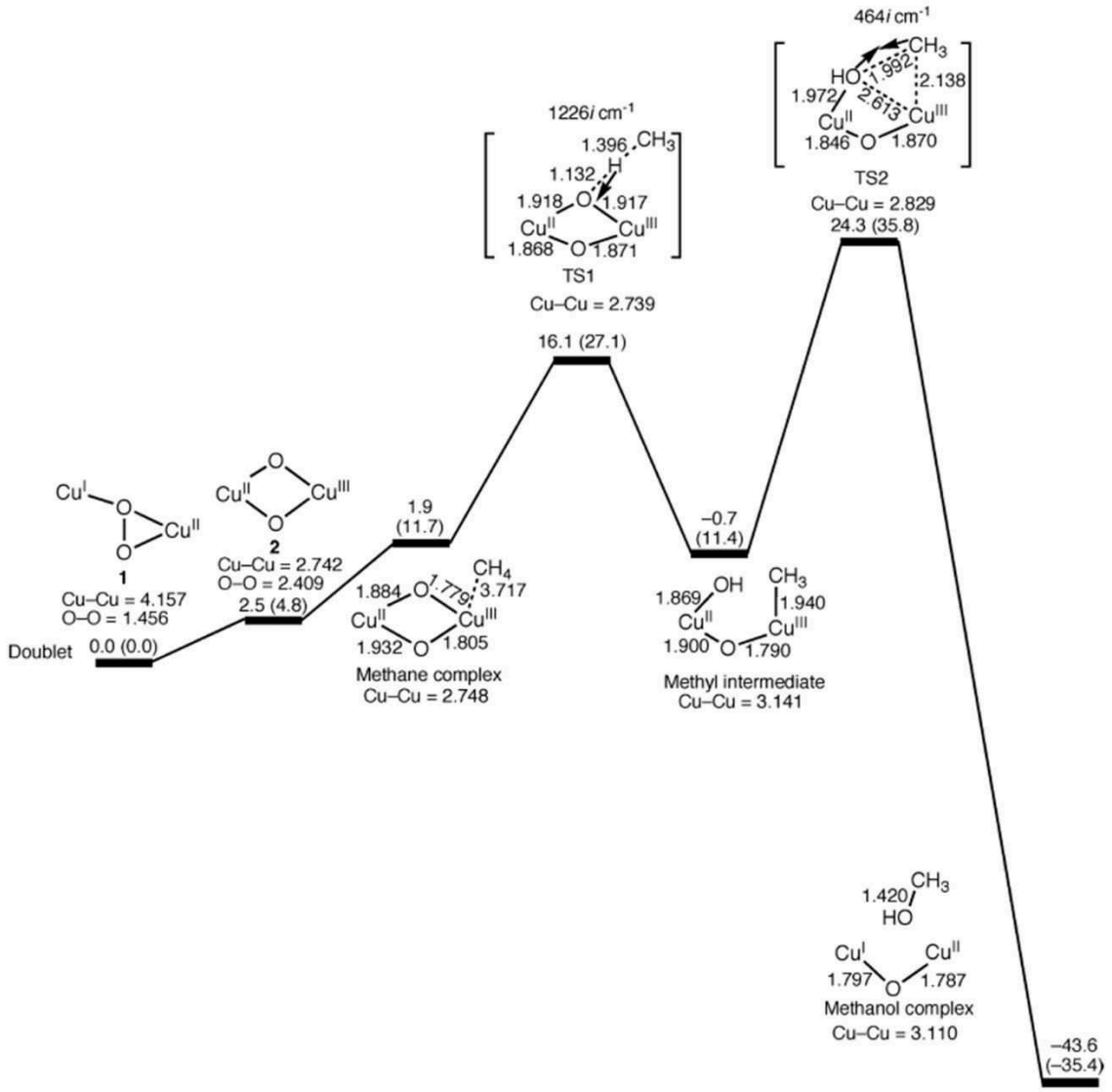

Figure I.9. Energy diagram for methane hydroxylation starting from **1**. Values in parentheses are Gibbs free energies. Units are in kcal/mol and Å. Reproduced from Ref. [41].

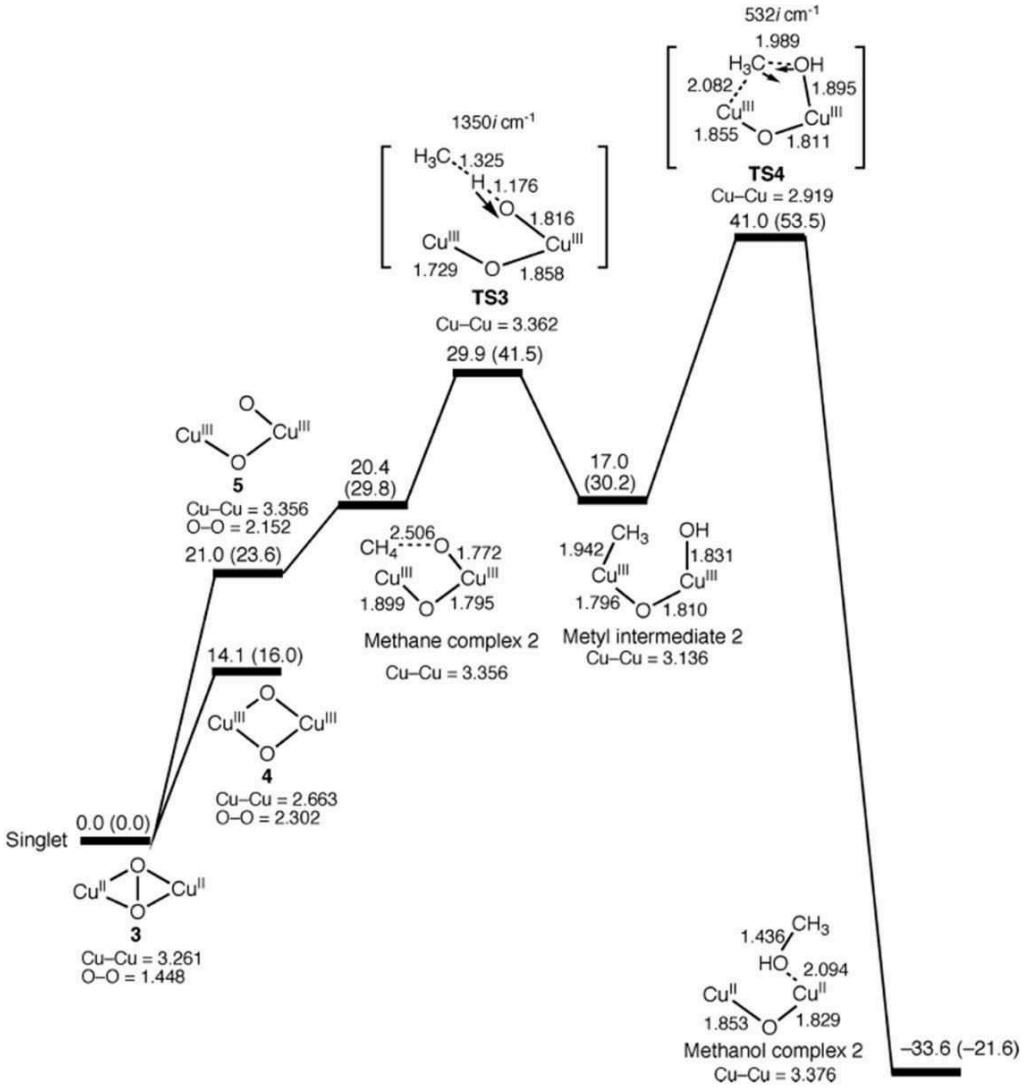

Figure I.10. Energy diagram for methane hydroxylation starting from **3**. The energies are corrected by zero-point vibrational energies and Gibbs free energies. Values in parentheses are Gibbs free energies. Units are in kcal/mol and Å. Reproduced from Ref. [41].

The comparison between the two pathways (starting from species **1** or **3)** seems to indicate that the mechanism presented in Figure I.9 is the most realistic. Indeed, the energy barrier to form the bis(μ-oxo)$Cu^{III}Cu^{III}$ species **4** from the (μ-η^2:η^2-peroxo)$Cu^{II}Cu^{II}$ **3** is relatively high, whereas the **1** to **2** transformation is kinetically more facile. Hence, the O-O bond breaking is unlikely to occur for **3** in comparison to **1**. Moreover, the activation barrier for the C-H bond dissociation is 16.1 kcal/ mol in the bis(μ-oxo)$Cu^{II}Cu^{III}$ **2** species, whereas neither the bis(μ-oxo)$Cu^{III}Cu^{III}$ species **4** nor the (μ-oxo)$Cu^{III}Cu^{III}$ **5** species is likely to mediate the C-H bond activation of methane.[41]

II.2. Tyrosinase and Catechol oxidase

Tyrosinase (Ty) and Catechol Oxidase (CO) enzymes are the members of the type III copper proteins commonly referred to as phenoloxidases (PPOs).[6] These enzymes display similar active sites in which two copper ions, Cu_A and Cu_B, are coordinated by six histidines and can reversibly bind dioxygen as peroxide in a side-on bridging coordination. Tyrosinase mediates the monooxygenation of tyrosine, a monophenol precursor of melanin and diverse neurotransmitters (monophenolase activity). Tyrosinase can also hydroxylate other monophenols than tyrosine. It also oxidizes the resulting o-diphenol into o-quinones (diphenolase activity). In contrast, catechol oxidase displays only a diphenolase activity, i.e. the dehydrogenetation of catechol to the corresponding *o*-quinones (Figure I.11).[42],[43] This functional discrimination between these two enzymes is still unclear.

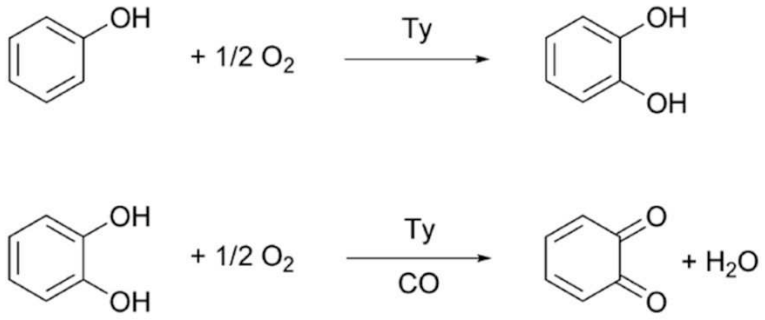

Figure I.11. Hydroxylation step (top) and subsequent oxidation (bottom) mediated by tyrosinase (Ty). The latter reaction is also catalyzed by the related enzyme catechol oxidase (CO). Reproduced from Ref. [43].

High-resolution crystal structures of PPOs (plant CO, bacterial Ty, fungal Ty, and insect Ty) display a central, globular domain that is mainly α-helical.[7] This domain contains a four-α-helix bundle. Structural characterizations of tyrosinase have shown a protein with two monomers glued together through extensive hydrophobic and charge-charge interactions. For each monomer two structural domains have been examined: the N-terminal and C-terminal sides are designed as copper-binding domain and the shielding domain. The core structure of four helix bundles of the copper-binding domain is highly conserved with the six histidine residues. The Cu-Cu distance (3.5 Å) suggests a met-form dinuclear copper (II) state. The Catechol Oxidase (CO) structure has been characterized from *Lycopus europaeus* (perennial plant in the *Lycopus* genus) and sweet potatoes. The only one monomer of 55×45×45 Å is primarily characterized by α-helical bundles. The catalytic core is composed of helices α2, α3, α6 and α7. The disulfide bridges (Cys 11-Cys 28 and Cys 27-Cys 89) anchor the loop rich N-terminal region of the protein to helix α2. Each copper of the two sites is coordinated by three histidine residues.[44]

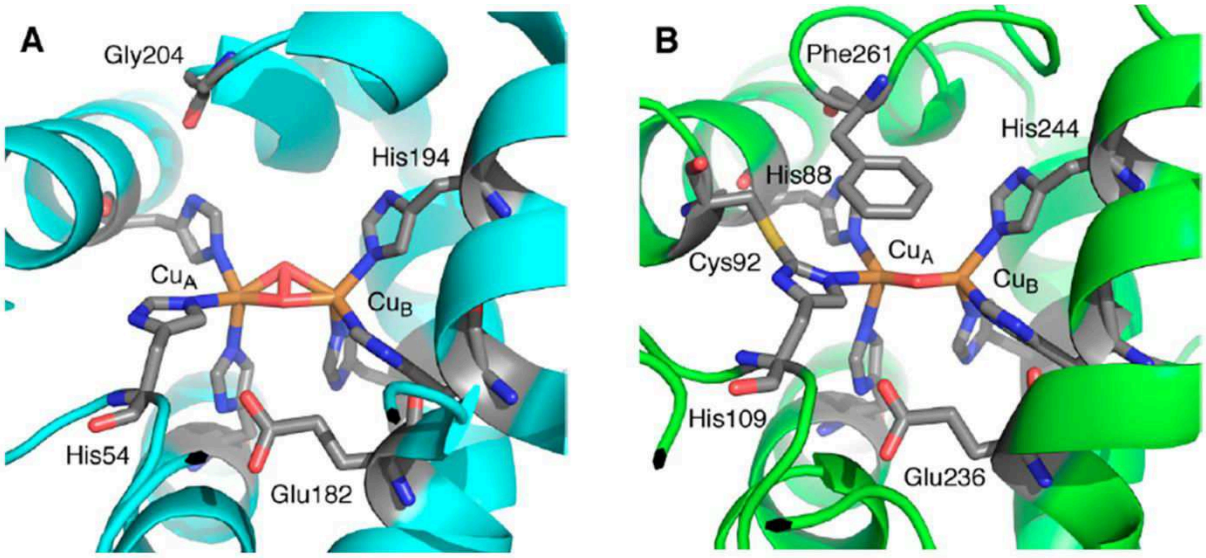

Figure I.12. Active site of oxy-tyrosinase (A) from the bacteria *S.castaneoglobisporus* and a structure of met-catechol oxidase from *I.batatas* (B). Reproduced from Ref. [7].

Crystal structures of deoxy (Cu^ICu^I), oxy ($Cu^{II}(O_2^{2-})Cu^{II}$) and met ($Cu^{II}Cu^{II}$) forms of the binuclear copper active site in the PPOs have been obtained (Figure I.12).[7],[45],[46] In the deoxy form, the copper coordination environment is characterized as a distorted tetrahedron with a fourth, bridging water-derived ligand. Despite the presence of a bridging solvent ligand, the Cu^I coordination environment is mostly planar, resulting in a Cu-Cu separation greater than 4.0 Å. Dioxygen binds the deoxy site as a peroxide in a μ-η^2:η^2 coordination mode, decreasing the distance between the two copper atoms (3.8 and 3.4 Å in oxy-CO and oxy-Ty, respectively). At the met form, crystal structures have shown that the distance between the coppers is extremely flexible, ranging from 4.9 to 2.9 Å and depending on the nature of the bridging solvent molecules.

The mechanism of oxidation of catechol through the four-electron reduction of molecular oxygen to water is shown in Figure I.13.[46] The catalytic cycle begins with the met form of catechol oxidase, which is the resting form of the enzyme. The dicopper(II) center of the met form reacts with one equivalent of catechol, leading to the formation of quinone and to the reduced deoxy dicopper(I) state. Afterwards, dioxygen binds to the dicopper(I) active site replacing the solvent molecule bonded to Cu_A in the reduced enzyme form. The binding of the catechol substrate to the deoxy state prior to dioxygen binding seems less likely, from the experimental evidences which indicates a low binding affinity of the substrate to the dicopper(I) center. UV-Vis spectroscopy and Raman data suggested that dioxygen binds in the bridging side-on μ-η^2:η^2 binding mode with a copper–copper separation of 3.8 A° (EXAFS).

Noteworthy, it was demonstrated that secondary-sphere amino acids are essential for the CO catalytic process.[44] Hence, the catechol substrate binds the reduced enzyme Cu^ICu^I center thanks to

the rotation of the side chain of a Phe261 residue that opens the dicopper center site. In addition, the Glu 236 was shown to assist for the deprotonation of the substrate. Also, the departure of the *o*–quinone product is promoted by Glu 236 and the second non-coordinating hydroxyl group of the substrate. [47]

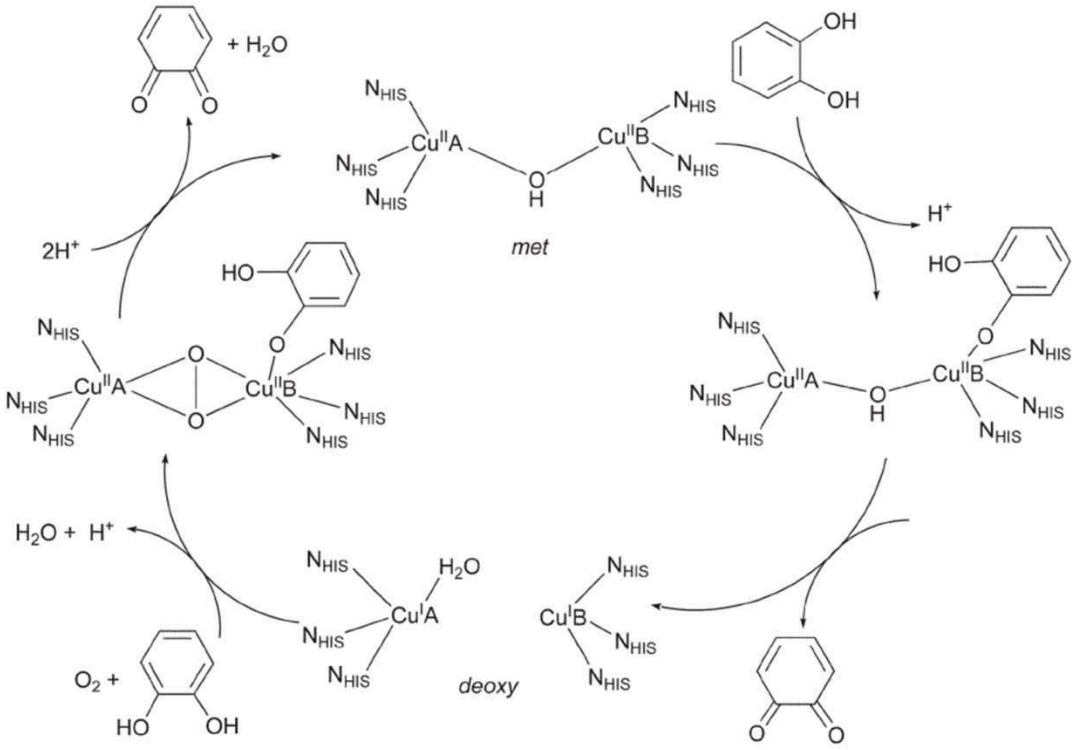

Figure I.13. Catalytic cycle of catechol oxidase from *Ipomoea batatas*, as proposed on the basis of structural, spectroscopic and biochemical data. Reproduced From Ref . [46].

The mono- and diphenolase activities of tyrosinase are displayed in Figure I.14.[7] The diphenolase cycle (the outer cycle) requires two equivalents of diphenol substrate and one dioxygen for each turnover. In the oxidative phase (left), dioxygen binds to the deoxy state to generate the oxy state, which subsequently reacts with catechol to generate the oxy-D state, finally releasing quinone and water to generate the met state. In the reductive phase (bottom right), the catechol binds to the met state to generate a dicopper(II) met-D state, as for catechol oxidase. The catechol substrate reduces the Cu^{II} ions to Cu^{I} concomitant with release of the quinone to generate the deoxy state, ready for a new cycle. Hence, the enzyme catalyzes the four-electron reduction of dioxygen to water in discrete two-electron steps using the substrate catechol as a two-electron donor without the release of hydrogen peroxide.

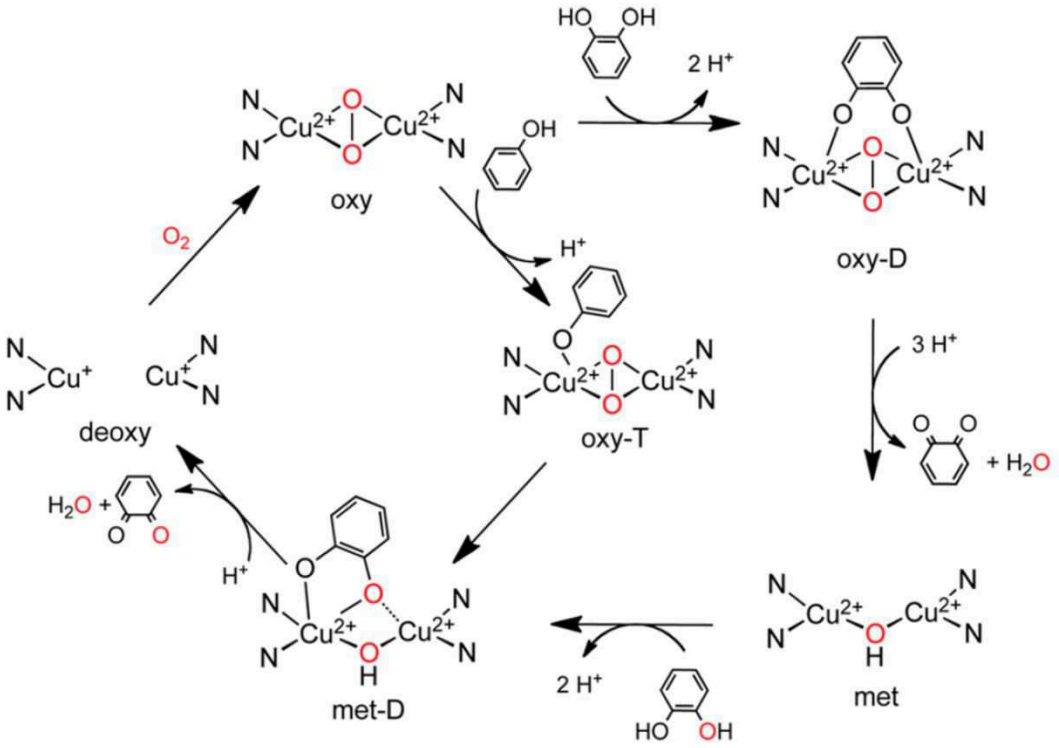

Figure I.14. Monophenolase (left) and diphenolase mechanisms of *o*-quinone formation mediated by tyrosinase. Reproduced From Ref. [7].

The functional differences between catechol oxidase, tyrosinase and hemocyanin (a type-III copper enzyme involved in O_2 transport in mollusks) has focused a lot of attention for many years since dioxygen is bound as peroxide in a side-on bridging coordination for these enzymes, within a poly-histidine environment. The absence of reactivity of hemocyanin towards tyrosine was demonstrated to be due to the proteic environment which inhibits substrate access to the binuclear site. Noteworthy, catechol oxidase activity in both arthropod and mollusk hemocyanins could be accomplished with protein denaturants.[48] Difference of functionality between monophenolase and diphenolase activities was only evidenced very recently.[42] Indeed, it was shown that deprotonation of monophenols in tyrosinase was triggered by activation of an adjacent water molecule through both glutamate (239) and asparagine (241) residues (Figure I.15). The conserved water molecule becomes basic enough to bind the proton released by phenolic substrates upon coordination to the active site. Interaction with a single residue, such as glutamate, did not increase the basicity of the water molecule sufficiently to induce monophenolase activity. In this case only diphenolase activity was possible because it does not rely on a deprotonation pathway.

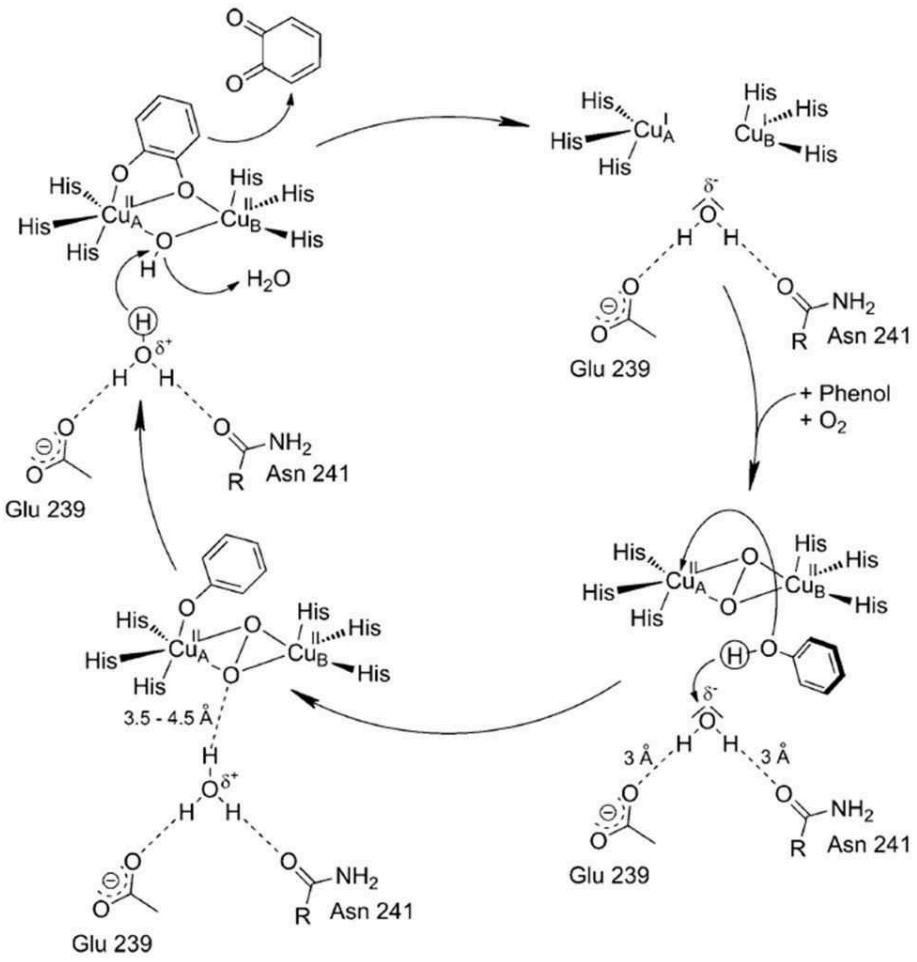

Figure I.15. Monophenolase catalytic cycle of tyrosinase showing the importance of adjacent amino-acids residues in the deprotonation process. Reproduced From Ref . [42].

II.3. Galactose Oxidase (GO)

Galactose Oxidase is a monomeric enzyme that contains a copper ion: it catalyzes the regioselective two-electron oxidation of primary alcohols into aldehydes, coupled to the two-electron reduction of molecular dioxygen into hydrogen peroxide.[6] Although the natural substrate for the enzyme is D-galactose, GO accepts a broad range of substrates, from sugars to aromatic alcohols. It can also oxidize aldehydes to carboxylates, but at a much slower rate. To achieve this task, the enzyme generates an organic radical cofactor on its own peptidic chain to complete metal-driven electron transfers. It is now believed that the physiological role of GO is to generate H_2O_2 as an anti-bacterial agent or fuel for lignin peroxidase.

GO is a monomer of 68 kDa molecular mass, containing one copper center per protein.[6],[7] The mature enzyme from *Fusarium* spp. comprises three β-sheet domains. Domain I consists of eight β-strands in a circle motif with a five-stranded antiparallel β-sheet. Domain II is the largest one and it is composed by seven-bladed β-propeller fold surrounding a central cavity. The active site is situated on the surface of this domain in which Tyr 272, Tyr 495 and His 496 coordinate the copper. Domain III contains antiparallel β-strands surrounding a hydrophobic core. The fourth protein ligand to the copper, His 581 is provided by this domain (Figure I.16).

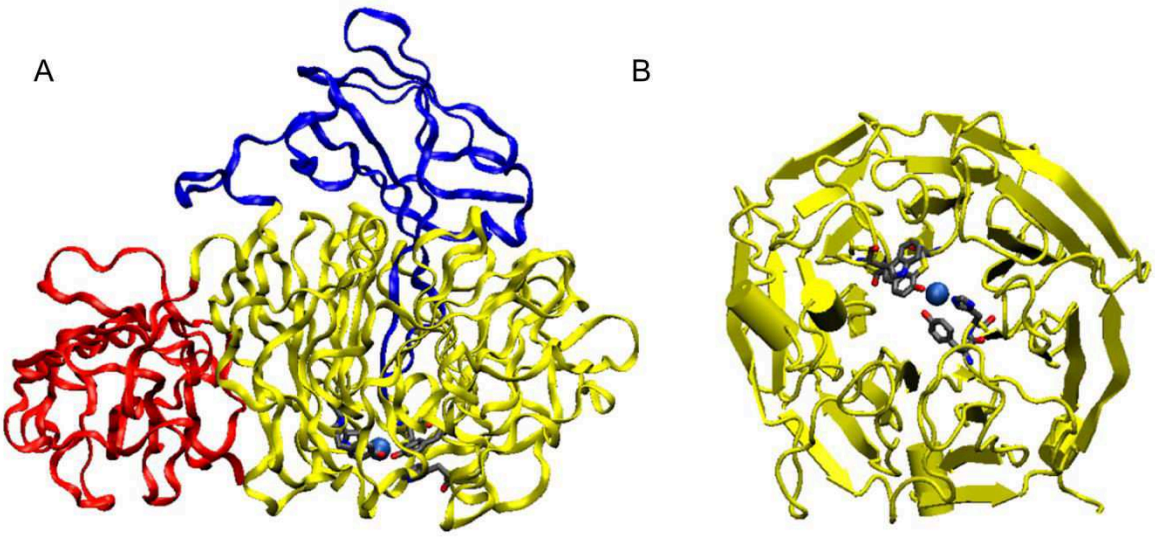

Figure I.16. A) Molecular model of galactose oxidase, showing the three domains (red, domain 1; yellow, domain 2; blue, domain 3); B) Computer generated model of the second domain showing the 7-fold axis and the location of the copper ion inside the domain. Reproduced from Ref. [7].

The active site of GO contains a copper atom in a distorted square-based pyramidal geometry with Tyr 495 in the axial position (Figure I.17). Copper is coordinated to two tyrosines (Tyr 272 and Tyr 496) and two histidines (His 496 and His 581), while a fifth coordination position is occupied by a molecule of water. X-ray data are limited to the inactive form of the enzyme, and show a trigonal bipyramidal geometry for the copper ion, with the long axis aligned with the coordinated solvent molecule. The catalytic activity, as alcohol oxidation and oxygen reduction are both two-electron processes, could be interpreted as dihydrogen transfer. In biological systems, this kind of transfer involves a cofactor, such as flavines or nicotinamides. Galactose Oxidase does not contain any of these cofactors and utilizes a free radical-coupled copper complex (Tyr 272) to perform the reaction.[49]

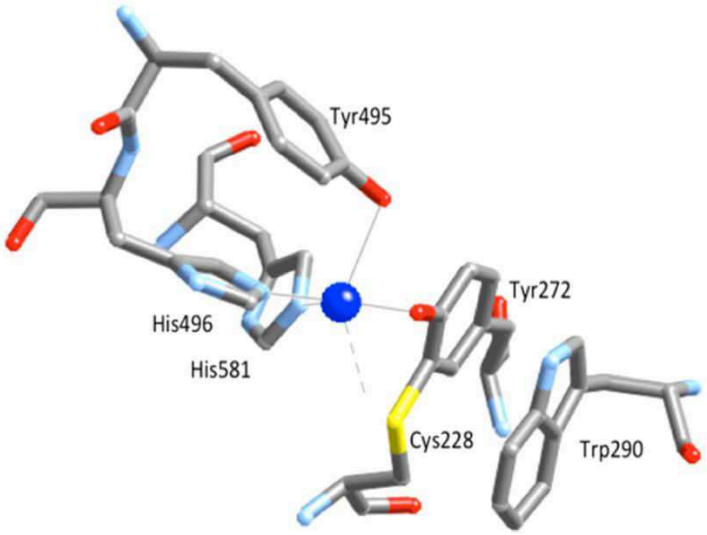

Figure I.17. X-ray structure of GAO active site in its inactive form. Reproduced from Ref. [7].

The crystal structure at 1.7 Å resolution, reported by Ito and co-workers has elucidated interesting and unique features of the active site.[50] Tyr 272, directly implicated in the coordination of copper, was found to be bound to the sulphur atom of Cys 228. This peculiar bond seems to have the character of a partial double bond, extending the aromatic system, as the C_β of cysteine lies on the same plan of the tyrosine aromatic ring. This modification identifies the real redox-active site in the protein, as it forms a stabilized free radical upon oxidation in mild conditions. Further stabilization of the free radical complex may come from the outer sphere tryptophan residue (Trp 290), which perhaps shields the Tyr-Cys dimer from interaction with the solvent (Figure I.17).

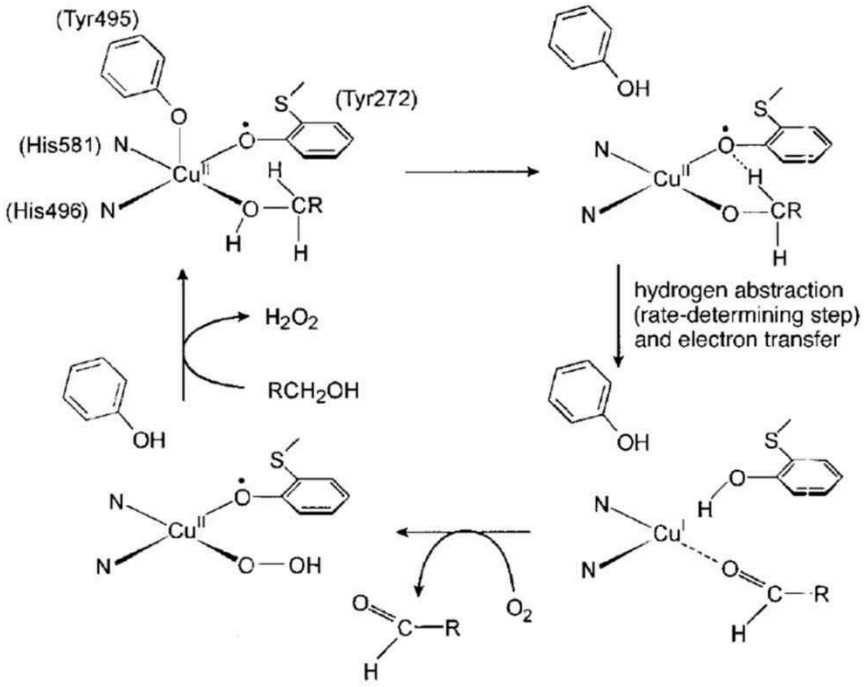

Figure I.18. Schematic representation of a proposed catalytic cycle of Galactose Oxidase. Reproduced from Ref. [51].

The catalytic reaction can be formally divided into two separated reduction and re-oxidation reactions, consistent with a ping-pong mechanism (Figure I.18). The reduction step involves the reaction of the free radical-Cu^{2+} complex with the primary alcohol to give the aldehyde (Figure I.18, right). In the second step, the reduced form reacts with dioxygen to generate the metal-radical complex accompanied by the formation of hydrogen peroxide (Figure I.18, bottom).[52] There is no crystal structure of the active site with the D-galactose bound, but the fact that the open coordination site of copper(II) in the crystal structures is usually occupied by water or an anion of the crystallization buffer indicates that the galactose coordinates to replace the labile equatorial ligand.

The enzyme can exist in three well-defined oxidation levels: the Cu^{II}-tyrosyl(495) radical oxidized form, an intermediate Cu^{II}-tyrosinate form, and the reduced Cu^{I}-tyrosine form. A key factor in this structure is represented by the thioether crosslink between Tyr and Cys (Figure I.17). The Cu^{I} binding to the tyrosil moiety affords a trigonal copper (I) complex that reacts with O_2. The reactive Cu^{II}-$O_2^{\bullet-}$ compound abstracts a hydrogen atom from Cys 228, forming a hydroperoxo adduct and releases H_2O_2. A re-aromatization occurs by proton and electron transfer to the metal to produce the fully reduced form of the mature GO. At this stage, two-electron oxidation by O_2 gives the catalytically active Cu^{II}-tyrosyl radical form of the enzyme and H_2O_2. Although the catalytic reaction of GO has been well resolved, little is known about the biogenesis formation of the Cys−Tyr radical cofactor.

III. Biomimetic models of copper enzymes for C-H oxidative cleavage

III.1. General aspects of synthetic models of copper-enzymes

Copper complexes of active-oxygen species have been invoked as key reactive intermediates in a wide variety of redox reaction involved not only in biological systems, but also in numerous catalytic oxidation processes. Many synthetic molecular systems, inspired by the structural and functional features of the active sites of copper proteins, have been widely developed for more than 30 years. The target objective has been to obtain biomimetic catalysts which can mediate fundamental reactions with high efficiency, such as oxidation and oxygenation of C−H bonds for the sustainable generation of chemical feedstocks and fuels. This approach has produced a number of discrete Cu_xO_y complexes which have been structurally and spectroscopically described and surveyed for reactivity toward organic substrates, looking at their nucleophilic or electrophilic character (Figure I.19).

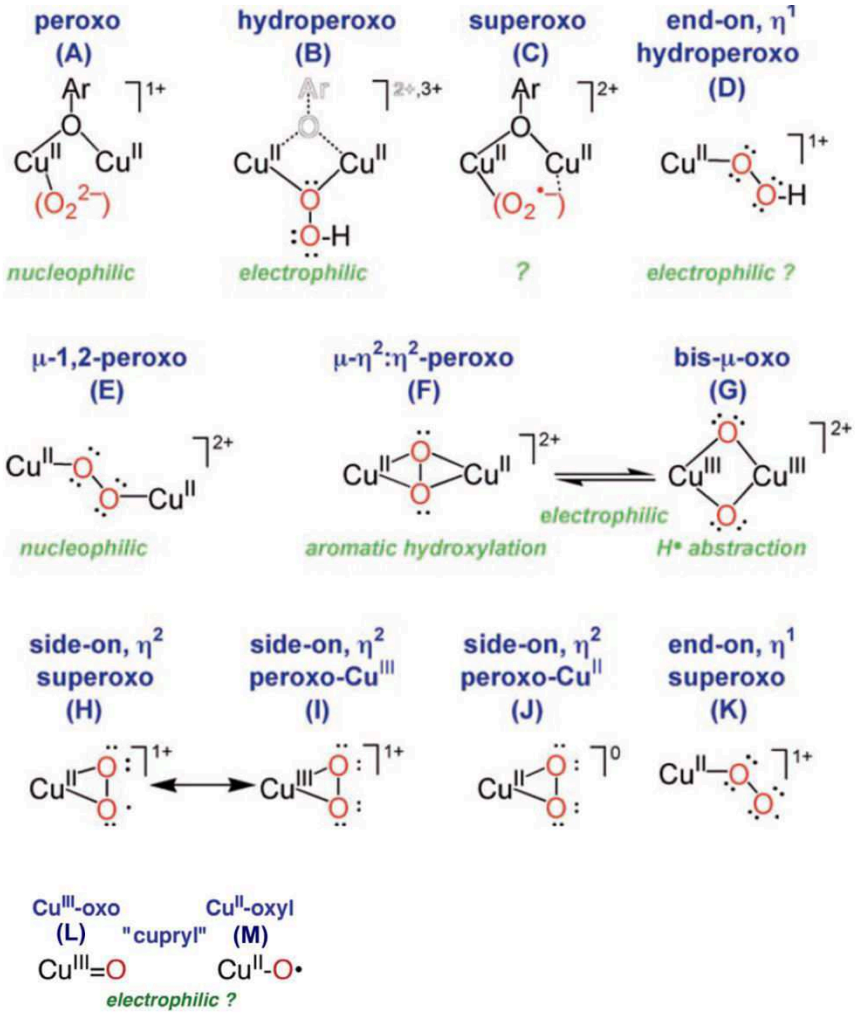

Figure I.19. Structure and reactivity of diverse Cu_nO_2 adducts obtained from biomimetic copper complexes. Reproduced from Refs. [53] and [54].

Due to the lability and coordination flexibility of Cu^{I} and Cu^{II} complexes, the ligand dictates the pathway for Cu/O_2 reactivity and accommodates the multiple oxidation states of the metal. The ligand that generates well-characterized Cu/O_2 species upon oxygenation of their Cu^{I} complexes differs by donor atoms, chelating ring sizes or their formal charge. Aromatic nitrogen ligands like pyrazol, pyridine and imidazole have been extensively used in biomimetic studies contrarily to sulphur and phosphorous ligation. The polydentate ligation is researched in ligand synthesis to restrict the Cu speciation.[55] The high lability and geometric flexibility of Cu^{I} complexes allow numerous geometries. Tetrahedral or trigonal-monopyramidal four-coordinated complexes are most common, but T- or Y-shaped three-coordinated and linear two-coordinated complexes are frequently observed.[17] Five-coordinated Cu^{I} complexes are rare and in all cases have at least one Cu-ligand bond that is significantly longer than the others. Cu^{II} complexes commonly have square-planar or square-pyramidal geometries with ligands weakly associated in the axial positions, or trigonal-bipyramidal conformations. In either case, two or more Cu^{II} ions are linked by anionic ligands (oxide, hydroxide) and an antiferromagnetic or a ferromagnetic coupling between the Cu^{II} ions is observed. The less common Cu^{III} complexes are generally stabilized by strongly basic, anionic ligands that accommodate a square-planar geometry.

Numerous examples of polydentate ligands have been developed in order to accommodate the $Cu\text{-}O_2$ cluster in different oxidation states.[17] *Tmpa* and its derivatives ligands (*R_3tmpa*, *$tmpa^{R4}$*, *tmpae*, *D^1* and *D^0*, Figure I.20) are probably the most studied examples of transient Cu/O_2 end-on superoxo (**K**) species and its related (μ-1,2-peroxo) (**E**) dicopper form (Figure I.19). *Tren* and derivatives are tripodal tetraamine ligands related to *tmpa* but possess better aliphatic amine donor groups; the *bisp* ligand and its derivatives are tetradentate ligands with two aliphatic amine and two pyridine. *Bpia* and *bipa* ligands are obtained changing the pyridine groups of *tmpa* with imidazoles. Modification with two quinolyl subunits (*bqpa* ligands, Figure I.20) is recognized as a common ligand in bis(μ-oxo)dicopper(III) complex (**G**) (Figure I.19).

One of the first well-characterized Cu/O_2 systems is based on the binucleating ligand $Xyl\text{-}O^-$ (Figure I.21). Oxygenation of the dicopper(I) complex of the protonated ligand XylOH produces a hydroperoxide species (**B**, **D**) (Figure I.19). Pyrazoles and mixed pyrazole/pyridine subunits in binucleating ligands are common for similar peroxo and/or hydroperoxo species. A side-on (superoxo)copper(II) (**H**) is favoured when the Cu^{II} shows a distorted square-pyramidal coordination environment. Some examples of tridentate ligands shown in Figure I.22 are supposed to support this geometry like the tris(pyrazolyl) borate ligands (*Tp* and derivatives).[56] Tridentate ligands are extensively used in (μ-η^2:η^2-peroxo)dicopper(II) (**F**) complexes and bis(μ-oxo)dicopper(III) (**G**) complexes. Bidentate ligands (Figure I.23) exploit charge and steric demands to stabilize 1:1 Cu/O_2 species. The series of ligands $^{H,Me}Dk^{iPr}$ and $^{H,tBu}Dk^{iPr}$ reported by Tolman and co-workers show that the O_2 moiety binds in a side-on conformation and Cu ion adopts a distorted square-planar geometry.[57]

These species are currently considered as hybrid species between a Cu^{II} -superoxide (**J**) and a Cu-(III)-peroxide (**I**) (Figure I.19).

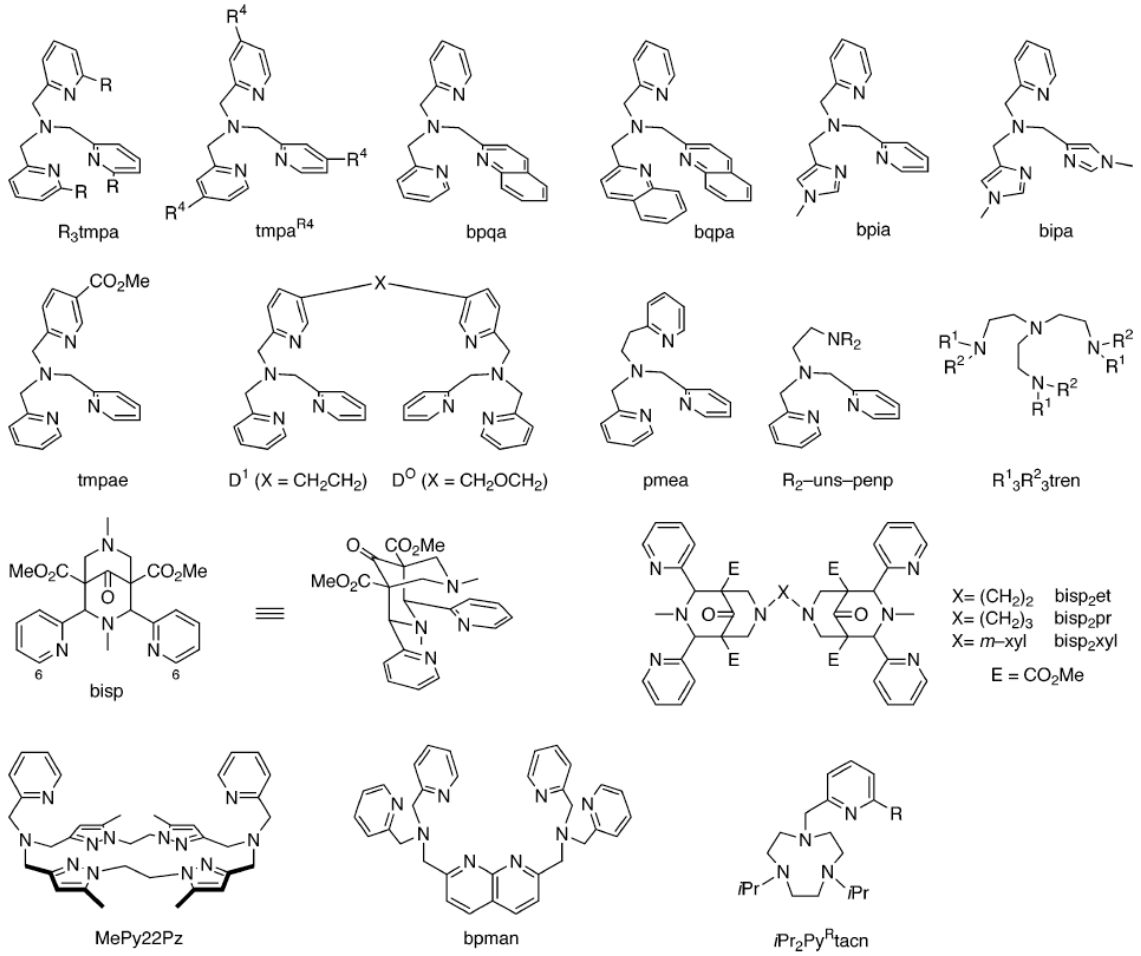

Figure I.20. Selected tetradentate N-ligands for Cu complexes leading to copper-oxygen adducts. Reproduced from Ref. [17].

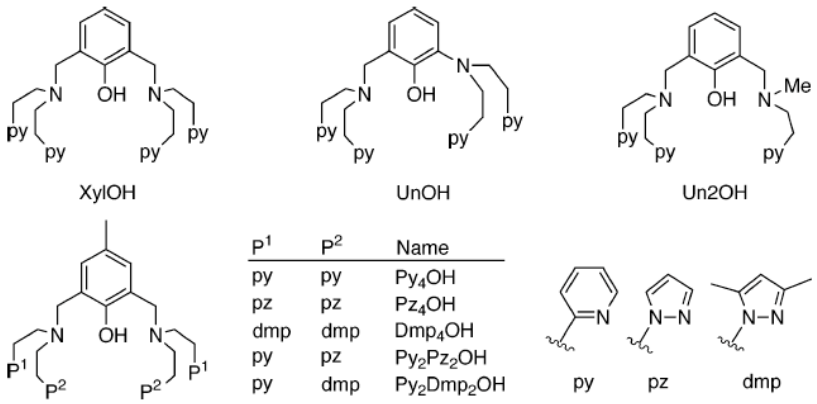

Figure I.21. Phenoxo-bridged dinucleating ligands derived from XylOH. Reproduced from Ref. [17].

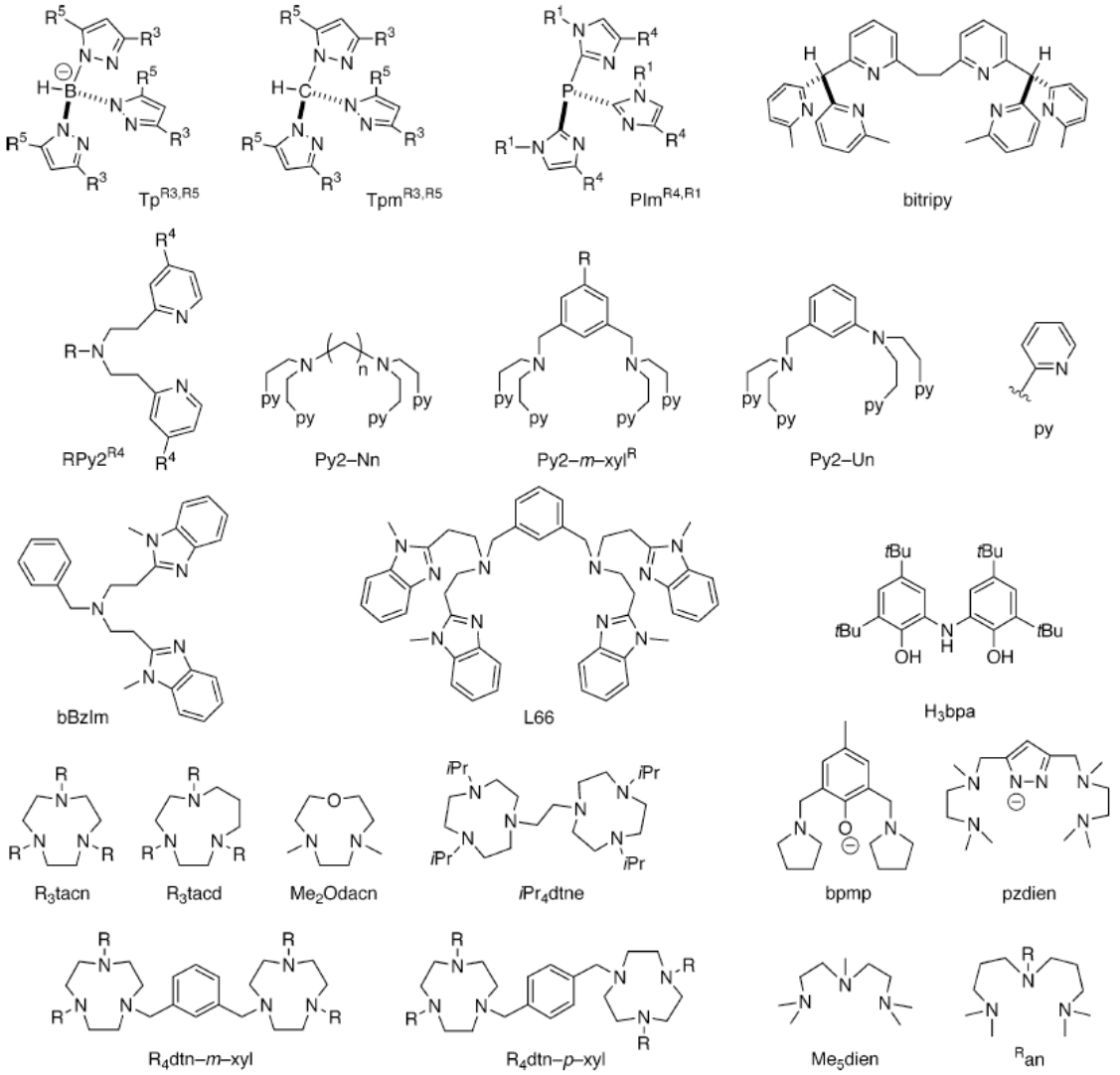

Figure I.22. Selected tridentate N-ligands for Cu complexes leading to copper-oxygen adducts. Reproduced from Ref. [17].

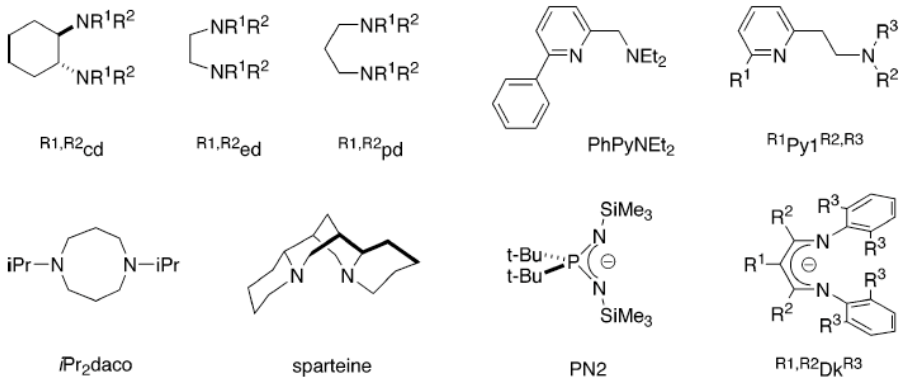

Figure I.23. Selected bidentate N-ligands for Cu complexes leading to copper-oxygen adducts. Reproduced from Ref. [17].

III.2. Reactivity of copper-oxygen adducts

Copper complexes leading to (μ-η^2:η^2-peroxo)Cu_2^{II} adducts have been probably the most extensively studied copper-dioxygen complexes due to their strong relevance in the intermediate oxy-forms of type III copper proteins: hemocyanin, tyrosinase, and catechol oxidase. Bis(μ-oxo)Cu_2^{III} complexes have been also well characterized in synthetic copper-oxygen adducts. Both of these specific adducts, supported by different kinds of coordinating ligands, exhibit various types of reactivity toward external substrates or in some cases intramolecularly towards its own ligand by oxidative modification. Aromatic ligand hydroxylation, epoxidation, dimerization of phenols, oxygenation of phenolates, oxidative N-dealkylation and aliphatic hydroxylation are some of the many possible reactions that they allow due to their electrophilic character.[58] Figure I.24 displays a list of reactions for (μ-η^2:η^2-peroxo)Cu_2^{II} and bis(μ-oxo)Cu_2^{III} complexes, investigated over time. The reactions represent the conversation either of substrate added in the reaction medium during catalysis or of the own ligand of the complexes.

The interconversion between bis(μ-oxo)Cu^{III}_2 and the isomeric (μ-η^2:η^2-peroxo)Cu_2^{II} species have been examined over several decades and the role of ligand structural variations on the reactivity of Cu^I complexes has been widely described.[18] The pyridyl-amine ligands have been probably the most used moieties to investigate copper-oxygen chemistry. Oxidation potential and rate of reaction with O_2 change with the substituent on the ligand structure. For example, the 6-methyl substituent in pyridyl-amine ligands can reduce the electron-donating power of the ligand framework, inhibiting O-O bond scission (Figure I.25). For this reason the formation of a bis(μ-oxo)Cu_2^{III} species is advantaged for the unsubstituted pyridyl ligand with one methyl chain spacer. Hence, both complexes bearing quinolyl groups and the methylpyridyl moieties yield preferentially a (μ-η^2:η^2-peroxo)Cu_2^{II} form. The increase of the chain length between the amine and the unsubstituted pyridyl groups also lead to the formation of the (μ-η^2:η^2-peroxo)Cu_2^{II} complex.[59]

The reactivity of bis(μ-oxo)Cu_2^{III} complexes has been widely discussed. In 2014 Stack *et al*.[60] reported experimental and computational studies of three copper complexes with bidentate ligands to activate C-H bond by a bis(μ-oxo)Cu_2^{III} complexes. Primary amines, propylenediamine, and N,N,-dimethyl propylenediamine were used as ligand substituent. Spectroscopy, structure and reactivity studies showed that the H-atom abstraction of 9,10-dihydromethylacridine substrate was detected only for the complex bearing at least one primary amine for accessibility reasons (Figure I.26).

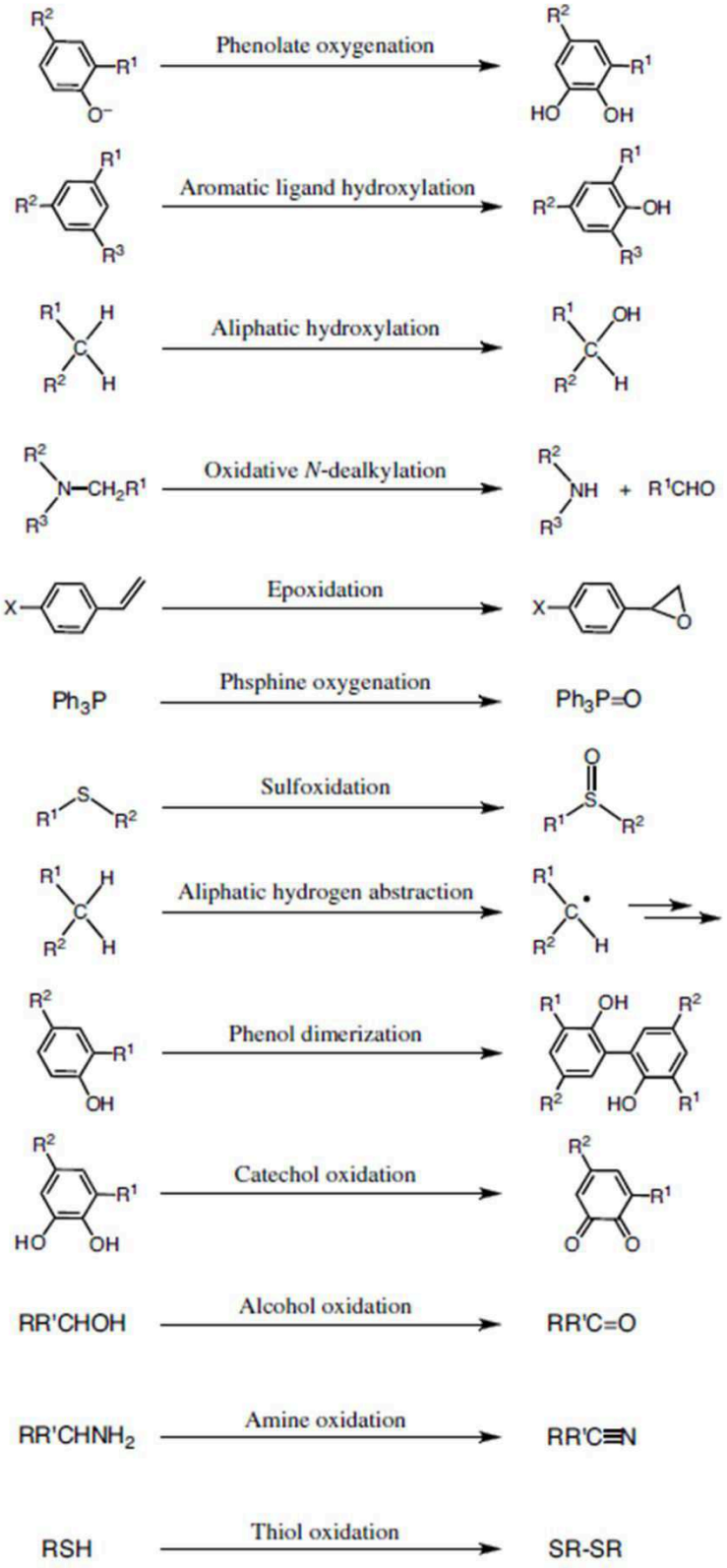

Figure I.24. General examples of catalytic reactions by (μ-η^2:η^2-peroxo)Cu_2^{II} and bis(μ-oxo)Cu_2^{III} complexes. Reproduced from Ref. [58].

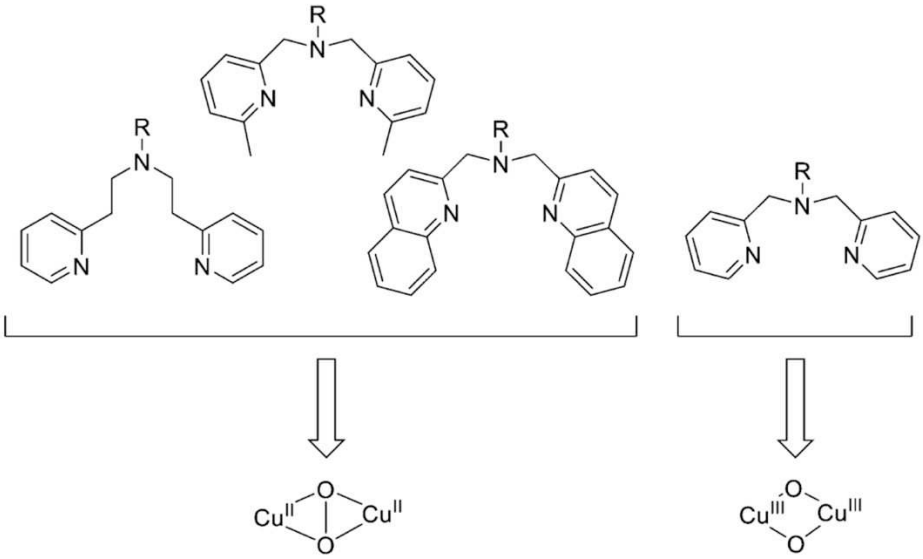

Figure I.25. Ligands yielding either the (μ-η²:η²-peroxo)Cu_2^{II} or the bis(μ-oxo)Cu_2^{III} (R = CH_2CH_2Ph). Reproduced from Ref. [18].

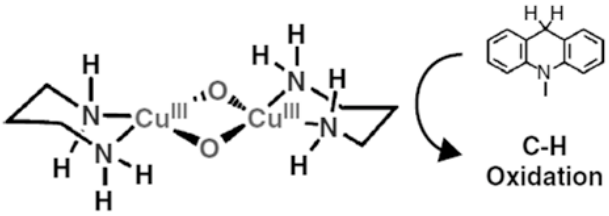

Figure I.26. H-atom abstraction in 9,10-dihydromethylacridine by a bis(μ-oxo)Cu_2^{III} complex. Reproduced from Ref. [19].

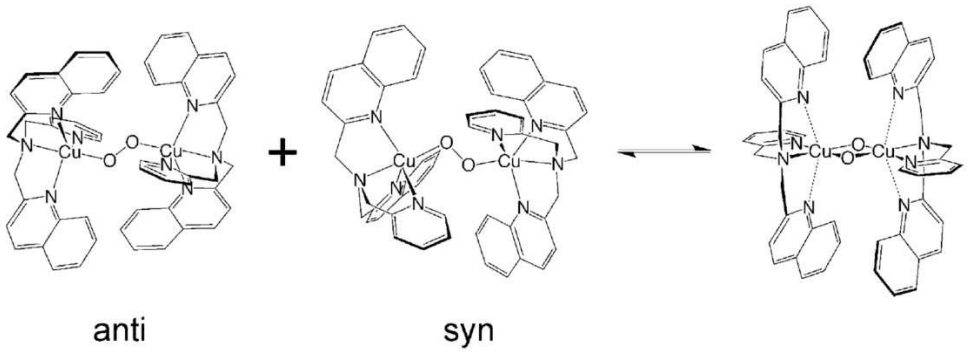

Figure I.27. End-on peroxo/bis-μ-oxo isomerization. Reproduced from Ref. [61].

In contrast to bis(μ-oxo)Cu_2^{III} and (μ-η²:η²-peroxo)Cu_2^{II} species which display electrophilic properties, (μ-1,2-peroxo)Cu_2^{II} (end-on) adducts typically behave as nucleophiles (Figure I.19).[16] Hence, they can react with H^+ (leading to H_2O_2) or trisphenylphosphines PPh_3 for example.

Noteworthy, Solomon and co-coworkers recently demonstrated by spectroscopic studies a possible interconversion of an end-on (μ-1,2-peroxo) dinuclear species to a thermodynamically more stable bis-μ-oxo derivative at low temperature, for a *tmpa*-based complex (Figure I.27).[61] DFT calculations suggested that the unexplained electrophilic reactivity (phenolate ortho-hydroxylation) previously ascribed to end-on peroxo species for this complex could result through an accessible electrophilic bis-μ-oxo isomer.

The reactivity of synthetic hydroperoxo-bridged dicopper complexes has also been investigated. It was demonstrated that (μ-η^1:η^1-hydroperoxo)dicopper(II) complexes react with sulfides quantitatively to give sulfoxides [RS(O)R].[62] Aromatic ligand hydroxylation and N-dealkylation were observed for the reaction of a *tmpa*-based dicopper(II) complex with H_2O_2.[63],[64] A high-valent copper-oxo species was suggested as the real active species for these oxidation reaction. Moreover, Karlin and co-workers investigated the reactivity of binucleating phenol-containing a (μ-phenoxo-μ-hydroperoxo)dicopper(II) complex. Although this species was unable to oxidize externally added substrates, for instance, PPh_3, 2,4-butylphenol, or 9,10-dihydroanthracene, it hydroxylated copper-bound organocyanides (e.g., benzylcyanide), leading to the corresponding aldehyde while releasing cyanide.[65] On the other hand, Suzuki and co-workers characterized a (hydroxo)dicopper(II) complex supported by a tetradentate tripodal ligand possessing three sterically bulky imidazolyl groups.[66] Decomposition of the complex induced aliphatic ligand hydroxylation at one of the methylene groups of the pendant arms.

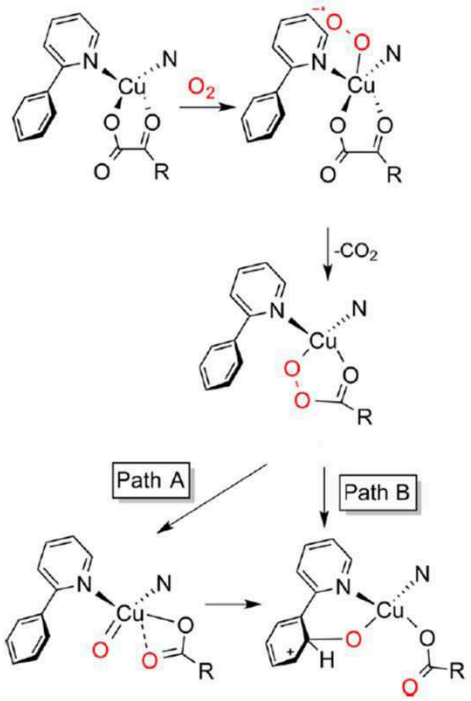

Figure I.28. Aromatic ligand hydroxylation mechanism in Cu^I-ketocarboxylate complex proposed from theoretical calculations. Reproduced from Ref. [67].

Copper-oxo adducts have been the object of high interest during the last years, because they have been postulated as a possible reactive intermediate in several fundamental biological reactions (PHM, DβH, pMMO). However, such a mononuclear copper–oxo species has never been isolated in enzymes and only has been detected in a gas-phase reaction.[67] Tolman and co-workers studied the oxygenation reaction of copper(I)–aketocarboxylate complexes to find oxidative decarboxylation of the α-ketocarboxylate ligand and arene hydroxylation of the supporting ligands (Figure I.28).[68] The electron-donating substituent on the phenyl group enhances the reaction, indicating that the active oxygen species generated has an electrophilic character. Theoretical studies on this reaction have suggested that a Cu-oxo species, best described as $Cu^{II}O^{\bullet-}$, is generated by O-O bond cleavage, and this oxygenates the phenyl substituent of the supporting ligand (Figure I.28).

At last, the reactivity of mononuclear copper-superoxo adducts has been also well investigated since these species are implicated in oxidation process of type II copper proteins, as shown by the structural resolution of the end-on Cu-O_2 active site in oxy-PHM (Figure I.2). During the last few years, relatively stable mononuclear end-on (superoxo)copper(II) complexes were synthesized and characterized from different N-ligands: *MG3tren*, *calix[6]amidotren*, *R_3TPA (R=NMe_2* and *OMe)* and *$L3^X$* (diazacyclooctane).[69],[70],[71],[72],[73],[74],[75] Hydrogen atom abstraction on phenolic substrates (*MG3tren*, *R_3TPA)* and/or from the ligand itself (*NMe_2TPA*, *calix[6]amidotren*, *$L3^X$*) was obtained with these complexes. For *MG3tren*, it was suggested that a Cu^{II} hydroperoxo complex generated *in situ* is involved as a key intermediate, leading to $Cu^{II}O^{\bullet-}$ or $Cu^{III}O^{-}$ species by O-O bond homolysis of the hydroperoxo adduct.[69] Recently, Karlin and co-workers have investigated the mechanisms of hydrogen atom abstraction for differently substituted phenolic substrates by using a *$(OMe)_3$TPA*-based Cu complex (Figure I.29).[71] They concluded from their studies that two-electron oxidation or four-electron oxygenation occurred according to the nature of the substituting group in para position of the phenol.

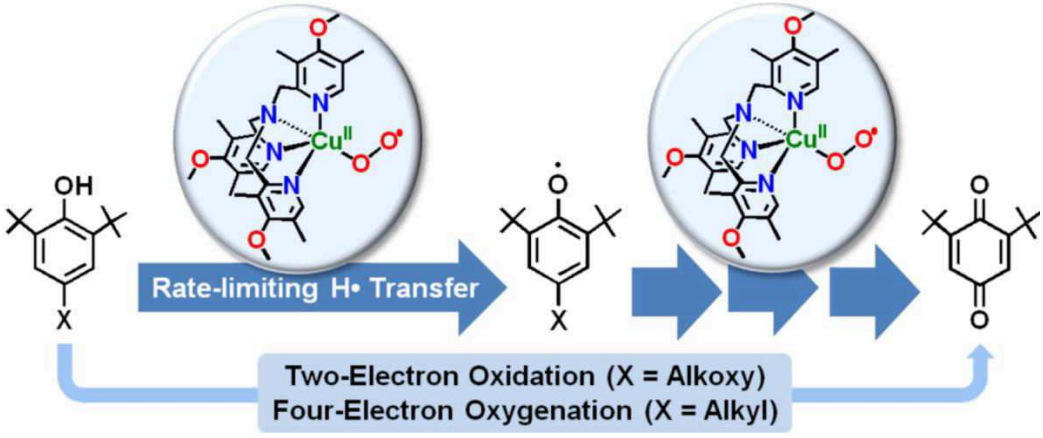

Figure I.29. Hydrogen atom abstraction on differently substituted phenolic substrates by a *$(OMe)_3$TPA*-Cu superoxo complex . Reproduced from Ref. [71].

III.3 Biomimetic models of pMMO

As mentioned previously, the nuclearity and structure of the active site of pMMO have been the subject of a controversy for a long time. Different synthetic models of the active site (tri-, di- and mononuclear) of pMMO have been developed over years. [55],[54],[76]

First trinuclear copper μ^3-oxo species in which copper ions are in the +2, +2, and +3 oxidation states have been reported by Stack and co-workers.[77] Although such a species was demonstrated to oxidize phenolic substrates and dihydroanthracene, [78] they seemed to possess limited reactivity. Other trinuclear Cu models of the putative trinuclear Cu cluster in pMMO have been developed and displayed oxidative properties for the functionalization of cyclohexane, but without mechanistic details.[54] Interestingly, Chan and co-workers have reported a trinuclear complex μ^3-oxo (Figure I.30) which could promote conversion of benzyl into its anhydride.[79] The authors suggested a singlet 'oxene' insertion pathway in agreement with DFT calculations, but without supporting mechanistic studies (Figure I.30).

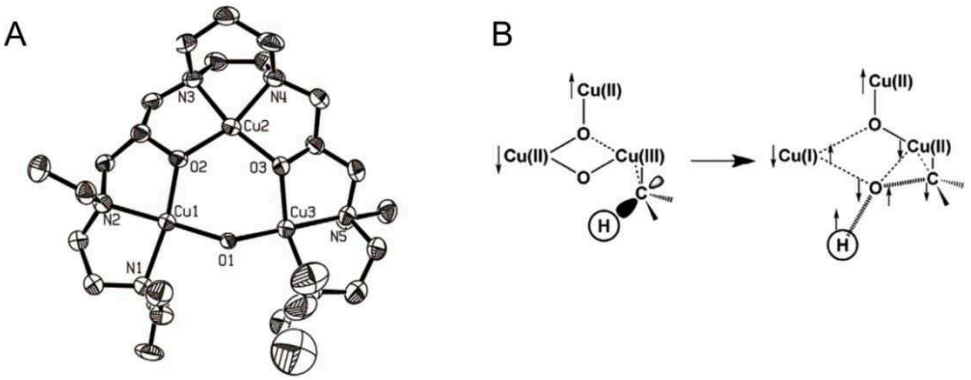

Figure I.30. A) Tricopper μ^3-oxo complex developped by Chan and co-workers. B) Proposed oxene insertion reaction for C-H activation. Reproduced from Ref. [79].

Dinuclear models of pMMO have also been developed, in line with experimental data on the enzyme which showed that the site of oxidation of methane into methanol is a dicopper site.[54],[76] Bis(μ-oxo)Cu_2^{III} and (μ-η^2:η^2-peroxo)Cu_2^{II} species have been both envisaged as active species capable of performing C-H activation in alkanes. Mechanistic studies of intramolecular N-dealkylation and benzylic C-H hydroxylation in side-on (peroxo)Cu_2^{II} complexes have shown that the rate-determining step was not the C–H abstraction but rather the isomerization to the bis(μ-oxo)Cu_2^{III} core.[78] This suggested that the methane hydroxylation at a copper dinuclear site, via C–H abstraction, would likely involve a bis(μ-oxo)Cu_2^{III} rather than a (μ-η^2:η^2-peroxo)Cu_2^{II} intermediate. Accordingly, Stack and co-workers have used a series of amino-based ligands to prepare bis(μ-oxo)Cu_2^{III} complexes as models of the active site of pMMO (Figure I.31). [60],[76] For this family of copper-oxygen adducts, it was shown that the rate of hydrogen atom abstraction of different substrates such as DHA (dihydroanthracene)

(Figure I.31) was correlated with ligand steric effects since the most accessible structures oxidize substrates with the greatest rate.

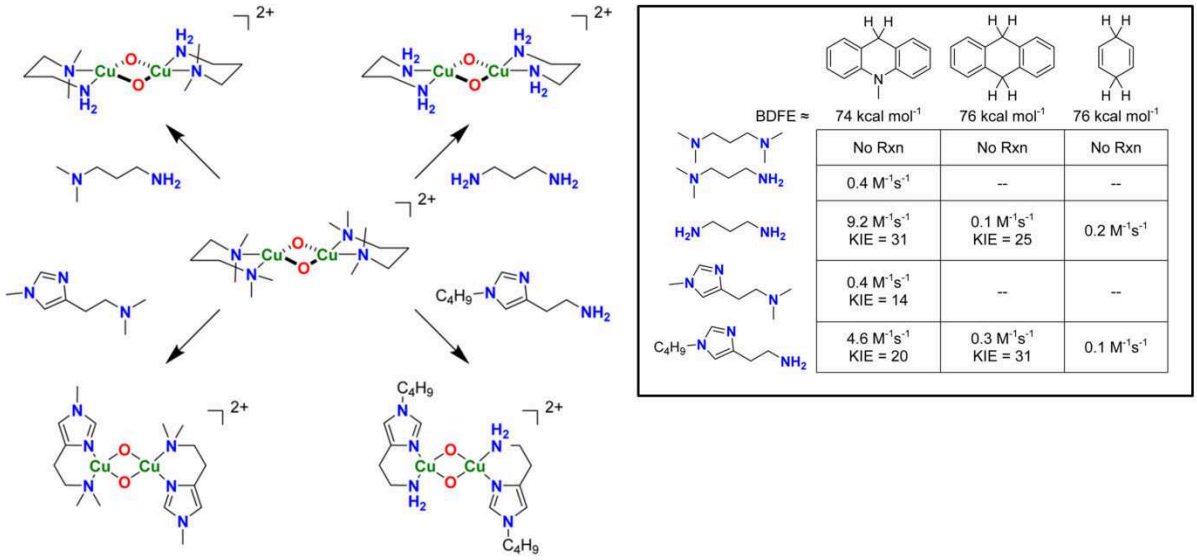

Figure I.31. Schematic representation and reactivity towards organic substrates of the dicopper bis(μ-oxo) models of pMMO developed by Stack and co-workers. Reproduced from Ref. [76].

Alternatively, Itoh early proposed to rationalize the second-order rate dependence on $[Cu_2(O)_2]$ in the oxidation of exogenous C–H substrates by considering the disproportionation of the bis(μ-oxo)Cu_2^{III} into mixed-valent oxygen adducts. Réglier and co-workers demonstrated that intramolecular hydroxylation for a polypyridine-based Cu complex occurred only in the presence of excess benzoin reductant, hence suggesting a mixed-valent $Cu^{II}Cu^{III}$ active species formed by electron transfer to the initial Cu_2O_2 complex (Figure I.32).[80] The $Cu^{II}Cu^{III}$ bis(μ-oxo), proposed as the active species which achieves oxidation of methane in pMMO, was validated latter by DFT calculations by Chan *et al.*[40] and Yoshizawa *et al.*[41]. More recently, Tolman and co-workers reported a relatively stable mixed-valent Cu^{II}(μ-OH)Cu^{III} species based on a macrocyclic ligand (Figure I.33).[81] This species was obtained from monoelectronic oxidation of the corresponding Cu_2^{II}(μ-OH) species by chemical or electrochemical means. In a related manner, Solomon and co-workers developed (μ-oxo)Cu_2^{II} species which can activate methane oxidation in Cu-loaded zeolites (Cu-ZSM-5)[82] at low temperature with high selectivity.[83] They provided definitive evidence of the formation of $[Cu_2O]^{2+}$ cores in Cu-MOR. Experimental data highlighted the participation of the zeolite lattice in the reaction.

At last, oxidation of methane at a mononuclear copper site has also been envisaged. Indeed, theoretical studies have suggested that a mononuclear copper-oxo ('cupryl') could oxidize methane.[41],[54] Such species has been indeed invoked in many oxidation mechanisms, (cyclohexadiene oxidation into benzene for example) by evolution of peroxo, hydroperoxo or alkylperoxo precursors. However, as discussed by Karlin and co-workers,[54] the formation of a cupryl from Cu^{II}OOH in

pMMO is unlikely for many reasons (mechanistic pathway, low reactivity of hydroperoxo species with methane to form the cupryl species).

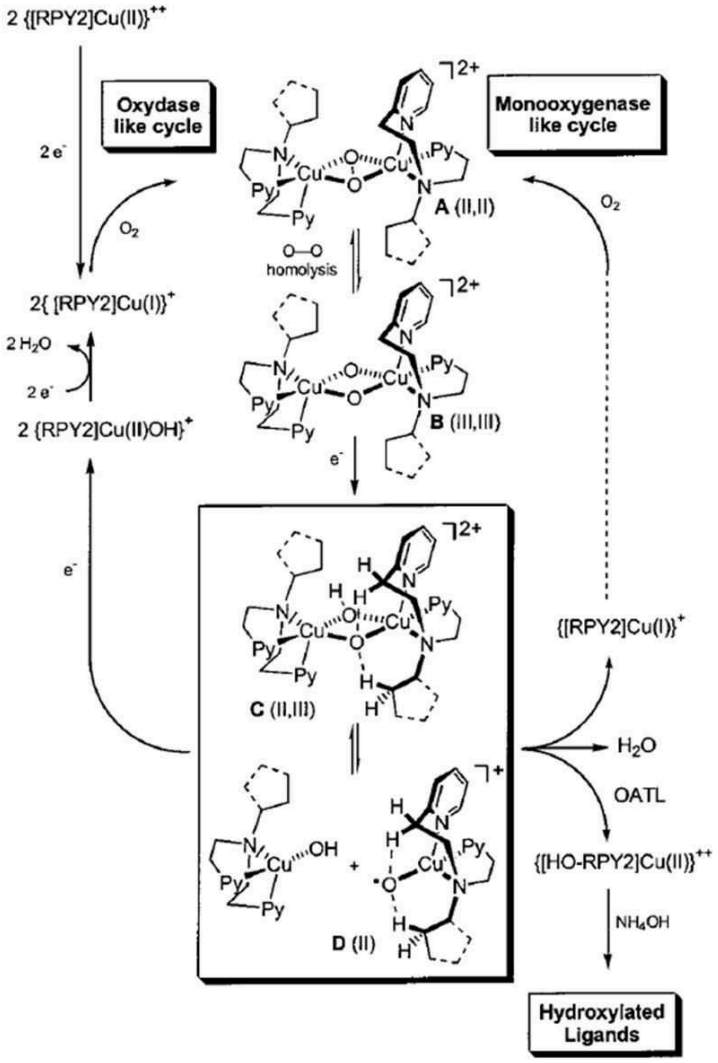

Figure I.32. Intramolecular hydroxylation of the Ind.-Py_2 ligand by the hypothetic $Cu^{II}Cu^{III}$ bis(μ-oxo) species (C) upon monoelectronic reduction of species B. Reproduced from Ref. [80].

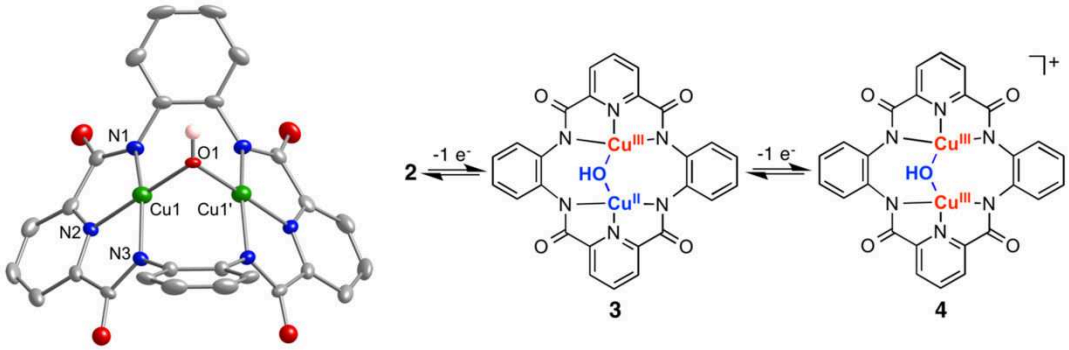

Figure I.33. X-ray structure and oxidation of the hydroxo-bridged dicopper(II,II) complex developed by Tolman and co-workers. Reproduced from Ref. [81].

III.4. Biomimetic models of Ty and CO

Many synthetic models of the active site of tyrosinase have been developed for almost 30 years.[18],[43],[84] N-donor ligands such as imines, pyridines, pyrazoles, imidazoles and benzimidazoles have been used to mimic the histidine residues of the surrounding environment in enzymes (Figure I.34). Hence, mononuclear and dinuclear ligands have been designed to perform the catalytic hydroxylation of a substrate 2,4-di-tert-butylphenol (DTBP-H) or para-substituted phenols. The first catalytically active model was reported by Réglier and co-workers in 1990 with the dinucleating ligand BiPh(impy)$_2$.[85] The substrate DTBP-H conversion into orthoquinone was obtained with a turnover number (TON) of 16 in one hour. In the following years, other catalytically active model systems with different N-donor ligands were reported with higher TONs.[84]

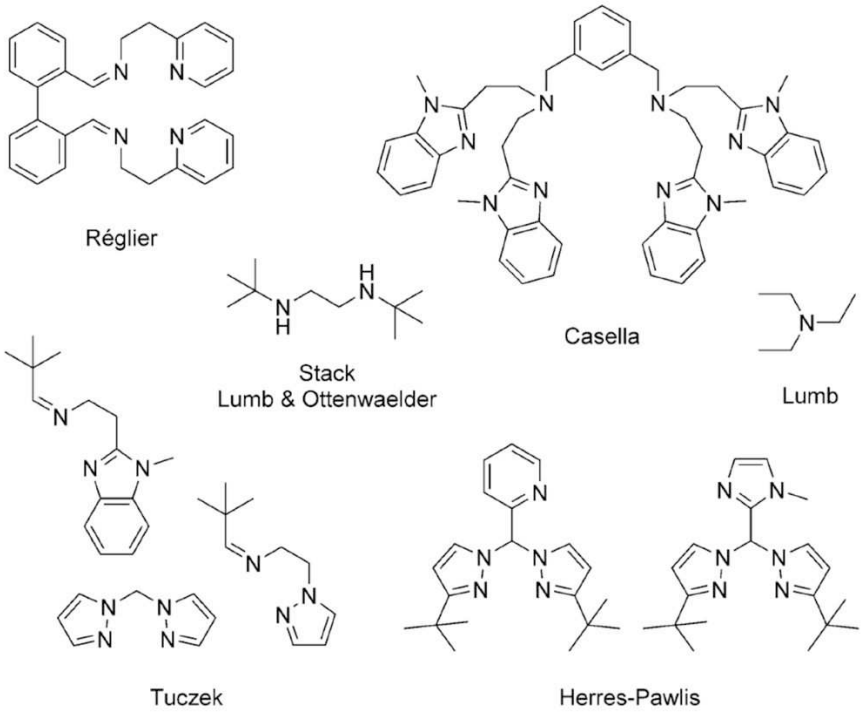

Figure I.34. Selected ligands designed for mimicking tyrosinase with the names of principal investigators. Reproduced from Ref. [84].

Although the crystal structure of tyrosinase displays a (μ-η^2:η^2-peroxide) dicopper(II) core, it has been uncertain whether this species or an isomeric bis(μ-oxo) dicopper(III) core is the reactive species. Tolman and co-workers have shown that such bis(μ-oxo) species can perform intramolecular arene hydroxylation.[86] Moreover, Stack and co-workers investigated the oxidation of 2,4-di-tert-butylphenol by a copper-O_2 complex supported by a substituted aliphatic diamine DBED ligand.[87],[88] The interconversion of the (μ-η^2:η^2-peroxo) into an bis(μ-oxo) complexes was shown to trigger the H

atom abstraction reaction. More recently, Costas and co-workers demonstrated that a stabilized bis(μ-oxo)Cu_2^{III} species could directly achieve *o*-hydroxylation of phenol derivatives (Figure I.35).[89]

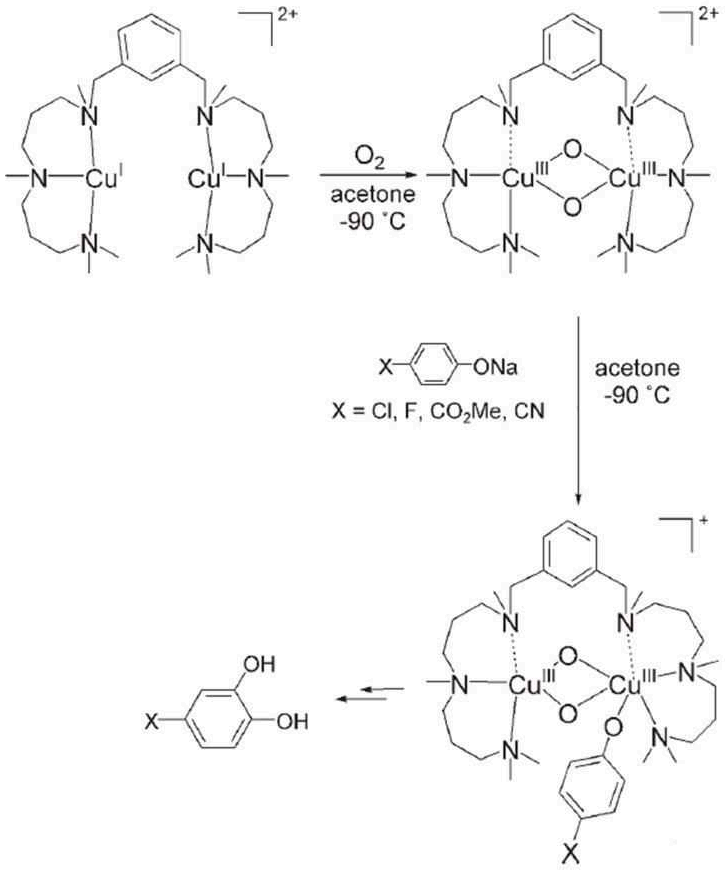

Figure I.35. Hydroxylation of phenol derivatives by a bis(μ-oxo)Cu_2^{III} complex. Reproduced from Ref. [89].

Notably, Casella and co-workers reported a tyrosinase model able to achieve the stereoselective hydroxylatation of chiral catechols.[90] The supposed reaction mechanism proceeds with a starting (hydroxo)Cu^{II} complex, which facilitates the formation of a bridged catecholate adduct. In the first step the catechol is oxidized by the dicopper(II) complex and the resulting dicopper(I) complex reacts with dioxygen; a second molecule of catechol is then oxidized by the intermediate dicopper-dioxygen species. The results showed that the L-Dopa substrate allows a disposition of the copper-bound catechol group that facilitates the electron transfer to the dicopper active species. Very recently, Herres-Pawlis described a dinucleating ligand bearing unsymmetrical N-donor moieties (Figure I.34).[84] The reaction of the dicopper(I) precursor complex with oxygen resulted in the formation of a (μ-η^2:η^2peroxo) dicopper(II) species. This peroxo adduct was shown to be the fastest catalytic system reported to date with the largest half-life at room temperature.

III.5. Biomimetic models of GO

As previously mentioned, Galactose Oxidase (GO) is a mononuclear enzyme which uses a tyrosyl radical coordinated to a copper(II) ion as an organic radical cofactor to catalyze the two electrons oxidation of primary alcohols to their corresponding aldehydes coupled to hydrogen peroxide production by dioxygen two-electron reduction.[6] This unusual biological entity has driven chemists toward the development of new synthetic systems that incorporate a Cu^{II}-phenoxyl radical unit in complexes.[91] Models were designed to reproduce the reactivity and the spectroscopic properties of the enzyme. More recently, research has focused on how asymmetry in phenolate coordination coupled to the axial/equatorial copper coordination, affects the electronic structure of this tyrosyl radical species.[92],[93]

The *o*-aminophenols are the most common class of redox active ligands that can be used to mimic the tyrosyl residue in the active site of GO. It coordinates the copper metal and three oxidation forms (aminophenol, iminosemiquinone and iminoquinone) (Figure I.36) can be considered as intermediate states of catalytic cycle in GO.

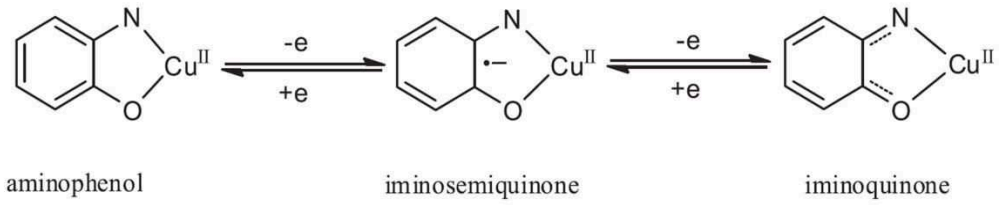

Figure I.36. Redox state of aminophenol. Reproduced from Ref. [94].

Salen-type ligands of copper(II) complexes have been widely used as model of GO active site.[91],[95] Ligands synthesis is typically operated by condensation of two equivalents of salicylaldehyde with one equivalent of diamine (Figure I.37,A), allowing the incorporation of various functional groups on the phenolate moieties and the introduction of different diamine linkers. A large number of these symmetrical and unsymmetrical complexes (Figure I.37, B) has been designed with a substituent at the *ortho*- and *para*- positions of each phenol to prevent the dimer formation by coupling phenolate units and in order to stabilize the phenoxyl radical. For instance, Stack and co-workers used a binaphthyl linker between the phenolate moieties to stabilized the phenoxyl radical with a significant tetrahedral distortion around the copper(I) ion due to the electron-donating character of the group substituent.

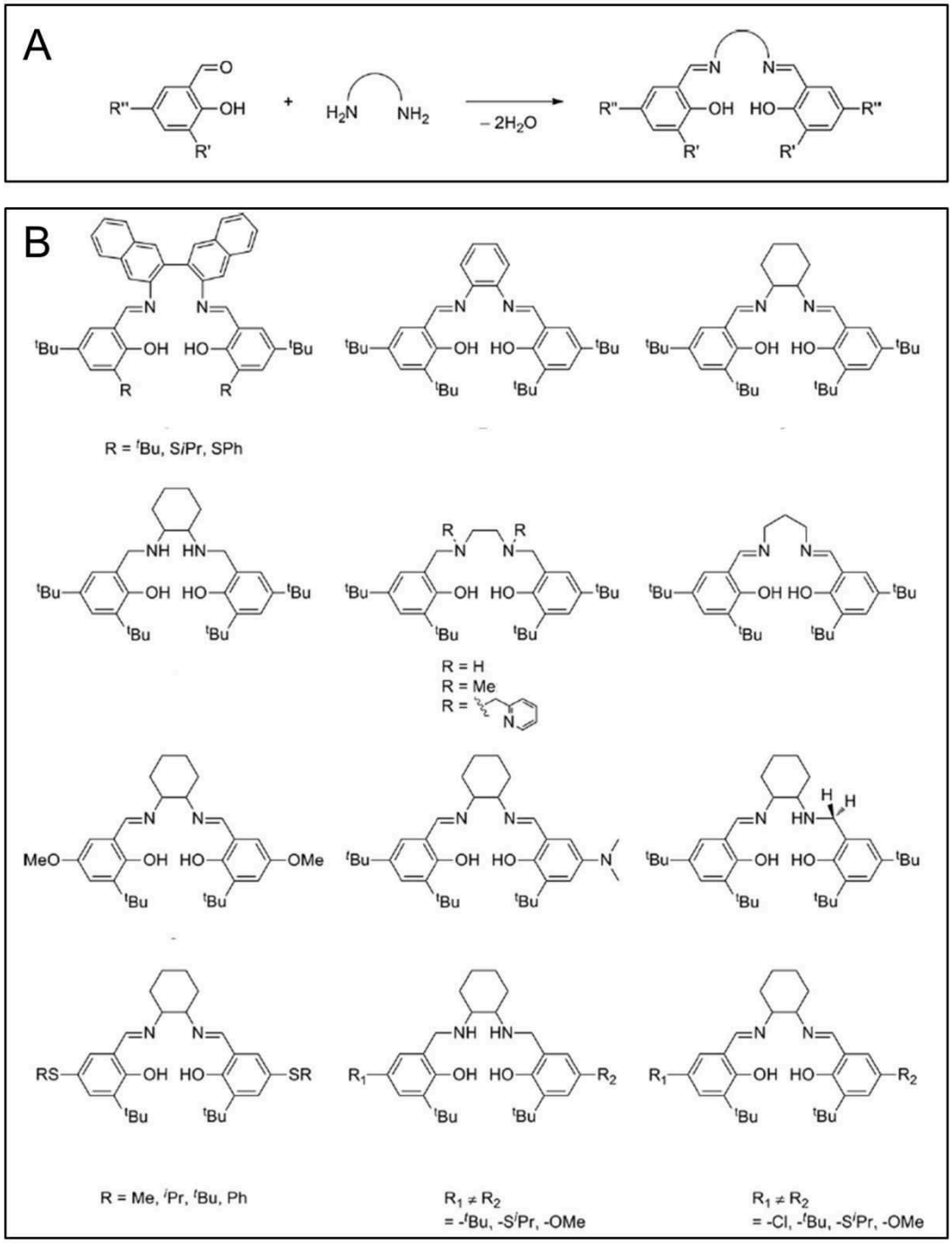

Figure I.37. Salen-based ligands designed to mimic the GO active site. Reproduced from Ref. [95].

Non-salen types of catalytically biomimetic models of GO have been also reported.[91],[96],[97] This is the case of Cu-phenoxo complexes which do not display any steric hindrance in *ortho*-position (Figure I.38). Dimeric complexes were obtained from complexation of Cu^{II} salt with ligand in the presence of a base. The two copper ions were bridged by the oxygen atoms of two phenolates. The conversion in mononuclear complex was induced by adding exogenous donor ligands as pyridine, acetate groups or protons. In some cases the chemical or electrochemical oxidation was sufficient for

the dimer-to-monomer conversion. The electrochemical behaviour of the mononuclear complexes showed an anodic, one-electron redox wave that corresponds to the oxidation of the phenolate moiety to a phenoxyl radical. The oxidation potential and the chemical stability of the Cu^{II}-phenoxyl radical complexes are correlated to the electron-donating properties of substituent in *para*-phenolate position.

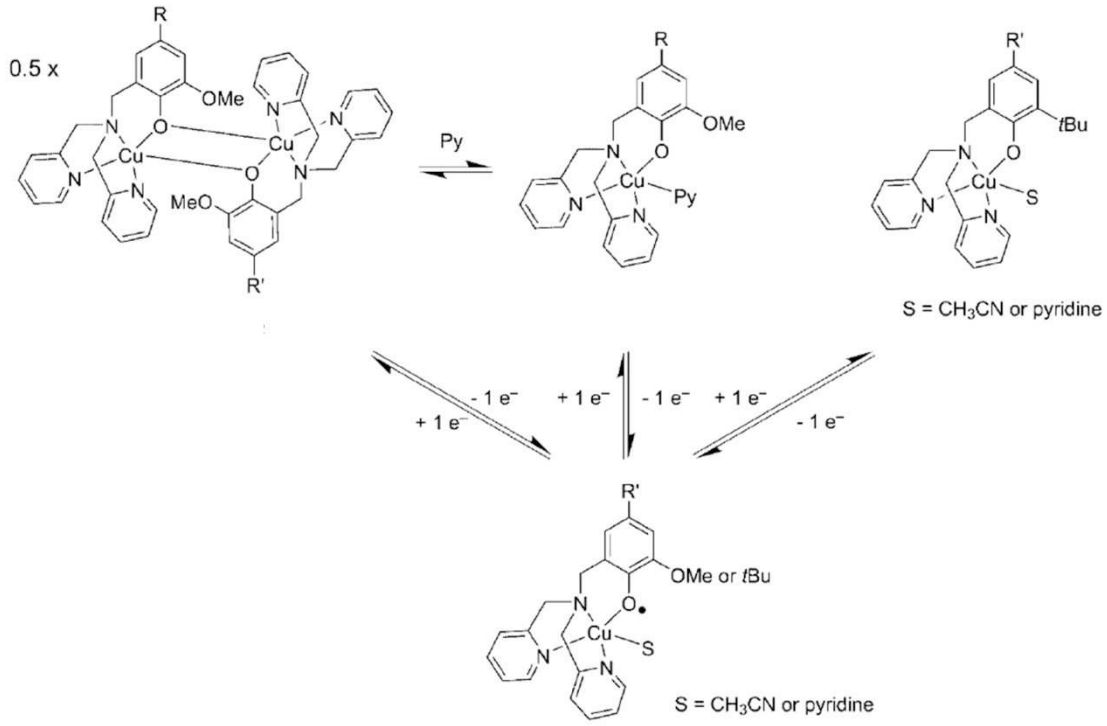

Figure I.38. Oxidative chemistry of mono-phenoxocopper complexes. Reproduced from Ref. [91].

Copper complexes bearing pyridine or bipyridine ligands were reported by several groups and the catalytic oxidation of alcohols to aldehydes has been widely described.[98],[99],[100] Recently, the synthesis of a mononuclear redox non-innocent *o*-aminophenol N_3O based ligand and its performance as efficient catalyst of benzylic alcohol oxidation were described.[94] The complete transformation of substrates has been carried in THF for 4h at room temperature. It was demonstrated that the nature of the ligand could affect the alcohol conversion.

Catalytic oxidation of alcohols using nitroxyl radicals such as TEMPO or ABNO has been also investigated, but remains less studied compared to classical systems. For instance, Stahl and co-workers have shown the redox cooperativity between Cu^{II} and TEMPO as co-catalyst for the oxidation of alcohols.[101] The authors described one of the supposed pathways involved for highly versatile and efficient benzylic and aliphatic alcohol and amine oxidation reactions (Figure I.39). Their results suggest a synergistic collaboration between copper complexes with highly efficient TEMPO units.

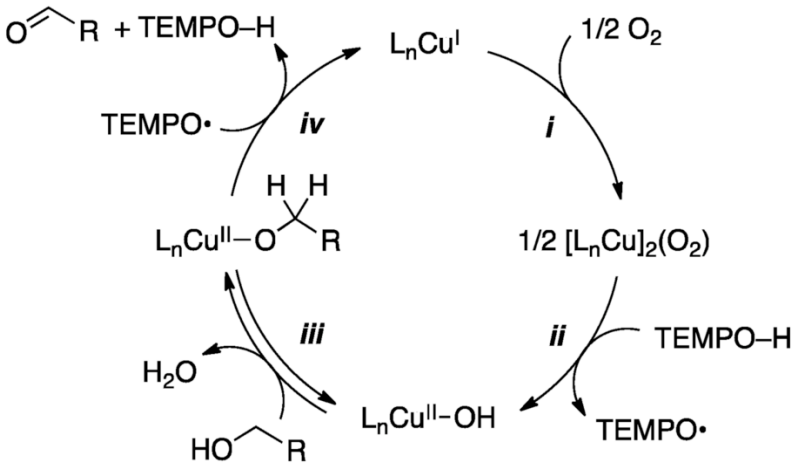

Figure I.39. Redox cooperativity with TEMPO co-catalyst. Reproduced from Ref. [101].

III.6. Nitrosoarene-based copper models of peroxo and superoxo Cu-oxygen adducts

Recent investigations have been conducted on a new class of compounds which are iso-electronic substitutes of dioxygen.[102],[103] Hence, nitrosoarene compounds can react with Cu^I complexes and form Cu-nitrosoarene species which can be considered as isoelectronic species of end-on superoxo complexes, but much more stable (Figure I.40).[104] By using a Cu^I(tren) complex, Ottenwaelder and co-workers obtained structural characterization of a couple of Cu-PhNO complexes, differentiated by their counter-ion. Magnetism measurements showed that spin state (singlet, triplet) was different depending on the counter-ion (OTf^- or SbF_6^-). Clearly, they showed that electron transfer occurred upon reaction for the OTf^- derivative, leading to the $Cu^{II}(PhNO^{\bullet-})$ species.

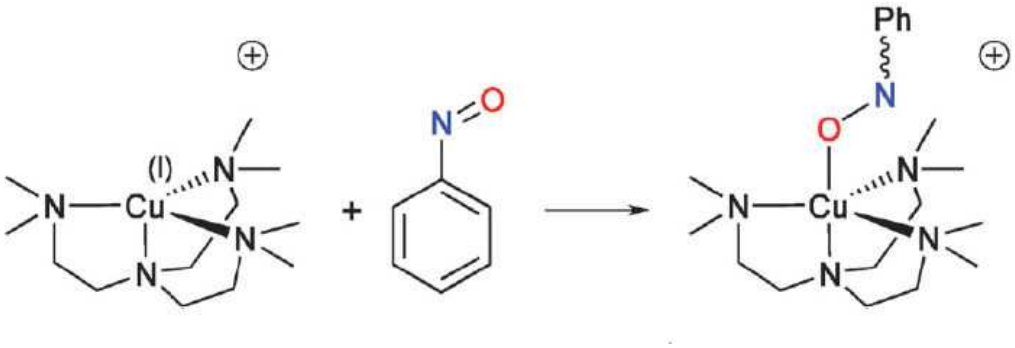

Figure I.40. Synthesis of copper-nitrosoarene complex. Reproduced from Ref. [104].

So far, no reactivity studies have been performed with copper-nitrosarene complexes. However, it has been carried out with Nickel-based analogues. Indeed, Warren and co-workers reported in 2016 the isolation of a Nickel complex bearing a PhNO unit.[105] The β-diketiminato $[Ni^{II}](\eta^2\text{-ONPh})^{\bullet/-}$

complex allowed the H-atom abstraction (HAA) of substrates and the reactivity pattern was similar to that observed for superoxide ($O_2^{\bullet-}$) and peroxide (O_2^{2-}) ligands. One-electron reduction of this $[Ni^{II}](\eta^2\text{-ONPh})^{\bullet-}$ species was ligand-centered and provided a $[Ni^{II}](\eta^2\text{-ONPh})^{2-}$ complex. Figure I.41 shows a possible reactivity pattern of the β-diketiminato $[Ni^{II}](\eta^2\text{-superoxo})$ and $([Ni^{II}](\mu\text{-}\eta^2\text{:}\eta^2\text{-peroxo}))K$ complexes. The radical $[Ni^{II}](\eta^2\text{-ONPh})^{\bullet-}$ complex undergoes H-atom abstraction of 1,4-cyclohexadiene (C-H BDE = 76 kcal mol^{-1}) at 65°C to give Ni^{II} nitroxide (η^2-ONHPh). The X-ray structure of this resulting complex revealed its square-planar geometry featuring a η^2-ONHPh nitroxide ligand with short Ni-N and N-O distances. The same complex may also prepared by protonation of the anionic $(\eta^2\text{-ONPh})^{2-}$ complex.

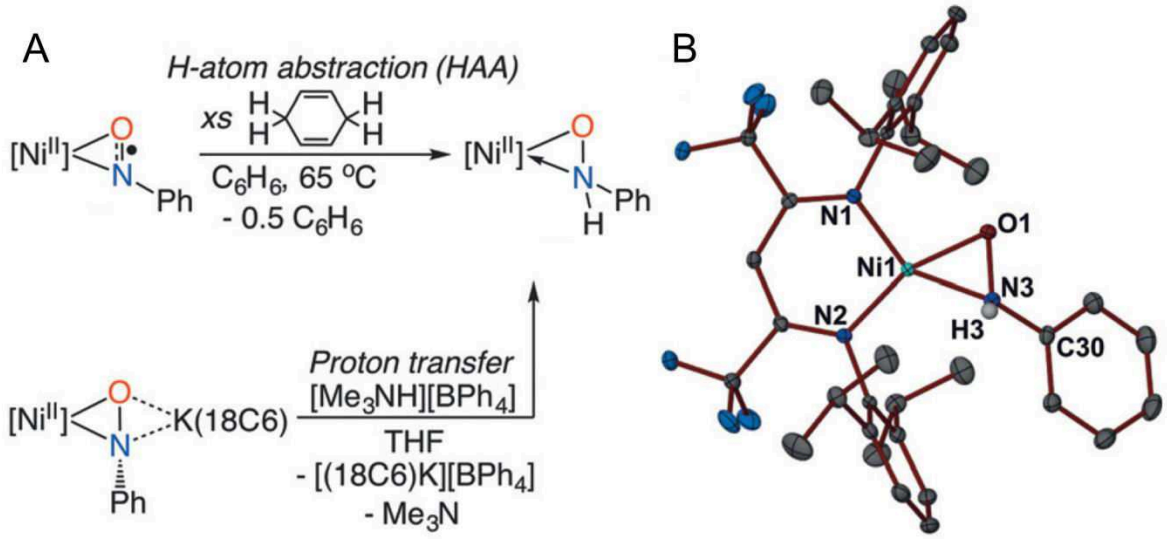

Figure I.41. A) Supposed pathway of conversion of Ni-nitrosoarene complexes via H-atom abstraction (HAA) and proton transfer (PT) routes. B) X-ray Structure of the final Ni product. Reproduced from Ref. [105].

IV. Objectives of the thesis

As shown by the short literature survey presented above, copper-oxygen adducts are involved in many essential processes. The design of bioinspired or biomimetic systems which are able to reproduce their properties remains a great challenge for the development of new devices in many areas (chemical industry, energy, medicinal chemistry…). In particular, three enzymes have focused our attention: (i) the particulate methane monoxygenase because of its high potential in being a catalyst for the mass conversion of methane into methanol, (ii) the tyrosinase/catechol oxidase for the environmental aspects of phenol/diphenol removal in polluted media, as well as the essential understanding of the role of melanin on living systems, (iii) the galactose oxidase for its ability to use a radical cofactor for the two-electron reduction of water into hydrogen peroxide, which is also of high interest in medicinal chemistry. As previously mentioned, many biomimetic systems have been developed over the last 30 years, leading to great progress in the understanding of their associated mechanisms and their specific reactivity through structural and spectroscopic (UV-Vis, Raman) characterization.

Curiously, very few are known about redox properties of copper oxygen adducts, since they are, for a vast majority, very unstable at room temperature. Recent works have shown the possibility to use chemical reagents to estimate redox potential values, but this approach does not provide direct measurement, and lack essential data such as kinetics of electron transfer. Hence the development of a cryogenic (-90°C) electrochemical and spectroelectrochemical setup was the first targeted objective of this doctoral work since there was (and still is) no commercially available equipment for such experimental conditions. Moreover, very few cryo-electrochemical and cryo-spectroelectrochemical systems have been reported so far in the literature.[106],[107],[108],[109],[110],[111],[112],[113] In particular, this doctoral work has focused on UV-Vis-NIR and EPR coupled techniques because copper-oxygen adducts display well-resolved signatures in UV-Vis spectroscopy, and unpaired electron can be detected by EPR spectroscopy.

Another objective of this doctoral work has been to characterize mixed-valent bis(μ-oxo) $Cu_2^{II,III}$ or bis(μ-OH, μ-O)$Cu_2^{II,III}$ species which were shown to be plausible active species in pMMO.[7],[41] Such characterization was not reported at the beginning of this work and only Tolman and co-workers have published very recently (2015) the spectroscopic and electrochemical features of a (μ-OH)$Cu_2^{II,III}$ complex.[81]

Two strategies can be envisaged for the preparation of the mixed-valent species. The first one ("Strategy 1" on Figures I.42 and I.43) is based on the favored reaction between dioxygen and Cu^I, as enzymes do, to allow the formation of a bis(μ-oxo)Cu^{III} species, which can further be reduced into a $Cu^{II}Cu^{III}$ species in a monoelectronic manner. This approach is attractive but needs the preparation of Cu^I species which are highly sensitive to dioxygen for most of them and can decompose very rapidly. Hence, it requires cautious manipulation of the samples under inert atmosphere.

The second approach ("Strategy 2" on Figures I.42 and I.43) starts from a (μ-hydroxo) or bis(μ-hydroxo)$Cu_2^{II,II}$ species which can be oxidized mono-electronically to produce a mixed-valent $Cu^{II}Cu^{III}$ intermediate. This strategy has the advantage to use stable precursors (i.e. not oxygen-sensitive) and leads in a one-step reaction to the mixed-valent species. Nevertheless, the question of simple or proton-coupled electron transfer (PCET) can be raised since the final mixed-valent species can be either a bis(μ-OH), a (μ-OH,μ-O), or a bis(μ-O) $Cu^{II}Cu^{III}$ complex. These three possible intermediates can indeed display different catalytic properties for C-H activation.

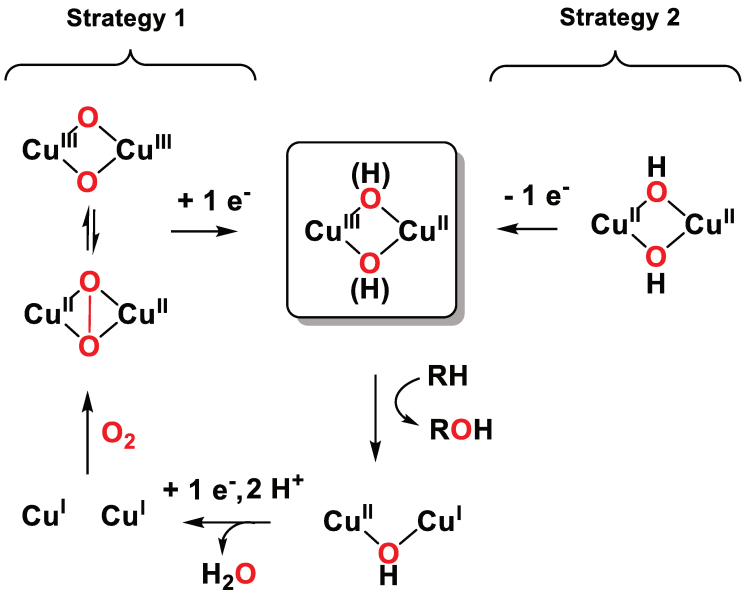

Figure I.42. Two different strategies to access a bis(μ-oxo)$Cu^{II}Cu^{III}$ species by using monoclear liagnds, and starting from mononuclear Cu^{I} (strategy 1) or bis(μ-hydroxo)$Cu_2^{II,II}$ (strategy 2) complexes.

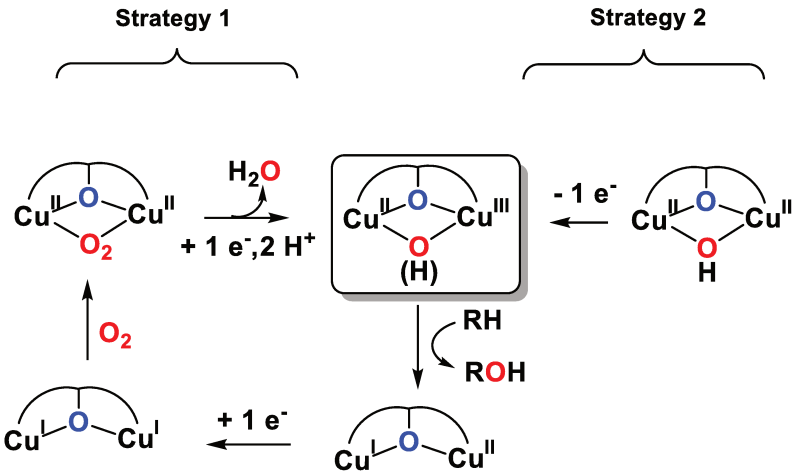

Figure I.43. Two different strategies to access a bis(μ-oxo)$Cu^{II}Cu^{III}$ species by using dinucleating bridging ligand, and starting from dinuclear Cu^{I} (strategy 1) or (μ-hydroxo)$Cu_2^{II,II}$ (strategy 2) complexes.

These two approaches can be applied to mono and dinucleating ligands. Due to the large number of possibilities to access the mixed-valent species, we have mainly limited our studies to the strategy 2 (oxidation of μ-hydroxo species) applied to bridged-dicopper complexes (Figure I.43, right). Several experiments have been conducted with mononuclear complexes using strategy 1 (Figure I.42, left), but are not reported here.

The next step has been to define the identity of (i) the ligand bridging the copper ions, as well as (ii) the ligands surrounding both copper ions on each side of the bridge. Looking at the active site of pMMO two parameters had to be considered: the short distance between the two copper ions (2.6 Å) and the coordination of the histidine units in the polypeptidic chain around the metals. For these reasons, our choice has been directed towards ligands bearing rigid spacers between two copper ions. Different bridging group were hence envisaged, depending on their redox activity (such as phenoxo) which could be at use, their flexibility and their distance to the copper ions. Figure I.44 displays the three bridges which have been used for this work: phenoxo, alkoxo and naphthyridyl. Another point of interest was to be able to design unsymmetrical ligand such that the mixed-valence state could be favored. For that purpose, and on the basis of previous works, we have envisaged polypyridyl ligands in order to stabilize the Cu^{II} redox state, and polyamidate ligands to favor Cu^{III} redox state (Figure I.44). Of course, for full comparison, symmetrical complexes have been synthesized.

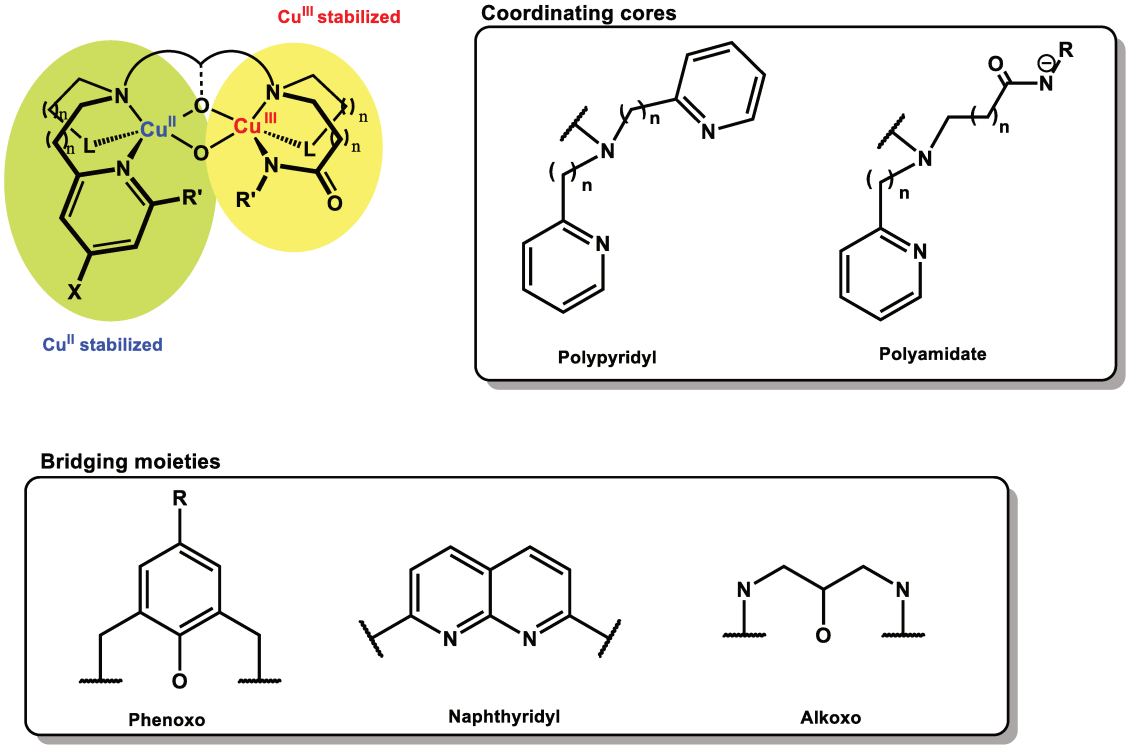

Figure I.44. Bridging and coordinating moieties designed to access the bis(μ-oxo)$Cu^{II}Cu^{III}$ mixed-valent species.

Due the large scope of this work, all syntheses of ligands and copper complexes related in this manuscript have been performed by collaborating teams in Marseille (Dr M. Réglier, Dr J. Simaan) and Grenoble (Dr C. Belle, Dr. A Thibon-Pourret). Theoretical calculations have been computed by Dr. H. Jamet (Grenoble) and Dr. A. Kochem (Marseille).

This manuscript thus reports the room- and low-temperature electrochemical and spectroelectrochemical studies of the different copper complexes described above. These characterizations were possible thanks to a new set up of spectroelectrochemical equipments developed in parallel during this research work.

BIBLIOGRAPHY

[1] W. B. Tolman, *J. Biol. Inorg. Chem.* **2006**, *11*, 261-271.
[2] C. F. Bucholz, *Repert. Pharm.* **1816**, *2*, 253.
[3] W. Meissner, *Deutsch. Jahrb. Pharm.* **1817**, *18*, 19.
[4] C. A. Elvehjem, W. Lindow, *J Biol. Chem.* **1929**, *81*, 435.
[5] J. S. McHargue, *Am. J. Physiol* **1925**, *72*, 538.
[6] A. Messerschmidt, R. Huber, T. Poulas, K. Wieghardt, *Handbook of metalloproteins*, **2006**.
[7] E. I. Solomon, D. E. Heppner, E. M. Johnston, J. W. Ginsbach, J. Cirera, M. Qayyum, M. T. Kieber-Emmons, C. H. Kjaergaard, R. G. Hadt, L. Tian, *Chem. Rev.* **2014**, *114*, 3659-3853.
[8] A. Walli, S. Dechert, M. Bauer, S. Demeshko, F. Meyer, *Eur. J. Inorg. Chem.* **2014**, *2014*, 4660-4676.
[9] S. T. Prigge, B. A. Eipper, R. E. Mains, L. M. Amzel, *Science* **2004**, *304*, 864-867.
[10] J. P. Bacik, S. Mekasha, Z. Forsberg, A. Y. Kovalevsky, G. Vaaje-Kolstad, V. G. H. Eijsink, J. C. Nix, L. Coates, M. J. Cuneo, C. J. Unkefer, J. C. Chen, *Biochemistry* **2017**, *56*, 2529-2532.
[11] K. A. Magnus, B. Hazes, H. Ton-That, C. Bonaventura, J. Bonaventura, W. G. Hol, *Proteins* **1994**, *19*, 302-309.
[12] K. A. Magnus, H. Ton-That, J. E. Carpenter, *Chem. Rev.* **1994**, *94*, 727-735.
[13] N. Kitajima, K. Fujisawa, Y. Morooka, K. Toriumi, *J. Am. Chem. Soc.* **1989**, *111*, 8975-8976.
[14] Y. Matoba, T. Kumagai, A. Yamamoto, H. Yoshitsu, M. Sugiyama, *J. Biol. Chem.* **2006**, *281*, 8981-8990.
[15] Y. Li, Y. Wang, H. Jiang, J. Deng, *Proc. Natl. Acad. Sci. USA* **2009**, *106*, 17002-17006.
[16] E. A. Lewis, W. B. Tolman, *Chem. Rev.* **2004**, *104*, 1047-1076.
[17] L. M. Mirica, X. Ottenwaelder, T. D. Stack, *Chem. Rev.* **2004**, *104*, 1013-1045.
[18] C. E. Elwell, N. L. Gagnon, B. D. Neisen, D. Dhar, A. D. Spaeth, G. M. Yee, W. B. Tolman, *Chem. Rev.* **2017**, *117*, 2059-2107.
[19] J. Y. Lee, K. D. Karlin, *Curr. Opin. Chem. Biol.* **2015**, *25*, 184-193.
[20] T. J. Lawton, A. C. Rosenzweig, *J. Am. Chem. Soc.* **2016**, *138*, 9327-9340.
[21] S. E. Allen, R. R. Walvoord, R. Padilla-Salinas, M. C. Kozlowski, *Chem. Rev.* **2013**, *113*, 6234-6458.
[22] X. W. Liu, W. W. Li, H. Q. Yu, *Chem. Soc. Rev.* **2014**, *43*, 7718-7745.
[23] X. Wang, X. Lu, L. Wu, J. Chen, *ChemElectroChem* **2014**, *1*, 808-816.
[24] K. R. Rogers, J. Y. Becker, J. Cembrano, *Electrochim. Acta* **2000**, *45*, 4373-4379.
[25] M. Florescu, M. David, *Sensors* **2017**, *17*.
[26] L. Wu, D. Deng, J. Jin, X. Lu, J. Chen, *Biosens. Bioelectron.* **2012**, *35*, 193-199.
[27] S. Tembe, M. Karve, S. Inamdar, S. Haram, J. Melo, S. F. D'Souza, *Anal. Biochem.* **2006**, *349*, 72-77.
[28] F. Bedioui, D. Quinton, S. Griveau, T. Nyokong, *Phys. Chem. Chem. Phys.* **2010**, *12*, 9976-9988.
[29] Y. Tian, L. Mao, T. Okajima, T. Ohsaka, *Anal. Chem.* **2004**, *76*, 4162-4168.
[30] J. Di, S. Bi, M. Zhang, *Biosens. Bioelectron.* **2004**, *19*, 1479-1486.
[31] X. Zhu, T. Liu, H. Zhao, L. Shi, X. Li, M. Lan, *Biosens. Bioelectron.* **2016**, *79*, 449-456.
[32] R. L. Lieberman, A. C. Rosenzweig, *Nature* **2005**, *434*, 177-182.
[33] A. S. Hakemian, K. C. Kondapalli, J. Telser, B. M. Hoffman, T. L. Stemmler, A. C. Rosenzweig, *Biochemistry* **2008**, *47*, 6793-6801.
[34] S. M. Smith, S. Rawat, J. Telser, B. M. Hoffman, T. L. Stemmler, A. C. Rosenzweig, *Biochemistry* **2011**, *50*, 10231-10240.
[35] S. Sirajuddin, A. C. Rosenzweig, *Biochemistry* **2015**, *54*, 2283-2294.
[36] R. Balasubramanian, A. C. Rosenzweig, *Acc. Chem. Res.* **2007**, *40*, 573-580.
[37] S. I. Chan, V. C. Wang, J. C. Lai, S. S. Yu, P. P. Chen, K. H. Chen, C. L. Chen, M. K. Chan, *Angew. Chem. Int. Ed. Engl.* **2007**, *46*, 1992-1994.

[38] V. C. Wang, S. Maji, P. P. Chen, H. K. Lee, S. S. Yu, S. I. Chan, *Chem. Rev.* **2017**, *117*, 8574-8621.
[39] S. Maji, J. C. M. Lee, Y.-J. Lu, C.-L. Chen, M.-C. Hung, P. P. Y. Chen, S. S. F. Yu, S. I. Chan, *Chem. Eur. J.* **2012**, *18*, 3955-3968.
[40] P. P. Y. Chen, S. I. Chan, *J. Inorg. Biochem.* **2006**, *100*, 801-809.
[41] Y. Shiota, K. Yoshizawa, *Inorg. Chem.* **2009**, *48*, 838-845.
[42] E. Solem, F. Tuczek, H. Decker, *Angew. Chem. Int. Ed. Engl.* **2016**, *55*, 2884-2888.
[43] M. Rolff, J. Schottenheim, H. Decker, F. Tuczek, *Chem. Soc. Rev.* **2011**, *40*, 4077-4098.
[44] T. Klabunde, C. Eicken, J. C. Sacchettini, B. Krebs, *Nat. Struct. Biol.* **1998**, *5*, 1084-1090.
[45] Y. Matoba, T. Kumagai, A. Yamamoto, H. Yoshitsu, M. Sugiyama, *J. Biol. Chem.* **2006**, *281*, 8981-8990.
[46] I. A. Koval, P. Gamez, C. Belle, K. Selmeczi, J. Reedijk, *Chem. Soc. Rev.* **2006**, *35*, 814-840.
[47] T. Klabunde, C. Eicken, J. C. Sacchettini, B. Krebs, *Nat. Struct. Biol.* **1998**, *5*, 1084-1090.
[48] B. Salvato, M. Santamaria, M. Beltramini, G. Alzuet, L. Casella, *Biochemistry* **1998**, *37*, 14065-14077.
[49] M. S. Rogers, E. M. Tyler, N. Akyumani, C. R. Kurtis, R. K. Spooner, S. E. Deacon, S. Tamber, S. J. Firbank, K. Mahmoud, P. F. Knowles, S. E. V. Phillips, M. J. McPherson, D. M. Dooley, *Biochemistry* **2007**, *46*, 4606-4618.
[50] N. Ito, S. E. Phillips, C. Stevens, Z. B. Ogel, M. J. McPherson, J. N. Keen, K. D. Yadav, P. F. Knowles, *Nature* **1991**, *350*, 87-90.
[51] P. Chaudhuri, M. Hess, U. Flörke, K. Wieghardt, *Angew. Chem. Int. Ed. Engl.* **1998**, *37*, 2217-2220.
[52] Y. Wang, T. D. P. Stack, *J. Am. Chem. Soc.* **1996**, *118*, 13097-13098.
[53] L. Q. Hatcher, K. D. Karlin, *J. Biol. Inorg. Chem.* **2004**, *9*, 669-683.
[54] R. A. Himes, K. D. Karlin, *Curr. Opin. Chem. Biol.* **2009**, *13*, 119-131.
[55] W. Keown, J. B. Gary, T. D. P. Stack, *J. Biol. Inorg. Chem.* **2017**, *22*, 289-305.
[56] S. Trofimenko, *Chem. Rev.* **1993**, *93*, 943-980.
[57] D. J. Spencer, A. M. Reynolds, P. L. Holland, B. A. Jazdzewski, C. Duboc-Toia, L. Le Pape, S. Yokota, Y. Tachi, S. Itoh, W. B. Tolman, *Inorg. Chem.* **2002**, *41*, 6307-6321.
[58] K. D. Karlin, S. Itoh, *Copper Oxygen Chemistry*, **2011,** Eds Wiley.
[59] T. Osako, S. Terada, T. Tosha, S. Nagatomo, H. Furutachi, S. Fujinami, T. Kitagawa, M. Suzuki, S. Itoh, *Dalton Trans.* **2005**, 3514-3521.
[60] C. Citek, B. L. Lin, T. E. Phelps, E. C. Wasinger, T. D. Stack, *J. Am. Chem. Soc.* **2014**.
[61] M. T. Kieber-Emmons, J. W. Ginsbach, P. K. Wick, H. R. Lucas, M. E. Helton, B. Lucchese, M. Suzuki, A. D. Zuberbühler, K. D. Karlin, E. I. Solomon, *Angew. Chem. Int. Ed. Engl.* **2014**, *53*, 4935-4939.
[62] T. Fujii, A. Naito, S. Yamaguchi, A. Wada, Y. Funahashi, K. Jitsukawa, S. Nagatomo, T. Kitagawa, H. Masuda, *Chem. Commun.* **2003**, 2700.
[63] D. Maiti, H. R. Lucas, A. A. Sarjeant, K. D. Karlin, *J. Am. Chem. Soc.* **2007**, *129*, 6998-6999.
[64] D. Maiti, A. A. Sarjeant, K. D. Karlin, *J. Am. Chem. Soc.* **2007**, *129*, 6720-6721.
[65] L. Li, A. A. Sarjeant, K. D. Karlin, *Inorg. Chem.* **2006**, *45*, 7160-7172.
[66] K. Itoh, H. Hayashi, H. Furutachi, T. Matsumoto, S. Nagatomo, T. Tosha, S. Terada, S. Fujinami, M. Suzuki, T. Kitagawa, *J. Am. Chem. Soc.* **2005**, *127*, 5212-5223.
[67] N. Gagnon, W. B. Tolman, *Acc. Chem. Res.* **2015**, *48*, 2126-2131.
[68] S. Hong, S. M. Huber, L. Gagliardi, C. C. Cramer, W. B. Tolman, *J. Am. Chem. Soc.* **2007**, *129*, 14190-14192.
[69] D. Maiti, D. H. Lee, K. Gaoutchenova, C. Wurtele, M. C. Holthausen, A. A. Sarjeant, J. Sundermeyer, S. Schindler, K. D. Karlin, *Angew. Chem. Int. Ed. Engl.* **2008**, *47*, 82-85.
[70] S. Kim, J. Y. Lee, R. E. Cowley, J. W. Ginsbach, M. A. Siegler, E. I. Solomon, K. D. Karlin, *J. Am. Chem. Soc.* **2015**, *137*, 2796-2799.
[71] J. Y. Lee, R. L. Peterson, K. Ohkubo, I. Garcia-Bosch, R. A. Himes, J. Woertink, C. D. Moore, E. I. Solomon, S. Fukuzumi, K. D. Karlin, *J. Am. Chem. Soc.* **2014**, *136*, 9925-9937.
[72] R. L. Peterson, R. A. Himes, H. Kotani, T. Suenobu, L. Tian, M. A. Siegler, E. I. Solomon, S. Fukuzumi, K. D. Karlin, *J. Am. Chem. Soc.* **2011**, *133*, 1702-1705.

[73] A. Kunishita, M. Kubo, H. Sugimoto, T. Ogura, K. Sato, T. Takui, S. Itoh, *J. Am. Chem. Soc.* **2009**, *131*, 2788-2789.
[74] D. Maiti, H. C. Fry, J. S. Woertink, M. A. Vance, E. I. Solomon, K. D. Karlin, *J. Am. Chem. Soc.* **2007**, *129*, 264-265.
[75] G. De Leener, D. Over, C. Smet, D. Cornut, A. G. Porras-Gutierrez, I. Lopez, B. Douziech, N. Le Poul, F. Topic, K. Rissanen, Y. Le Mest, I. Jabin, O. Reinaud, *Inorg. Chem.* **2017**, *56*, 10971-10983.
[76] C. Citek, S. Herres-Pawlis, T. D. Stack, *Acc. Chem. Res.* **2015**, *48*, 2424-2433.
[77] A. P. Cole, D. E. Root, P. Mukherjee, E. I. Solomon, T. D. P. Stack, *Science* **1996**, *273*, 1848-1850.
[78] M. Taki, S. Teramae, S. Nagatomo, Y. Tachi, T. Kitagawa, S. Itoh, S. Fukuzumi, *J. Am. Chem. Soc.* **2002**, *124*, 6367-6377.
[79] P. P. Chen, R. B. Yang, J. C. Lee, S. I. Chan, *Proc. Natl. Acad. Sci. USA* **2007**, *104*, 14570-14575.
[80] I. Blain, M. Giorgi, I. De Riggi, M. Réglier, *Eur. J. Inorg. Chem.* **2000**, *2000*, 393-398.
[81] M. R. Halvagar, P. V. Solntsev, H. Lim, B. Hedman, K. O. Hodgson, E. I. Solomon, C. J. Cramer, W. B. Tolman, *J. Am. Chem. Soc.* **2014**, *136*, 7269-7272.
[82] J. S. Woertink, P. J. Smeets, M. H. Groothaert, M. A. Vance, B. F. Sels, R. A. Schoonheydt, E. I. Solomon, *Proc. Natl. Acad. Sci. USA* **2009**, *106*, 18908-18913.
[83] P. Vanelderen, B. E. Snyder, M. L. Tsai, R. G. Hadt, J. Vancauwenbergh, O. Coussens, R. A. Schoonheydt, B. F. Sels, E. I. Solomon, *J. Am. Chem. Soc.* **2015**, *137*, 6383-6392.
[84] P. Liebhauser, K. Keisers, A. Hoffmann, T. Schnappinger, I. Sommer, A. Thoma, C. Wilfer, R. Schoch, K. Stuhrenberg, M. Bauer, M. Durr, I. Ivanovic-Burmazovic, S. Herres-Pawlis, *Chem. Eur. J.* **2017**, *23*, 12171-12183.
[85] M. Reglier, C. Jorand, B. Waegell, *J. Chem. Soc., Chem. Commun.* **1990**, 1752-1755.
[86] S. Mahapatra, S. Kaderli, A. Llobet, Y.-M. Neuhold, T. Palanché, J. A. Halfen, V. G. Young, T. A. Kaden, L. Que, A. D. Zuberbühler, W. B. Tolman, *Inorg. Chem.* **1997**, *36*, 6343-6356.
[87] L. M. Mirica, M. Vance, D. J. Rudd, B. Hedman, K. O. Hodgson, E. I. Solomon, T. D. P. Stack, *Science* **2005**, *308*, 1890-1892.
[88] L. M. Mirica, D. J. Rudd, M. A. Vance, E. I. Solomon, K. O. Hodgson, B. Hedman, T. D. Stack, *J. Am. Chem. Soc.* **2006**, *128*, 2654-2665.
[89] A. Company, S. Palavicini, I. Garcia-Bosch, R. Mas-Balleste, L. Que, E. V. Rybak-Akimova, L. Casella, X. Ribas, M. Costas, *Chem. Eur. J.* **2008**, *14*, 3535-3538.
[90] M. L. Perrone, E. Lo Presti, S. Dell'Acqua, E. Monzani, L. Santagostini, L. Casella, *Eur. J. Inorg. Chem.* **2015**, *21*, 3493-3500.
[91] F. Thomas, *Eur. J. Inorg. Chem.* **2007**, *2007*, 2379-2404.
[92] P. Verma, R. C. Pratt, T. Storr, E. C. Wasinger, T. D. Stack, *Proc. Natl. Acad. Sci. USA* **2011**, *108*, 18600-18605.
[93] R. C. Pratt, C. T. Lyons, E. C. Wasinger, T. D. Stack, *J. Am. Chem. Soc.* **2012**, *134*, 7367-7377.
[94] E. Safaei, H. Bahrami, A. Pevec, B. Kozlevčar, Z. Jagličić, *J. Mol. Struct.* **2017**, *1133*, 526-533.
[95] C. T. Lyons, T. D. P. Stack, *Coord. Chem. Rev.* **2013**, *257*, 528-540.
[96] Z. Alaji, E. Safaei, L. Chiang, R. M. Clarke, C. Mu, T. Storr, *Eur. J. Inorg. Chem.* **2014**, *2014*, 6066-6074.
[97] S. E. Balaghi, E. Safaei, L. Chiang, E. W. Wong, D. Savard, R. M. Clarke, T. Storr, *Dalton Trans.* **2013**, *42*, 6829-6839.
[98] J. A. Halfen, V. G. Young, W. B. Tolman, *Angew. Chem. Int. Ed. Eng.* **1996**, *35*, 1687-1690.
[99] J. A. Halfen, B. A. Jazdzewski, S. Mahapatra, L. M. Berreau, E. C. Wilkinson, L. Que, W. B. Tolman, *J. Am. Chem. Soc.* **1997**, *119*, 8217-8227.
[100] P. Gamez, I. W. C. E. Arends, J. Reedijk, R. A. Sheldon, *Chem. Commun.* **2003**, 2414-2415.
[101] S. D. McCann, S. S. Stahl, *Acc. Chem. Res.* **2015**, *48*, 1756-1766.
[102] M. R. Kumar, A. Zapata, A. J. Ramirez, S. K. Bowen, W. A. Francisco, P. J. Farmer, *Proc. Natl. Acad. Sci. USA* **2011**, *108*, 18926-18931.

[103] R. S. Srivastava, N. R. Tarver, K. M. Nicholas, *J*. *Am*. *Chem*. *Soc*. **2007**, *129*, 15250-15258.
[104] M. S. Askari, B. Girard, M. Murugesu, X. Ottenwaelder, *Chem*. *Commun*. **2011**, *47*, 8055-8057.
[105] S. Kundu, S. C. Stieber, M. G. Ferrier, S. A. Kozimor, J. A. Bertke, T. H. Warren, *Angew*. *Chem*. *Int*. *Ed*. *Engl*. **2016**, *55*, 10321-10325.
[106] R. P. Van Duyne, C. N. Reilley, *Anal*. *Chem*. **1972**, *44*, 142-152.
[107] J. T. McDevitt, S. Ching, M. Sullivan, R. W. Murray, *J*. *Am*. *Chem*. *Soc*. **1989**, *111*, 4528-4529.
[108] A. M. Bond, D. A. Sweigart, *Inorg*. *Chim*. *Acta* **1986**, *123*, 167-173.
[109] N. Le Poul, S. J. Green, Y. Le Mest, *J*. *Electroanal*. *Chem*. **2006**, *596*, 47-56.
[110] R. Baron, N. M. Kershaw, T. J. Donohoe, R. G. Compton, *J*. *Phys*. *Org*. *Chem*. **2009**, *22*, 1136-1141.
[111] F. Hartl, H. Luyten, H. A. Nieuwenhuis, G. C. Schoemaker, *Appl*. *Spectr*. *Rev*. **1994**, *48*, 1522-1528.
[112] M. Górski, F. Hartl, T. Szymańska-Buzar, *Organometallics* **2007**, *26*, 4066-4071.
[113] F. Gaillard, E. Levillain, *J*. *Electroanal*. *Chem*. **1995**, *398*, 77-87.

Chapter II

Phenoxo-bridged polypyridyl dicopper complexes

I. Introduction

As defined in Chapter I, this doctoral work aims at characterizing mixed-valent bis(μ-oxo)$Cu_2^{II,III}$ or bis(μ-OH, μ-O)$Cu_2^{II,III}$ species which have been suggested as being the active species which oxidizes methane into methanol in pMMO.[1],[2] The strategy that we have chosen, is based on the mono-electronic oxidation of a stable (μ-hydroxo) or bis(μ-hydroxo)$Cu_2^{II,II}$ species to produce a mixed-valent $Cu^{II}Cu^{III}$ intermediate. According to the structural features of the active site of pMMO,[2] the optimal dinucleating ligand should lead to a 2.6 Å Cu-Cu distance when complexed, allowing μ-OH and μ-O bridging. As a first example described in this chapter, we have focused on the specific family of phenoxo-bridged polypyridyl ligands which have been largely investigated and characterized in the last thirty years.[3]

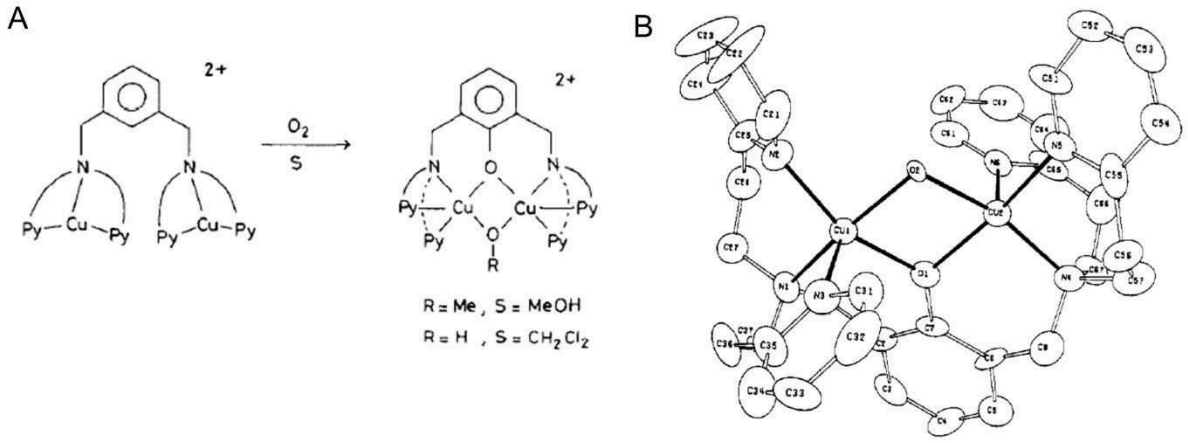

Figure II.1. A) Synthesis of the first phenoxo-bridged dicopper complex from a xylyl (NPy_2) ligand by reaction with dioxygen. B) X-ray structure of the resulting phenoxo-μ(OH) dicopper(II) complex. Reproduced from Refs. [4] and [5], respectively.

Dicopper complexes bearing both phenoxo and hydroxo bridged were initially developed and studied by Karlin and co-workers as resulting from the intramolecular oxidation of the bridging xylyl ligand by a Cu_2:O_2 (μ-η^2-η^2-peroxo) species (Figure II.1).[4],[5] The dinucleating ligand displayed the remarkable property to constrain the Cu ions at a define distance one from each other through the phenoxo linker. Moreover, the presence of a hydroxo moiety was suggested to have a beneficial effect for the deprotonation of diphenol (catechol).[5] The reaction of the bis(μ-phenoxo, μ-hydoxo) complex with H_2O_2 led to a μ-phenoxo, μ-hydroperoxo species[6] which was further shown to be a precursor for oxidation of nitriles.[7] In this family of complexes, most of investigations have been dedicated to dinucleating ligands bearing polyaza groups.[5],[8],[9],[10],[11],[12],[13],[14],[15],[16],[17],[18],[19],[20] Figure II.2 displays selected examples of phenoxo-based bis(μ-oxo) or bis(μ-methoxo) dicopper complexes with significant contributions from both groups of Karlin and Belle. Polypyridyl coordinating cores such as

DPA (2,2'-dipicolylamine) have been particularly used to mimic the first coordination sphere in the enzyme active site. The pKa and coordinating properties of pyridyl moieties are indeed close to those of imidazole groups present in the amino acid histidine residues of the protein. Different substituting moieties were also grafted on the phenoxo bridge in order to modify the reactive properties towards specific substrates.

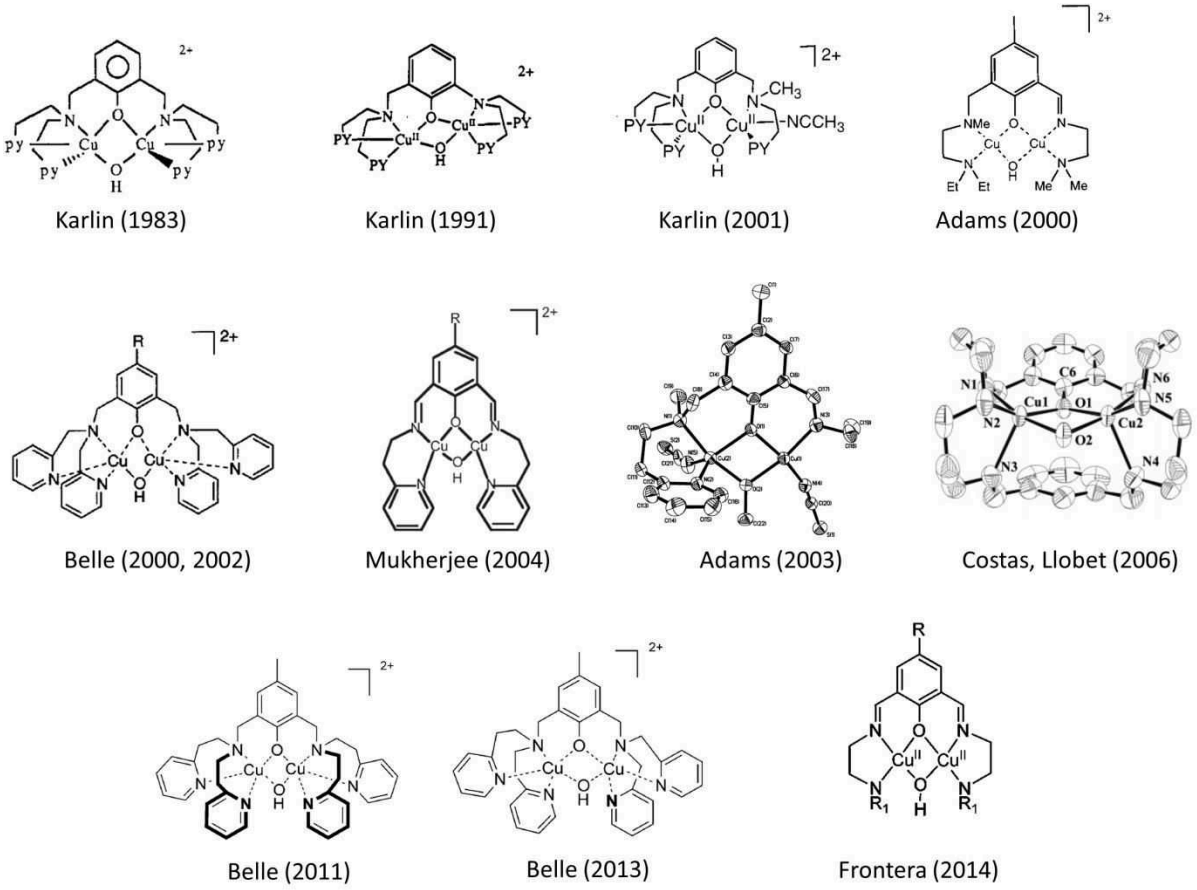

Figure II.2. Selected examples (μ-phenoxo) (μ-OH) dicopper complexes. [4],[8],[9],[10],[11],[12],[13],[14],[15],[17],[18],[19],[20]

Most of these complexes have been designed in order to mimic the active site type III copper proteins, catechol oxidase and tyrosinase. One main reason is that the structural pattern of the complexes (μ-OH bridge between two copper(II) ions) reproduces the met form of these enzymes. Various coordination modes of coordination of catechol substrates to the Cu ions (monodentate/ bidentate, bridging/not bridging) have been evidenced.[11],[21] Figure II.3 displays one reactive pathway proposed by Frontera and co-workers for the catalytic oxidation of catechol by μ-OH phenoxo-dicopper complexes supported by DFT calculations.[17] The authors suggested from their results two consecutive one-electron transfer reactions with formation of a mixed-valent $Cu^{I}Cu^{II}$ intermediate (B′ on Figure II.3). The catalytic cycle ends up with the reaction of a (μ-η^2:η^2 peroxo) species (D) with

the catechol giving E. An alternative pathway has also been proposed by Mukherjee and co-workers for the regeneration of the (μ-OH) initial species (A).[16]

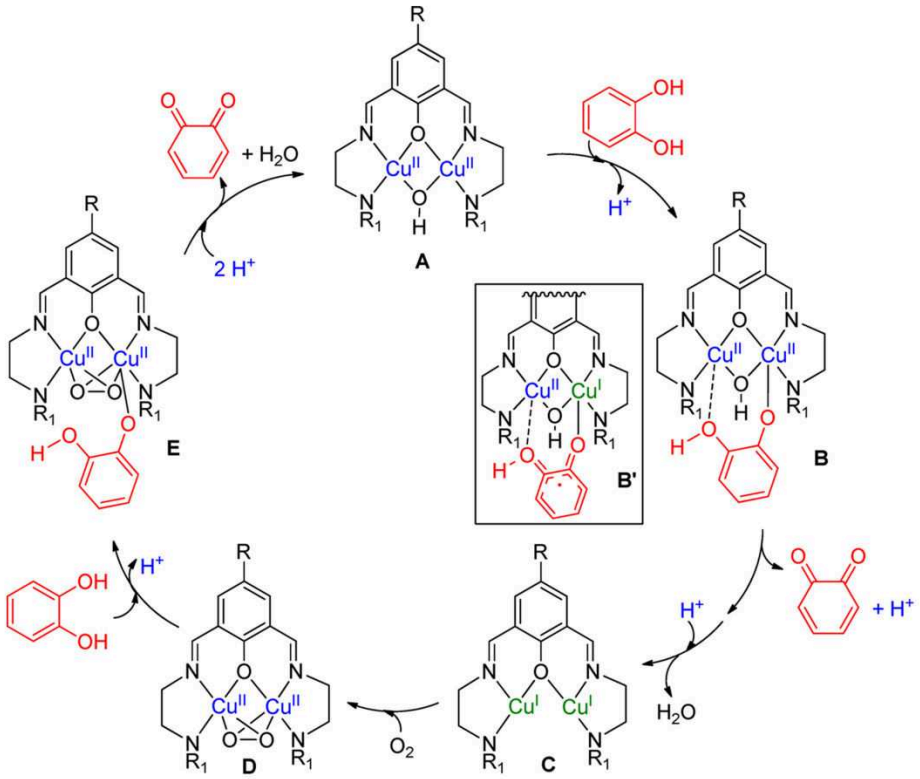

Figure II.3. Mechanistic pathway for the catalytic oxidation of catechol by a (μ-phenoxo) (μ-OH) dicopper complex. Reproduced from Ref. [17].

So far, few studies have reported unsymmetrical dinuclear models of copper oxidases despite the good evidence for the non-equivalence of copper sites in some proteins.[22],[23],[24] Recent structural resolutions of metalloproteins have emphasized that the dissymmetry of the active-site, allowing different geometries, is essential to perform their functionality.[2] Unsymmetry in phenoxo-bridged dicopper complexes has been achieved either by tuning the length of the linker that separates the phenoxo bridge and the coordinating groups, or by differentiating the coordinating cores around copper ions. In 1991, Karlin and co-workers designed an unsymmetrical dicopper complex displaying a coordinating core directly attached to the phenoxo group by the N atom of the tertiary amine (Figure II.2, top).[20] This system was originally designed for modelling monooxygenase activity. A similar unsymmetrical complex was reported by the same team in 2001 (Figure II.2).[19] Adams and co-workers developed unsymmetrical ligands bearing a picolyl-imine group on one side and a diamine core on the other side (Figure II.2). Belle and co-workers extensively developed symmetrical ligands with bis(2-pyridylmethyl)amine (BPMP)[9],[10],[11] and bis(2-pyridylethyl)amine (BPEP)[14] entities, as well as an unsymmetrical dinucleating ligand (BPMEP[15]: bis(2-pyridylmethylethyl)amine) (Figures

II.2 and II.4). For the corresponding copper complexes, EPR spectra were silent due to the antiferromagnetic coupling of the unpaired electrons localized on each Cu. Interestingly, UV-vis spectroscopic characterization at -40°C of the oxidized methoxy-substituted BPMP dicopper complex after exhaustive electrolysis evidenced the formation of phenoxyl radical. X-band EPR studies (T = 4K) of the μ-hydroxo methoxy complex showed a dominating S_{Cu} = 1/2 signal (attributed to a degraded complex containing non interacting copper(II) nuclei) at g = 2.[25] Electrochemical studies of the differently R-substituted μ-hydroxo BPMP-based dicopper complexes in acetonitrile at room temperature suggested two sequential reduction processes on each copper center and one oxidation process ascribed to the phenoxo bridge. However, for the BPEP and BPMEP complexes, no voltammetric studies were performed so far.

From this literature basis, our studies have been motivated by the following objectives:

(i) Investigating the effect of the different topologies on the redox properties in both oxidation and reduction of the family of copper complexes shown in Figure II.4: substituent effects, flexibility and unsymmetry. A main goal is to analyze how / if it is possible to promote a mixed valence $Cu^{III}Cu^{II}$ state vs phenoxyl form by oxidation. To this end, correlating experimental results with theoretical data is indeed necessary for the development of a reliable calculation method which can give access to theoretical redox potential, spectroscopic features and charge density mapping for analogous complexes.

(ii) Exploring the oxidation properties towards external substrates of the *in-situ* generated oxidized complexes. More specifically, it is well known that oxidation of a phenoxo moiety lead to a phenoxyl radical which can further perform benzyl alcohol oxidation or DNA cleavage. If one excepts the dinuclear reported by Mukherjee and co-workers (which dissociates upon oxidation),[26] there is no example of dinuclear model of galactose oxidase.[27],[28],[29],[30] One probable reason is that the active site of galactose oxidase contains one single copper ion, and chemists have felt no need to add a supplementary metal ion, even for structural reasons.

This work has required the development of new electrochemical and spectroelectrochemical devices for the determination of the redox properties of the intermediate species.

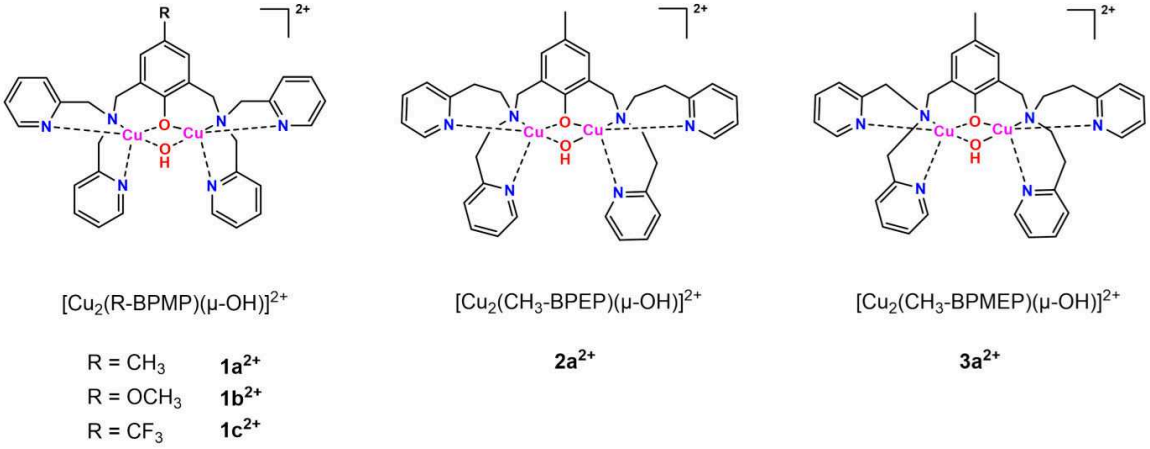

Figure II.4. Schematic representation of the studied phenoxo dicopper complexes bearing the R-BPMP, Me-BPEP, and Me-BPMEP ligands.

II. Synthesis and characterization of dinucleating BPMP, BPEP and BPMEP ligands and their copper complexes

The syntheses and solid state characterization of the ligands and dinuclear complexes were previously reported.[9],[10],[11],[14],[15] Below is presented the X-ray structures of some of these complexes with a short description as well as their UV-Vis spectroscopic properties in solution which have been previously published.

II.1. X-ray Structures of dicopper complexes

ORTEP views of dicationic complexes **1a**$^{2+}$**, 1b**$^{2+}$**, 2a**$^{2+}$ **and 3a**$^{2+}$ are displayed on Figure II.5. Selected data and angles are gathered in Table II.1. All crystal structures showed that the two copper atoms are doubly bridged by the phenoxo and a hydroxo group. The pentacoordination of Cu1 and Cu2 is achieved by the tertiary amine and two pyridine nitrogens. The coordination polyhedrons of both copper atoms depend on the length the aliphatic chain linking the phenoxo bridge to the coordination core. For complexes **1a**$^{2+}$ and **1b**$^{2+}$, polyhedrons are best described as distorted trigonal bipyramids with (O, N, N) trigonal planes. The two pyridine groups are cis to each other. The four atoms Cu1, Cu2, O1, and O2 are in the same plane. For complexes **2a**$^{2+}$, both coordination polyhedra around copper atoms are square pyramidal, with a *trans* spatial arrangement of the two pyridines. The X-ray structure of **3a**$^{2+}$ revealed that the complex possesses geometrical unsymmetry because the environment around the Cu2 center is found to be intermediate between square pyramidal and trigonal bipyramidal (τ = 0.53, τ being the Addison parameter defining the geometrical feature of a penta-

coordinated Cu core[31]), unlike that around the Cu1 center which is fully square pyramidal (τ=0.06). Cu-N and Cu-O distances do not vary significantly with the complexes. However, the Cu-Cu distance increases as well as the <Cu-O-Cu> angle when an ethyl linker is introduced instead of a methyl one, as an indication of a release of geometric constraint around copper centre.

Table II.1. Selected bond distances and angles from X-ray data for **$1a^{2+}$, $1b^{2+}$, $2a^{2+}$ and $3a^{2+}$**.

	$1a^{2+}$	**$1b^{2+}$**	**$2a^{2+}$**	**$3a^{2+}$**
Cu-N (Å)	1.995-2.19	2.010-2.245	1.991-2.228	1.982-2.242
Cu-O (Å)	1.891-2.039	1.905-2.039	1.928–1.961	1.8995-1.9876
Cu1-Cu2 (Å)	2.966	2.980	3.077	3.045
<Cu1O1Cu2> (°)	95.7	95.2	103.7	101.0
<Cu1O2Cu2> (°)	102.1	102.6	105.5	104.6

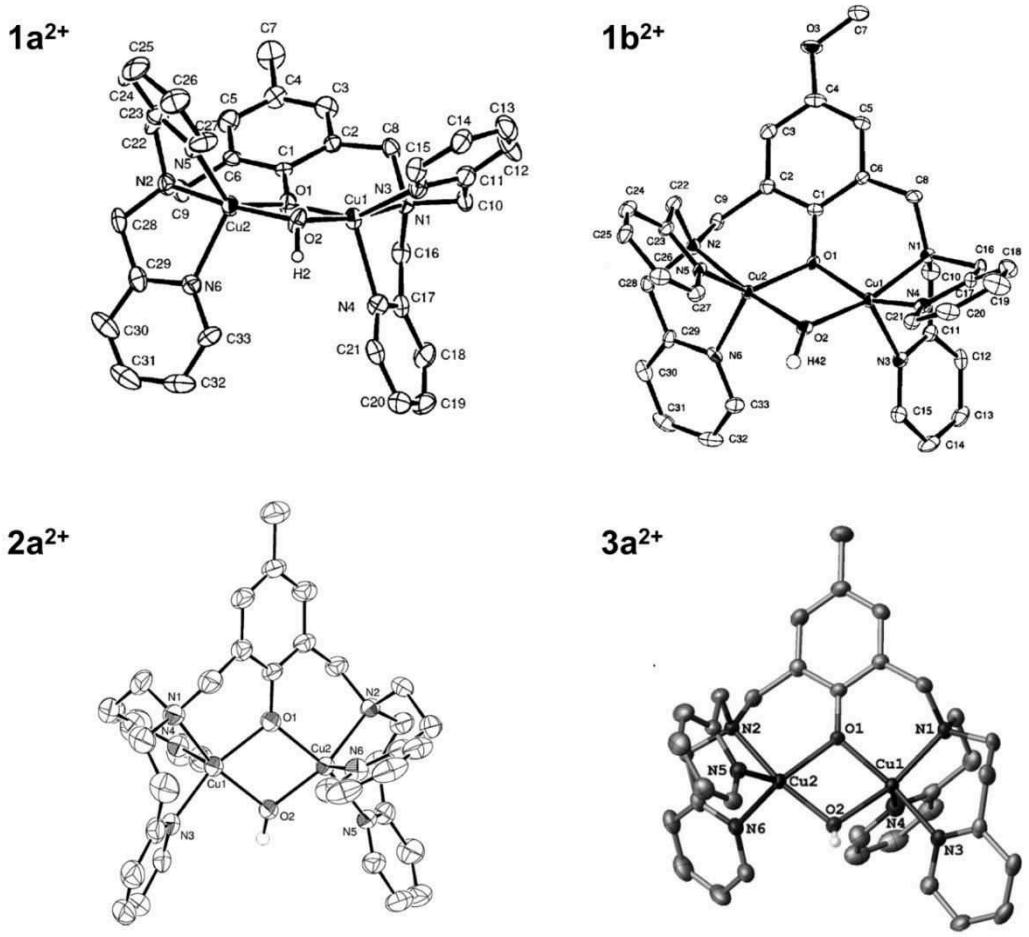

Figure II.5. ORTEP views of complexes **$1a^{2+}$, $1b^{2+}$, $2a^{2+}$ and $3a^{2+}$**. (Probability 30%) Reproduced from Refs. [9],[10],[14],[15].

II.2. UV-Vis spectroscopic properties of complexes [1a-c]$^{2+}$, 2a^{2+} and 3a^{2+}

As shown in Table II.2, all complexes are characterized by a ligand-to-metal charge-transfer (LMCT) transition between the bridging phenoxo and copper ions in the 350–450 nm region and a d–d transition in the 600–750 nm region. Nevertheless, discrepancies are observed between complexes. The variation in molar absorption coefficient (ε) for the LMCT suggests that the increase of the chain length induces a better overlap between the phenolate donor and the half-filled copper orbital. This can be ascribed with a less strained structure for **2a**$^{2+}$, as deduced from solid sate data. Moreover, the shift of the d–d bands is consistent with geometric modifications from trigonal-bipyramidal to square-pyramidal coordination around the copper(II) centers, in agreement with the X-ray structures. These data are a first indication that strcuctural features of the complexes remain the same at solid state and in solution.

Table II.2. UV-Vis spectroscopic data (λ /nm (ε/M^{-1} cm^{-1})) of **1a**$^{2+}$, **1b**$^{2+}$, **1c**$^{2+}$, **2a**$^{2+}$ **and 3a**$^{2+}$ in H_2O/DMSO.

	1a^{2+}	**1b**$^{2+\,a}$	**1c**$^{2+\,a}$	**2a**$^{2+}$	**3a**$^{2+}$
d-d	730 (280)	787 (300)	806 (251)	621 (206)	645 (200)
LMCT	410 (480)	440 (560)	340 (760)	391 (2600)	386 (1220)

[a] Determined in CH_3CN.

III. Electrochemical and theoretical studies of the BPMP, BPEP and BPMEP Cu complexes

In order to investigate the R-substitution, chain length and dissymetrisation effects on the redox properties for all series (H-BPMP, BPEP and BPMEP), electrochemical studies at room temperature have been performed under inert atmosphere (Glovebox) with a home-designed 3-electrodes cell (glassy carbon working electrode). NBu_4PF_6 was used as supporting salt (0.1 M). Three different organic solvents were tested: acetonitrile (MeCN) as coordinating and polar solvent, tetrahydrofuran (THF) as poorly-coordinating and non-polar solvent, and propylene carbonate (PC) as poorly-coordinating polar medium. To model these electronic/geometric ligand effects on the redox properties, DFT calculations have been performed by using different basis sets and functional. An optimal combination of two complementary methods was obtained by using the IEFPCM/M11L level to compute the redox potential, and the IEFPCM/PBE0 level for geometry optimization, hence spin localization i.e. redox site. The objective was to determine as accurately as possible the redox site of electron transfer by comparison with coupled electrochemical/spectroscopic techniques.

As a basis for the calculations, different spin states have to be considered depending on the redox states of the complexes (Figure II.6). The synthesized $Cu^{II}(O^{-})Cu^{II}$ complex can display two spin states, a singlet (S = 0) or a triplet (S=1), in the ground state, depending respectively on the antiferro- or ferro-magnetic respective interactions between Cu^{II} centers (Figure II.6, top). One-electron reduction of the starting complex leads to a $Cu^{II}(O^{-})Cu^{I}$ with S = 1/2, doublet state, (paramagnetic species) and a second reduction will lead to a $Cu^{I}(O^{-})Cu^{I}$ diamagnetic singlet state species with S = 0. For the oxidation, the spin state depends on the site of the redox reaction, which is either the metal, through the Cu^{III}/Cu^{II} process, or the phenoxo center, $PhO^{-}/PhO^{\bullet}$ process. If oxidation is localized on one copper ion, it leads to a $Cu^{II}(O^{-})Cu^{III}$ species in a doublet state with S = 1/2 . (Figure II.6, middle). At last, if oxidation occurs on the phenoxo process, the $Cu^{II}(O^{\bullet})Cu^{II}$ phenoxyl species gives rise to a magnetic situation depending on the delocalization and coupling processes in the ground state with either a global doublet spin state with S = 1/2, through an antiferromagnectic coupling, or a quartet state with S = 3/2 in the case of a ferromagnetic coupling (Figure II.7, bottom). For the calculation of redox potentials, only high spin states of complexes were computed even if they are not ground states. This is justified since the energy difference between spin states is very small compared to that between two redox states. Hence, only the triplet state of the $Cu^{II}(O^{-})Cu^{II}$ complexes and quartet state of its mono-oxidized $Cu^{II}(O^{\bullet})Cu^{II}$ were considered, respectively.

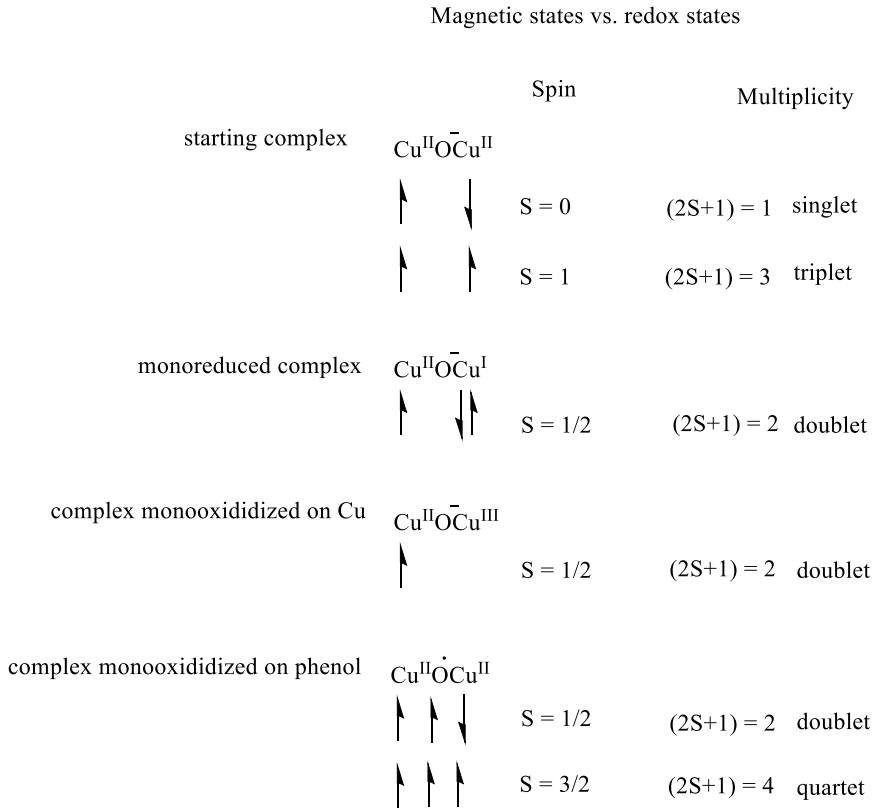

Figure II.6. Schematic representation of spin states of the different redox states of the phenoxo-dicopper complexes.

III.1. Symmetrical complexes R-BPMP ($1a^{2+}$, $1b^{2+}$ and $1c^{2+}$)

Room temperature electrochemical studies of this family have been previously reported in acetonitrile.[9],[10],[11],[25] The next section provides with a full investigation in the three media above-mentioned and the comparison of experimental data with DFT computed values.

III.1.1 Electrochemical studies of complexes $1a^{2+}$, $1b^{2+}$ and $1c^{2+}$

Cyclic voltammetry (CV) of the first series of complexes (R-BPMP) reveals a single oxidation peak for all three different R-substituent complexes, as well as two successive monoelectronic reduction peaks whatever the solvent used (see for instance CVs in PC/NBu_4PF_6, Figure II.7 A). Depending on the R-substituent, different redox behaviors have been observed (Table II.3). Indeed, changing from the strong (-OCH_3) to the less electron donating substituent (-CH_3, -CF_3) on the phenoxo spacer, induces a positive shift of the oxidation potential on the CV (Figure II.7 B). For instance, the -OCH_3 BPMP displays a reversible system at E^0 = 0.51 V vs Fc at v = 0.1 V/s in acetonitrile. With lower σ-donors (-CH_3 or -CF_3), the oxidation potential is shifted positively: for –CF_3 substituent, the change is particularly important (+500 mV *vs* -OCH_3, +700 mV –CH_3) and the system becomes irreversible. Exhaustive electrolysis at E = 0.60 V vs Fc for R = –OCH_3 shows that the mono-oxidized species is unstable at room temperature in the experiment timescale (1 hour). The resulting species is characterized by several reduction peaks in the 0 to -0.5 V potential range, meaning that strong rearrangement occurs at long timescale. In contrast, reduction peaks are slightly modified with the nature of R. A reversible redox wave at ca. -1.0 V followed by an irreversible cathodic peak at ca. -1.3 V vs Fc are ascribed to two sequential mono-electronic reduction processes on each copper(II) center. Exhaustive electrolysis at -1.1 V gives n = 1 electron attributed to the $Cu_2^{II,II}/Cu_2^{II,I}$ redox couple for the first system. Consequently, the second reduction process is ascribed to the formation of the $Cu_2^{I,I}$ species, which undergoes fast and irreversible decomposition.[10] Moreover, reduction on the Cu^{II} centers was further evidenced by UV-vis spectroelectrochemical measurement (decrease of the d-d band at 700 nm).

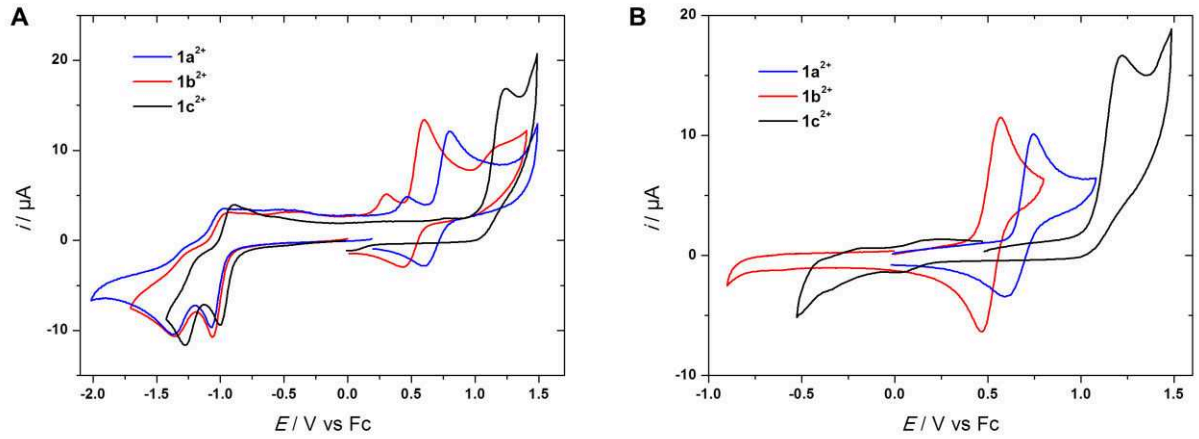

Figure II.7. CVs (v = 0.1 V/s) at a glassy carbon electrode (E /V *vs* Fc) of complexes **1a**$^{2+}$, **1b**$^{2+}$ and **1c**$^{2+}$ (1.5 mM) in PC/NBu_4PF_6 0.1 M: R=CF_3 (black), OCH_3 (red), CH_3 (blue). A: starting cathodic direction; B: starting anodic direction.

Table II.3. Experimental voltammetric data [E^0/ V *vs* Fc (ΔEp / mV)] for complexes **1a**$^{2+}$, **1b**$^{2+}$ and **1c**$^{2+}$ in Solvent/NBu_4PF_6 0.1 M (Solvent = MeCN, THF, PC).

	Solvent	**1a**$^{2+}$	**1b**$^{2+}$	**1c**$^{2+}$
Oxyd.	MeCN	0.71 (170)	0.51 (70)	1.20[a]
	THF	0.60 (280)	0.45 (90)	1.05[a]
	PC	0.67 (150)	0.49 (100)	1.22[a]
Reduct. I	MeCN	-1.03 (110)	-1.02 (105)	-0.95 (90)
	THF	-1.11 (130)	-1.09 (130)	-1.03 (100)
	PC	-1.03 (105)	-1.03 (100)	-0.95 (100)
Reduct. II	MeCN	-1.34[a]	-1.39[a]	-1.29[a]
	THF	-1.44 (130)	-1.41 (140)	-1.31 (140)
	PC	-1.38[a]	-1.38[a]	-1.27[a]

[a] Irreversible peak potential value.

These results prove that the complex does not dissociate in PC and CH_3CN and that µ-hydroxo and phenolate-bridged species are preserved. In THF the redox properties are slightly different probably because of the low polarity of the solvent as a slightly difference is detected in the cathodic part (Table II.3). Hence, electrochemical studies show that oxidation process is fully R-dependent whereas the reduction process is not. It also shows that the solvent has no significant effect, as anticipated by UV-Vis spectroscopy.

III.1.2. Theoretical calculations for complexes $1a^{2+}$, $1b^{2+}$ and $1c^{2+}$

For the theoretical calculations, the redox potential in both THF and MeCN solvents was determined by calibration on the Fc^{+}/Fc couple as reference. Theoretical potential values were calculated for the respective monoelectronic oxidation and reduction of complexes. As indicated above, only high spin states of complexes were computed for this calculation, namely doublet for the dicopper(II), quartet for the monooxidized form and doublet for the reduced form. Analysis of the electronic structure of the dicopper(II) complex was performed on the basis of an antiferromagnetic coupling, singlet state with S = 0, as previously reported.[14] Good agreement between theory and experimental data has been obtained for both oxidation and reduction processes (Tables II.4 and II.5). This indicates that the computed data and structures are reliable for analysis. They correctly reproduced the trends observed experimentally with regards to the effect of the substituting groups. The discrepancies observed in THF, can be explained by the fact that calibration was done in CH_3CN. Moreover, weaker effects for reduction than for oxidation process, is consistent with a solvent effect, more pronounced for highly charged species such as $\mathbf{1b^{3+}}$, compared to $\mathbf{1b^{+}}$.

Table II.4. Experimental and theoretical voltammetric data [E^0 / V *vs* Fc] for the monoelectronic oxidation of dinuclear μ-hydroxo complexes $\mathbf{1a^{2+}}$, $\mathbf{1b^{2+}}$ and $\mathbf{1c^{2+}}$ in Solvent/NBu_4PF_6 0.1 M (Solvent = MeCN, THF).

Solvent	$\mathbf{1a^{3+/2+}}$		$\mathbf{1b^{3+/2+}}$		$\mathbf{1c^{3+/2+}}$	
	Theor	*Exp*	*Theor*	*Exp*	*Theor*	*Exp*
MeCN	0.85	0.71	0.59	0.51	1.39	1.20[a]
THF	1.28	0.60	1.11	0.45	1.85	1.05[a]

[a] Irreversible peak

Table II.5. Experimental and theoretical voltammetric data [E^0 / V *vs* Fc] for the monoelectronic reduction of dinuclear μ-hydroxo complexes $\mathbf{1a^{2+}}$, $\mathbf{1b^{2+}}$, $\mathbf{1c^{2+}}$ in Solvent/NBu_4PF_6 0.1 M (Solvent = MeCN, THF).

Solvent	$\mathbf{1a^{2+/1+}}$		$\mathbf{1b^{2+/1+}}$		$\mathbf{1c^{2+/1+}}$	
	Theor	*Exp*	*Theor*	*Exp*	*Theor*	*Exp*
MeCN	-1.05	-1.03	-1.00	-1.02	-0.95	-0.95
THF	-0.86	-1.11	-0.89	-1.09	-0.74	-1.03

[a] Irreversible peak.

Since good agreement was obtained for redox potentials between theoretical and experimental values, further analysis were performed in order to determine the redox site of the oxidation or reduction process. Plots of spin density (difference between α and β densities) for the oxidized or reduced species were considered for the analysis. Figure II.8 displays plots of spin density for the mono-oxidized and mono-reduced species of the dicationic **1b**$^{2+}$ complex, calculated respectively on the basis of a quartet and a doublet state. For the mono-oxidized state (**1b**$^{3+}$), spin densities are localized on both copper atoms and phenoxo moiety, hence suggesting a dinuclear complex with two Cu(II) cations and one phenoxyl radical, $Cu^{II}(O^{\bullet})Cu^{II}$. For the reduced state (**1b**$^{+}$), spin density shows no more density on one of the copper in agreement with experimental data, hence indicating the formation of a localized mixed valence $Cu^{I}(O^{-})Cu^{II}$ species.

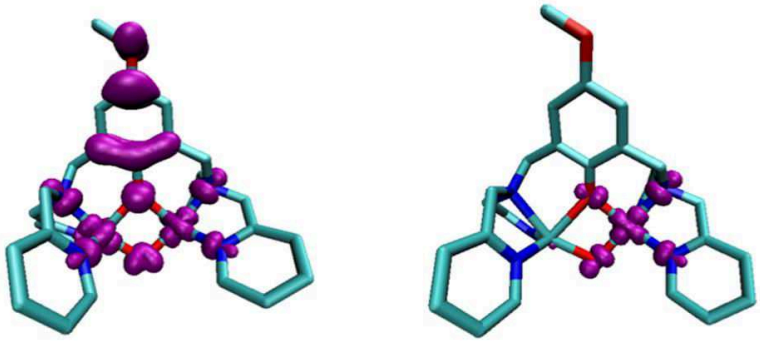

1b^{3+} **1b**$^{+}$

Figure II.8. Spin density plot for the high spin state of the mono-oxidized **1b**$^{3+}$ species (left) and the mono-reduced species **1b**$^{+}$ (right).

Interestingly, geometries display an unsymmetrical structure with an increase of distances around the copper atom at the reduced site. Same description was obtained for the mono-oxidized and mono-reduced species of **1a**$^{2+}$ and **1c**$^{2+}$ dinuclear copper complexes (Figure II.9). Looking at the effect of R on the alpha singled occupied orbital on the phenoxo group (Figures II.10), the charge is slightly less delocalized for the lower electron donors -CH_3 and -CF_3 *vs* -OCH_3 on the phenoxo spacer. This indicates a better stability for the R = –OCH_3 complex hence explaining its less positive redox potential compared to – CH_3 and –CF_3 analogous.

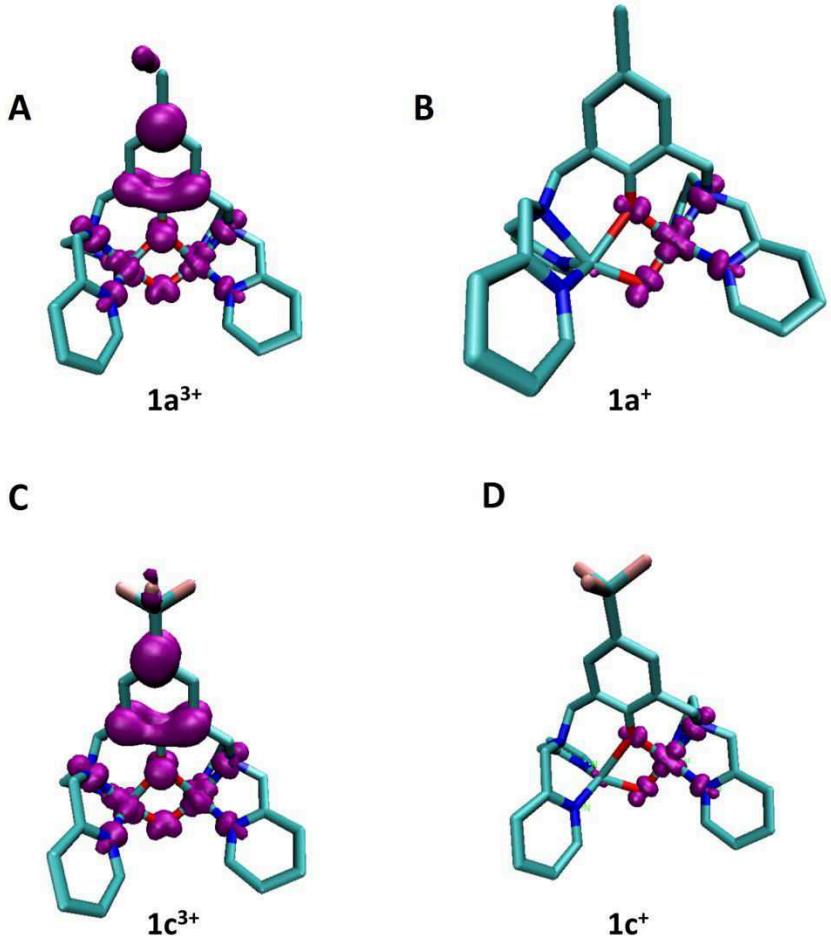

Figure II.9. Spin density plot for A) $\mathbf{1a^{3+}}$ (quadruplet state), B) $\mathbf{1a^{+}}$ (doublet state), C) $\mathbf{1c^{3+}}$ (quadruplet state) and D) $\mathbf{1c^{+}}$ (doublet state) .

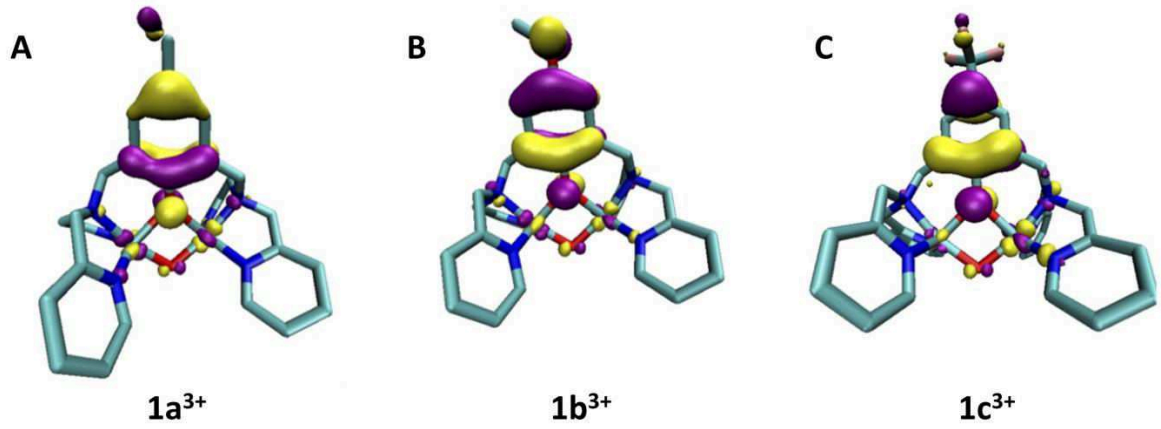

Figure II.10. Schematic representation of the alpha singled occupied orbital localized on the phenoxy group for A) $\mathbf{1a^{3+}}$, B) $\mathbf{1b^{3+}}$ and C) $\mathbf{1c^{3+}}$ complexes, showing slight better charge delocalization for $\mathbf{1b^{3+}}$.

III.2. Symmetrical complex BPEP ($2a^{2+}$)

III.2.1. Electrochemical studies of complex $2a^{2+}$

The symmetrical complex **$2a^{2+}$** bearing the ligand CH_3-BPEP, displays a rather different redox behavior than its CH_3-BPMP analogue (**$1a^{2+}$**), in both oxidation and reduction parts. As shown in Figure II.11-A (green curve), a single and irreversible reduction peak was detected at E_{pc} = -1.09 V *vs* Fc in acetonitrile (see Table II.6 for other solvents) when scanning negatively, in contrast to the two successive peaks observed for the analogue CH_3-BPMP. On the oxidation part, an irreversible peak was identified at E_{pa} = 1.04 V. This behavior differs from **$1a^{2+}$** which is oxidized quasi-reversibly at a lower potential value (E_{pa} = 0.79 V) (Figure II.11-A blue curve). Plots of anodic and cathodic peak current i_p *vs* $v^{1/2}$ for **$2a^{2+}$** show similar slope values (Figure II.11-D), indicating that both processes involve the same number of electrons. Comparison of anodic and cathodic peak currents for the two series, in analogous conditions, strongly suggests the occurrence monoelectronic oxidation and reduction processes for this complex.

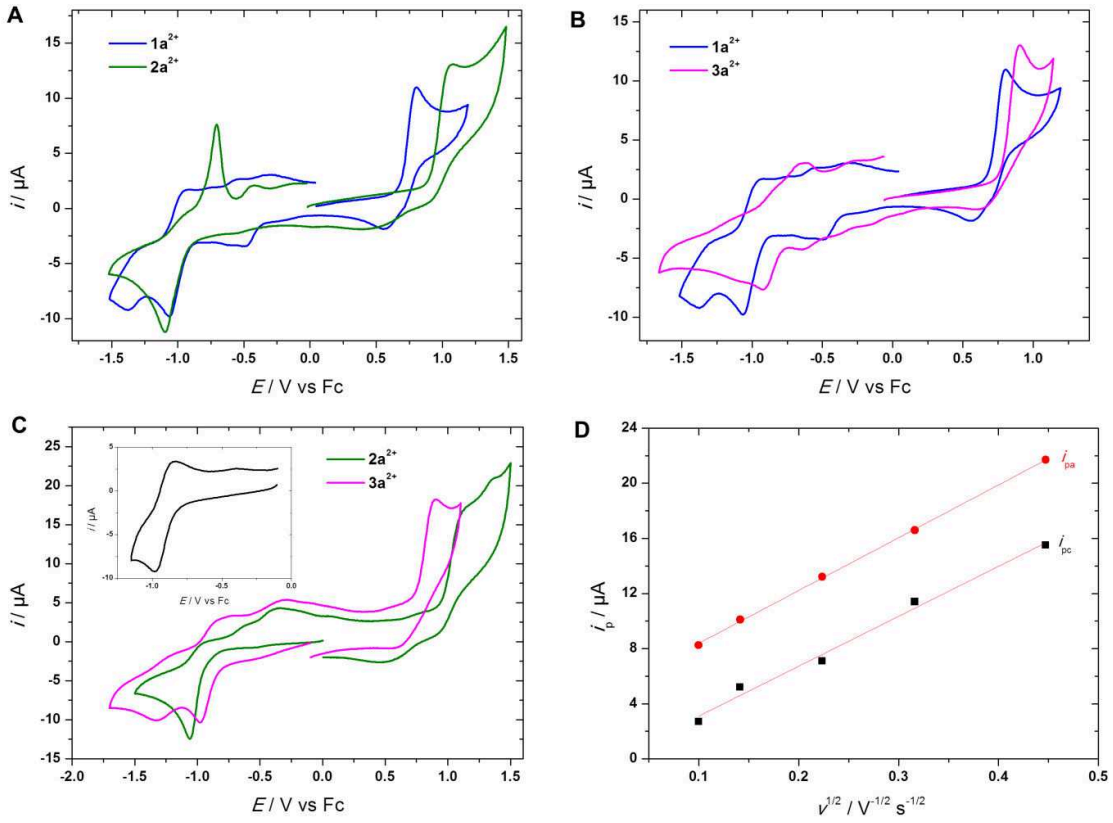

Figure II.11. A, B and C) CVs (v = 0.1 V/s) at a vitreous carbon electrode (E / V *vs* Fc) in CH_3CN /NBu_4PF_6 0.1 M of : A) **$1a^{2+}$** (blue) and **$2a^{2+}$** (green) with positive scanning; B) **$1a^{2+}$** (blue) and **$3a^{2+}$** (pink) with positive scanning; C) **$2a^{2+}$** (green) and **$3a^{2+}$** (pink) with negative scanning; inset: CV at 0.1 V/s of **$3a^{2+}$** showing the reversibility for the first system in reduction. D) Plots of i_{pa} (red circles) and i_{pc} (black squares) against $v^{1/2}$ taken from CVs for **$2a^{2+}$** in CH_3CN /NBu_4PF_6 0.1 M.

Table II.6. Experimental voltammetric data [E^0/ V *vs* Fc (ΔEp / mV)] for complexes **2a**$^{2+}$ in Solvent/NBu_4PF_6 0.1 M (Solvent = MeCN, THF, PC).

	Solvent	**2a**$^{2+}$
Oxyd.	MeCN	1.04[a]
	THF	1.01[a]
	PC	1.05[a]
Reduct. I	MeCN	-1.09[a]
	THF	-1.08[a]
	PC	-1.11[a]
Reduct. II	MeCN	[b]
	THF	[b]
	PC	[b]

[a] Irreversible peak potential value; [b] No second reduction peak observed

III.2.2 Theoretical Calculations for complex 2a^{2+}

The basis sets and functional is the same as that used for **1a**$^{2+}$, **1b**$^{2+}$ and **1c**$^{2+}$. The good agreement between theory and experiment data is obtained for both the oxidation and reduction processes (Table II.7). Spin density plots have been obtained for the oxidized or reduced species of **2a**$^{2+}$ complex. For the mono-oxidized species, analysis has been carried out on the quartet state. Results are similar to that obtained for complex **1b**$^{2+}$, i.e. a mono-reduced species **2a**$^{+}$ with a Cu_2(II,I) character and a mono-oxidized **2a**$^{3+}$ $Cu^{II}Cu^{II}$ phenoxyl species. Figure II.12-B displays spin density plots for the mono-oxidized species derived from the dicationic **2a**$^{2+}$ complex. The charge is more localized on the phenoxo moiety at the mono-oxidized state (**2a**$^{3+}$), in contrast to the delocalization of spin on the copper atoms for the mono-oxidized complex **1a**$^{3+}$.

Table II.7. Experimental and theoretical voltammetric data [E^0 / V *vs* Fc] for **2a**$^{2+}$ in Solvent/NBu_4PF_6 0.1 M (Solvent = MeCN, THF) for the oxidation and reduction process.

Solvent	**2a**$^{3+/2+}$		**2a**$^{2+/1+}$	
	Theor	*Exp*	*Theor*	*Exp*
MeCN	1.05	1.04[a]	-1.01	-1.09
THF	1.53	1.01[a]	-0.91	-1.08

[a] Irreversible peak.

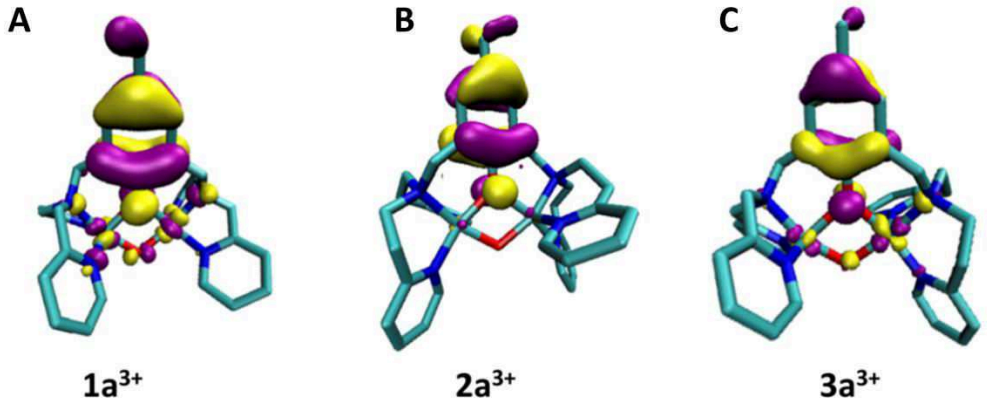

Figure II.12. Schematic representation of the alpha singled occupied orbital localized on the phenoxy group for the quartet state of A) **1a**$^{3+}$, B) **2a**$^{3+}$ and C) **3a**$^{3+}$.

III.3. Unsymmetrical complex BPMEP (3a^{2+})

III.3.1. Electrochemical studies of complex 3a^{2+}

The same investigations have been performed with the unsymmetrical CH_3-BPMEP complex **3a**$^{2+}$. On the cathodic part (Figure II.11-C, pink curve), two reduction peaks are detected at *ca*. -0.9 and -1.3 V, whatever the solvent. The first system at E^0 = -0.91 V *vs* Fc is reversible (ΔE_p = 140 mV at v = 0.1 V/s, Figure II.11-C, inset) and noticeably appears at a more positive value than that observed for the symmetrical complex **1a**$^{2+}$ (E^0 = -1.03 V). Scanning below -1.5 V induces the loss of reversibility of the first system and appearance of new oxidation peaks on the back scan. On the anodic part (Figure II.11-B), an irreversible anodic peak is detected at E_{pa} = 0.90 V *vs* Fc. Variation of solvent does not induce significant modification of the redox properties (Table II.8).

Table II.8. Experimental voltammetric data [E^0/ V *vs* Fc (ΔEp / mV)] for complexes **2a**$^{2+}$ in different solvent/NBu_4PF_6 0.1 M (Solvent = MeCN, THF, PC).

	Solvent	**3a^{2+}**
Oxyd.	MeCN	0.90[a]
	THF	0.84[a]
	PC	0.93[a]
Reduct. I	MeCN	-0.91 (140)
	THF	-1.04 (140)
	PC	-0.96[a]
Reduct. II	MeCN	-1.32[a]
	THF	-1.41[a]
	PC	-1.36[a]

[a] Irreversible peak potential value.

III.3.2. Theoretical calculations for complex $3a^{2+}$

As for the other series, redox potential values have been computed using the IEFPCM/M11L level and the IEFPCM/PBE0 level for geometry optimization. As shown in Table II.9, good agreement is obtained between theoretical and experimental data. Spin density plots were obtained for the oxidized or reduced species of $\mathbf{3a}^{2+}$ complex. For the mono-oxidized species, analysis has been carried out on the quartet state. As for $\mathbf{2a}^{2+}$, results show a mono-reduced species $\mathbf{3a}^{+}$ with a Cu_2(II,I) character and a mono-oxidized $\mathbf{3a}^{3+}$ phenoxyl species. The spin density plot for the mono-oxidized species $\mathbf{3a}^{3+}$ (Figure II.12-C) reveals an intermediate case between $\mathbf{1a}^{3+}$ and $\mathbf{2a}^{3+}$: the charge is partially delocalized on the copper atoms, but not as much as found for $\mathbf{1a}^{3+}$.

Table II.9. Experimental and theoretical voltammetric data [E^0 / V *vs* Fc] for $\mathbf{3a}^{2+}$ in Solvent/NBu_4PF_6 0.1 M (Solvent = MeCN, THF) for the oxidation and reduction process.

Solvent	$\mathbf{3a}^{3+/2+}$		$\mathbf{3a}^{2+/2+}$	
	Theor	*Exp*	*Theor*	*Exp*
MeCN	1.01	0.90[a]	-0.98	-0.91
THF	1.49	0.84[a]	-0.82	-1.04

[a] Irreversible peak.

III.4. Conclusions on the electrochemical and theoretical studies of $\mathbf{1(a\text{-}c)}^{2+}$, $\mathbf{2a}^{2+}$ and $\mathbf{3a}^{2+}$

The combination of electrochemical studies and theoretical calculations lead to the following conclusions:

(i) Effect of R substituent for the R-BPMP series

The R substituent plays a significant role only for the oxidation process. A positive shift of the oxidation potential ($\mathbf{1b}^{2+}$ <$\mathbf{1a}^{2+}$ < $\mathbf{1c}^{2+}$) is detected experimentally when the donor ability of the substituent decreases. This is consistent with the theoretical calculations which show that the charge delocalization in their final tricationic mono-oxidized species is slightly less delocalized on the phenoxo group for $\mathbf{1a}^{3+}$ (CH_3) and $\mathbf{1c}^{3+}$ (CF_3) than for $\mathbf{1b}^{3+}$ (OCH_3). Hence, with the highest electronic density on the phenoxo core, $\mathbf{1b}^{2+}$ is the easiest oxidizable species.

(ii) Effect of chain length for CH_3-substitued symmetrical complexes: comparison between $\mathbf{1a}^{2+}$ and $\mathbf{2a}^{2+}$

The variation of the chain length between the tertiary amine and the picolyl groups on both sides of the ligand induces a modification of the redox behavior. For $\mathbf{2a}^{2+}$ a single and irreversible

peak is detected in both reduction and oxidation, whereas two peaks are observed for $\mathbf{1a}^{2+}$ in reduction and a quasi-reversible system at a lower potential value in oxidation. One possible explanation is that the charge for the tricationic species is more delocalized on the copper core for $\mathbf{1a}^{3+}$ than $\mathbf{2a}^{2+}$, as shown by DFT calculations. Indeed, theoretical studies suggest that the angle between the phenoxo moiety and the Cu1-O1-O2-Cu2 core is more twisted in $\mathbf{2a}^{3+}$ (-48°) than in $\mathbf{1a}^{3+}$ (-40°). This would indicate a better stabilization of $\mathbf{1a}^{3+}$ (vs $\mathbf{2a}^{2+}$), hence a lower redox potential value.

(iii) Effect of unsymmetry: comparison between $\mathbf{1a}^{2+}$, $\mathbf{2a}^{2+}$ and $\mathbf{3a}^{2+}$

Unsymmetrical design of the ligand affects the redox signature of the resulting dicopper complex (Figure II.13). Two reduction peaks are detected for $\mathbf{3a}^{2+}$ with a slightly more positive value than for $\mathbf{1a}^{2+}$ and $\mathbf{2a}^{2+}$. Moreover, a 110 mV positive shift (vs $\mathbf{1a}^{2+}$, E_{pa} = 0.79 V) of the oxidation peak and loss of reversibility are observed for the unsymmetrical complex $\mathbf{3a}^{2+}$ (E_{pa} = 0.90 V vs Fc). The oxidation potential for the $\mathbf{3a}^{2+}$ remains below that of $\mathbf{2a}^{2+}$ (E_{pa} = 1.04 V) (Figure II.13). This redox behaviour can be explained thanks to the distances taken from computed structures (Table II.10).

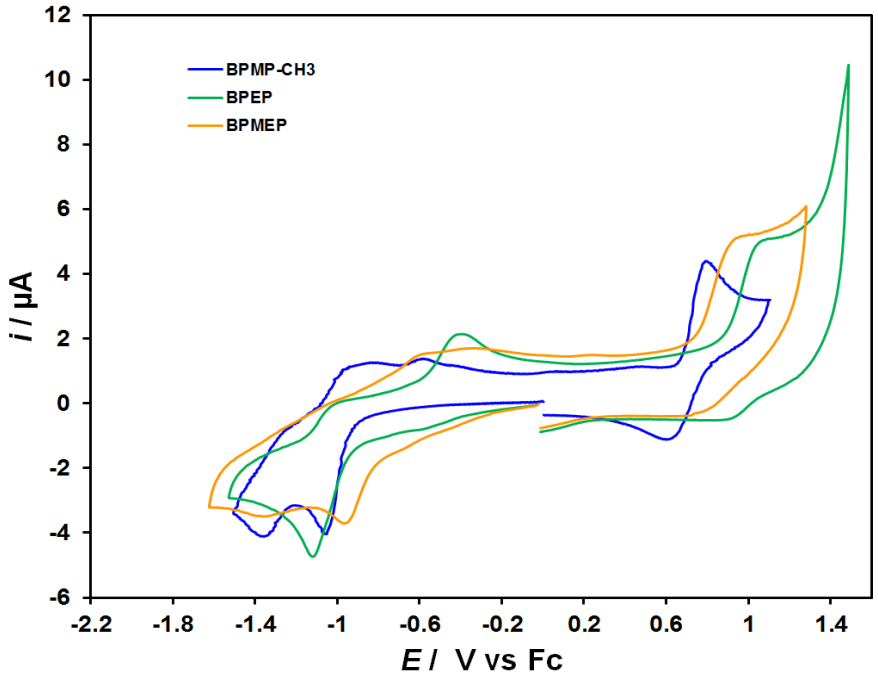

Figure II.13. CVs (v = 0.1 V/s) at a vitreous carbon electrode (E /V *vs* Fc) of complexes $\mathbf{1a}^{2+}$ (blue), $\mathbf{2a}^{2+}$ (green) and $\mathbf{3a}^{2+}$ (orange) (0.5 mM) in CH_3CN/NBu_4PF_6 0.1 M.

Table II.10. Selection of bond distances for the initial and monoreduced states of complexes $\mathbf{1a}^{2+}$, $\mathbf{2a}^{2+}$ and $\mathbf{3a}^{2+}$ from DFT calculations.[a]

	Cu1-O1 / Cu2-O1	Cu1-O2 / Cu2-O2	Cu1-N1 / Cu2-N2	Cu1-N2 / Cu2-N2	Cu1-N3 / Cu2-N3
$\mathbf{1a}^{2+}$	2.06/1.99	1.95/1.96	2.05/2.04	2.05/2.03	2.11/2.21
$\mathbf{1a}^{+}$	2.36/1.98	2.10/1.92	2.38/2.05	2.08/2.07	2.08/2.25
$\mathbf{2a}^{2+}$	1.98/1.98	1.97/1.98	2.09/2.10	2.03/2.03	2.24/2.24
$\mathbf{2a}^{+}$	2.32/1.97	2.21/1.93	2.33/2.11	2.06/2.07	2.07/2.27
$\mathbf{3a}^{2+}$	1.99/1.99	1.95/1.99	2.05/2.10	2.03/2.03	2.20/2.23
$\mathbf{3a}^{+}$	2.10/2.04	3.64/1.89	2.18/2.19	2.04/2.11	2.00/2.07

[a] Atom numbering: O1: phenoxy oxygen atom; O2 : hydroxo oxygen atom; N1: amine nitrogen atom; N2 and N3: picolyl nitrogen atoms

Upon reduction, the unsymmetrical complex $\mathbf{3a}^{+}$ displays a significant increase of the Cu1-O2 / Cu2-O2 distance, correlated to the reduced copper ion on the ethyl-spacer side and the hydroxo-bridging oxygen (from 1.99 A to 3.64 Å). In contrast, $\mathbf{1a}^{+}$ and $\mathbf{2a}^{+}$ do not show large modification of the coordination sphere. Hence, the reduced Cu^{I} center on the ethyl side is better stabilized than on the methyl side, due probably to the higher flexibility of the ethyl linker *vs* the methyl one. This modification could explain the more positive potential associated with the first reduction process for $\mathbf{3a}^{2+}$ vs $\mathbf{1a}^{2+}$ and $\mathbf{2a}^{2+}$.

The positively shift of the oxidation potential ($\mathbf{1a}^{2+} < \mathbf{3a}^{2+} < \mathbf{2a}^{2+}$) can find an explanation by considering the stability of their final tricationic mono-oxidized species through the charge delocalization of their alpha singled occupied orbital localized on the phenoxo group. Figure II.12 shows the more delocalized charge on copper atoms for $\mathbf{1a}^{3+}$ than for $\mathbf{2a}^{3+}$ and the intermediate case for the unsymmetrical complex $\mathbf{3a}^{3+}$. As an evidence, the angle between the phenoxo moiety and the Cu1-O1-O2-Cu2 plane for $\mathbf{3a}^{3+}$ (-46°) is indeed intermediate between that of $\mathbf{1a}^{3+}$ (-40°) and $\mathbf{3a}^{3+}$ (-48°). The geometry effect induces a variation of the charge delocalization on the phenoxo group, explaining the lowest value of the oxidation potential.

IV. UV-Vis-NIR spectroelectrochemical studies of the oxidized species

IV.1. Room and low temperature analysis.

In order to analyze the formation of the species electrochemically-generated on the electrode surface upon oxidation potential, and the existence of transient intermediates, UV-Vis-NIR-spectroelectrochemical experiments have been performed in thin layer conditions at room and low temperature. In addition, studies with chemical oxidant were carried out (with spectroscopic characterizations).

IV.1.1. Symmetrical complexes R-BPMP ($1a^{2+}$, $1b^{2+}$)

As previously explained, the oxidation of the symmetrical R-BPMP complexes is likely centered on the phenoxo spacer, leading to a phenoxyl radical species. Indeed, previous UV-Vis studies on the $\mathbf{1b^{2+}}$ complex (OCH_3-BPMP) at low temperature, revealed an intense absorption band at λ_{max}= 440 nm, inferred to a π-π transition occurring on the phenoxyl radical, after low-*T* exhaustive electrolysis at 0.9 0V vs Fc.[25] In order to reproduce this behavior, room temperature spectroelectrochemical experiments have been carried out in thin-layer conditions. As shown in Figure II.14, upon oxidation potential (0.90 V vs Fc), a single band at 440 nm increases in a short time scale. This confirms the formation of the phenoxyl radical upon our spectroelectrochemical conditions.

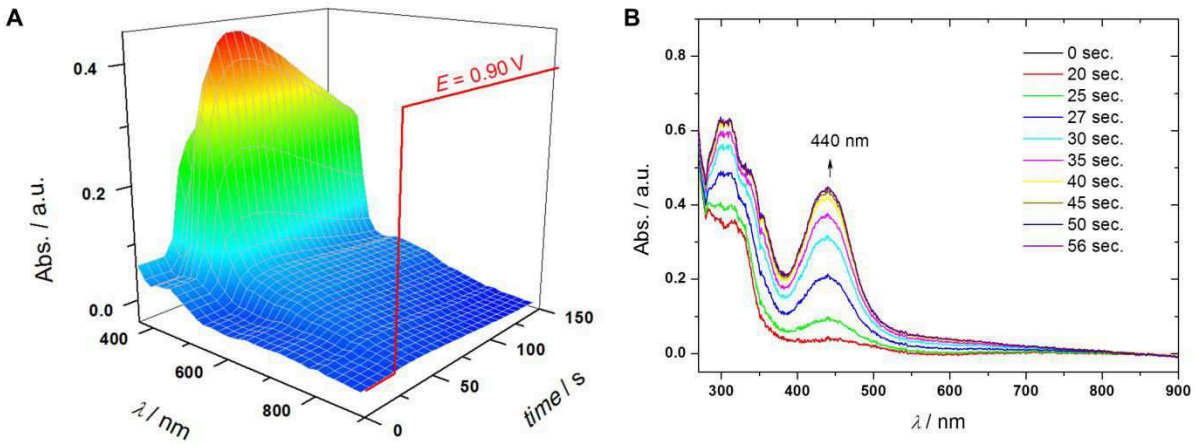

Figure II.14. A) 3D spectroelectrochemical data obtained for $\mathbf{1b^{2+}}$ upon electrochemical oxidation at 0.90 V in CH_3CN/NBu_4PF6 (thin layer conditions, optical path 0.2 mm, *C* = 4 mM). B) Monitoring of UV-Vis spectra of the complex according to spectroelectrochemical experiments at 293 K.

The same experiments have been performed with $\mathbf{1a^{2+}}$ (CH_3-BPMP). By application of an oxidation potential at 1.10 V vs Fc, an absorption band appeared at λ_{max}= 438 nm that decayed rapidly (50 seconds) (Figure II.15). By analogy with the $\mathbf{1b^{2+}}/\mathbf{1b^{3+}}$ system, it can be inferred to a π-π transition occurring on the phenoxyl radical, indicating that oxidation occurs on the phenolate ligand as for $\mathbf{1b^{2+}}$.

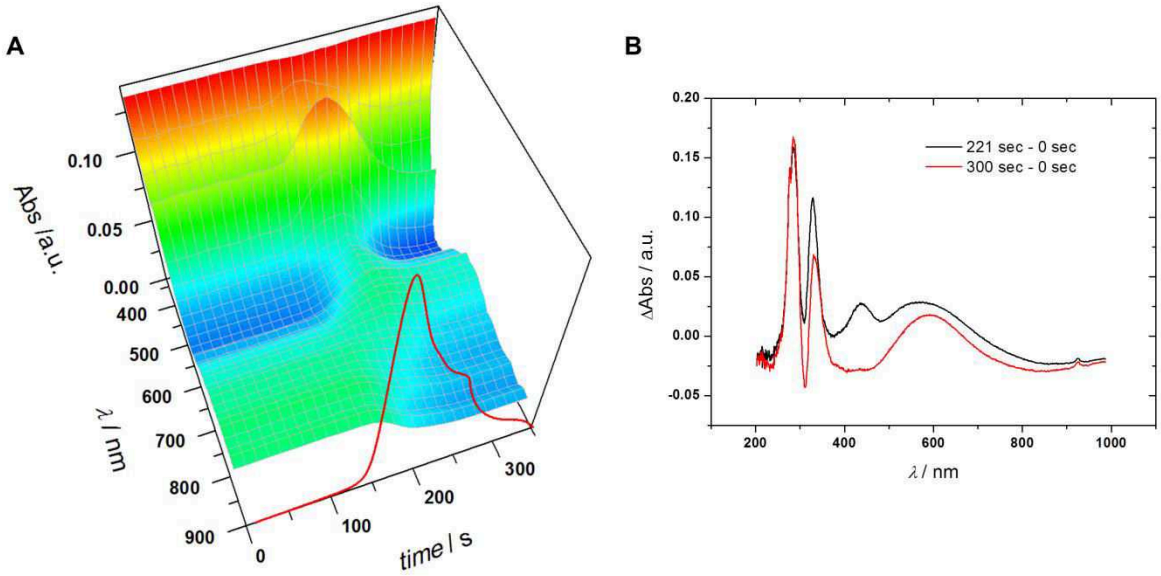

Figure II.15. A) 3D spectroelectrochemical data obtained for **1a**$^{2+}$ upon electrochemical oxidation (red curve, CV) in CH_3CN/NBu_4PF_6 (thin layer conditions, optical path 0.2 mm, C = 4 mM). B) 2D UV-Vis graphics at 221 s (*vs* initial curve at 0 s, black curve) and 300 s (*vs* initial curve at 0 s, red curve) obtained from spectroelectrochemical monitoring of the oxidation of **1a**$^{2+}$.

IV.1.2. Symmetrical complex BPEP (2a^{2+})

The oxidation process of the symmetrical complex with pyridylethyl arms has also been investigated by room temperature spectroelectrochemistry. The initial UV-Vis spectra of the complex **2a**$^{2+}$ displays a band at λ_{max} = 630 nm ascribed to a d-d transition. Noticeably, the oxidation at 1.00 V *vs* Fc leads to the disappearance of this band and the appearance of a weak one at λ_{max} = 532 nm. The latter converts rapidly (30 seconds) into a new band at λ_{max} = 361 nm (Figure II.16).

IV.1.3. Unsymmetrical complex BPMEP (3a^{2+})

The spectroelectrochemical studies of the unsymmetrical complex **3a**$^{2+}$ show a similar behavior as complex **2a**$^{2+}$: its oxidation leads to the appearance of a transient band at λ_{max} = 518 nm ($t_{½}$ = 14s) that evolves rapidly toward a new species λ_{max} = 393 nm (Figure II.17). Note that by comparison with **2a**$^{2+}$, the band at *ca*. 520 nm is much more intense. According to these results, two oxidized species are formed in oxidation. Specifically, the isosbestic point at 460 nm (Figure II.17 B) indicates the total conversation of the first species into the second one. Complementary room-temperature NIR-spectroelectrochemical experiments do not display any appearance of an intervalence band upon electrochemical oxidation, hence suggesting probable charge localization (Figure II.18).

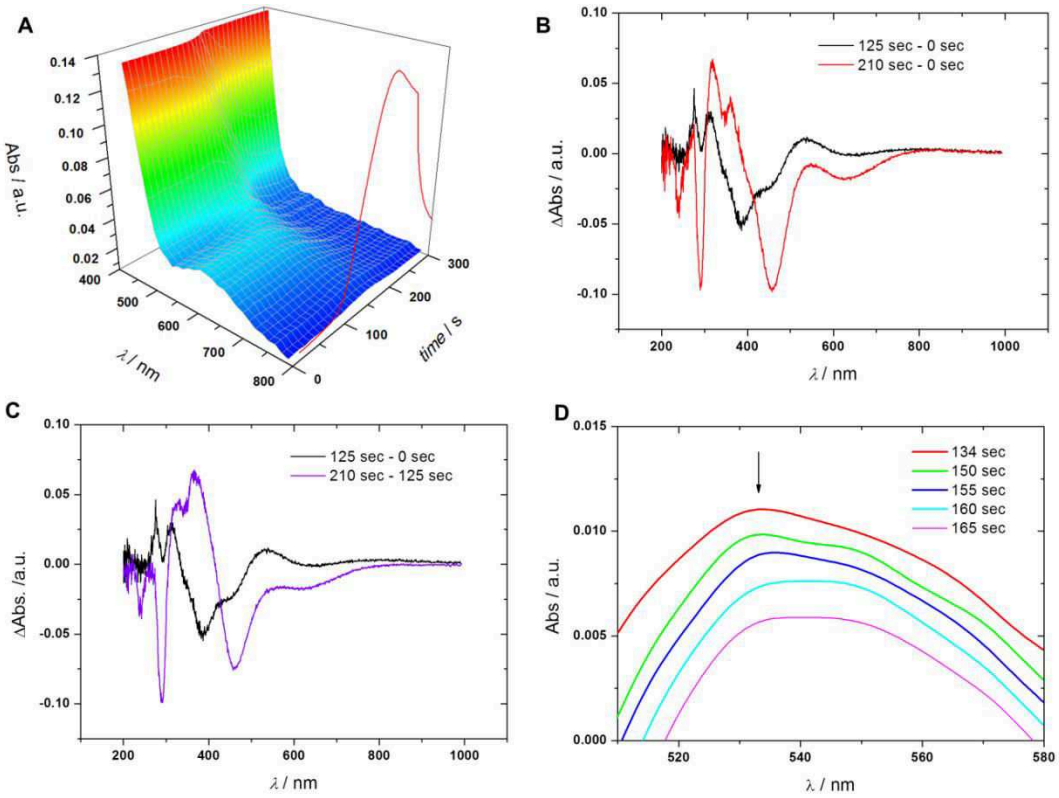

Figure II.16. A) 3D UV-Vis spectroelectrochemical data obtained for $\mathbf{2a}^{2+}$ upon electrochemical oxidation (red curve, CV 5 mV/s) in CH_3CN/NBu_4PF_6 (thin layer conditions, optical path 0.2 mm, *C* = 4 mM, 298 K). B) 2D UV-Vis spectrum at 125 s (*vs* initial curve at 0 s, black curve) and 210 s (*vs* initial curve at 0 s, red curve) obtained from spectroelectrochemical monitoring of the oxidation of $\mathbf{2a}^{2+}$. C) 2D UV-Vis spectra at 125 s (*vs* initial curve at 0 s, black curve) and 300 s (*vs* initial curve at 125 s, purple curve) obtained from spectroelectrochemical monitoring of the oxidation of $\mathbf{2a}^{2+}$. D) Monitoring of the absorption band at 532 nm with time upon electrochemical oxidation.

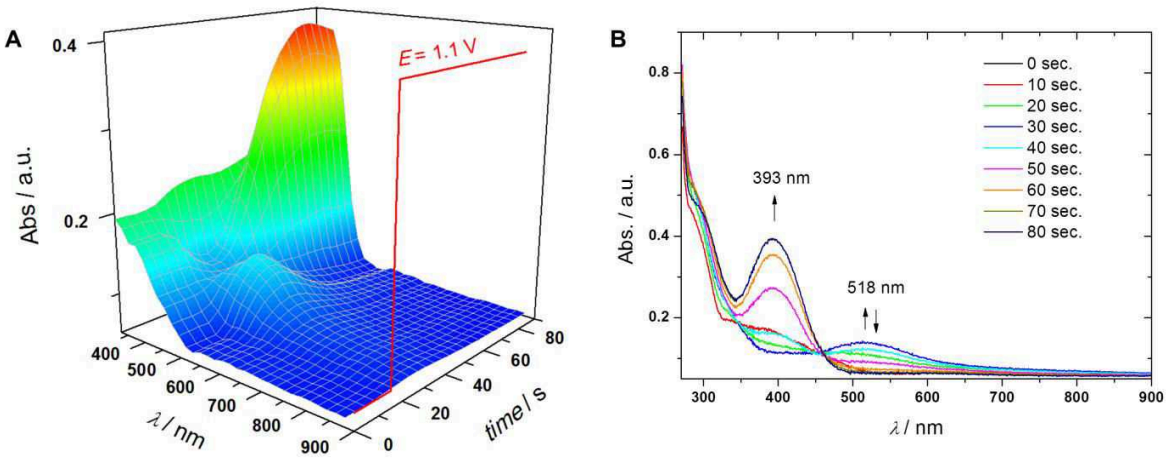

Figure II.17. A) 3D spectroelectrochemical data obtained for $\mathbf{3a}^{2+}$ upon electrochemical oxidation at 1.10 V in CH_3CN/NBu_4PF_6 (thin layer conditions, optical path 0.2 mm, *C* = 4 mM). B) Monitoring of UV-Vis spectra of the complex according to spectroelectrochemical experiment at 293 K.

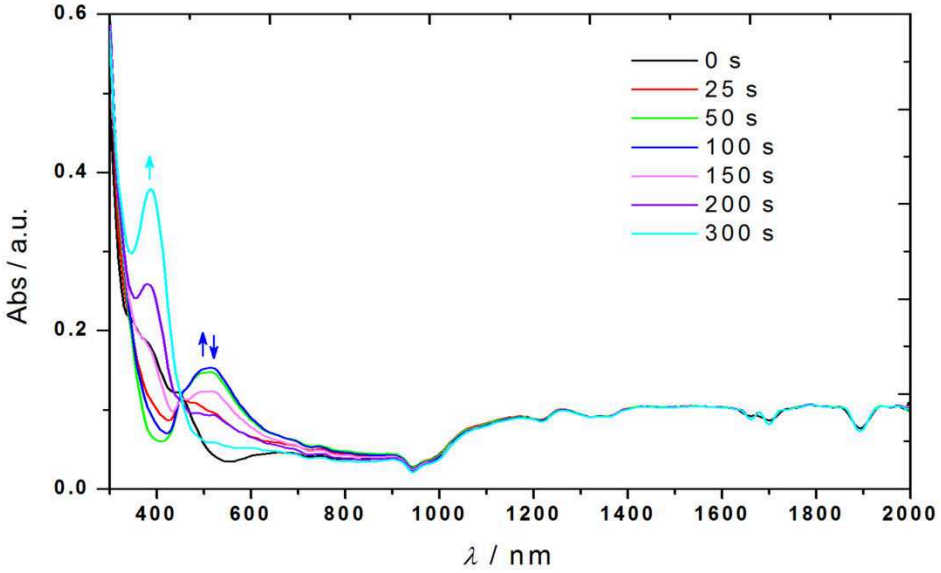

Figure II.18. 2D UV-Vis-NIR spectroelectrochemical data obtained for **3a**$^{2+}$ upon electrochemical oxidation in CH_3CN/NBu_4PF_6 (thin layer conditions, optical path 0.2 mm, C = 4 mM) at room temperature. The maximum detection of the transient (III,II,O$^-$) phenolate **3a**$^{3+}$ species (at λ_{max} = 518 nm, blue curve) occurs after 100 seconds. It decays progressively and gives a new band at λ_{max} = 393 nm (cyan curve, 300 seconds) characterizing the (II,II,O$^\bullet$) phenoxyl **3a**$^{3+}$ species. No significant change is observed in the NIR region (900-2000 nm) upon oxidation.

Hence, these spectrolectrochemical studies allow producing and analyzing by time-resolved manner the transient species formed upon oxidation. The results obtained show the influence of the chain length and of the unsymmetry on the oxidation potential. We can observe two different behaviors for the three series. Indeed for the BPMP series (**1a**$^{2+}$ and **1b**$^{2+}$), the monoelectronic oxidation is fully R-dependent and the experimental data as well the theoretical calculations show the oxidation on the phenoxo ligand leading to the formation of a phenoxyl radical (Figure II.21). In contrast, an increase of the chain length induces the formation of a transient species with λ_{max} = 520 nm upon oxidation. This intermediate species is particularly visible for the unsymmetrical complex **3a**$^{2+}$. According to previous studies on salen-type Cu^{II} complex which showed the formation of Cu(III)-phenolate systems within the [535 – 555] nm wavelength range,[32],[33],[34] we postulate that the intermediate species at λ_{max} = 532 nm for **2a**$^{3+}$ and at λ_{max} = 518 nm for **3a**$^{3+}$ are Cu^{III}O$^\bullet$Cu^{II} mixed-valent complexes.

In order to characterize this transient species, oxidation of complex **3a**$^{3+}$ was carried out at room temperature by using with $NOBF_4$ as chemical reagent. As shown in Figure II.19, after addition of one molar equivalent of oxidant, a slight decrease of the absorption band at 660 nm was detected with the appearance of a new one at 475 nm. After several minutes, a second band appears at 365 nm. The spectrum did not evolve after 60 minutes. Low-temperature EPR spectroscopy of the species

displayed a typical signature of a monocopper center in a square-base pyramidal geometry (Figure II.20). The discrepancy of these results compared to those obtained by spectroelectrochemistry might be due to the NO species which can potentially react with the Cu center.[35] Other chemical oxidants are envisaged for future characterizations.[36]

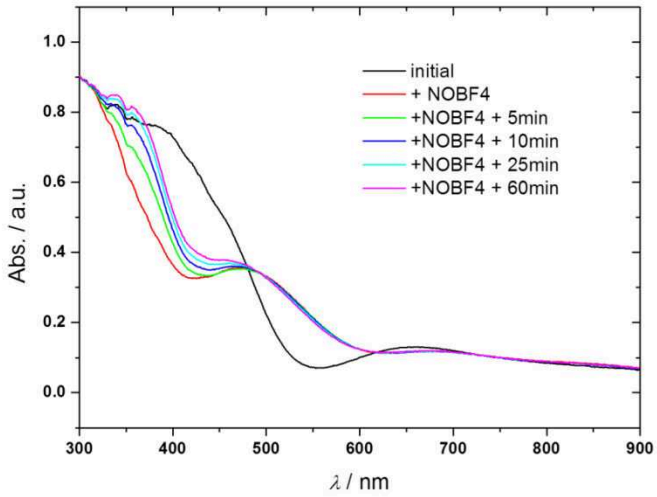

Figure II.19. UV-Vis spectroscopic data obtained for **3a**$^{2+}$ upon chemical oxidation with one molar equivalent of $NOBF_4$ in CH_3CN/NBu_4PF_6 (optical path 10 mm, C = 1 mM).

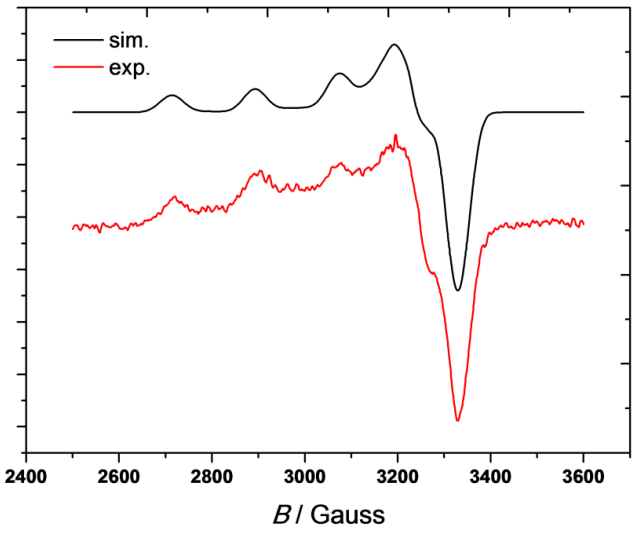

Figure II.20. Experimental (red curve) and simulated (black curve) X-band EPR spectra (T = 150 K) of the solution resulting from the chemical oxidation of **3a**$^{2+}$ with one molar equivalent of $NOBF_4$ in CH_3CN/NBu_4PF_6. Simulation was performed with the XSophe© software assuming a copper complex with a single copper center environed by 3 N atoms. Parameters for the simulated curve: $g_{//}$ = 2.24; $g_{\perp}$=2.06; $A_{//}$ = 183 Gauss. (T = 150 K, ν = 9.35 GHz)

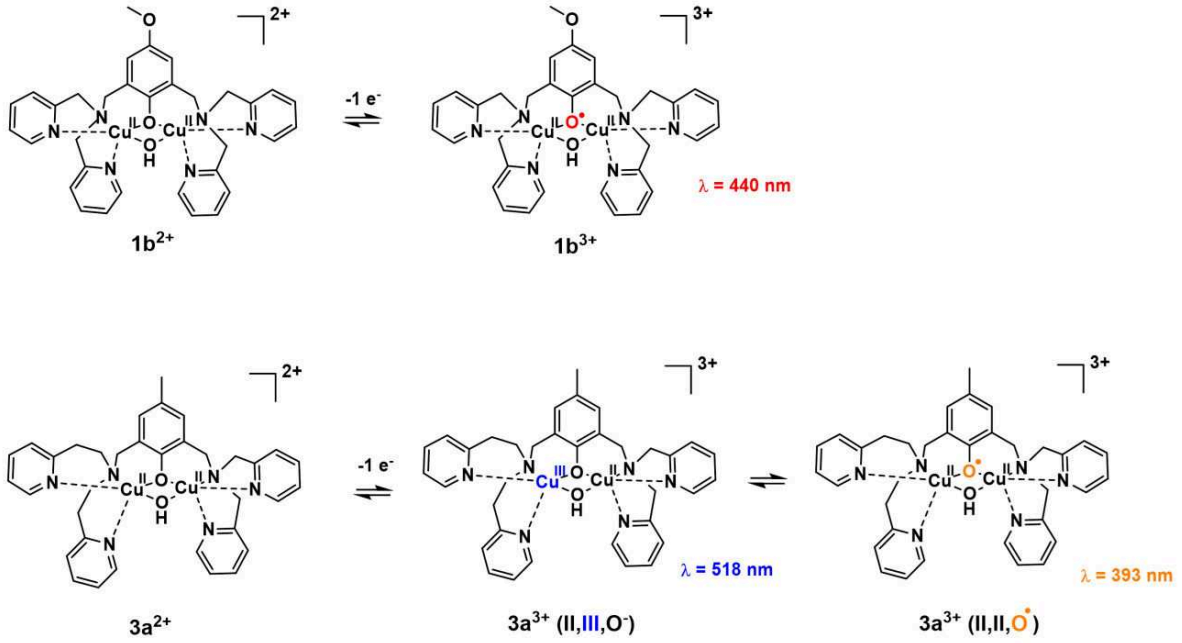

Figure II.21. Postulated transient oxidized complexes detected by spectroelectrochemistry illustrated for $\mathbf{1b}^{2+}$ (top) and $\mathbf{3a}^{2+}$ (bottom).

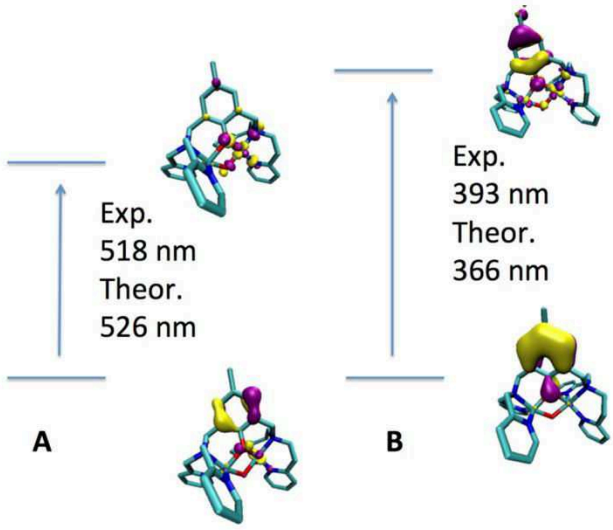

Figure II.22. Natural transition orbitals of the excited state associated to the absorption band detected successively for $\mathbf{3a}^{3+}$ by spectroelectrochemistry A) at 518 nm and B) at 393 nm.

Theoretical TD-DFT investigations have also been performed to account for the two mono-oxidized species for the unsymmetrical BPMEP series ($\mathbf{3a}^{2+}$): Cu-Cu(III,II)-phenolate and Cu-Cu(II,II)-phenoxyl (Figure II.21). As shown in Figure II.22, two bands at 526 nm and 366 nm are formed for intramolecular charge transfer for $\mathbf{3a}^{2+}$. By comparison with theoretical results, the

experimental band at λ_{max} = 518 nm is assigned to the charge transfer essentially between the phenolate ligand and the Cu^{III} ion (Figure II.22-A). Instead the mono-oxidized Cu-Cu(II,II)-phenoxyl species was found at 366 nm close to the absorption band detected experimentally at 393 nm. This band is attributed to a $\pi - \pi^*$ transition occurring on the phenoxyl radical (Figure II.22-B).

In conclusion, the chain length influences the stability of the Cu-Cu(II,III)-phenolate species found only for the symmetrical **2a**$^{2+}$ (BPEP) and unsymmetrical **3a**$^{2+}$ (BPMEP) complexes. It is not detected for the symmetrical **1a**$^{2+}$ (BPMP) complex probably because the better flexibility of the ligand for the ethyl-spacer compared to a methyl-spacer induces a better stability for the conformation of the copper center in its oxidized form.

V. Reactivity studies

V.1. Electrocatalytic activity of the complexes by electrochemical generation of the phenoxyl radical in acetonitrile

Electrochemical studies of the R-BPMP (**1a**$^{2+}$, **1b**$^{2+}$ and **1c**$^{2+}$), BPEP (**2a**$^{2+}$) and BPMEP (**3a**$^{2+}$) hydroxo-bridged dinuclear Cu copper complexes have shown that slight modifications could impact in a strong manner the redox behavior, particularly in oxidation. On the basis of these results, we have focused the reactivity studies on the complex displaying the lowest oxidation potential **1b**$^{2+}$, *i.e*. Cu_2-OCH_3-BPMP. Our ultimate goal was to generate electrochemically the phenoxyl radical in order to perform electrocatalytic processes for oxidation of the benzyl alcohol. We have first investigated the reactivity of the one-electron oxidized Cu_2-OCH_3-BPMP (**1b**$^{2+}$) complex toward a simple substrate which is likely to coordinate to Cu^{II} and cannot be oxidized at low potential values (E > 1 V vs Fc). A primary aliphatic amine (*n*-butylamine) was chosen because of its well-known coordination properties towards copper ion and its high oxidation potential. In order to better characterize the process of substrate coordination to Cu^{II}, two different OCH_3-BPMP dicopper complexes, $[Cu_2(OCH_3\text{-BPMP})(\mu\text{-OH})]^{2+}$ (**1b**$^{2+}$) and the previously described $[Cu_2(OCH_3\text{-BPMP})(L)_2]^{4+}$ (**1d**$^{4+}$, L= H_2O, Figure II.23),[9] have been used. As shown in Figure II.24, both complexes display a very close oxidation potential value (0.40 V vs Fc in CH_3CN), but strongly differ in reduction: **1d**$^{4+}$ complex is reduced at a much higher potential value (-0.50 V vs Fc) than **1b**$^{2+}$ (-1.0 V), as a result of the different σ-donor properties of μOH and L ligands (L= CH_3CN in acetonitrile probably).

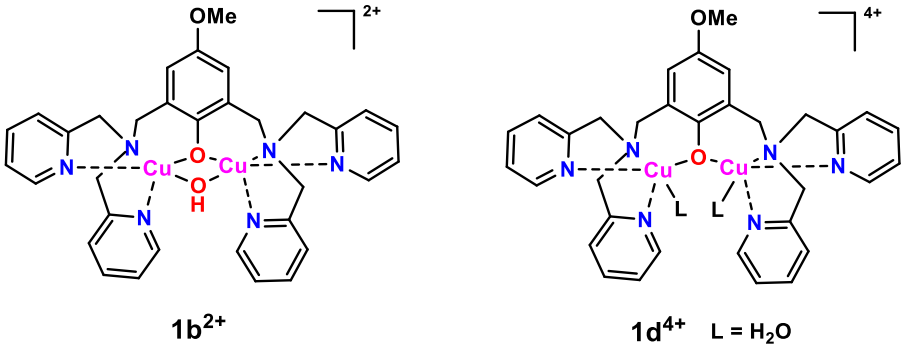

Figure II.23. Schematic representation of **1b**$^{2+}$ and **1d**$^{4+}$.

Cyclic voltammetry has been carried out to study the electrocatalytic reaction as well as the coordination properties of the complexes. As shown in Figures II.24-A and II.24-B, addition of butylamine to the solution of complex induces a modification of the CV on the cathodic part, but only for **1d**$^{4+}$. After addition of more than one equivalent of amine on **1d**$^{4+}$, the CV did not evolve significantly, which suggests that $[Cu_2(O\text{-}BPMP)(L)(BuNH_2)]^{4+}$ is the major species formed.

Low scan rate voltammetry (0.005 V/s) has then been performed to scrutinize the electrocatalyzed oxidation of butylamine by the phenoxyl radical. Both complexes display electrocatalytic properties as shown by the increase of the anodic peak current (i_{pa}) as well as the loss of reversibility (Figure II.24-A-B-C). Plots of anodic peak current against butylamine concentration display a progressive increase of i_{pa} until a maximum value which does not evolve after further increase of $[BuNH_2]$ (Figure II.24-D). This plateau is attained after addition of 5 molar equivalents. The non-linearity of i_{pa} vs $[BuNH_2]^{1/2}$ plots indicates that the catalyst activity is hindered by secondary processes involving butylamine (Inset Figure 24 D). On this basis, voltammetric fitting of the curves was performed by assuming that the oxidized amine reacts with the initial complex and its oxidized form. Experimental trends were reproduced, as shown by the red curve in Figure 24 D. Hence, the similarity of results between the μ-OH and bis-nitrilo complexes strongly suggests that coordination of butylamine to Cu^{II} is not necessary for the catalytic reaction. In other words, the electron transfer reaction seems likely to occur between a non-coordinated amine and the electrochemically generated phenoxyl radical. Increasing the concentration in substrate does not increase the current intensity, probably because of passivation of the electrode surface. Indeed, the electrochemical oxidation of amines in organic solvent (like acetonitrile) can produce the polymerization of radical cations onto the surface.[37],[38] As a result the wave shifts and decreases in intensity. This can be improved by polishing the electrode with alumina after each measurement, but the deposition is inevitable if one scans at very slow scan (5 mV/s), as required to study the electrocatalytic system.

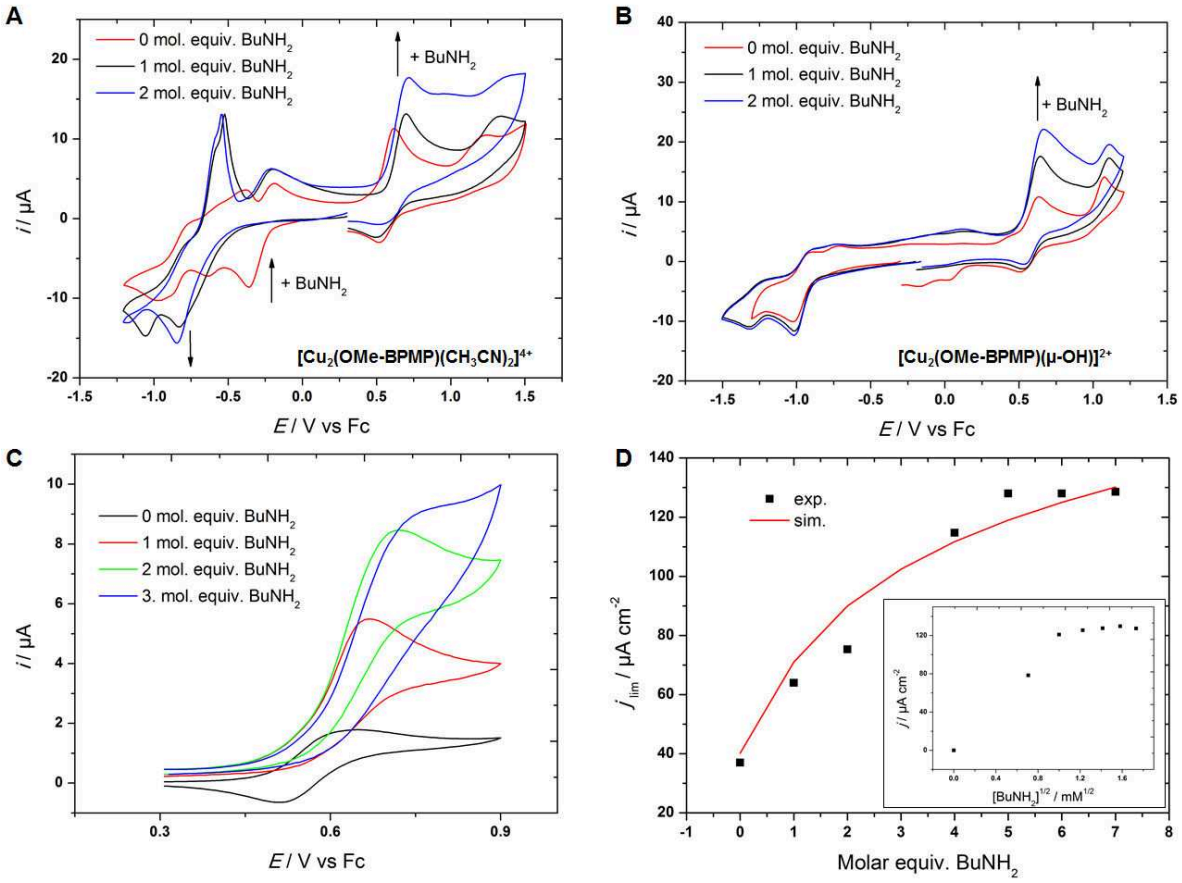

Figure II.24. CVs (v = 0.1 V/s) at a vitreous carbon electrode (E / V vs Fc) of **1d^{4+}** (Panels A and C) and of $[Cu_2(OCH_3\text{-BPMP})(\mu\text{-}OH)_2]^{2+}$ (Panel B) in CH_3CN/NBu_4PF_6 0.1 M upon progressive addition of butylamine. A) and B) v = 0.1 V/s; C) v = 0.005 V/s. D) Plots of current density vs $[BuNH_2]$ (black square); red curve : Simulated curve assuming an electrocatalytic process.

V.2. Electrocatalytic oxidation of benzyl alcohol

On the basis of the results obtained with the butylamine, similar voltammetric studies were performed with benzyl alcohol to mimic a galactose oxidase activity. Figure II.25-A displays the voltammetric behavior of **1d^{4+}** upon addition of 40 molar equivalents of benzyl alcohol. Slight modifications of the CV are observed on the cathodic part: the reduction peak at -0.35 V slightly decreases in favor of a new peak at lower potential. The same experiment performed with the bis-µ-hydroxo species did not change the voltammetric behavior. Hence, for both complexes, formation of the $PhCH_2OH$-Cu adduct is not favored under these experimental conditions. This indicates that coordination of $PhCH_2OH$ to Cu^{II} is difficult to proceed because of the strong binding of the µ-hydroxo or nitrilo ligands to the Cu^{II} centers.

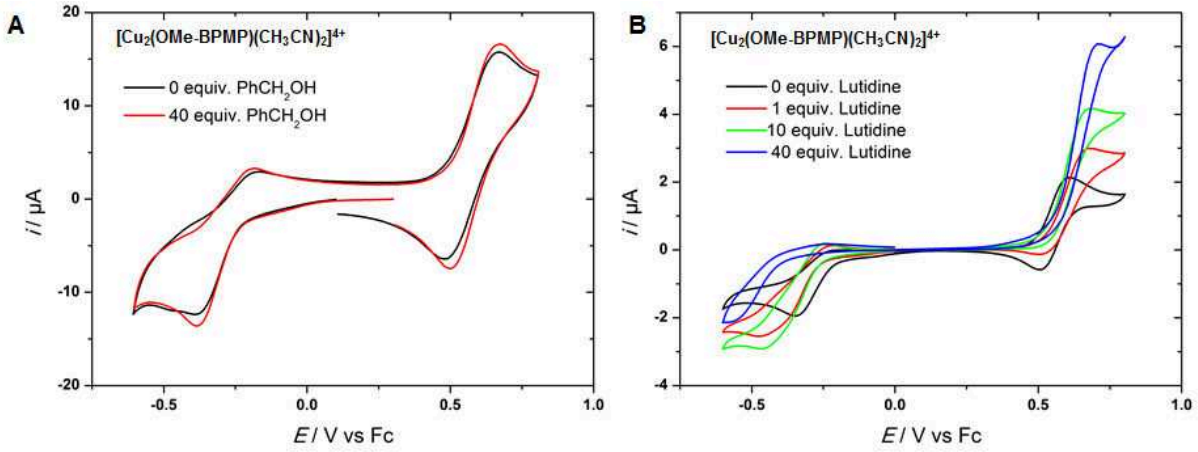

Figure II.25. CVs (v = 0.1 V/s) at a vitreous carbon electrode (E / V vs Fc) of **1d**$^{4+}$ in CH_3CN/NBu_4PF_6 0.1 M: A) upon addition of 40 equiv. of benzyl alcohol (v = 0.1 V/s); B) Upon progressive addition of lutidine (40 equiv.) (v = 0.005 V/s).

CV of the complex has then been performed to possibly trigger the substrate oxidation by reaction with the electrochemically-generated phenoxyl radical. Low scan rate voltammetry did not induce the appearance of any electrocatalytic wave. This result may be ascribed to the poor coordination affinity of benzyl alcohol towards Cu^{II}. Another possible reason is that deprotonation of the alcohol, which is necessary for Hydrogen Atom Transfer (HAT), did not occur. To further understand this behavior, the same experiments have been performed in basic media. We have first investigated the CV response in presence of sodium benzyl alcoholate instead of benzyl alcohol. Unfortunately, the benzyl alcoholate alone displays an oxidation peak which occurs at a lower potential value (0.4 V) than that of the complex itself (0.5 V), meaning that electrocatalytic process cannot proceed. The second approach has consisted then in performing the experiments in presence of benzyl alcohol and 2,5-lutidine (methylpyridine). The latter is a weak base which is electrochemically oxidized at high potential (E = 1.2 V vs Fc). Interestingly, the voltammetric behavior is modified: slight increase of peak current, S-shape of the curve at low scan rate and irreversibility. Such behavior is typical of an electrocatalytic process, as observed with butylamine. To further understand this process, control experiments have been performed with lutidine under anaerobic conditions and/or without benzyl alcohol. As shown in Figure II.25-B, addition of lutidine only leads also to the appearance of an electrocatalytic wave, which evidences the reactivity of the phenoxyl radical toward the weak base, and probably not the alcohol.

VI. Conclusions

Thorough electrochemical and theoretical studies of hydroxo-phenoxo-bridged dinuclear copper complexes have shown that redox properties could be finely tuned by slight modification of the ligand topology. In particular, the effect has been fully demonstrated by voltammetric studies of symmetrical BPMP (**1a**$^{2+}$, **1b**$^{2+}$, **1c**$^{2+}$), BPEP (**2a**$^{2+}$) and unsymmetrical BPMEP (**3a**$^{2+}$) complexes for both oxidation and reduction processes. In full correlation with DFT calculations, the increase of spacer length or breakage of the symmetry of the molecule induces a positive shift of the redox potential value associated with the oxidation of the bridging phenoxo part. *In situ* UV-Vis spectro-electrochemical monitoring of the formation of the phenoxyl radical has been performed at room temperature. The results suggest the formation of a transient mixed valence $Cu_2^{III,II}$ species for the unsymmetrical BPMEP (**3a**$^{2+}$) and symmetrical (BPEP, **2a**$^{2+}$) families. The more intense signal for the unsymmetrical series compared to the symmetrical one (BPEP, **2a**$^{2+}$) may be due to the better stability of the $Cu_2^{III,II}$ species when it is accommodated in this distorted geometry. It was shown to be unreactive toward benzyl alcohol by low scan rate voltammetry. Substrate accessibility and phenoxyl radical reactivity were however clearly evidenced by electrocatalytic oxidation of an aliphatic primary amine. The results also emphasize that the reaction with the phenoxyl radical could occur in an outer-sphere manner. With the aim of developing functional models of GAO, future phenoxo-dinucleating ligands can be designed in such a way that their complex will favor substrate coordination and proton removal, while keeping low oxidation potential (E < 0.5 V vs Fc).

BIBLIOGRAPHY

[1] Y. Shiota, K. Yoshizawa, *Inorg*. *Chem*. **2009**, *48*, 838-845.
[2] E. I. Solomon, D. E. Heppner, E. M. Johnston, J. W. Ginsbach, J. Cirera, M. Qayyum, M. T. Kieber-Emmons, C. H. Kjaergaard, R. G. Hadt, L. Tian, *Chem*. *Rev*. **2014**, *114*, 3659-3853.
[3] C. E. Elwell, N. L. Gagnon, B. D. Neisen, D. Dhar, A. D. Spaeth, G. M. Yee, W. B. Tolman, *Chem*. *Rev*. **2017**, *117*, 2059-2107.
[4] K. D. Karlin, J. C. Hayes, J. P. Hutchinson, J. Zubieta, *Inorg*. *Chim*. *Acta* **1983**, *78*, L45-L46.
[5] K. D. Karlin, J. C. Hayes, Y. Gultneh, R. W. Cruse, J. W. McKown, J. P. Hutchinson, J. Zubieta, *J*. *Am*. *Chem*. *Soc*. **1984**, *106*, 2121-2128.
[6] P. Ghosh, Z. Tyeklar, K. D. Karlin, R. R. Jacobson, J. Zubieta, *J*. *Am*. *Chem*. *Soc*. **1987**, *109*, 6889-6891.
[7] L. Li, A. A. Sarjeant, K. D. Karlin, *Inorg*. *Chem*. **2006**, *45*, 7160-7172.
[8] H. Adams, D. E. Fenton, S. R. Haque, S. L. Heath, M. Ohba, H. Okawa, S. E. Spey, *J*. *Chem*. *Soc*., *Dalton*. *Trans*. **2000**, 1849-1856.
[9] S. Torelli, C. Belle, I. Gautier-Luneau, J. L. Pierre, E. Saint-Aman, J. M. Latour, L. Le Pape, D. Luneau, *Inorg*. *Chem*. **2000**, *39*, 3526-3536.
[10] C. Belle, C. Beguin, I. Gautier-Luneau, S. Hamman, C. Philouze, J. L. Pierre, F. Thomas, S. Torelli, E. Saint-Aman, M. Bonin, *Inorg*. *Chem*. **2002**, *41*, 479-491.
[11] S. Torelli, C. Belle, S. Hamman, J.-L. Pierre, E. Saint-Aman, *Inorg*. *Chem*. **2002**, *41*, 3983-3989.
[12] H. Adams, S. Clunas, L. R. Cummings, D. E. Fenton, P. E. McHugh, *Inorg*. *Chem*. *Commun*. **2003**, *6*, 837-840.
[13] S. P. Foxon, D. Utz, J. Astner, S. Schindler, F. Thaler, F. W. Heinemann, G. Liehr, J. Mukherjee, V. Balamurugan, D. Ghosh, R. Mukherjee, *Dalton Trans*. **2004**, 2321-2328.
[14] M. Orio, C. Bochot, C. Dubois, G. Gellon, R. Hardre, H. Jamet, D. Luneau, C. Philouze, M. Reglier, G. Serratrice, C. Belle, *Chem*. *Eur*. *J*. **2011**, *17*, 13482-13494.
[15] C. Bochot, E. Favre, C. Dubois, B. Baptiste, L. Bubacco, P. A. Carrupt, G. Gellon, R. Hardre, D. Luneau, Y. Moreau, A. Nurisso, M. Reglier, G. Serratrice, C. Belle, H. Jamet, *Chem*. *Eur*. *J*. **2013**, *19*, 3655-3664.
[16] S. Mandal, J. Mukherjee, F. Lloret, R. Mukherjee, *Inorg*. *Chem*. **2012**, *51*, 13148-13161.
[17] P. Chakraborty, J. Adhikary, B. Ghosh, R. Sanyal, S. K. Chattopadhyay, A. Bauzá, A. Frontera, E. Zangrando, D. Das, *Inorg*. *Chem*. **2014**.
[18] M. Costas, X. Ribas, A. Poater, J. M. Lopez Valbuena, R. Xifra, A. Company, M. Duran, M. Sola, A. Llobet, M. Corbella, M. A. Uson, J. Mahia, X. Solans, X. Shan, J. Benet-Buchholz, *Inorg*. *Chem*. **2006**, *45*, 3569-3581.
[19] N. N. Murthy, M. Mahroof-Tahir, K. D. Karlin, *Inorg*. *Chem*. **2001**, *40*, 628-635.
[20] M. S. Nasir, K. D. Karlin, D. McGowty, J. Zubieta, *J*. *Am*. *Chem*. *Soc*. **1991**, *113*, 698-700.
[21] I. A. Koval, P. Gamez, C. Belle, K. Selmeczi, J. Reedijk, *Chem*. *Soc*. *Rev*. **2006**, *35*, 814-840.
[22] T. N. Sorrell, *Tetrahedron* **1989**, *45*, 3-68.
[23] J. H. Satcher, M. W. Droege, T. J. R. Weakley, R. T. Taylor, *Inorg*. *Chem*. **1995**, *34*, 3317-3328.
[24] J. Serrano-Plana, M. Costas, A. Company, *Inorg*. *Chem*. **2014**, *53*, 12929-12938.
[25] F. Michel, S. Torelli, F. Thomas, C. Duboc, C. Philouze, C. Belle, S. Hamman, E. Saint-Aman, J. L. Pierre, *Angew*. *Chem*. *Int*. *Ed*. *Engl*. **2005**, *44*, 438-441.
[26] A. Mukherjee, F. Lloret, R. Mukherjee, *Inorg*. *Chem*. **2008**, *47*, 4471-4480.
[27] Z. Alaji, E. Safaei, L. Chiang, R. M. Clarke, C. Mu, T. Storr, *Eur*. *J*. *Inorg*. *Chem*. **2014**, *2014*, 6066-6074.
[28] V. B. Arion, S. Platzer, P. Rapta, P. Machata, M. Breza, D. Vegh, L. Dunsch, J. Telser, S. Shova, T. C. Mac Leod, A. J. Pombeiro, *Inorg*. *Chem*. **2013**, *52*, 7524-7540.
[29] C. T. Lyons, T. D. Stack, *Coord*. *Chem*. *Rev*. **2013**, *257*, 528-540.
[30] A. Kochem, A. Carrillo, C. Philouze, M. van Gastel, A. du Moulinet d'Hardemare, F. Thomas, *Eur*. *J*. *Inorg*. *Chem*. **2014**, *2014*, 4263-4267.

[31] A. W. Addison, T. N. Rao, J. Reedijk, J. van Rijn, G. C. Verschoor, *J*. *Chem*. *Soc*., *Dalton Trans*. **1984**, 1349-1356.
[32] T. Storr, P. Verma, R. C. Pratt, E. C. Wasinger, Y. Shimazaki, T. D. Stack, *J*. *Am*. *Chem*. *Soc*. **2008**, *130*, 15448-15459.
[33] L. Chiang, K. Herasymchuk, F. Thomas, T. Storr, *Inorg*. *Chem*. **2015**, *54*, 5970-5980.
[34] K. Asami, K. Tsukidate, S. Iwatsuki, F. Tani, S. Karasawa, L. Chiang, T. Storr, F. Thomas, Y. Shimazaki, *Inorg*. *Chem*. **2012**, *51*, 12450-12461.
[35] M. Sarma, B. Mondal, *Inorg*. *Chem*. **2011**, *50*, 3206-3212.
[36] N. G. Connelly, W. E. Geiger, *Chem*. *Rev*. **1996**, *96*, 877-910.
[37] J. Ghilane, P. Martin, H. Randriamahazaka, J.-C. Lacroix, *Electrochem*. *Commun*. **2010**, *12*, 246-249.
[38] A. Adenier, M. M. Chehimi, I. Gallardo, J. Pinson, N. Vila, *Langmuir* **2004**, *20*, 8243-8253.

Chapter III

Dicopper complex with a naphthyridine spacer

I. Introduction

In the precedent Chapter, the phenoxo-bridged dicopper complexes bearing polypyridyl moieties displayed a first oxidation on the spacer rather than on the metal ions, except for the unsymmetrical complex (transient mixed-valent Cu^{III} Cu^{II} species). Such situation was due to the poor donor strength of the polypyridyl groups combined to the relative easiness of oxidation of the redox non-innocent phenolate moiety into a phenoxyl radical. From this conclusion and in order to form a mixed valent bis(μ-oxo)$Cu_2^{III\,II}$ complex, we have modified our strategy by adjusting the nature of the spacer without changing the DPA coordinating cores on each side on the dinucleating ligand. Several parameters have to be considered for the modeling of the active site of pMMO: (i) a suitable short distance between the two copper ions in the catalytic site, (ii) a rigid ligand to enforce a fixed coordination environment around the metal centers. In order to respect these conditions, we chose the 1,8-naphthyridine group (*np*) as a spacer ligand (Figure III.1) as it displays interesting specifications proper to model Cu-Cu coordination in pMMO (2.6 Å distance). First, the two donor atoms are separated by only a single C atom. Second, this well-known neutral bidentate ligand displays a good planarity and no redox activity. Moreover it has the capability of forming strained four members ring chelate without ionic charge.

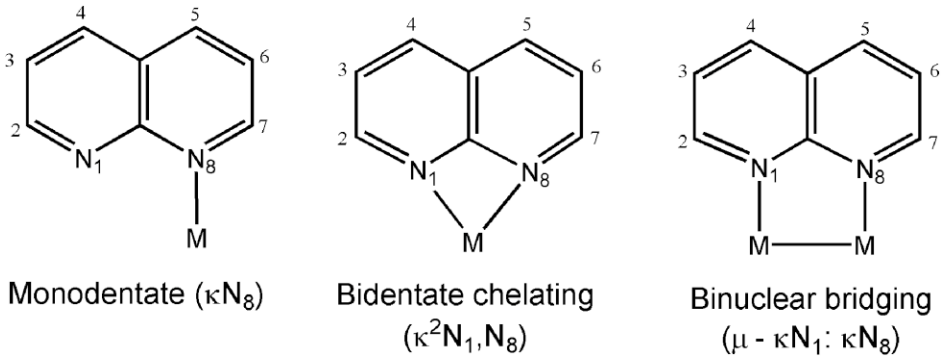

Figure III.1. Schematic representation of the different coordination modes for the 1,8-naphthyridine (*np*) group. Reproduced from Ref. [1].

The first synthesis and isolation of a fully aromatic 1,8-naphthyridine derivative was reported by Koller.[2] Later, several authors have described the synthesis of other 1,8-naphthyridine derivatives.[3],[4] The use of 1,8-naphthyridine as a ligand for the preparation of coordination compound was reported for the first time by Enwall for his PhD thesis.[5] His objective was to synthesize metal complexes similar to dicopper acetate monohydrate for a better understanding of the magnetic exchange interaction between two copper(II) ions maintained in a close distance. This first compound isolated was however a monocopper(II) dichloro-bis-(1,8-naphthyridine) complex in which the copper(II) ion stands in a square planar geometry, through binding of naphthyridine in a monodentate mode. Later on, other works described the versatile coordination chemistry of *np* which can be

monodentate, bidentate or bridging in mononuclear and dinuclear complexes (Figure III.1). In most of cases, it afforded a bidentate coordination mode, with 1[6] up to 3, 4, or 6 *np* units per metal ion.[7],[8],[9],[10] For example, Emerson and coworkers reported the first example of a bis-naphthyridine dicopper complex in which each *np* unit is coordinated in a bidentate mode to one copper ion, the bridging interaction being ensured through chloro bridges.[11] This complex was the first of this family displaying "subnormal magnetic properties" (magnetic exchange).

Bridging two metal ions (Ni and Cu) with a single *np* derivative was achieved by Sacconi and co-workers by using 4-methyl-1,8-naphthyridine (Me*np*) ligands (Figure III.2).[12],[13] For the dicopper, complex, the characterization by single-crystal X-ray diffraction revealed a bimetallic core bridged by two Me-naphthyridine units and one chloride ion. The Cu-Cu distance was found to be 2.386 Å, hence suggesting a possible metal-metal orbital overlap. The coordination geometry for each copper atom was described as a highly distorted tetrahedron. ESR and NIR spectroscopies the complex revealed a mixed valence compound, $Cu^{III}Cu^{II}$, of class III in the Robin and Day's classification, hence strong electronic delocalization. These properties were correlated to the rigidity of the naphthyridine ligand which probably enforces a tetrahedral geometry around Cu^{II} ions making them highly oxidant, and inducing a distorted structure with a very short Cu-Cu distance. This constraint was overcome by introducing a second bridging chloride ion in the coordination sphere (by changing the stoichiometry during synthesis), leading to the formation of a dicopper(II) complex displaying higher metal-metal distance (2.659 Å) (Figure III.2).[14] Later, a bis-Cu^{I} complex was also obtained with intermediate Cu-Cu distance value (2.506 Å).[15] These results emphasized the interest of the naphthyridine ligand in promoting copper dinuclear complexes with very short metal-metal distances and controlled geometry.

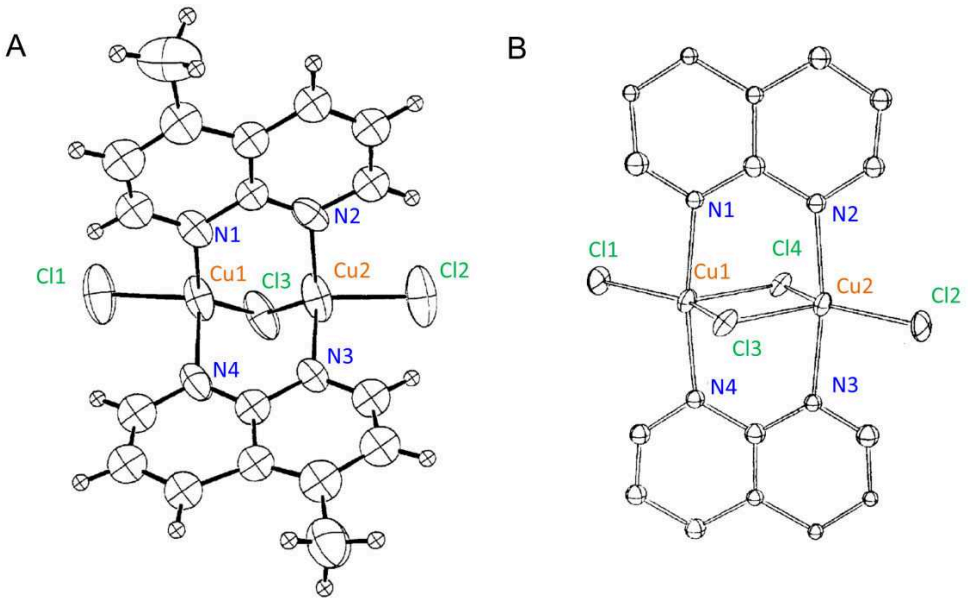

Figure III.2. X-ray structures of the complexes A) $[Cu_2Cl_3(Me\mathit{np})_2]$ and B) $[Cu_2Cl_4(\mathit{np})_2]$. Reproduced from Refs [13] and [14].

Functionalization of the *np* core with coordinating arms opened the range of applications for this family of metal complexes. An interesting derivative of the naphthiridine ligand was synthesized by Caluwe and co-workers[16] in which the naphthyridine moeity displayed two pyridine groups in ortho position leading to the *bpnp* ligand (Figure III.3). Kaska and Ford used this motif to coordinate two rhodium(II) ions and study the physical and electrochemical properties.[17] The same group reported the synthesis and properties of several copper(I) and copper(II) mononuclear and dinuclear complexes with the *bpnp* ligand. For instance, they reported the formation of a dinuclear complex where two metal ions are bridged by the *np* unit, a chloride ion and a hydroxo motif (Figure III.3). They found a Cu-Cu distance of 3.022 Å without substantive metal-metal bonding.[18]

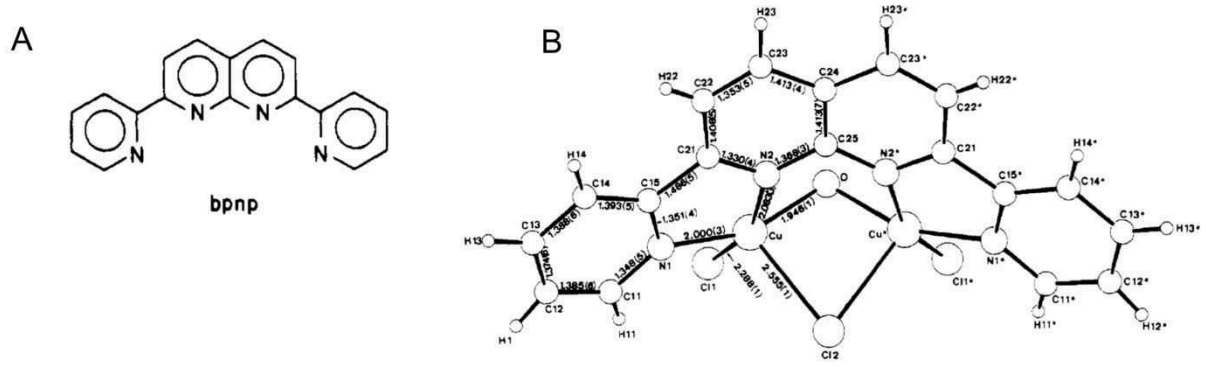

Figure III.3. Schematic representation of A) the *bpnp* ligand (2,7-bis(2-pyridyl)-1,8-naphthyridine) and B) the $[Cu_2Cl_2(bpnp)(\mu\text{-}OH)(\mu\text{-}Cl)]$ complex. Reproduced from Ref. [18].

Various metal complexes derived from other substituted symmetrical and unsymmetrical *np* ligands were synthesized over years.[1],[18],[19],[20],[21],[22],[23],[24],[25] Noticeably in 2011, Davenport and co-workers incorporated a 2,2'-dipyridylethyl group into the 2 and 7 positions of the *n*p core giving rise to the potentially six-donor dinucleating *dpen* ligand (Figure III.4).[26] A dicopper(I) bridged by the *dpen* ligand and a nitrile was reported (Figure III.4). The metal-metal distance was found as 2.44 Å. A cuprophilic "electron-deficient" interaction was suggested on the basis of a three-center (Cu-N-Cu) two-electron bond. More recently, the same group investigated the coordination chemistry of a 2,7-bis(di(2-pyridyl)fluoromethyl)-1,8-naphthyridine (*dpfn*) scaffold.[27] Figure III.5 shows the various mono and dinuclear complexes derived from this ligand with Cu, Mn, Co and Ni metal ions. All *dpfn*-based metal complexes displayed a metal-metal distance ranging between 2.8 and 3.2 Å. The structural properties of *dpfn* led to the formation of pseudo-octahedral metal centers with two one-atom bridging ligands to give "diamond-shaped" dinuclear complexes. As shown in Figure III.5 the metal centers can be bridged by Cl^- or OH^- groups.

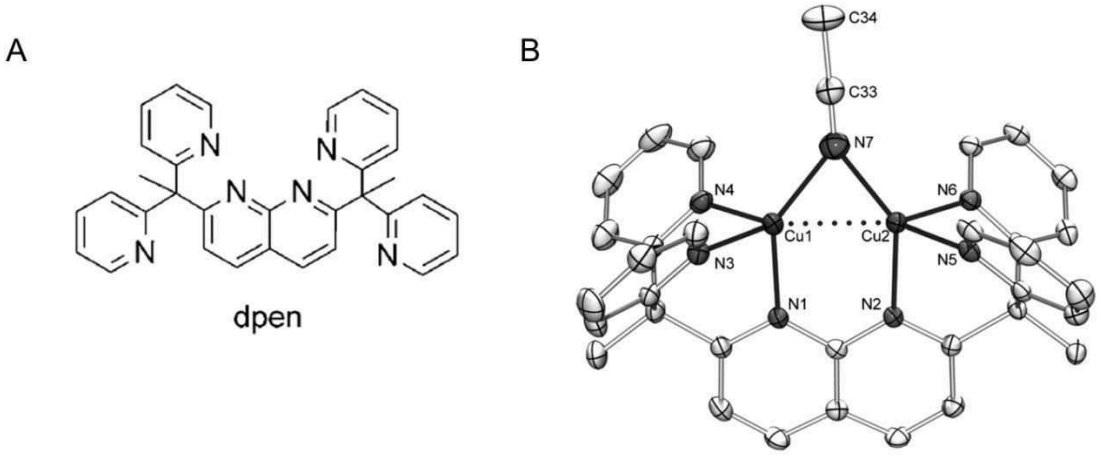

Figure III.4. Schematic representation of the *dpen* ligand and the bis-copper(I) complexes. Reproduced from Ref. [26].

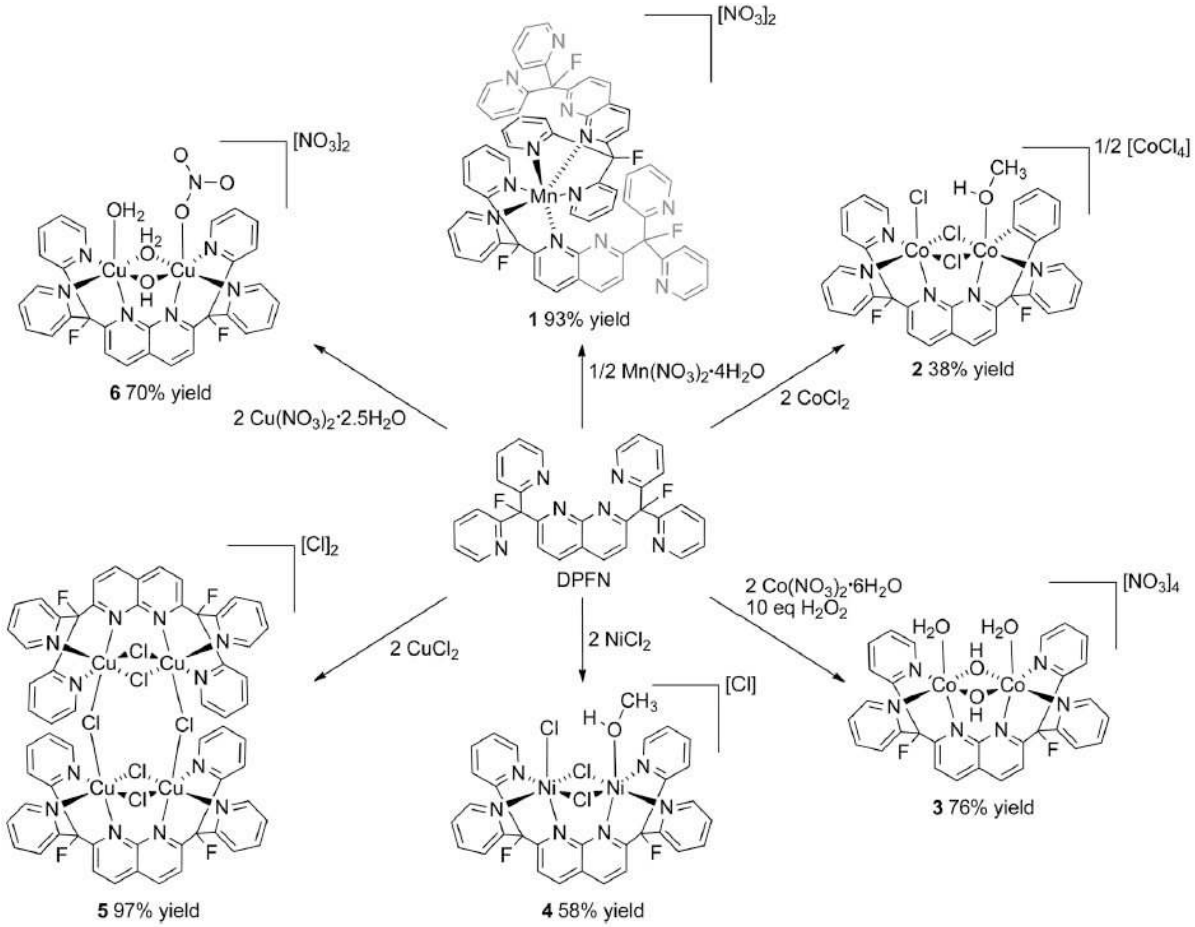

Figure III.5. Metal complexes derived from the ligand *dpfn*. Reproduced from Ref. [27].

Metal-naphthyridyne complexes were also investigated for their reactivity towards different chemical reagents. Hence, Lippard and co-workers studied the reaction of a bis-Cu(I) complex bearing the *bpman* ligand with dioxygen (Figure III.6).[28] A (μ-1,2-peroxo)dicopper(II) species was characterized by UV-Vis spectroscopy at low temperatures. EXAFS studies revealed a short Cu-Cu distance of about 2.84 Å, similar to those determined previously for bis(μ-oxo) dicopper(III) complexes.[29],[30],[31] This property was ascribed to the rigid structure of the ligand. A (μ-hydroxo)dizinc(II) complex was also synthesized by Lippard *et al*. to carry out the hydrolysis of phosphodiesters and the hydrolysis of β-lactams.[32] The low reactivity of the complex was assigned to the *trans* position of the μ-OH group in respect to the coordinated substrate, as well as its reduced nucleophilicity by coordination to two zinc(II) ions. Recently, a $[Cu_2(bpman)(\mu\text{-}OH)]^{3+}$ complex demonstrated catalytic properties for water oxidation upon electrochemical oxidation at neutral pH. Theoretical calculations suggested that the O-O bond formation occurs after a ($2e^-$, $2H^+$) process according to an intramolecular coupling mechanism.[33] In 2001, Liu and co-workers investigated the catalytic properties of $[Cu_2(bpnp)(OH)(CF_3COO)_3]$ for the oxidative coupling of phenols in mild conditions.[23] In addition, they studied the diamination of phenylene dihalides with aqueous ammonia to give the corresponding phenylenediamines.[22]

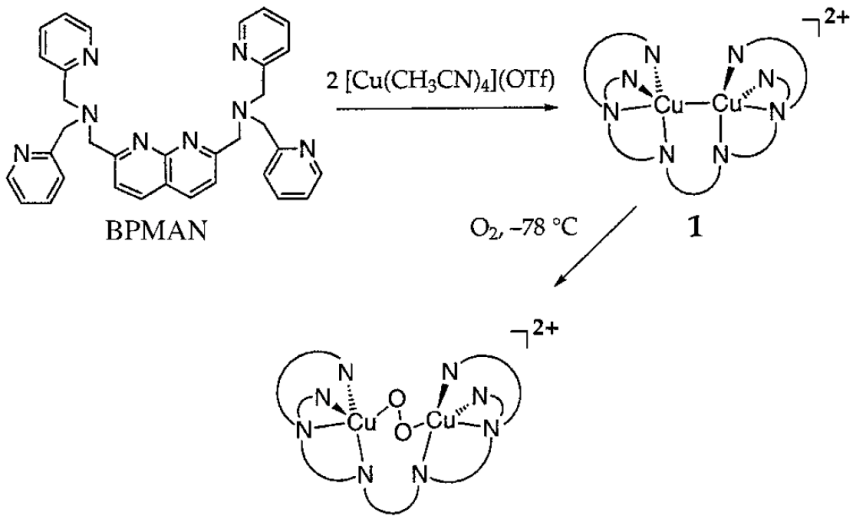

Figure III.6. Reactivity of the *bpman*-Cu^I_2 complex with O_2. Reproduced from Ref. [28].

Naphthyridine-based copper complexes were also investigated to isolate mixed-valent species since the rigid bridging ligand is supposed to favour cooperative interaction between the two metal ions.[34],[35] Hence, Lippard and co-workers developed a series of copper complexes binding a 1,8-naphthyridine ligand in order to perform the spin-delocalized dinuclear mixed-valence copper(II,I) cluster. A fully delocalized mixed-valence Cu(II,I) of class III was thus obtained from a dicopper(I) naphthyridine compound bridged by O_2CCPh_3 and treated with silver(I) triflate.[36]

In summary, coordination chemistry of naphthyridine-based metal complexes has shown that the *np* core can be easily derived to obtain various mono or bimetallic systems with versatile properties. In particular dicopper complexes in which the copper ions are bridged by the *np* unit and environed by polypyridyl ligands displayed remarkable Cu-Cu short distances ascribed to the rigid *np* backbone. From this basis and aiming at characterizing mixed-valent $Cu_2^{III,II}$ (μ-O(H)) species, our purpose has been to develop and characterize a new bis(μ-OH) dicopper complex **4** bearing the *dpen* ligand previously reported by Tilley and co-workers.[26]

II. Synthesis, characterization and redox properties of complex 4

II.1. Synthesis and solid-state characterization of complex 4

The synthesis of complex **4** was performed by reaction of 2 equivalents Cu^{II} triflate with one equivalent of *dpen* in THF in the presence of triethylamine and water (Figure III.7). The resulting powder was characterized by NMR and UV-Vis spectroscopies, as well as mass spectrometry (ESI).

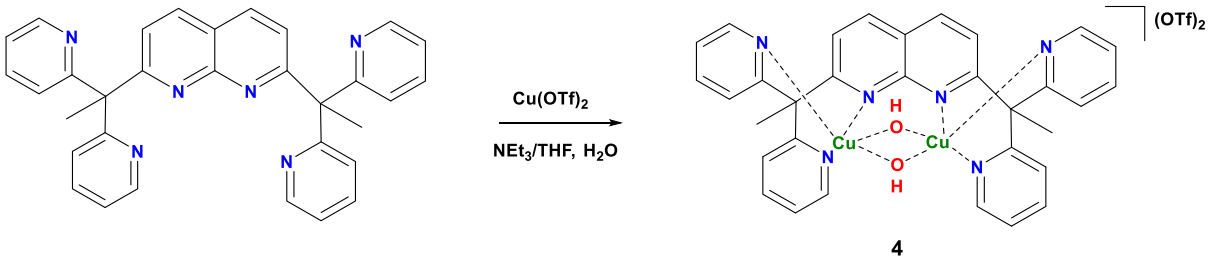

Figure III.7. Synthesis of complex **4**.

Crystals of the powder were obtained by vapor diffusion of diisopropylether into CH_3CN. The unit cell contains two independent $[Cu_2^{II}(dpen)(\mu\text{-}OH)_2(OTf)](OTf)\cdot 1.8CH_3CN$ entities **4A** and **4B**. Both show almost no significant differences in their bond distances and angles. Table III.1 gathers selected bond distances and angles for **4A**. The cationic unit of **4A** is shown in Figure III.8. Each unit consists of two Cu atoms bridged by two hydroxo moieties with Cu1−OH−Cu2 angles in the range of 90.11−90.67°. The Cu1···Cu2 bond distance (~2.75 Å) is one of the shortest reported for bis(μ-hydroxo)dicopper(II) complexes bridged by a spacer[37],[38],[39] and close to the ~2.6 Å value observed in the dinuclear site of pMMO.[40],[41] The coordination polyhedron around the Cu1A atom is a distorted square pyramid whose apical position is occupied by the naphthyridine N1 atom at 2.276 Å (Figure III.8). Because of the presence of a triflate anion at the Cu2A site, the two Cu atoms are not in identical coordination environments in the solid state. Cu2 is found in a distorted octahedral geometry with axial positions occupied by the N2 atom at an elongated distance of 2.352 Å compared to 2.276 Å for Cu1−N1 and the O3 atom from a triflate at 2.615 Å.

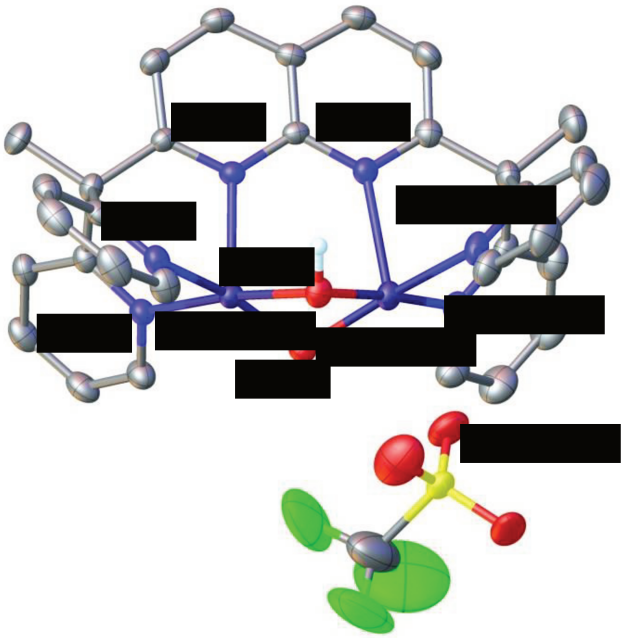

Figure III.8. Molecular structure of the cationic part of **4A** determined by X-ray diffraction with thermal ellipsoids set at 50%. H atoms (except from the OH) were omitted for clarity.

Table III.1. Selected bond lengths and angles for complex **4A**.

Bond lengths in Å		Angles in °	
Cu1-Cu2	2.7511(12)	Cu1-O1-Cu2	90.38(12)
Cu1-O1	1.936(3)	Cu1-O2-Cu2	90.58(12)
Cu1-N1	2.276(3)	O2-Cu2-O1	82.11(12)
Cu1-N3	1.989(3)	O1-Cu2-O2	82.41(12)
Cu1-N4	1.987(3)	O1-Cu1-N3	93.45(13)
Cu2-O1	1.942(3)	N1-Cu1-N4	88.14(13)
Cu2-O2	1.946(3)	N1-Cu1-N3	88.21(14)
Cu2-O3	2.615(3)	N1-Cu1-O1	103.08(12)
Cu2-N2	2.352(3)	N1-Cu1-O2	100.72(12)
Cu2-N5	1.995(3)	N5-Cu2-N6	88.77(14)
Cu2-N6	1.978(3)	N2-Cu2-O2	98.31(12)
		N2-Cu2-O1	98.97(11)
		N2-Cu2-N5	84.40(13)
		N2-Cu2-N6	85.69(13)

II.2. Magnetism

Magnetic susceptibility measurements of **4** were carried out with a SQUID magnetometer equipped with a 5 T magnet in the range from 295 K to 2.0 K. The powdered samples were contained in a gel bucket and fixed in a nonmagnetic sample holder. Each raw data file for the measured magnetic moment was corrected for the diamagnetic contribution of the sample holder and the gel bucket. The molar susceptibility data were corrected for the diamagnetic contribution. At 295 K, the

$\chi_M T$ value is 0.96 cm^3 K mol^{-1}; it increases smoothly by cooling down to 50 K, to finally reach a plateau of *ca*. 1.06 cm^3 K mol^{-1}. Analysis of the experimental data yields a highly positive value for the exchange coupling constant (J = 113 cm^{-1}), indicating a strong ferromagnetic interaction between the two copper(II) (S = ½) ions. Structural and magnetic properties of $Cu^{II}(\mu\text{-}OH)_2Cu^{II}$ cores can be correlated:[42],[43] if the Cu-O-Cu angle is smaller than 97.55°, the magnetic coupling expected for the dinuclear complex is ferromagnetic. In complex **4A**, two hydroxo bridges are present: the Cu1-O1-Cu2 and the Cu1-O2-Cu2 angles are 90.11° and 90.58°, respectively. These angles are smaller than 97.55° which is in agreement with a strong ferromagnetic coupling between the two copper ions in the complex.[43]

II.3. Electrochemical and theoretical studies of complex 4

II.3.1. Room temperature electrochemical studies

Room temperature cyclic voltammetry (CV) of **4** at a glassy carbon electrode in CH_3CN/NBu_4PF6 0.1 M revealed a reversible system at E^0 = 1.26 V vs Fc for v > 0.1 V/s. At lower scan rate, the oxidation process was irreversible as shown by the scan-rate normalized CVs in Figure III.9. Plots of the current function ($i/v^{1/2}$) against v are shown in Figure III.10. The increase of the current function at low scan rate is typical of an ECE mechanism (E = electrochemical and C = chemical), which involves a transient oxidized species having a life time of several seconds.

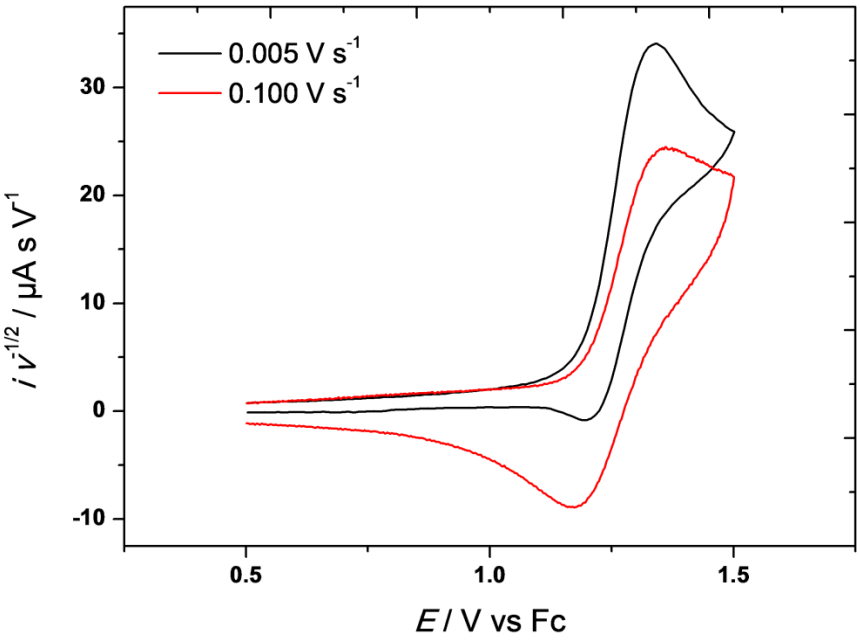

Figure III.9. Room-temperature scan-rate-normalized cyclic voltammograms (E /V vs Fc) of **4** (C = 1 mM) in 0.1 M Bu_4PF_6/CH_3CN at v = 0.005 V/s (black) and v = 0.1 V/s (red).

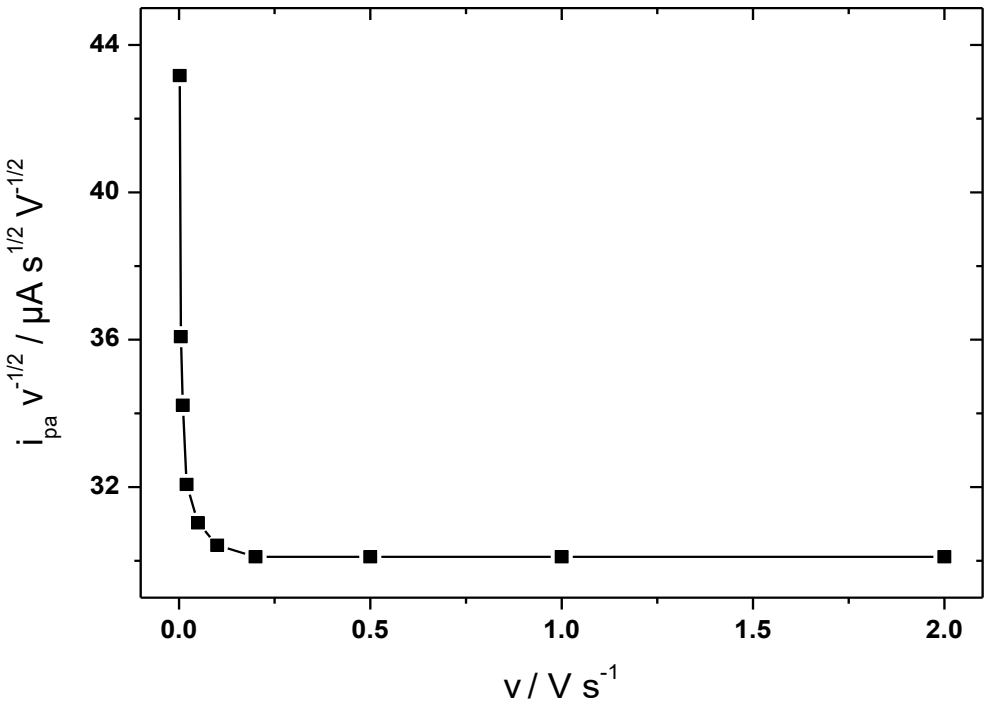

Figure III.10. Plots of current function ($i\, v^{-1/2}$) against v for 0.02 V/s < v < 2 V/s from CVs at a glassy carbon electrode of complex **4** (C = 1.0 mM) in CH_3CN / NBu_4PF_6 0.1 M at 298 K.

Indeed, at low scan rate, the chemical process is fast enough (*vs* time scale of the experiment) to allow the formation of a new species which can be oxidized at the same potential value than **4**. This second electron transfer induces a significant increase of the current. At higher scan rate, the chemical reaction is not fast enough to occur within the timescale of the experiment, thus leading to a simple monoelectronic transfer. Noteworthy, the absence of any cathodic peak at low scan rate likely suggests that a supplementary chemical process occurs after the ECE process of **4**, hence possibly leading to an ECEC mechanism.

Exhaustive electrolysis with coulometry is an usual electrochemical method for determining the number of electron implicated in a redox reaction. Indeed, according to Faraday's law (Equation III.1), the total amount of electricity Q (in C) involved in a redox process depends on the number of electrons involved in the process n_p, the Faraday's constant (96500 C mol^{-1}) and on the number of moles of the only one oxidized specie initially present in the solution (m in mole):

$$Q = n\, F\, m \qquad \text{(III.1)}$$

In our case, several oxidized species are involved at the same oxidation potential. Controlled potential coulometry yielded 9 electrons involved for the redox process. This result is due to the long-time range of the electrolysis which allows the ECE mechanism to occur.

The number of electrons was then determined according to an alternative approach based on the combination of short-time data obtained by CV (for v > 0.05 V/s to avoid the second E process) rotating-disk electrode voltammetry (RDEV) and chronoamperometry (CA). The first step has consisted in evaluating the diffusion coefficient value of **4**, D, for the complex at T = 293 K in this medium by ^{1}H NMR DOSY. The value found for the diffusion coefficient [D=1.0 (±0.1) 10^{-5} cm^2 s^{-1}] was then used in three different electrochemical equations to calculate the number of electrons n involved in oxidation of **4**.

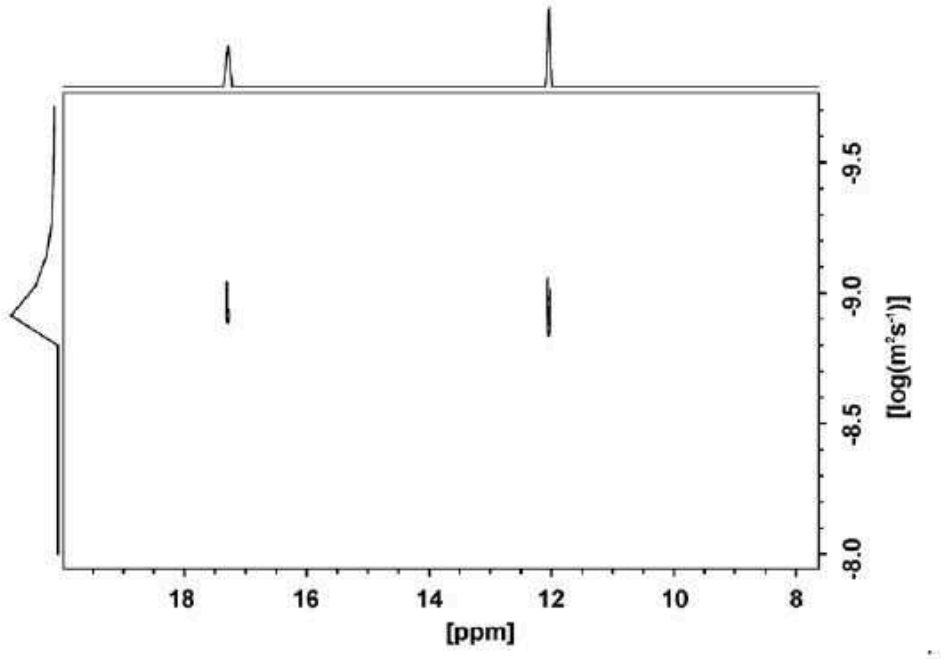

Figure III.11. ^{1}H NMR DOSY spectrum of **4** (12 mM) in presence of KPF_6 (0.1 M) in CD_3CN at 25°C.

As mentioned before, the complex **4** displays a reversible behaviour at high scan rate since the chemical reaction is not fast enough to occur. Therefore, the Randles−Sevcik equation (equation III.2) can be used assuming a simple E mechanism:[44],[45]

$$i_p = 0.446n^{3/2}FACD^{1/2}\left[\frac{F}{RT}\right]^{1/2}v^{1/2} \qquad \text{(III.2)}$$

where n = number of electrons, A = electrode surface area (cm^2), D = diffusion coefficient (cm^{2}s^{-1}), v = scan rate (V/s) and C = concentration of the complex (M).

From the value of D determined by 1H NMR DOSY, plots of i_{pa} versus $v^{1/2}$ ($v > 0.05$ V/s) show a linear trend yielding $n = 1.03$.

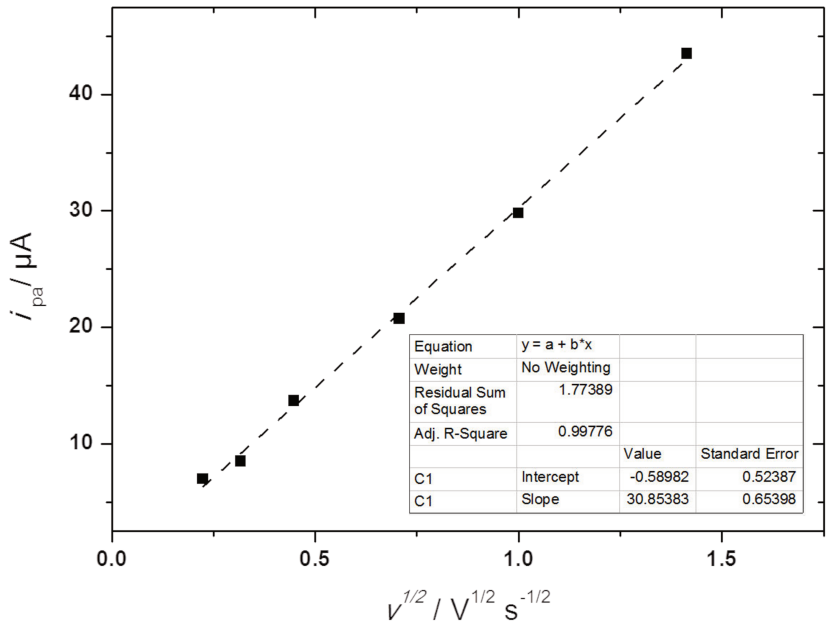

Figure III.12. Plots of i_{pa} versus $v^{1/2}$ for 0.05 V/s < v < 2 V/s from CVs at a glassy carbon electrode of **4** (C = 0.5 mM) in CH_3CN / NBu_4PF_6 0.1 M at 298 K (E / V vs Fc).

The same approach was used by using the Levich equation for RDEV (Equation III.3):[45]

$$i_{lim} = 0.62nFACD^{2/3}\omega^{1/2}\upsilon^{-1/6} \qquad \text{(III.3)}$$

[υ is the kinematic viscosity of the MeCN at 293 K.]

The Cottrell equation was also used for CA experiments (Equation III.4):[45]

$$i(t) = \frac{nFACD^{1/2}}{\pi^{1/2}t^{1/2}} \qquad \text{(III.4)}$$

From both CA and RDEV, the linear trend allowed the determination of n (1.07 and 1.10 respectively). As shown in Table III.2, the three methods are consistent with a monoelectronic transfer for the oxidation of complex **4**.

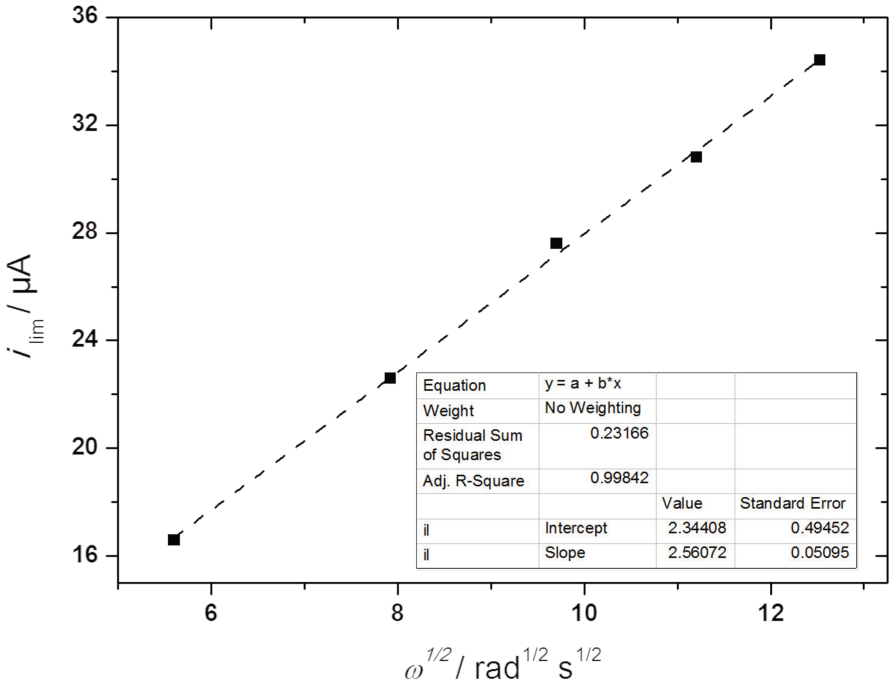

Figure III.13. Plots of i_{lim} versus $\omega^{1/2}$ for 300 RPM < ω < 2000 RPM from RDEVs at a glassy carbon electrode of **4** (C = 0.5 mM) in CH_3CN / NBu_4PF_6 0.1 M at 298 K (v = 0.02 V/s).

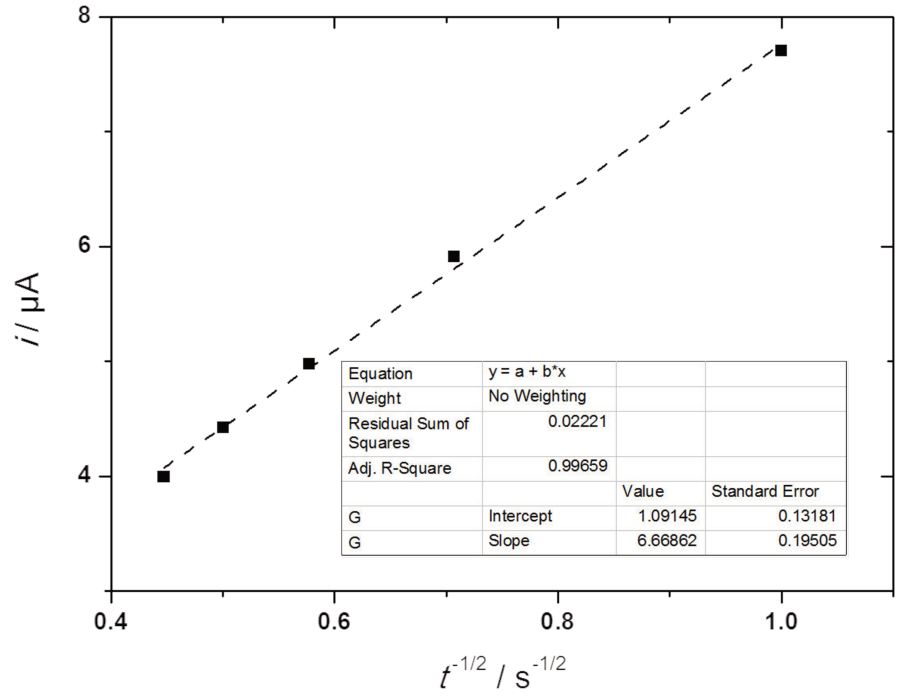

Figure III.14. Plots of i vs $t^{-1/2}$ for 1 s < t < 5 s from CAs at a glassy carbon electrode of **4** (C = 0.5 mM) in CH_3CN / NBu_4PF_6 0.1 M at 298 K.

Table III.2. Calculated values of the number of electrons (n) at 293 K for the oxidation of **4** from experimental electrochemical data

Method	Slope	*n*
CV	60.85µA $V^{-1/2}$ $s^{1/2}$	1.03[a]
CA	2.56 µA $s^{1/2}$	1.07[b]
RDEV	6.67 µA $rad^{-1/2}$ $s^{1/2}$	1.10[c]

[a]Calculated from i_{pa} vs $v^{1/2}$ plots (v > 0.05 V/s); [b]Calculated from plots of i vs $t^{-1/2}$ for t < 5 s; [c]Calculated from plots of i_{lim} vs $\omega^{1/2}$ for 300 RPM < ω < 2000 RPM.

II.3.2. Low temperature Electrochemical, UV-Vis Spectroscopic and EPR studies of 4

The oxidation of complex **4** has been investigated at low temperature in CH_3CN/NBu_4PF_6. At T = 233 K, the system became chemically reversible at v = 0.01 V/s (Figure III.15) in contrast to the irreversible system detected at room temperature at the same scan rate. As shown in Figure III.15, the decrease in temperature induced a higher peak-to-peak separation (ΔE_p) between the potentials of the forward and reverse peaks, as well as a decrease of the intensity. These effects are ascribed to slower kinetics of electron transfer and slower diffusion of the electroactive species.

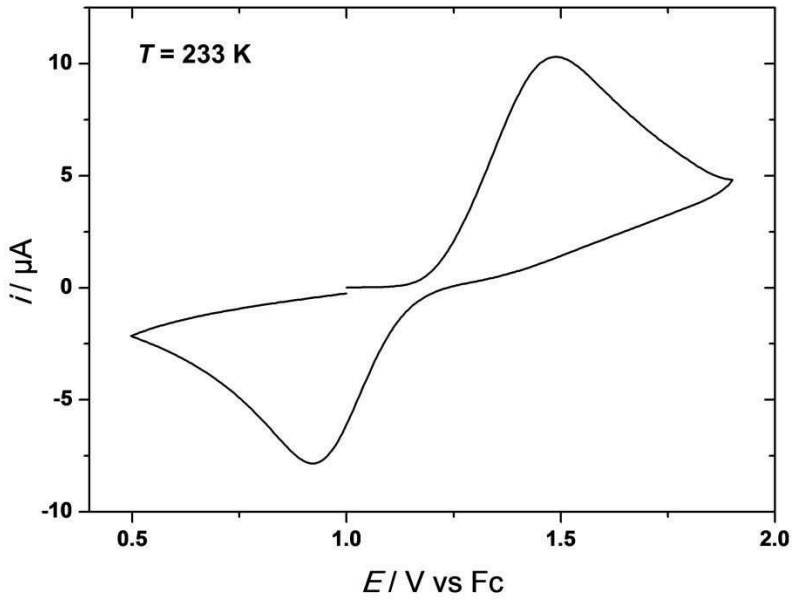

Figure III.15. CV at T = 233 K of **4** in CH_3CN / NBu_4PF_6; v = 0.01 V/s.

The one-electron oxidized species was then generated by exhaustive electrolysis of a solution of **4** at 233 K (E_{app} = 1.6 V vs Fc). Noticeably, the pale-purple solution turned to yellow-brown upon oxidation and rapidly (minutes) became decomposed in a greenish mixture. UV-Vis and X-band EPR characterization of the yellow product was performed and revealed the appearance of an UV-Visible

absorption band at *ca*. λ = 430 nm. An axial EPR spectrum with a 4-lines pattern in $g_{\parallel}$ was also recorded (Figure III.17). This indicated a hyperfine coupling to only one Cu^{II} consistent with a localized valence.[46] Fitting led to the following parameters: $g_{\parallel}$ = 2.21, $g_{\perp}$ = 2.02 and $A_{\parallel}$ = 174 × 10^{-4} cm^{-1} suggesting a square-pyramidal geometry for the Cu^{II} ion.

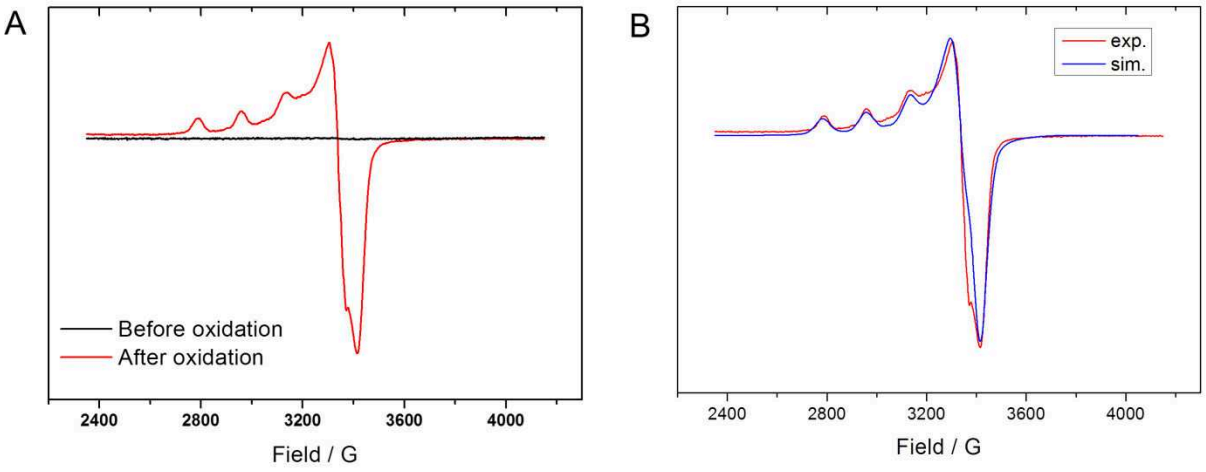

Figure III.16. A) Experimental EPR spectra (15 K) of **4** before (black) and after (red) low-temperature (233 K) bulk electrolysis in NBu_4ClO_4 / CH_3CN (ν = 9.419 GHz). B) Experimental (red, T = 15 K) and simulated (blue) EPR spectra of **4** after low-temperature bulk electrolysis in CH_3CN/TBAP at 233 K (ν = 9.419 GHz). Simulation was carried out assuming the following parameter: g_x = 2.020, g_y = 2.015, g_z = 2.210, A_x = 40 G, A_y = 10 G, A_z = 174 G.

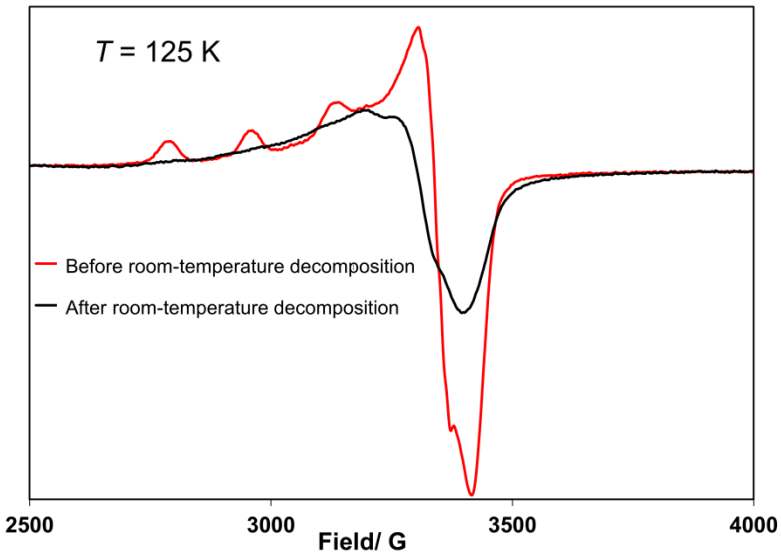

Figure III.17. Experimental EPR spectra after low-temperature bulk electrolysis of **4** in CH_3CN/TBAP at 233 K (ν = 9.419 GHz) recorded at T = 125 K after increasing to T = 200 K and returning to 125 K (red) and after room-temperature decomposition during 2h (black).

The yellow solution was stable for hours as long as the temperature was kept below 200 K. Warming the EPR tube up to room temperature for 2 hours and returning back to low temperature 125 K demonstrated an evolution of the oxidized species, as shown in Figure III.17 by EPR spectroscopy. The same decomposition reaction was obtained when leaving the low-temperature (233 K) electrolysis occurring for more than 1 hour. The resulting broad EPR spectrum suggested a mixture of several Cu^{II} complexes in solution.

II.4. UV-Vis-NIR spectroelectrochemical studies of complex 4

The UV−Vis time-resolved spectroelectrochemistry of **4** was carried out in CH_3CN/NBu_4PF_6 (optical path = 0.2 mm; one spectrum every 0.5 s). This experiment was conducted at room and low temperatures to study the stability of the species with time. At room temperature, an absorption band was detected at ca 430 nm under oxidation potential (E = 1.6 V vs Fc) and it disappeared progressively within tens of seconds, showing that the mono-oxidized species is relatively stable at RT (Figure III.18). Notably, the value of the transient absorption band was similar to that found for the yellow solution generated by exhaustive electrolysis of **4**.

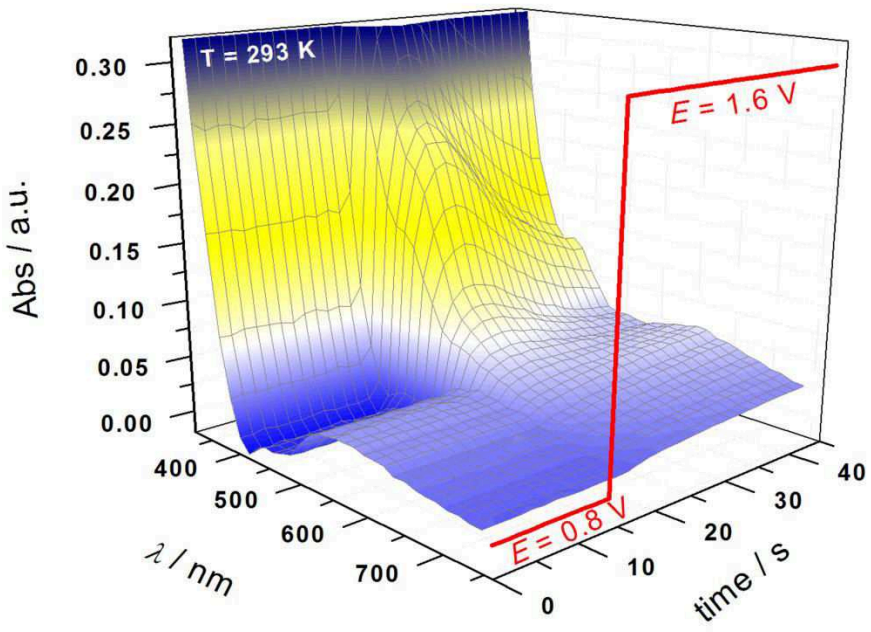

Figure II.18. 3D room-temperature time-resolved UV−Vis spectrum of complex **4** (C = 10 mM; optical path = 0.2 mm) in 0.1 M NBu_4PF_6/CH_3CN upon application of a potential at the working electrode E = 0.8 V *vs* Fc^+/Fc (first 15 s) and E = 1.6 V *vs* Fc^+/Fc (after 15 s).

Low-temperature (223 K) UV-Vis-NIR spectroelectrochemistry was also carried out in order to identify the intermediate oxidized species. Figures III.19 and III.20 show the variation of the spectroscopic responses of **4** upon variation of the applied potential with pulses at 2.0 V and 0.4 V vs Fc. An increase of the absorbance around 430 nm was observed upon oxidation, without decay of the band at this temperature. Successive cycling showed disappearance and regeneration of this band. The UV-Vis spectrum resulting from the difference between the spectra before and after oxidation yielded a maximum absorption wavelength at λ = 424 nm (Figure III.20, inset).

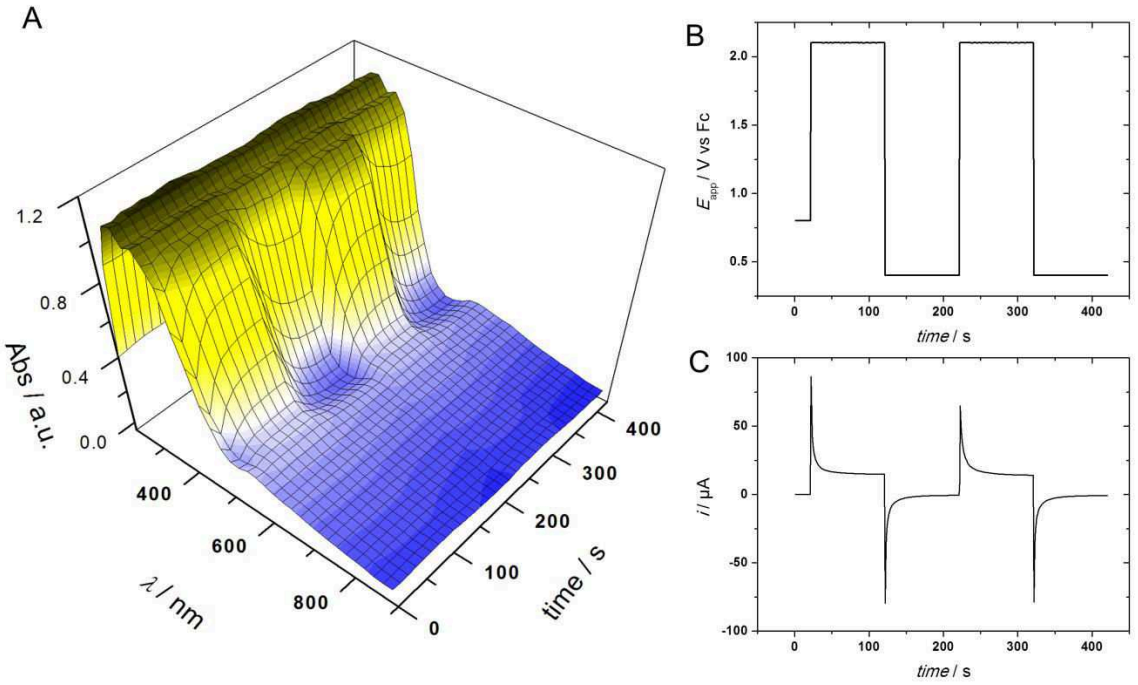

Figure III.19. A) 3D low-temperature (T = 223 K) time-resolved UV-Vis spectrum of **4** (C = 10 mM, optical path 0.2 mm) in CH_3CN/NBu_4PF_6 0.1 M upon variation of the applied potential with pulses at 2.0 V and 0.4 V vs Fc (B); C) Current response to applied potential pulses.

At 223 K the NIR region was also significantly modified by the potential value applied at the working electrode. Hence, a low-intensity and broad absorption band centred at λ = 1344 nm (ε = 90 M^{-1} cm^{-1}) appeared upon electrochemical oxidation (E = 1.6 V) (Figure III.21). Switching between 0.8 V and 1.6 V induced the disappearance and reappearance of this band (Figure III.22).

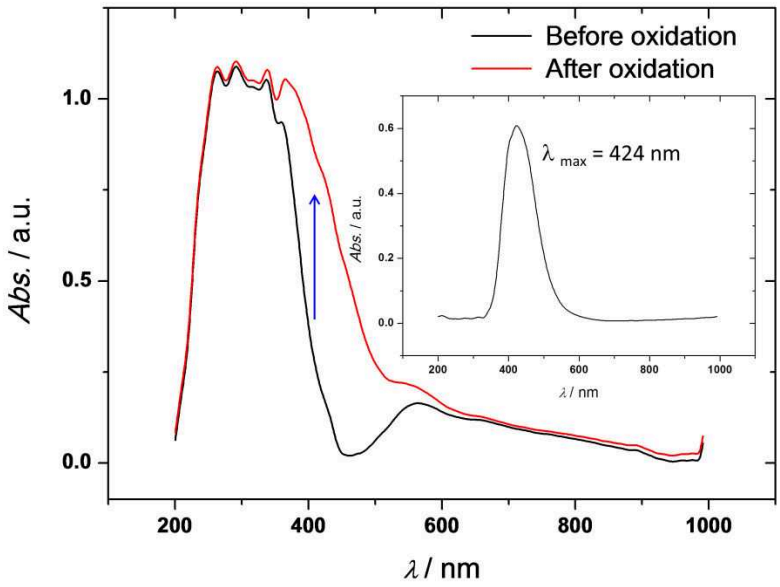

Figure III.20. 2D Low-temperature (T = 223 K) UV-Vis spectra of **4** (C = 10 mM, optical path 0.2 mm) in CH_3CN / NBu_4PF_6 0.1 before (black) and after (red) electrochemical oxidation at 1.6 V vs Fc (red curve). Inset: UV-Vis spectrum resulting from the difference between spectra (before/after oxidation), giving the maximum absorption wavelength at λ = 424 nm.

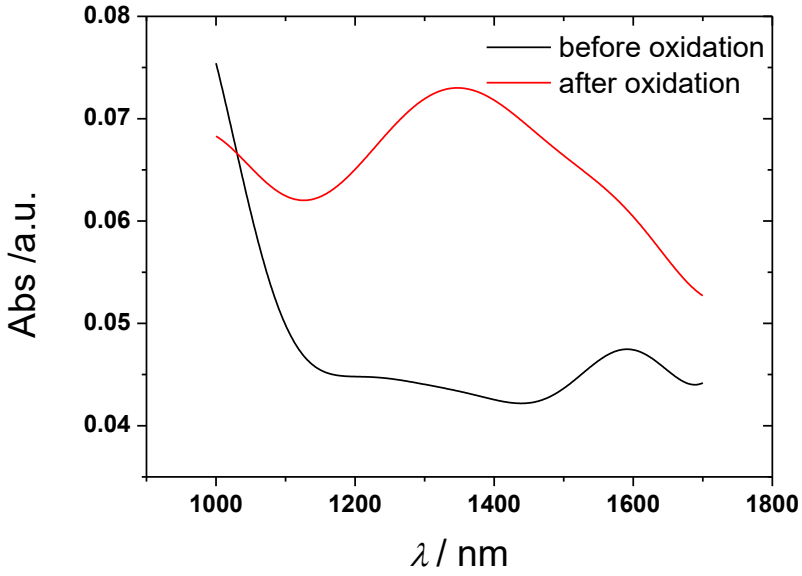

Figure III.21. NIR spectra (T = 223 K, optical path 0.2 mm) of **4** in CH_3CN/NBu_4PF_6 before (black) and after (red) application of a potential at the working electrode E = 0.8 V vs Fc (first 15 seconds) and E = 1.6 V (after 15 seconds).

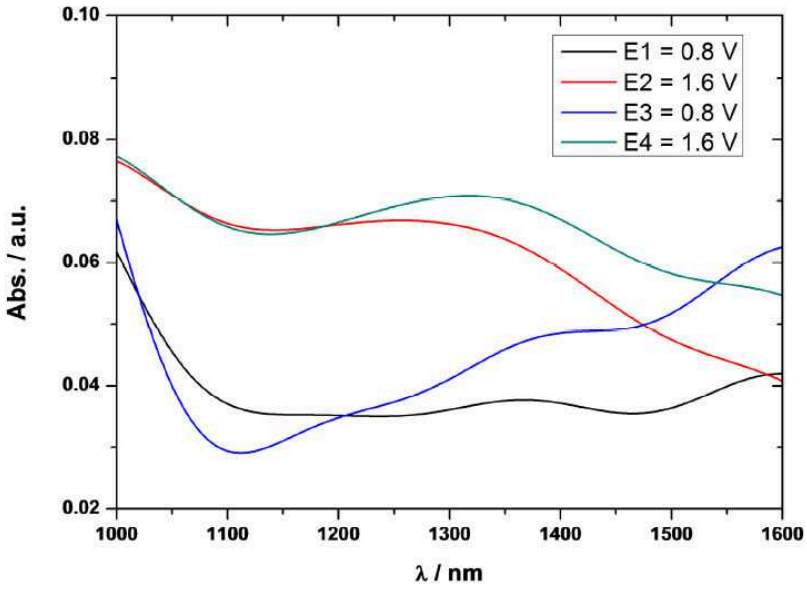

Figure III.22. NIR spectra (T = 223 K, optical path 0.2 mm) of **4** in CH_3CN/NBu_4PF_6 before (black and blue) and after (red and green) successive application of a potential at the working electrode E = 0.8 V vs Fc and E = 1.6 V.

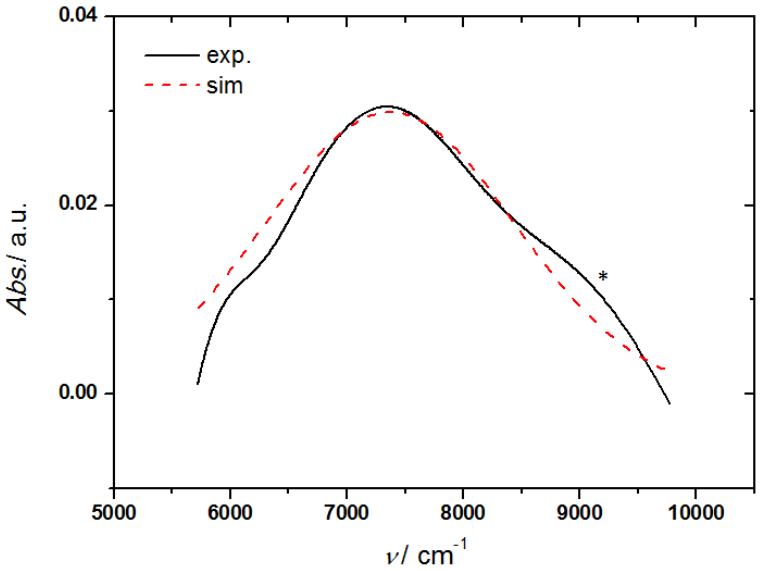

Figure III.23. Experimental (black) and simulated (red) NIR spectra of the oxidized form of **4** in CH_3CN/NBu_4PF_6 at T = 223 K. The small band at 9000 cm^{-1} (*) may be ascribed to remaining non-oxidized complex **4**.

In contrast to the EPR-spectrum (Figure III.16) which showed that the product of the electrolysis of **4** at 1.6 V is a valence localized $Cu_2^{III,II}$ species, the NIR spectra in Figure III.21 revealed a slight delocalization of the charge on the dicopper core. Fitting of the NIR band allowed the determination of the bandwidth at half height ($\Delta\tilde{\nu}_{1/2}$ = 2520 cm^{-1}) (Figure III.23). The presented experimental curve was obtained from the difference of spectra between the oxidized and initial

species. Simulation was performed by assuming a Gaussian curve (Equation III.5) with the following parameters: $y_0 = 0$; x_c =7370; w = 2410; A = 80.

$$y = y_0 + \frac{A}{w\sqrt{\pi/2}} e^{-2\frac{(x-xc)^2}{w^2}} \quad \text{(III.5)}$$

The electronic coupling matrix element H_{AB} was then determined from the Mulliken-Hush expression (equation III.6).[47] The calculations give H_{AB} = 305 cm^{-1}.

$$H_{AB} = 0.0206(\varepsilon_{max}\breve{\upsilon}_{max}\Delta\breve{\upsilon}_{1/2})/R_{AB} \quad \text{(III.6)}$$

where ε_{max} is the extinction coefficient at the band maximum (90 M^{-1} cm^{-1}), $\breve{\upsilon}_{max}$ the energy at the band maximum (7370 cm^{-1}), $\Delta\breve{\upsilon}_{1/2}$ the bandwidth at half-height (2520 cm^{-1}) and R_{AB} the effective charge transfer distance (2.75 Å).[46]

The parameter Γ relates to the ratio between the experimental and theoretical values of $\Delta\breve{\upsilon}_{1/2}$ as given by equation (III.7):[48],[49]

$$\Gamma = 1 - \frac{(\Delta\breve{\upsilon}_{1/2,exp})}{(\Delta\breve{\upsilon}_{1/2,theo})} \quad \text{(III.7)}$$

For a class II system, $\Delta\breve{\upsilon}_{1/2,theo}$ is given according to equation (III.8):

$$\Delta\breve{\upsilon}_{1/2,theo} = (2310\breve{\upsilon}_{max})^{1/2} \quad \text{(III.8)}$$

Hence, for $\breve{\upsilon}_{max}$ = 7370 cm^{-1}, $\Delta\breve{\upsilon}_{1/2,theo}$ = 4125 cm^{-1} and Γ = 0.39. Values found for H_{AB}= 322 cm^{-1} and Γ = 0.39 are typical of a class II system in the Robin-Day classification,[50] i.e. low delocalization of the charge. This result is different from that obtained by EPR, which suggested a localization of the charge. This discrepancy might be due to the difference of temperature at which the spectra are recorded (223 K vs 125 K), which may favor localization of the charge at the lowest T. Notably, the NIR features of the oxidized species are slightly different from those obtained for the previously reported mixed-valent $Cu_2^{III,II}$ complex by Tolman and co-workers.[46] Indeed, the present complex displays lower energy frequency and molar extinction coefficient and higher bandwidth at half-height than the above-mentioned analogue, consistent with a lower delocalization of the charge on the dicopper core.

III. DFT and TD-DFT theoretical calculations of complex 4

Further investigations were carried out by density functional theory (DFT) calculations to gain insight into the electronic structure, redox potential and UV−vis spectroscopic features of the monooxidized complex (collaboration Université Grenoble-Alpes). The redox potential for oxidation of **4** was computed and reported relative to the computed value of the Fc^{+}/Fc redox couple.[51] DFT calculations predicted a standard potential equal to 1.36 V v*s* Fc for sequential one-electron oxidation, in good agreement with the experimental data (E^0 = 1.26 V vs Fc). Figure III.24 displays a spin-density plot (difference between α and β densities) for the monooxidized complex. The remaining unpaired electron is mainly localized on only one Cu ion and its adjacent atoms (μ- OH and N_{pyr}). This result confirms the weakly delocalized nature of the mixed-valent $Cu_2^{III,II}$ species, in agreement with experimental NIR−vis spectroscopic data. It is also consistent with the EPR results (mono-Cu^{II} signature). The mixed-valent complex also displays Cu−N and Cu−O distances that decrease according to the valence state of the Cu ion. For instance, the Cu−N_{pyr} and Cu−O distances are equal to 1.97 and 2.00 Å for Cu^{II}, respectively, whereas they are significantly lower for Cu^{III} (1.88 and 1.85 Å, respectively). The Cu···Cu distance increases from 2.78 Å to 2.83 Å by monoelectronic oxidation.

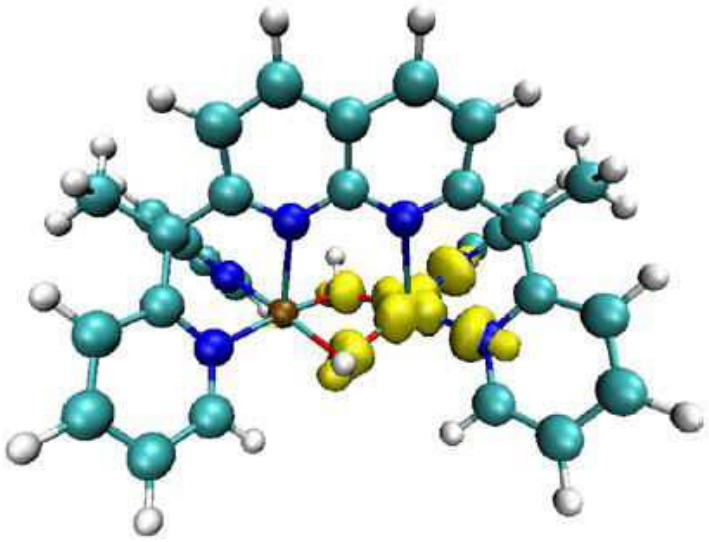

Figure III.24. Spin-density plot for the oxidized species (yellow).

Time dependent - density functional theory (TD-DFT) calculations were performed to consider the UV-vis spectroscopic features of the oxidized form of **4**. A band at λ_{max} = 430 nm, corresponding to a ligand-to-metal charge transfer, essentially between pyridine rings and the Cu^{III} ion, was found (Figure III.25). In order to better identify the nature of the oxidized species, theoretical calculations of the Cu-O distances were performed by considering three different cores, bis(μ-O), (μ-O)(μ-OH) and bis(μ-OH), for the final oxidized species (Table III.3). The relative values of both Cu-O distance are indeed a relatively good indicator of the redox state of the metal ion ("+2", "+2.5" or "+3"). Geometry

optimization showed for the bis(μ-O) and (μ-O)(μ-OH) species, that both Cu−O distances are similar (Table III.3), in agreement with a fully delocalized charge ($Cu_2^{2.5}$) mixed-valent state. Interestingly, the Cu-O distances were different only for the oxidized species bearing a bis(μ-OH) core. These results indicate that the oxidation does not lead to the deprotonation of any of the OH bridges. In agreement with the experimental data, the oxidized species is a bis(μ-hydroxo) mixed-valent dicopper(III,II) complex.

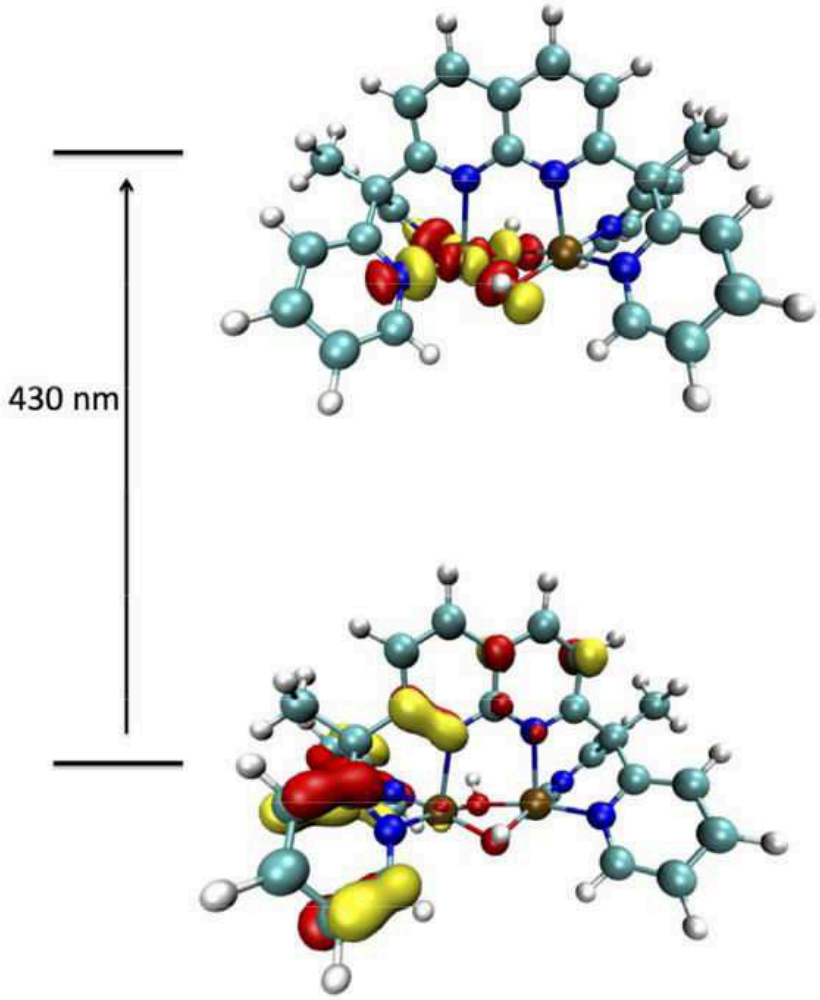

Figure III.25. Natural transition orbitals of the excited state associated with the absorption band detected experimentally.

Table III.3. Cu-O distances in Å for different protonation states of the mono-oxidized dicopper core after geometry optimizations at IEFPCM/wB97XD level.

	Cu-O	Cu-OH	Cu-O	Cu-OH
$Cu_2(\mu\text{-}OH)_2$		1.97-2.00		1.88-1.85
$Cu_2(\mu\text{-}OH)(\mu\text{-}O)$	1.95	1.96	1.95	1.96
$Cu_2(\mu\text{-}O)_2$	1.88		1.88	

IV. Conclusions on complex 4

The objective is this work was to develop and characterize a new bis(μ-OH) dicopper complex **4** bearing the *dpen* ligand, since the naphthyridine moiety is coordinating, redox inactive and rigid enough to enforce short Cu-Cu interaction. The X-ray study of crystals of the complex demonstrated that the choice of this ligand was judicious in structural terms, since a short Cu-Cu distance (2.75 Å) was found. This value is close to that suggested for the active site in pMMO (2.6 Å). The electrochemical studies in acetonitrile demonstrated that the oxidation of the complex occurs at a relatively high potential value (1.26 V vs Fc, confirmed at 1.36 V by DFT calculations) corresponding to a one-electron transfer. The oxidation led to the formation of a new species which evolved within seconds, as shown by variable scan rate cyclic voltammetry. Nevertheless, the mixed-valent bis(μ-OH) dicopper(III,II) was characterized by using time-resolved UV-Vis-NIR spectroelectrochemistry at room and low temperatures. Upon oxidation, an absorption band was detected at λ_{max} = 424 nm. According to TD-DFT calculations, this transition corresponds to a ligand-to-metal charge transfer between pyridine rings and Cu^{III} ion. In the NIR region, a band at λ_{max} = 1344 nm was also observed, suggesting a weak delocalization of the charge density. Analysis of the spectra suggested that the $Cu_2^{III,II}$ complex belongs to a class II mixed-valent species according to the Robin−Day classification. EPR spectroscopy of the product of oxidation of **4** obtained by electrolysis displayed a signature typical of mononuclear Cu^{II} centre, as a proof of a weak dissymmetry.

The overall studies demonstrated that the incorporation of a *np* unit instead a phenoxo one into the dinucleating ligand scaffold was beneficial for the generation of a mixed-valent species. Indeed, the monoelectronic oxidation occurs on one copper ion and not on the bridging unit as observed for the phenoxo-based dicopper complex. Unfortunately, the oxidation potential (E^0 = 1.26 V vs Fc) of the complex **4** is too high to envisage its application in electrocatalysis. This is due to the poor donor properties of the polypyridyl arms environing the copper ions. Another aspect of interest of these studies is that a weakly delocalized mixed-valent species was obtained from a symmetrical complex. This means that asymmetry is not absolutely necessary to produce and stabilize a mixed-valent species. Such result is interesting for the development of synthetic dicopper models of the catalytic site of pMMO. Future work should then be focused on new complexes bearing better-donating N-ligands than polypyridyl systems in order to reduce the oxidation potential.

BIBLIOGRAPHY

[1] J. K. Bera, N. Sadhukhan, M. Majumdar, *Eur. J. Inorg. Chem.* **2009**, *2009*, 4023-4038.
[2] G. Koller, *Ber. Dtsch. Chem. Ges* **1927**, *60*, 407-410.
[3] C. F. H. Allen, *Chem. Rev.* **1950**, *47*, 275-305.
[4] E. V. Brown, *J. Org. Chem.* **1965**, *30*, 1607-1610.
[5] E. L. Enwall, *PhD Thesis*, *Montana State University* **1968**.
[6] D. G. Hendricker, T. E. Reed, *Inorg. Chem.* **1969**, *8*, 685-687.
[7] P. Singh, A. Clearfield, I. Bernal, *J. Coord. Chem.* **1971**, *1*, 29-37.
[8] R. L. Bodner, D. G. Hendricker, *Inorg. Nucl. Chem. Lett.* **1970**, *6*, 421-423.
[9] D. G. Hendricker, R. J. Foster, *Inorg. Chem.* **1973**, *12*, 349-352.
[10] D. G. Hendricker, R. L. Bodner, *Inorg. Chem.* **1970**, *9*, 273-277.
[11] K. Emerson, A. Emad, R. W. Brookes, R. L. Martin, *Inorg. Chem.* **1973**, *12*, 978-981.
[12] L. Sacconi, C. Mealli, D. Gatteschi, *Inorg. Chem.* **1974**, *13*, 1985-1991.
[13] D. Gatteschi, C. Mealli, L. Sacconi, *Inorg. Chem.* **1976**, *15*, 2774-2778.
[14] C. Mealli, F. Zanobini, *J. Chem. Soc., Chem. Commun.* **1982**, 97-98.
[15] M. Munakata, M. Maekawa, S. Kitagawa, M. Adachi, H. Masuda, *Inorg. Chim. Acta* **1990**, *167*, 181-188.
[16] G. Evens, P. Caluwe, *Macromolecules* **1979**, *12*, 803-808.
[17] W. R. Tikkanen, E. Binamira-Soriaga, W. C. Kaska, P. C. Ford, *Inorg. Chem.* **1984**, *23*, 141-146.
[18] W. R. Tikkanen, C. Krueger, K. D. Bomben, W. L. Jolly, W. Kaska, P. C. Ford, *Inorg. Chem.* **1984**, *23*, 3633-3638.
[19] C. He, A. M. Barrios, D. Lee, J. Kuzelka, R. M. Davydov, S. J. Lippard, *J. Am. Chem. Soc.* **2000**, *122*, 12683-12690.
[20] A. E. M. Boelrijk, T. X. Neenan, J. Reedijk, *J. Chem. Soc., Dalton Trans.* **1997**, 4561-4570.
[21] J.-F. Zhang, M.-M. Yu, Y. Chen, X.-M. Ou, W.-F. Fu, *Acta Cryst. Sect. E* **2006**, *62*, m2758-m2760.
[22] B. S. Liao, S. T. Liu, *J. Org. Chem.* **2012**, *77*, 6653-6656.
[23] B.-S. Liao, Y.-H. Liu, S.-M. Peng, S.-T. Liu, *Dalton Trans.* **2012**, *41*, 1158-1164.
[24] B.-S. Liao, Y.-H. Liu, S.-M. Peng, K. R. Reddy, S.-H. Liu, P.-T. Chou, S.-T. Liu, *Dalton Trans.* **2014**, *43*, 3557-3562.
[25] B.-C. Tsai, Y.-H. Liu, S.-M. Peng, S.-T. Liu, *Eur. J. Inorg. Chem.* **2016**, *2016*, 2783-2790.
[26] T. C. Davenport, T. D. Tilley, *Angew. Chem. Int. Ed. Engl.* **2011**, *50*, 12205-12208.
[27] T. C. Davenport, T. D. Tilley, *Dalton Trans.* **2015**, *44*, 12244-12255.
[28] C. He, J. L. DuBois, B. Hedman, K. O. Hodgson, S. J. Lippard, *Angew. Chem. Int. Ed. Engl.* **2001**, *40*, 1484-1487.
[29] J. A. Halfen, S. Mahapatra, E. C. Wilkinson, S. Kaderli, V. G. Young, Jr., L. Que, Jr., A. D. Zuberbuhler, W. B. Tolman, *Science* **1996**, *271*, 1397-1400.
[30] H. Hayashi, S. Fujinami, S. Nagatomo, S. Ogo, M. Suzuki, A. Uehara, Y. Watanabe, T. Kitagawa, *J. Am. Chem. Soc.* **2000**, *122*, 2124-2125.
[31] V. Mahadevan, Z. Hou, A. P. Cole, D. E. Root, T. K. Lal, E. I. Solomon, T. D. P. Stack, *J. Am. Chem. Soc.* **1997**, *119*, 11996-11997.
[32] N. V. Kaminskaia, C. He, S. J. Lippard, *Inorg. Chem.* **2000**, *39*, 3365-3373.
[33] X. J. Su, M. Gao, L. Jiao, R. Z. Liao, P. E. Siegbahn, J. P. Cheng, M. T. Zhang, *Angew. Chem. Int. Ed. Engl.* **2015**, *54*, 4909-4914.
[34] M. S. Ziegler, D. S. Levine, K. V. Lakshmi, T. D. Tilley, *J. Am. Chem. Soc.* **2016**, *138*, 6484-6491.
[35] M. S. Ziegler, K. V. Lakshmi, T. D. Tilley, *J. Am. Chem. Soc.* **2017**, *139*, 5378-5386.
[36] C. He, S. J. Lippard, *Inorg. Chem.* **2000**, *39*, 5225-5231.
[37] L. J. Farrugia, P. A. Lovatt, R. D. Peacock, *J. Chem. Soc., Dalton Trans.* **1997**, 911-912.
[38] M. Kodera, H. Shimakoshi, M. Nishimura, H. Okawa, S. Iijima, K. Kano, *Inorg. Chem.* **1996**, *35*, 4967-4973.

[39] E. Monzani, G. Battaini, A. Perotti, L. Casella, M. Gullotti, L. Santagostini, G. Nardin, L. Randaccio, S. Geremia, P. Zanello, G. Opromolla, *Inorg*. *Chem*. **1999**, *38*, 5359-5369.
[40] M. A. Culpepper, G. E. Cutsail, B. M. Hoffman, A. C. Rosenzweig, *J*. *Am*. *Chem*. *Soc*. **2012**, *134*, 7640-7643.
[41] A. C. Rosenzweig, *Biochem*. *Soc*. *Trans*. **2008**, *36*, 1134-1137.
[42] V. H. Crawford, H. W. Richardson, J. R. Wasson, D. J. Hodgson, W. E. Hatfield, *Inorg*. *Chem*. **1976**, *15*, 2107-2110.
[43] E. Ruiz, P. Alemany, S. Alvarez, J. Cano, *Inorg*. *Chem*. **1997**, *36*, 3683-3688.
[44] J.-M. Savéant, *Elements of Molecular and Biomolecular Electrochemistry: An Electrochemical Approach to Electron Transfer Chemistry*, Wiley ed., **2006**.
[45] A. J. Bard, L. R. Faulkner, *Electrochemical Methods: Fundamentals and Applications, 2nd Edition*, Wiley ed., **2001**.
[46] M. R. Halvagar, P. V. Solntsev, H. Lim, B. Hedman, K. O. Hodgson, E. I. Solomon, C. J. Cramer, W. B. Tolman, *J*. *Am*. *Chem*. *Soc*. **2014**, *136*, 7269-7272.
[47] K. D. Demadis, C. M. Hartshorn, T. J. Meyer, *Chem*. *Rev*. **2001**, *101*, 2655-2686.
[48] R. F. Winter, *Organomet*. **2014**, *33*, 4517-4536.
[49] B. S. Brunschwig, C. Creutz, N. Sutin, *Chem*. *Soc*. *Rev*. **2002**, *31*, 168-184.
[50] M. B. Robin, P. Day, *Adv*. *Inorg*. *Chem*. *Radiochem*. **1968**, *10*, 247-422.
[51] S. J. Konezny, M. D. Doherty, O. R. Luca, R. H. Crabtree, G. L. Soloveichik, V. S. Batista, *J*. *Phys*. *Chem*. *C* **2012**, *116*, 6349-6356.

Chapter IV

Bis-amide dicopper complexes with alkoxo or phenoxo spacers

I. Introduction

Our previous electrochemical studies on various hydroxo and phenoxo-bridged dinuclear copper complexes bearing polypyridyl cores have led to the conclusion that mono-electronic oxidation of one Cu^{II} ion was possible if (i) the spacer is not easily oxidized (such as for the naphthyridyl-based complex **4**) or (ii) dissymmetry or flexibility is introduced in the ligand framework (such as for the unsymmetrical phenoxo-hydroxo dicopper complex **3a**). Even if one of this condition is fulfilled, we have observed that the oxidation potential to access the mixed-valent species is very high (1.3 V vs Fc for **4**), or the complex quickly evolves towards a new species by internal electron-transfer with the phenoxo spacer (**3a**). Since our target objective is to characterize a $Cu^{III}(\mu\text{-}O(H))Cu^{II}$ species, we have pursued our investigations by focusing on the development of ligands that could stabilize a Cu^{III} redox state and lower the reduction potential.

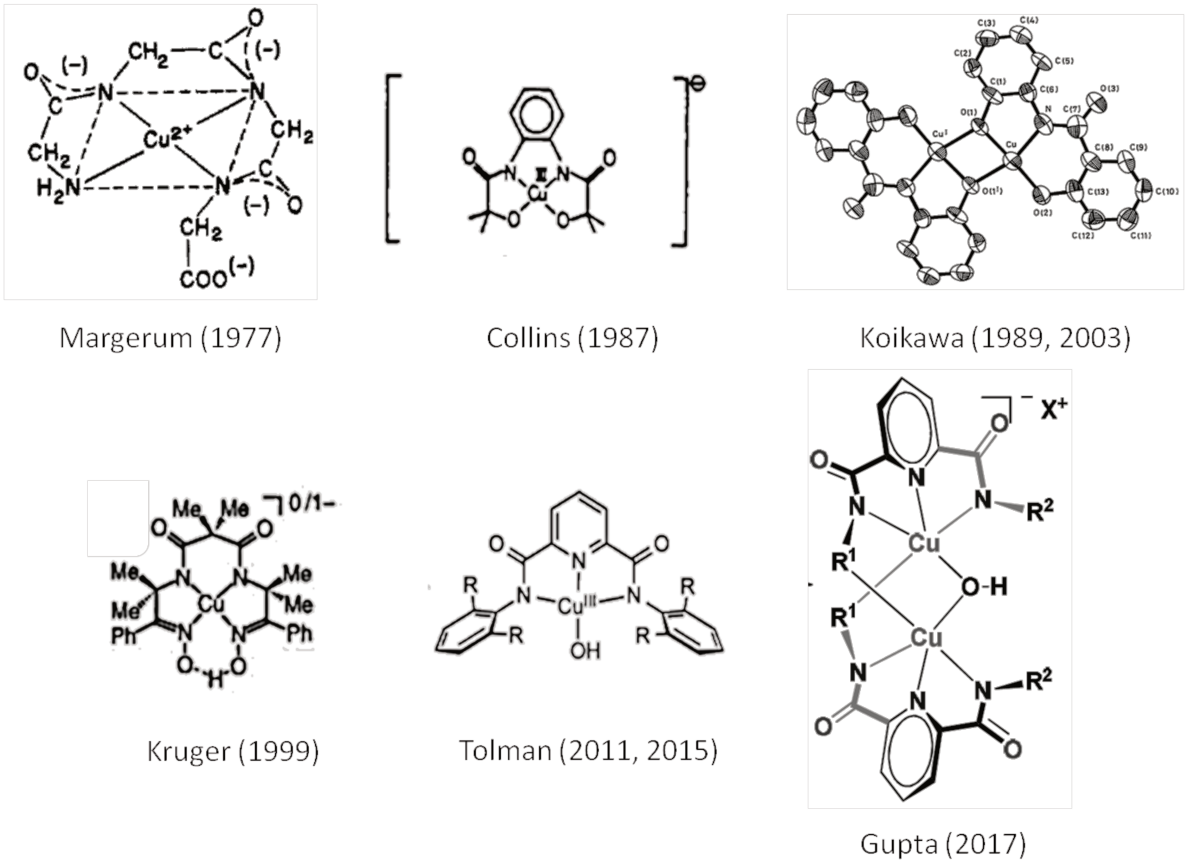

Figure IV.1. Structures of copper complexes.[1],[2],[3],[4],[5],[6],[7],[8]

Cu^{III} state has not yet been observed in biology,[9] and only bioinspired models have been able to emphasize its existence by the employment of anionic ligands which decrease the redox potential value.[10] Among the many possibilities, amides scaffolds have been largely used because they display the ability, when deprotonated, to stabilize metal ions in high oxidation state. Numerous examples of mono-copper complexes bearing amide groups have thus been reported, the redox

potential of the $Cu^{III/II}$ couple varying within the 0.5 to 1.5 V range (vs NHE) (Figure IV.2).[1],[11],[12],[2],[13],[14],[15],[16],[17] Margerum and co-workers were among the first to use deprotonated amide groups to lower the $Cu^{III/II}$ redox potential of a copper complex (Figure IV.1).[1],[11] Collins *et al*. developed several bis-amide copper(III) complexes in which the two amide donor groups are linked by various units (Figure IV.1).[2] These authors demonstrated that the substitution of aliphatic for aromatic groups addressed the oxidation state on the metal and not on the ligand. A series of polyvalent ligands containing two amide and two oxime functionalities as donor groups were also investigated by Kruger and co-workers.[5] Electronic spectroscopy showed that the geometry around the tetra-coordinated Cu^{III} is square-planar in solution, as determined by X-ray diffraction.

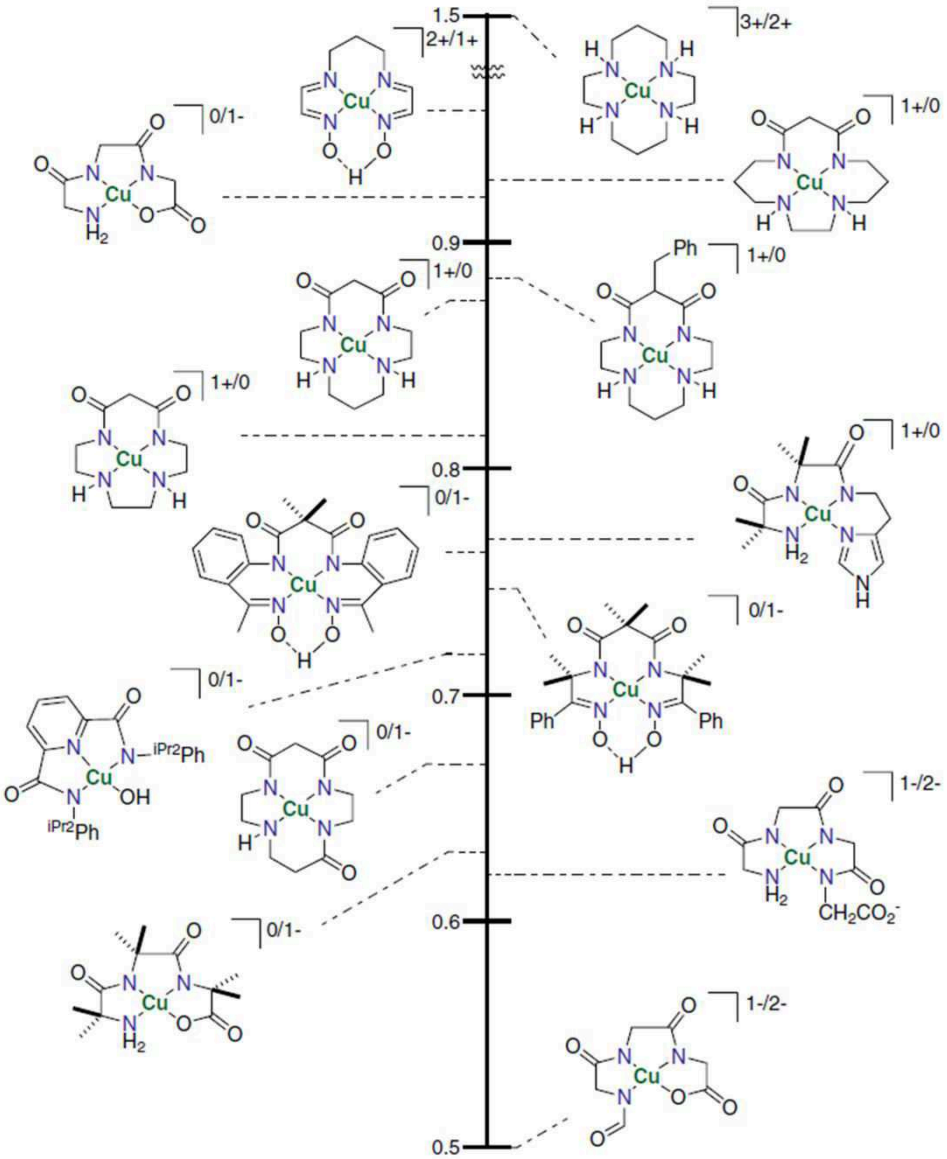

Figure IV.2. Comparison of $Cu^{III/II}$ redox potentials for Cu^{III} complexes with varied donor strengths and overall complex charge. *E*/ V vs NHE. Reproduced from Ref. [18].

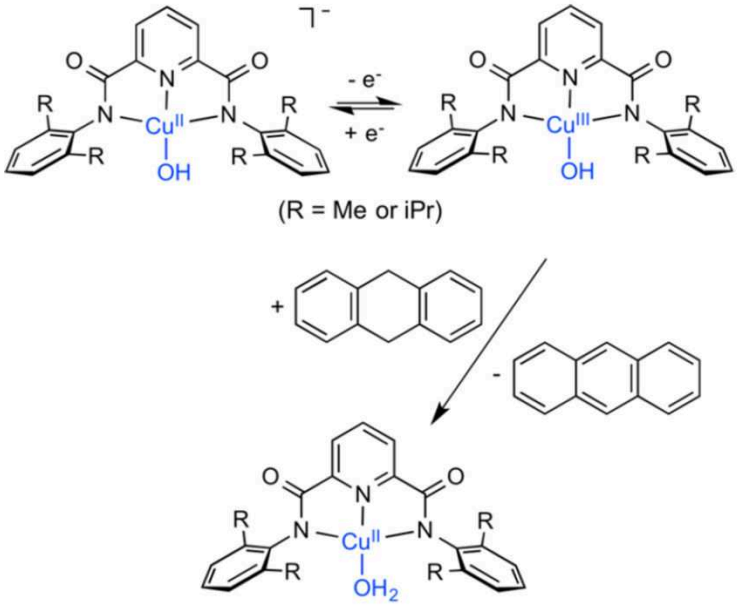

Figure IV.3. Hydrogen Atom Transfer (HAT) from dihydroanthracene to a pyridinedicarboxamide copper(III) hydroxo complex. Reproduced from Ref. [7].

More recently, Tolman *et al*. used a pyridinedicarboxamide ligand (Figure IV.1) to investigate the reactivity a mononuclear Cu^{III} hydroxo complex towards dihydroanthracene for abstraction of a hydrogen atom (HAT).[6] Thermodynamic measurements were performed to determine the bond dissociation enthalpy (BDE) for the O-H bond for the formed aqua complex (Figure IV.3) with the aim of understanding the basis for the observed HAT rates.[7]

Few examples of dinuclear system bearing amide groups have been reported.[3],[4],[13],[8],[19] Koikawa and co-workers used two units of tridentate chelate ligand to afford dinuclear copper complexes bridged by one of the phenolic oxygens (Figure IV.1). Electrochemical oxidation on the copper core led to the formation $Cu_2^{III,II}$ and $Cu_2^{III,III}$ species .[3],[4] The mixed-valent (III,II) species was however unstable in dichloromethane at room temperature. Gupta and co-workers reported the synthesis of hydroxo-bridged dicopper(II) complexes bridging two pyridine-2,6-dicarboxamide units (Figure IV.1). The series of complexes investigated were evaluated for their catecholase (o-diphenol oxidation) activity. The secondary coordination sphere on the Cu-μ(OH)-Cu core was modified in order to control the bond distance between the copper ions and influence the reactivity affecting the Cu^{II}/Cu^{I} redox potentials.[20],[21] Recently, Tolman and co-workers investigated the chemistry of a pyridine(dicarboxamide) dicopper complex (Figure IV.4) bridged by a hydroxo moiety. These authors demonstrated by low-temperature cyclic voltammetry in DMF that monoelectronic oxidation of the dicopper(II) complex leads to the reversible formation of a mixed-valent hydroxo-bridged (III,II) complex. The first and second oxidation processes were detected at 0.18 V and 0.47 V vs Fc,

respectively. EPR spectroscopy revealed the formation of a localized mixed-valent species at low temperatures.

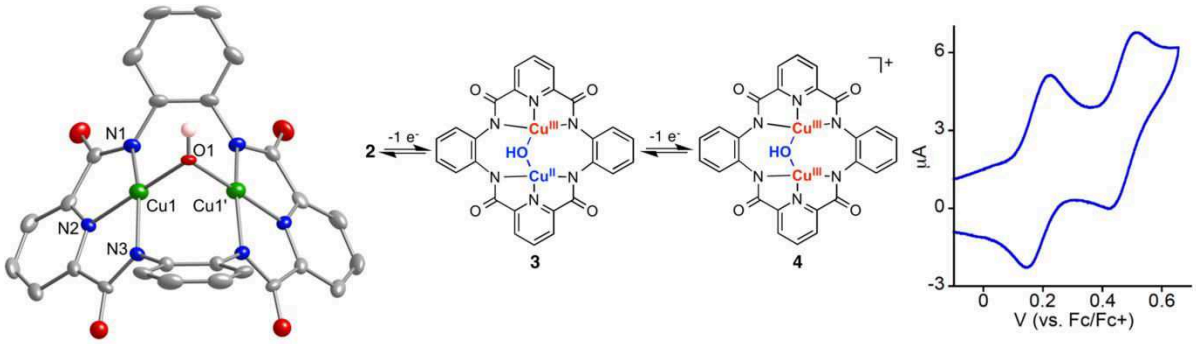

Figure IV.4. X-ray structure and voltammetric behavior in DMF at T = 223 K of the pyridine(dicarboxamide) dicopper complex developed by Tolman and co-workers. Reproduced from Ref.[22].

Hence, this short literature survey demonstrates that the Cu^{III} redox state in both mononuclear and dinuclear complexes can be accessed and stabilized by the employment of amide ligands. On this basis, our objectives have been to develop new dicopper complexes bearing amide groups in order to favor a mixed valent $Cu_2^{III,II}$ species at low oxidation potential (*ca*. 0 V vs Fc). Two different dicopper(II) complexes have been envisaged, depending on the type of spacer (phenoxo or alkoxo), as well as the number (1 or 2) of bis-amide cores (Figure IV.5).

As stated earlier, phenoxo bridges display the interesting property to be relatively rigid, which is of interest for designing ligand with specific intermetallic distance (see Chapter I and II). However, their main drawback is their relatively low oxidation potential into phenoxyl radicals. To avoid this situation, a ligand design with strongly donating groups (such as bis-amides) is necessary. On the other hand, alkoxo bridges are of interest because of their relative redox inertia. So far, numerous dicopper complexes bridged by an alkoxo unit have been reported.[1],[23],[24],[25],[26],[27],[28],[29],[30],[31],[32],[33],[34],[35],[36],[37],[38],[39] Most of the time, the purpose was to accommodate the intermetallic bond distance, by playing with second bridging group such as carboxylate, pyrazolate, azide and nitrite.[27],[28],[40],[41],[42],[43] Most of these systems were shown to be antiferromagnetically coupled; ferromagnetic interactions were observed only in few µ-alkoxo-µ-carboxylato bridged complexes.[44],[45],[46]

Our first objective was to develop a dicopper complex bearing two bis-amide units which are separated by an alkoxo bridging ligand (Figure IV.5-A). The use of the alkoxo spacer is expected to avoid ligand oxidation before the metal ion(s). The second complex is unsymmetrical and displays a DPA unit separated from a bis-amide core by a phenoxo bridge. For this complex, it is expected that the donor properties of the bis-amide ligand would favor the oxidation of the metal ion rather than

that of the phenoxo bridge, hence yielding a mixed-valent dicopper(III,II) species. For these two complexes, special emphasis will be placed on electrochemical, spectoelectrochemical and DFT analyses to rationalize the redox properties upon oxidation.

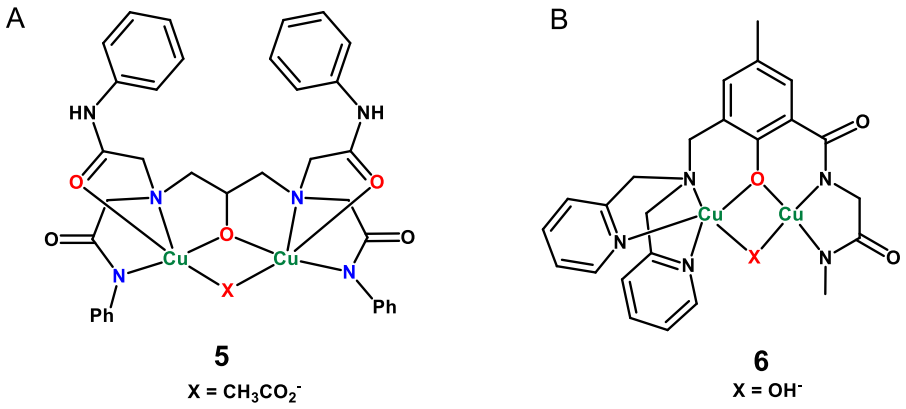

Figure IV.5. Targeted dicopper(II) complexes **5** and **6** bearing amide groups with A) alkoxo and B) phenoxo bridges.

II. Synthesis, characterization and redox properties of complex 5

II.1. Synthesis and solid-state characterization of complex 5

The bis-amide ligand was obtained in a high yield (87%), in one single step by condensation of 2-chloro-N-phenylacetamide and 1,3-diamino-2-propanal (Figure IV.6). The double metalation of the ligand in methanol by using two equivalents of copper(II) acetate salt in the presence of Et_3N as a base afforded the μ-alkoxo-μ-acetato dinuclear Cu^{II} complex **5** with good yield.

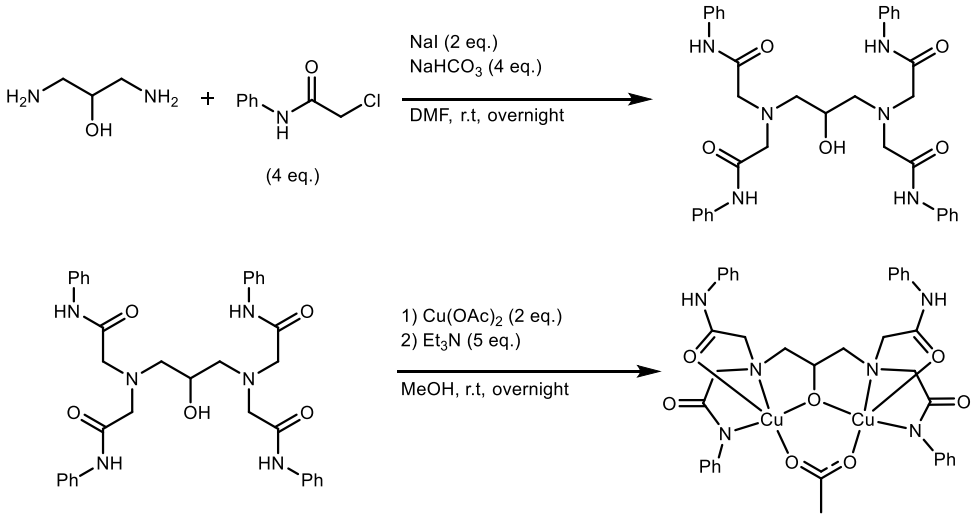

Figure IV.6. Synthesis of the bis-amide ligand and its corresponding dinuclear Cu(II) complex **5**.

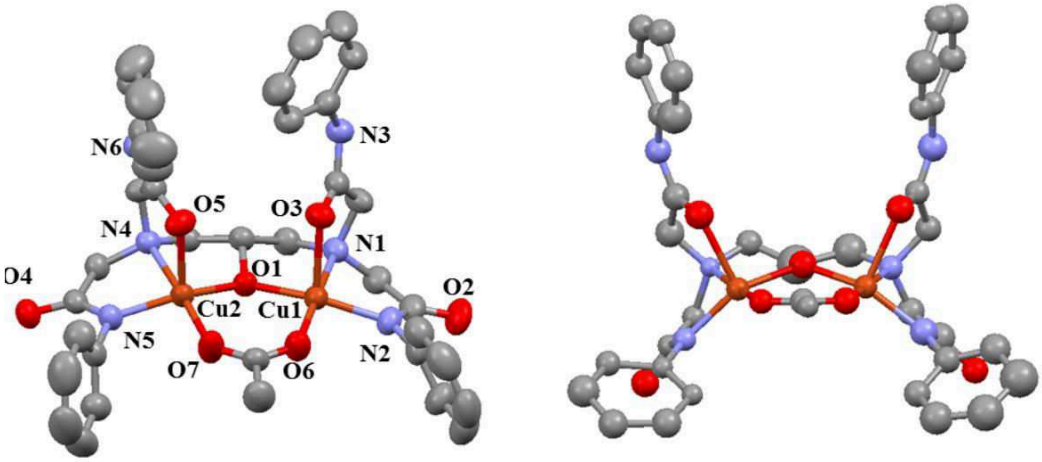

Figure IV.7. X-ray crystal structure of **5a** (left) and **5b** (right).

As shown in Figure IV.7, the crystallization of the complex **5** revealed two different X-ray crystal structures (**5a** and **5b**). The two crystals were obtained by slow evaporation of a solution in either ethanol/dichloromethane/N,N-dimethylformamide (DMF) at room temperature (**5a**) or in dichloromethane/DMF at 48°C (**5b**).

Table IV.1. Selected bond lengths and angles for complex **5**

Bond lengths in Å		Angles in °	
Cu1-O1	1.9225(17)	O1-Cu1-O6	96.12(8)
Cu1-O6	1.937(2)	O1-Cu1-N1	83.89(8)
Cu1-N1	2.064(2)	N1-Cu1-N2	82.78(9)
Cu1-N2	1.963(2)	N2-Cu1-O6	96.12(9)
Cu1-O3	2.3359(18)	O3-Cu1-O1	90.78(7)
Cu2-O1	1.9022(18)	O3-Cu1-N1	79.18(7)
Cu2-O7	1.931(3)	O1-Cu2-O7	95.92(9)
Cu2-N4	2.095(2)	O1-Cu2-N4	85.31(8)
Cu2-N5	1.935(2)	N4-Cu2-N5	83.59(8)
Cu2-O5	2.2257(18)	N5-Cu2-O7	94.09(9)
		O5-Cu2-N4	80.44(7)
		O5-Cu2-N5	98.23(8)

The binuclear complex shows two copper ions bridged by the alkoxide group of the ligand and an acetate moiety. The ligand is tri-deprotonated and two amide functions remain protonated (N3 and N6). Each copper is coordinated in equatorial positions with the nitrogen atom from deprotonated amide groups (N2 and N5), the nitrogen (N1 and N4) and oxygen (O1) atoms of the ethanolamine moieties, and two oxygen atoms (O6 and O7) from the bridging acetate ligand. The apical position is occupied by the oxygen atoms (O3 and O5) from the pendant amide arms that remained protonated. Selected bond lengths and angles of complex **5a** are gathered in Table IV.1. The two Cu1 and Cu2 atoms are in square-pyramidal geometries as shown by the value of the Addison parameter[47] (τ = 0.02). The two structures of the complex **5** are very similar to each other. The only difference is the distance between the two apical arms (O3-O5), and the two equatorial amide arms (N2-N5). In **5a** and **5b**, the Cu1-Cu2 distance remains very similar (3.41 Å). These two structures, closed (**5a**) and open (**5b**), of the same complex **5** can be visualized as a butterfly flapping its wings.

II.2. Electrochemical studies of complex 5

Cyclic voltammetry (CV) of complex **5** (0.50 mM) was performed at a glassy carbon electrode in DMF/NBu_4PF_6 under argon at room temperature. The cyclic voltammetry of **5** revealed an irreversible oxidation peak at $E_{pa}(1)$ = 0.63 V vs Fc (v = 0.1 V s^{-1}, Figure IV.8). The peak remained irreversible in the investigated scan-rate range (0.005 V s^{-1} < v < 30 V s^{-1}) (Figures IV.8-A, inset and IV.8-B). The same behavior was found at low temperature (233 K). On the back scan, two broad reduction peaks were detected at -1.1 V and -1.4 V (Figures IV.8-B and IV.8-C). A sharp oxidation peak at -0.25 V was observed after reduction and can be ascribed to the dissolution of an electrogenerated Cu^0 complex.

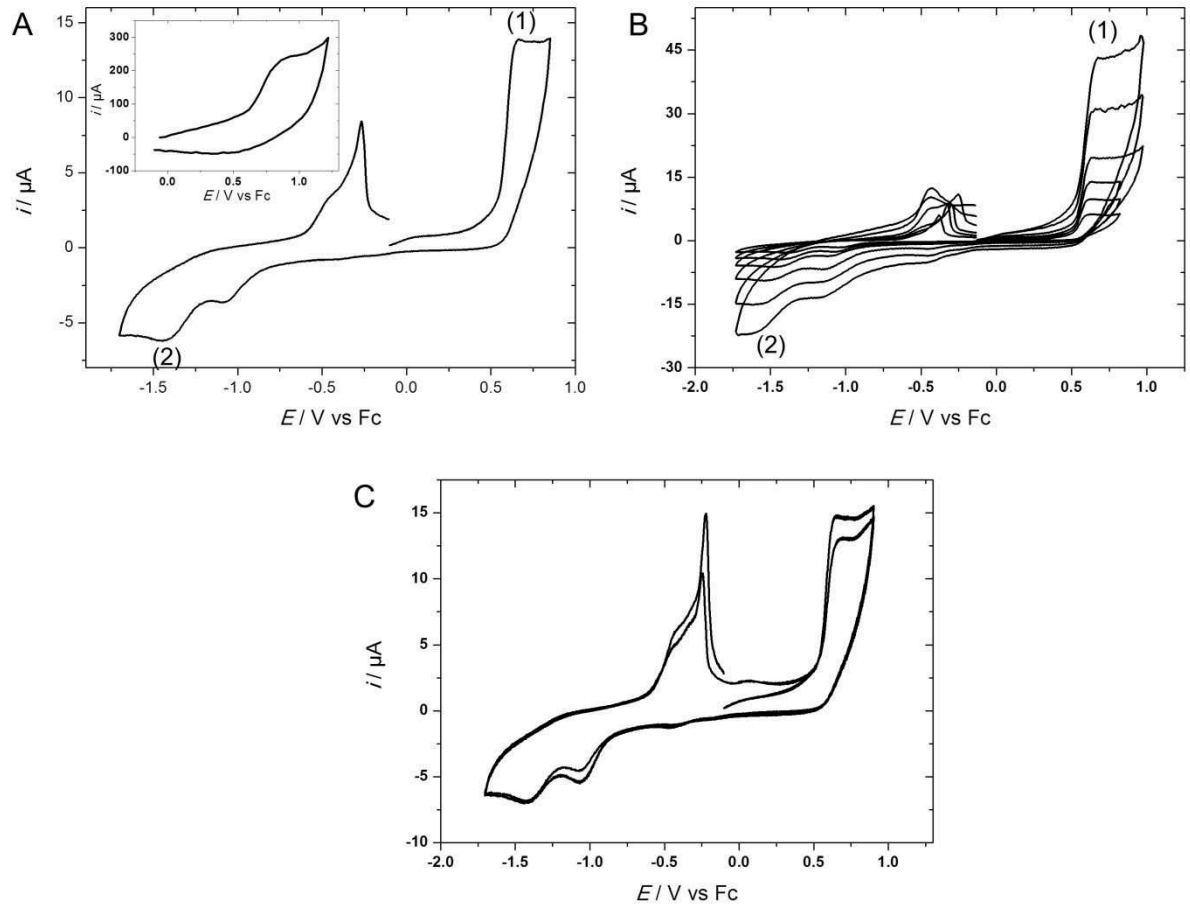

Figure IV.8. CVs on positive scanning of complex **5** (0.5 mM) in DMF /NBu_4PF_6 A) v = 0.1 V s^{-1}, inset: v = 30 V s^{-1}; B) 0.02 V s^{-1}< v < 1 V s^{-1}; C) 2 cycles, v = 0.1 V s^{-1}.

When scanning negatively, a single reduction peak was detected at $E_{pc}(2)$ = -1.34 V vs Fc while several oxidation peaks of low intensity, associated to the reduction process were observed on the reverse scan between -0.6 V and 0.2 V (Figure IV.9) .

Plots of anodic or cathodic peaks current ($i_{pa}(1)$ or $i_{pc}(2)$, respectively) against $v^{1/2}$ follow a linear variation, as expected for a diffusion-controlled electrochemical process (Figure IV.10). Notably, the ratio between anodic (1) and cathodic (2) peak currents is more than 1 and remains almost constant over the investigated scan rates ($i_{pa}(1)/i_{pc}(2)$ = 2.5 /+- 0.2).

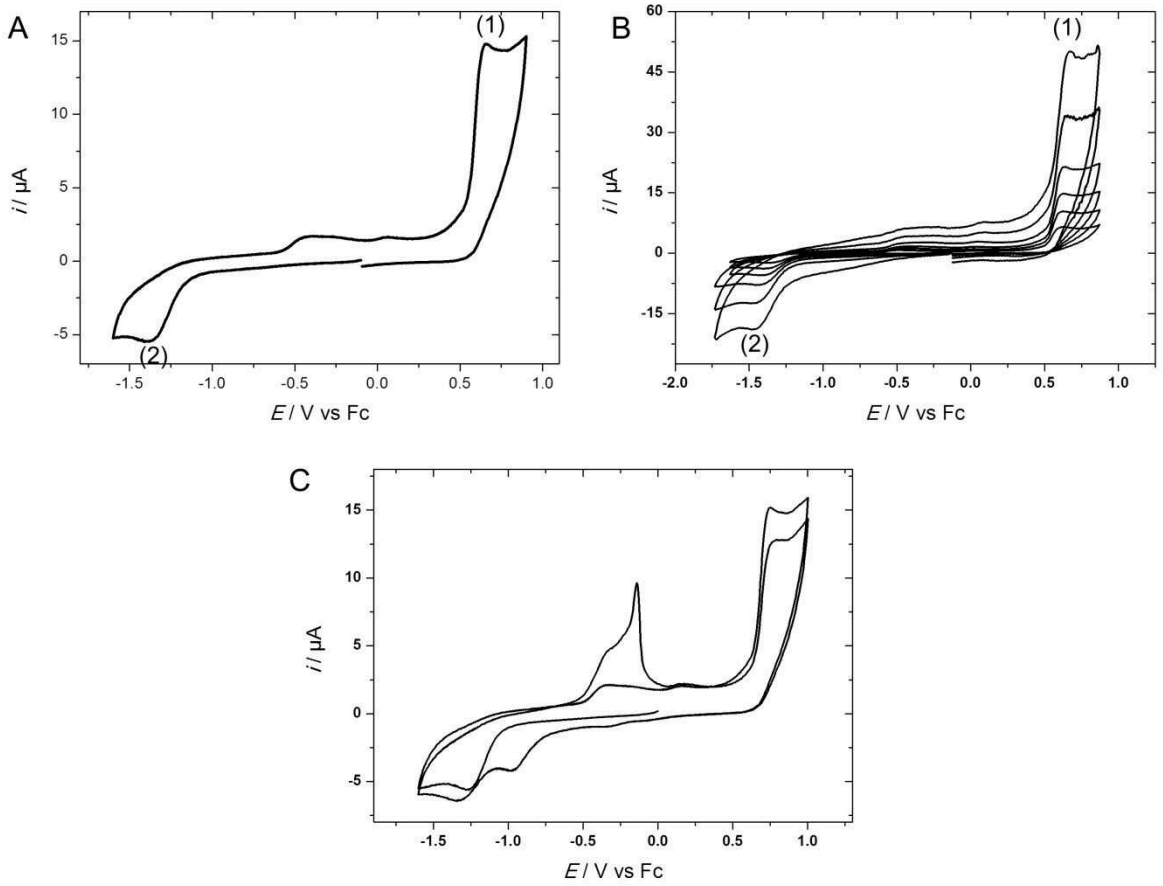

Figure IV.9. CVs on negative scanning of complex **5** (0.5 mM) in DMF /NBu_4PF_6 A) v = 0.1 V s^{-1}; B) 0.02 V s^{-1}< v < 1 V s^{-1}; C) 2 cycles, v = 0.1 V s^{-1}.

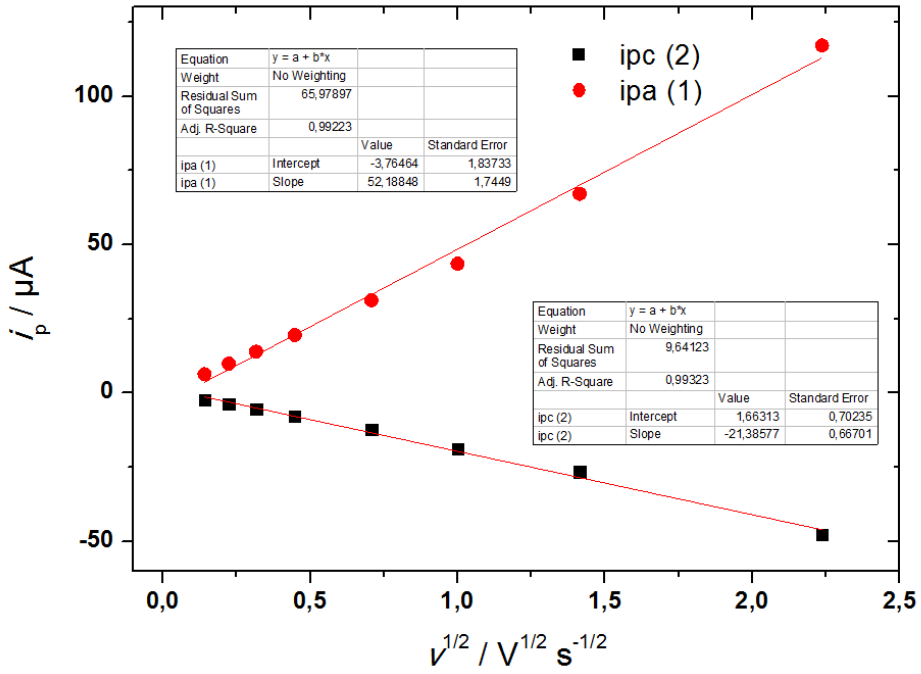

Figure IV.10. Plots of i_{pa}(1) and i_{pc}(2) vs $v^{1/2}$ from CVs at different scan rates 0.02 V s^{-1}< ν < 5 V s^{-1}.

In order to determine the number of electrons (n) involved in the oxidation and reduction processes, exhaustive electrolyses of the solution were carried out at room temperature at E = 1.0 V vs Fc for the oxidation and -1.5 V for the reduction. After an hour of bulk electrolysis, the solution color changed from blue to yellow in both cases, showing the transformation of complex **5**. Coulometric analyses indicated that n = 8 for the oxidation and n = 3 for the reduction. These results suggest complicated mechanisms involving new redox-active species generated during long-time scaled electrolysis, through ECE (E=electrochemical, C=Chemical) pathways.

Another approach was then employed by using short-time voltammetric data and NMR spectroscopy. The number of exchanged electrons in the redox processes can be indeed determined knowing the value of i_p, since the peak current includes a diffusional term as well as the number of electrons. The diffusion coefficient can be extracted from DOSY NMR experiments (D = 5.4 10^{-6} cm^2s^{-1}) (Figure IV.11). Then, if one assumes a simple EC mechanism for the redox processes (1) and (2), the variation of i_p vs $v^{1/2}$ yields n knowing the diffusion coefficient (D), the concentration in complex **5** (C = 0.50 mM) and the area of the electrode (A = 0.07 cm^2).[48]

$$i_p = 0.496n^{3/2}FACD^{1/2}\left[\frac{F}{RT}\right]^{1/2}v^{1/2} \qquad \text{(IV.1)}$$

Using the equation IV.1 yielded n = 0.9 and 1.6 for the reduction and oxidation processes respectively. This indicates that an ECE mechanism, with C being fast (vs timescale of the experiment) occurs for the electrochemical oxidation of the complex. In order to further understand this mechanism, cyclic voltammetry of acetate was performed. An irreversible oxidized peak was detected at $E_{pa}(3)$ = 0.78 V (Figure IV.12).

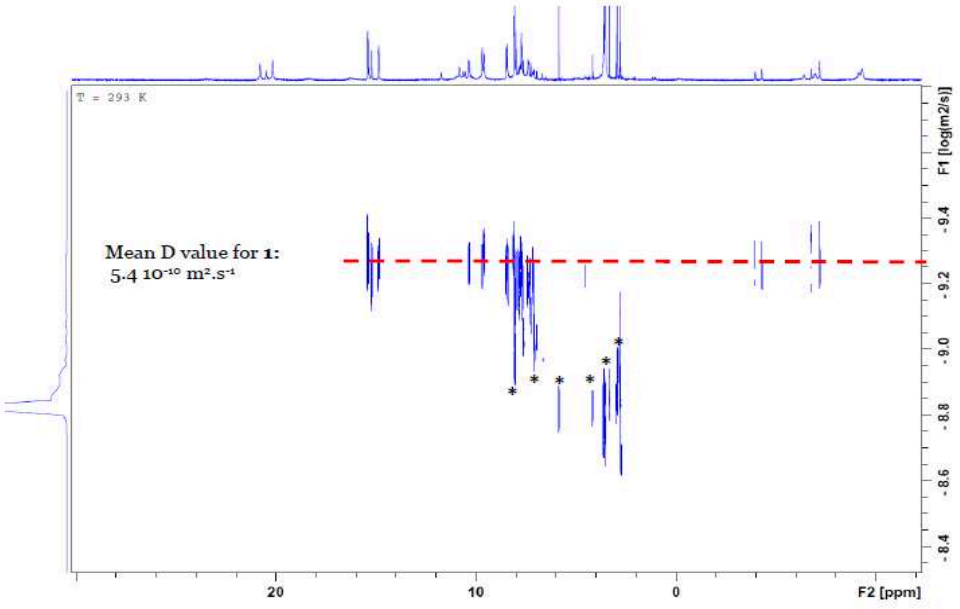

Figure IV.11. DOSY spectrum of complex **5** (1.5 10^{-2} M) in N,N-Dimethylformamide-d_7 at 293 K.

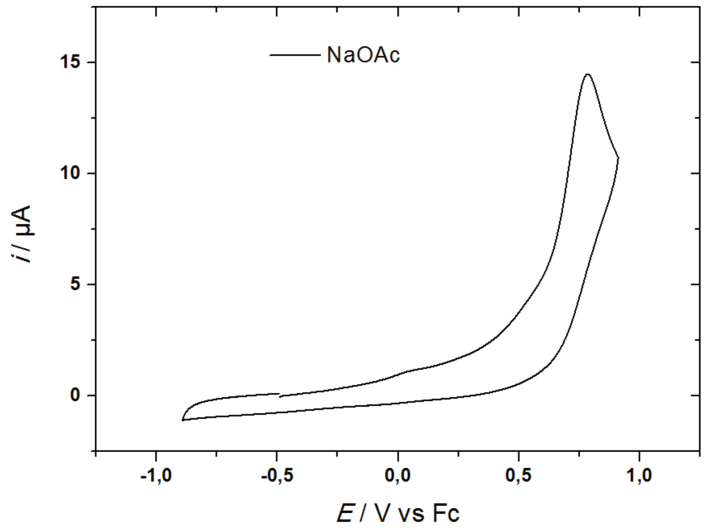

Figure IV.12. CV of NaOAc (2.5 mM) at a glassy carbon electrode in DMF/NBu_4PF_6 0.1 M under Ar (v = 0.1 V s^{-1}).

This result accounts for the number of electron involved in the oxidation process greater than one. The oxidation of the complex at $E_{pa}(1)$ = 0.63 V induces probably fast release of the acetate ligand which starts being oxidized when scanning positively beyond 0.6 V. Hence, the complex can be reduced or oxidized in a monoelectronic manner, but the oxidation process induces a fast chemical unbinding of acetate and possible binding of DMF solvent (Figure IV.13). Noteworthy, the release of acetate is triggered by electron input since ESI mass spectrometry of **5** in DMF/MeOH exhibits two fragments centered at m/z = 805.1466 and 827.1285 assigned to $[M+H]^+$ and $[M+Na]^+$, respectively, suggesting that the complex retains its coordination sphere in DMF solution, therefore implying that the bridging acetate is maintained in solution.

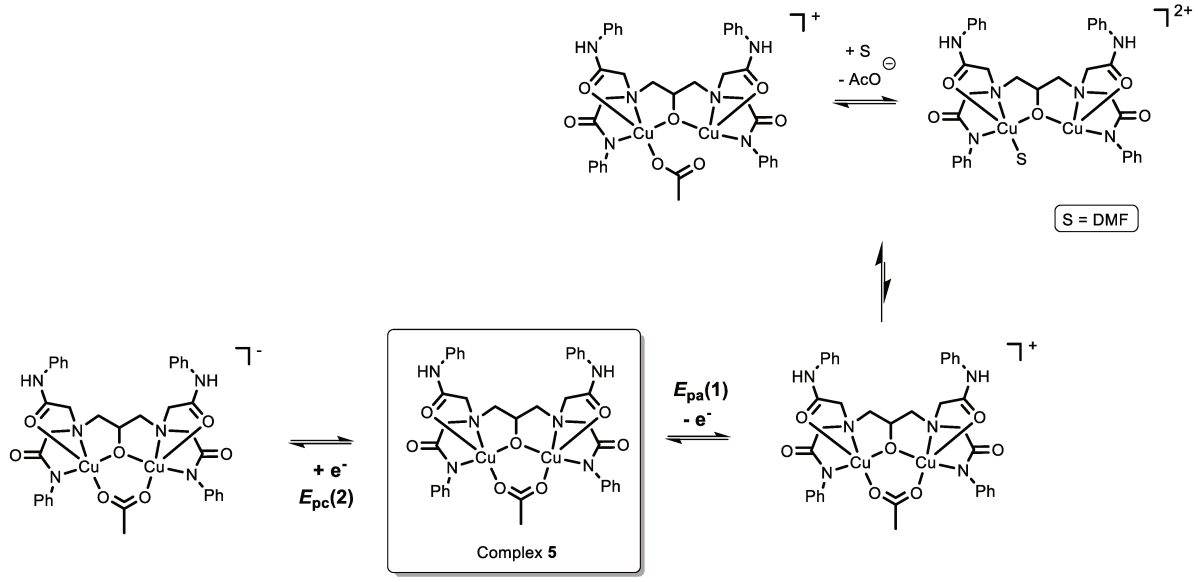

Figure IV.13. Proposed redox pathway for complex **5** for oxidation and reduction in DMF.

II.3. Spectroelectrochemical studies of complex 5

Spectroelectrochemical experiments at room temperature were performed in order to characterize the transient oxidized species ($\mathbf{5}^{+}$). Thin-layer cyclic voltammetry (TLCV) upon oxidation was used to monitor a time-resolved UV-Vis spectroscopic response of the oxidized species. The 3D spectroscopic response of the complex **5** is displayed in Figure IV.14. Thorough analysis of the time-resolved UV-Vis spectra is shown in Figure IV.15.

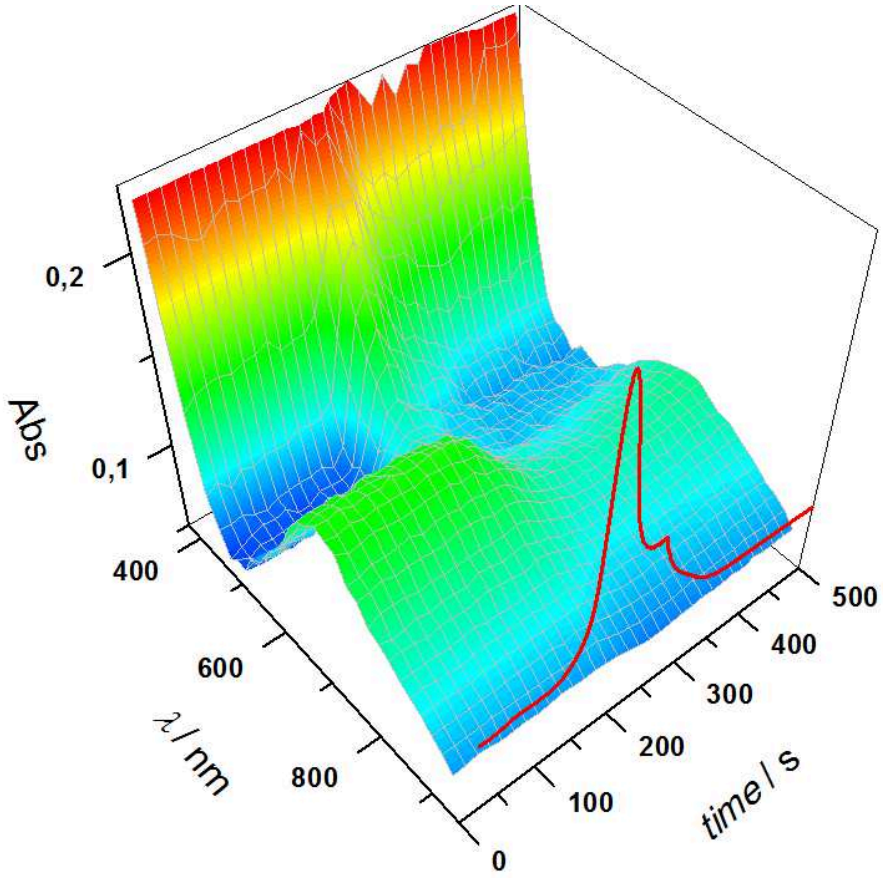

Figure IV.14. 3D spectroscopic response of **5** (5 mM) under electrochemical oxidation in DMF/NBu_4PF_6 (0.1 M) under argon and at a glassy carbon electrode (optical path 0.2 mm); red curve: corresponding TLCV results (v = 5 mV s^{-1}).

Complex **5** showed two absorption bands at λ_{max} = 711 nm and λ_{max} = 380 nm, corresponding to a d-d and a LMCT transition, respectively. At 150 seconds, when oxidation started, the two bands decreased and a new one appeared in the λ_{max} = 400-500 nm wavelength range. Beyond 220 seconds, this new band decreased, showing the transient character of the generated oxidized species. A maximum absorption was reached at 220 seconds for λ_{max} = 463 nm (Figure IV.15-C). This wavelength value was obtained by subtraction of the initial spectrum for all recorded spectra. Reverse scanning revealed a slight increase of the d-d band at λ_{max} = 711 nm, but without reaching the initial absorbance level, consistently with the irreversible behavior of the CV.

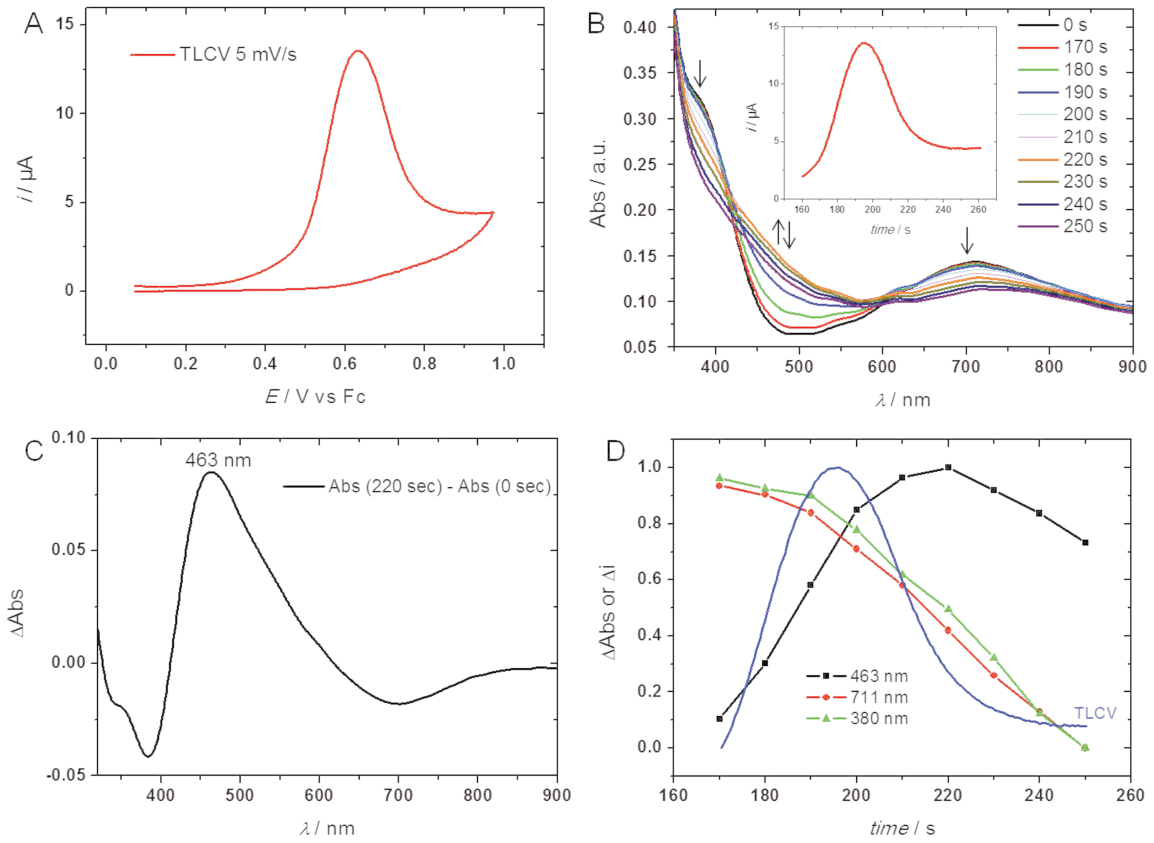

Figure IV.15. A) Room-temperature TLCV at v = 5 mV s^{-1} at a glassy carbon electrode of **5** (5 mM) in DMF/NBu_4PF_6 (0.1 M) under argon; B) 2D UV-Vis spectra of complex **5** after TLCV experiments (5 mV s^{-1}), inset: variation of current with time during CV; C) UV-Vis differential spectrum at λ_{max} = 463 nm between t = 220 s and 0 s; D) Plots of relative absorbance versus time during spectro-electrochemical measurements at different wavelengths: λ = 463 (black), 711 (red), and 380 nm (green). Blue curve: corresponding TLCV results (5 mV s^{-1}).

These results show that oxidation occurs on the copper core because the d-d transition is affected by the electron-transfer reaction. To investigate the $\mathbf{5}^{+}$ species, EPR experiments were performed after generation of the oxidized species by chemical oxidation. Indeed, 1 molar equivalent of $NOSbF_6$ was added in a solution of complex **5** in CH_2Cl_2/DMF (9/1) at 213 K. The complex **5** was EPR silent; after chemical oxidation a transient EPR signal was detected (Figure IV.16). After few minutes at 213 K, the signal decreased, in agreement with the electrochemical results. The spectrum of $\mathbf{5}^{+}$ displays a typical S = 1/2 axial signal with a four-line pattern in the $g_{//}$ region consistent with a hyperfine interaction with only one Cu^{II} ion. This result supports a valence-localized $Cu^{II}Cu^{III}$ species. The copper(II) ion bound axially to two nitrogen atoms and one or two oxygen-containing ligands ($g_{//}$ = 2.356 and $A_{//}$(Cu) = 126 G). The inset of Figure IV.16 shows the expanded second derivative of the perpendicular region of the EPR spectrum of $\mathbf{5}^{+}$. It represents the superhyperfine

lines from the interaction between one nitrogen nucleus (I = 1) from the first coordination sphere and the single unpaired electron (S = 1/2) of the copper(II) ion, providing a coupling constant of A_N = 16.8 G. This strong superhyperfine interaction indicates that the copper(II) ion interacts with an axially bound nitrogen most likely the deprotonated amide ligand, and that only a small deviation from planarity is expected. The overall structure of the complex is maintained in solution; altogether the EPR data indicate a localized mixed-valent $Cu^{III}Cu^{II}$ formulation for **5**$^{+}$.

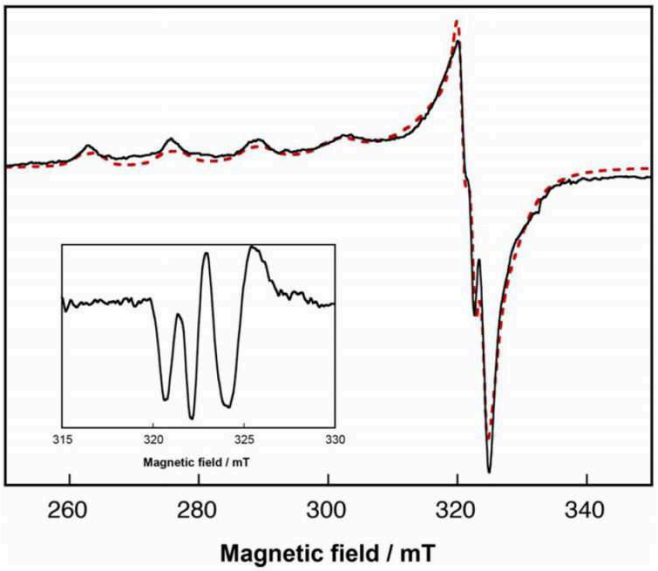

Figure IV.16. X-band EPR spectrum of a 0.5 mM solution of chemically generated **5**$^{+}$ at 213 K in CH_2Cl_2 + 10% DMF. Solid line: experimental spectrum, dotted red line: simulation. Parameters: g_z = 2.356, g_y = 2.058, g_x = 2.058, $A_{//}$(Cu)=126 G, $A_{//}(^{14}N)$ = 16.8 G; inset: derivative spectrum. Experimental conditions: microwave frequency = 9.31 GHz, microwave power = 20 mW, modulation amplitude = 0.3 mT, T = 120 K.

II.4. Electrochemical studies of complex 5 in presence of MeONa

Further electrochemical experiments were performed to investigate ligand exchange properties of the complex. A solution of sodium methoxide was prepared in DMF/NBu_4PF_6. Addition of one molar equivalent of sodium methoxide to a solution of complex **5** led to the appearance of a new irreversible peak at a lower potential value [E_{pa}(4) = 0.40 V] (Figure IV.17-A). The peak at E_{pa}(1) also increased but in lower extent. The disappearance of the peak at E_{pc}(2) in favor of a new one at a more negative value [E_{pc}(5) = -1.72 V] suggested the formation of a new species probably including one methoxide coordinated (complex **5-OMe-DMF**, Figure IV.21).

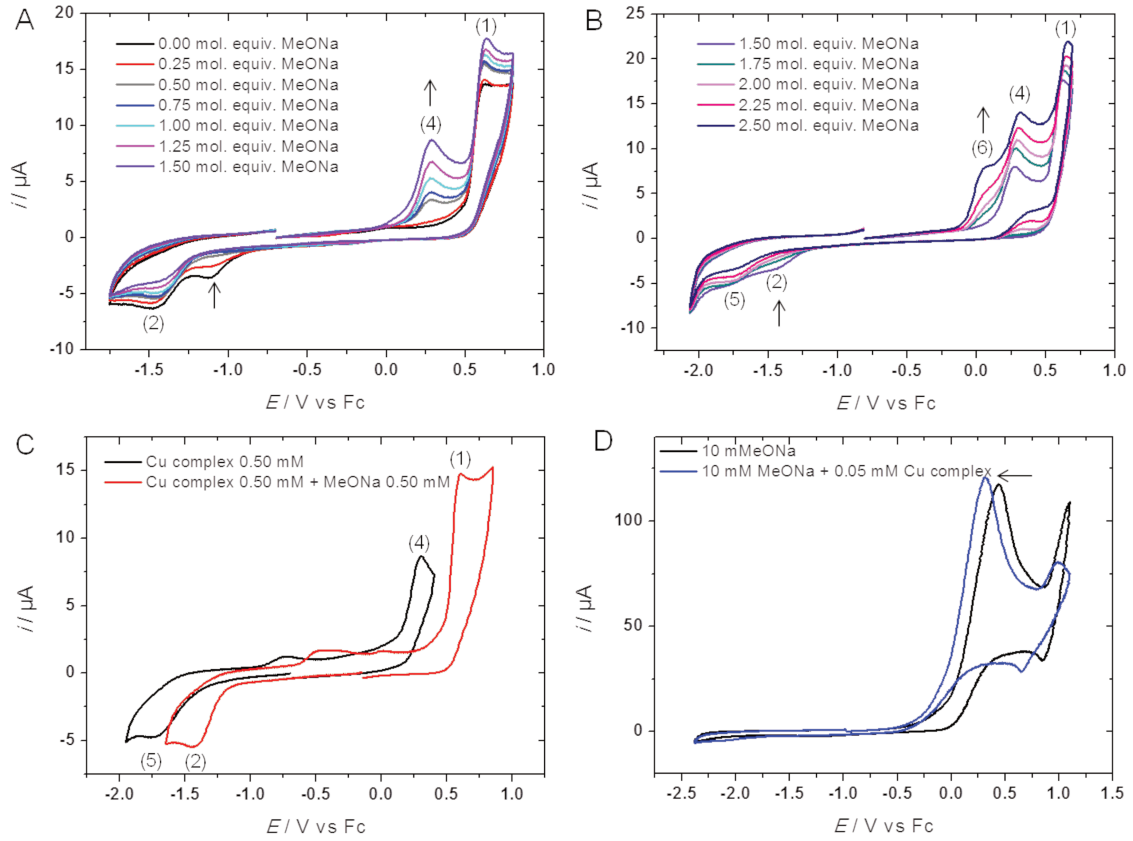

Figure IV.17. CVs at a glassy carbon electrode in DMF / NBu_4PF_6 0.1 M under Ar (v = 0.1 V s^{-1}). A) Addition of 0 to 1.50 molar equiv. of MeONa on a solution of complex **5** (0.50 mM), and B) 1.50 to 2.50 molar equiv. of MeONa on a solution of complex **5** (0.50 mM); C) Comparative CVs of complex **5** before (red) and after (black) addition of one molar equiv. of MeONa; D) CV of MeONa (10 mM) before (black) and after (blue) addition of 0.005 molar equiv. (0.05 mM) of complex **5**.

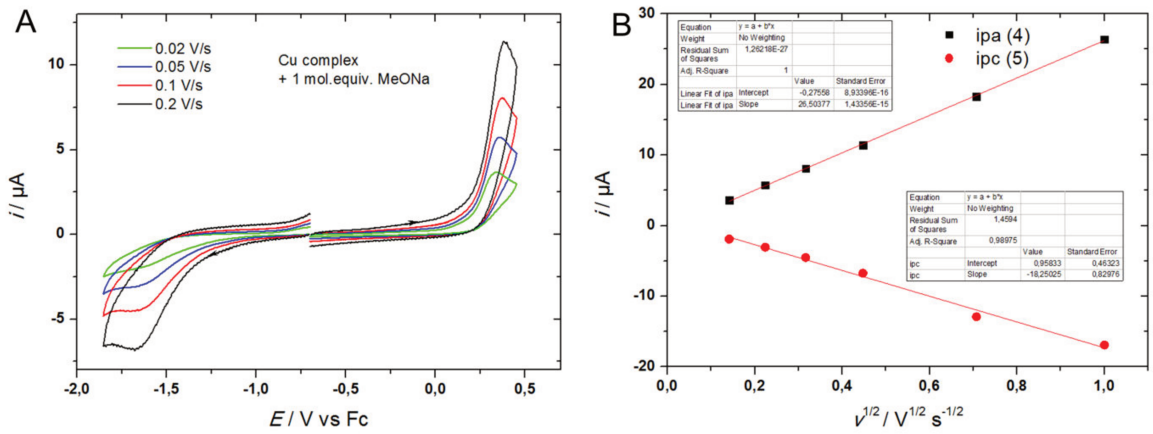

Figure IV.18. CVs at a glassy carbon electrode in DMF / NBu_4PF_6 0.1 M under Ar of complex **5** (0.50 mM) + 1 molar equiv. MeONa A) CVs at different scan rate (0.02 V s^{-1} < v < 0.2 V s^{-1}), starting from 0 V vs Fc in oxidation or reduction; B) plots of i_{pa}(4) and i_{pc}(5) vs $v^{1/2}$ from CVs at different scan rate (0.02 V s^{-1} < v < 5 V s^{-1}).

Plots of $i_{pa}(4)$ and $i_{pc}(5)$ vs $v^{1/2}$ for **5-OMe-DMF** gave similar slope values (Figures IV.18-A and IV.18-B), hence yielding n=0.9+/-0.1 using the assumption that the diffusion coefficient is similar to that of **5** (D = 5.4 10^{-6} cm^2 s^{-1}). These result contrasts with that obtained for complex **5**. Indeed, the analysis of the oxidation peak for **5** gave n = 1.6. This value was proposed to be due to the acetate oxidation after release in solution. Further addition of methoxide led to the appearance of a supplementary peak at $E_{pa}(6)$ = 0.10 V (Figure IV.17-B). This peak corresponds to the oxidation of free methoxide in solution (Figure IV.19).

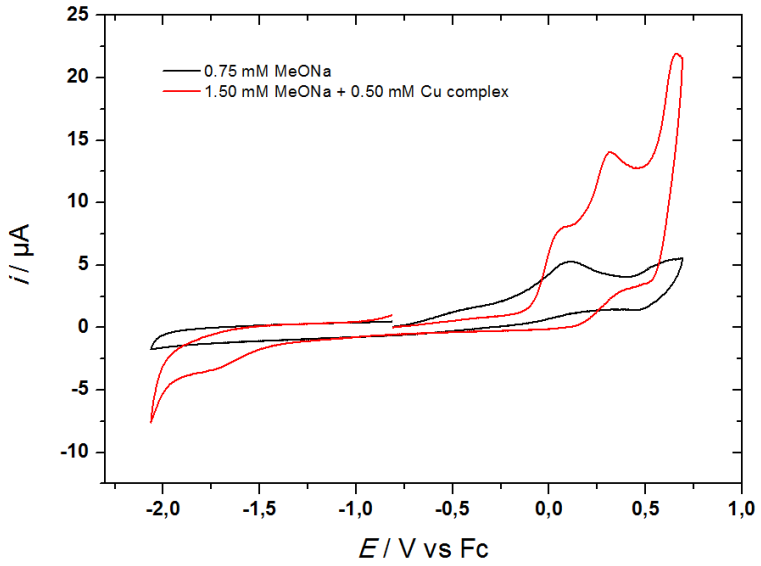

Figure IV.19. CVs (v = 0.1 V s^{-1}) at a glassy carbon electrode in DMF / NBu_4PF_6 0.1 M under Ar of MeONa (0.75 mM) (black); MeONa (1.50 mM) + 0.50 mM Cu complex **5** (red).

Electrochemical investigations were then carried out with the addition of sub-stoichiometric amounts of complex **5** in methoxide solution. Sodium methoxide (10 mM) displayed an irreversibly oxidation peak at 0.10 V (Figures IV.20) at a vitreous carbon electrode. When 0.05 mM of **5** were added, a negative shift of 125 mV of the oxidation potential was observed without significant variation of the anodic peak current. Further addition led to a progressive decrease of the peak intensity with concomitant increase of a several peaks at higher potential (Figure IV.20). The results evidenced an additional competitive reaction involving the oxidized form of methoxide. Indeed, the occurrence of a supplementary chemical process with a high rate of reaction for an existing EC oxidation reaction induces a negative shift of the peak potential. Figure IV.21 displays a mechanism in which the complex **5** binds the methoxide group to produce the complex **5-OMe-DMF**.

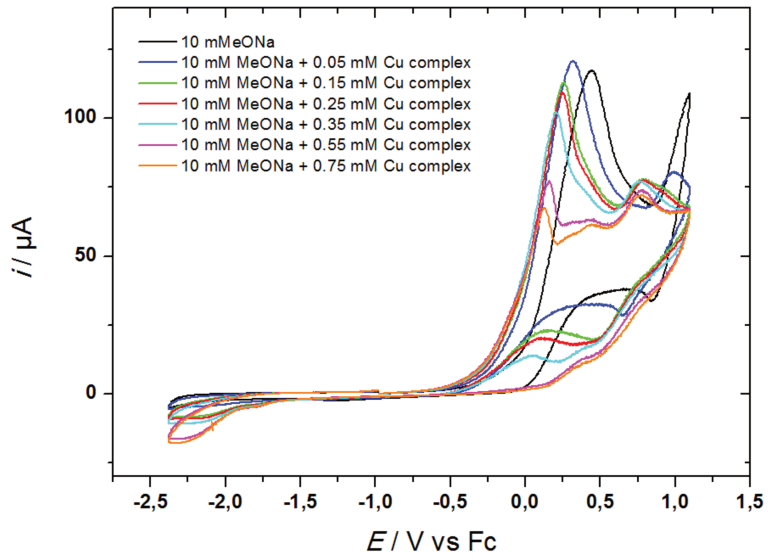

Figure IV.20. CVs at a glassy carbon electrode in DMF / NBu_4PF_6 0.1 M under Ar (v = 0.1 V s^{-1}) of MeONa (10 mM) before (black) and after (blue) addition of 0.05 mM (blue), 0.15 mM (green), 0.25 mM (red), 0.35 mM (cyan), 0.55 mM (pink), 0.75 mM (orange) of complex **5**.

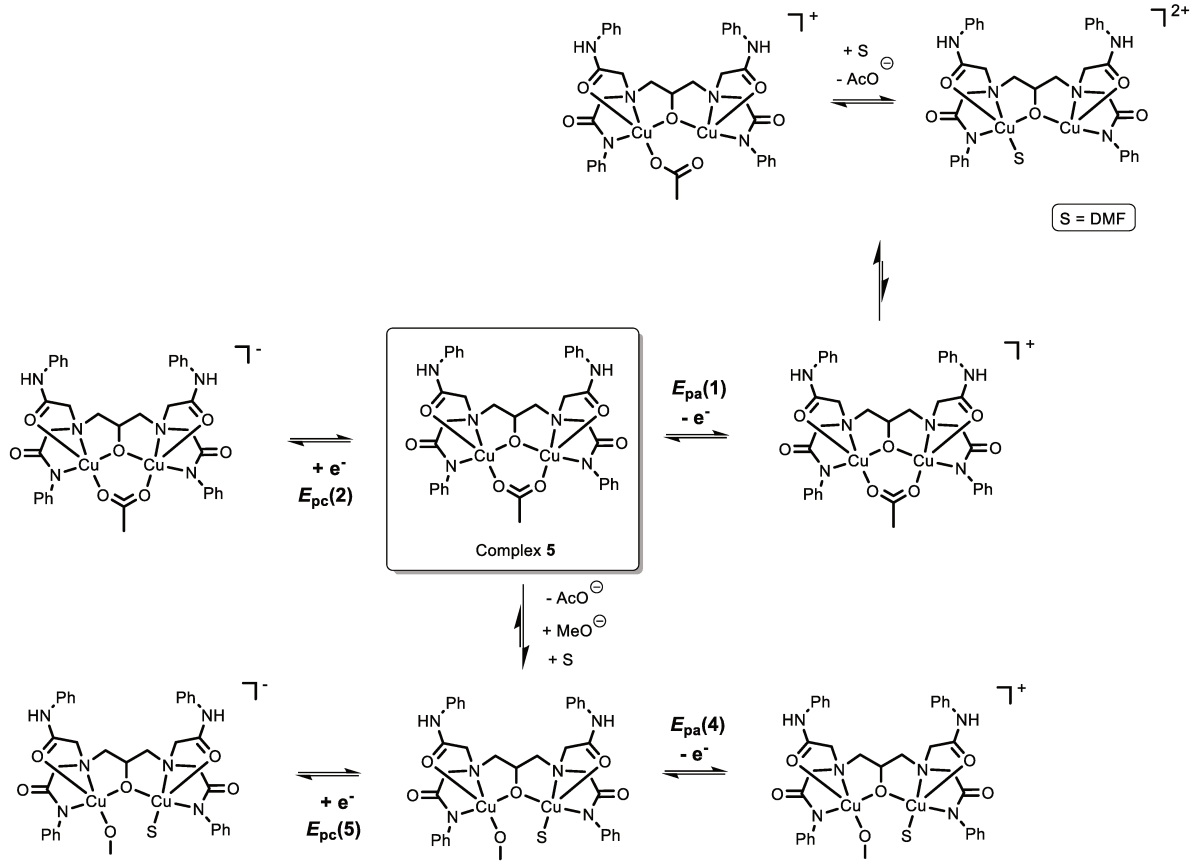

Figure IV.21. Proposed redox pathway for complex **5** upon electrochemical oxidation and reduction in DMF with addition of sodium methoxide

II.5. Theoretical calculations on complex 5

Further investigations were carried out by DFT calculations to evaluate the first oxidation potentials of the different complexes (before and after addition of MeONa) and get insight into the oxidation site (ligand vs metal centered). The evaluation of the redox potential value was performed according to the computational method used for the phexoxo-DPA complexes (Chapter II). In the case of **5**, DFT calculations predicted an oxidation potential of 0.62 V vs Fc, very close to the experimental value of the irreversible peak at $E_{pa}(1)$ (0.63 V). As shown in Figure IV.22, different structures were also computed for the oxidized state of complex **5**: i) form *a* with the bridging acetate ligand, ii) form *b* with one acetate bound in a monodentate fashion on one copper, iii) form *c* with one DMF on one copper and one monodentate acetate on the other copper, and iv) form *d* with one monodentate DMF bound on one copper (Figure IV.22).

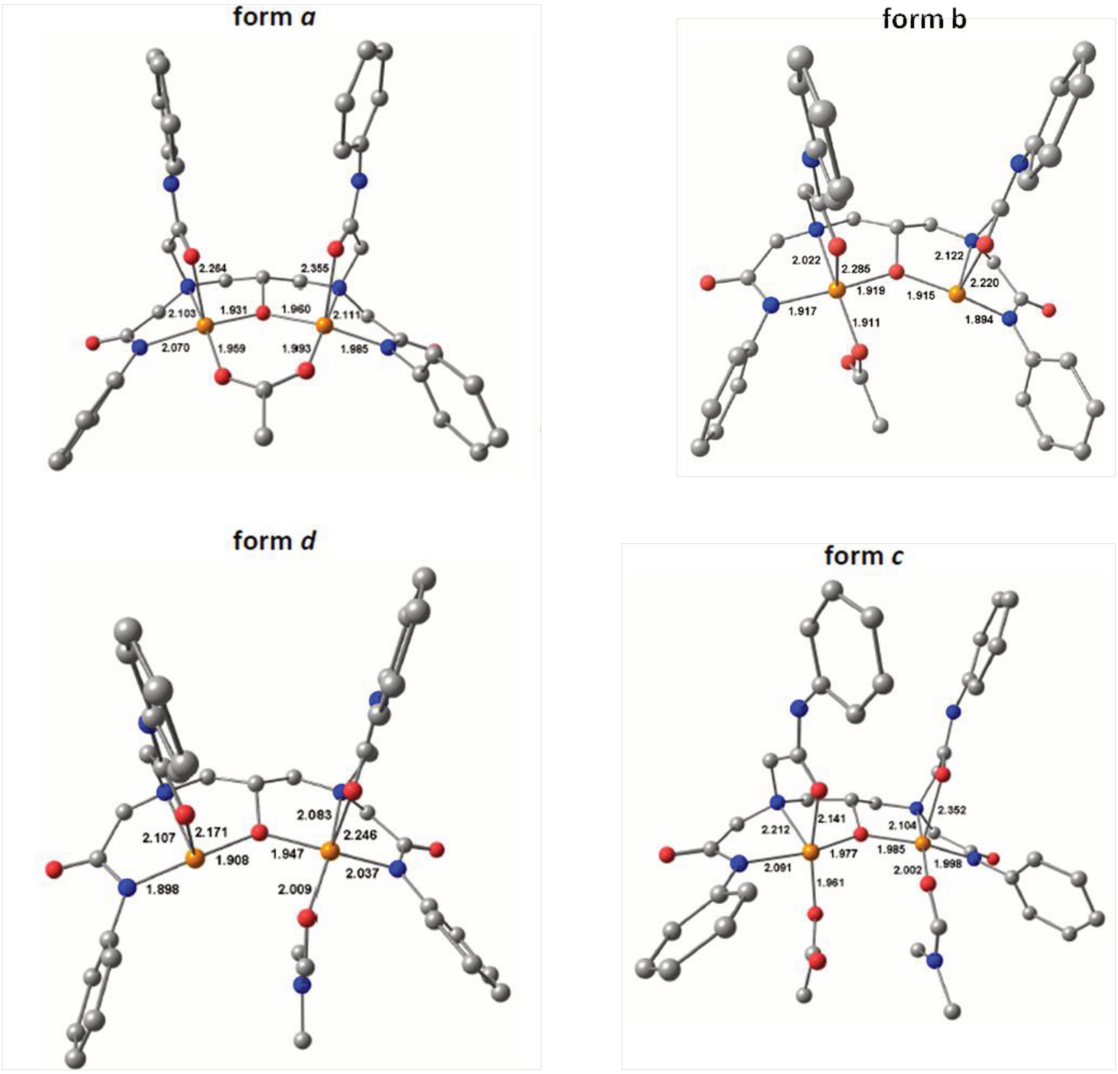

Figure IV.22. DFT-optimized structures and selected bond distances parameters for alternative oxidized forms of **5** (a, b, c and d).

Singly occupied molecular orbitals (SOMOs) were calculated for a, c and d optimized forms of $\mathbf{5}^{+}$. For the form *a*, *c* and *d* the SOMOs were found partly delocalized on both copper centers and on one phenyl of the ligand (Figure IV.23). This situation does not account for a localized mixed-valent $Cu^{III}Cu^{II}$ species. The calculations performed on form *b* (Figure IV.24) support a localized mixed-valent $Cu^{III}Cu^{II}$ species that could be formed upon oxidation of **5**. The SOMO localized on the Cu^{II} center displayed a dominant Cu $3d_{x2-y2}$ character, which is in agreement with the experimental EPR spectrum (Figure IV.16). This result is however not fully consistent with that suggested on the basis of cyclic voltammetry (release of acetate in solution by oxidation, the free acetate ion being then oxidized at this potential value). One possible explanation is that forms b and d (or equivalent with two DMF ligands) of $\mathbf{5}^{+}$ are in equilibrium. Due to the structural pattern, only form b would be detected by EPR spectroscopy at low temperatures.

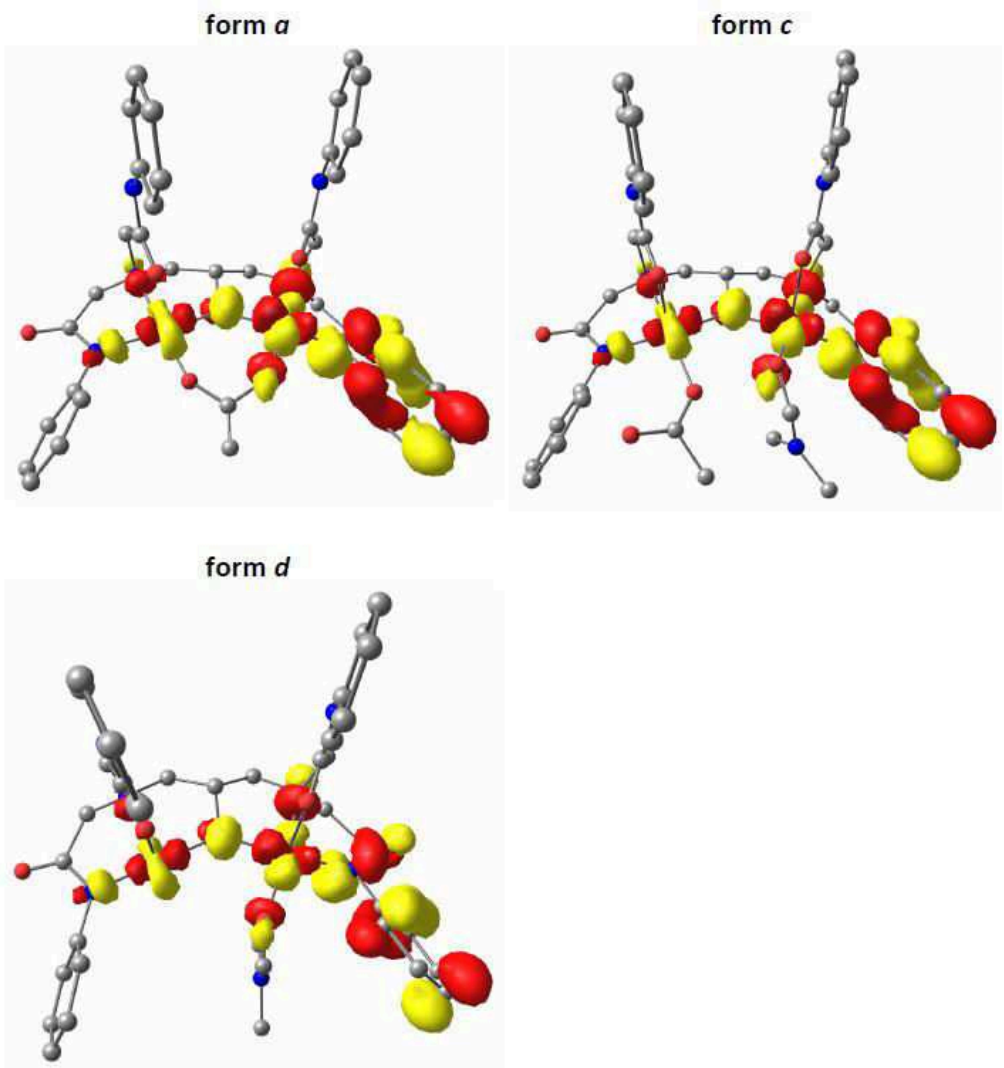

Figure IV.23. Localized SOMO for different oxidized forms of **5** (a, c and d).

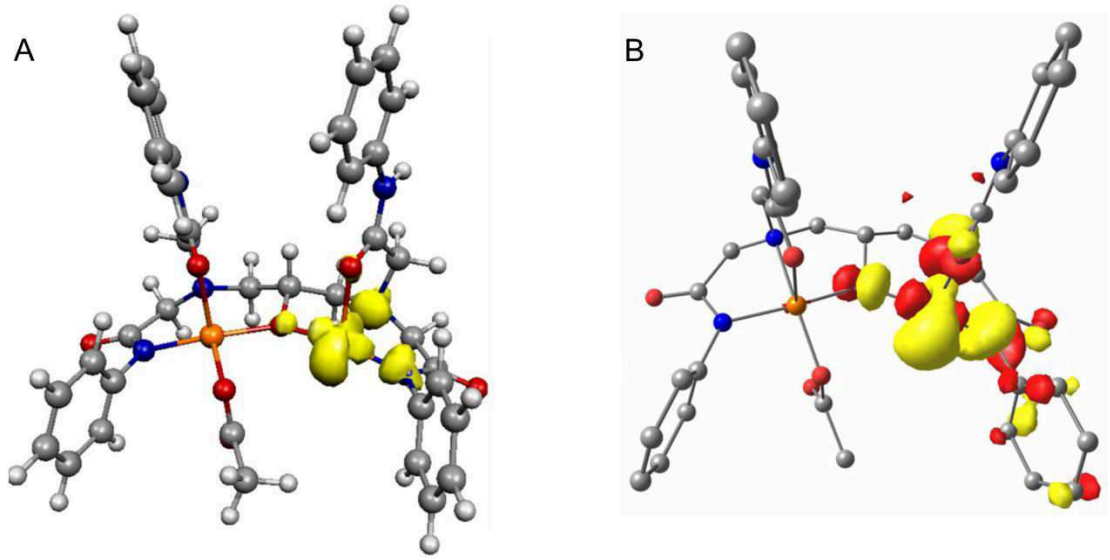

Figure IV.24. A) Spin density plot and B) localized SOMO for the relevant oxidized form b of **5**.

Time-dependent DFT calculations were performed to predict the UV-Vis spectrum. The λ_{max} = 457 nm was found to correspond to ligand-to-copper(III) transition, which is in agreement with the observed transition at λ = 463 nm during spectro-electrochemical experiments. So, according to the calculations, the form b seems to be the major intermediated oxidized form of **5**, corresponding to the mixed- valent $Cu^{III}Cu^{II}$ species with one acetate bound in a monodentate fashion.

DFT calculations were also employed for the series of complexes putatively formed upon addition of sodium methoxide to **5** (Figure IV.25). Three complexes were considered depending on the mode of coordination of the methoxide/acetate: i) one bidendate bridging methoxide (**5-OMe**), ii) one monodentate methoxide and one DMF (**5-OMe-DMF**) or iii) one monodentate methoxide and one monodentate acetate (**5-OMe-OAc**). Redox potentials (vs Fc) were computed for all dicopper(II,II) structures: 0.52 V for **5-OMe**, 0.32 V for **5-OMe-DMF** and 0.16 V for **5-OMe-OAc**. Analysis of spin densities indicates that the oxidation of **5-OMe** is copper-centered, hence resulting in a $Cu^{III}Cu^{II}$ species (Figure IV.26).

From the computed redox potential values, it seems reasonable to propose that the addition of sodium methoxide to a solution of complex **5** releases the acetate ion into the solution, while methoxide and DMF bind to copper ions in a monodentate coordination mode, as suggested by cyclic voltammetry. Indeed, the experimental value found after addition of one molar equivalent of methoxide is 0.40 V, which is close to the 0.32 V value found by DFT for **5-OMe-DMF**. Hence, the release of acetate and methoxide binding results in a lower oxidation potential (0.40 V vs 0.63 V) due to the better donor properties of the methoxide ion. Mono-electronic oxidation of the resulting complex led to the generation of a $Cu^{III}Cu^{II}$ species. The oxidation process is irreversible, supposing a degradation of the complex after oxidation (Figure IV.21).

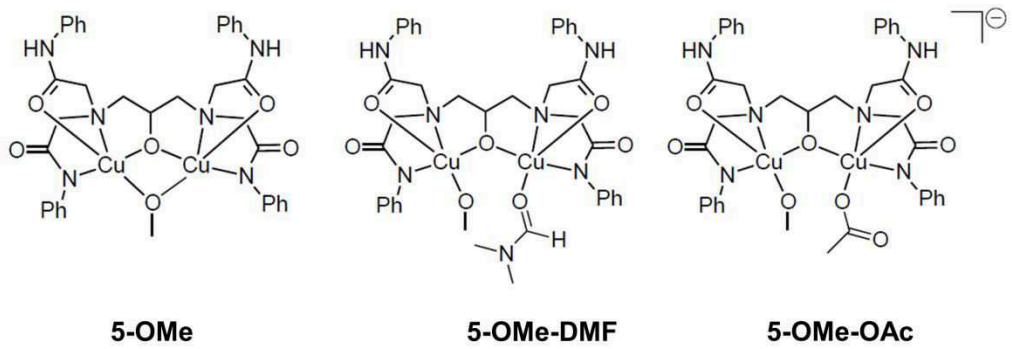

Figure IV.25. Different structures considered for the resulting complex after addition of sodium methoxide on **5**.

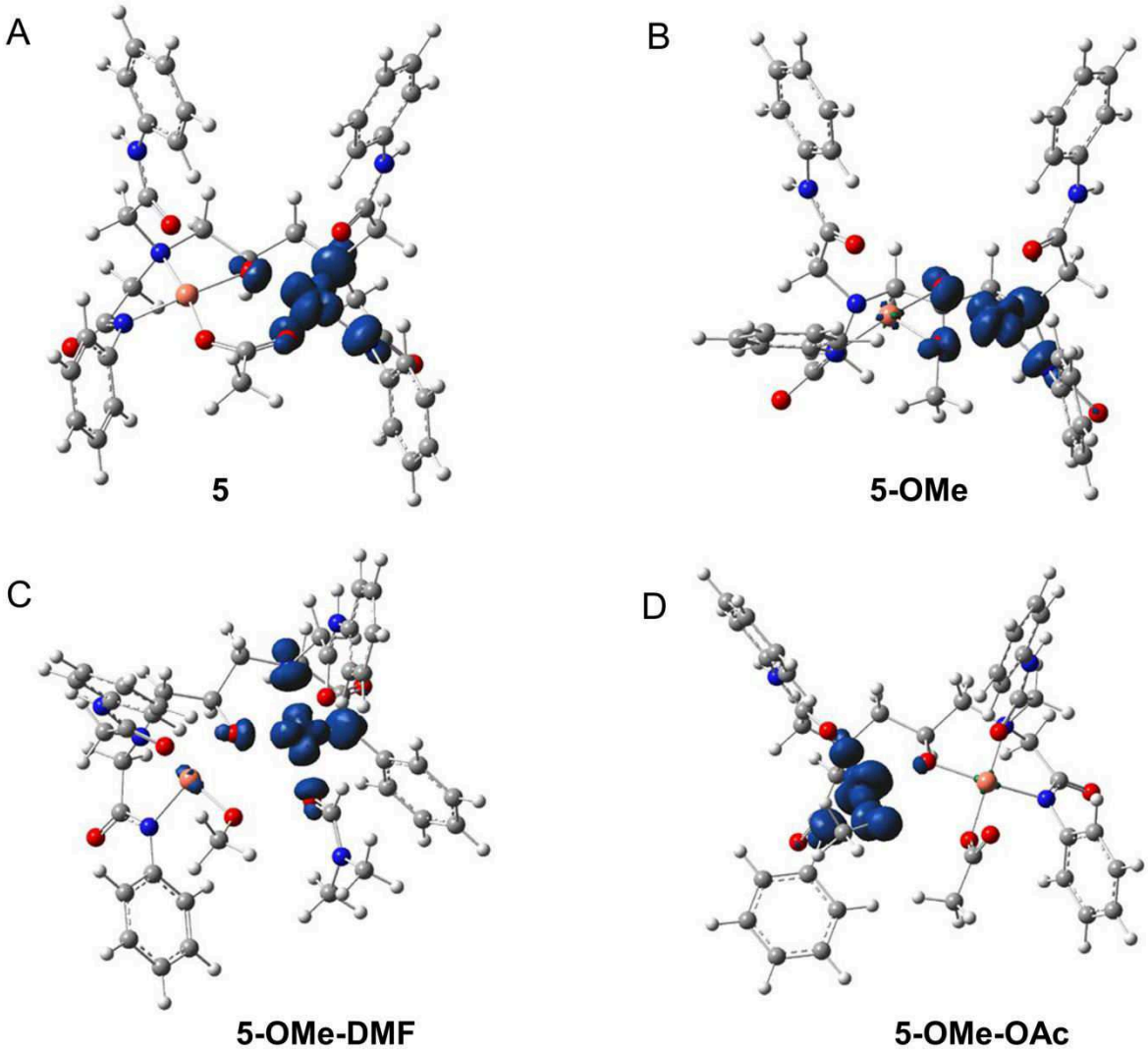

Figure IV.26. Spin density plot for mono-oxidized form of complexes A) **5**, B) **5-OMe**, C) **5-OMe-DMF**, and D) **5-OMe-OAc**.

II.6. Conclusions on the studies of complex 5

The objective of this study was to develop a dicopper complex bearing two bis-amide units separated by an alkoxo bridge. Crystals of a μ-alkoxo, μ-acetato dicopper complex were obtained and analyzed by X-ray diffraction. Electrochemical studies in DMF of the complex showed an irreversible monoelectronic oxidation at 0.63 V and a reduction at -1.34 V vs Fc. Spectroelectrochemical analysis and DFT calculations suggest that: (i) the oxidation process is centered on one of the copper ion leading to a mixed-valent $Cu_2^{III,II}$ species, (ii) oxidation is coupled with the decoordination of the bridging acetate from one copper ion, leading to a mixed-valent complex which absorbs at λ_{max} = 463 nm and displays an EPR signal typical of an isolated Cu^{II}, (iii) the acetate may be totally dissociated from the (III,II) dicopper species and is oxidized at the electrode surface, (iv) substitution of the acetate ligand by a methoxide anion leads to the formation of a dicopper copper with a monodentate methoxo group and a DMF ligand. This new complex is mono-oxidized irreversibly at 0.40 V vs Fc and reduced at -1.72 V.

Hence, the μ-acetato,μ-alkoxo dicopper complex displays limited features due to the hemi-lability of the acetate ligand. Despite an interesting decrease of the redox potential, this complex is not exploitable for catalytic studies. However, the μ-methoxo, μ-alkoxo complex formed by reaction of **5** with sodium methoxide displays more interesting properties since its redox potential is lower than its precursor (due to the donor effect of the MeO^-), and its oxidation seems not being perturbed by an unbinding process such as for the acetato species. Future work will aim at developing unsymmetrical complexes which will favor the stabilization of a mixed-valent species using a bis-amide core, methoxo and alkoxo bridges.

III. Synthesis, characterization and redox properties of complex 6

III.1. Synthesis and characterization complex 6

The unsymmetrical phenoxo-bridged dinucleating ligand, decorated with a DPA and a bis-amide site, was synthesized in three reaction steps. The first one is a reaction between 5-methylsalicyclic acid with hydrochloric acid and paraformaldehyde, to give the corresponding chloromethylated product quantitatively. Substitution of this product by N,N-bis(2-pyridyl)methylamine (BPA) and subsequent peptide coupling reaction afforded the ligand as a crystalline material with a global yield of 30%. The dinuclear copper(II) complex was prepared by the successive addition of 4 equiv. of tetramethylammonium hydroxide to a solution of the ligand and then the addition of 2 equiv. of $Cu(ClO_4)_2.6H_2O$ (Figure IV.27). Crystals suitable for X-Ray diffraction of the complex were obtained by slow diffusion of ethyl acetate into a solution of the complex in dimethylformamide. The structure of complex reveals that the ligand is three time deprotonated and that the copper centers are doubly bridged by the phenoxo and by a hydroxo group (Figure IV.28).

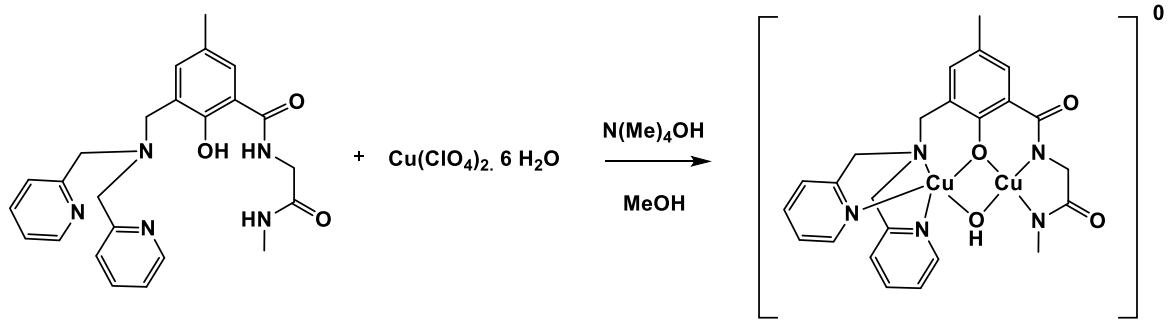

Figure IV.27. Synthesis of the bis-amide-DPA dicopper complex

The unsymmetrical ligand confers two different coordination environments to the two copper centers. Cu1 is tetracoordinated, in a distorted square planar geometry, by the two deprotonated amide (N2, N3) and by the oxygen atoms from the phenoxo (O1) and hydroxo (O2), both bridging Cu1 with Cu2. The coordination of Cu2 is completed by the two *N*-pyridines (N4, N5) and the nitrogen N1, forming a distorted trigonal bipyramid with N1 and O2 occupying the axial positions forming. The Addison parameter, τ,[47] of the pentacoordinated Cu2 is 0.59 indicating a distorted trigonal bipyramid with N1 and O2 occupying the axial positions. The Cu-Cu separation is 3.007 Å for this complex. The bond distances observed in complex **6** are in agreement with those found in copper(II) complexes coordinated by similar N,O-donor groups. Selected bond distances and angles are given in Table IV.2. Considering the angles, a dihedral angle of 44.4° exists between the Cu1-O1-Cu2 and the plane containing the phenyl ring of the spacer indicating that the ligand is relatively twisted.

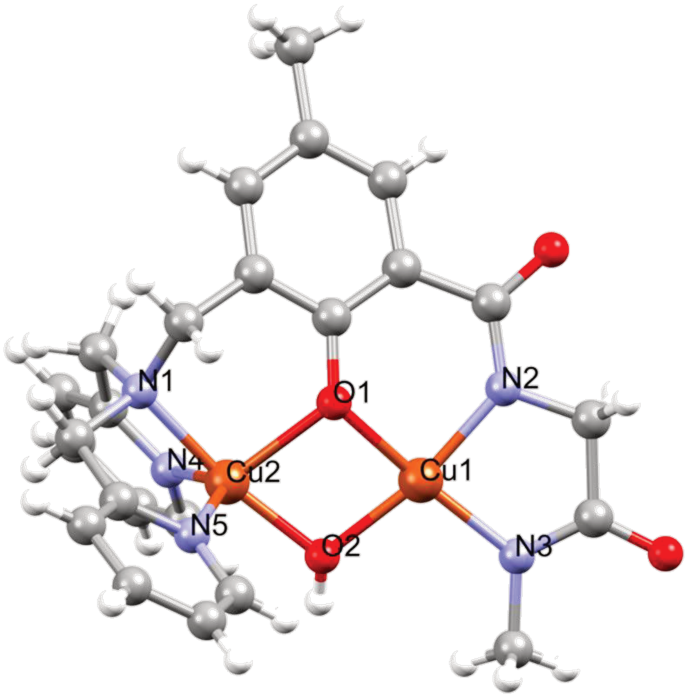

Figure IV.28. Crystal structure of complex **6** crystallized in DMF/EtOAc with partial numbering scheme.

Table IV.2. Selected bond lengths and angles for complex **6**

Bond lengths in Å		Angles in °	
Cu1-O1	1.960(2)	O1-Cu1-N2	91.4(1)
Cu1-N2	1.914(3)	O1-Cu1-O2	81.6(1)
Cu1-O2	1.924(3)	O1-Cu1-N3	167.3(1)
Cu1-N3	1.928(3)	N2-Cu1-O2	167.7(1)
Cu2-O1	2.118(2)	N2-Cu1-N3	85.8(1)
Cu2-O2	1.903(2)	O2-Cu1-N3	103.2(1)
Cu2-N1	2.025(3)	O1-Cu2-O2	78.0(1)
Cu2-N4	2.036(2)	O1-Cu2-N1	93.2(1)
Cu2-N5	2.043(3)	O1-Cu2-N4	120.0(1)
		O1-Cu2-N5	103.7(1)
		O2-Cu2-N1	171.0(1)
		O2-Cu2-N4	102.8(1)
		O2-Cu2-N5	97.9(1)
		N1-Cu2-N4	82.9(1)
		N1-Cu2-N5	82.5(1)
		N4-Cu2-N5	134.5(1)
		Cu1-O1-Cu2	94.92(9)
		Cu1-O2-Cu2	103.6(1)

III.2. Spectroscopic studies of complex 6

Solubilization of complex **6** was possible in either H_2O, MeOH or DMF. The spectroscopic response was shown to be solvent-dependent (Figure IV.29). The shoulder observed in the 380 nm < λ < 550 nm wavelength range was ascribed to a LMCT transition between the bridging phenoxo and copper ions. This transition explains the brown color of the solution. The band observed at 700 nm < λ < 800 nm is characteristic of a Cu^{II} d-d transition. In DMF, the LMCT band at 460 nm (ε = 780 mol^{-1} cm^{-1}) is more intense than in the other solvents, and it was shifted toward higher wavelength. The band detected at λ = 313 nm (ε = 5900 mol^{-1} cm^{-1}) was attributed to the $\pi \rightarrow \pi^*$ transition of the ligand.

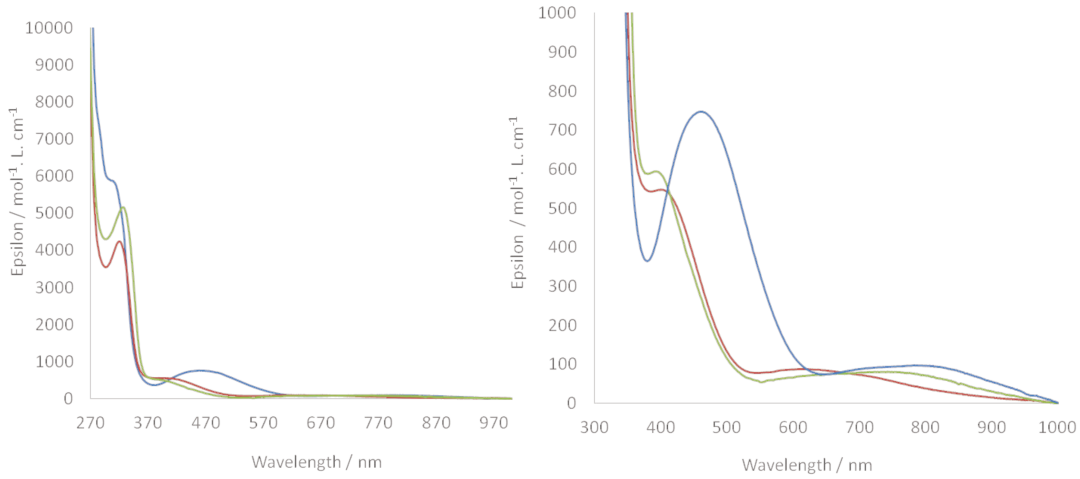

Figure IV.29. UV-Vis spectra of complex **6** in H_2O (red), MeOH (green) and DMF (blue) on different wavelength ranges.

III.3. Electrochemical studies of complex 6

Cyclic voltammetry (CV) of complex **6** was recorded in DMF/NBu_4ClO_4 (0.1 M). At room temperature (T=293 K), three oxidation peaks were detected at E_{pa} = 0.19, 0.68 and 0.87 V vs Fc (Figure IV.30-A). The first system is irreversible at low scan rate, but became partly reversible when v was increased (> 0.5 V/s) (Figure IV.31). This behaviour is typical of an EC mechanism (E=electrochemical, C=Chemical), for which a rather slow chemical process follows the electrochemical oxidation.

As expected, lowering the temperature until 213 K induced a modification of the redox behaviour as shown by cyclic voltammetry (Figure IV.30). Indeed, the first system became fully reversible at $E_{1/2}$ (1) = 0.12 V vs Fc (ΔE_p = 75 mV at v = 0.1 V/s). Increase (decrease) of the scan rate (0.02 V/s < v < 1 V/s) resulted in an increase (decrease) of peak current and peak separation, without loss of chemical reversibility (Figure IV.32-A). On the cathodic part, a quasi-reversible system was detected at $E_{1/2}$ (2) = -1.27 V by CV (ΔE_p = 91 mV at v = 0.1 V/s) (Figure IV.30-B).

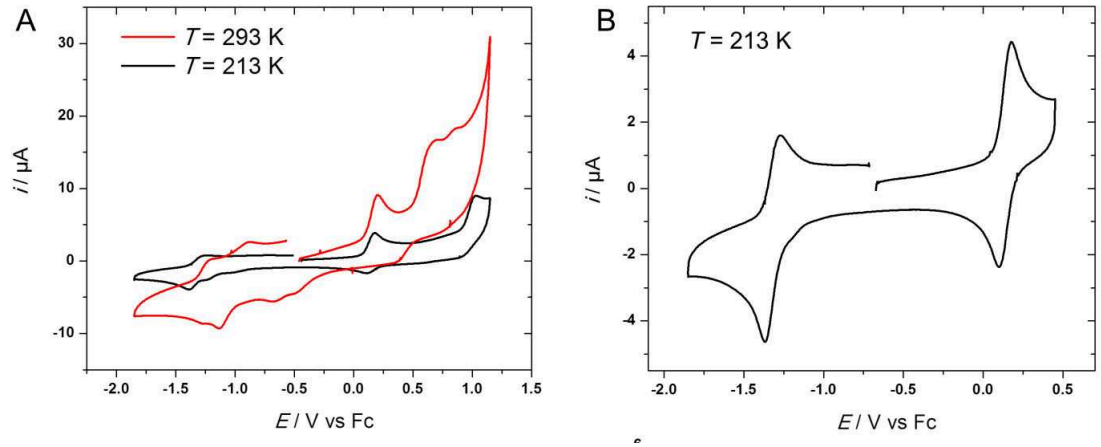

Figure IV.30. CVs of complex **6** in DMF/NBu_4ClO_4 0.1 M (C WE, *E* /V vs Fc): A) at two different temperatures (*T* = 293 K and 213 K) on the -1.8 to 1.2 V potential range (*v* = 0.1 V/s); B) CV at 0.1 V/s at *T* = 213 K for the first oxidation and reduction processes.

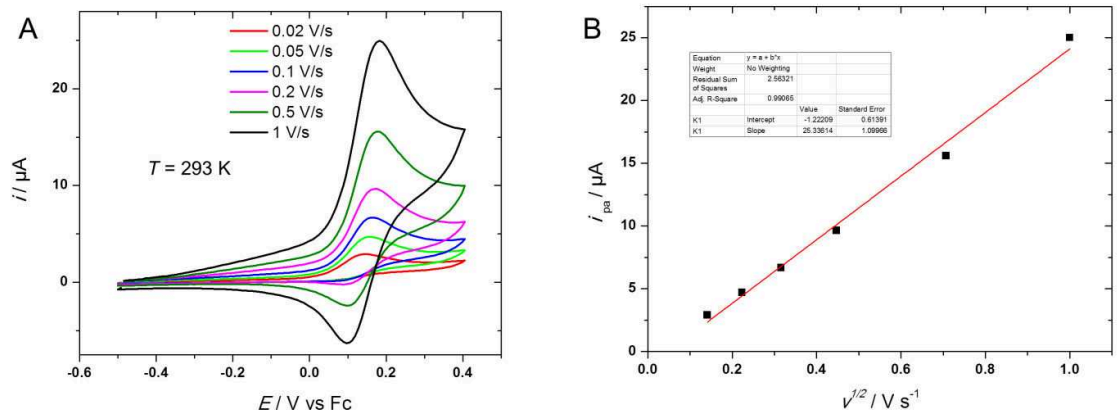

Figure IV.31. A) CVs of complex **6** in DMF/NBu_4ClO_4 0.1 M (C WE, *E* /V vs Fc) at *T* = 293 K for 0.02 V/s < *v* < 1 V/s; B) Plots of i_{pa} vs $v^{1/2}$.

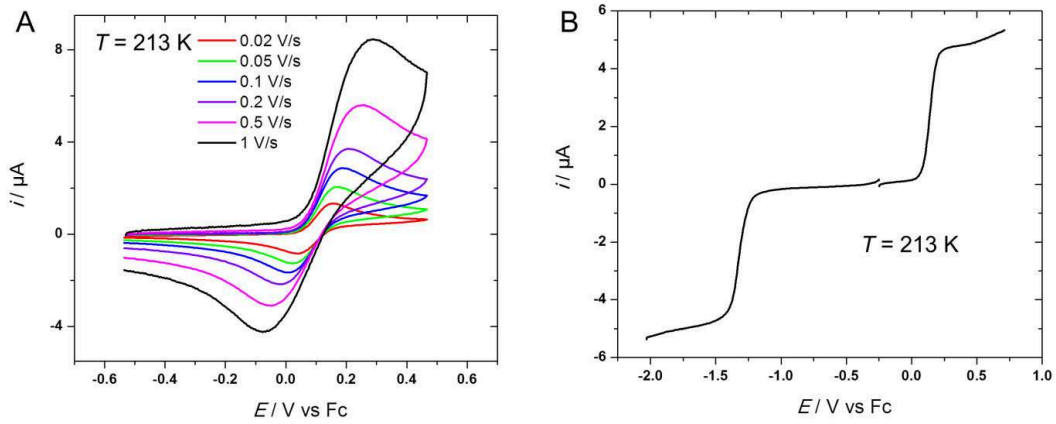

Figure IV.32. A) CVs of complex **6** in DMF/NBu_4ClO_4 0.1 M (C WE, *E* /V vs Fc) at *T* = 213 K for 0.02 V/s < *v* < 1 V/s; B) RDEVs of complex **6** in DMF/NBu_4ClO_4 0.1 M (C WE, *E* /V vs Fc) at *T* = 293 K (ω = 500 RPM, *v* = 0.02 V/s).

From CV and RDEV data at this temperature, it appears clearly that both reduction of oxidation processes involve the same number of electrons (*n*) (Figures IV-30-B and IV.32-B). Three different electrochemical methods were thus combined to calculate *n*: cyclic voltammetry (CV), chronoamperometry (CA) and rotating-disk electrode voltammetry (RDEV). The first step consisted in determining the type of mechanism associated with the oxidation of **6** at 293 K. Hence, the current function (i_{pa} /$v^{1/2}$) was plotted against scan rate *v* to discriminate between two possible mechanisms, EC and ECE. The resulting linear trend was clearly indicative of an EC mechanism, rather than an ECE one. From this basis, we used the equation (IV.1) previously mentioned in this chapter (and rewritten below for convenience) to determine the diffusion coefficient (*D*) for *n*=1 or *n*=2, knowing the area of the electrode (*A*) and the concentration (*C*):[48],[49]

$$i_p = 0.496n^{3/2}FACD^{1/2}\left[\frac{F}{RT}\right]^{1/2}v^{1/2} \qquad \text{(IV.1)}$$

The same approach was used by using the Levich equation for RDEV:[49]

$$i_{lim} = 0.62nFACD^{2/3}\omega^{1/2}\upsilon^{-1/6} \qquad \text{(IV.2)}$$

And the Cottrell equation for CA:[49]

$$i(t) = \frac{nFACD^{1/2}}{\pi^{1/2}t^{1/2}} \qquad \text{(IV.3)}$$

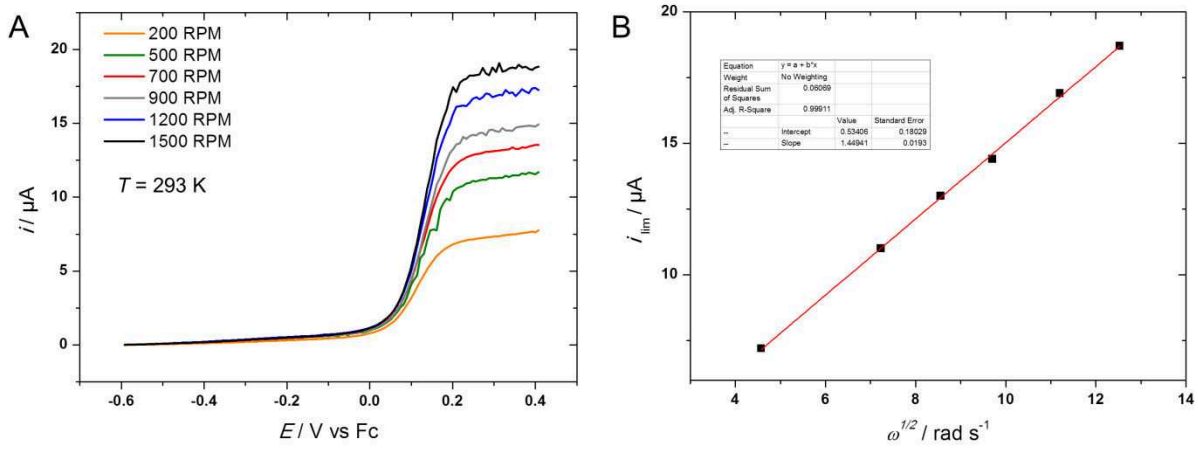

Figure IV.33. A) RDEVs of complex **6** in DMF/NBu_4ClO_4 0.1 M (C WE, *E* /V vs Fc) at *T* = 293 K for 200 RPM < ω < 1500 RPM (v = 0.02 V/s); B) Plots of i_{lim} vs $\omega^{1/2}$.

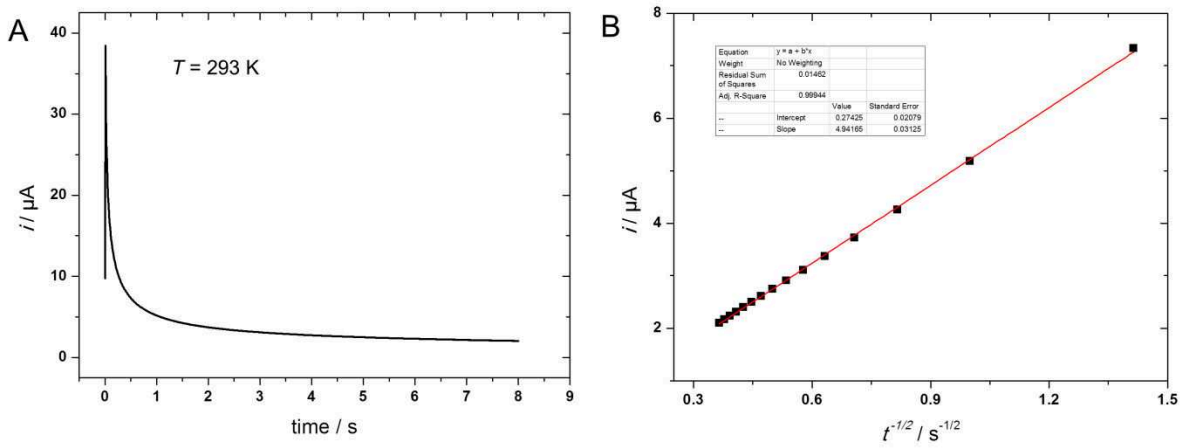

Figure IV.34. A) Chronoamperogram of complex **6** in DMF/NBu_4ClO_4 0.1 M (C WE, *E* /V vs Fc) at *T* = 293 K upon oxidation (E_{app} = 0.3 V vs Fc); B) Plots of *i* vs $t^{-1/2}$.

Plots of i_{pa} vs $v^{1/2}$ (Figure IV.31-B), of i_{lim} vs $\omega^{1/2}$ (Figure IV.33-B) and of *i* vs $t^{-1/2}$ (Figure IV.34-B) displayed a linear trend for the three different techniques. Table IV.3 gives the slopes extracted from these plots and the calculated values of *D*, assuming that either *n*=1 or *n*=2. Best agreement between the three approaches was found for *n*=1, giving *D* = 2.2 +/- 0.2 10^{-6} cm^2/s at 293 K, which is a reasonable value considering the unsymmetrical topology of the ligand and assuming that oxidation/reduction processes occurs on the metal ions. Thus, electrochemical studies suggest that complex **6** is mono-electronically oxidized at $E_{1/2}$ (1) and mono-electronically reduced at $E_{1/2}$ (2).

Table IV.3. Calculated values of the diffusion coefficients (*D*) at 293 K for the oxidation of **6** from experimental electrochemical data, assuming that the number of electrons (*n*) equals 1 or 2.

		***n*=1**	***n*=2**
Method	**Slope**	**10^6 *D* (cm/s)**	**10^6 *D* (cm/s)**
CV	25.3 µA $V^{-1/2}$ $s^{1/2}$	2.2[a]	0.27[a]
CA	4.94 µA $s^{1/2}$	2.1[b]	0.53[b]
RDEV	5.44 µA $rad^{-1/2}$ $s^{1/2}$	2.4[c]	0.84[c]

[a]Calculated from i_{pa} vs $v^{1/2}$ plots (0.02 V/s < *v* < 1 V/s); [b]Calculated from plots of *i* vs $t^{-1/2}$ for *t* < 5 s; [c]Calculated from plots of i_{lim} vs $\omega^{1/2}$ for 200 RPM < ω < 1500 RPM.

Attempts to prepare the one-electron oxidized species by exhaustive electrolysis of a solution of complex **6** at low temperature (213 K) were carried out. After 1 hour electrolysis, RDEV showed that complex **6** was transformed in its oxidized form $\mathbf{6^+}$ (approximatively 1/5th of the solution) as well as a new species which is oxidized at 0.6 V (Figure IV.35-A). This evolution towards a new species is not surprising given the electrochemical data at room temperature (EC mechanism).

Hence, the oxidized species $\mathbf{6}^{+}$ is not stable and evolves towards a new complex which can be oxidized at higher redox potential. Interestingly, X-band EPR characterization at 10 K of the electrolyzed solution displayed a weak signal at $g = 2$ with a four line pattern (Figure IV.35-B). Simulation of the experimental result provided the following parameters: $g_{//} = 2.246$, $g_{\perp} = 2.0575$, $A_{//}$ =193 Gauss, which are typical of a mononuclear Cu^{II} center in a square-based geometry. Since complex **6** is EPR silent in DMF (X band at 6 K and 100 K), these results show that the antiferromagnetic coupling between the copper ions was broken by electrochemical oxidation. Probably, the EPR signal detected at low temperature originates from the mixed-valent species (III,II) dicopper species $\mathbf{6}^{+}$.

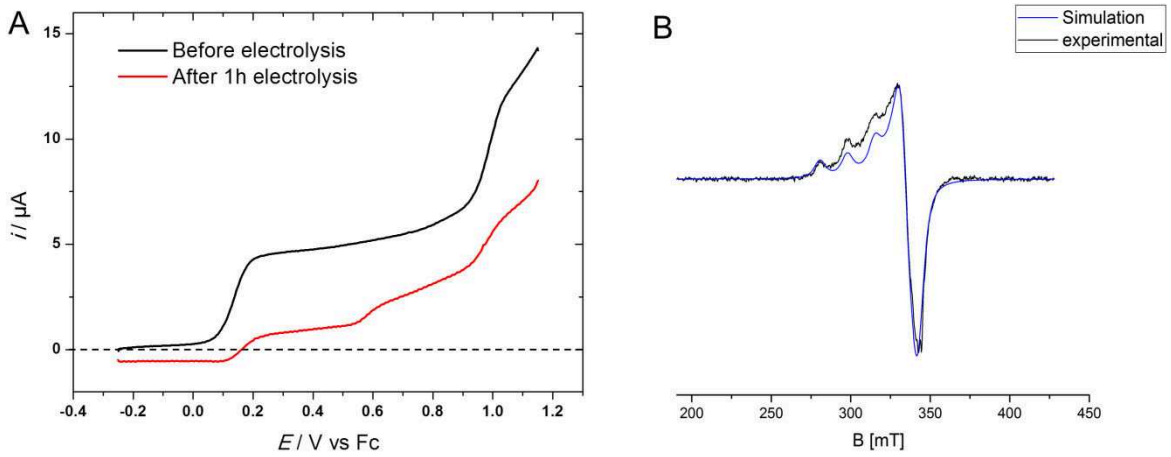

Figure IV.35. A) RDEVs of complex **6** in DMF/NBu_4ClO_4 0.1 M (C WE, E /V vs Fc) at T = 213 K (ω = 500 RPM, v = 0.02 V/s) before (red) and after (black) low-temperature electrolysis (E_{app} = 0.4 V vs Fc); B) X-Band EPR spectrum of the dicopper complex **6** after electrolysis (1h), T = 10K. Black: experimental, Blue: simulated. From simulation: $g_{//} = 2.246$, $g_{\perp} = 2.0575$, $A_{//}$=193 Gauss.

III.4. Cryo-spectroelectrochemical studies of complex 6

To further investigate the electrochemical oxidation of complex **6** in a short timescale and at low temperature, a cryo-spectroelectrochemical setup was employed for the generation and characterization of $\mathbf{6}^{+}$ within a thin layer (<200 µm) at the electrode surface. As shown before, this method offers the advantage to be fast (few seconds) which is of interest when the generated species is not very stable, even at low temperatures, as found for complex **6**. Figure IV.36-A displays the UV-Vis monitoring of the complex **6** upon electrochemical oxidation by CV (red curve) at T = 213 K. Clearly, when electrochemical oxidation occurred, an increase of the band was observed around 400 nm. This band decreased when the potential was swept back to its initial value. An important point here is that the redox process is fully reversible as attested by the CV shape, meaning that the species detected by UV-Vis spectroscopy is effectively the one-electron oxidized complex $\mathbf{6}^{+}$. In

order to better analyze the variation of the spectroscopic data with applied potential, we extracted the initial UV-Vis spectrum (t = 0 sec) from the set of data. The resulting UV-Vis spectra are displayed in a 2D manner in Figure IV.36-B, together with the applied potential and resulting current (red curves). It shows the appearance of a band at λ_{max} = 386 nm at approximatively 17 seconds, which corresponds to the foot of the reduction wave, (i.e. before the electrochemically generated **6**$^{+}$ is reduced). This band can be confidently ascribed to a UV feature of the one-electron oxidized species **6**$^{+}$.

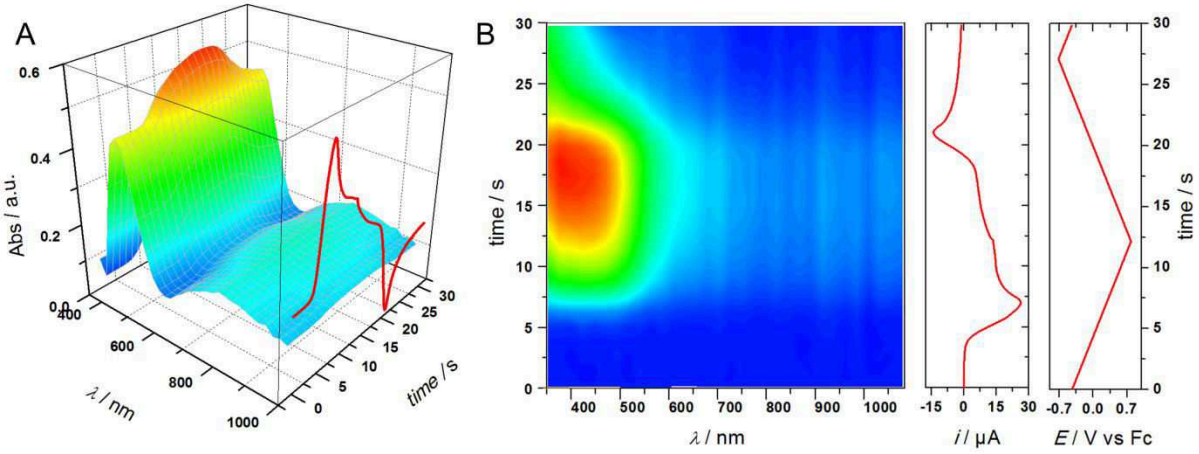

Figure IV.36. A) 3D UV-Vis spectroscopic monitoring of the electrochemical oxidation of complex **6** in DMF/NBu_4ClO_4 at T = 213 K under thin-layer conditions (200 µm). The red curve represents the current intensity (i) response (vs time) upon variation of potential; B) 2D differential (vs initial spectrum) spectroscopic response of complex **6** upon electrochemical oxidation. The red curves on the right panels represents the variation of the current intensity (i) and potential (E) with time.

III.5. Chemical oxidation of complex 6

Chemical oxidation (instead of electrochemical) of **6** was also implemented in order to better characterize the mono-oxidized species. First attempts in DMF were unsuccessful because of the very low stability of many chemical oxidants in this solvent. We then switched our investigation to acetonitrile despite the low solubility of the complex **6** at room temperature (0.5 mM). The chemical oxidation was carried out using ferroceniumcarboxaldehyde ($FcCHO^{+}$) (E^0 = 0.29 V vs Fc)[50] which was generated by exhaustive electrolysis of a solution of ferrocenecarboxaldehyde (FcCHO) in CH_3CN/NBu_4PF_6. Figure IV.37-A shows the CVs and RDEVs of FcCHO before and after 1h electrolysis. The conversion of FcCHO into $FcCHO^{+}$ was almost total after 1h. The generated ferrocenium compound remained stable in this solvent in absence of water traces. The UV-Vis-spectra of both neutral and oxidized species are shown in Figure IV.37-B. The initial band at λ_{max} =

458 nm (ε = 570 M^{-1} cm^{-1}) disappeared in favour of a new band at λ_{max} = 630 nm (ε = 285 M^{-1} cm^{-1}) typical of a $FcCHO^+$ species.[50]

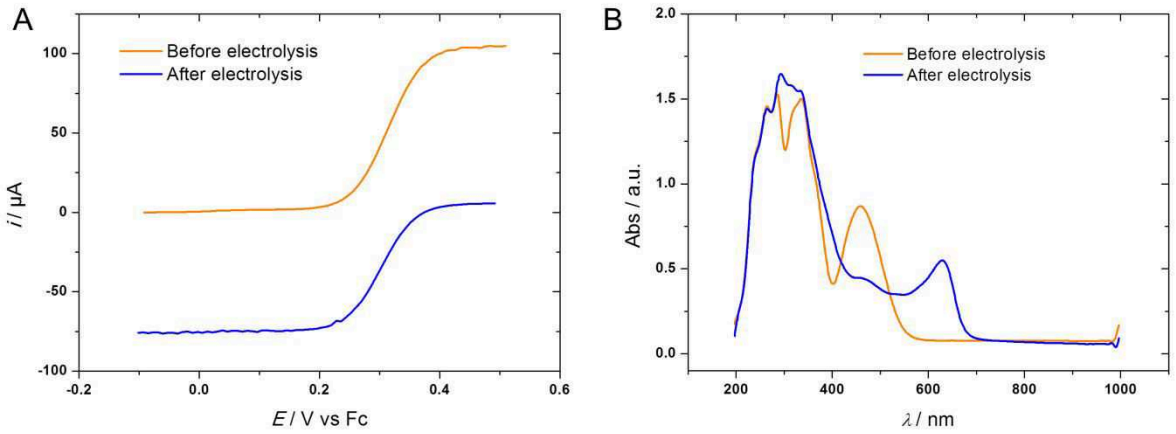

Figure IV.37. A) RDEVs (ω = 1500 RPM) and UV-Vis spectra (optical path: 10 mm) of FcCHO (0.5 mM) before (orange) and after (blue) room-temperature electrolysis at 0.6 V in CH_3CN/NBu_4PF_6 0.1 M.

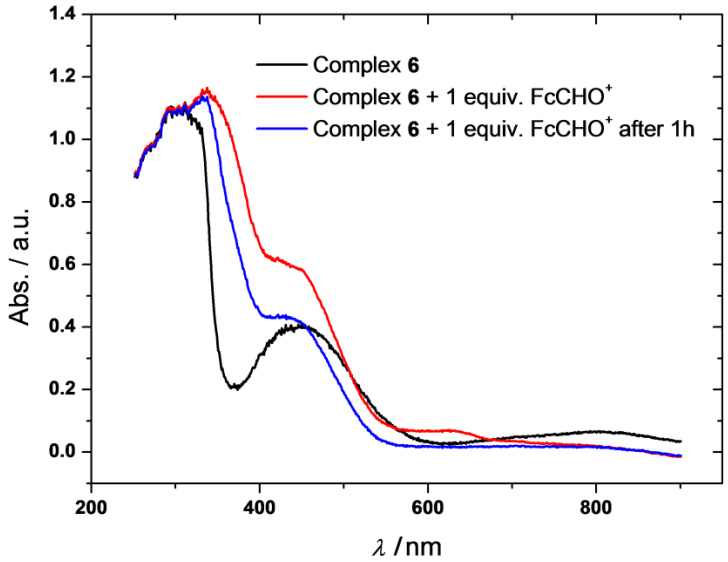

Figure IV.38. Low-temperature (233 K) UV-Vis spectra of complex **6** (*C* = 0.5 mM, optical path 10 mm) in CH_3CN/NBu_4PF_6 0.1 M before (black) and after (red) addition of 1 equiv. of $FcCHO^+$. The blue curve is the spectrum taken after 1h.

The reaction of complex **6** with $FcCHO^+$ at low temperature (233 K) was monitored by UV-Vis spectroscopy. The initial spectrum of **6** displayed an absorption band at λ_{max} = 448 nm (ε = 780 mol^{-1} cm^{-1}) (Figure IV.38, black curve). After addition of one equivalent of oxidant, we observed an increase of the absorbance in the 350-500 nm wavelength range band. A new intense band was detected at λ_{max} = 335 nm (Figure IV.38, red curve) which may be partly ascribed to an electronic

transition for the resulting FcCHO compound. Moreover, the detection of a small band at 630 nm attested for the presence of $FcCHO^+$ in solution, probably in small excess. The increase of the absorbance around 400 nm strongly resembles to what was obtained by cryo-spectroelectrochemical methods, even if the analysis of the spectra is more difficult here due to the presence of supplementary chromophoric species in solution (FcCHO and $FcCHO^+$). Interestingly, after 1h at low temperature, the signal decreased (Figure IV.38, blue curve), hence showing the relatively instability of the oxidized species produced. EPR measurements at 130 K were also performed from samples of the solution, before and after addition of the chemical reagent. No signal could be detected at this temperature.

III.6. Conclusions on the studies of complex 6

The dinuclear complex **6** was synthesized mainly in order to investigate the effect of the bis-amide core as well as the unsymmetrical topology of the ligand on the redox properties. The synthesis has led to the formation of a dicopper complex bearing a μ-phenoxo, μ-hydroxo bridge as shown by X-ray diffraction analysis. Notably, the complex showed a reversible monoelectronic oxidation at 0.12 V vs Fc at low temperature in DMF, and a reversible monoelectronic reduction at -1.27 V. This low value of the oxidation potential contrasts by - 600 mV to that obtained for its bis-DPA μ-phenoxo, μ-hydroxo analogue (**1a,** $E_{1/2}$ = 0.71 V vs Fc in MeCN), hence showing the effect of the strongly donating bis-amide core. This result suggests that the oxidation occurs on the metallic core rather than on the phenoxo moiety (Figure IV.39). Electrolysis of the solution allowed the characterization by EPR (10 K) of a copper(II) species, which could be ascribed to a dicopper(III,II) complex $\mathbf{6^+}$ with a localized charge on one copper ion (probably the copper environed by the DPA unit). Cryo-spectroelectrochemical analysis showed that the oxidation of **6** led to the formation of a new species $\mathbf{6^+}$ which displayed a maximum of absorbance at λ_{max} = 386 nm. This absorption band may be ascribed to a LMCT, according to our previous results with analogous complexes. Unfortunately, DFT calculations have not yet been performed to confirm this result. At last, the trends obtained by cryo-spectroelectrochemistry were reproduced in acetonitrile using a chemical oxidant.

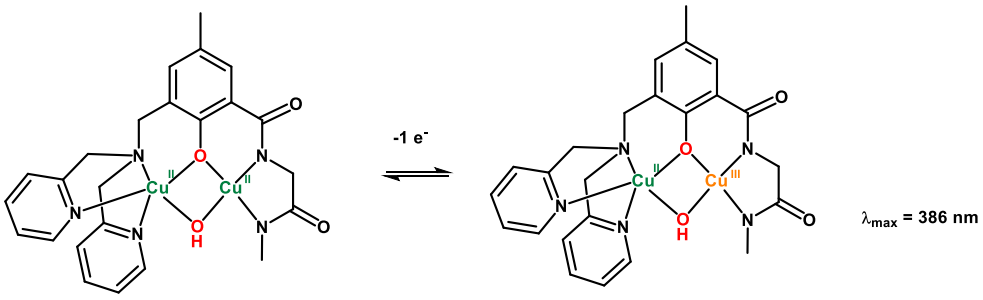

Figure IV.39. Proposed structure for the mono-electronic oxidation of complex **6**.

IV. Concluding remarks on complexes 5 and 6

The main goal of these studies was to investigate the effect of introducing one or two bis-amide units on a binucleating scaffold bridged by a phenoxo or an alkoxo moiety. Two different dicopper complexes have been synthesized. On one hand, complex **5** displayed two bis-amide cores separated by a μ-alkoxo bridge, with a μ-acetato unit being incorporated between the two copper ions, as shown by X-ray diffraction. On the second hand, complex **6** exhibited an unsymmetrical topology, with one bis-amide arm on one side of a phenoxo bridge, and one DPA unit on the other side, in complement to a μ-OH bridging core linking the two metals.

Voltammetric analysis in DMF of these two neutral complexes suggested that the monoelectronic oxidation occurs on the Cu^{II} ion environed by the bis-amide core. The redox potential was significantly different depending on the phenoxo or alkoxo bridge (E_{pa} = 0.63 V vs Fc and $E_{1/2}$ = 0.12 V for **5** and **6**, respectively). In both cases, the oxidation process was followed by a chemical reaction at room temperature (unbinding of the acetate from copper in **5**). For the complex **6**, it was possible to stabilize the oxidized species for several minutes.

Spectroelectrochemical analysis, supported by DFT calculations for **5**, suggested that a mixed-valent $Cu_2^{III,II}$ species was formed upon oxidation. For complex **5**, the release of the bridging acetate after oxidation is very fast (even at low temperature), and the detected species which absorbs at 463 nm may have either the acetate, either monodentate or uncoordinated. For complex **6**, since reversibility could be obtained at 213 K, the mixed-valent species $\mathbf{6}^{+}$ is likely similar to **6**, with one of the copper ions oxidized into Cu^{III}, logically that bearing the bis-amide unit. According to spectroelectrochemistry, this mixed-valent species has a maximum absorption at 386 nm. Interestingly for **5**, substitution of the acetate ligand by a methoxide anion led to the formation of a dicopper copper with a monodentate methoxo group and a DMF ligand, from DFT calculations. This new complex was mono-oxidized irreversibly at 0.40 V vs Fc, *i.e.* at a lower potential value than **5**.

In conclusion, the introduction of the bis-amide ligand was shown to be effective to have access to a mixed-valent dicopper (III,II) species at relatively low potential value. Nevertheless, these preliminary studies have shown the importance of the bridging functions on the redox properties, either between the two arms (phenoxo/alkoxo) or between the copper ions upon crystallization (hydroxo, acetate, methoxo). Also, unsymmetrical design of the ligand seems to favor the stabilization of such mixed-valent species. Future work will thus aim at developing bis-amide dinuclear systems in order to understand how these species evolve when there are mono-oxidized.

BIBLIOGRAPHY

[1] F. P. Bossu, K. L. Chellappa, D. W. Margerum, *J. Am. Chem. Soc.* **1977**, *99*, 2195-2203.
[2] F. C. Anson, T. J. Collins, T. G. Richmond, B. D. Santarsiero, J. E. Toth, B. G. R. T. Treco, *J. Am. Chem. Soc.* **1987**, *109*, 2974-2979.
[3] M. Koikawa, H. Okawa, N. Matsumoto, M. Gotoh, S. Kida, T. Kohzuma, *J. Chem. Soc., Dalton Trans.* **1989**, 2089-2094.
[4] M. Koikawa, H. Yamashita, T. Tokii, *Inorg. Chem. Commun.* **2003**, *6*, 157-161.
[5] J. Hanss, A. Beckmann, H.-J. Krüger, *Eur. J. Inorg. Chem.* **1999**, *1999*, 163-172.
[6] P. J. Donoghue, J. Tehranchi, C. J. Cramer, R. Sarangi, E. I. Solomon, W. B. Tolman, *J. Am. Chem. Soc.* **2011**, *133*, 17602-17605.
[7] D. Dhar, W. B. Tolman, *J. Am. Chem. Soc.* **2015**, *137*, 1322-1329.
[8] D. Bansal, R. Gupta, *Dalton Trans.* **2017**, *46*, 4617-4627.
[9] E. I. Solomon, D. E. Heppner, E. M. Johnston, J. W. Ginsbach, J. Cirera, M. Qayyum, M. T. Kieber-Emmons, C. H. Kjaergaard, R. G. Hadt, L. Tian, *Chem. Rev.* **2014**, *114*, 3659-3853.
[10] C. E. Elwell, N. L. Gagnon, B. D. Neisen, D. Dhar, A. D. Spaeth, G. M. Yee, W. B. Tolman, *Chem. Rev.* **2017**, *117*, 2059-2107.
[11] M. R. McDonald, F. C. Fredericks, D. W. Margerum, *Inorg. Chem.* **1997**, *36*, 3119-3124.
[12] A. Casitas, X. Ribas, *Chem. Sci.* **2013**, *4*, 2301-2318.
[13] P. Kumar, R. Gupta, *Dalton Trans.* **2016**, *45*, 18769-18783.
[14] A. I. Buvailo, E. Gumienna-Kontecka, S. V. Pavlova, I. O. Fritsky, M. Haukka, *Dalton Trans.* **2010**, *39*, 6266-6275.
[15] K. P. Neupane, A. R. Aldous, J. A. Kritzer, *Inorg. Chem.* **2013**, *52*, 2729-2735.
[16] S. Kumar, M. Munjal, J. Singh, R. Gupta, *Eur. J. Inorg. Chem.* **2014**, *2014*, 4957-4965.
[17] S. L. Jain, P. Bhattacharyya, H. L. Milton, A. M. Z. Slawin, J. A. Crayston, J. D. Woollins, *Dalton Trans.* **2004**, 862-871.
[18] W. Keown, J. B. Gary, T. D. P. Stack, *J. Biol. Inorg. Chem.* **2017**, *22*, 289-305.
[19] S. Louhibi, A. Y. Nour, L. Vendier, J.-P. Costes, J.-P. Tuchagues, *Polyhedron* **2007**, *26*, 3448-3454.
[20] P. Kumar, R. Gupta, *Dalton Trans.* **2016**, *45*, 18769-18783.
[21] D. Bansal, R. Gupta, *Dalton Trans.* **2017**, *46*, 4617-4627.
[22] M. R. Halvagar, P. V. Solntsev, H. Lim, B. Hedman, K. O. Hodgson, E. I. Solomon, C. J. Cramer, W. B. Tolman, *J. Am. Chem. Soc.* **2014**, *136*, 7269-7272.
[23] T. Gajda, A. Jancso, S. Mikkola, H. Lonnberg, H. Sirges, *J. Chem. Soc., Dalton Trans.* **2002**, 1757-1763.
[24] R. Murugavel, R. Pothiraja, N. Gogoi, R. Clerac, L. Lecren, R. J. Butcher, M. Nethaji, *Dalton Trans.* **2007**, 2405-2410.
[25] S. Striegler, N. A. Dunaway, M. G. Gichinga, L. K. Milton, *Tetrahedron* **2010**, *66*, 7927-7932.
[26] K. Selmeczi, M. Giorgi, G. Speier, E. Farkas, M. Réglier, *Eur. J. Inorg. Chem.* **2006**, *2006*, 1022-1031.
[27] S. Striegler, N. A. Dunaway, M. G. Gichinga, J. D. Barnett, A.-G. D. Nelson, *Inorg. Chem.* **2010**, *49*, 2639-2648.
[28] A. Patra, S. Haldar, G. Vijay Kumar, L. Carrella, A. K. Ghosh, M. Bera, *Inorg. Chim. Acta* **2015**, *436*, 195-204.
[29] H. W. L. Fraser, G. S. Nichol, G. Velmurugan, G. Rajaraman, E. K. Brechin, *Dalton Trans.* **2017**, *46*, 7159-7168.
[30] M. N. Akhtar, M. A. AlDamen, Y.-C. Chen, M. Sadakiyo, J. Khan, M.-L. Tong, *Inorg. Chem. Commun.* **2017**, *83*, 49-51.
[31] M. S. Ziegler, K. V. Lakshmi, T. D. Tilley, *J. Am. Chem. Soc.* **2017**, *139*, 5378-5386.
[32] B.-S. Liao, Y.-H. Liu, S.-M. Peng, S.-T. Liu, *Dalton Trans.* **2012**, *41*, 1158-1164.
[33] K.-S. Burger, P. Chaudhuri, K. Wieghardt, *J. Chem. Soc., Dalton Trans.* **1996**, 247-248.
[34] H. Nie, S. M. J. Aubin, M. S. Mashuta, R. A. Porter, J. F. Richardson, D. N. Hendrickson, R. M. Buchanan, *Inorg. Chem.* **1996**, *35*, 3325-3334.

[35] K. Takashi, Y. Michinari, O. Shigeru, N. Yuzo, N. Megumi, T. Tadashi, K. Michinobu, S. O. W., *Bull*. *Chem*. *Soc*. *Jap*. **1992**, *65*, 2739-2747.
[36] S. Meenakumari, S. K. Tiwari, A. R. Chakravarty, *J*. *Chem*. *Soc*., *Dalton Trans*. **1993**, 2175-2181.
[37] C. J. Boxwell, R. Bhalla, L. Cronin, S. S. Turner, P. H. Walton, *J*. *Chem*. *Soc*., *Dalton Trans*. **1998**, 2449-2450.
[38] M. Elie, M. D. Weber, F. Di Meo, F. Sguerra, J. F. Lohier, R. B. Pansu, J. L. Renaud, M. Hamel, M. Linares, R. D. Costa, S. Gaillard, *Chem*. *Eur*. *J*. **2017**.
[39] D. Y. Shopov, L. S. Sharninghausen, S. B. Sinha, J. E. Borowski, B. Q. Mercado, G. W. Brudvig, R. H. Crabtree, *New J*. *Chem*. **2017**, *41*, 6709-6719.
[40] S. Striegler, M. G. Gichinga, *Chem*. *Commun*. **2008**, 5930-5932.
[41] M. G. Gichinga, S. Striegler, *Tetrahedron* **2009**, *65*, 4917-4922.
[42] S. Striegler, M. Dittel, *J*. *Am*. *Chem*. *Soc*. **2003**, *125*, 11518-11524.
[43] S. Striegler, *Macromolecules* **2003**, *36*, 1310-1317.
[44] W. Mazurek, B. J. Kennedy, K. S. Murray, M. J. O'Connor, J. R. Rodgers, M. R. Snow, A. G. Wedd, P. Zwack, *Inorg*. *Chem*. **1985**, *24*, 3258-3264.
[45] Y. Nishida, S. Kida, *Inorg*. *Chem*. **1988**, *27*, 447-452.
[46] G. Christou, S. P. Perlepes, E. Libby, K. Folting, J. C. Huffman, R. J. Webb, D. N. Hendrickson, *Inorg*. *Chem*. **1990**, *29*, 3657-3666.
[47] A. W. Addison, T. N. Rao, J. Reedijk, J. van Rijn, G. C. Verschoor, *J*. *Chem*. *Soc*., *Dalton Trans*. **1984**, 1349-1356.
[48] J.-M. Savéant, *Elements of Molecular and Biomolecular Electrochemistry: An Electrochemical Approach to Electron Transfer Chemistry*, Wiley ed., **2006**.
[49] A. J. Bard, L. R. Faulkner, *Electrochemical Methods: Fundamentals and Applications, 2nd Edition*, Wiley ed., **2001**.
[50] C. Orain, P. Le Poul, Y. Le Mest, N. Le Poul, *J*. *Electroanal*. *Chem*. **2013**, *710*, 48-58.

Conclusion

CONCLUSION

The objective of this PhD project was to develop and to characterize mono- or bis(μ-OH) dicopper complexes in order to mimic the functionality of the pMMO upon monoelectronic oxidation. In particular, the work has focused on the design of dinucleating ligands which could promote the formation of a mixed-valent bis(μ-oxo), (μ-OH, μ-O) or bis(μ-OH) $Cu_2^{III,II}$ species, which have been suggested to be key intermediates for the oxidation of methane in pMMO. Hence, several ligands have been synthesized by varying either the bridging unit (phenoxo, alkoxo, naphthyridine), or the surrounding coordinating arms (polypyridyl, bis-amide). The effect of the switch of the μ-hydroxo ligand by μ-acetato and μ-methoxo units has also been investigated. For these studies, particular emphasis has been placed on the development of cryo-electrochemical and cryo-spectroelectrochemical techniques since the targeted species were very unstable at room temperature. At the beginning of this work, there was no cryo-equipment readily available in the laboratory.

We have started our studies with a series of μ-hydroxo dicopper complexes bearing a phenoxo bridge and DPA coordinating cores (complexes **1**-**3**). Slight modifications of the structure of the complex were shown to impact significantly the oxidation properties. Hence, increasing the spacer length between the bridge and the arms induced a positive shift of the oxidation potential. For symmetrical complexes **1a-c**, mono-electronic oxidation led to the formation of a phenoxyl radical, as shown by spectroelectrochemistry. Interestingly, a transient mixed valence $Cu_2^{III,II}$ species was detected for complexes **3a** and **2a** upon electrochemical oxidation (Figure V.1). For **3a**, the oxidized species displayed an absorption band at λ_{max} = 518 nm. DFT calculations assigned this band to the charge transfer essentially between the phenolate ligand and the Cu^{III} ion. Electrocatalytic studies were carried with **1b** in order to investigate the reactivity of the phenoxyl radical towards hydrogenated substrates. The complex displayed electrocatalytic properties for the oxidation of an aliphatic primary amine, but no activity for benzyl alcohol. Detailed analysis suggested an outer-sphere mechanism (no substrate coordination to the catalyst).

From these results, a new bis(μ-OH) dicopper complex, **4**, bearing two DPA coordinating cores and a non-electroactive naphthyridine bridging ligand was synthesized and characterized at solid state and in solution. The X-ray study of crystals of the complex emphasized a short Cu-Cu distance (2.75 Å), close to that suggested for the active site in pMMO (2.6 Å). Electrochemical studies showed that the mono-electronic oxidation of the complex occurs at a relatively high potential value (1.26 V vs Fc). The oxidized species evolves slowly (seconds) towards a new species. A mixed-valent bis(μ-OH) dicopper(III,II) was characterized by using time-resolved UV-Vis-NIR spectroelectrochemistry at room and low temperatures (Figure V.1). Upon oxidation, an absorption band was detected at λ_{max} = 424 nm. According to TD-DFT calculations, this transition corresponds to a ligand-to-metal charge transfer between pyridine rings and Cu^{III} ion. In the NIR region, a band at λ_{max} = 1344 nm was also

observed, suggesting a weak delocalization of the charge density. Hence, the incorporation of a naphthyridine bridging unit instead a phenoxo one allowed a monoelectronic oxidation on one of the copper(II) ion and not on the bridging unit. Unfortunately, the oxidation potential (E^0 = 1.26 V vs Fc) of the complex **4** is too high to envisage its application in electrocatalysis. This is due to the poor donor properties of the polypyridyl arms environing the copper ions.

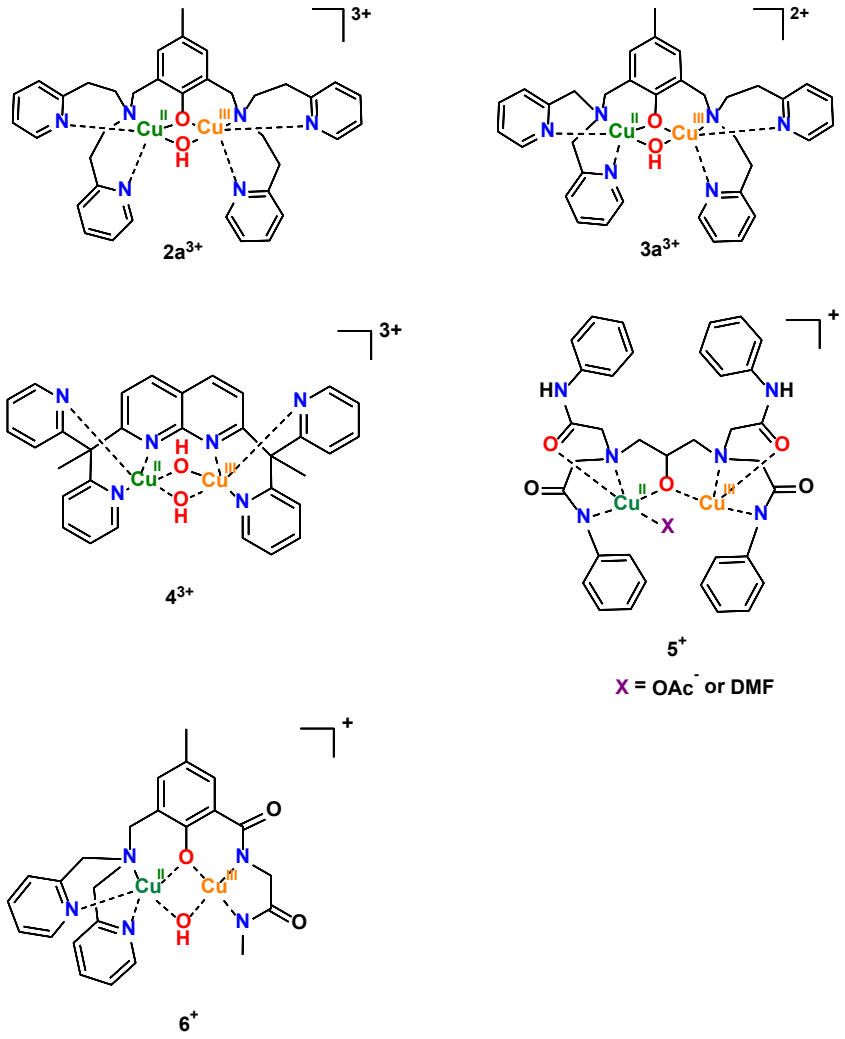

Figure V.1. Mixed-valent $Cu_2^{III,II}$ complexes characterized in this work.

At last, new chelating ligands were developed to decrease the redox potential. The new models were designed with amidate coordinating cores combined an alkoxo (complex **5**) or phenoxo (complex **6**) bridge. Amidate groups were chosen because of their good σ-donating character. On one hand, the symmetrical alkoxo-based complex **5** was obtained with a μ-acetato, μ-hydroxo units bridging the Cu^{II} ions. The X-ray structures have shown the butterfly character of the complex due to the high flexibility of the system through its open and close forms. Electrochemical investigations evidenced the irreversible monoelectronic oxidation of **5** at 0.63 V vs Fc, with probable unbinding of the bridging acetate (Figure V.1). The mono-oxidized species, generated by spectroelectrochemistry, displayed an

absorption band at λ_{max} = 463 nm. Exchange of bridging ligand, methoxo against acetato, was detected by cyclic voltammetry. The newly formed complex exhibited an oxidation potential at 0.40 V (1 electron process). On the other hand, the unsymmetrical complex **6** bearing one bis-amide group, a phenoxo bridge and a DPA core showed probably the most interesting properties in redox terms. This ligand design allowed the stabilization of a mixed-valent $Cu_2^{III,II}$ species at low potential (E^0 = 0.12 V vs Fc) (Figure V.1). Chemical reversibility of the oxidation process was detected at low temperature by cyclic voltammetry. The number of electrons involved in the oxidation was determined by electrochemical procedures. Cryo-spectroelectrochemical investigations on the mixed-valent species yielded an absorption band at λ_{max} = 378 nm. This may be ascribed to a LMCT from phenoxo to copper.

Table 1. Oxidation potential of studied complexes **1-6** and spectroscopic data of the transient mixed-valent $Cu_2^{III,II}$ complexes.

Complex	Solvent	E^0 /V vs Fc (ΔE_p /mV)	λ_{max} (nm) $Cu_2^{III,II}$
1a	CH_3CN	0.71 (170)	b
1b	CH_3CN	0.51 (70)	b
1c	CH_3CN	1.20[a]	b
2a	CH_3CN	1.04[a]	532
3a	CH_3CN	0.90[a]	520
4	CH_3CN	1.26 (190)	424
5	DMF	0.63[a]	463
6	DMF	0.124 (75)	386

[a]Irreversible peak potential value. b Not determined

The oxidation potential values of the initial complexes and UV-Vis features of the five different mixed-valent (III,II) dicopper species characterized in these studies are given in Table 1. The complex **5** displays the lowest oxidation potential as a result of the incorporation of one bis-amide group to the ligand scaffold. Probably, the stabilization of the mixed-valent species may be helped by the unsymmetrical design of the ligand.

In conclusion, this work has demonstrated the possible preparation and characterization of mixed-valent Cu^{III}-$(\mu\text{-}OH)_n$-Cu^{II} species. These systems remain the only ones described so far since the (μ-OH) complex described by Tolman and co-workers in 2014.[1] The identification of the unstable intermediates was possible thanks to the time-resolved cryo-spectroelectrochemical set up, developed in our laboratory during the last few years.

From these preliminary studies, several perspectives can be envisaged. The first one concerns the catalytic studies which can be carried out with these mixed-valent complexes for H-atom

abstraction (HAT) on classical substrates, such as dihydroanthracene, cyclohexane, toluene… In particular, it would be of interest to correlate the bond-dissociation enthalpy (BDE) for HAT to the redox and pKa properties of the dicopper complexes. Another point of interest would be the design of new ligands which could allow stabilization and (solid-state) characterization of a mixed-valent species at room temperature. The studies on complex **6** have shown that it was close to that point, and this complex could probably be a starting system. At last, the cryo-spectroelectochemical method could be used to detect other reactive species. For instance, Cu^{III}-OH has been suggested as being a key intermediate in the supposed catalytic mechanism of LPMO (lytic polysaccharide monooxygenases).[2],[3],[4],[5],[6],[7],[8],[9],[10],[11] Hence, Tolman and co-workers recently described the oxidizing power of a mononuclear Cu^{III}-OH complex vs substrates. They discovered that the $[CuOH]^{2+}$ moiety attacks the C-H bonds with BDE values > 80 kcal mol^{-1}, including THF (BDE = 92 Kcal mol^{-1}) and cyclohexane (BDE = 99 Kcal mol^{-1}), despite a relatively low redox potential (-0.08 V vs Fc).[12] From the results obtained in this doctoral work about the stabilization of Cu^{III} redox state, new oxidizable hydroxo-mononuclear copper(II) complexes could be synthesized in future. The time-resolved cryo-spectroelectrochemistry (UV-Vis and NIR) could enhance the detection of their intermediate species, and reactivity towards hydrogenated substrates could be investigated.

References

[1] M. R. Halvagar, P. V. Solntsev, H. Lim, B. Hedman, K. O. Hodgson, E. I. Solomon, C. J. Cramer, W. B. Tolman, *J. Am. Chem. Soc.* **2014**, *136*, 7269-7272.
[2] R. A. Himes, K. D. Karlin, *Curr. Op. Chem. Biol.* **2009**, *13*, 119-131.
[3] P. Chen, E. I. Solomon, *J. Am. Chem. Soc.* **2004**, *126*, 4991-5000.
[4] A. Decker, E. I. Solomon, *Curr. Op. Chem. Biol.* **2005**, *9*, 152-163.
[5] K. Yoshizawa, N. Kihara, T. Kamachi, Y. Shiota, *Inorg. Chem.* **2006**, *45*, 3034-3041.
[6] A. Crespo, M. A. Martí, A. E. Roitberg, L. M. Amzel, D. A. Estrin, *J. Am. Chem. Soc.* **2006**, *128*, 12817-12828.
[7] B. F. Gherman, D. E. Heppner, W. B. Tolman, C. J. Cramer, *J. Biol. Inorg. Chem.* **2006**, *11*, 197-205.
[8] S. M. Huber, M. Z. Ertem, F. Aquilante, L. Gagliardi, W. B. Tolman, C. J. Cramer, *Chem. Eur. J.* **2009**, *15*, 4886-4895.
[9] N. Dietl, C. van der Linde, M. Schlangen, M. K. Beyer, H. Schwarz, *Angew. Chem. Int. Ed. Eng.* **2011**, *50*, 4966-4969.
[10] S. Kim, J. Ståhlberg, M. Sandgren, R. S. Paton, G. T. Beckham, *Proc. Ntln. Acad. Sci. USA* **2014**, *111*, 149-154.
[11] A. Conde, L. Vilella, D. Balcells, M. M. Díaz-Requejo, A. Lledós, P. J. Pérez, *J. Am. Chem. Soc.* **2013**, *135*, 3887-3896.
[12] D. Dhar, W. B. Tolman, *J. Am. Chem. Soc.* **2015**, *137*, 1322-1329.

Appendix

General aspects of electrochemistry

Electrochemistry is defined as the branch of chemistry that examines the phenomena resulting from combined chemical and electrical effects. It is essentially based on the relationships between chemical changes and flows of electrons. The electrochemical technique expects adding or removing electrons in a controlled manner, which leads to the formation of new bonds or to the breakage of existing bonds. The effects of these electron addition/removal processes give information about the properties of the studied species. Electrochemical experiments are carried out in an electrochemical cell. Figure A.1 shows one example of a 3-electrodes electrochemical cell, including a working electrode (WE), a reference electrode (RE) and a counter electrode (CE). The working and counter electrode act as electron donors or acceptors at the interface with the electrolytic solution, according to a redox reaction: Ox + n e^- = Red involving n electrons. The potential of the working electrode is defined against that of the reference electrode.

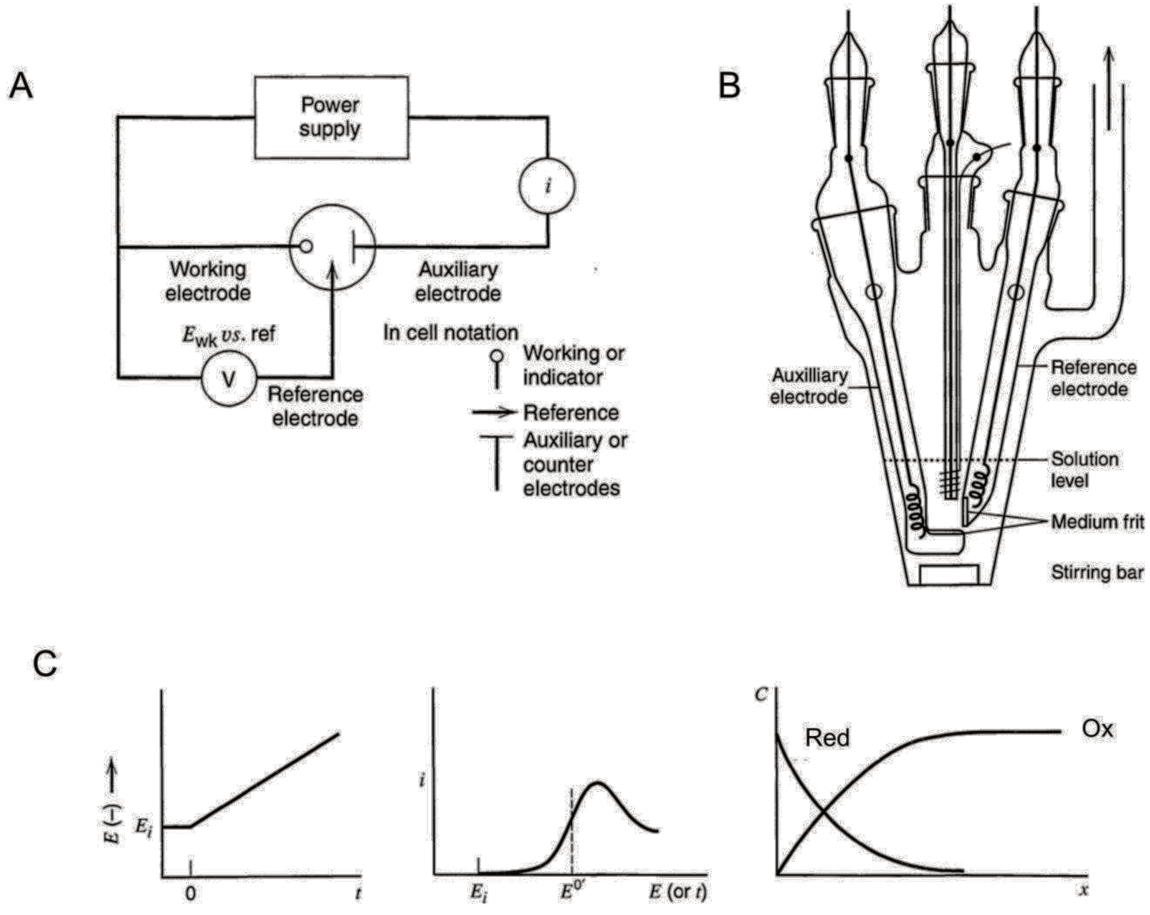

Figure A.1. Representation of a 3-electrodes electrochemical cell (A and B), and principle of linear sweep voltammetry (C).[1]

Probably the most used electrochemical technique is the linear sweep voltammetry which consists in a sweep of potential (*E*) at a defined and constant rate as shown in Figure A1. The variation of the WE electrode potential in respect to the RE leads to the production of current (*i*) when the potential at the WE reaches the standard potential of the electroactive species. When the variation of potential is performed according to a cycle, i.e. two different senses of scanning, the technique is named as cyclic voltammetry (CV). The resulting *i-E* curves (CVs), give information about the thermodynamics (redox potential) associated to the electroactive species in solution, as well as the kinetics of the electron transfer, the number of electrons involved, and the possible occurrence of associated chemical processes. Such information is generally obtained by variation of the scan rate (*v* in V/s). Figure A.2 depicts the different voltammetric responses obtained for a coupled electrochemical-chemical (EC) process upon modulation of *v*.

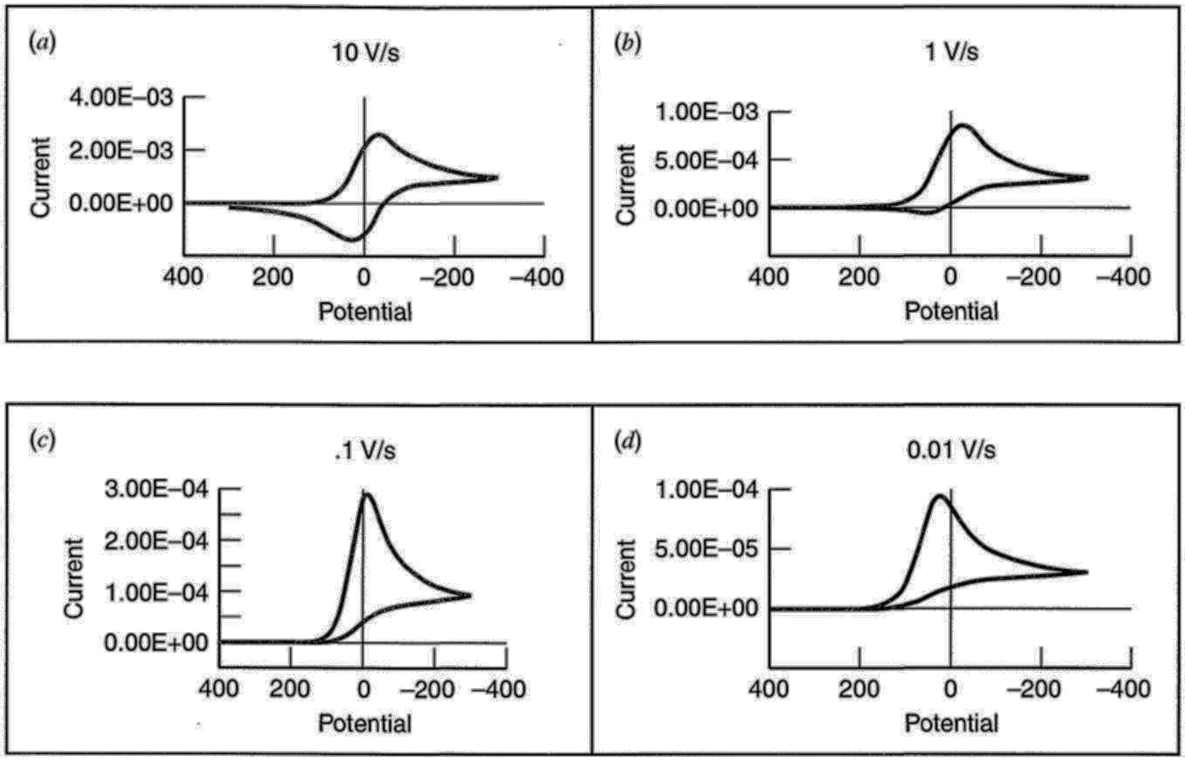

Figure A.2. Typical cyclic voltammetry profile for a EC process by variation of *v*.[1]

Electrochemical studies

Electrochemical studies of the copper complex have been performed in a glovebox (Jacomex) (O_2 < 1 ppm, H_2O < 1 ppm) with a home-designed 3-electrodes cell (WE: glassy carbon or platinum disk (3 mm diameter), carefully polished before each measurement with 1 µm alumina powder, sonicated in water bath and then washed with acetone; RE: Pt wire in a Fc^+/Fc solution, CE: Pt or graphite rod). Ferrocene was added at the end of the experiments to determine redox potential values.

The potential of the cell was controlled by an AUTOLAB PGSTAT 100 (Metrohm) potentiostat monitored by the NOVA software. Extra-dry solvents (DMF, THF, PC) were stored into the glovebox and used as received. CH_3CN and CH_2Cl_2 were distilled over CaH_2 and stored in the glovebox. The supporting salt NBu_4PF_6 was synthesized from NBu_4OH (Acros) and HPF_6 (Aldrich). It was then purified, dried under vacuum for 48 hours at 100° C, then kept under argon in the glovebox. NBu_4ClO_4 was purchased from Acros and used without purification. Electrolyses were carried out with a home-designed 3-electrodes cell (WE: Graphite rod, RE: Pt wire in a Fc^+/Fc solution, CE: graphite rod).

UV-Vis and NIR spectroscopy

UV-Vis and NIR spectroscopic measurements have been performed with Ocean Optics apparatus, including a deuterium-halogen light source (DH-2000-BAL, 230-2500 nm), and UV-Vis (QEPRO or MAYA models (200-1100 nm, minimum integration time: 8 ms), and NIR (NQ256-2.5 model, 900-2500 nm, minimum integration time: 1 ms) detectors. Transmission of the optical signal was operated by optic fibers (UV/SR-VIS and Vis/NIR). UV-Vis and NIR probes (Ocean Optics T300 model) were used for spectroelectrochemical experiments.

Theoretical calculations

a) Computational method

All calculations have been performed using the GAUSSIAN 09 package.[2] Different basis set functionals and solvent models have been used. Best results have been obtained at the IEFPCM/M11L level to compute redox potential and at IEFPCM/PBE0 level for geometry optimization with the def2-TZVDP for copper atoms and the 6-311+G(d,p) for other atoms. Vibrational frequency calculations were performed to ensure that each geometry optimization converged to a real minimum. Orbital population analysis was done using the pop=(biorthogonalize, save) keyword to transform the canonical α and β orbitals in orbitals which match up as much as possible α and β orbitals to determine without ambiguity the spin states of the system. Spin densities, orbitals were computed using the program cubegen of GAUSSIAN 09 package, and their representations were done using the software VMD.[3]

b) Calculation of redox potential by DFT

The absolute potential of a redox couple E_{calc}^{abs} is typically calculated using equation (A1) where the ΔG_{sol} is the Gibbs free energy in solution of the reaction, F is the faraday constant and n the number of moles of electrons of the reaction:

$$E_{calc}^{abs}(V) = -\frac{\Delta G_{sol}}{nF} \quad \text{(A1)}$$

For comparison with experimental data, the value of this potential has to be reported relatively to a reference couple (RC), such as for example the standard hydrogen electrode (SHE) in water, or ferrocenium/ferrocene (Fc^+/Fc) in organic solvents. Hence, the relative (*vs* RC) standard potential value (E_{calc}^{0}) is calculated according to equation (A2) by using the absolute redox potential of the reference ($E_{exp,RC}^{abs}$), which is experimentally determined:

$$E_{calc}^{0}(V\ vs\ RC) = E_{calc}^{abs}(V) - E_{exp,RC}^{abs}(V) \quad \text{(A2)}$$

Hence, theoretical relative standard potential values (E_{calc}^{0}) are fully dependent on the accuracy of $E_{exp,RC}^{abs}$. One major problem of this approach originates from the solvent and electrolyte dependency of $E_{exp,RC}^{abs}$, which can induce shifts up to one hundred of millivolts. One solution proposed by Batista *et al.*[4] to avoid this situation has been to substitute the $E_{exp,RC}^{abs}$ term in equation (A2) by a theoretical value of the absolute potential of the reference, $E_{calc,RC}^{abs}$, as shown in equation (A3):

$$E_{calc}^{0}(V\ vs\ RC) = E_{calc}^{abs}(V) - E_{calc,RC}^{abs}(V) \quad \text{(A3)}$$

Here, $E_{calc,RC}^{abs}$ is calculated at the same level than the redox couple used as reference

For the calculation of redox potentials, only high spin states of complexes were computed even if they are not ground states. This is justified since the energy difference between spin states is very small compared to that between two redox states.

EPR spectroscopy

EPR spectra were obtained from a Bruker Elexsys E500 spectrometer, at a perpendicular-mode X band (9.50 GHZ); simulations were performed using the Bruker Spin-Count software.

Cryogenic systems

Two different apparatus have been used for low-temperature measurements:

1) A liquid-nitrogen cryostat (Optistat DN-V, Oxford Instruments) 77-500K (± 0.1 K), controlled by a multi-channel-Mercury iTC temperature controller.
2) A Lauda Pro-line cryogenic system (T_{min} = 283 K)

UV-Vis-NIR cryo-spectroelectrochemistry

Spectroelectrochemistry (SEC) is a combined methodology that couples spectroscopic and electrochemical analysis, to get spectroscopic information about the *in situ* electrogenerated species.[5] Performing UV-Vis-NIR spectroelectrochemistry at low-temperature ("cryo-spectroelectrochemistry") has been rarely reported for experimental reasons (solubility, ohmic drop…).[6],[7],[8],[9],[10],[11],[12] Such technique is indeed interesting to obtain informative data about i) short-lived intermediate species that undergo rapid follow-up reaction (mixed valent species, radicals…), ii) reaction mechanisms occurring at the electrode surface and iii) thermodynamic and kinetic parameters relevant to the coupled chemical processes

Two main types of cryo-spectroelectrochemical cells have been reported in the literature. The system developed in 1991 by Hartl *et al*. is based on an OTTLE (optically transparent thin layer electrochemical) cell incorporated into a liquid nitrogen cryostat.[13],[14] Like a classical spectroelectrochemical OTTLE cell used at room temperature, the low-*T* one works in a transmission mode, i.e. the optical signal crosses a small portion of the solution and is analyzed on the other side of the cell. Another type of cryo-spectroelectrochemical cell has been developed by Levillain *et al.*.[7] In contrast to the OTTLE cell, their system relies on the reflection of the optical beam on the electrode surface (reflection-mode). The spectroelectrochemical PTFE cell is cooled by the flow of cold liquid inside a jacket. This set up allows analysis in thin layer (~2–200 μm) or semi-infinite conditions (>200 μm). Indeed, by moving the distance between the electrode and the probe, it is possible to follow the reactions of the species on the surface of the electrode with limited diffusion in solution.[7]

From this basis and with the aim at detecting unstable dicopper(II,III) complexes, we have designed two types of cryo-spectroelectrochemical cell working in a reflection mode. The first one is based on a Schlenk tube which can be introduced in a liquid-nitrogen cryostat. The choice of a Schlenk tube is motivated by the high sensitivity of solutions of Cu^{I} complexes towards dioxygen and water. These solutions can be prepared under inert atmosphere in the glovebox, transferred into the Schlenk tube, and taken out from the glovebox without risk of decomposition. The system, which is air-tight, is shown in Figure A.3.

As mentioned, the optical beam coming from the source crosses the solution from a probe (inside the Schlenk cell), and it is reflected on the surface of the working electrode to pass again thought the solution and finally to be detected by the UV-Vis or NIR spectrophotometer. The counter and reference electrodes are two Pt wires dipping into the solution. The principle of the cell is shown in Figure A.4.

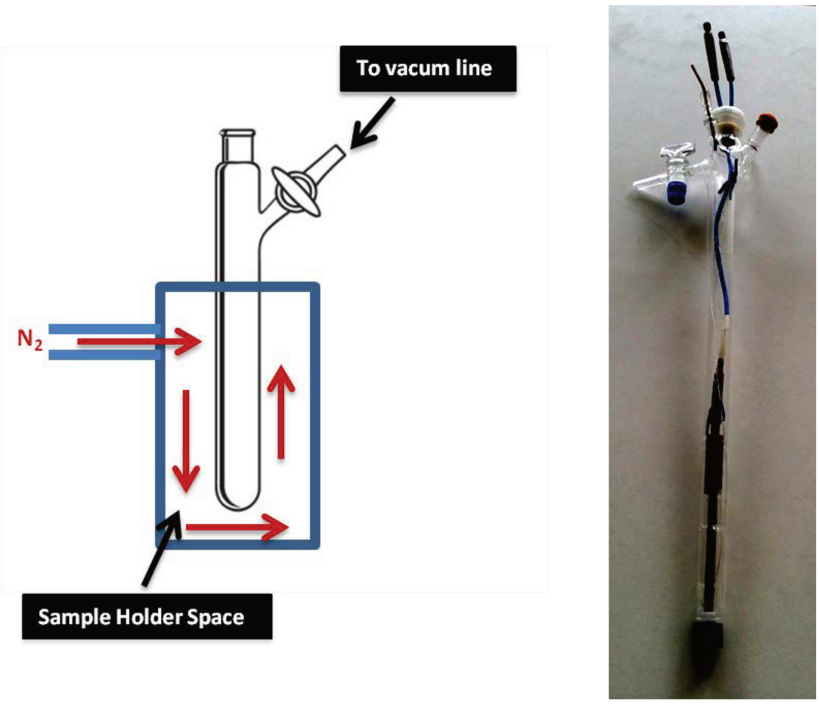

Figure A.3. Left: Schematic representation of cryo-spectroelectrochemical set up: cryostat and Schlenk tube. Right: picture of the Schlenk tube working as cryo-spectroelectrochemical cell.

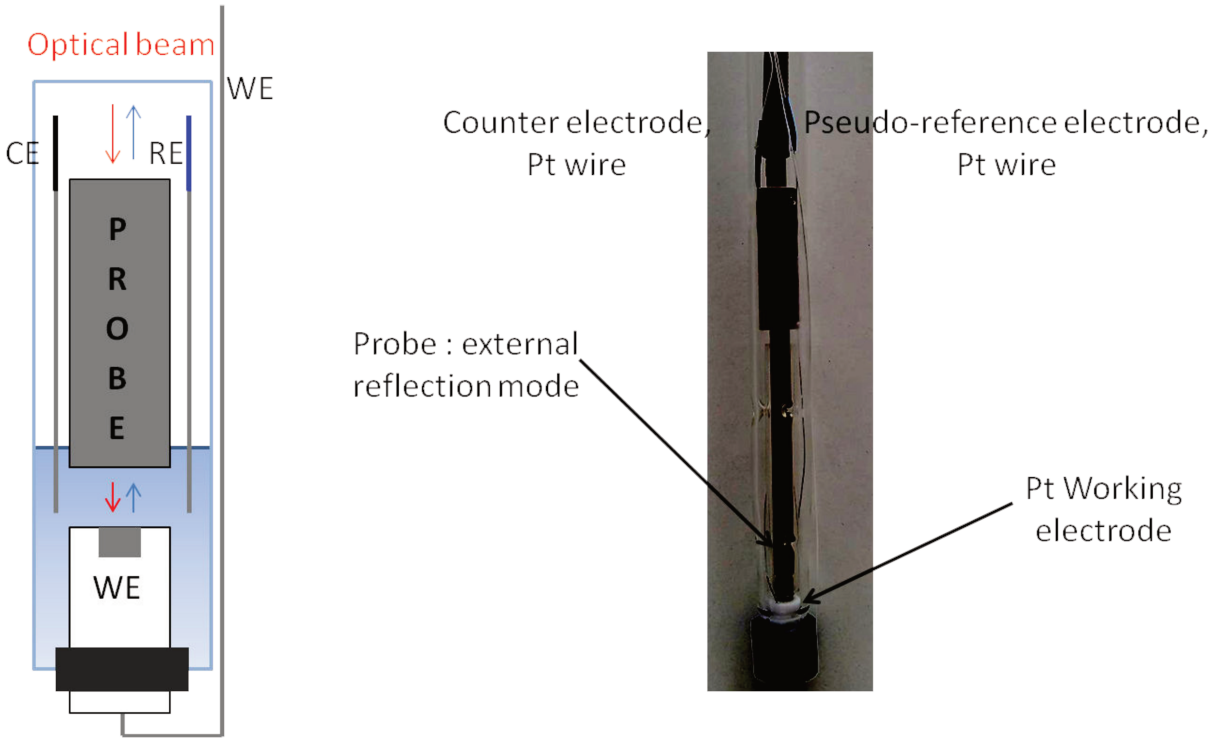

Figure A.4. Schematic representation and picture of the cryo-spectroelectrochemical cell.

A second cryo-spectroelectrochemical cell has been designed. It is based on the reflection-mode type of cell designed by Levillain *et al.*.[7] The difference is that our system is at work in the glovebox, then avoiding all problems of a moisture contamination and water condensation on the cell walls. The Figure A.5 shows the representation of two cells that can work at room and low temperature in and outside the glovebox. Thin layer and semi-infinite diffusion conditions can be reached in the same electrochemical cell and solution, moving the working electrode. The working electrode can be easily removed and replaced to be cleaned after each measurement. With these set up small volumes of solution (~ 200-500 µl) are used. Noteworthy, UV-Vis-NIR cryo-pectroelectrochemical measurements are time-resolved with the help of adapted detectors.

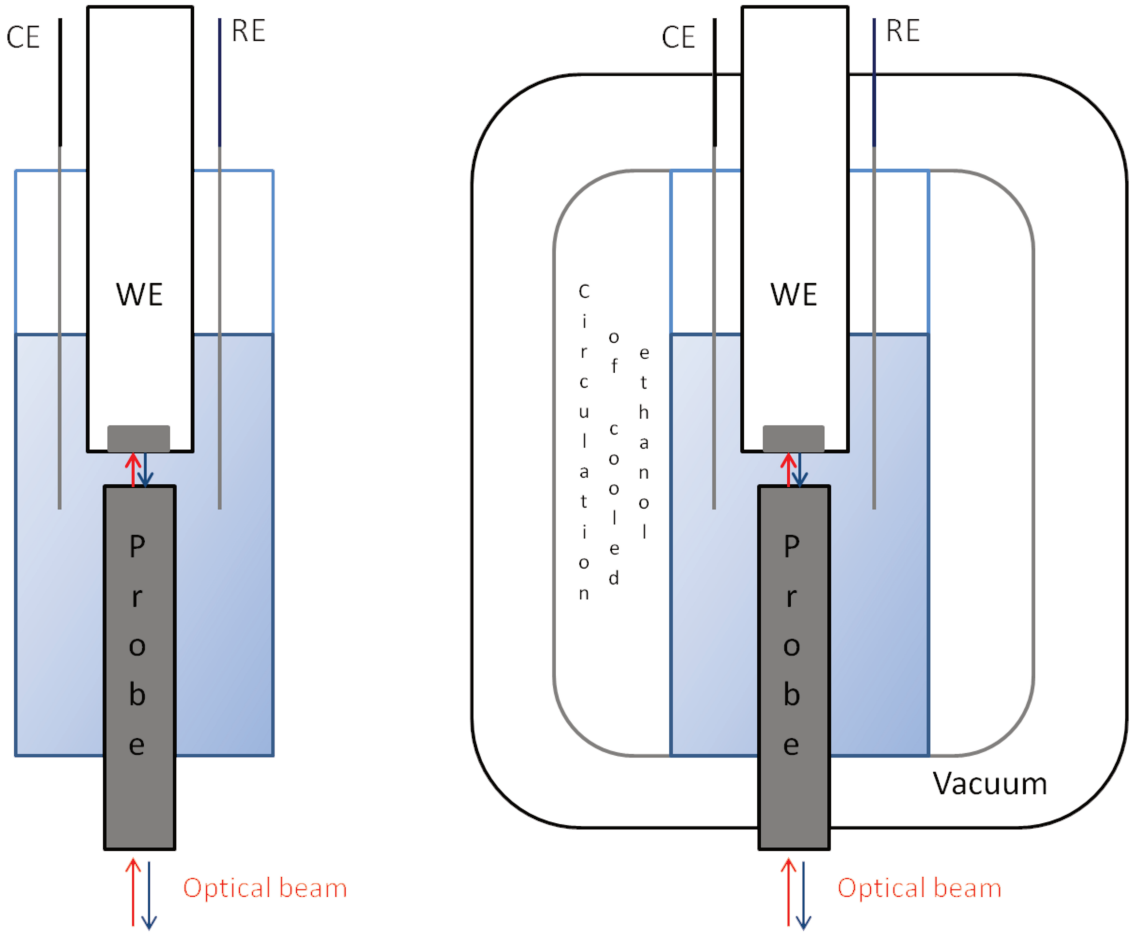

Figure A.5. Two set-ups of spectro-electrochemial cell are represented. Left: room temperature cell that can work in and outside glovebox. Right: low temperature cell used in the glovebox; the jacket surrounding the cell allows to reach the low temperature (~213K) due to a circulation of cooled alcohol by cryocooling system.

References

[1] A. J. Bard, L. R. Faulkner, *Electrochemical Methods: Fundamentals and Applications, 2nd Edition*, Wiley ed., **2001**.

[2] G. W. T. M. J. Frisch, H. B. Schlegel, G. E. Scuseria, M. A. Robb, J. R. Cheeseman, G. Scalmani, V. Barone, B. Mennucci, G. A. Petersson, H. Nakatsuji, M. Caricato, X. Li, H. P. Hratchian, A. F. Izmaylov, J. Bloino, G. Zheng, J. L. Sonnenberg, M. Hada, M. Ehara, K. Toyota, R. Fukuda, J. Hasegawa, M. Ishida, T. Nakajima, Y. Honda, O. Kitao, H. Nakai, T. Vreven, J. A. Montgomery, Jr., J. E. Peralta, F. Ogliaro, M. Bearpark, J. J. Heyd, E. Brothers, K. N. Kudin, V. N. Staroverov, R. Kobayashi, J. Normand, K. Raghavachari, A. Rendell, J. C. Burant, S. S. Iyengar, J. Tomasi, M. Cossi, N. Rega, J. M. Millam, M. Klene, J. E. Knox, J. B. Cross, V. Bakken, C. Adamo, J. Jaramillo, R. Gomperts, R. E. Stratmann, O. Yazyev, A. J. Austin, R. Cammi, C. Pomelli, J. W. Ochterski, R. L. Martin, K. Morokuma, V. G. Zakrzewski, G. A. Voth, P. Salvador, J. J. Dannenberg, S. Dapprich, A. D. Daniels, Ö. Farkas, J. B. Foresman, J. V. Ortiz, J. Cioslowski, D. J. Fox, *Gaussian 09 (Gaussian, Inc., Wallingford CT)*. **2009**.

[3] W. Humphrey, A. Dalke, K. Schulten, *J. Mol. Graph.* **1996**, *14*, 33-38.

[4] S. J. Konezny, M. D. Doherty, O. R. Luca, R. H. Crabtree, G. L. Soloveichik, V. S. Batista, *J. Phys. Chem. C* **2012**, *116*, 6349-6356.

[5] W. Kaim, J. Fiedler, *Chem. Soc. Rev.* **2009**, *38*, 3373-3382.

[6] R. P. Van Duyne, C. N. Reilley, *Anal. Chem.* **1972**, *44*, 142-152.

[7] F. Gaillard, E. Levillain, *J. Electroanal. Chem.* **1995**, *398*, 77-87.

[8] G. A. Heath, R. G. Raptis, *J. Am. Chem. Soc.* **1993**, *115*, 3768-3769.

[9] M. P. Cifuentes, M. G. Humphrey, G. A. Heath, *Inorg. Chim. Acta* **1997**, *259*, 273-280.

[10] S. Chardon-Noblat, P. D. Costa, A. Deronzier, T. Mahabiersing, F. Hartl, *Eur. J. Inorg. Chem.* **2002**, *2002*, 2850-2856.

[11] S. Santi, L. Orian, C. Durante, A. Bisello, F. Benetollo, L. Crociani, P. Ganis, A. Ceccon, *Chem. Eur. J.* **2007**, *13*, 1955-1968.

[12] A. Takahashi, T. Kurahashi, H. Fujii, *Inorg. Chem.* **2011**, *50*, 6922-6928.

[13] M. Krejčik, M. Daněk, F. Hartl, *J. Electroanal. Chem. Interfacial Electrochem.* **1991**, *317*, 179-187.

[14] F. Hartl, H. Luyten, H. A. Nieuwenhuis, G. C. Schoemaker, *Appl. Spectr. Rev.* **1994**, *48*, 1522-1528.

Published articles

Inorganic Chemistry

Article

pubs.acs.org/IC

Influence of Asymmetry on the Redox Properties of Phenoxo- and Hydroxo-Bridged Dicopper Complexes: Spectroelectrochemical and Theoretical Studies

Federica Gennarini,[†] Rolf David,[‡] Isidoro López,[†] Yves Le Mest,[†] Marius Réglier,[§] Catherine Belle,[‡] Aurore Thibon-Pourret,[‡,∥] Hélène Jamet,*[,‡] and Nicolas Le Poul*[,†]

[†]Université de Bretagne Occidentale, CNRS UMR 6521, Laboratoire CEMCA, 6 Avenue Le Gorgeu, CS 93837, 29238 Brest Cedex 3, France

[‡]Université Grenoble Alpes - Grenoble1, CNRS-UGA UMR 5250, Laboratoire DCM/Cire, CS 40700, 38058 Grenoble Cedex 9, France

[§]Université Aix Marseille, CNRS UMR 7313, Laboratoire de ISM2/BiosCiences, 52 avenue Escadrille Normandie-Niemen, 13397 Marseille Cedex 20, France

[∥]Institut de Chimie, CLAC, UMR 7177 CNRS, Université de Strasbourg, 67008 Strasbourg, France

Supporting Information

ABSTRACT: The redox properties and electronic structures of a series of phenoxo- and hydroxo-bridged dicopper(II) complexes have been explored. Complexes $(\mathbf{1a-c})^{2+}$ are based on symmetrical ligands with bis(2-methylpyridyl)aminomethyl as complexing arms bearing different substituting R groups (CH_3, OCH_3, or CF_3) in the *para* position of the phenol moiety. Complex $\mathbf{2a}^{2+}$ is based on a symmetrical ligand with bis(2-ethylpyridyl)aminomethyl arms and R = CH_3, while complex $\mathbf{3a}^{2+}$ involves an unsymmetrical ligand with two different complexing arms (namely bis(2-ethylpyridyl)aminomethyl and bis(2-methylpyridyl)aminomethyl). Investigations have been done by electrochemical and spectroelectrochemical means and correlated to theoretical calculations as this series of complexes offers a unique opportunity of an in-depth comparative analysis. The voltammetric studies have shown that the redox behavior of the dicopper complexes is not influenced by the nature of the solvent. However, the increase of the spacer chain length and the unsymmetrical design induce significant modifications of the voltammetric responses for both oxidation and reduction processes. DFT calculations of the redox potentials using a computational reference redox couple calculated at the same level of theory to reduce systematic errors confirm these results. Ligand contributions to the electronic structure of the different species have been analyzed in detail. The good agreement between experimental and theoretical results has validated the developed calculation method, which would be used in the following to design new dinuclear copper complexes. These studies demonstrate that subtle modification of the ligand topology can significantly affect the redox and spectroscopic properties. In particular, the unsymmetrical design allows the formation of a transient mixed-valent Cu(II)-Cu(III) phenoxo complex detected upon spectroelectrochemical experiments at room temperature, which evolves toward a dicopper (II,II) phenoxyl complex. The latter displays an intense $\pi \rightarrow \pi^*$ transition band at 393 nm in the UV−vis spectrum compared to the less intense ligand to metal charge transfer band at 518 nm observed for the mixed-valent Cu(II)-Cu(III) phenoxo complex.

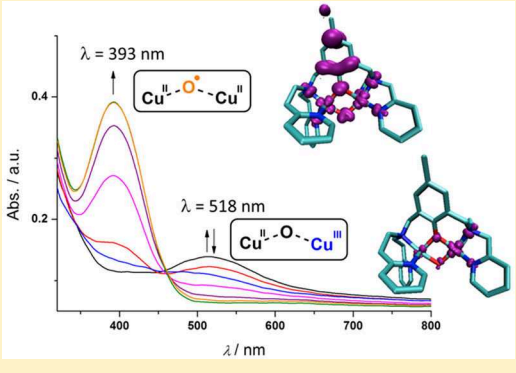

1. INTRODUCTION

Most of the dinuclear active sites of metalloproteins are characterized by unsymmetrical patterns, either in the proteic backbone or within the active sites.[1] Asymmetry is indeed essential for performing the specific functionalities (enzymatic reaction, electron transfer, substrate transport...), through cooperative processes between nonequivalent centers. For both heterobimetallic and homobimetallic systems, each metal ion displays a definite task related to its redox/coordination properties as well as its environment. This is particularly true in the field of copper oxygenases.[2] For example, type II copper enzymes such as PHM and DβH possess two copper sites with different first coordination spheres such that one Cu ion serves as electron reservoir, whereas the other performs the O_2 activation and the oxidation of the biosubstrate.[3,4] In a subtle manner, type III copper enzymes, such as tyrosinase (Tyr) and catechol oxidase (CO), are characterized by copper centers with similar first coordination environments (three histidines and one bridging hydroxide ion) but different secondary coordination

Received: February 7, 2017
Published: June 30, 2017

DOI: 10.1021/acs.inorgchem.7b00338
Inorg. Chem. 2017, 56, 7707−7719

Chart 1. Schematic Representation of the Studied Phenoxo Dicopper Complexes

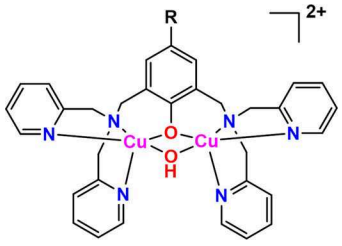

$[Cu_2(R\text{-}BPMP)(\mu\text{-}OH)]^{2+}$

R = CH_3 $\mathbf{1a}^{2+}$
R = OCH_3 $\mathbf{1b}^{2+}$
R = CF_3 $\mathbf{1c}^{2+}$

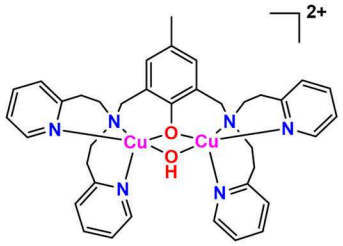

$[Cu_2(CH_3\text{-}BPEP)(\mu\text{-}OH)]^{2+}$

$\mathbf{2a}^{2+}$

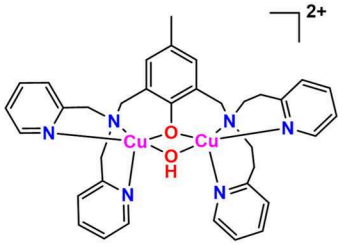

$[Cu_2(CH_3\text{-}BPMEP)(\mu\text{-}OH)]^{2+}$

$\mathbf{3a}^{2+}$

spheres.[2] A large number of model complexes described in the literature display a symmetrical binuclear copper site,[5−9] and the use of unsymmetrical dicopper model complexes in terms of structure and reactivity has been underexplored compared to the symmetrical ones. Nevertheless, some models of dinuclear copper oxidases have been designed with unsymmetrical cores.[10−27] For instance, Itoh et al. reported two different pentapyridine dicopper(I) complexes that both yield μ-η^1:η^1 peroxo dicopper complexes in the presence of dioxygen.[15,19] Interestingly, it was found that one of the peroxo complexes displays unusual both electrophilic and nucleophilic properties associated with the specific design of the ligand. In another example, an unsymmetrical ligand with different coordination cores separated by a phenyl (*m*-xylyl) linker was reported. The corresponding dicopper(I) species was reacted with dioxygen and yielded a symmetrical tetranuclear peroxo/oxo species.[23,26] For phenoxo-bridged dinuclear complexes, asymmetry was achieved either by playing with the linker length that separates the phenoxo bridge and the coordinating atoms[10] or by differentiating the coordinating cores around copper ions.[12−14,16,17,21,22] As compared to the parent symmetrical copper complexes, or with complexes involving other metallic centers,[28,29] several interesting effects were reported. For example, with dicopper compounds, a mixed-valent (I,II) dicopper complex could be obtained by shortening of the linker length on one side of the *m*-xylyl unit.[10,24] Such species was shown to be reactive toward dioxygen to yield a transient dinuclear complex that incorporates a superoxide radical anion.[24] Alternatively, an unsymmetrical dinucleating ligand, BPMEP[21] (BPMEP: bis(2-pyridylmethylethyl)amine), based on two different complexing arms was recently reported. In comparison to its symmetrical analogues (BPMP[30−32] and BPEP;[33] see Chart 1), the resulting phenoxo- and hydroxo-bridged dicopper (II,II) complex displayed a particular affinity for a tyrosinase inhibitor (2-hydroxypyridine-*N*-oxide, HOPNO) through an unsymmetrical binding. However, asymmetry was shown not to be critical for the catalytic oxidation of catechol derivatives.[21] So far, very few studies have focused on the redox properties of unsymmetrical dicopper complexes and the formation of mixed-valent species (II,I) or (II,III) starting from homovalent (I,I) or (II,II) complexes.[13,15,17,19,22] Noteworthy, there has been recently renewed interest for generating Cu_2:$(\mu\text{-}O)_2$ (II,III) mixed-valent complexes since such species is postulated to be one key intermediate for the oxidation of methane in the active site of particulate methane monooxygenases (pMMOs).[34] The strategy used so far is to generate such mixed-valent species from μ-hydroxo dicopper(II) complexes by chemical or electrochemical means, including possible deprotonation of the hydroxo bridge through proton-coupled electron transfer. To our knowledge, only symmetrical dinucleating ligands have been used for this purpose,[35−37] and no attempt was made to reach such an intermediate via the design of unsymmetrical ligands.

In this paper, we report electrochemical, spectroelectrochemical, and computational studies of symmetrical and unsymmetrical μ-hydroxo dinuclear complexes, which may lead to the formation of mixed-valent (II,III) dicopper species through oxidation. In that purpose, we have focused our investigations on symmetrical R-BPMP (R = CH_3, OCH_3, CF_3) ($\mathbf{1a}^{2+}$, $\mathbf{1b}^{2+}$, and $\mathbf{1c}^{2+}$), CH_3-BPEP ($\mathbf{2a}^{2+}$), and unsymmetrical CH_3-BPMEP ($\mathbf{3a}^{2+}$) dicopper complexes, which display both phenoxo and hydroxo bridging ligands as previously reported (Chart 1).[21,30−33] Previous studies have reported the synthesis for all complexes, X-ray structures in the solid state for $(\mathbf{1a-b})^{2+}$, $\mathbf{2a}^{2+}$, and $\mathbf{3a}^{2+}$, and the electrochemical properties of complexes $(\mathbf{1a-c})^{2+}$ in acetonitrile at room temperature.[30,31] Monoelectronic oxidation was detected at a redox potential value, which is R-dependent. Formation of a phenoxyl radical upon oxidation was evidenced by UV−vis spectroscopy at low temperature after exhaustive electrolysis of the solution containing the methoxy-substituted complex.[32] For complexes $\mathbf{2a}^{2+}$ and $\mathbf{3a}^{2+}$, no electrochemical data have been reported so far. On this basis, our purpose has been to investigate the possible formation of a transient mixed-valent (II,III) Cu_2:$(\mu\text{-}O)_2$ or its monoprotonated form, Cu_2:$(\mu\text{-}O)(\mu\text{-}O(H))$, species for this series of complexes through spectroelectrochemical means. In support of the electrochemical and spectroelectrochemical studies, we also present a calibration method for DFT calculations for the determination of theoretical redox potential values. A computational reference redox couple, calculated using identical conditions (e.g., same level of theory and solvent parameters), has been used in order to reduce systematic errors.[38] Noticeably, room-temperature spectroelectrochemical experiments clearly demonstrate that unsymmetrical design of the ligand induces the formation of a transient mixed-valence (II,III) species upon electrochemical oxidation.

2. EXPERIMENTAL SECTION

2.1. Synthesis. The syntheses and solid state characterizations of the dinuclear complexes were previously reported.[21,30−33]

DOI: 10.1021/acs.inorgchem.7b00338
Inorg. Chem. 2017, 56, 7707−7719

Table 1. Experimental Voltammetric Data [E^0/V vs Fc (ΔE_p/mV)] for Complexes $1a^{2+}$, $1b^{2+}$, $1c^{2+}$, $2a^{2+}$, and $3a^{2+}$ in Different Solvent/NBu_4PF_6 0.1 M (Solvent = MeCN, THF, PC)

	solvent	$1a^{2+}$	$1b^{2+}$	$1c^{2+}$	$2a^{2+}$	$3a^{2+}$
oxyd.	MeCN	0.71 (170)	0.51 (70)	1.20[a]	1.04[a]	0.90[a]
	THF	0.60 (280)	0.45 (90)	1.05[a]	1.01[a]	0.84[a]
	PC	0.67 (150)	0.49 (100)	1.22[a]	1.05[a]	0.93[a]
reduct. I	MeCN	−1.03 (110)	−1.02 (105)	−0.95 (90)	−1.09[a]	−0.91 (140)
	THF	−1.11 (130)	−1.09 (130)	−1.03 (100)	−1.08[a]	−1.04 (140)
	PC	−1.03 (105)	−1.03 (100)	−0.95 (100)	−1.11[a]	−0.96[a]
reduct. II	MeCN	−1.34[a]	−1.39[a]	−1.29[a]	[b]	−1.32[a]
	THF	−1.44 (130)	−1.41 (140)	−1.31 (140)	[b]	−1.41[a]
	PC	−1.38[a]	−1.38[a]	−1.27[a]	[b]	−1.36[a]

[a]Irreversible peak potential value. [b]No second reduction peak observed.

2.2. Cyclic Voltammetry, Spectroelectrochemistry. Room-temperature electrochemical studies of the copper complex were performed in a glovebox (Jacomex) (O_2 < 1 ppm, H_2O < 1 ppm) with a home-designed 3-electrode cell (WE: glassy carbon or platinum, RE: Pt wire in a Fc^+/Fc solution, CE: Pt or graphite rod). Ferrocene was added at the end of the experiments to determine redox potential values. The potential of the cell was controlled by an AUTOLAB PGSTAT 100 (Metrohm) potentiostat monitored by the NOVA software. THF was dried over Na/benzophenone and distilled before being stocked in the glovebox (Argon) over molecular sieves. Propylene carbonate was kept under N_2 in the glovebox and dried over molecular sieves. Acetonitrile was distilled over CaH_2 and kept in the glovebox. The supporting salt NBu_4PF_6 was synthesized from NBu_4OH (Acros) and HPF_6 (Aldrich). It was then purified, dried under vacuum for 48 h at 100 °C, and then kept under argon in the glovebox. Thin layer room-temperature UV−vis−NIR spectroelectrochemistry was performed with a specific home-designed cell in a reflectance mode (WE: glassy carbon or platinum, RE: Pt wire, CE: Pt wire). The UV−vis and vis−NIR optic fiber probes were purchased from Ocean Optics. Time-resolved UV−vis detection was performed with QEPro and NIR-Quest spectrometers (Ocean optics). X-band EPR spectroscopy was performed with a Bruker Elexsys instrument. Simulations of the EPR spectra were carried out with the XSophe software.

2.3. Theoretical Calculations. All calculations were performed using the Gaussian 09 package.[39] Different basis set functionals and solvent models were used (see Table 2). Best results were obtained at the IEFPCM/M11L level to compute redox potential and at the IEFPCM/PBE0 level for geometry optimization with the def2-TZVDP for copper atoms and the 6-311+G(d,p) for other atoms as it was already described.[35] Vibrational frequency calculations were performed to ensure that each geometry optimization converged to a real minimum. Orbital population analysis was done using the pop = (biorthogonalize, save) keyword to transform the canonical α and β orbitals in orbitals which match up as much as possible α and β orbitals to determine without ambiguity the spin states of the system. Spin densities, orbitals were computed using the program cubegen of the Gaussian 09 package, and their representations were done using the software VMD.[40]

Different spin states are possible. The ground state of dicopper (II,II) complexes can be a triplet or a singlet state. For the monoreduced species, reduction occurs on one copper atom and the only spin state possible in this case is a doublet state. For the mono-oxidized species, according to the oxidation site, only a doublet state (oxidation on copper atom) or a doublet state and quartet state (oxidation on the phenoxo group) were possible. We thus have first considered calculations on a doublet state to determine the oxidation site. Mulliken populations and spin density has allowed us quickly to perform this task. For all complexes, oxidation occurs on the phenoxo group and two spin states, a doublet or a quartet state, have to be considered.

For the calculation of redox potentials, only high spin states of complexes were computed even if they are not ground states, so the triplet state for the dicopper (II,II) complexes and the quartet state for the mono-oxidized species. This is justified since the energy difference between spin states is very small compared to that between two redox states. To give an example, a hypothetical value of high antiferromagnetic coupling such as 300 cm^{-1} corresponds to an energy difference between the triplet and the singlet states of 0.86 kcal/mol. It is well negligible regarding the energy difference between the two redox states which equals approximatively 130 kcal/mol for $\mathbf{1b}^{2+}$ with a computed redox potential of 0.56 vs Fc for the oxidation process.

Analysis of the electronic structure of dicopper (II,II) complexes was performed on their broken symmetry state since experimentally magnetization measurements reveal an antiferromagnetic coupling for these systems.[21,30,33] Single-point calculation was performed using the PBE0 functional. A high-spin wave function was used with its optimized geometry, and the guess = (read, mix) keyword of Gaussian 09 was used to generate the unrestricted broken symmetry singlet wave function. For all complexes studied, the broken symmetry state was found to have an electronic energy lower than that of the triplet state, in agreement with an antiferromagnetic coupling (see Table S1).

Analysis of the electronic structure of the mono-oxidized species was performed on their quartet state. There is no experimental information on their ground states. Calculations were done for the compound $\mathbf{1b}^{2+}$ by using the fragment keyword of Gaussian 09, and the optimized geometry of the quartet state to generate different configurations for a doublet state using the PBE0 functional. The unrestricted doublet state associated with a configuration Cu(1/2)L(1/2)Cu(−1/2) (respectively, a configuration Cu(1/2)L(−1/2)Cu(1/2)) was found to have an electronic energy less than 0.57 kcal/mol (respectively, more than 0.49 kcal/mol) that of the quartet state. These weak differences, added to the fact that there is no experimental proof to confirm the spin state, make it difficult to conclude on the ground state for this complex. Hence, we made the choice, even if quartet states are not necessarily the ground state of these systems, to use their electronic structures to help us to rationalize experimental data observed on the mono-oxidized species.

Finally, for the mono-oxidized species of $\mathbf{3a}^{2+}$, TD-DFT calculations were performed for two configurations. For the mono-oxidized Cu-Cu(III,II)-phenolate species, only a doublet spin state is possible. For the mono-oxidized Cu-Cu(II,II)-phenoxyl species, as seen before, calculations were performed on the quartet state. Solutions for the 50 lowest states were computed. TD-DFT is recognized to provide accurate results for closed shell systems,[41] but in the case of open shell systems such as the mono-oxidized species described here, spin contamination problems can induce errors on the nature of the excited states.[42] Benchmarks were tested previously using different functionals.[36] The functional wB97XD, associated with the IEFPCM solvent model and the basis set used for geometry optimizations and calculations of redox potentials, gives the lowest spin contamination.

3. RESULTS AND DISCUSSION

3.1. Electrochemical Studies. As mentioned in the Introduction, only the electrochemical properties of complexes $(\mathbf{1a-c})^{2+}$ in acetonitrile at room temperature were previously reported.[30,31] Indeed, it was shown that two successive reduction processes occur at ca. −1.0 and −1.3 V vs Fc when scanning negatively, independently of R. Such results were ascribed to

DOI: 10.1021/acs.inorgchem.7b00338
Inorg. Chem. 2017, 56, 7707−7719

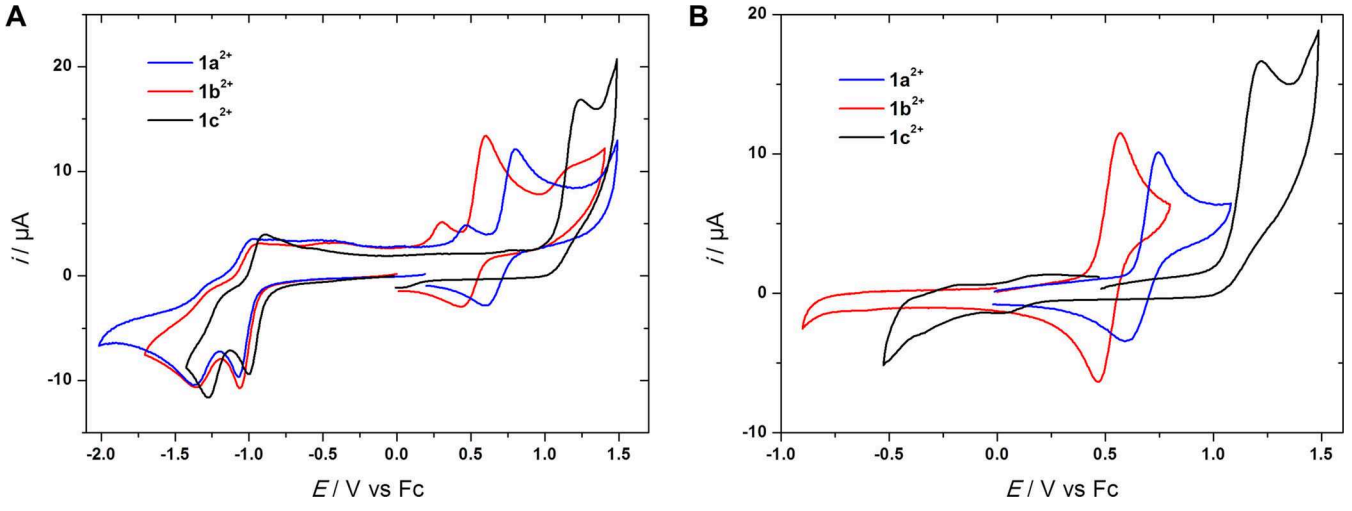

Figure 1. CVs (v = 0.1 V/s) at a vitreous carbon electrode (E/V vs Fc) of complexes $\mathbf{1a}^{2+}$, $\mathbf{1b}^{2+}$, and $\mathbf{1c}^{2+}$ (1.5 mM) in PC/NBu_4PF_6 0.1 M: R = CF_3 (black), OCH_3 (red), CH_3 (blue). A: full scan, B: enlarged anodic part.

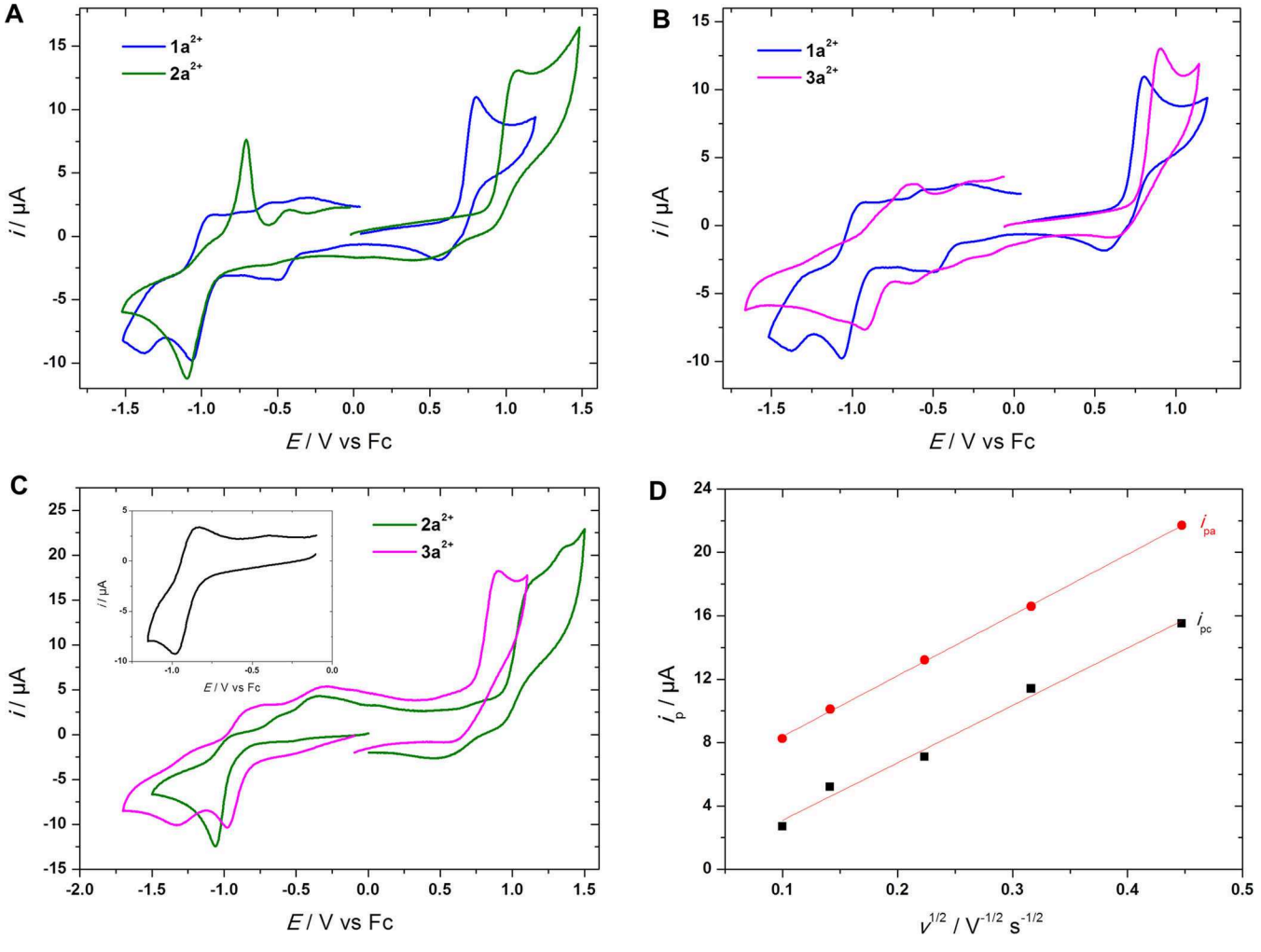

Figure 2. (A–C) CVs (v = 0.1 V/s) at a vitreous carbon electrode (E/V vs Fc) in CH_3CN/NBu_4PF_6 0.1 M of: (A) $\mathbf{1a}^{2+}$ (blue) and $\mathbf{2a}^{2+}$ (green) with positive scanning; (B) $\mathbf{1a}^{2+}$ (blue) and $\mathbf{3a}^{2+}$ (pink) with positive scanning; (C) $\mathbf{2a}^{2+}$ (green) and $\mathbf{3a}^{2+}$ (pink) with negative scanning; inset: CV at 0.1 V/s of $\mathbf{3a}^{2+}$ showing the reversibility for the first system in reduction. (D) Plots of i_{pa} (red circles) and i_{pc} (black squares) against $v^{1/2}$ taken from CVs at different scan rates for $\mathbf{2a}^{2+}$ in CH_3CN/NBu_4PF_6 0.1 M.

sequential monoelectronic reduction of each copper(II) center. On the oxidation side, the complexes display a monoelectronic oxidation at a redox potential value which depends on the nature of R. A phenoxyl radical was characterized by low-temperature UV–vis spectroscopy after exhaustive electrolysis of the solution containing $\mathbf{1b}^{2+}$.[32] Electrochemical studies of complexes $\mathbf{2a}^{2+}$ and

DOI: 10.1021/acs.inorgchem.7b00338
Inorg. Chem. 2017, 56, 7707−7719

$\mathbf{3a}^{2+}$ have not been reported so far. Hence, in order to develop a reliable calculation method which can give access to theoretical redox potential, spectroscopic features, and charge density mapping for this family of copper complexes, we have first investigated the effect of (i) solvent medium, (ii) spacer chain length, and (iii) asymmetry on the electrochemical properties of all complexes.

3.1.1. Solvent Effect. A first set of studies was carried out by investigating the effect of the medium on the redox properties on the R-BPMP series (complexes $\mathbf{1a}^{2+}$, $\mathbf{1b}^{2+}$, and $\mathbf{1c}^{2+}$). Three different organic solvents were used: acetonitrile (MeCN) as coordinating and polar solvent, tetrahydrofuran (THF) as poorly coordinating and nonpolar solvent, and propylene carbonate (PC) as poorly coordinating polar medium. As shown in Table 1, voltammetric investigations show that the medium has very little influence on the redox signature. The electrochemical features are indeed almost identical in propylene carbonate and acetonitrile, which is a first indication that the complexes do not dissociate in these media (no coordination of the solvent or electrolyte) and remain as a μ-hydroxo- and phenolate-bridged species. In THF, redox potential values are slightly different than those determined in PC and MeCN, probably because of the difference of polarity. On the cathodic part, two redox systems are systematically detected, the first one being reversible, as previously observed in acetonitrile[30,31] (see Figure 1 for experiments in PC). Exhaustive electrolysis (n = 1 e^-) at E = −1.0 V on a graphite rod leads to the formation of a new species which is oxidized at E = −0.4 V as shown by rotating-disk electrode voltammetry. The 500 mV difference in potential difference before/after electrolysis indicates that a large rearrangement (ligand decoordination and/or geometrical change) has occurred upon monoelectronic reduction. UV−vis spectroelectrochemical measurements in thin layer conditions (short time electrolysis) show a significant decrease of the d−d band at 700 nm upon reduction, which strongly suggests that the reduction process occurs on one of the Cu(II) centers, as previously proposed in acetonitrile.[30,31]

On the anodic side, oxidation of the complex depends on R but not on the solvent (see Table 1). For instance, $\mathbf{1b}^{2+}$ displays a reversible system at E^0 = 0.51 V vs Fc at 0.1 V/s in acetonitrile. With lower σ-donors (CH_3, CF_3), the oxidation potential is shifted positively in all media (Figure 1A). For $\mathbf{1c}^{2+}$, the positive shift is particularly important (+500 mV vs $\mathbf{1a}^{2+}$, +700 mV vs $\mathbf{1b}^{2+}$) and the system becomes irreversible. Exhaustive electrolysis at E = 0.60 V vs Fc of $\mathbf{1b}^{2+}$ shows that the mono-oxidized species is unstable at room temperature in the experiment time scale (1 h). The resulting species is characterized by several reduction peaks in the 0 to −0.5 V potential range, meaning that a large rearrangement occurs on this time scale.

3.1.2. Spacer Length Effect. The symmetrical CH_3-BPEP dicopper complex $\mathbf{2a}^{2+}$ displays a rather different redox behavior than its CH_3-BPMP analogue $\mathbf{1a}^{2+}$ in both oxidation and reduction parts. As shown in Figure 2C (green curve), a single and irreversible reduction peak is detected in acetonitrile at E_{pc} = −1.09 V vs Fc when scanning negatively, in contrast to the two successive peaks observed for $\mathbf{1a}^{2+}$. The same behavior is observed in THF and PC (Table 1). On the oxidation part, an irreversible peak is identified at E_{pa} = 1.04 V in MeCN (see Table 1 for values in THF and PC). This behavior differs from $\mathbf{1a}^{2+}$ which is oxidized quasi-reversibly at a lower potential value (E_{pa} = 0.79 V) (Figure 2A, blue curve). For both reduction and oxidation processes, variation of the scan rate does not induce the appearance of new peaks. Plots of anodic and cathodic peak current i_p vs $v^{1/2}$ for $\mathbf{2a}^{2+}$ in MeCN show similar slope values (Figure 2D), indicating that both processes involve the same number of electrons. Comparison of anodic and cathodic peak currents for $\mathbf{1a}^{2+}$ and $\mathbf{2a}^{2+}$ in analogous conditions strongly suggests the occurrence of monoelectronic oxidation and reduction processes for this complex.

3.1.3. Effect of Asymmetry. The same investigations were then performed with the unsymmetrical CH_3-BPMEP complex $\mathbf{3a}^{2+}$. On the cathodic part (Figure 2C, pink curve), two reduction peaks were detected at ca. −0.9 and −1.3 V, whatever the solvent (see Table 1). The first system at E^0 = −0.91 V vs Fc in acetonitrile is reversible (ΔE_p = 140 mV at v = 0.1 V s^{-1}, Figure 2C, inset) and noticeably appears at a more positive value than that observed for $\mathbf{1a}^{2+}$ (E^0 = −1.03 V). Scanning below −1.5 V induces the loss of reversibility of the first system and the appearance of new oxidation peaks on the back scan. On the anodic part (Figure 2B), an irreversible anodic peak was detected at E_{pa} = 0.90 V vs Fc in acetonitrile (0.84 V in THF and 0.93 V in PC; see Table 1). This value lies between those obtained for $\mathbf{1a}^{2+}$ (E_{pa} = 0.79 V) and $\mathbf{2a}^{2+}$ (E_{pa} = 1.04 V).

In summary, the voltammetric studies have led to the following conclusions:

(i) The redox behavior of all studied μ-hydroxo, μ-phenoxo dicopper complexes is not influenced by the nature of the solvent, hence indicating that the basic structure, i.e., bonding pattern, of the complex remains intact in solution.
(ii) The increase of spacer chain length between the tertiary amine and the picolyl groups on both sides of the ligand induces significant modifications of the voltammetric response: detection of only one cathodic peak (instead of two), positive shift of the oxidation peak by more than 300 mV, irreversibility of the anodic process in the experimental time scale (v = 0.1 V s^{-1}).
(iii) The unsymmetrical design of the ligand affects the redox signature of the resulting dicopper complex: positive shift of the first reduction potential by approximately 100 mV, positive shift of the oxidation potential by ca. 150 mV, and loss of reversibility for the oxidation reaction.

3.2. Theoretical Investigations. DFT calculations have been performed to determine the theoretical redox potential for this family of copper complexes.

3.2.1. Theoretical Model Calibration. The absolute potential of a redox couple E^{abs}_{calc} is typically calculated using eq 1, where the ΔG_{sol} is the Gibbs free energy in solution of the reaction, F is the Faraday constant, and n the number of moles of electrons of the reaction:

$$E^{abs}_{calc}(\mathrm{V}) = -\frac{\Delta G_{sol}}{nF} \quad (1)$$

For comparison with experimental data, the value of this potential has to be reported relative to a reference couple (RC), such as, for example, the standard hydrogen electrode (SHE) in water, or ferrocenium/ferrocene (Fc^+/Fc) in organic solvents. Hence, the relative (vs RC) standard potential value (E^0_{calc}) is calculated according to eq 2 by using the absolute redox potential of the reference ($E^{abs}_{exp,RC}$), which is experimentally determined:

$$E^0_{calc}(\mathrm{V\ vs\ RC}) = E^{abs}_{calc}(\mathrm{V}) - E^{abs}_{exp,RC}(\mathrm{V}) \quad (2)$$

Hence, theoretical relative standard potential values (E^0_{calc}) are fully dependent on the accuracy of $E^{abs}_{exp,RC}$. One major problem of this approach originates from the solvent and electrolyte

DOI: 10.1021/acs.inorgchem.7b00338
Inorg. Chem. 2017, 56, 7707−7719

Table 2. Basis Set, Functionals, Solvent Methods Tested To Compute Absolute Redox Potential Values of Fc (E^{abs}(Fc)/V) and Standard Potential (E^0_{ox} and E^0_{red}/V vs Fc) Values of Complex $1b^{2+}$

basis set	geometry optimization	redox potential	E_{abs} (Fc)[e]	E^0_{ox}[f]	E^0_{red}[g]
A[a]	B3LYP*[c]/IEFPCM	B3LYP*/IEFPCM	5.19	0.03	−1.16
	B3LYP*[c]/IEFPCM	B3LYP*/SMD	4.95	−0.11	−1.25
	B3LYP*[c]/IEFPCM	M11L/IEFPCM	4.91	0.69	−0.84
	B3LYP*[c]/IEFPCM	M11L/SMD	4.67	0.57	−0.94
B[b]	PBE0/IEFPCM	PBE0/IEFPCM	5.25	0.12	−1.28
	PBE0/IEFPCM	M11L/IEFPCM	5.00	0.59	−1.00
	[d]PBE0/IEFPCM	M11L/SMD	4.76	0.49	−1.32

[a]Basis set A: 6-311+G* Cu/Fe, D95** on other atoms. [b]Basis set B: def2-TZVDP Cu/Fe, 6-311+G(d,p) on N and O atoms, 6-311G(d,p) on other atoms. [c]B3LYP*: new parametrization of B3LYP with an HF value of 0.15 (from ref 34). [d]Basis set and method used in ref 35. [e]Exp. value: E^{abs} (Fc) = 4.98 V. [f]Exp. value: 0.51 V vs Fc. [g]Exp.: −1.02 V vs Fc.

Table 3. Experimental and Theoretical Voltammetric Data [E^0/V vs Fc (ΔE_p/mV)] for Dinuclear μ-Hydroxo Complexes $1a^{2+}$, $1b^{2+}$, $1c^{2+}$, $2a^{2+}$, and $3a^{2+}$ in Solvent/NBu_4PF_6 0.1 M (Solvent = MeCN, THF) for the First Oxidation Process

	$1a^{2+}$		$1b^{2+}$		$1c^{2+}$		$2a^{2+}$		$3a^{2+}$	
solvent	theor	exp	theor	exp	theor	exp	theor	exp	theor	exp
MeCN	0.85	0.71	0.59	0.51	1.39	1.20[a]	1.05	1.04[a]	1.01	0.90[a]
THF	1.28	0.60	1.11	0.45	1.85	1.05[a]	1.53	1.01[a]	1.49	0.84[a]

[a]Irreversible peak.

Table 4. Experimental and Theoretical Voltammetric Data [E^0/V vs Fc (ΔE_p/mV)] for Dinuclear μ-Hydroxo Complexes $1a^{2+}$, $1b^{2+}$, $1c^{2+}$, $2a^{2+}$, and $3a^{2+}$ in Solvent/NBu_4PF_6 0.1 M (Solvent = MeCN, THF) for the First Reduction Process

	$1a^{2+}$		$1b^{2+}$		$1c^{2+}$		$2a^{2+}$		$3a^{2+}$	
solvent	theor	exp	theor	exp	theor	exp	theor	exp	theor	exp
MeCN	−1.05	−1.03	−1.00	−1.02	−0.95	−0.95	−1.01	−1.09[a]	−0.98	−0.91
THF	−0.86	−1.11	−0.89	−1.09	−0.74	−1.03	−0.91	−1.08[a]	−0.82	−1.04

[a]Irreversible peak.

dependency of $E^{abs}_{exp,RC}$, which can induce shifts up to one hundred of millivolts. One solution proposed by Batista et al.[38] to avoid this situation has been to substitute the $E^{abs}_{exp,RC}$ term in eq 2 by a theoretical value of the absolute potential of the reference, $E^{abs}_{calc,RC}$, as shown in eq 3:

$$E^0_{calc}(\text{V vs RC}) = E^{abs}_{calc}(\text{V}) - E^{abs}_{calc,RC}(\text{V}) \quad (3)$$

Here, $E^{abs}_{calc,RC}$ is calculated at the same level than the redox couple used as reference.

On this basis, we have calculated the redox potential values for all dinuclear complexes against the experimentally used Fc^+/Fc reference. We tested two basis sets of similar quality associated with different functionals and solvation methods. The choice of these basis sets was governed by our own expertise for similar systems for the first one and by works by Tolman et al. for the second one.[35] Calibration was done to obtain the best correlation between theoretical and experimental data, for both the absolute potential values in acetonitrile for the ferrocenium/ferrocene redox system and for the first oxidation E^0_{ox} and reduction E^0_{red} potentials of complex $1b^{2+}$. The results are given in Table 2. The best correlation was obtained at the M11L/IEFPCM level to compute redox potential and at the PBE0/IEFPCM level for geometry optimization (entry 6, Table 2).

3.2.2. Calculated Redox Values for Dinuclear Complexes. From the calibration data, experimental and theoretical potential values (vs Fc^+/Fc) were calculated for the respective monoelectronic oxidation and reduction of all complexes in both acetonitrile and tetrahydrofuran. As shown in Tables 3 and 4, calculations are able to correctly reproduce the trends observed experimentally according to the ligand design, i.e., the effect of the substituting group and spacer length on the oxidation and reduction potentials. In particular, excellent agreement between theory and experiment was obtained for both the oxidation and the reduction processes in acetonitrile.

In tetrahydrofuran, discrepancies were found between calculated and theoretical results. Such an effect can be explained by the fact that the calibration was done in acetonitrile. Noticeably, discrepancies in THF are weaker for the reduction (Table 4) than for the oxidation process (Table 3). This is consistent with the solvent model used (polarizable continuum): the solvent effect is more pronounced for highly charged species such as the mono-oxidized species $1b^{3+}$ than the monoreduced complex $1b^+$.

3.2.3. Effect of R in the R-BPMP Series: Theoretical Considerations. Since good agreement was obtained between theoretical and experimental redox potential values in acetonitrile, further analysis was performed in order to rationalize the effect of the R substituting group on the oxidation and reduction processes. Plots of spin density (difference between α and β densities) for the oxidized or reduced species are of interest to consider the final species obtained after oxidation and reduction. For the reduced species, only the doublet state is possible, but for the oxidized species, different spins states can be considered. There is no experimental proof that can give an indication about the nature of the ground state. Some investigations were done (see more details in the Theoretical Calculations section), but it is difficult to conclude definitively on the nature of the ground state. Thus, all analyses have been performed on the quartet state, which is the only pure spin state accessible by DFT calculations.

DOI: 10.1021/acs.inorgchem.7b00338
Inorg. Chem. 2017, 56, 7707−7719

It is assumed to be a good indicator of the electronic structure of the real system. Figure 3 displays spin density plots for the high spin state of the mono-oxidized of the dicationic $\mathbf{1b}^{2+}$ complex and for its monoreduced species. For the quartet state ($\mathbf{1b}^{3+}$), spin densities are localized on both copper atoms and phenoxo moiety, hence suggesting a dinuclear complex with two Cu(II) cations and one phenoxyl radical. For the reduced state ($\mathbf{1b}^{+}$), spin density shows a localized mixed-valence species in agreement with a Cu-Cu (I,II) pair of cations, suggesting that reduction occurs on one Cu atom. Interestingly, geometries display an unsymmetrical structure with an increase of distances around the copper atom at the reduced site. The same description was obtained for the mono-oxidized and mono-reduced species of $\mathbf{1a}^{2+}$ and $\mathbf{1c}^{2+}$ dinuclear copper complexes (see their plots of spin density in Figure S1).

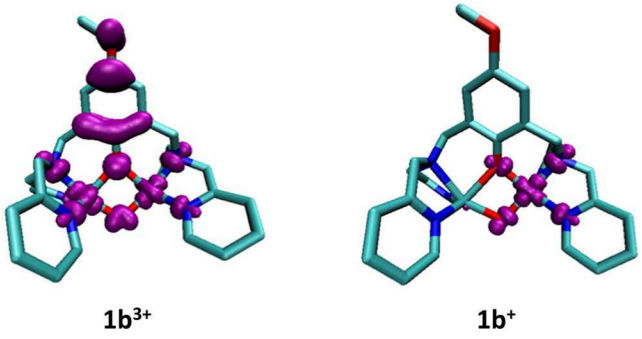

Figure 3. Spin density plot (isosurface equals to 0.04 au) for the high spin state of the mono-oxidized $\mathbf{1b}^{3+}$ species (left) and for the monoreduced species $\mathbf{1b}^{+}$ (right).

Like experimental data, theoretical calculations were able to show that the monoelectronic oxidation of the complexes is fully R-dependent (see Table 3, in MeCN, E_{ox} = 0.85 V for $\mathbf{1a}^{2+}$, 0.60 V for $\mathbf{1b}^{2+}$, and 1.39 V vs Fc for $\mathbf{1c}^{2+}$). To analyze the charge delocalization in their final tricationic mono-oxidized species (always in quartet state), we used biorthogonalized unrestricted orbitals. These orbitals are obtained using a subroutine of Gaussian09 (see the Theoretical Calculations section). For the quartet state of $\mathbf{1a}^{3+}$ and $\mathbf{1c}^{3+}$, the alpha singled occupied orbital for which spin is on the phenoxo group is less delocalized on the phenoxo moiety than for the quartet state of $\mathbf{1b}^{3+}$ (Figure S2). In particular, the instability of the radical $\mathbf{1c}^{3+}$ is a consequence of the withdrawing effect of CF_3. For $\mathbf{1a}^{3+}$ and $\mathbf{1b}^{3+}$, the difference of stability can be ascribed to the donor property of the substituting group (OCH_3 > CH_3). Hence, this data suggests a better stability for this state of $\mathbf{1b}^{3+}$ compared to that of $\mathbf{1a}^{3+}$ and $\mathbf{1c}^{3+}$. These differences can explain the less positive redox potential computed and observed experimentally.

3.2.4. Effect of Linker Length and Asymmetry: Theoretical Considerations. Similar analysis was performed in order to understand the impact of the linker length and the asymmetry on the redox potential. Spin density plots were obtained for the stable species after monoreduction and mono-oxidation of methyl-substituted complexes $\mathbf{1a}^{2+}$, $\mathbf{2a}^{2+}$, and $\mathbf{3a}^{2+}$. For the mono-oxidized species, analysis was still carried out on the quartet state. Results are similar to that obtained for complex $\mathbf{1b}^{2+}$, i.e., a monoreduced species with a Cu_2(I,II) character and a mono-oxidized phenoxyl species.

For the reduction process, distances around the reduced copper atom increased for all complexes (Table 5). Noticeably, a change of coordination was found for the unsymmetrical $\mathbf{3a}^{+}$ since the distance between the reduced copper on the ethyl-spacer side and the hydroxo-bridging oxygen increases from 1.99 to 3.64 Å. Reduction on the ethyl side may result from the higher flexibility of the ethyl linker vs the methyl one, such that the final reduced Cu(I) center is better stabilized. This modification could explain the more positive value obtained for both redox and experimental potential values associated with the first reduction process for $\mathbf{3a}^{2+}$ vs $\mathbf{1a}^{2+}$ and $\mathbf{2a}^{2+}$ as shown in Table 4 (−0.98 V, −1.05 V, and −1.01 V vs Fc, respectively).

For the oxidation process, the calculated redox potential is significantly more negative for $\mathbf{1a}^{2+}$ (0.85 V vs Fc) than for $\mathbf{2a}^{2+}$ (1.05 V) and $\mathbf{3a}^{2+}$ (1.01 V) (Table 3) as observed experimentally. This result is difficult to rationalize if one only considers that oxidation occurs on the phenoxo moiety. Indeed, it is not intuitively expected that the carbon chain between amine and picolyl groups affects the redox properties of the phenolate bridge. One explanation can be found when considering the stability of the quartet states of their final tricationic mono-oxidized species through the charge delocalization of their alpha singly occupied orbital localized on the phenoxo group as previously seen for the quartet states of $\mathbf{1a}^{3+}$, $\mathbf{1b}^{3+}$, and $\mathbf{1c}^{3+}$ complexes. Figure 4 shows a schematic representation of this orbital for the three complexes. Clearly, charge is more delocalized on copper atoms for the quartet states of $\mathbf{1a}^{3+}$ than for that of $\mathbf{2a}^{3+}$, the unsymmetrical complex $\mathbf{3a}^{3+}$ being an intermediate case. Close inspection of the geometry of these species indicates that the angle between the phenoxo moiety and the Cu1-O1-O2-Cu2 plane equals −40° for $\mathbf{1a}^{3+}$. For $\mathbf{2a}^{3+}$ and $\mathbf{3a}^{3+}$, the twist is significantly higher (−48° and −46°, respectively). These differences induce the bigger delocalization of the alpha singled occupied orbital localized on the phenoxo group for $\mathbf{1a}^{3+}$ and could explain the lowest value of the oxidation potential.

3.3. Oxidation of Dicopper(II) Complexes: Spectroelectrochemical and TD-DFT Investigations. *3.3.1. UV−vis−NIR Spectroelectrochemical Oxidation Monitoring.* In order to better understand the effect of ligand topology on the oxidation

Table 5. Selection of Bond Distances for the Initial and Monoreduced States of Complexes $\mathbf{1a}^{2+}$, $\mathbf{2a}^{2+}$, and $\mathbf{3a}^{2+}$ from DFT Calculations[a]

	Cu1−O1/Cu2−O1	Cu1−O2/Cu2−O2	Cu1−N1/Cu2−N2	Cu1−N2/Cu2−N2	Cu1−N3/Cu2−N3
$\mathbf{1a}^{2+}$	2.06/1.99	1.95/1.96	2.05/2.04	2.05/2.03	2.11/2.21
$\mathbf{1a}^{+}$	2.36/1.98	2.10/1.92	2.38/2.05	2.08/2.07	2.08/2.25
$\mathbf{2a}^{2+}$	1.98/1.98	1.97/1.98	2.09/2.10	2.03/2.03	2.24/2.24
$\mathbf{2a}^{+}$	2.32/1.97	2.21/1.93	2.33/2.11	2.06/2.07	2.07/2.27
$\mathbf{3a}^{2+}$	1.99/1.99	1.95/1.99	2.05/2.10	2.03/2.03	2.20/2.23
$\mathbf{3a}^{+}$	2.10/2.04	3.64/1.89	2.18/2.19	2.04/2.11	2.00/2.07

[a]Atom numbering: O1: phenoxy oxygen atom; O2: hydroxo oxygen atom; N1: amine nitrogen atom; N2 and N3: picolyl nitrogen atoms.

DOI: 10.1021/acs.inorgchem.7b00338
Inorg. Chem. 2017, 56, 7707−7719

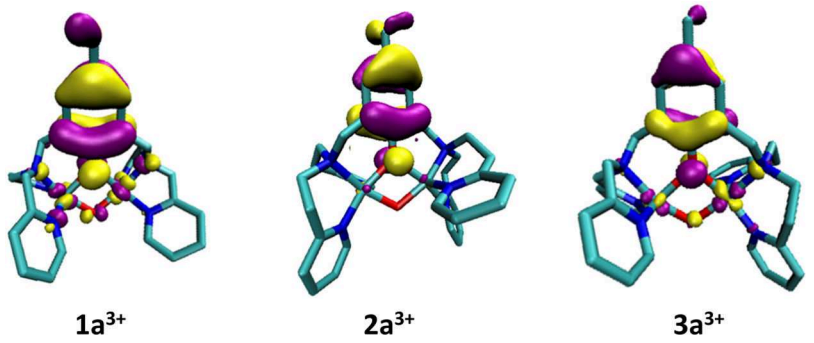

Figure 4. Schematic representation (isosurface is equal to ±0.04 au) of the alpha singled occupied orbital localized on the phenoxy group for the quartet state of $\mathbf{1a}^{3+}$ (left), $\mathbf{2a}^{3+}$ (middle), and $\mathbf{3a}^{3+}$ (right) showing better charge delocalization complex on copper atoms for $\mathbf{1a}^{3+}$.

process, UV−vis−NIR spectroelectrochemical experiments have been carried out at room temperature using thin-layer conditions, as previously performed for other species.[36] In comparison to the classical approach based on the exhaustive electrolysis of the solution at low temperatures, this method offers the possibility of working in a much lower time scale (ms), thus allowing the characterization of the transient species, which are electrogenerated on the electrode surface. Experimental data are gathered in Table 6.

Table 6. Experimental and Theoretical UV−vis Data (λ/nm) Obtained for the Dinuclear Copper Complexes upon Electrochemical Oxidation in CH_3CN/NBu_4PF_6 (Experimental Conditions: Thin Layer, Optical Path 0.2 mm, C = 4 mM), with the Assumption of the Successive Formation of (II,III,O$^-$) and (II,II,O$^\bullet$) Species for 2a and 3a

	λ_{max} (II,II,O$^\bullet$)		λ_{max} (II,III,O$^-$)	
	exp	theor	exp	theor
$\mathbf{1a}^{3+}$	438	363		
$\mathbf{2a}^{3+}$	361	404	532	567
$\mathbf{3a}^{3+}$	393	366	518	526
$\mathbf{1b}^{3+}$	440	380		

First investigations have been performed with the R-BPMP series. Complex $\mathbf{1b}^{2+}$ displays an intense absorption band at λ_{max} = 440 nm when a potential of 0.90 V is applied, without the appearance of any intermediate (Figure S3). This band decreases slowly ($t_{1/2}$ = 150 s) even if the applied potential remains at 0.90 V vs Fc. According to previous studies, it can be inferred to a $\pi-\pi^*$ transition occurring on the phenoxyl radical, suggesting that oxidation occurs on the phenolate ligand.[32] The same behavior was obtained with the oxidation of $\mathbf{1a}^{2+}$: an absorption band appears at λ_{max} = 438 nm upon application of an oxidation potential (1.10 V) and decays rapidly ($t_{1/2}$ = 30 s) as shown by the 3D and 2D time-resolved spectra in Figure 5. By analogy with $\mathbf{1b}^{2+}$, this band is ascribed to the $\pi-\pi^*$ transition on the phenoxyl radical.

Interestingly, a different behavior was obtained with the unsymmetrical complex $\mathbf{3a}^{2+}$. As shown in Figure 6, oxidation of the complex leads first to the appearance of a band at λ_{max} = 518 nm. This band decays rapidly ($t_{1/2}$ = 14 s) for the benefit of a new one at 393 nm. Monitoring of the spectroscopic response shows an isosbestic point at 460 nm (Figure 6B), hence evidencing the full conversion of the primary oxidized species into the second one. Close inspection in the NIR wavelength range shows no appearance of any new band (Figure S5) and no informative EPR signal (150 K) upon oxidation. Assuming that the entire amount of dinuclear complex was electrolyzed in the thin layer, molar extinction coefficients were calculated for these two species from the UV−vis spectra. Calculations yield ε = 1250 cm^{-1} M^{-1} and 3400 cm^{-1} M^{-1} at 518 and 393 nm, respectively. In a complementary way, the symmetrical complex $\mathbf{2a}^{2+}$ was investigated with the same approach. The oxidation leads to the disappearance of the initial band at 630 nm (d−d transition). This is accompanied by the increase of a band at 532 nm which rapidly (30 s) converts into a new one at 361 nm (Figure S4). Note that, in comparison to its unsymmetrical analogous complex $\mathbf{3a}^{2+}$, these spectral modifications are much less intense (8 times lower in absorbance) and hard to detect.

Oxidation of $\mathbf{3a}^{2+}$ was also performed by using a chemical oxidant in order to potentially characterize $\mathbf{3a}^{3+}$. Addition of 1 molar equiv of $NOBF_4$ to a solution of $\mathbf{3a}^{2+}$ at room temperature led to a slight decrease of the absorption band at 660 nm and the appearance of a new one at 475 nm (Figure S6). After several minutes, a second band appeared at 365 nm. The spectrum did not evolve after 60 min. Low-temperature EPR spectroscopy of the species displayed a signature which is typical of a monocopper center in a square-base pyramidal geometry (Figure S7). We may note here that previous EPR studies[32] performed on complex $\mathbf{1b}^{3+}$ essentially exhibited a signal attributed to a degraded compound. Altogether, these results clearly show that the intermediate species $\mathbf{3a}^{3+}$ (mixed-valent (II,III,O$^-$) and phenoxyl (II,II,O$^\bullet$)) were not detected by chemical oxidation with NO^+.

Thus, these results clearly demonstrate that the oxidation process is strongly influenced by the chain length and asymmetry. Noticeably, both complexes $\mathbf{3a}^{2+}$ and $\mathbf{2a}^{2+}$ display a remarkable behavior since an increase by one methylene unit of the spacer affords the formation of two successive species. This effect is particularly observable for the unsymmetrical complex $\mathbf{3a}^{2+}$. In an analogous manner, reported studies on mononuclear bis(phenolato)salen copper complexes have shown that chemical oxidation could lead in specific conditions to the formation of Cu(III)-phenolate complexes instead of an expected Cu(II)-phenoxyl species.[43−45] Such a Cu(III) complex is characterized by an absorption band in the 18 000−18 700 cm^{-1} energy range (i.e., λ = 535−555 nm), consistent with the experimental value found for the primary oxidation of $\mathbf{2a}^{3+}$ and $\mathbf{3a}^{3+}$.

3.3.2. Theoretical Investigation of the Oxidized Species. Close inspection of the electronic structure for these complexes is useful to explain the discrepancies in the oxidation processes between the complexes $\mathbf{1a}^{2+}/\mathbf{1b}^{2+}$ and $\mathbf{2a}^{2+}/\mathbf{3a}^{2+}$ complexes. To further understand the influence of the chain length, analysis was done on methyl-substituted systems $\mathbf{1a}^{2+}$, $\mathbf{2a}^{2+}$, and $\mathbf{3a}^{2+}$. Since

DOI: 10.1021/acs.inorgchem.7b00338
Inorg. Chem. 2017, 56, 7707−7719

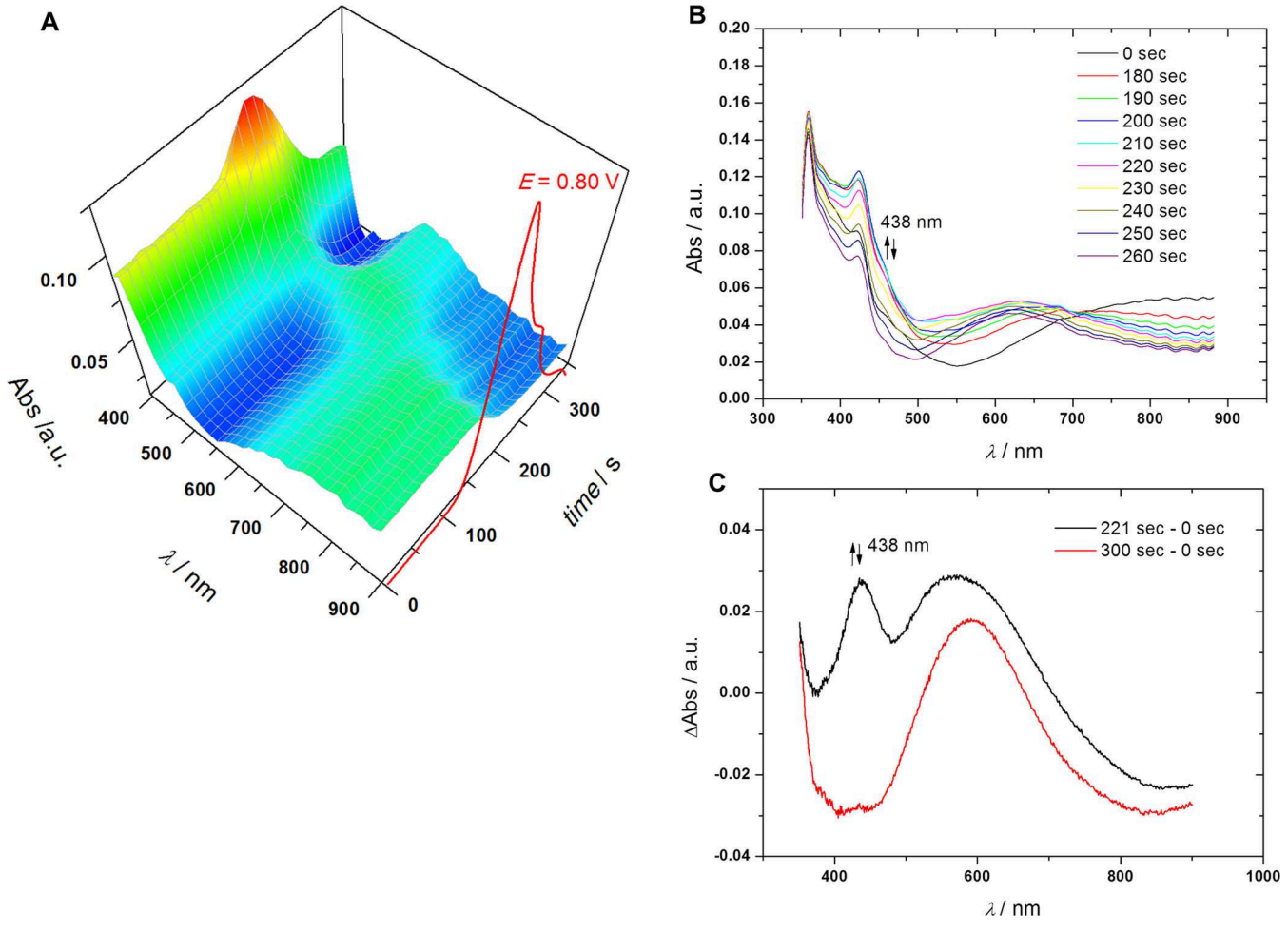

Figure 5. (A) 3D and (B) 2D UV−vis spectroelectrochemical data obtained for $\mathbf{1a}^{2+}$ upon electrochemical oxidation (red curve, CV 5 mV/s) in CH_3CN/NBu_4PF_6 (thin layer conditions, optical path 0.2 mm, C = 4 mM, 298 K). (C) 2D UV−vis graphics at 221 s (vs initial curve at 0 s, black curve) and 300 s (vs initial curve at 0 s, red curve) obtained from spectroelectrochemical monitoring of the oxidation of $\mathbf{1a}^{2+}$.

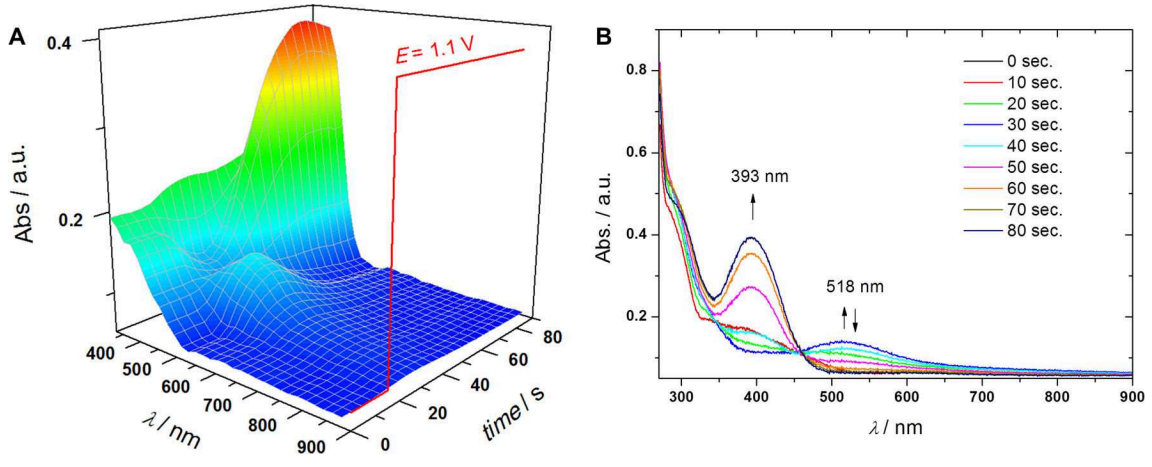

Figure 6. (A) 3D UV−vis spectroelectrochemical data obtained for $\mathbf{3a}^{2+}$ upon electrochemical oxidation at 1.10 V in CH_3CN/NBu_4PF_6 (thin layer conditions, optical path 0.2 mm, C = 4 mM, 298 K). (B) Monitoring of UV−vis spectra of the complex according to spectroelectrochemical experiment at 293 K.

experimental magnetic measurements reveal antiferromagnetic coupling for $\mathbf{1a}^{2+}$,[30] $\mathbf{2a}^{2+}$,[33] and $\mathbf{3a}^{2+}$,[21] a broken symmetry state was computed for these systems (Table S1). For all complexes, the electronic energies of this state were found to be lower than that of the triplet state, in agreement with experimental data. Therefore, inspection of the electronic structure was done on this state in the same way previously performed for similar systems.[46] Figure 7 displays the alpha highest occupied orbitals, HOMO, HOMO-1, HOMO-2, for the broken symmetry states of these complexes.

For systems where electron transfer is associated with conformational reorganization, oxidation can occur on orbitals

DOI: 10.1021/acs.inorgchem.7b00338
Inorg. Chem. 2017, 56, 7707−7719

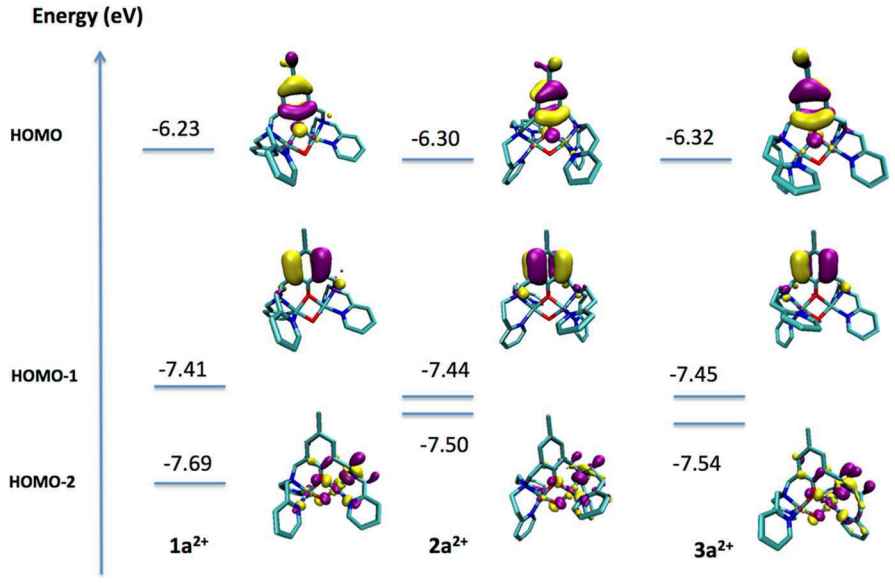

Figure 7. Schematic representation of the alpha highest occupied orbitals, HOMO, HOMO-1, HOMO-2 for the broken symmetry state of $\mathbf{1a}^{2+}$ (left), $\mathbf{2a}^{2+}$ (middle), and $\mathbf{3a}^{2+}$ (right). Numbers represent the energy (eV) of the different orbitals.

close to the HOMO, but not necessarily on the HOMO,[47] since orbitals ordering is modified with reorganization. For the three complexes $\mathbf{1a}^{2+}$, $\mathbf{2a}^{2+}$, and $\mathbf{3a}^{2+}$, HOMO and HOMO-1 are localized on the phenoxo group but HOMO-2 is localized on the copper atoms and its energy is close to each of HOMO-1 (0.06 eV for $\mathbf{2a}^{2+}$, 0.09 eV for $\mathbf{3a}^{2+}$, and a slightly larger difference for $\mathbf{1a}^{2+}$ with 0.28 eV). This difference could explain the formation of the other primary oxidized species observed experimentally before the oxidation of the phenoxo ligand for $\mathbf{3a}^{2+}$ and $\mathbf{2a}^{2+}$ and not for $\mathbf{1a}^{2+}$. To confirm this hypothesis, further calculations for $\mathbf{3a}^{2+}$ were performed by specifying the spin multiplicity of each copper atom in order to constrain the oxidation on one copper atom and to obtain a mono-oxidized Cu-Cu (III,II)-phenolate species. Then, TD-DFT calculations were carried out on both mono-oxidized Cu-Cu(III,II)-phenolate and Cu-Cu(II,II)-phenoxyl species $\mathbf{3a}^{3+}$. For the mono-oxidized Cu-Cu(III,II)-phenolate complex, only a doublet state is possible and calculations were done on this state. For the Cu-Cu(II,II)-phenoxyl species, calculations were performed as seen previously on the quartet state.

For the former, a transition at λ = 526 nm with a high value of oscillator strength (0.0804) and a weak spin contamination (S^2 = 0.771 against 0.75 for a doublet state) was found, which can correspond to the absorption band detected experimentally at 518 nm (Table 1). Natural transition orbital analysis provides a reasonable assignement of this band with a charge transfer essentially between the phenolate ligand and the Cu(III) (Figure 8A). For the mono-oxidized Cu-Cu(II,II)-phenoxyl species $\mathbf{3a}^{3+}$, a band with a high oscillator strength (0.0779) and also a weak spin contamination (S^2 = 3.876 against 3.75 for a quartet state) was found at 366 nm close also to the absorption band detected experimentally at 393 nm (Table 6). This band is attributed to a $\pi-\pi^*$ transition occurring on the phenoxyl radical (Figure 8B).

These results are illustrated in Scheme 1 for the oxidation process of $\mathbf{3a}^{2+}$ and $\mathbf{2a}^{2+}$. For these two complexes, oxidation occurs first on the copper atom on the ethyl-spacer side and forms a mono-oxidized Cu-Cu(II,III)-phenolate species which is rapidly transformed in the more stable Cu-Cu(II,II)-phenoxyl species. The chain length influences directly the stability of this species and could explain why it is not detected for $\mathbf{1a}^{2+}$, and

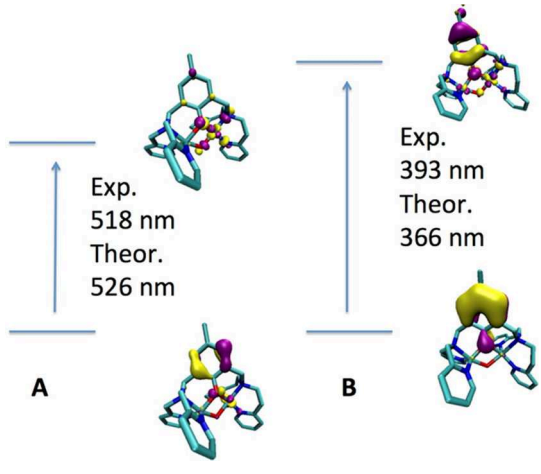

Figure 8. Natural transition orbitals of the excited state associated with the absorption band detected successively for $\mathbf{3a}^{3+}$ by spectroelectrochemistry (A) at 518 nm and (B) at 393 nm.

more generally for the R-BPMP series. Indeed, the value of the energy of the Cu-Cu(II,III)-phenolate complex was found to be 30.1 kcal·mol^{-1} higher than that of the Cu-Cu(II,II)-phenoxyl one for $\mathbf{1a}^{2+}$. This difference is significantly lower for $\mathbf{2a}^{2+}$ and $\mathbf{3a}^{2+}$ (23.9 and 24.1 kcal·mol^{-1}, respectively). This can be explained by the flexibility of the ligand, since the oxidized copper center can adopt a preferred conformation with an ethyl spacer compared to a methyl spacer.

4. CONCLUSIONS

In summary, the electrochemical and spectroelectrochemical studies, supported by theoretical calculations, of a series of symmetrical and unsymmetrical phenoxo- and hydroxo-bridged dicopper complexes have demonstrated that subtle modification of the ligand design can significantly affect the redox and spectroscopic properties. Good agreement between experimental and theoretical data has corroborated the proposed calculation method. TD-DFT calculations and spectroelectrochemical methods have demonstrated the formation of transient

DOI: 10.1021/acs.inorgchem.7b00338
Inorg. Chem. 2017, 56, 7708−7719

Scheme 1. Postulated Transient Oxidized Species Detected by Spectroelectrochemistry Illustrated for $1b^{2+}$ (Top) and $3a^{2+}$ (Bottom)

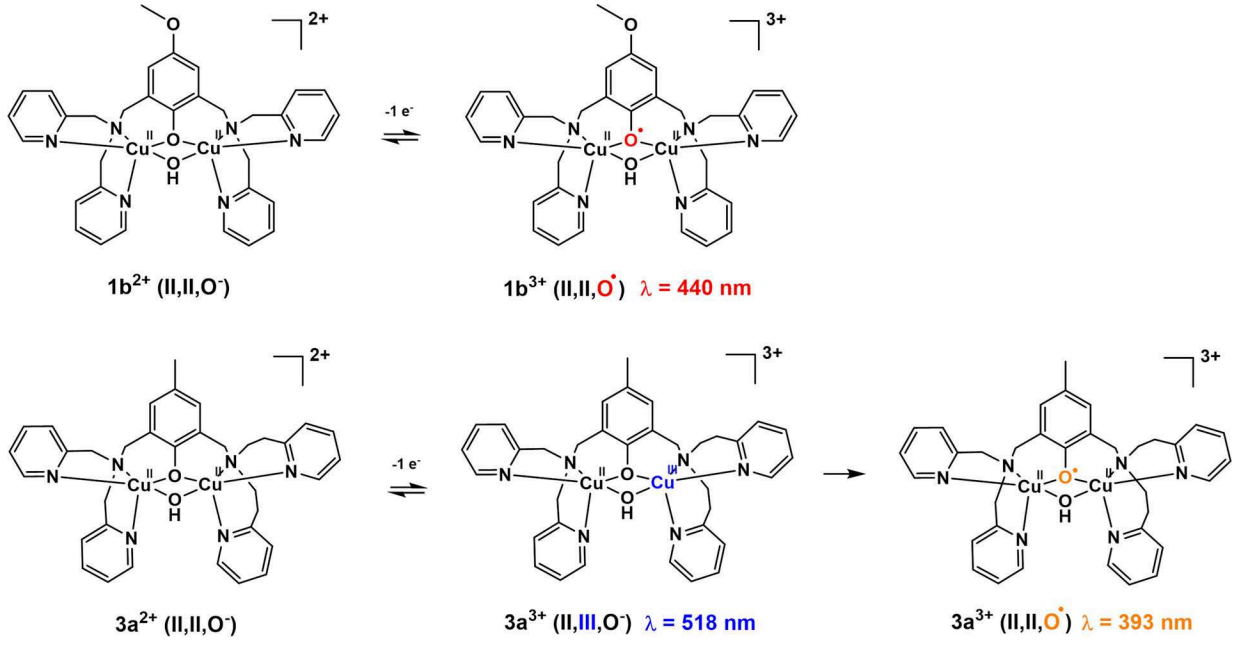

mixed-valent Cu(II)-Cu(III) phenolate complexes upon electrochemical oxidation, associated with the increase of the chain length between the tertiary amine and the pyridyl groups on one coordinating site. The intermediate species have evolved toward dicopper (II,II) phenoxyl complexes as shown by UV−vis spectroscopy, before decaying. Hence, two main points can be raised from these results. First, from a methodological point of view, the dicopper (II,III) mixed-valent species would not have been characterized unless spectroelectrochemical experiments were carried out. Thus, future experiments on analogous systems would gain, if possible, in characterizing the intermediates to determine whether oxidation takes place on the metallic core or on the ligand (phenolate); such data is of interest particularly if one wishes to investigate the nature of the reactive species. Another interesting aspect of these results originates from the mixed-valent (II,III) phenolate dicopper species obtained with $\mathbf{3a}^{2+}$, which could be relevant for modeling the postulated active species in pMMO, as previously done with symmetrical species.[35−37] For instance, the coordination site could become accessible to a defined substrate by modification of one of the N-coordinating groups, the unsymmetrical environment favoring the formation of the mixed-valent (II,III) species. Further work will be devoted to such investigations.

■ ASSOCIATED CONTENT

Supporting Information

The Supporting Information is available free of charge on the ACS Publications website at DOI: 10.1021/acs.inorgchem.7b00338.

Spectroelectrochemical and theoretical data for the dicopper complexes (PDF)

■ AUTHOR INFORMATION

Corresponding Authors

*E-mail: helene.jamet@univ-grenoble-alpes.fr (H.J.).
*E-mail: nicolas.lepoul@univ-brest.fr (N.L.P.).

ORCID

Rolf David: 0000-0001-5338-6267
Nicolas Le Poul: 0000-0002-5915-3760

Author Contributions

The manuscript was written through contributions of all authors. All authors have given approval to the final version of the manuscript.

Funding

Financial support by ANR-13-BSO7-0018, Conseil Général du Finistère (I.L.), Université de Bretagne Occidentale (F.G.).

Notes

The authors declare no competing financial interest.

■ ACKNOWLEDGMENTS

The authors are grateful to the Labex Arcane (ANR-11-LABX-0003-01), the COST CM1305, and for providing computer facilities the CECIC center. We also thank Laurianne Wojcik for EPR measurements and analyses (simulations).

■ REFERENCES

(1) Belle, C.; Pierre, J.-L. Asymmetry in bridged binuclear metalloenzymes: lessons for the chemist. *Eur. J. Inorg. Chem.* **2003**, *2003*, 4137−4146.

(2) Solomon, E. I.; Heppner, D. E.; Johnston, E. M.; Ginsbach, J. W.; Cirera, J.; Qayyum, M.; Kieber-Emmons, M. T.; Kjaergaard, C. H.; Hadt, R. G.; Tian, L. Copper active sites in biology. *Chem. Rev.* **2014**, *114*, 3659−3853.

(3) Prigge, S. T.; Mains, R. E.; Eipper, B. A.; Amzel, L. M. New insights into copper monooxygenases and peptide amidation: structure, mechanism and function. *Cell. Mol. Life Sci.* **2000**, *57*, 1236−1259.

(4) Francisco, W. A.; Wille, G.; Smith, A. J.; Merkler, D. J.; Klinman, J. P. Investigation of the pathway for inter-copper electron transfer in peptidylglycine alpha-amidating monooxygenase. *J. Am. Chem. Soc.* **2004**, *126*, 13168−13169.

(5) Mirica, L. M.; Ottenwaelder, X.; Stack, T. D. Structure and spectroscopy of copper-dioxygen complexes. *Chem. Rev.* **2004**, *104*, 1013−1045.

DOI: 10.1021/acs.inorgchem.7b00338
Inorg. Chem. 2017, 56, 7708−7719

(6) Elwell, C. E.; Gagnon, N. L.; Neisen, B. D.; Dhar, D.; Spaeth, A. D.; Yee, G. M.; Tolman, W. B. Copper-oxygen complexes revisited: structures, spectroscopy, and reactivity. *Chem. Rev.* **2017**, *117*, 2059−2107.
(7) Rolff, M.; Schottenheim, J.; Decker, H.; Tuczek, F. Copper-O_2 reactivity of tyrosinase models towards external monophenolic substrates: molecular mechanism and comparison with the enzyme. *Chem. Soc. Rev.* **2011**, *40*, 4077−4098.
(8) Hamann, J. N.; Herzigkeit, B.; Jurgeleit, R.; Tuczek, F. Small-molecule models of tyrosinase: From ligand hydroxylation to catalytic monooxygenation of external substrates. *Coord. Chem. Rev.* **2017**, *334*, 54−66.
(9) Koval, I. A.; Gamez, P.; Belle, C.; Selmeczi, K.; Reedijk, J. Synthetic models of the active site of catechol oxidase: mechanistic studies. *Chem. Soc. Rev.* **2006**, *35*, 814−840.
(10) Nasir, M. S.; Karlin, K. D.; McGowty, D.; Zubieta, J. Unsymmetrical dicopper complexes. Direct observation of reversible oxygen binding in a copper monooxygenase model system. *J. Am. Chem. Soc.* **1991**, *113*, 698−700.
(11) Adams, H.; Bailey, N. A.; Fenton, D. E.; Papageorgiou, G. A mononuclear copper(II) complex of an unsymmetrical dinucleating ligand. *J. Chem. Soc., Dalton Trans.* **1995**, 1883−1886.
(12) Adams, H.; Fenton, D. E.; Haque, S. R.; Heath, S. L.; Ohba, M.; Okawa, H.; Spey, S. E. Diversity in the reactions of unsymmetric dinucleating Schiff base ligands with Cu^{II} and Ni^{II}. *Dalton Trans.* **2000**, 1849−1856.
(13) Murthy, N. N.; Mahroof-Tahir, M.; Karlin, K. D. Dicopper(I) complexes of unsymmetrical binucleating ligands and their dioxygen reactivities. *Inorg. Chem.* **2001**, *40*, 628−635.
(14) Adams, H.; Clunas, S.; Cummings, L. R.; Fenton, D. E.; McHugh, P. E. Copper(II) complexes of unsymmetric compartmental ligands bearing adjacent {N2O}, {N,S,O} donor sets and {N2O}, {N,O} donor sets. *Inorg. Chem. Commun.* **2003**, *6*, 837−840.
(15) Tachi, Y.; Aita, K.; Teramae, S.; Tani, F.; Naruta, Y.; Fukuzumi, S.; Itoh, S. Dicopper-dioxygen complex supported by asymmetric pentapyridine dinucleating ligand. *Inorg. Chem.* **2004**, *43*, 4558−4560.
(16) Merkel, M.; Möller, N.; Piacenza, M.; Grimme, S.; Rompel, A.; Krebs, B. Less symmetrical dicopper(II) complexes as catechol oxidase models-an adjacent thioether group increases catecholase activity. *Chem. - Eur. J.* **2005**, *11*, 1201−1209.
(17) Peralta, R. A.; Neves, A.; Bortoluzzi, A. J.; Dos Anjos, A.; Xavier, F. R.; Szpoganicz, B.; Terenzi, H.; de Oliveira, M. C.; Castellano, E.; Friedermann, G. R.; Mangrich, A. S.; Novak, M. A. New unsymmetric dinuclear Cu(II)Cu(II) complexes and their relevance to copper(II) containing metalloenzymes and DNA cleavage. *J. Inorg. Biochem.* **2006**, *100*, 992−1004.
(18) Sander, O.; Näther, C.; Tuczek, F. Chiral dicopper complexes with a doubly Asymmetric ligand as models for the tyrosinase active site: synthesis, structure, O_2-reactivity and comparison with their symmetric analogs. *Z. Anorg. Allg. Chem.* **2009**, *635*, 1123−1133.
(19) Tachi, Y.; Matsukawa, Y.; Teraoka, J.; Itoh, S. A stable Cu_2O_2 complex supported by an asymmetric dinucleating pentapyridine ligand involving an amide linkage. *Chem. Lett.* **2009**, *38*, 202−203.
(20) Garcia-Bosch, I.; Company, A.; Frisch, J. R.; Torrent-Sucarrat, M.; Cardellach, M.; Gamba, I.; Guell, M.; Casella, L.; Que, L.; Ribas, X.; Luis, J. M.; Costas, M. O_2 activation and selective phenolate ortho hydroxylation by an unsymmetric dicopper μ-η^1:η^1-peroxido complex. *Angew. Chem., Int. Ed.* **2010**, *49*, 2406−2409.
(21) Bochot, C.; Favre, E.; Dubois, C.; Baptiste, B.; Bubacco, L.; Carrupt, P. A.; Gellon, G.; Hardre, R.; Luneau, D.; Moreau, Y.; Nurisso, A.; Reglier, M.; Serratrice, G.; Belle, C.; Jamet, H. Unsymmetrical binding modes of the HOPNO inhibitor of tyrosinase: from model complexes to the enzyme. *Chem. - Eur. J.* **2013**, *19*, 3655−3664.
(22) Chakraborty, P.; Adhikary, J.; Ghosh, B.; Sanyal, R.; Chattopadhyay, S. K.; Bauzá, A.; Frontera, A.; Zangrando, E.; Das, D. Relation between the catalytic efficiency of the synthetic analogues of catechol oxidase with their electrochemical property in the free state and substrate-bound state. *Inorg. Chem.* **2014**, *53*, 8257−8263.
(23) Serrano-Plana, J.; Costas, M.; Company, A. Building complexity in O_2-binding copper complexes. Site-selective metalation and intermolecular O_2-binding at dicopper and heterometallic complexes derived from an unsymmetric ligand. *Inorg. Chem.* **2014**, *53*, 12929−12938.
(24) Cao, R.; Saracini, C.; Ginsbach, J. W.; Kieber-Emmons, M. T.; Siegler, M. A.; Solomon, E. I.; Fukuzumi, S.; Karlin, K. D. Peroxo and superoxo moieties bound to copper ion: electron-transfer equilibrium with a small reorganization energy. *J. Am. Chem. Soc.* **2016**, *138*, 7055−7066.
(25) Li, S. T.; Braun-Cula, B.; Hoof, S.; Dürr, M.; Ivanović-Burmazović, I.; Limberg, C. Ligands with two different binding sites and O_2 reactivity of their copper(I) complexes. *Eur. J. Inorg. Chem.* **2016**, *2016*, 4017−4027.
(26) Serrano-Plana, J.; Garcia-Bosch, I.; Company, A.; Costas, M. Structural and reactivity models for copper oxygenases: cooperative effects and novel reactivities. *Acc. Chem. Res.* **2015**, *48*, 2397−2406.
(27) Rammal, W.; Selmeczi, K.; Philouze, C.; Saint-Aman, E.; Pierre, J.-L.; Belle, C. Thiomethyl substituted dicopper complexes: attempts to reproduce the asymmetry of the active site from type 3 copper enzymes. *Z. Anorg. Allg. Chem.* **2013**, *639*, 1477−1482.
(28) Bosch, S.; Comba, P.; Gahan, L. R.; Schenk, G. Dinuclear zinc(II) complexes with hydrogen bond donors as structural and functional phosphatase models. *Inorg. Chem.* **2014**, *53*, 9036−9051.
(29) Daumann, L. J.; Schenk, G.; Gahan, L. R. Metallo-β-lactamases and their biomimetic complexes. *Eur. J. Inorg. Chem.* **2014**, *2014*, 2869−2885.
(30) Torelli, S.; Belle, C.; Gautier-Luneau, I.; Pierre, J. L.; Saint-Aman, E.; Latour, J. M.; Le Pape, L.; Luneau, D. pH-controlled change of the metal coordination in a dicopper(II) complex of the ligand H−BPMP: crystal structures, magnetic properties, and catecholase activity. *Inorg. Chem.* **2000**, *39*, 3526−3536.
(31) Belle, C.; Beguin, C.; Gautier-Luneau, I.; Hamman, S.; Philouze, C.; Pierre, J. L.; Thomas, F.; Torelli, S.; Saint-Aman, E.; Bonin, M. Dicopper(II) complexes of H-BPMP-type ligands: pH-Induced changes of redox, spectroscopic (^{19}F NMR studies of fluorinated complexes), structural properties, and catecholase activities. *Inorg. Chem.* **2002**, *41*, 479−491.
(32) Michel, F.; Torelli, S.; Thomas, F.; Duboc, C.; Philouze, C.; Belle, C.; Hamman, S.; Saint-Aman, E.; Pierre, J. L. An unprecedented bridging phenoxyl radical in dicopper(II) complexes: evidence for an S = 3/2 spin state. *Angew. Chem., Int. Ed.* **2005**, *44*, 438−441.
(33) Orio, M.; Bochot, C.; Dubois, C.; Gellon, G.; Hardre, R.; Jamet, H.; Luneau, D.; Philouze, C.; Reglier, M.; Serratrice, G.; Belle, C. The versatile binding mode of transition-state analogue inhibitors of tyrosinase towards dicopper(II) model complexes: experimental and theoretical investigations. *Chem. - Eur. J.* **2011**, *17*, 13482−13494.
(34) Shiota, Y.; Yoshizawa, K. Comparison of the reactivity of bis(μ-oxo)Cu(II)Cu(III) and Cu(III)Cu(III) species to methane. *Inorg. Chem.* **2009**, *48*, 838−845.
(35) Halvagar, M. R.; Solntsev, P. V.; Lim, H.; Hedman, B.; Hodgson, K. O.; Solomon, E. I.; Cramer, C. J.; Tolman, W. B. Hydroxo-bridged dicopper(II,III) and -(III,III) complexes: models for putative intermediates in oxidation catalysis. *J. Am. Chem. Soc.* **2014**, *136*, 7269−7272.
(36) Isaac, J. A.; Gennarini, F.; Lopez, I.; Thibon-Pourret, A.; David, R.; Gellon, G.; Gennaro, B.; Philouze, C.; Meyer, F.; Demeshko, S.; Le Mest, Y.; Reglier, M.; Jamet, H.; Le Poul, N.; Belle, C. Room-temperature characterization of a mixed-valent μ-hydroxodicopper-(II,III) complex. *Inorg. Chem.* **2016**, *55*, 8263−8266.
(37) Kochem, A.; Gennarini, F.; Yemloul, M.; Orio, M.; Le Poul, N.; Rivière, E.; Giorgi, M.; Faure, B.; Le Mest, Y.; Réglier, M.; Simaan, A. J. Characterization of a dinuclear copper(II) complex and its fleeting mixed-valent copper(II)/copper(III) counterpart. *ChemPlusChem* **2017**, *82*, 615−624.
(38) Konezny, S. J.; Doherty, M. D.; Luca, O. R.; Crabtree, R. H.; Soloveichik, G. L.; Batista, V. S. Reduction of systematic uncertainty in DFT redox potentials of transition-metal complexes. *J. Phys. Chem. C* **2012**, *116*, 6349−6356.

DOI: 10.1021/acs.inorgchem.7b00338
Inorg. Chem. 2017, 56, 7708−7719

(39) Frisch, M. J.; Trucks, G. W.; Schlegel, H. B.; Scuseria, G. E.; Robb, M. A.; Cheeseman, J. R.; Scalmani, G.; Barone, V.; Mennucci, B.; Petersson, G. A.; Nakatsuji, H.; Caricato, M.; Li, X.; Hratchian, H. P.; Izmaylov, A. F.; Bloino, J.; Zheng, G.; Sonnenberg, J. L.; Hada, M.; Ehara, M.; Toyota, K.; Fukuda, R.; Hasegawa, J.; Ishida, M.; Nakajima, T.; Honda, Y.; Kitao, O.; Nakai, H.; Vreven, T.; Montgomery, J. A., Jr.; Peralta, J. E.; Ogliaro, F.; Bearpark, M.; Heyd, J. J.; Brothers, E.; Kudin, K. N.; Staroverov, V. N.; Kobayashi, R.; Normand, J.; Raghavachari, K.; Rendell, A.; Burant, J. C.; Iyengar, S. S.; Tomasi, J.; Cossi, M.; Rega, N.; Millam, J. M.; Klene, M.; Knox, J. E.; Cross, J. B.; Bakken, V.; Adamo, C.; Jaramillo, J.; Gomperts, R.; Stratmann, R. E.; Yazyev, O.; Austin, A. J.; Cammi, R.; Pomelli, C.; Ochterski, J. W.; Martin, R. L.; Morokuma, K.; Zakrzewski, V. G.; Voth, G. A.; Salvador, P.; Dannenberg, J. J.; Dapprich, S.; Daniels, A. D.; Farkas, Ö.; Foresman, J. B.; Ortiz, J. V.; Cioslowski, J.; Fox, D. J. *Gaussian 09*, Revision D.01; Gaussian, Inc.: Wallingford, CT, 2009.

(40) Humphrey, W.; Dalke, A.; Schulten, K. VMD: Visual molecular dynamics. *J. Mol. Graphics* **1996**, *14*, 33−38.

(41) Laurent, A. D.; Jacquemin, D. TD-DFT benchmarks: A review. *Int. J. Quantum Chem.* **2013**, *113*, 2019−2039.

(42) Li, Z.; Liu, W. Critical Aassessment of TD-DFT for excited states of open-shell systems: I. Doublet-doublet transitions. *J. Chem. Theory Comput.* **2016**, *12*, 238−260.

(43) Asami, K.; Tsukidate, K.; Iwatsuki, S.; Tani, F.; Karasawa, S.; Chiang, L.; Storr, T.; Thomas, F.; Shimazaki, Y. New insights into the electronic structure and reactivity of one-electron oxidized copper(II)-(disalicylidene)diamine complexes. *Inorg. Chem.* **2012**, *51*, 12450−12461.

(44) Chiang, L.; Herasymchuk, K.; Thomas, F.; Storr, T. Influence of electron-withdrawing substituents on the electronic structure of oxidized Ni and Cu salen complexes. *Inorg. Chem.* **2015**, *54*, 5970−5980.

(45) Storr, T.; Verma, P.; Pratt, R. C.; Wasinger, E. C.; Shimazaki, Y.; Stack, T. D. Defining the electronic and geometric structure of one-electron oxidized copper-bis-phenoxide complexes. *J. Am. Chem. Soc.* **2008**, *130*, 15448−15459.

(46) Park, G. Y.; Qayyum, M. F.; Woertink, J.; Hodgson, K. O.; Hedman, B.; Narducci Sarjeant, A. A.; Solomon, E. I.; Karlin, K. D. Geometric and electronic structure of $[\{Cu(MeAN)\}2(\mu\text{-}\eta^2\text{:}\eta^2(O_2^{2-})]^{2+}$ with an unusually long O-O bond: O-O bond weakening vs activation for reductive cleavage. *J. Am. Chem. Soc.* **2012**, *134*, 8513−8524.

(47) Talipov, M. R.; Boddeda, A.; Lindeman, S. V.; Rathore, R. Does Koopmans' paradigm for 1-electron oxidation always hold? Breakdown of IP/E_{ox} relationship for p-hydroquinone ethers and the role of methoxy group rotation. *J. Phys. Chem. Lett.* **2015**, *6*, 3373−3378.

DOI: 10.1021/acs.inorgchem.7b00338
Inorg. Chem. 2017, 56, 7708−7719

Inorganic Chemistry

Communication

pubs.acs.org/IC

Room-Temperature Characterization of a Mixed-Valent μ-Hydroxodicopper(II,III) Complex

James A. Isaac,[†] Federica Gennarini,[‡] Isidoro López,[‡] Aurore Thibon-Pourret,[†,§] Rolf David,[†] Gisèle Gellon,[†] Béatrice Gennaro,[†] Christian Philouze,[†] Franc Meyer,[∥] Serhiy Demeshko,[∥] Yves Le Mest,[‡] Marius Réglier,[⊥] Hélène Jamet,[†] Nicolas Le Poul,*[,‡] and Catherine Belle*[,†]

[†]DCM (UMR CNRS 5250), Université Grenoble-Alpes, CS 40700, 38058 Grenoble, France

[‡]CEMCA (UMR CNRS 6521), Université de Bretagne Occidentale, 6 avenue Le Gorgeu, 29238 Brest, France

[§]Institut de Chimie, CLAC, UMR 7177 CNRS, Université de Strasbourg, 67008 Strasbourg, France

[∥]Institut für Anorganische Chemie, Georg-August Universität Göttingen, Tammannstraße 4, 37077 Göttingen, Germany

[⊥]Aix-Marseille, CNRS, Centrale Marseille, ISM2 UMR 7313, 13397 Marseille, France

Supporting Information

ABSTRACT: Bis(μ-hydroxo)dicopper(II,II) bearing a naphthyridine-based ligand has been synthesized and characterized in the solid state and solution. Cyclic voltammetry at room temperature displays a reversible redox system that corresponds to the monoelectronic oxidation of the complex. Spectroscopic and time-resolved spectroelectrochemical data coupled to theoretical results support the formation of a charge-localized mixed-valent $Cu^{II,III}_2$ species.

In past decades, significant progress has been achieved in the field of Cu/O_2 chemistry relevant to metalloenzymes capable of oxidizing substrates.[1,2] Numerous biomimetic dicopper complexes have provided structural and spectroscopic data about Cu_2/O_2 species involved in such processes.[3−8] Interestingly, theoretical studies have postulated that a mixed-valent $Cu^{II,III}_2/O_2$ cluster in the active site could be the oxidizing intermediate in the catalytic cycle in the particulate methane monooxygenase (pMMO) enzyme.[9−11] So far, only one example of such a $Cu^{II,III}_2$ species has been characterized by spectroscopic means at low temperatures.[12]

In the present work, we have prepared and characterized a mixed-valent $Cu^{II,III}_2$ species that is stable for several seconds at room temperature (RT) in CH_3CN. The chosen ligand [DPMN = 2,7-bis(dipyridyl)methyl-1−8-naphthyridine] displays interesting properties,[13,14] such as (i) two well-defined coordination sites with a short metal−metal distance and (ii) a redox-innocent bridging spacer. In this context, a new bis(μ-hydroxo)dicopper(II,II) complex, $[Cu^{II}_2(DPMN)(\mu\text{-}OH)_2(OTf)](OTf)$ (**1**·$(OTf)_2$, where $OTf^- = CF_3SO_3^-$), was synthesized from a reaction in tetrahydrofuran between the DPMN ligand, Cu$(OTf)_2$, triethylamine, and water (details in the Supporting Information, SI). Crystals suitable for X-ray diffraction (XRD) were obtained from the resulting powder by vapor diffusion of diisopropyl ether into CH_3CN. The unit cell contains two independent $[Cu^{II}_2(DPMN)(\mu\text{-}OH)_2(OTf)](OTf)\cdot 1.8CH_3CN$ entities, **1A**·$(OTf)_2$ and **1B**·$(OTf)_2$. Both show no significant differences in their bond distances and angles (see the SI). The cationic unit of **1A**·$(OTf)_2$ is shown in Figure 1. Each unit consists of two Cu atoms bridged by two hydroxo moieties with Cu1−OH−Cu2 angles in the range of 90.11−90.67°.

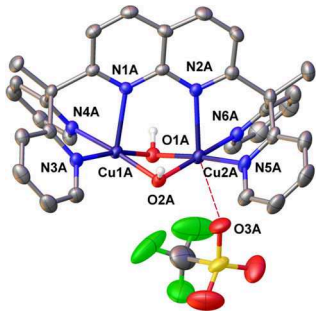

Figure 1. Molecular structure of the cationic part of **1A**·$(OTf)_2$ determined by XRD with thermal ellipsoids set at 50%. H atoms (except from the OH) were omitted for clarity. Selected bond and distances are given in the SI.

The Cu1···Cu2 bond distance (~2.75 Å) is one of the shortest reported for bis(μ-hydroxo)dicopper(II) complexes bridged by a spacer[15−17] and close to the ~2.6 Å value observed in the dinuclear site of pMMO.[11,18] The coordination polyhedron around the Cu1A atom is a distorted square pyramid whose apical position is occupied by the naphthyridine N1A atom at 2.276 Å. Because of the presence of a triflate anion at the Cu2A site, the two Cu atoms are not in identical coordination environments. Cu2A is found in a distorted octahedral geometry with axial positions occupied by the N2A atom at an elongated distance of 2.353 Å compared to 2.276 Å for Cu1−N1A and the O3A atom from a triflate at 2.615 Å. The temperature-dependent magnetic susceptibility for **1**·$(OTf)_2$ was measured at 5000 Oe from 295 to 2 K. The $\chi_M T$ versus T curve for the dinuclear complex (Figure S2) was simulated by using the isotropic exchange Hamiltonian $\hat{H} = -2J\hat{S}_1\hat{S}_2$. The exchange coupling constant, J = +113 cm^{-1}, is large and positive, indicating the presence of strong ferromagnetic interactions between the two

Received: June 23, 2016
Published: August 12, 2016

DOI: 10.1021/acs.inorgchem.6b01504
Inorg. Chem. 2016, 55, 8263−8266

Cu^{II} ($S = {}^1/_2$) ions within the dinuclear complex, in accordance with the acute Cu−O(H)−Cu angles (see the SI) and previous studies on μ-OH $Cu^{II,II}_2$ complexes.[19,20]

In CD_3CN, the paramagnetic ^1H NMR spectrum displays seven observable signals (7.7−133 ppm range; Figures S3−S5), which are consistent with a more symmetrical structure in solution. On the ^{19}F NMR spectrum (+460 to −140 ppm range), a unique peak at +85 ppm versus C_6F_6 is observed upon dissolution of **1**·$(OTf)_2$ in CD_3CN, suggesting that all triflate anions are in the same environment and not coordinated to Cu cations in solution or exchanging rapidly on the NMR time scale (Figure S6). The X-band electron paramagnetic resonance (EPR) spectrum (CH_3CN, 15 K) is silent (Figure 2B). In

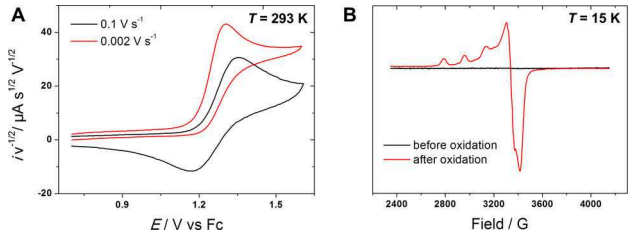

Figure 2. (A) RT scan-rate-normalized cyclic voltammograms (E/V vs Fc^+/Fc) of **1**·$(OTf)_2$ (C = 1 mM) in 0.1 M NBu_4PF_6/CH_3CN at v = 0.002 V s^{-1} (red) and v = 0.1 V s^{-1} (black). (B) EPR spectra (15 K) of **1**·$(OTf)_2$ before (black) and after (red) low-temperature (233 K) bulk electrolysis in NBu_4ClO_4/CH_3CN (ν = 9.419 GHz).

CH_3CN, **1**·$(OTf)_2$ exhibits intense electronic transitions (Figure S13) in the UV region similar to the free ligand, and these have been assigned as $\pi-\pi^*$ transitions[14] at 262, 307, 311, and 320 nm. The low-energy band of the d → d transition is observed at 580 nm ($\varepsilon \sim 70$ M^{-1} cm^{-1}). Cyclic voltammetry (CV) of **1**·$(OTf)_2$ in NBu_4PF_6/CH_3CN shows an oxidation process that is fully irreversible at low scan rate (v) but becomes quasi-reversible for $v \geq 0.1$ V s^{-1} [E^0 = 1.26 V vs Fc^+/Fc (=1.66 V vs SCE); ΔE_p = 190 mV; Figure 2A]. Plots of the current function ($i/v^{1/2}$) against potential E and v (Figure S8) indicate the occurrence of an ECE mechanism (E = electrochemical and C = chemical), which involves a transient oxidized species having a lifetime of several seconds at T = 293 K (see the SI for further explanations).[21,22] Aiming at calculating the number of electrons (n) involved in the oxidation process, we first performed NMR DOSY experiments (Figure S7) to determine the diffusion coefficient value for **1**·$(OTf)_2$ in KPF_6/CH_3CN at 293 K [D = 1.0 (±0.1) 10^{-5} cm^2 s^{-1}]. CV at different scan rates was then used to calculate n by assuming the reversible case for v > 0.1 V s^{-1}. Indeed, plots of i_{pa} versus $v^{1/2}$ yielded n = 1 knowing D, according to the Randles−Sevcik equation (Figure S9).[23] In the same manner, chronoamperometry and rotating-disk electrode voltammetry confirmed the monoelectronic character of the oxidation (Figures S10 and S11 and Table S1). The high value of the oxidation potential determined for **1**·$(OTf)_2$ (ca. 1.3 V vs Fc^+/Fc) precludes chemical oxidation.[24] Nevertheless, in order to further investigate the oxidation process, electrochemical and spectroelectrochemical studies were carried out at −40 °C. Decreasing the temperature induced a different redox behavior. Indeed, the system at E = 1.26 V versus Fc^+/Fc became reversible at a low scan rate (v = 0.01 V s^{-1}; Figure S12) in contrast to the irreversible system at RT. This was accompanied by an increase of the peak-to-peak separation due to a decrease of the electron-transfer kinetics with T. The one-electron-oxidized species was then generated by exhaustive electrolysis of the solution at −40 °C (details in the SI). Noticeably, the pale-purple solution turned to yellow-brown upon oxidation and decomposed into a greenish mixture in less than 1 h. Interestingly, UV−vis and X-band EPR characterization of the transient yellow product was performed and revealed the appearance of an UV−vis absorption band at λ = 424 nm (ε = 1250 M^{-1} cm^{-1}; Figure S13) as well as an axial EPR spectrum with a four-line pattern in $g_{\|}$ from 15 to 200 K (Figures 2B and S16).[25] This indicates hyperfine coupling to only one Cu^{II} consistent with a localized valence similar to the one previously described.[12] The fitting led to the following parameters: $g_{\|}$ = 2.21, $g_{\perp}$ = 2.02, and $A_{\|}$ = 174 × 10^{-4} cm^{-1} (Figure S17), suggesting a square-pyramidal geometry for the Cu^{II} ion. Spectroscopic EPR characterization of the final greenish product showed a broad spectrum, which suggested a mixture of several Cu^{II} complexes in solution (Figure S15).

UV−vis time-resolved spectroelectrochemistry was then carried out for the RT detection of the transient species in a time-resolved manner (thin-layer conditions; one spectrum every 0.5 s). An absorption band was detected at λ = 424 nm upon application of a high potential value (E = 1.6 V) starting from the open-circuit potential (E = 0.8 V; Figure 3). This band

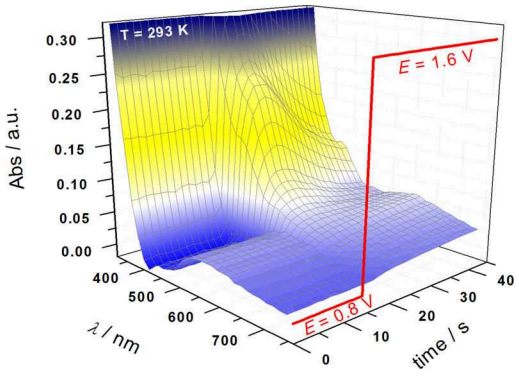

Figure 3. RT time-resolved UV−vis spectrum of **1**·$(OTf)_2$ (C = 10 mM; optical path = 0.2 mm) in 0.1 M NBu_4PF_6/CH_3CN upon application of a potential at the working electrode E = 0.8 V versus Fc^+/Fc (first 15 s) and E = 1.6 V (after 15 s).

disappeared progressively within tens of seconds, indicating that the mixed-valent species is relatively stable at RT in agreement with CV at v = 0.1 V s^{-1}. The same experiment performed at −40 °C led to full stabilization of the monooxidized complex, as shown by UV−vis spectroscopy (Figure S14). In the near-IR (NIR) region, a low-intensity and broad absorption band centered at λ = 1344 nm (ε = 90 M^{-1} cm^{-1}) was detected (Figure S18). This band disappeared and reappeared reversibly by switching between 0.8 and 1.6 V (Figure S19). Fitting of the NIR band allowed the determination of the bandwidth at half-height ($\Delta\tilde{\nu}_{1/2}$ = 2520 cm^{-1}; Figure S20). This gives access to the minimum value for the electronic coupling matrix element H_{ab} assuming a Cu−Cu distance of 2.75 Å.[12] The Γ parameter[26,27] (ratio between the experimental and theoretical values of $\Delta\tilde{\nu}_{1/2}$) was also calculated (see the SI). Values found for H_{ab} = 322 cm^{-1} and Γ = 0.39 are typical of a class II system in the Robin−Day classification, i.e., low delocalization of the charge.[28] Hence, the NIR features of $\mathbf{1}^{3+}$ are slightly different from those obtained for the previously reported mixed-valent $Cu^{II,III}_2$ complex.[12] Indeed, the present complex displays lower energy frequency and molar extinction coefficient and higher bandwidth at half-height than the above-mentioned analogue. This suggests a lower delocalization of the charge on the dicopper core for $\mathbf{1}^{3+}$ at 233 K. Further

DOI: 10.1021/acs.inorgchem.6b01504
Inorg. Chem. 2016, 55, 8263−8266

investigations were then carried out by density functional theory (DFT) calculations to gain insight into the electronic structure, redox potential, and UV−vis spectroscopic features of the monooxidized complex.[29] For the redox potential, the absolute value of $\mathbf{1}^{2+}$ was computed and reported relative to the computed value of the Fc^+/Fc redox couple (see the SI).[30] DFT calculations predicted a standard potential equal to 1.36 V versus Fc^+/Fc for sequential one-electron oxidation, in good agreement with the experimental data (E^0 = 1.26 V vs Fc^+/Fc). Figure 4 displays a

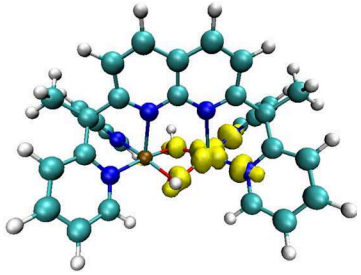

Figure 4. Spin-density plot for $\mathbf{1}^{3+}$ (yellow).

spin-density plot (difference between the α and β densities) for the monooxidized complex. The remaining unpaired electron is mainly localized on only one Cu ion and its adjacent atoms (μ-OH and N_{pyr}). This result confirms the weakly delocalized nature of the mixed-valent $Cu^{II,III}_2$ species, in agreement with experimental NIR−vis spectroscopic data. It is also consistent with the EPR results (mono-Cu^{II} signature). The mixed-valent complex also displays Cu−N and Cu−O distances that decrease according to the valence state of the Cu ion. For instance, the Cu−N_{pyr} and Cu−O distances are equal to 1.97 and 2.00 Å for Cu^{II}, respectively, whereas they are significantly lower for Cu^{III} (1.88 and 1.85 Å, respectively). The Cu···Cu distance increases to 2.83 Å for the mixed-valent state species against 2.78 and 2.75 Å for the computed and experimental values, respectively.

Considering the UV−vis spectroscopic features of the monooxidized complex, time-dependent DFT calculations were also performed for $\mathbf{1}^{3+}$ and $\mathbf{1}^{2+}$. Different benchmarks were done to obtain a good description of the absorption band detected experimentally at ∼430 nm. For $\mathbf{1}^{2+}$, there was no band computed at this value (Table S3). The best results were obtained at the wB97XD/IEFPCM level of theory with a transition computed with the lowest-spin contamination of the excited state (S^2 = 0.79 vs 0.75 for a good description of the excited state; Table S2). A band at 1367 nm was also found but with a heavy contamination of spin, which renders this result unreliable. Natural transition orbital analysis[31] provides a reasonable assignment of the band at ∼430 nm as a ligand-to-metal charge transfer essentially between pyridine rings and the Cu^{III} ion (Figure S21). For the monooxidized species, different protonation states of the bridging hydroxo moieties to form a μ-oxo, μ-hydroxo, or a bis(μ-oxo) species were considered. Only $\mathbf{1}^{3+}$ with a bis(μ-hydroxo) core gives different distances between the two Cu and O atoms after geometry optimization (see the description above). For the μ-oxo, μ-hydroxo, and bis(μ-oxo) species, both Cu−O distances stay similar (Table S4), in agreement with a fully delocalized charge ($Cu_2^{2.5}$) of the mixed-valent state. These results, added to the experimental data and the computed redox potential of $\mathbf{1}^{3+}$, seem to indicate that no deprotonation occurs during the oxidation process.

In summary, the use of a bis(tridendate) ligand based on a naphthyridine spacer has provided access to the RT experimental characterization of a mixed-valent μ-hydroxodicopper(II,III) complex with a predominant charge localization on one of the two Cu ions as fully supported by theoretical data. So far, this work displays a rare example of RT spectroscopic and electrochemical identification of such mixed-valent species. The relatively good stability of the mixed-valent complex at RT provides insight for the challenging development of synthetic $Cu^{II,III}_2$ models of copper oxygenases such as pMMO. Future work will aim at designing new bioinspired copper complexes with lower oxidation potentials for comparative studies of their reactivity toward C−H activation.

■ ASSOCIATED CONTENT

Supporting Information

The Supporting Information is available free of charge on the ACS Publications website at DOI: 10.1021/acs.inorgchem.6b01504.

Synthesis, electrospray ionization mass spectrometry, magnetism, NMR, electrochemistry, UV−vis, EPR, NIR, and theoretical calculations (PDF)

X-ray crystallographic data in CIF format (CIF)

■ AUTHOR INFORMATION

Corresponding Authors

*E-mail: nicolas.lepoul@univ-brest.fr

*E-mail: catherine.belle@univ-grenoble-alpes.fr

Notes

The authors declare no competing financial interest.

■ ACKNOWLEDGMENTS

Financial support by ANR-13-BSO7-0018 and COST action CM1003 including a STSM grant are acknowledged. This work has been carried out in the frameworks of Labex Arcane (ANR-11-LABX-003) and COST action CM1305 (ECOSTBio). The authors thank C. Calvarin and G. Leroux for the manufacturing of the cryospectroelectrochemical cell and F. Molton for EPR spectra.

■ REFERENCES

(1) Solomon, E. I.; Heppner, D. E.; Johnston, E. M.; Ginsbach, J. W.; Cirera, J.; Qayyum, M.; Kieber-Emmons, M. T.; Kjaergaard, C. H.; Hadt, R. G.; Tian, L. *Chem. Rev.* **2014**, *114*, 3659−3853.

(2) Lee, J. Y.; Karlin, K. D. *Curr. Opin. Chem. Biol.* **2015**, *25*, 184−193.

(3) Mirica, L. M.; Ottenwaelder, X.; Stack, T. D. P. *Chem. Rev.* **2004**, *104*, 1013−1046.

(4) Rolff, M.; Schottenheim, J.; Decker, H.; Tuczek, F. *Chem. Soc. Rev.* **2011**, *40*, 4077−4098.

(5) Citek, C.; Herres-Pawlis, S.; Stack, T. D. *Acc. Chem. Res.* **2015**, *48*, 2424−2433.

(6) Dalle, K. E.; Gruene, T.; Dechert, S.; Demeshko, S.; Meyer, F. *J. Am. Chem. Soc.* **2014**, *136*, 7428−7434.

(7) Kindermann, N.; Bill, E.; Dechert, S.; Demeshko, S.; Reijerse, E. J.; Meyer, F. *Angew. Chem., Int. Ed.* **2015**, *54*, 1738−1743.

(8) Lewis, E. A.; Tolman, W. B. *Chem. Rev.* **2004**, *104*, 1047−1076.

(9) Shiota, Y.; Yoshizawa, K. *Inorg. Chem.* **2009**, *48*, 838−845.

(10) Sirajuddin, S.; Rosenzweig, A. C. *Biochemistry* **2015**, *54*, 2283−2294.

(11) Culpepper, M. A.; Rosenzweig, A. C. *Crit. Rev. Biochem. Mol. Biol.* **2012**, *47*, 483−492.

(12) Halvagar, M. R.; Solntsev, P. V.; Lim, H.; Hedman, B.; Hodgson, K. O.; Solomon, E. I.; Cramer, C. J.; Tolman, W. B. *J. Am. Chem. Soc.* **2014**, *136*, 7269−7272.

(13) Davenport, T. C.; Tilley, T. D. *Angew. Chem., Int. Ed.* **2011**, *50*, 12205−12208.

DOI: 10.1021/acs.inorgchem.6b01504
Inorg. Chem. 2016, 55, 8263−8266

(14) Davenport, T. C.; Tilley, T. D. *Dalton Trans.* **2015**, *44*, 12244−12255.
(15) Farrugia, L. J.; Lovatt, P. A.; Peacock, R. D. *J. Chem. Soc., Dalton Trans.* **1997**, 911−912.
(16) Kodera, M.; Shimakoshi, H.; Tachi, Y.; Katayama, K.; Kano, K. *Chem. Lett.* **1998**, 441−442.
(17) Monzani, E.; Battaini, G.; Perotti, A.; Casella, L.; Gullotti, M.; Santagostini, L.; Nardin, G.; Randaccio, L.; Geremia, S.; Zanello, P.; Opromolla, G. *Inorg. Chem.* **1999**, *38*, 5359−5369.
(18) Lieberman, R. L.; Rosenzweig, A. C. *Nature* **2005**, *434*, 177−182.
(19) Ruiz, E.; Alemany, P.; Alvarez, S.; Cano, J. *Inorg. Chem.* **1997**, *36*, 3683−3688.
(20) Crawford, V. H.; Richardson, H. W.; Wasson, J. R.; Hodgson, D. J.; Hatfield, W. E. *Inorg. Chem.* **1976**, *15* (9), 2107−210.
(21) Zanello, P. *Inorganic electrochemistry: theory, practice and application*, 2nd ed.; Royal Society of Chemistry: Cambridge, U.K., 2003.
(22) Saveant, J.-M. *Elements of molecular and biomolecular electrochemistry: an electrochemical approach in electron transfer chemistry*; Wiley: Hoboken, NJ, 2006.
(23) Bard, A.; Faulkner, L. *Electrochemical Methods: Fundamentals and Applications*; Wiley: Hoboken, NJ, 2000; p 864.
(24) Connelly, N. G.; Geiger, W. E. *Chem. Rev.* **1996**, *96*, 877−910.
(25) The increase of *T* led to a broadening of the signal and a partial decomposition of the complex observable around 150−200K (Figure S15).
(26) Brunschwig, B. S.; Creutz, C.; Sutin, N. *Chem. Soc. Rev.* **2002**, *31*, 168−184.
(27) Winter, R. F. *Organometallics* **2014**, *33*, 4517−4536.
(28) Robin, M. B.; Day, P. *Adv. Inorg. Chem. Radiochem.* **1968**, *10*, 247−422.
(29) The OTf^- in interaction with Cu2, as observed in the solid state, was not taken into account for DFT calculations according to NMR.
(30) Konezny, S. J.; Doherty, M. D.; Luca, O. R.; Crabtree, R. H.; Soloveichik, G. L.; Batista, V. S. *J. Phys. Chem. C* **2012**, *116*, 6349−6356.
(31) Martin, R. L. *J. Chem. Phys.* **2003**, *118*, 4775−4777.

■ NOTE ADDED AFTER ASAP PUBLICATION

This paper was published on the Web on August 12, 2016, with errors to Table S1 in the Supporting Information. The corrected version was reposted on August 25, 2016.

DOI: 10.1021/acs.inorgchem.6b01504
Inorg. Chem. 2016, 55, 8263−8266

ChemPubSoc Europe

DOI: 10.1002/cplu.201600636

CHEMPLUSCHEM Full Papers

SPECIAL ISSUE

Characterization of a Dinuclear Copper(II) Complex and Its Fleeting Mixed-Valent Copper(II)/Copper(III) Counterpart

Amélie Kochem,*[a] Federica Gennarini,[b] Mehdi Yemloul,[a] Maylis Orio,[a] Nicolas Le Poul,[b] Eric Rivière,[c] Michel Giorgi,[d] Bruno Faure,[a] Yves Le Mest,[b] Marius Réglier,[a] and A. Jalila Simaan*[a]

In memory of T. Silviu Balaban

The synthesis of a dinuclear copper(II) complex, supported by a 1,3-diamino-2-propanol-based tetraamide ligand, is reported. Structural properties in the solid state and in solution, by means of XRD analysis and NMR spectroscopy, respectively, provide evidence of a highly flexible complex that can display several conformations, leading to the image of the wings of a butterfly. The complex was fully characterized and the redox properties were investigated. Room-temperature spectro-electrochemistry was used to monitor the formation of a metastable mono-oxidized product that displayed an absorption band centered at $\lambda = 463$ nm. EPR investigation of the low-temperature, chemically generated, mono-oxidized product reveals the presence of an intermediate described as a mixed-valent $Cu^{II}Cu^{III}$ species, which is a model of the possible highly oxidizing intermediate in particulate methane monooxygenase.

Introduction

In a time when our society needs to diversify its energy sources, the development of catalysts that can convert the greenhouse gas methane into methanol as alternative for traditional fuels is of major interest.[1] Currently, industrial methanol production from methane requires high temperatures and pressures. Thus, new processes for efficient methane oxidation into methanol at low temperatures need to be developed.[2] However, methane has the strongest C–H bond of any hydrocarbon (bond dissociation energy (BDE) = 104 kcal mol^{-1}) and its oxidation under mild conditions represents a major challenge in modern chemistry. On the other hand, in nature, methane monooxygenases (MMOs) accomplish the conversion of methane into methanol at ambient temperature and atmospheric pressure, allowing the harnessing of methane as an energy source for the synthesis of molecules required for life. MMOs exist as soluble and particulate forms.[3] The soluble form (sMMO) contains a diiron active site that achieves methane oxidation thanks to high-valent dinuclear bis(μ-oxo)$Fe^{IV}Fe^{IV}$ intermediate.[4,5] The particulate form (pMMO) is a membrane-bound enzyme that uses copper as a metallic cofactor, and the structure and mechanism of which are far less understood than those of the iron-containing sMMO.[6] X-ray crystallographic studies have shown that pMMO possesses several metal-binding sites.[7–9] Owing to moderate crystallographic resolution and low copper binding stoichiometry, the exact nature of the active site of pMMO is still a matter of controversy.[10,11] However, recent studies suggest that methane oxidation is achieved at a dinuclear copper center.[12,13] This active site was modeled as two copper ions located at a short Cu–Cu distance (2.5–2.7 Å) with one Cu ion bound by two histidine imidazoles and the other Cu bound by an imidazole and the amino group of the N-terminal histidine in a coordination motif named a histidine brace (Figure 1).

The mechanism and Cu_2/O_2 active species in methane oxidation are still under debate and different types of intermediates have been postulated as possible active species (Scheme 1).[14] In heterogeneous catalysis, copper-loaded zeolites (Cu-ZSM-5) were shown to produce methanol from methane at relatively low temperature (≈100 °C) with high selectivity through the formation of highly reactive (μ-oxo)Cu^{II}_2 (Cu_2O) intermediates; thus, these species are relevant for the pMMO catalytic cycle.[15] Synthetic Cu_2O species have been described, but their

[a] Dr. A. Kochem, Dr. M. Yemloul, Dr. M. Orio, Dr. B. Faure, Dr. M. Réglier, Dr. A. J. Simaan
Aix Marseille Université, CNRS
Centrale Marseille, iSm2
13397 Marseille (France)
E-mail: amelie.kochem@hotmail.fr
jalila.simaan@univ-amu.fr

[b] F. Gennarini, Dr. N. Le Poul, Dr. Y. Le Mest
Université de Bretagne occidentale
CEMCA, UMR CNRS, 6521 Brest (France)

[c] Dr. E. Rivière
Institut de Chimie Moléculaire et des Matériaux d'Orsay
Univ Paris Sud, Université Paris-Saclay, CNRS
91400 Orsay (France)

[d] Dr. M. Giorgi
Aix Marseille Université, CNRS
Spectropole FR1739, 13397 Marseille (France)

Supporting information and the ORCID identification number(s) for the author(s) of this article can be found under http://dx.doi.org/10.1002/cplu.201600636.

This article is part of the "Biofest" Special Issue. To view the complete issue, visit: https://doi.org/10.1002/cplu.v82.4.

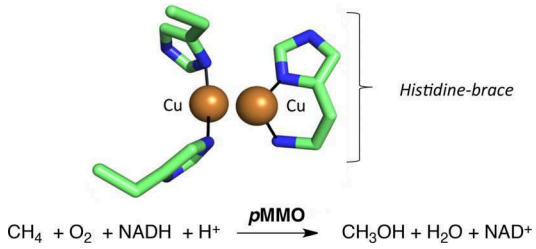

Figure 1. Structure of the dicopper active site of pMMO from *Methylococcus capsulatus* (Bath) and the reaction catalyzed by pMMO.

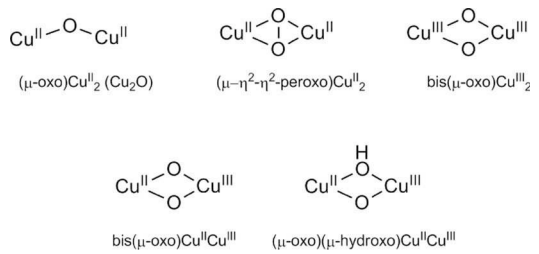

Scheme 1. Possible dicopper intermediates for methane oxidation at the pMMO active site.

ability to perform strong C–H bond oxidation has not yet been established.[16] Recently, theoretical calculations have shown that the dicopper site of pMMO can accommodate a (μ-η^2:η^2-peroxo)Cu$^{II}_2$ species, similar to that found in tyrosinase or hemocyanin.[17] Oxo-bridged high-valent bis(μ-oxo)Cu$^{III}_2$ species are able to perform various oxidation reactions, and have also been suggested as intermediates that may form during pMMO catalysis.[18] Stack and co-workers have shown that primary amine ligation reminiscent of the histidine brace motif provided greater stabilization to the bis(μ-oxo)Cu$^{III}_2$ intermediates without attenuation of their oxidizing power.[19] Finally, using computational analysis, Yoshizawa and co-workers suggested that mixed-valent Cu^{II}Cu^{III} species, such as bis(μ-oxo)Cu^{II}Cu^{III} or (μ-oxo)(μ-hydroxo)Cu^{II}Cu^{III} species, were more reactive towards C–H bonds than the bis(μ-oxo)Cu$^{III}_2$ species.[20–22] Their newer calculations suggested that methane oxidation in pMMO could be promoted by (μ-oxo)(μ-hydroxo)Cu^{II}Cu^{III} species that could arise from bis(μ-oxo)Cu^{III} after one-electron reduction followed by proton transfer from a nearby tyrosine residue.[22]

To the best of our knowledge, only two examples of synthetic mixed-valent Cu^{II}Cu^{III} species have been reported.[23,24] The group of Tolman reported the characterization of a hydroxo-bridged mixed-valent Cu^{II}Cu^{III} complex with a tetra-anionic macrocyclic ligand containing two pyridine(dicarboxamide) moieties. This intermediate was able to perform C–H bond activation of dihydroanthracene.[23] Recently, using a naphthyridyl-based ligand, Belle and co-workers generated a bis(hydroxo)-bridged mixed-valent Cu^{II}Cu^{III} species.[24] Because only two examples have been reported, a study of such mixed-valent complexes is of current interest to gain a deeper insight into their structure–function relationships. Herein, we report on the synthesis and characterization of a dinuclear copper

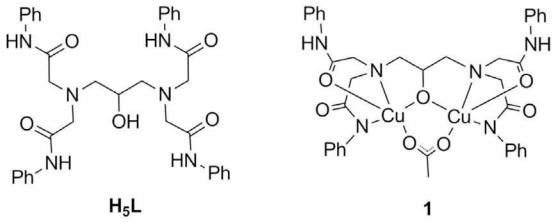

Scheme 2. Structures of the H_5L ligand and complex **1**.

complex based on a polydentate amide-containing ligand, H_5L (Scheme 2).

The choice of this ligand was driven by several features: 1) this kind of ligand is well known to accommodate two copper centers in close vicinity thanks to an alkoxo-bridging group;[25] 2) the coordination mode of this ligand should allow the incorporation of an exogenous bridging ligand or several nonbridging ligands; and 3) hard ligands, such as deprotonated amide groups, are well known to stabilize metal ions in their high oxidation states, such as Cu^{III}.[26] By using ligand H_5L, a dinuclear alkoxo- and acetato-bridged complex, $[(H_2L)Cu_2(OAc)](H_2O)_2$ (**1**), was prepared and characterized. Starting from complex **1**, we have focused on the generation and characterization of a new mixed-valent Cu^{II,III} dinuclear species by chemical and electrochemical oxidation.

Results and Discussion

Synthesis and X-ray crystallography

Ligand H_5L was obtained in high yield (87%), in one step, by the reaction of commercially available 2-chloro-*N*-phenylacetamide with 1,3-diamino-2-propanal. The metalation of H_5L was performed in methanol by using two equivalents of copper(II) acetate salt in the presence of Et_3N as a base to yield complex **1**. Two different X-ray crystal structures (**1a** and **1b)** were obtained from the crystallization of complex **1** by slow evaporation of a solution in either ethanol/dichloromethane/*N*,*N*-dimethylformamide (DMF) at room temperature (**1a**) or dichloromethane/DMF at 4 °C (**1b**). Crystals of **1a** were of good quality and allowed complete structure refinement and determination. On the contrary, data collected for **1b** provided a structure that was not refined according to standard crystallographic criteria and is therefore presented in Figure S1 in the Supporting Information. The ORTEP view of **1a** is depicted in Figure 2.

Compound **1a** is a binuclear complex in which the copper ions are bridged by the alkoxide group of the ligand and an acetate moiety. In both cases, the ligand was tri-deprotonated and two amide functions remained protonated. The equatorial positions of each copper are occupied by the nitrogen atom from deprotonated amide groups, the nitrogen and oxygen atoms of the ethanolamine moieties, and one oxygen atom from the bridging acetate ligand. The oxygen atoms from the pendant amide arms that remained protonated were found in the apical positions. Selected bond lengths and angles are listed in Table 1. The structural index calculated, as defined by Addison et al.,[27] was $\tau = 0.02$ for both Cu1 and Cu2, which in-

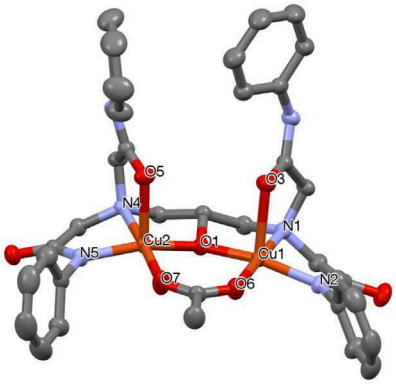

Figure 2. ORTEP representation (30% ellipsoid probability) obtained for the X-ray crystal structure of **1a**. Solvent molecules and hydrogen atoms were omitted for clarity.

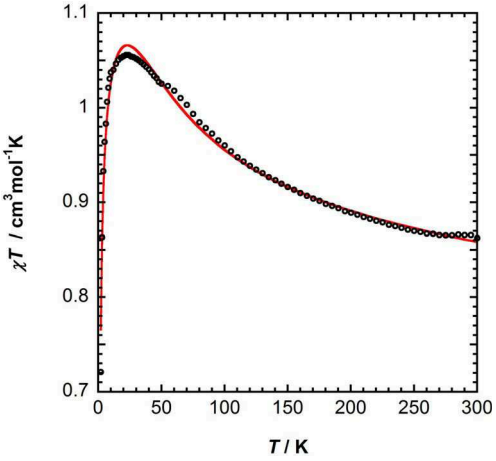

Figure 3. Temperature dependence of **1** in the solid state. Parameters from the fit: $J = 53.8\ cm^{-1}$, $g = 2.20$, $zJ' = -0.97\ cm^{-1}$, $C_{/Cu} = -60.6.10^{-6}\ cm^3 mol^{-1}$ goodness of fit $R = 7.6.10^{-5}$. C is the diamagnetic contribution.

Table 1. Selected bond lengths [Å] and angles [°] for **1a**.

Cu1–O1	1.9225(17)	O1-Cu1-O6	96.12(8)
Cu1–O6	1.937(2)	O1-Cu1-N1	83.89(8)
Cu1–N1	2.064(2)	N1-Cu1-N2	82.78(9)
Cu1–N2	1.963(2)	N2-Cu1-O6	96.12(9)
Cu1–O3	2.3359(18)	O3-Cu1-O1	90.78(7)
Cu2–O1	1.9022(18)	O3-Cu1-N1	79.18(7)
Cu2–O7	1.931(3)	O1-Cu2-O7	95.92(9)
Cu2–N4	2.095(2)	O1-Cu2-N4	85.31(8)
Cu2–N5	1.935(2)	N4-Cu2-N5	83.59(8)
Cu2–O5	2.2257(18)	N5-Cu2-O7	94.09(9)
		O5-Cu2-N4	80.44(7)
		O5-Cu2-N5	98.23(8)

dicated that the copper ions were in square-pyramidal geometries. The structure of **1b** is very similar to that of **1a**. Although the main geometric features are generally similar in both cases, one striking difference is observed in the distances between the two apical arms (materialized by distance O5–O3) and the two equatorial amide arms (materialized by distance N5–N2). The O5–O3 distance is elongated in **1b** compared with that in **1a**. Meanwhile, the N5–N2 distance is shortened in **1b** relative to that in **1a**, whereas the Cu1–Cu2 distance remains very similar. These two structures possibly describe two limiting conformations adopted by **1**—closed (**1a**) and open (**1b**)—leading to the image of a complex resembling a butterfly flapping its wings.

Magnetic properties

Magnetic susceptibility measurements were performed for **1** both in the solid state (crystals of **1a**) and in DMF. In the solid state, the temperature dependence of the product of the molar susceptibility and temperature, χT, shows a typical profile of ferromagnetic coupling interactions (Figure 3). The rapid decrease of χT below 20 K may be due to intermolecular antiferromagnetic interactions.[28] The data could be fitted by using a model for two coupled spins ($S = 1/2$) described by the spin-Hamiltonian $\mathbf{H} = -J\mathbf{S}_1\mathbf{S}_2$ and with the use of an additional mean field approximation to reproduce intermolecular interactions. Parameter optimization yielded a coupling constant of $J = 53.8\ cm^{-1}$ with $g = 2.20$. Other μ-alkoxo-μ-monocarboxylato dinuclear copper(II) complexes have been structurally and magnetically studied in the literature, allowing the establishment of magnetostructural correlations.[28–30] From these studies, a Cu1-O1-Cu2 angle (θ) greater than 116.5°, as it is the case in **1** (127.54°), should lead to an antiferromagnetic coupling, whereas ferromagnetism appears for smaller values of θ.[28] However, complex **1** exhibits a significant roof-shaped distortion, which is measured by the dihedral (δ) angle between two copper coordination planes (4.64° in **1a**), as well as a significant out-of-plane displacement of the carbon atom of the alkoxo group with respect to the Cu1-O1-Cu2 plane (0.76 Å in **1a**).[31,32] These factors suppress antiferromagnetic interactions, leading to ferromagnetic coupling, and may explain that ferromagnetic coupling prevails in **1**. Surprisingly, magnetic susceptibility measurements performed for **1** in DMF (Figure S3 in the Supporting Information) lead to different results, that is, small antiferromagnetic coupling ($J = -3.1\ cm^{-1}$). The switch from ferro- to antiferromagnetic coupling in solution might, however, be the result of a small geometric rearrangement, in particular around the alkoxo-bridging motif.

Studies of 1 in DMF

To obtain a better picture of the structure of **1** in DMF, we first performed mass spectrometry analysis. The ESI-MS spectrum of **1** in DMF/MeOH (Figure S2 in the Supporting Information) exhibits two fragments centered at *m/z* 805.1466 and 827.1285, which are assigned to $[M+H]^+$ and $[M+Na]^+$, respectively; this suggests that **1** retains its coordination sphere in DMF, including the bridging acetate moiety.

NMR spectroscopy studies of **1** in deuterated DMF were also performed. ^1H NMR spectra of **1** and of the sodium acetate salt were recorded in deuterated DMF. A comparison of the two spectra allows us to conclude that no resonance attributed to

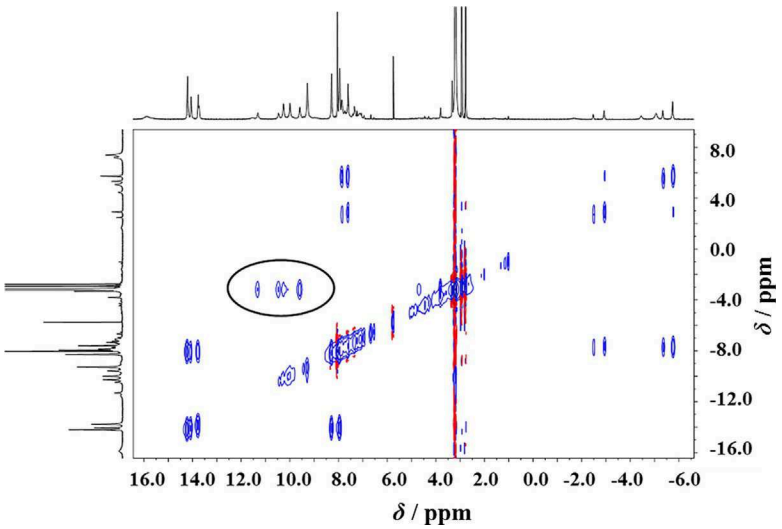

Figure 4. NOESY spectrum of **1** in [D_7]DMF at 343 K. Cross peaks in the black circle correspond to the correlation between protons from protonated amide arms and residual water molecules.

free acetate, which could have been released in solution, are detected (Figures S4 and S5 in the Supporting Information); this supports the fact that acetate is maintained in the coordination sphere of the copper ions, as already suggested by ESI-MS experiments. The ^{1}H NMR spectrum of **1** is rather complicated with numerous resonances (33 resonances detected) over a large range of chemical shifts from $\delta = +25$ to -10 ppm, as expected for a paramagnetic compound (Figure S4 in the Supporting Information).[33,34] The numerous resonances detected are consistent with the presence of several conformers in solution. To further investigate the behavior of the complex in DMF, 2D ^{1}H NMR spectroscopy experiments were performed. The NOESY spectrum of **1** at 343 K (Figure 4) exhibits four cross peaks ($\delta = 11.33$, 10.48, 10.27, and 9.60 ppm) attributed to the correlation between labile protons from the protonated amide arms of **1** and residual water molecules (cross peaks in the black circle). These results suggest that two to four different conformations for complex **1** coexist in solution, possibly a mixture between asymmetric conformations that display two inequivalent protonated amide arms for each conformation and/or different symmetric conformations. Integration of the resonances attributed to the NH amide groups of the different conformers based on NOESY experiments gives a ratio of 1:1:1:2 at 343 K. Similar ratios for different conformers were determined in the temperature range of 273 to 343 K and no equilibrium between the different conformers could be detected in this temperature range (Figure S6 and Table S1 in the Supporting Information). These results suggest that at least three different conformers coexist in solution at room temperature and at higher temperatures. As already observed in the solid state, the ligand provides great flexibility around the dicopper center. The two limiting conformations characterized in the solid state display different conformations of protonated amide arms. It is therefore not surprising that different conformations of these pendant amide arms can also be found in solution, without significantly altering the dicopper core. Finally, DOSY ^{1}H NMR spectroscopy experiments were performed to evaluate the diffusion coefficient of **1**, which was calculated as the average of the *D* values determined for each signal attributed to the different conformers (Figure S7 in the Supporting Information). The mean *D* value for **1** is 5.4×10^{-10} m^2 s^{-1} at 293 K.

Electrochemical studies

Cyclic voltammetry (CV) of **1** was performed in DMF in the presence of 0.1 M NBu_4PF_6 under argon and at room temperature. All potentials are referenced versus the ferrocene (Fc^+/Fc) redox couple. As shown in Figure 5, an oxidation peak is detected at $E_{pa}(1) = 0.63$ V at a scan rate $v = 0.1$ V s^{-1}. It is fully irreversible over the investigated scan-rate range (0.005 V s^{-1} < v < 30 V s^{-1}) and even at low temperature (−40 °C). This oxidation peak is associated with several reduction peaks on the reverse scan (Figure 5 and Figure S8 in the Supporting Information). The sharp oxidation peak at −0.25 V on the reverse scan can

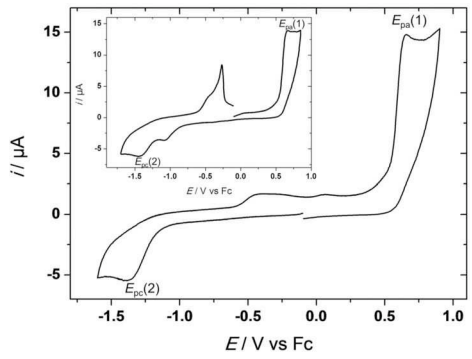

Figure 5. CV results at a glassy carbon electrode of complex **1** (0.50 mM) in DMF/NBu_4PF_6 0.1 M under argon at $v = 0.1$ V s^{-1}, negative scanning; inset: $v = 0.1$ V s^{-1}, positive scanning.

be ascribed to dissolution of an electrogenerated copper(0) complex. When scanning towards negative potentials, a single reduction peak is detected at $E_{pc}(2) = -1.34$ V versus Fc^+/Fc, whereas several oxidation peaks associated with the reduction process are observed on the reverse scan between −0.6 and 0.2 V (Figure 5 and Figure S9 in the Supporting Information). Room-temperature exhaustive electrolysis in either oxidation or reduction leads to the degradation of electrochemically oxidized or reduced complexes. The bulk electrolysis timescale is approximately an hour, so the observed degradation is not surprising.

Plots of anodic or cathodic peak currents ($i_{pa}(1)$ and $i_{pc}(2)$, respectively) versus $v^{1/2}$ follow linear variations, as expected for a diffusion-controlled electrochemical process (Figures S10 in the Supporting Information).[35] The dependence of the current intensity, i_p, versus $v^{1/2}$ was used to determine the number of electrons exchanged in the redox processes (n). This was performed by assuming a simple electrochemical–chemical (EC) mechanism to account for irreversibility, knowing the value of the diffusion coefficient from DOSY experiments ($D = 5.4 \times 10^{-6}$ $cm^2 s^{-1}$). Calculations give $n = 0.9$ and 1.6 for the cathodic and anodic processes, respectively.[36] In agreement with CV studies that show that free acetate can be oxidized irreversibly at $E_{pa}(3) = 0.78$ V versus Fc^+/Fc under the same experimental conditions (Figure S11 in the Supporting Information), it seems likely that the oxidation of complex **1** at $E_{pa}(1)$ leads to fast release of acetate and possible binding of DMF solvent (Scheme 3). In that case, acetate can itself be oxidized when scanning positively beyond $E_{pa}(3)$. As a result, the number of electrons involved in the oxidation process is greater than one. Hence, these voltammetric studies strongly suggest that complex **1** can be reduced or oxidized in a monoelectronic manner, and that the oxidation process induces fast chemical unbinding of acetate. Notably, unbinding of acetate before oxidation of **1** can be excluded on the basis of previously mentioned ESI-MS and NMR spectroscopy experiments. Thus, the redox behavior of **1** is somewhat similar to those obtained with analogous dinuclear hydroxo-bridged copper(II) complexes that can also be oxidized in a monoelectronic manner.[23,24] The potential required for the oxidation of **1** ($E_{pa} = 0.63$ V) lies between those found for naphthyridine- ($E^0 = 1.26$ V) and pyridine(dicarboxamide)-based ($E^0 = 0.18$ V) dinuclear complexes. By assuming similar donor properties for acetate and hydroxo bridging groups, such differences can be correlated to the charge of the resulting complexes (neutral for **1**, dicationic for the naphthyridine-based complex, and monoanionic for macrocycle-based species).

Characterization of one-electron oxidized species 1^+

Spectro-electrochemical experiments were performed at room temperature for the UV/Vis spectroscopic characterization of the transient oxidized species 1^+ generated by electrochemistry. The 3D spectroscopic response of the complex obtained by thin-layer cyclic voltammetry (TLCV) upon oxidation is displayed in Figure 6.

Three zones can be drawn from the experimental data. Before oxidation, complex **1** displays two absorption bands at $\lambda_{max} = 711$ (d–d transition) and 380 nm (charge transfer (CT)). When oxidation starts ($t > 150$ s), both bands decrease in intensity and a new transition appears in the $\lambda = 400$–500 nm wavelength range (Figure 7B). A maximum absorption is reached for this newly formed band at $t = 220$ s. Differential superposition of the spectra indicates that a maximal absorption is obtained at $\lambda_{max} = 463$ nm (Figure 7C). Beyond 220 s, this band decreases, showing the transient character of the generated oxidized species (Figures 6 and 7D). Reverse cycling toward negative potential ($t > 260$ seconds) shows a slight increase of the d–d band at $\lambda = 711$ nm, but without reaching the initial absorbance level (Figure 6), as expected from the irreversible character of the TLCV. These results indicate that oxidation is likely to occur on one copper center because the d–d transi-

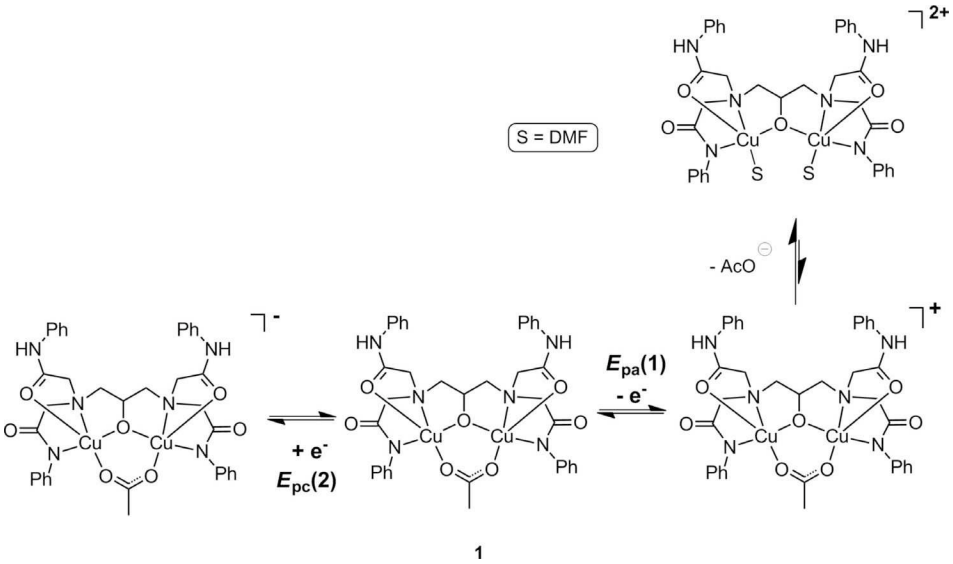

Scheme 3. Proposed redox pathways for complex **1** from voltammetric data.

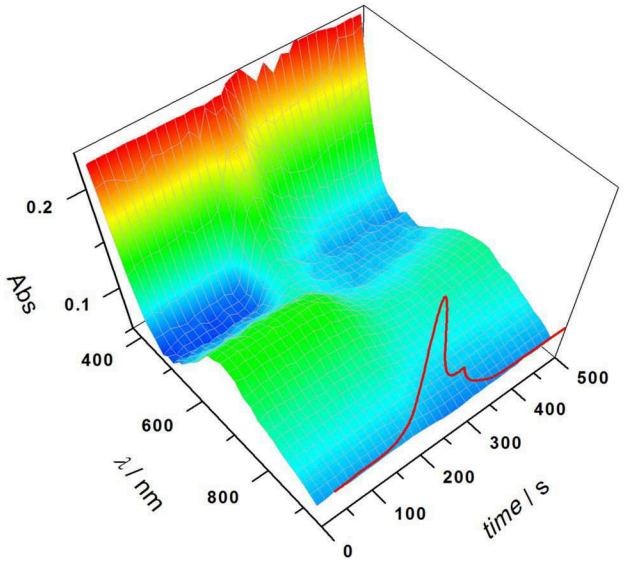

Figure 6. Room-temperature 3D UV/Vis spectroscopic monitoring of electrochemical oxidation of complex **1** (0.50 mM) in DMF/NBu_4PF_6 (0.1 M) under argon and at a glassy carbon electrode (optical path 0.2 mm); red curve: corresponding TLCV results ($v = 5$ mV s^{-1}).

tion is affected by the electron-transfer reaction. The generated species, which displays an absorption band at $\lambda = 463$ nm, is transiently stable for several seconds at room temperature before decaying into a new species.

To further investigate $\mathbf{1}^+$, EPR experiments were performed. Complex **1** is EPR silent (X-band, 120 K). Oxidation of the neutral complex **1** was performed in CH_2Cl_2/DMF (9/1) at −60 °C by adding $NOSbF_6$ (1 equiv) as a one-electron oxidant. The chemical generation of $\mathbf{1}^+$ causes the appearance of a transient EPR signal. The 120 K continuous-wave (CW) X-band EPR spectrum of unstable species $\mathbf{1}^+$ is depicted in Figure 8. The EPR signal of $\mathbf{1}^+$ quickly decreases after a few minutes at −60 °C to completely disappear; this is consistent with the unstable character of the oxidized species and in agreement with the electrochemical studies. The maximum intensity of the signal accounts for approximately 20% of intensity, as referenced to the initial concentration of **1**. The spectrum of $\mathbf{1}^+$ displays a typical $S = 1/2$ axial signal with a four-line pattern in the $g_{\|}$ region consistent with hyperfine interaction with only one Cu^{II} ion, and therefore, with a valence-localized $Cu^{II}Cu^{III}$ species, as observed for the two previously reported complexes.[23,24] The simulation parameters indicate a dominant $d_{x^2-y^2}$ electronic ground state and are consistent with a copper(II) ion bound axially to two nitrogen atoms and one or two oxygen-containing ligands ($g_{\|} = 2.356$ and $A_{\|}(Cu) = 126$ G).[37,38] The expanded second derivative of the perpendicular region of the EPR spectrum of $\mathbf{1}^+$ is also shown in Figure 8 (inset). It reveals the presence of superhyperfine lines that result from the interaction between one nitrogen nucleus ($I = 1$) from the first coordination sphere and the single unpaired electron ($S = {}^1/_2$) of the copper(II) ion, providing a coupling constant of $A_N = 16.8$ G. This relatively strong superhyperfine interaction indicates that the copper(II) ion interacts with an axially bound nitrogen (most likely the deprotonated amide ligand),[39] and that only a small deviation from planarity is expected. This strongly sup-

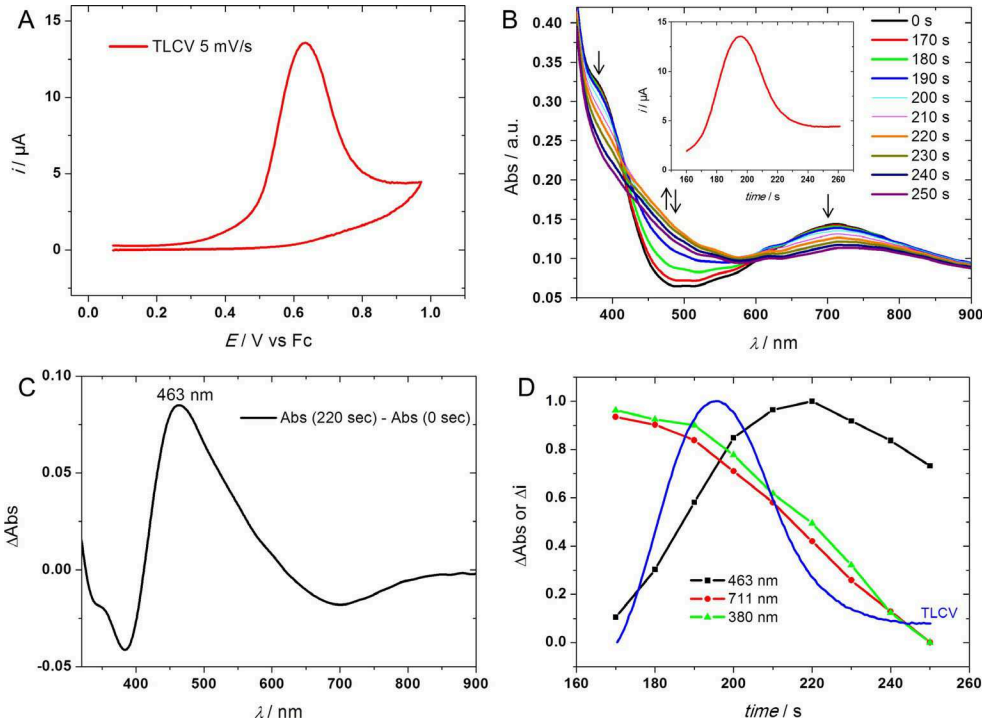

Figure 7. A) Room-temperature TLCV results ($v = 5$ mV s^{-1}) at a glassy carbon electrode of **1** (0.50 mM) in DMF/NBu_4PF_6 (0.1 M) under argon. B) 2D UV/Vis spectra of complex **1** after TLCV experiments (5 mV s^{-1}); inset: variation of current with time during CV. C) UV/Vis differential spectrum at $\lambda = 463$ nm between $t = 220$ 0 s. D) Plots of relative absorbance versus time during spectro-electrochemical measurements at different wavelengths: $\lambda = 463$ (black), 711 (red), and 380 nm (green). Blue curve: corresponding TLCV results (5 mV s^{-1}).

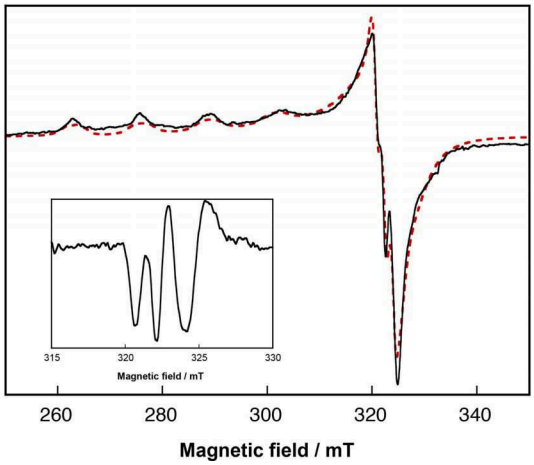

Figure 8. X-band EPR spectrum of a 0.5 mM solution of chemically generated 1^+ at −60 °C in CH_2Cl_2 + 10% DMF. Solid line: experimental spectrum, dotted red line: simulation. Parameters: $g_z = 2.356$, $g_y = 2.058$, $g_x = 2.058$, $A_{||}(Cu) = 126$ G, $A_{\perp}(^{14}N) = 16.8$ G; inset: derivative spectrum. Experimental conditions: microwave frequency = 9.31 GHz, microwave power = 20 mW, modulation amplitude = 0.3 mT, $T = 120$ K.

ports the fact that the overall structure of the complex is maintained in solution. Altogether, the EPR data indicate a localized mixed-valent $Cu^{II}Cu^{III}$ formulation for 1^+.

DFT calculations

DFT calculations were performed to propose a structure for the oxidized form of **1**. Different structures, with or without the acetate moiety, were computed: a structure similar to the starting complex with the bridging acetate ligand (form a), a structure with the acetate bound in a monodentate fashion on one copper (b), a structure with one DMF on one copper and one monodentate acetate ligand on the other copper (form c), and a structure with one monodentate DMF bound on one copper (form d; Figure 9 and Figure S12 in the Supporting Information). Singly occupied molecular orbitals (SOMOs) were calculated for different optimized forms of 1^+. The SOMOs of oxidized forms a, c, and d of **1** were all found on both copper centers and on one phenyl moiety of the ligand (Figure S13 in the Supporting Information). These data are not in agreement with the experimental description of 1^+ as a localized mixed-valent intermediate.

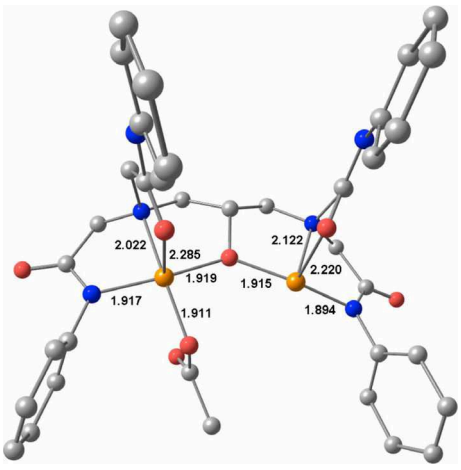

Figure 9. DFT-optimized structure and selected parameters for the relevant oxidized form of **1** (form b).

The oxidized form of **1**, including one monodendate acetate ligand (form b), is the only structure that provided a localized mixed-valent $Cu^{II}Cu^{III}$ species (Figure 9). This structure could be formed upon oxidation of **1** before complete acetate release and DMF binding. This assignment is supported by the spin density plot and the SOMO that are found mainly on one copper center (Figure 10). The SOMO, located on the Cu^{II} center, displays a dominant Cu $3d_{x^2-y^2}$ character, which is in agreement with the experimental EPR spectrum. In addition, time-dependent DFT calculations were performed to predict the UV/Vis spectrum (Figure S14 in the Supporting Information). A ligand-to-copper(III) transition is predicted at $\lambda \approx 457$ nm (Figure S15 in the Supporting Information), which is in fair agreement with the observed transition at $\lambda = 463$ nm during spectro-electrochemistry experiments.

Altogether, our data indicate that form b of 1^+ can account for the experimentally observed properties of the intermediate, and therefore, represents a possible structure for the mixed-valent $Cu^{II}Cu^{III}$ species.

Conclusion

We have shown that the use of polydentate amide-containing ligand, such as H_5L, provides a high flexibility of the corresponding dicopper complex, which can adopt several conformations in both the solid state and solution. The presence of amide ligands favors the formation of the copper(III) redox state and spectroscopic characterizations of the mono-oxidized complex indicate the formation of a mixed-valent $Cu^{II}Cu^{III}$ species. DFT calculations were performed to propose a possible structure for this intermediate. To date, this study represents the third example of characterization of such mixed-valent species generated from bridged dicopper complexes. Interestingly, because replacement of the acetate bridge is possible and acetate seems to unbind from copper upon oxidation, further studies will aim to stabilize the mono-oxidized species through suitable ligand design. The development of new $Cu^{II}Cu^{III}$ complexes with different bridges/cores will be coupled to catalytic studies for the activation of C–H bonds, as mimics of the pMMO metalloenzyme active site.

Experimental Section

General

The solvents used for chemical reactions, electrochemistry, and spectroscopic characterization were purified by using the solvent purification system Innovative Technology PS-MD-5. The supporting electrolyte, NBu_4BF_4, was synthesized from NBu_4OH (Acros) and HPF_6 (Aldrich). It was dried under vacuum for 48 h at 100 °C then kept under argon in a glove box. Microanalysis was performed on an Elementar Thermo Finnigan EA 1112 instrument. ^1H NMR spectra

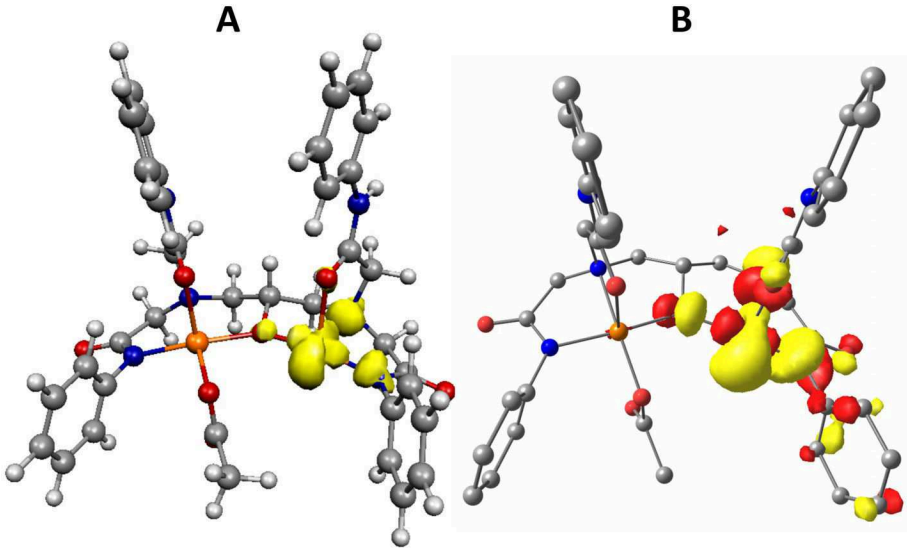

Figure 10. A) Spin density plot and B) localized SOMO for the relevant oxidized form of **1**.

were recorded at room temperature by using a Brucker-Avance III Nanobay spectrometer operating at 300 MHz. A Bruker Avance III spectrometer operating at 600MHz, equipped with a variable-temperature control unit and a triple resonance high-resolution probe producing gradients with a maximum strength of 60 G cm^{-1}, was used for the collection of 1D, 2D, and DOSY NMR spectra of complex **1** at the required temperature. All chemical shifts are given relative to the residual solvent signal ($CHCl_3$: $\delta = 7.26$ ppm). Standard DOSY spectra were recorded by a conventional pulse sequence, based on the stimulated echo and incorporated bipolar gradient pulses and an eddy-current delay (BPP-LED);[40,41] the diffusion delay (Δ) was set at 25 ms, the gradient strength (g) was linearly incremented in 32 steps from 2 to 9% of its maximum value, and 8 scans were recorded for each experiment.

ESI-MS analyses were performed by using a SYNAPT G2 HDMS (Waters) spectrometer equipped with a pneumatically assisted atmospheric pressure ionization (API) source. Samples were ionized by positive electrospray mode as follows: ion-spray voltage: 2.8 kV; orifice lens: 60 and 80 V for H_5L and **1**, respectively; nitrogen flux (nebulization): 100 L h^{-1}. HRMS was performed on a QStar Elite (Applied Biosystems SCIEX) spectrometer equipped with a pneumatically assisted API source. Complex **1** was placed in a solution of methanol/DMF/0.1 mM sodium chloride, and H_5L was placed in a solution of methanol/3 mM sodium acetate. All measurements were performed in triplicate. UV/Vis spectra were recorded on a Varian Cary 50 spectrophotometer. CW X-band EPR measurements were conducted at 120 K in frozen solution by using a BRUKER ELEXSYS E500 instrument equipped with a digital temperature controller (80–300 K). Simulations with automatic parameter fitting were performed for axial symmetry.[42]

Synthesis of H_5L

1,3-Diamino-2-propanol (0.34 g, 3.8 mmol) was dissolved in DMF (60 mL) and 2-chloro-*N*-phenylacetamide (2.58 g, 15.2 mmol), NaI (1.14 g, 7.6 mmol), and $NaHCO_3$ (1.28 g, 15.2 mmol) were added. The resulting suspension was stirred at room temperature overnight. The solvent was removed until dryness. The product was then extracted with chloroform and washed three times with water (40 mL). The organic phase was dried over Na_2CO_3. The product was washed with diethyl ether (3×30 mL) and dried under vacuum to give a white powder (2.05 g, 87%). ^{1}H NMR (300 MHz; $CDCl_3$): $\delta = 9.54$ (s, 4H), 7.55 (d, $J = 7.8$ Hz, 8H), 7.19 (t, $J = 7.8$ Hz, 8H), 7.05 (t, $J = 7.4$ Hz, 4H), 3.87 (m, 1H), 3.60–3.30 (m, 8H), 2.71 (d, $J = 13.0$ Hz, 2H), 2.46 ppm (m, 2H); HRMS (ESI): *m/z* calcd for $C_{35}H_{39}N_6O_5^+$ $[M+H]^+$: 623.2976; found: 623.2979.

Synthesis of 1

$Cu(OAc)_2$ (0.17g, 0.87 mmol) in EtOH (10 mL) and Et_3N (0.30 µL, 2.16 mmol) were added sequentially to a solution of H_5L (0.27 g, 0.43 mmol) in EtOH (4 mL). The solution turned green and was stirred at RT overnight. A blue precipitate was collected by filtration, washed with diethyl ether (10 mL), and dried under vacuum (0.273 g, 75%). HRMS (ESI): *m/z* calcd for $C_{37}H_{39}N_6O_7Cu_2$ $[M+H]^+$: 805.1467; found: 805.1466; calcd for $C_{37}H_{38}N_6O_7Cu_2Na$ $[M+Na]^+$: 827.1286; found: 827.1285; elemental analysis calcd (%) for $C_{37}H_{42}Cu_2N_6O_9$: C 52.79, H 5.03, N 9.98; found: C 52.50, H 4.76, N 9.97.

Magnetic properties

Magnetic measurements were performed with a Quantum Design SQUID magnetometer with an applied field of 1000 *G*. The independence of the susceptibility value with regard to the applied field was checked at room temperature. The powder sample was measured in a gelatin capsule. For solution measurements, the frozen sample (molar concentration 4.5×10^{-2} mol L^{-1}) was sealed under vacuum in a quartz glass tube. To avoid artifacts, this sample holder was symmetrized with another quartz glass tube.[43] The susceptibility data were corrected for the sample holder recorded under the same conditions and diamagnetic contributions, as calculated from tables of Pascal's constants.

The data were fitted by using a model for two coupled spins ($S = 1/2$) described by the spin-Hamiltonian $\mathbf{H} = -J\mathbf{S}_1\mathbf{S}_2$. An additional mean field approximation was added to reproduce intermolecular interactions: $\chi T = [\chi_{dimer}/(1 - zJ'\chi_{dimer}/Ng^2\beta^2) + C]T$, in which C was

a diamagnetic contribution. The error in the fit was calculated from the following expression, in which χ_{exptl} and χ_{calcd} were the observed and calculated magnetic susceptibilities, respectively: $R = \Sigma(\chi T_{calcd} - \chi T_{exptl})^2 / \Sigma(\chi T_{exptl})^2$.

X-ray crystallographic data collection and refinement of the structures

Single crystals were grown by slow evaporation of a concentrated solution of compound **1** in either ethanol/dichloromethane/DMF (1/1/1; conformer **1a**) or dichloromethane/DMF (9/1; conformer **1b**). The intensity data for both compounds were collected at 293 K on a Rigaku Oxford Diffraction SuperNova diffractometer by using $Cu_{K\alpha}$ radiation ($\lambda = 1.54184$ Å). Data collection, cell refinement, and data reduction were performed with CrysAlisPro (Rigaku Oxford Diffraction). By using Olex2,[44] the structures were solved with ShelXS[44] by using direct methods and refined with the ShelXL[45] refinement package by using least-squares minimization. Unfortunately, crystals of **1b** were not suitable to complete a good structure refinement, despite the fact that the main features of the complex could be characterized without ambiguities. Both forms cocrystallized with solvent molecules: one ethanol and one water molecule for **1a**; two dichloromethane and several highly unidentified disordered solvent molecules for **1b**. The hydrogen atoms were found experimentally for **1a** and were refined with riding coordinates to their parent atoms and with their U_{iso} parameters fixed to 1.2 U_{eq}(parent atom) for the C(H) and C(H,H) groups and to 1.5 U_{eq}(parent atom) for the C(H,H,H) groups. The crystallographic data for **1a** are reported in Table 2.

CCDC 1521875 contains the supplementary crystallographic data for this paper. These data are provided free of charge by The Cambridge Crystallographic Data Centre.

Table 2. Crystallographic data for compound **1a**.

formula	$C_{39}H_{46}Cu_2N_6O_9$
M_r [g mol^{-1}]	869.9
crystal system	monoclinic
space group	$P2_1/c$
a [Å]	16.4055(2)
b [Å]	20.8433(2)
c [Å]	12.38931(17)
β [°]	106.4933(14)
V [Å^3]	2069.83(12)
Z	4
λ [Å]	1.54184
ρ_{calcd} [g cm^{-3}]	1.422
crystal size [mm^3]	0.18×0.1×0.03
color	blue
T [K]	293(2)
μ [mm^1]	1.797
unique data, parameters	8238, 511
no. observed reflns ($F^2 > 4\sigma F^2$)	6776
R_1 ($F^2 > 4\sigma F^2$)	0.0409
R_2 (all reflns)	0.0509
wR_1[a] ($F^2 > 4\sigma F^2$)	0.1057
wR_2[a] (all reflns)	0.1134
GoF	1.021
residual Fourier [e Å^{-3}]	−0.181; 0.636
CCDC	1521875

[a] $w = 1/[\sigma^2(F_o^2) + (0.0578P)^2 + 1.2308P]$, in which $P = (F_o^2 + 2F_c^2)/3$.

Electrochemical studies

Electrochemical studies of the copper complex were performed in a glove box (Jacomex) ($O_2 < 1$ ppm, $H_2O < 1$ ppm) with a home-designed three-electrode cell (working electrode (WE): glassy carbon, reference electrode (RE): Pt wire in a solution of Fc^+/Fc, counter electrode (CE): Pt or graphite rod). The cell potential was controlled by using an AUTOLAB PGSTAT 100 (Metrohm) potentiostat monitored by the NOVA software. Extra-dry DMF (Acros) was stored in the glove box and used as received. Electrolysis was performed with a home-designed three-electrode cell (WE: Graphite rod, RE: Pt wire in a Fc^+/Fc solution, CE: graphite rod). Thin-layer room-temperature UV/Vis spectro-electrochemistry was performed with a specific home-designed cell in reflectance mode (WE: glassy carbon, RE: Pt wire, CE: Pt wire). The UV/Vis optical fiber probe was purchased from Ocean Optics. Time-resolved UV/Vis/near-IR detection was performed with a QEPro spectrometer (Ocean optics).

DFT calculations

All theoretical calculations were performed with the ORCA program package.[46] Full geometry optimizations were undertaken for all complexes by using the GGA functional BP86[47] and by taking advantage of the resolution of the identity (RI) approximation in the Split-RI-J variant[48] with the appropriate Coulomb fitting sets[49] Scalar relativistic effects were included with ZORA paired by using the SARC def2-TZVP(-f) basis sets[50,51] and the uncontracted def2-TZVP/J Coulomb fitting basis sets for all atoms. Increased integration grids (Grid4 and GridX4 in ORCA convention) and tight self-consistent field (SCF) convergence criteria were used. Electronic structures and molecular orbital diagrams were obtained from single-point calculations by using the hybrid functional B3LYP.[52] Increased integration grids (Grid4 and GridX4 in ORCA convention) and tight SCF convergence criteria were used in the calculations. In accordance with experimental conditions, solvent effects were accounted for and we used DMF as a solvent ($\varepsilon = 37$) within the framework of the conductor-like screening (COSMO) dielectric continuum approach.[53] Optical properties were also predicted from additional single-point calculations by using the hybrid functional B3LYP. Electronic transition energies and dipole moments for all models were calculated by using time-dependent DFT[54] within the Tamm–Dancoff approximation.[55] To increase computational efficiency, the RI approximation[56] was used to calculate the Coulomb term, and at least 30 excited states were calculated in each case. For each transition, difference density plots were generated by using the ORCA plot utility program and were visualized with the Chemcraft program.[57]

Acknowledgements

We acknowledge the French Research Agency (COMEBAC/ ANR-13-BS-0070-0018-01) for financial support.

Keywords: bioinorganic chemistry · copper · electrochemistry · enzyme models · mixed-valent species

[1] G. A. Olah, *Angew. Chem. Int. Ed.* **2005**, *44*, 2636–2639; *Angew. Chem.* **2005**, *117*, 2692–2696.

[2] R. A. Periana, G. Bhalla, W. J. Tenn, K. J. H. Young, X. Y. Liu, O. Mironov, C. J. Jones, V. R. Ziatdinov, *J. Mol. Catal. A* **2004**, *220*, 7–25.

[3] a) S. Sirajuddin, A. C. Rosenzweig, *Biochemistry* **2015**, *54*, 2283 – 2294; b) M. O. Ross, A. C. Rosenzweig *J. Biol. Inorg. Chem.*, DOI: 10.1007/s00775-016 – 1419-y.
[4] R. Banerjee, Y. Proshlyakov, J. D. Lipscomb, D. A. Proshlyakov, *Nature* **2015**, *518*, 431 – 434.
[5] P. K. Grzyska, E. H. Appelman, R. P. Hausinger, D. A. Proshlyakov, *Proc. Natl. Acad. Sci. USA* **2010**, *107*, 3982 – 3987.
[6] E. I. Solomon, D. E. Heppner, E. M. Johnston, J. W. Ginsbach, J. Cirera, M. Qayyum, M. T. Kieber-Emmons, C. H. Kjaergaard, R. G. Hadt, L. Tian, *Chem. Rev.* **2014**, *114*, 3659 – 3853.
[7] R. L. Lieberman, A. C. Rosenzweig, *Nature* **2005**, *434*, 177 – 182.
[8] A. S. Hakemian, K. C. Kondapalli, J. Telser, B. M. Hoffman, T. L. Stemmler, A. C. Rosenzweig, *Biochemistry* **2008**, *47*, 6793 – 6801.
[9] S. M. Smith, S. Rawat, J. Telser, B. M. Hoffman, T. L. Stemmler, A. C. Rosenzweig, *Biochemistry* **2011**, *50*, 10231 – 10240.
[10] S. I. Chan, S. S.-F. Yu, *Acc. Chem. Res.* **2008**, *41*, 969 – 979.
[11] R. A. Himes, K. Barnese, K. D. Karlin, *Angew. Chem. Int. Ed.* **2010**, *49*, 6714 – 6716; *Angew. Chem.* **2010**, *122*, 6864 – 6866.
[12] R. Balasubramanian, S. M. Smith, S. Rawat, L. A. Yatsunyk, T. L. Stemmler, A. C. Rosenzweig, *Nature* **2010**, *465*, 115 – 119.
[13] M. A. Culpepper, G. E. Cutsail III, W. A. Gunderson, B. M. Hoffman, A. C. Rosenzweig, *J. Am. Chem. Soc.* **2014**, *136*, 11767 – 11775.
[14] D. A. Quist, D. E. Diaz, J. J. Liu, K. D. Karlin, *J. Biol. Inorg. Chem.*, DOI: 10.1007/s00775-016 – 1415-2.
[15] J. S. Woertink, P. J. Smeetsa, M. H. Groothaert, M. A. Vance, B. F. Sels, R. A. Schoonheydt, E. I. Solomon, *Proc. Natl. Acad. Sci. USA* **2009**, *106*, 18908 – 18913.
[16] P. Haack, C. Limberg, *Angew. Chem. Int. Ed.* **2014**, *53*, 4282 – 4293; *Angew. Chem.* **2014**, *126*, 4368 – 4380.
[17] S. Itoyama, K. Doitomi, T. Kamachi, Y. Shiota, K. Yoshizawa, *Inorg. Chem.* **2016**, *55*, 2771 – 2775.
[18] a) W. Keown, J. B. Gary, T. D. P. Stack, *J. Biol. Inorg. Chem.*, DOI: 10.1007/s00775-016 – 1420-5; b) J. Serrano-Plana, I. Garcia-Bosch, A. Company, M. Costas, *Acc. Chem. Res.* **2015**, *48*, 2397 – 2406; c) J. Y. Lee, K. D. Karlin, *Curr. Op. Chem. Biol.* **2015**, *25*, 184 – 193.
[19] a) C. Citek, B. L. Lin, T. E. Phelps, E. C. Wasinger, T. D. P. Stack, *J. Am. Chem. Soc.* **2014**, *136*, 14405 – 14408; b) C. Citek, S. Herres-Pawlis, T. D. P. Stack, *Acc. Chem. Res.* **2015**, *48*, 2424 – 2433.
[20] K. Yoshizawa, Y. Shiota, *J. Am. Chem. Soc.* **2006**, *128*, 9873 – 9881.
[21] Y. Shiota, K. Yoshizawa, *Inorg. Chem.* **2009**, *48*, 838 – 845.
[22] Y. Shiota, G. Juhaśz, K. Yoshizawa, *Inorg. Chem.* **2013**, *52*, 7907 – 7917.
[23] M. R. Halvagar, P. V. Solntsev, H. Lim, B. Hedman, K. O. Hodgson, E. I. Solomon, C. J. Cramer, W. B. Tolman, *J. Am. Chem. Soc.* **2014**, *136*, 7269 – 7272.
[24] J. A. Isaac, F. Gennarini, I. López, A. Thibon-Pourret, R. David, G. Gellon, B. Gennaro, C. Philouze, F. Meyer, S. Demeshko, Y. Le Mest, M. Réglier, H. Jamet, N. Le Poul, C. Belle, *Inorg. Chem.* **2016**, *55*, 8263 – 8266.
[25] K. Selmeczi, M. Giorgi, G. Speier, E. Farkas, M. Réglier, *Eur. J. Inorg. Chem.* **2006**, 1022 – 1031.
[26] a) A. Casitas, X. Ribas, *Chem. Sci.* **2013**, *4*, 2301 – 2318; b) P. J. Donoghue, J. Tehranchi, C. J. Cramer, R. Sarangi, E. I. Solomon, W. B. Tolman, *J. Am. Chem. Soc.* **2011**, *133*, 17602 – 17605; c) J. Tehranchi, P. J. Donoghue, C. J. Cramer, W. B. Tolman, *Eur. J. Inorg. Chem.* **2013**, 4077 – 4084.
[27] A. W. Addison, T. N. Rao, J. Reedijk, J. van Rijn, G. C. Verschoor, *J. Chem. Soc. Dalton Trans.* **1984**, 1349 – 1348.
[28] C. H. Weng, S. C. Cheng, H. M. Wei, H. H. Wei, C. J. Lee, *Inorg. Chim. Acta* **2006**, *359*, 2029 – 2040.
[29] E. Ruiz, P. Alemany, S. Alvarez, J. Cano, *J. Am. Chem. Soc.* **1997**, *119*, 1297 – 1303.
[30] *Magnetic Molecular Materials, NATO ASI Series C, Vol. 140* (Eds.: D. Gatteschi, O. Khan, J. S. Miller, F. Palacio), Kluwer, Dordrecht, **1985**.
[31] a) M. F. Charlot, O. Kahn, S. Jeannin, Y. Jeannin, *Inorg. Chem.* **1980**, *19*, 1410 – 1411; b) I. Negodaev, C. de Graaf, R. Cabalool, V. V. Lukov, *Inorg. Chim. Acta* **2011**, *375*, 166 – 172.
[32] E. Ruiz, P. Alemany, S. Alvarez, J. Cano, *Inorg. Chem.* **1997**, *36*, 3683 – 3688.
[33] G. N. La Mar, W. D. W. Horrocks, R. H. Holm, *NMR of Paramagnetic Molecules*, Academic Press, New York, **1973**.
[34] I. Bertini, C. Luchinat, G. Parigi, *Solution NMR of Paramagnetic Molecules*, Elsevier, Amsterdam, **2001**.
[35] A. J. Bard, L. R. Faulkner, *Electrochemical Methods: Fundamentals and Applications*, Wiley, New York, **2000**.
[36] J.-M. Savéant, *Elements of Molecular and Biomolecular Electrochemistry*, Wiley, New York, **2006**. p. 83.
[37] J. Peisach, W. E. Blumberg, *Arch. Biochem. Biophys.* **1974**, *165*, 691 – 708.
[38] O. M. Rasia, C. W. Bertoncini, D. Marsh, W. Hoyer, D. Cherny, M. Zweckstetter, C. Griesinger, T. M. Jovin, C. O. Fernandez, *Proc. Natl. Acad. Sci. USA* **2005**, *102*, 4294 – 4299.
[39] R. Pogni, G. Della Lunga, R. Basosi, *J. Am. Chem. Soc.* **1993**, *115*, 1546 – 1550.
[40] M. Shukla, K. A. Dorai, *Appl. Magn. Reson.* **2012**, *43*, 485 – 497.
[41] D. H. Wu, A. D. Chen, C. S. Johnson, *Magn. Reson. A* **1995**, *115*, 260 – 264.
[42] A. Rockenbauer, L. Korecz, *Appl. Magn. Reson.* **1996**, *10*, 29 – 43.
[43] N. Casañ-Pastor, P. Gomez-Romero, L. C. W. Baker, *J. Appl. Phys.* **1991**, *69*, 5088 – 5091.
[44] O. V. Dolomanov, L. J. Bourhis, R. J. Gildea, J. A. K. Howard, H. Puschmann, *Appl. Crystallogr.* **2009**, *42*, 339 – 341.
[45] G. M. Sheldrick, *Acta Crystallogr. Sect. A* **2015**, *71*, 3 – 8.
[46] F. Neese, *Wiley Interdiscip. Rev.: Comput. Mol. Sci.* **2012**, *2*, 73 – 78.
[47] a) J. P. Perdew, *Phys. Rev. B* **1986**, *33*, 8822 – 8824; b) J. P. Perdew, *Phys. Rev. B* **1986**, *34*, 7406 – 7406; c) A. D. Becke, *Phys. Rev. A* **1988**, *38*, 3098 – 3100.
[48] F. Neese, *J. Comput. Chem.* **2003**, *24*, 1740 – 1747.
[49] F. Weigend, *Phys. Chem. Chem. Phys.* **2006**, *8*, 1057 – 1065.
[50] D. A. Pantazis, X.-Y. Chen, C. R. Landis, F. Neese, *J. Chem. Theory Comput.* **2008**, *4*, 908 – 919.
[51] D. A. Pantazis, F. Neese, *J. Chem. Theory Comput.* **2009**, *5*, 2229 – 2238.
[52] a) A. D. Becke, *J. Chem. Phys.* **1993**, *98*, 1372 – 1377; b) C. T. Lee, W. T. Yang, R. G. Parr, *Phys. Rev. B* **1988**, *37*, 785 – 789.
[53] A. Klamt, G. Schürmann, *J. Chem. Soc. Perkin Trans. 2* **1993**, 799 – 805.
[54] a) M. E. Casida in *Recent Advances in Density Functional Theory, Part I* (Ed.: D. P. Chong), World Scientific, Singapore, **1995**; b) R. E. Stratmann, G. E. Scuseria, M. J. Frisch, *J. Chem. Phys.* **1998**, *109*, 8218 – 8224; c) R. Bauernschmitt, R. Ahlrichs, *Chem. Phys. Lett.* **1996**, *256*, 454 – 464.
[55] a) S. Hirata, M. Head-Gordon, *Chem. Phys. Lett.* **1999**, *314*, 291 – 299; b) S. Hirata, M. Head-Gordon, *Chem. Phys. Lett.* **1999**, *302*, 375 – 382.
[56] F. Neese, *J. Chem. Phys.* **2001**, *115*, 11080 – 11080.
[57] Chemcraft, http://chemcraftprog.com.

Manuscript received: December 18, 2016
Revised: February 14, 2017
Accepted Article published: February 14, 2017
Final Article published: March 6, 2017

Inorganica Chimica Acta xxx (2017) xxx–xxx

Contents lists available at ScienceDirect

Inorganica Chimica Acta

journal homepage: www.elsevier.com/locate/ica

Research paper

Effect of ligand exchange on the one-electron oxidation process of alkoxo or phenoxo bridged binuclear copper(II) complexes

Federica Gennarini [1,c], Amélie Kochem [1,a], James Isaac [b], Ali-Taher Mansour [b], Isidoro López [c], Yves Le Mest [c], Aurore Thibon-Pourret [b], Bruno Faure [a], Hélène Jamet [b], Nicolas Le Poul [c,*], Catherine Belle [b,*], A. Jalila Simaan [a,*], Marius Réglier [a]

[a] Aix Marseille Univ, CNRS, Centrale Marseille, iSm2, Marseille, France
[b] Université Grenoble Alpes – Grenoble1, CNRS-UGA UMR 5250, Laboratoire DCM/Cire, CS 40700, 38058 Grenoble Cedex 9, France
[c] Université de Bretagne Occidentale, CNRS UMR 6521, Laboratoire CEMCA, 6 Avenue Le Gorgeu, CS 93837, 29238 Brest Cedex 3, France

ARTICLE INFO

Article history:
Received 4 August 2017
Received in revised form 26 September 2017
Accepted 30 September 2017
Available online xxxx

Keywords:
Copper
Electrochemistry
DFT calculations

ABSTRACT

In the present paper, we report on the influence of methanol/methoxide on the structure and the mono-electronic oxidation process of two different dicopper(II,II) complexes: a binuclear μ-alkoxo μ-acetato dicopper(II,II) complex obtained with a tetraamide-containing ligand (**1**) or a new unsymmetric μ-phenoxo, μ-hydroxo dicopper(II,II) complex based on a ligand bearing one bis(2-pyridylmethyl)aminomethyl arm (BPA) and one thiosemicarbazone (**2**). Structural data obtained from X-ray diffraction analysis showed that, in the case of complex **2**, bridging hydroxide was replaced by a methoxide bound in a bridging mode (**2-OMe**). Concerning complex **1**, redox properties were investigated by electrochemistry and rationalized using theoretical calculations. Our studies indicate that (i) the acetate bridge of **1** is decoordinated from the copper ions after mono-oxidation (ii) in presence of methoxide, acetate is released and a complex with two pendant exogen ligands (one methoxide and one solvent, **1-OMe-DMF**) is a plausible structure although bridging methoxide cannot be excluded. In the case of **2** the anodic potentials are not influenced by the nature of the bridge (hydroxo in **2** or methoxo in **2-OMe**). Finally, the computed redox potentials using DFT calculations are in good agreement with the experimental ones and indicates that in the case of the complexes derived from **1**, oxidation is copper-centered therefore leading to Cu(II)Cu(III) species although oxidation is ligand-centered in the case of **2** and **2-OMe**.

1. Introduction

Copper-containing proteins have essential roles in many biological processes ranging from electron transfer processes, dioxygen binding or redox catalysis [1]. In particular, several biological systems containing binuclear copper sites have been characterized and are found involved in dioxygen binding (hemocyanin), aromatic ring oxidation (catechol oxidase, tyrosinase), or methane oxidation into methanol (particulate methane monooxygenase, *p*MMO). The preparation of low molecular-weight models in relevance to copper-containing metalloenzymes is a very important tool for a better understanding of the structure and mechanism of the enzymes [2]. In the case of dioxygen activation, rational design of the ligand allows modulation of the structural properties, the nuclearity and the nature of the active copper-oxygen species formed upon reaction with dioxygen [3]. Armed with the data provided by synthetic systems, it has been shown that dioxygen binding on binuclear Cu(I) centers leads to peroxo-bridged Cu_2^{II} species [2a,2b]. The (μ-η^2-η^2-peroxo)Cu_2^{II} can further be converted into high-valent bis(μ-oxo)Cu_2^{III} species (Scheme 1) [2a,2b,4]. Both (μ-η^2-η^2-peroxo)Cu_2^{II} and bis(μ-oxo)Cu_2^{III} intermediates have been shown to be able to perform oxidation reactions However, since the hypothesis that methane oxidation into methanol by *p*MMO is performed at an asymmetric dinuclear copper sites [5], several additional active copper-oxygen species have been discussed as relevant for strong C—H bond oxidation. In particular, (μ-oxo)Cu_2^{II} intermediates have been proposed as active species for methane oxidation in copper-loaded zeolites (Scheme 1) [6]. Synthetic Cu_2O species have been described, but their ability to perform strong C—H bond oxidation has not yet been established [7]. Using DFT calculations, it has been suggested that bis(μ-oxo)$Cu^{II}Cu^{III}$ or (μ-oxo)(μ-hydroxo)$Cu^{II}Cu^{III}$ are more reactive toward oxidative chemistry involving very strong

* Corresponding authors.
E-mail addresses: lepoul@univ-brest.fr (N. Le Poul), catherine.belle@univ-grenoble-alpes.fr (C. Belle), jalila.simaan@univ-amu.fr (A.J. Simaan).
[1] These authors contributed equally to the work.

https://doi.org/10.1016/j.ica.2017.09.067
0020-1693/

Please cite this article in press as: F. Gennarini et al., Inorg. Chim. Acta (2017), https://doi.org/10.1016/j.ica.2017.09.067

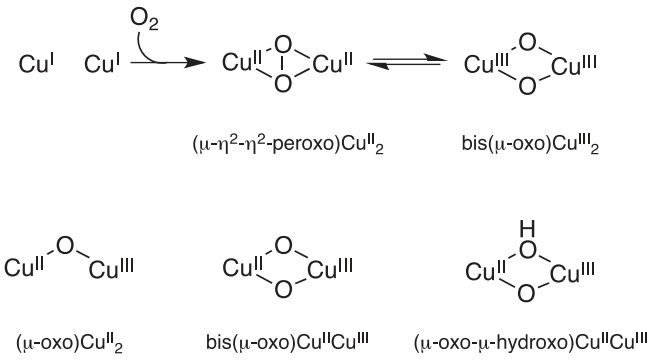

Scheme 1. Example of relevant copper-oxygen species.

C—H bonds than the corresponding bis(μ-oxo)Cu^{III}_2 species [8]. So far, only few synthetic mixed-valent $Cu^{II}Cu^{III}$ species have been characterized in the recent years [9].

Understanding the structure-function relationships, the electronic properties, substrate binding, ligand exchanges as well as the redox properties of binuclear copper centers therefore remains of high importance. To accommodate binuclear copper sites in appropriate proximity and spatial arrangements, multidentate ligands are often prepared. We have recently reported on the structure and properties of several dinuclear copper(II) complexes using binucleating ligands featuring alkoxo or phenoxo bridging units [9c,9d]. In particular, we have reported recently on the synthesis and characterization of a dinuclear μ-alkoxo μ-acetato dicopper (II,II) complex obtained with a tetraamide-containing ligand (**1,** Scheme 2) [9c]. Monoelectronic oxidation of complex **1** led to the formation of a $Cu^{II}Cu^{III}$ intermediate that was characterized by UV–visible spectroscopy and Electron Paramagnetic Resonance spectroscopy. Electrochemical studies have suggested that, upon oxidation the acetate moiety is probably decoordinated and replaced by solvent molecules.

In the present work, we were interested in getting insight into the effect of ligand exchange on the redox properties of two different dicopper(II,II) complexes (Scheme 2): complex **1** and a new unsymmetric μ-phenoxo, μ-hydroxo dicopper(II,II) complex based on a ligand bearing one bis(2-pyridylmethyl)aminomethyl arm (BPA) and one thiosemicarbazone (**2**). In particular, we have investigated the effect of bridging moiety exchange (μ-actetato or μ-hydroxo for **1** and **2** respectively) upon methoxide addition on the structure and redox properties of the resulting complexes. Upon addition of methoxide on complex **2**, we were able to get structural data and the structure of **2-OMe** was solved unraveling a bridging methoxide moiety. The redox properties of the different complexes were investigated in absence and in presence of methoxide and the results were rationalized using DFT calculations.

2. Experimental section

2.1. General

The solvents used for chemical reactions, electrochemistry and spectroscopic characterization were purified using the solvent purification system Innovative Technology PS-MD-5. Microanalysis was performed on an Elementar Thermo Finnigan EA 1112. Electrospray mass spectra were recorded on an Esquire 3000 plus Bruker Daltonics with nanospray inlet. A Unity Plus 400 MHz spectrometer was used for collection of NMR spectra. X-band EPR spectra were recorded at 100K with a EMX Bruker spectrometer equipped with a standard ER4102ST Bruker cavity.

2.2. Synthesis of $[(L^aH_2)Cu_2(\mu\text{-}OAc)]$ (1)

The ligand L^aH_4 and the complex **1** were prepared according to already described procedures [9c].

2.3. Synthesis of the ligand L^pH

3-{[Bis(2-pyridinylmethyl)amino]}-2-hydroxybenzaldehyde was prepared from commercially available 5-methyl-2-hydroxybenzaldehyde in two steps *via* a previously described method [10]. To a solution of 3-{[Bis(2-pyridinylmethyl)amino]}-2-hydroxybenzaldehyde (1g, 2.8 mmol) in methanol, a solution of 4,4-dimethyl-3-thiosemicarbazide (0.34 g, 2.8 mmol) in methanol (Scheme 3) was added and left to stir for 1 h then refluxed for another hour after which the reaction mixture was concentrated and L^pH was obtained as a yellow orange solid (53%). ^{1}H NMR (400 Mz DMSO d_6) δ: 11.89 (1H, s, N*H*), 11.15 (1H, s, O*H*), 8.49 (2H, d, J = 4.4 Hz, *H*), 8.47 (1H,s, –NC*H*), 7.76 (2H, td, J = 7.5 Hz, 1.5 Hz, Py-*oH*), 7.55 (2H, d, J = 7.7, Py-*pH*), 7.26 (1H, s, –NCH–Ar*H*), 7.24 (2H, dd, J = 6.7 Hz, 5.0 Hz, Py-*mH*), 7.12 (1H, s, –CH_2–Ar*H*), 3.77 (4H, s, Py-CH_2-N), 3.70 (2H, s, –N—CH_2–Ar), 3.29 (6H, s, N—CH_3), 2.25 (3H, s, CH_3). ^{13}C NMR (100 MHz DMSO d_6) δ:179.8, 159.5, 153.9, 149.2, 146.4, 137.0, 132.2, 128.9, 127.5, 125.7, 122.9, 122.6, 118.5, 59.7, 52.5, 41.5, 20.6. ESI-MS: m/z: 449.1 $[M + 1]^+$. Anal. Calcd. for $C_{24}H_{28}N_6O_1S_1 \cdot H_2O$: C, 61.76; H, 6.51; N, 17.86. Found C, 61.78; H, 6.48; N, 18.01.

2.4. Synthesis of $[(L^p)Cu_2(\mu\text{-}OH)](OTf)$ (2)

The complex was prepared according a known procedure [11], starting from $LHMe_2$ (0.157 g, 1 eq) dissolved in acetone (10 ml) and Et_3N (150 μl). A solution of $Cu(OTf)_2$ (0.272 g, 2.1 eq) in acetonitrile (10 ml) was added, and the mixture was stirred for 1 h. The mixture was then concentrated, di-isopropylether (10 ml) was added and the solution was placed at −20 °C for 1 week to give the pure complex $[Cu_2(LMe_2)(\mu\text{-}OH)][OTf]$ (73 mg, 28%) as a dark solid. ESI-MS (CH_3CN), m/z: z = 1, 589 $(M\text{-}OTf)^+$, UV–Vis (CH_3CN) (ε, $M^{-1}\,cm^{-1}$): 242 (23000), 281 (14000), 326 (16000) 338 (16000), 390 (18000), 760 (185) Anal. Calcd. for C25H27Cu2-N6O5S2F3: C, 40.59; H, 3.68; N, 11.36. Found C, 40.62; H, 3.85; N, 11.13.

2.5. Synthesis of $[(L^p)Cu_2(\mu\text{-}OMe)](ClO_4)$ (2-MeO)

$[Cu_2(LMe_2)(\mu\text{-}OH)](OTf)$ (25 mg, 3.4×10^{-4} mol, 1 eq) was dissolved in MeOH (10 ml). Then, $NaClO_4$ (40 mg, 10 eq) was added and a dark brown precipitate was immediately formed. The mixture was stirred for 20 min then the solution was removed with a pipette. The precipitate was dissolved in MeCN and X-ray quality crystals (15 mg, 63%) were obtained by slow diffusion of isopropyl ether. ESI-MS (MeOH), m/z: z = 1, 605 (M-ClO4)+. Anal. Calcd. for C25H29Cu2N6O6SCl: C, 42.64; H, 4.16; N, 11.94. Found C, 42.67; H, 3.95; N, 12.13.

2.6. Crystal structure determination and refinement

Measurements were made on a Bruker-Nonius Kappa CCD diffractometer with graphite monochromatized Mo(Kα) radiation (λ = 0.71073 Å). Crystallographic structures were solved using direct methods implemented by ShelxS-97 [12]. Refinement was performed using ShelxL-97 [12] run under Olex2 [13]. C, N, O, S, Cl, and Cu atoms were refined anisotropically by the full matrix least-squares method. H atoms were calculated on idealized positions and constrained on their bearing atoms. The crystal data of **2-OMe** and details of the data collections are given in Table 1. Supplementary data is available from the CCDC, 12 Union Road,

Please cite this article in press as: F. Gennarini et al., Inorg. Chim. Acta (2017), https://doi.org/10.1016/j.ica.2017.09.067

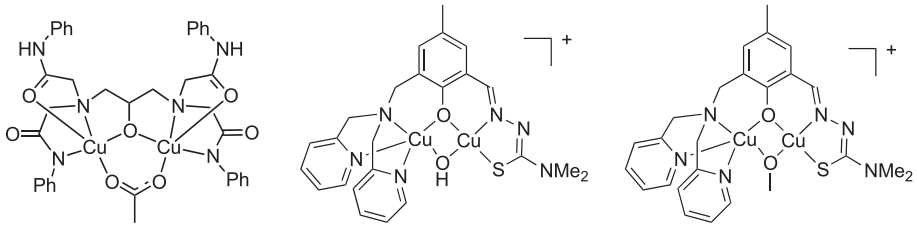

Scheme 2. Complexes used in the present work.

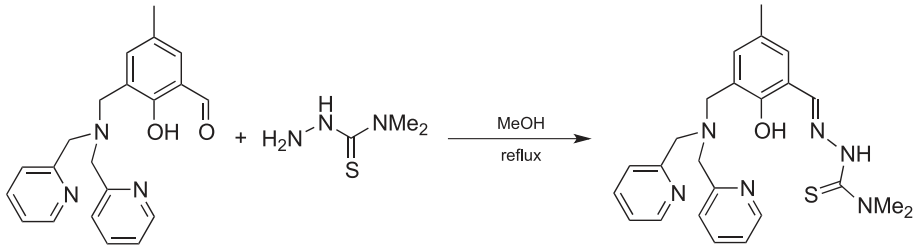

Scheme 3. Synthetic route for the ligand L^PH.

Cambridge CB2 1EZ, UK on request, quoting the deposition number CCDC–1520305. These data can be obtained free of charge at www.ccdc.cam.ac.uk/conts/retrieving.html or fax: +44 1223/336 033; E-mail: deposit@ccdc.cam.ac.uk].

2.7. Electrochemical studies

Electrochemical studies of the copper complex were performed in a glovebox (Jacomex) (O_2 < 1 ppm, H_2O < 1 ppm) with a home-designed 3-electrodes cell (WE: glassy carbon, RE: Pt wire in a Fc^+/Fc solution, CE: Pt or graphite rod). Ferrocene was added at the end of the experiments to determine redox potential values. The potential of the cell was controlled by an AUTOLAB PGSTAT 100 (Metrohm) potentiostat monitored by the NOVA software. Extra-dry DMF (99.8% Acros) was stored into the glovebox and used as received. The supporting salt NBu_4PF_6 was synthesized from NBu_4OH (Acros) and HPF_6 (Aldrich). It was then purified, dried under vacuum for 48 h at 100 °C, then kept under argon in the glovebox. Electrolyses were carried out with a home-designed 3-electrodes cell (WE: Graphite rod, RE: Pt wire in a Fc^+/Fc solution, CE: graphite rod).

2.8. Theoretical calculations

All calculations were performed using the GAUSSIAN 09 package [14]. Geometry optimizations were carried out for all systems using the hybrid exchange-correlation PBE0 functional accounting for MeCN solvation effects using the IEF-PCM continuum solvent model. A mixed basis set comprised of the Def2-TZVDP for copper and iron atoms, the 6-311 + G(d,p) for N and O atoms and 6-311G (d,p) for C and H atoms as already described [9a]. Vibrational frequency calculations were performed to ensure that each geometry optimization converged to a real minimum.

The ground-state of dicopper(II,II) complexes can be triplet or singlet state. For the mono-oxidized species, according to the oxidation site, only doublet states (arising from oxidation centered on one copper ion) or doublet and quartet states (arising from oxidation on the ligands) are possible. In order to determine the oxidation site (ligand *vs* metal) we first considered only the doublet state and computed Mulliken population and spin density. When oxidation occurs on the ligand, two spin states, a doublet or a quartet state, have to be considered. For the calculation of redox potentials, energetic calculations were carried from additional single point calculations on the previously optimized geometries using the M11-L functional and always the IEF-PCM continuum solvent model. Only high spin states of complexes were computed even if they are not ground states, so the triplet state for the dicopper (II,II) complexes and the quartet state for the

Table 1
Crystallographic data for **2-OMe.**

Compound	**2-OMe**
Formula	$[Cu_2(C_{25}H_{29}N_6O_2S)]\cdot ClO_4$
F_w	704.13
Morphology	Plate
Color	Brown
Crystal size mm	0.46 × 0.35 × 0.06
Crystal system	orthorhombic
Space group	P b c a
a [Å]	13.134(3)
b [Å]	14.738(3)
c [Å]	28.476(6)
α [°]	90.00
β [°]	90.00
γ [°]	90.00
Unit-cell volume [Å^3]	5512.0(19)
D_x (g cm^{-3})	1.697
T [K]	200
Z	8
μ [mm^{-1}]	1.769
Total reflections	54313
Unique reflections	8035
Obsd. reflections	5460 ($F > 2\sigma$)
Rint.	0.0816
R^a	0.0525
$R(w)^a$	0.0928
Goodness of fit *S*	1.116
$\Delta\rho_{min}/\Delta\rho_{max}$ (e Å^{-3})	−0.751/0.496

[a] Refinement based on *F* where $w = 1/[\sigma\ ^2(Fo)^2 + (0.0237p)^2 + 9.8733p]$ with $p = (Fo^2 + 2Fo^2)/3$.

Please cite this article in press as: F. Gennarini et al., Inorg. Chim. Acta (2017), https://doi.org/10.1016/j.ica.2017.09.067

mono-oxidized species. This is justified since the energy difference between spin states is very small compared to that between two redox states.

3. Results and discussions

3.1. Synthesis of complexes 1 and 2

The ligand L^aH_4 was obtained in one step by reaction of the commercially available 2-chloro-N-phenylacetamide with 1,3-diamino-2-propanol. The metallation was performed in methanol by using two equivalents of copper(II) acetate salt in the presence of Et_3N as a base yielding complex **1**. The structure of **1** has been previously reported [9c]. The two copper ions are bridged by the alkoxide group of the ligand and an acetate moiety. The equatorial positions of each copper are occupied by the N-atom from deprotonated amide groups, the N and the O-atoms of the ethanolamine moieties, as well as one O-atom from the bridging acetate ligand. The apical positions are occupied by the oxygen atoms from the pendant amide arms that remained protonated. The ligand L^pH_2 derives from bis(2-pyridylmethyl)aminomethyl-2-hydroxy-5-methylbenzaldehyde, the key intermediate available from chloromethyl-2-hydroxy-5-methylbenzaldehyde and bis(2-pyridylmethyl)aminomethyl in two steps *via* a previously described method [10]. The subsequent reaction in methanol with 4,4-dimethyl-3-semithiocarbazide led to the desired ligand (Scheme 3). Complex **2** was obtained by reacting with $Cu(OTf)_2$ in acetonitrile in the presence of Et_3N as a base. ESI-MS and elemental analysis confirm the formulation (see experimental part). The EPR spectra were measured at 100 K in a frozen solution in 1 mM in CH_3CN. Complex **2** is EPR silent, in accordance with doubly bridged structure and a short Cu...Cu distance as observed in previously described μ-phenoxo μ-hydroxo complexes, such structure resulting into strong antiferromagnetic coupling between the two copper atoms [11].

3.2. Effect of methoxide binding: Structural characterization of 2-OMe

Dissolution of complex **2** in methanol led to methoxide binding as confirmed by ESI-MS spectrometry (Fig. S1 in SI). Indeed, a peak at $m/z = 605$ was detected corresponding to the ion $[(L^p)Cu_2(OMe)]^+$. After dissolution of complex **2** in MeOH, addition of $NaClO_4$ immediately led to a dark precipitate. The precipitate was dissolved in MeCN and X-ray quality crystals were obtained by slow diffusion of isopropyl ether.

The molecular structure of the dinuclear complex **2-OMe** is depicted in Fig. 1. This structure clearly shows the replacement of the hydroxo bridge in **2** by a methoxo bridge in **2-OMe.** The two copper ions are found doubly bridged both by the phenoxo and the methoxo groups. The relevant crystal data and structural parameters are given in the experimental part (Table 1). In **2-OMe**, the two ligand compartments provide dissimilar coordination environments and thereby induce different coordination geometries for each copper. The Cu2 has a geometry that is best described as a distorted trigonal bipyramidal (τ value of 0.7) rather than a square pyramidal, with its N4, N5, O1 in the basal plane and N1, O2 in the axial positions. On the other hand, the Cu1 in **2-OMe** is tetracoordinated by oxygen atoms from phenoxo and methoxo bridges, and N2 and S1 atoms from the thiosemicarbazone arm, forming a distorted square planar geometry around the Cu1. The S1-C10 bond distance (1.745 Å), is in accordance with a thiolate form [15]. The former is generated from the thiol form which is probably the predominant tautomeric form of the ligand rather than the thione form and the subsequent loss of hydrogen from the SH occurring after the complexation in basic medium. It is consistent with the increased single bond character expected for the ligand in the thiolate form rather than the thione. The two copper ions are at a relatively close distance of 3.026 Å.

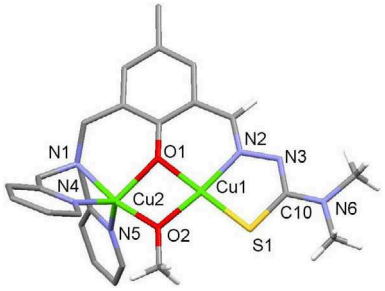

Fig. 1. Molecular structure of the cation $[(Cu_2(LMe_2)(OMe)]^+$. Hydrogen atoms (except on the methoxo bridge and thiosemicarbazone arm), solvent molecules and counterion were removed for clarity. Selected bond lengths (Å) and angles (°): Cu1 Cu2 3.0263, Cu1-S1 2.033, Cu1-O2 1.911, Cu1-O1 1.932, Cu1-N2 1.933, Cu2-O2 1.897, Cu2-O1 2.068, Cu2-N1 2.012, Cu2-N5 2.020, Cu2-N4 2.035, S1-C10 1.74-belle5, C10-N3 1.318; O2-Cu1-S1 101.03, O2-Cu1-O1 78.72, N2-Cu1-S1 87.47, N2-Cu1-O1 93.02, O2-Cu2-O1 75.71 O2-Cu2-N5 103.69, O2-Cu2-N4 100.55, N1-Cu2-O1 92.65, N1-Cu2-N5 82.56, N5-Cu2-O1 118.00, N4-Cu2-N1 83.14, N4-Cu2-N5 125.86, Cu1-O1-Cu2 98.30, Cu1-O2-Cu2 105.27.

3.3. Effect of methoxide binding: UV–visible spectroscopy

Complex **2** was placed in acetonitrile and the UV–visible spectrum was recorded (Fig. S2). Main LMCT transitions are found in the 300–400 nm range (326, 338 and 390 nm). **2-OMe** was generated by placing complex **2** in methanol and the transitions are found slightly shifted (323, 335 and 389 nm). Formation of methoxo bridged complexes has previously been observed in relevant μ-phenoxo, μ-hydroxo dicopper complexes [11]. Due to the poor solubility of **1** in methanol, the effect of methoxide binding was investigated in DMF. The complex was placed at 1 mM and 1–3 equivalents of MeONa were added. Slight modifications of the d-d transitions are detected indicating that MeO^- probably interacts at the copper centers.

3.4. Electrochemical studies

Cyclic voltammetry (CV) of **1** was performed in DMF with 0.1 M NBu_4PF_6 under argon at room temperature. All potentials are referenced *versus* the Fc^+/Fc redox couple. In a previous publication, we have reported that complex **1** undergoes an irreversible one-electron oxidation process at $E_{pa}(1) = 0.63$ V and a one electron reduction process at $E_{pc}(2) = -1.34$ V (at $v = 0.1$ V s^{-1}) [9c]. Electrochemical experiments were performed to investigate ligand exchange properties of complex **1**. Hence, addition of one molar equivalent of sodium methoxide to a solution of complex **1** leads to the appearance of a new irreversible peak at a lower potential value ($E_{pa}(4) = 0.40$ V) (Fig. 2). The peak at $E_{pa}(1)$ also increased but in a lower extent. This evidences the formation of a new species (complex **1-OMe**) probably including one methoxide coordinated. These results are in agreement with the known ability of methoxide to replace acetate coordinated at copper centers [16]. This process is also accompanied by the disappearance of the initial cathodic peak at $E_{pc}(2)$ and the appearance of a new cathodic peak at a more negative value ($E_{pc}(5) = -1.72$ V), without significant change of the peak intensity and shape (Fig. 2C). Plots of $i_{pa}(4)$ and $i_{pc}(5)$ *vs* $v^{1/2}$ for **1-OMe** give similar slope values (Figs. S3 and S4), hence yielding $n = 0.9 \pm 0.1$, n corresponding to the number of exchanged electrons associated to the oxidation and reduction processes respectively; n was determined using the assumption that the diffusion coefficient is similar to that of **1** that has been determined in our previous publication

Please cite this article in press as: F. Gennarini et al., Inorg. Chim. Acta (2017), https://doi.org/10.1016/j.ica.2017.09.067

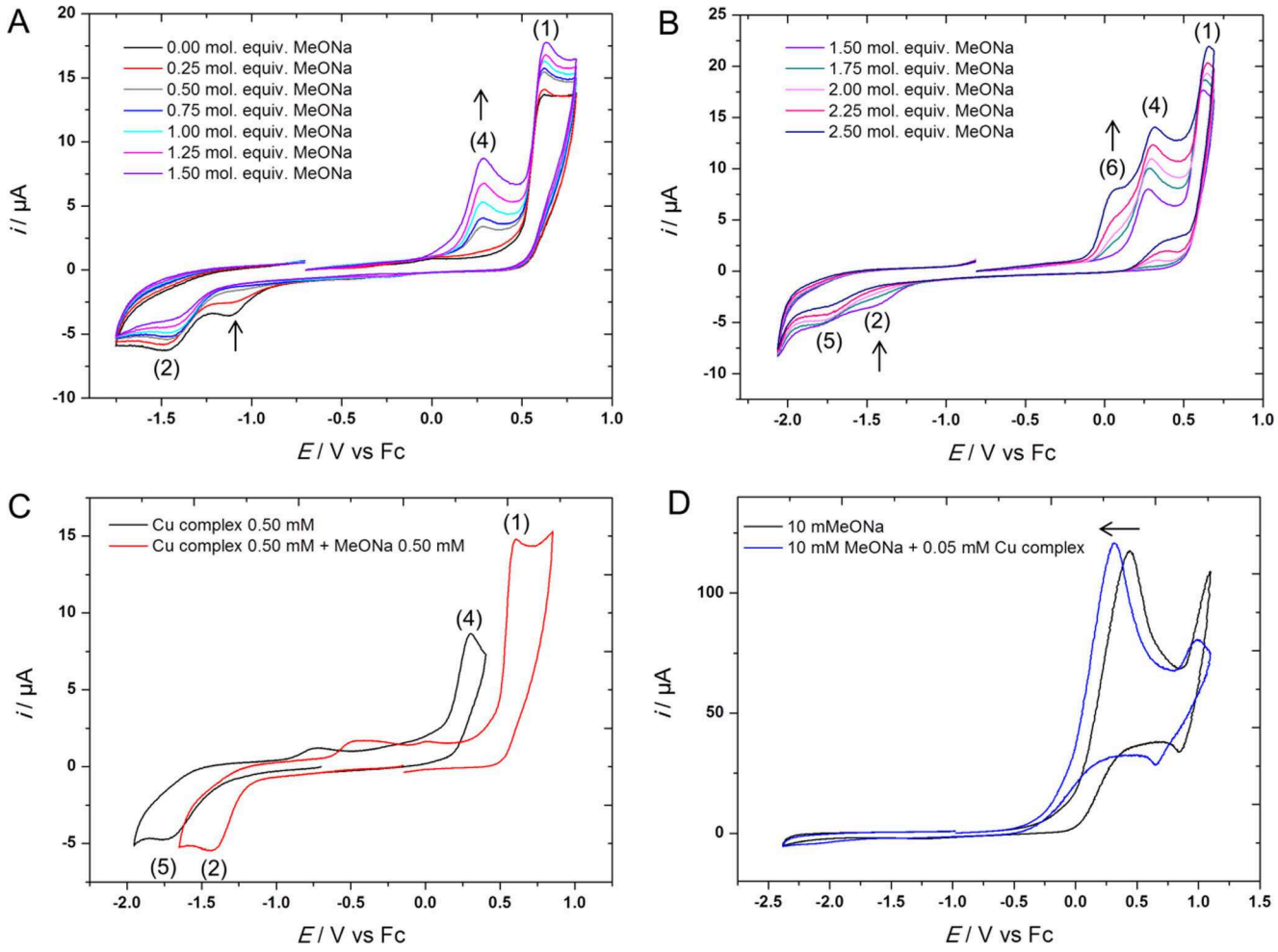

Fig. 2. CVs at a glassy carbon electrode in DMF/NBu_4PF_6 0.1 M under Ar (v = 0.1 V s^{-1}). A) Addition of 0–1.50 M equivalents of MeONa on a solution of complex **1** (0.50 mM), and B) 1.50–2.50 M equivalents of MeONa on a solution of complex **1** (0.50 mM); C) Comparative CVs of complex **1** before (red) and after (black) addition of one molar equivalent of MeONa; D) CV of MeONa (10 mM) before (black) and after (blue) addition of 0.005 M equivalent (0.05 mM) of complex **1**. Arrows are indicative of main changes on CVs. (For interpretation of the references to colour in this figure legend, the reader is referred to the web version of this article.)

($D = 5.4{\cdot}10^{-6}$ cm^2 s^{-1}) [9c]. These results contrast with those obtained for complex **1.** Indeed, the oxidation peak was found associated to n = 1.6 electrons and acetate release after oxidation was proposed to contribute to the increased number of exchanged electrons (free acetate is oxidized at 0.7 V vs. Fc^+/Fc) [9c]. Further addition of methoxide leads to the appearance of a supplementary peak at $E_{pa}(6)$ = 0.10 V which corresponds to the oxidation of free methoxide in solution (Figs. 2B, S5 and S6). Therefore, formation of a dinuclear copper(II) complex with two methoxide groups coordinated is precluded in these experimental conditions.

An interesting result was obtained when studying the effect of the addition of sub-stoichiometric amounts of complex **1** on the oxidation potential of free methoxide. As depicted in Fig. 2D, sodium methoxide is oxidized irreversibly at 0.10 V at a vitreous carbon electrode. With only 0.005 M equivalent of complex **1**, a 125 mV negative shift of the oxidation potential was observed without significant variation of the anodic peak current (Fig. 2D). Further addition leads to a progressive decrease of the peak intensity with concomitant increase of a several peaks at higher potential (Fig. S6). Hence, the shift of the anodic peak at sub-stoichiometric amounts of **1** in Fig. 2D likely results from additional competitive reactions involving the oxidized form of methoxide. Indeed, the occurrence of a supplementary chemical process with high rate of reaction for an existing EC oxidation reaction induces a negative shift of the peak potential.

The electrochemical behavior of complex **2** were investigated in CH_3CN solution containing 0.1 M NBu_4PF_6 as supporting electrolyte and the potentials are also referenced *versus* the Fc^+/Fc redox couple. Complex **2** displays two reversible redox waves, one in reduction at $E_{1/2} = -1.05$ V and one in oxidation at $E_{1/2}$ = 0.45 V. In the presence of one molar equivalent of MeONa, the oxidation peak of **2** remains unchanged indicating that, in contrast to the results obtained with complex **1**, the redox properties of the copper ions are not significantly affected by hydroxide exchange by methoxide (see DFT calculations part). However, addition of sub-stoichiometric amounts of complex **2** on MeONa solution leads to a shift of the methoxide oxidation peak at E_{pa} = 0.10 V (Fig. S7), similarly to what has been observed with complex **1**.

3.5. DFT calculations

Further investigations were carried out by DFT calculations to evaluate the first oxidation potentials of the different complexes and get insight into the oxidation site (ligand *vs.* metal centered). For evaluating the oxidation potentials, we have used our previously reported computational method [9d].

Please cite this article in press as: F. Gennarini et al., Inorg. Chim. Acta (2017), https://doi.org/10.1016/j.ica.2017.09.067

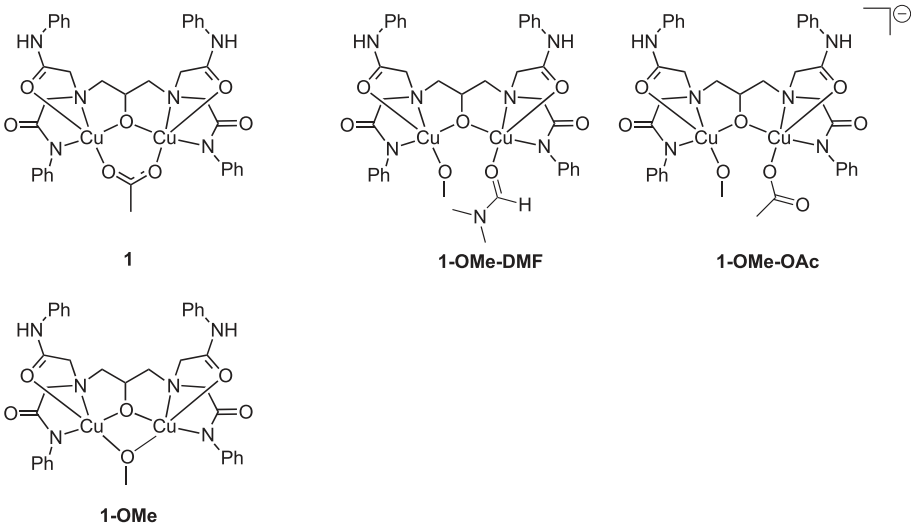

Scheme 4. Different structures that were considered for the resulting complex after addition of methoxide on **1.**

In the case of **1**, DFT calculations predicted an oxidation potential of 0.62 V *vs* Fc^+/Fc, very close to the experimental value (0.63 V *vs* Fc^+/Fc). Since no structural characterization of the species formed upon addition of sodium methoxide to **1** could be obtained, different complexes were considered (Scheme 4) bearing either *(i)* one bridging methoxide as found in the case of **2-OMe** (**1-OMe**), *(ii)* one methoxide and one DMF (**1-OMe-DMF**) or *(iii)* one methoxide and one acetate (**1-OMe-OAc**).

The different dicopper(II,II) structures were optimized and the redox potentials were computed. The potential values are found equal to 0.52 V for **1-OMe**, 0.32 V for **1-OMe-DMF** and 0.16 V **1-OMe-OAc**. Analysis of the spin densities indicates that in all

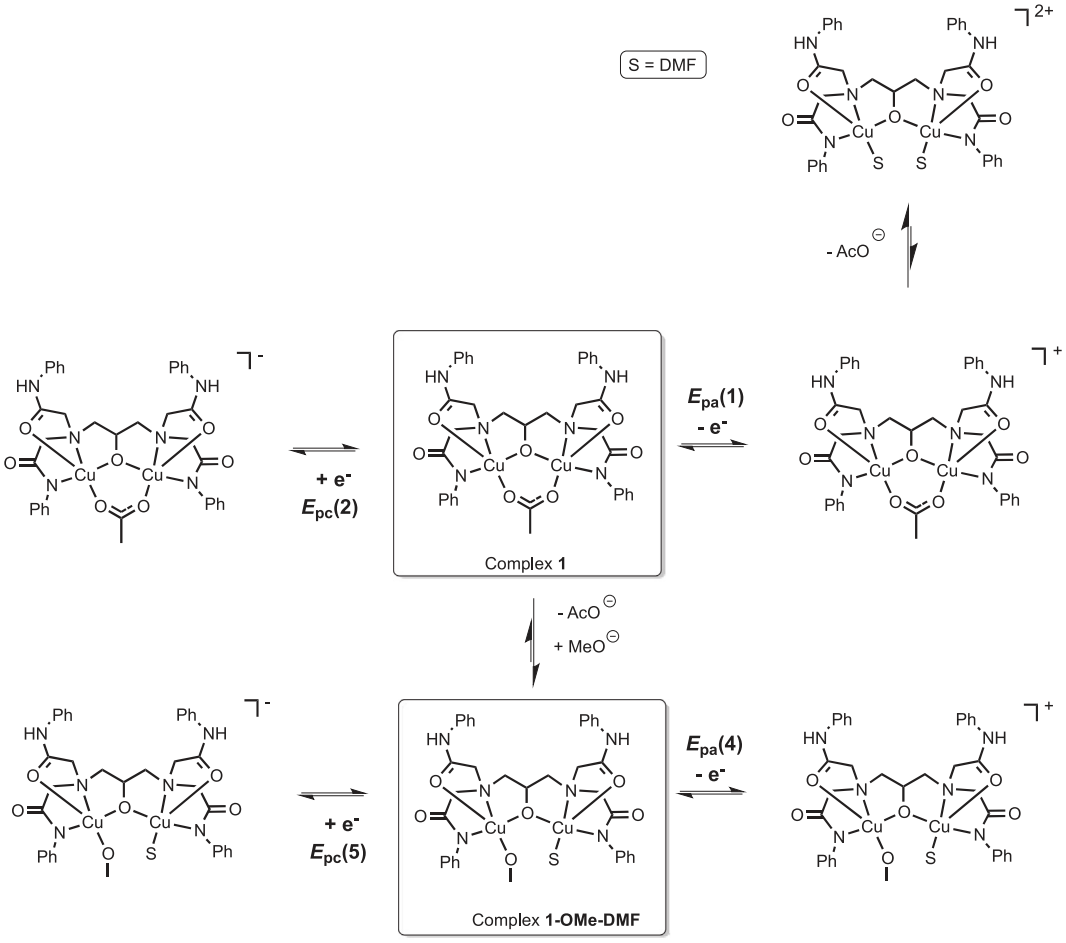

Scheme 5. Proposed redox pathway for complex **1** in absence and presence of methoxide from voltammetric and computational data.

Please cite this article in press as: F. Gennarini et al., Inorg. Chim. Acta (2017), https://doi.org/10.1016/j.ica.2017.09.067

cases, the one-electron oxidation is copper-centered resulting in a mixed-valent Cu(II)Cu(III) species with a predominant charge localization on one of the two copper ion supported by the theoretical calculations (Figs. S8 and S9). Comparisons of the different computed potentials with the experimental one suggest that binding of methoxide leads to acetate release since the computed potential for **1-OMe-OAc** (0.16 V) is far from the 0.4 V experimentally determined one. The experimental value is found relatively close to the computed values for both **1-OMe** and **1-OMe-DMF**. It is however slightly closer to the 0.32 V value computed for **1-OMe-DMF.** The structure **1-OMe-DMF** is therefore a plausible structure for the complex upon methoxide binding but bridging methoxide cannot be excluded.

Altogether, our data therefore suggest that upon methoxide addition to complex **1**, the acetate bridge is released leading to methoxide binding. This results in a lower oxidation potential (0.40 V *vs*. 0.63 V) and leads to the generation of a $Cu^{II}Cu^{III}$ species upon mono-electronic oxidation. The oxidation process being irreversible, further chemical processes certainly occur after oxidation, probably leading to the degradation of the complex. This is supported by the fact that we were not able to trap the resulting mixed-valent species upon bulk electrolysis, time-resolved thin layer spectroelectrochemistry or chemical oxidation, even at low temperature. The different redox pathways derived from the present experimental and theoretical studies upon methoxide binding on complex **1** are summarized in Scheme 5.

In the case of complexes **2** and **2-OMe**, DFT calculations predicted similar redox potential values equal to 0.46 V *vs* Fc^+/Fc for **2** and 0.45 V for **2-OMe** in good agreement with experimental data and with the absence of significant changes in redox properties upon methoxide binding. Analysis of the Mullliken population and spin density plots (Fig. S10) for the mono-oxidized species indicated that the oxidation is centered on the ligand and not on the copper ions. This can explain why the value of the oxidation potential is not significantly affected by the nature of the bridge between the two copper ions (methoxide or hydroxo bridge).

4. Conclusion

In this paper we have investigated the effect of methoxide binding on two different dicopper(II,II) complexes using experimental (spectroscopic tools, cyclic voltammetry) combined with DFT calculations. Our studies indicate that, in both cases, methoxide addition leads to decoordination of the bridging moiety (acetate and hydroxo in **1** and **2** respectively). In the case of **2**, structural data revealed a bridging mode of the methoxide between the two copper ions. In the case of **1**, a complex with two pendant exogen ligands (one methoxide and one solvent, **1-OMe-DMF**) is a plausible structure although bridging methoxide cannot be excluded. The computed redox potentials using DFT calculations are in good agreement with the experimental ones and indicates that in the case of the complexes derived from **1**, oxidation is copper-centered therefore leading to unstable Cu(II)Cu(III) species although oxidation is ligand-centered in the case of **2** and **2-OMe**.

Acknowledgments

Financial support by ANR-13-BSO7-0018 including grant for AK is acknowledged. This work has been carried out in the frameworks of Labex Arcane (ANR-11-LABX-003) and COST action CM1305 (ECOSTBio).

Appendix A. Supplementary data

Supplementary data associated with this article can be found, in the online version, at https://doi.org/10.1016/j.ica.2017.09.067.

References

[1] E.I. Solomon, D.E. Heppner, E.M. Johnston, J.W. Ginsbach, J. Cirera, M. Quyyum, M.T. Kieber-Emmons, C.H. Kjaergaard, R.G. Hadt, L. Tian, Chem. Rev. 114 (2014) 3659–3853.
[2] a) D.A. Quist, D.E. Diaz, J.J. Liu, K.D. Karlin, J. Biol. Inorg. Chem. 22 (2017) 253–288;
b) S. Itoh, Acc. Chem. Res. 48 (2015) 2066–2074;
c) C. Citek, S. Herres-Pawlis, T.D. Stack, Acc. Chem. Res. 48 (2015) 2424–2433;
d) N. Gagnon, W.B. Tolman, Acc. Chem. Rev. 48 (2015) 2126–2131.
[3] a) L.M. Mirica, X. Ottenwaelder, T.D.P. Stack, Chem. Rev. 104 (2004) 1013–1046;
b) E.A. Lewis, W.B. Tolman, Chem. Rev. 104 (2004) 1047–1076.
[4] N. Fujieda, S. Itoh, Bull. Chem. Soc. Jpn. 89 (2016) 733–742.
[5] a) S. Sirajuddin, A.C. Rosenzweig, Biochemistry 54 (2015) 2283–2294;
b) M.O. Ross, A.C. Rosenzweig, J. Biol. Inorg. Chem. 22 (2017) 307–319.
[6] J.S. Woertink, P.J. Smeets, M.H. Groothaert, M.A. Vance, B.F. Sels, R.A. Schoonheydt, E.I. Solomon, Proc. Natl. Acad. Sci. 106 (2009) 18908–18913.
[7] P. Haack, C. Limberg, Angew. Chem. Int. Ed. 53 (2014) 4282–4293.
[8] a) Y. Shiota, K. Yoshizawa, Inorg. Chem. 48 (2009) 838–845;
b) Y. Shiota, G. Juhász, K. Yoshizawa, Inorg. Chem. 52 (2013) 7907–7917.
[9] a) M.R. Halvagar, P.V. Solntsev, H. Lim, B. Hedman, K.O. Hodgson, E.I. Solomon, C.J. Cramer, W.B. Tolman, J. Am. Chem. Soc. 136 (2014) 7269–7272;
b) J.A. Isaac, F. Gennarini, I. López, A. Thibon-Pourret, R. David, G. Gellon, B. Gennaro, C. Philouze, F. Meyer, S. Demeshko, Y. Le Mest, M. Réglier, H. Jamet, N. Le Poul, C. Belle, Inorg. Chem. 55 (2016) 8263–8266;
(c) A. Kochem, F. Gennarini, M. Yemloul, M. Orio, N. Le Poul, E. Rivière, M. Giorgi, B. Faure, Y. Le Mest, M. Réglier, A.J. Simaan, ChemPlusChem 82 (2017) 615–624;
d) F. Gennarini, R. David, I. López, Y. Le Mest, M. Réglier, C. Belle, A. Thibon-Pourret, H. Jamet, N. Le Poul, Inorg. Chem. 56 (2017) 7707–7719.
[10] a) G. Lock, Ber. Dtsch. Chem. Ges. 63 (1930) 551–559;
b) I.A. Koval, D. Pursche, A.F. Stassen, P. Gamez, B. Krebs, J. Reedjik, Eur. J. Inorg. Chem. (2003) 1669–1674.
[11] S. Torelli, C. Belle, I. Gautier-Luneau, J.L. Pierre, E. Saint-Aman, J.M. Latour, L. Le Pape, D. Luneau, Inorg. Chem. 39 (2000) 3526–3536.
[12] G.M. Sheldrick, Acta Cryst. A64 (2008) 112–122.
[13] O.V. Dolomanov, L.J. Bourhis, R.J. Gildea, J.A.K. Howard, H. Puschmann, J. Appl. Cryst. 42 (2009) 339–341.
[14] Gaussian 09: G. W. T. M. J. Frisch, H. B. Schlegel, G. E. Scuseria, M. A. Robb, J. R. Cheeseman, G. Scalmani, V. Barone, B. Mennucci, G. A. Petersson, H. Nakatsuji, M. Caricato, X. Li, H. P. Hratchian, A. F. Izmaylov, J. Bloino, G. Zheng, J. L. Sonnenberg, M. Hada, M. Ehara, K. Toyota, R. Fukuda, J. Hasegawa, M. Ishida, T. Nakajima, Y. Honda, O. Kitao, H. Nakai, T. Vreven, J. A. Montgomery, Jr., J. E. Peralta, F. Ogliaro, M. Bearpark, J. J. Heyd, E. Brothers, K. N. Kudin, V. N. Staroverov, R. Kobayashi, J. Normand, K. Raghavachari, A. Rendell, J. C. Burant, S. S. Iyengar, J. Tomasi, M. Cossi, N. Rega, J. M. Millam, M. Klene, J. E. Knox, J. B. Cross, V. Bakken, C. Adamo, J. Jaramillo, R. Gomperts, R. E. Stratmann, O. Yazyev, A. J. Austin, R. Cammi, C. Pomelli, J. W. Ochterski, R. L. Martin, K. Morokuma, V. G. Zakrzewski, G. A. Voth, P. Salvador, J. J. Dannenberg, S. Dapprich, A. D. Daniels, A. Farkas, J. B. Foresman, J. V. Ortiz, J. Cioslowski, and D. J. Fox, Revision D01 ed. (Ed.: I. Gaussian, Wallingford CT), 2009.
[15] A.G. Bingham, H. Bögge, A. Müller, E.W. Ainsscough, A. Brodddie, J. Chem. Soc. Dalton Trans. (1987) 493–499.
[16] J. Kendrick, J.K. Nelson, A.I. Guzei, S.G. Lund, W.R. McGaff, Polyhedron 21 (2002) 2017–2020.

Please cite this article in press as: F. Gennarini et al., Inorg. Chim. Acta (2017), https://doi.org/10.1016/j.ica.2017.09.067

Résumé français

Principaux résultats des travaux de thèse

1. Etat de l'art et objectifs de la thèse.

Les protéines à cuivre sont impliquées dans de nombreuses réactions fondamentales.[1] Le cuivre joue en effet un rôle important dans de multiples réactions biologiques telles que le métabolisme énergétique (cytochrome *c* oxydase), la production de mélanine (tyrosinase) ou la régulation d'hormones (PHM, DβM). Le cuivre est également impliqué dans de nombreux processus de formation/régulation d'espèces réactives du dioxygène. Il participe au transport du dioxygène dans les mollusques (hémocyanine), ou bien à l'oxydation de méthane en méthanol (méthane monoxygénase particulaire, pMMO, Figure VI.1).[2] De manière générale, une grande majorité des enzymes à cuivre a pour fonction d'activation le dioxygène pour son incorporation dans des biomolécules (oxygénases) ou bien sa réduction en H_2O (oxydases), servant alors d'accepteur d'électrons. Le rôle de ces catalyseurs est essentiel car O_2 n'est pas un bon oxydant d'un point de vue cinétique pour les substrats organiques, du fait de sa configuration en état triplet.

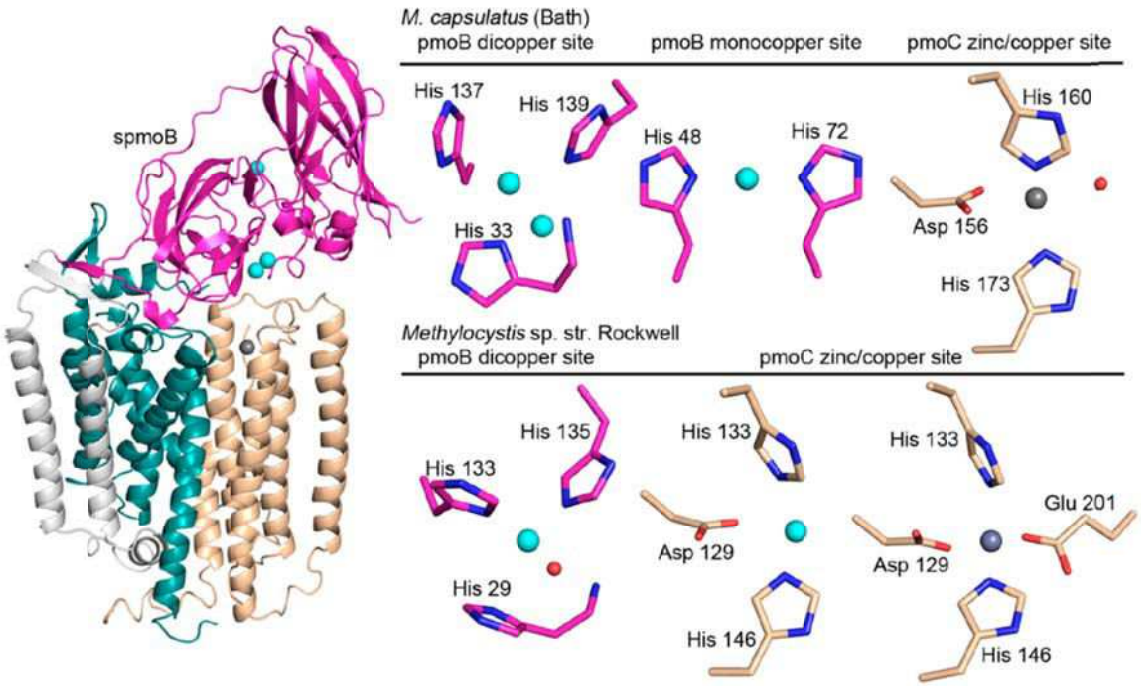

Figure VI.1. Structure RX de la pMMO contenant trois sous-unités (pmoB (magenta), pmoA (cyan), pmoC (marron)) et deux hélices transmembranaires (gris).[3]

L'activation de l'oxygène moléculaire par les sites actifs des enzymes à cuivre s'opère par réaction de l'oxygène moléculaire avec un ou plusieurs centres Cu^I, aboutissant à la formation d'espèces transitoires oxydantes superoxyde, peroxyde ou autres (Figure VI.2).[4] Tout particulièrement, les oxygénases à cuivre sont des oxydoréductases qui permettent le transfert d'un

atome d'oxygène provenant du dioxygène à un substrat défini. Cette famille inclut les monoxygénases (transfert d'un atome) et les dioxygénases (transfert de deux atomes).

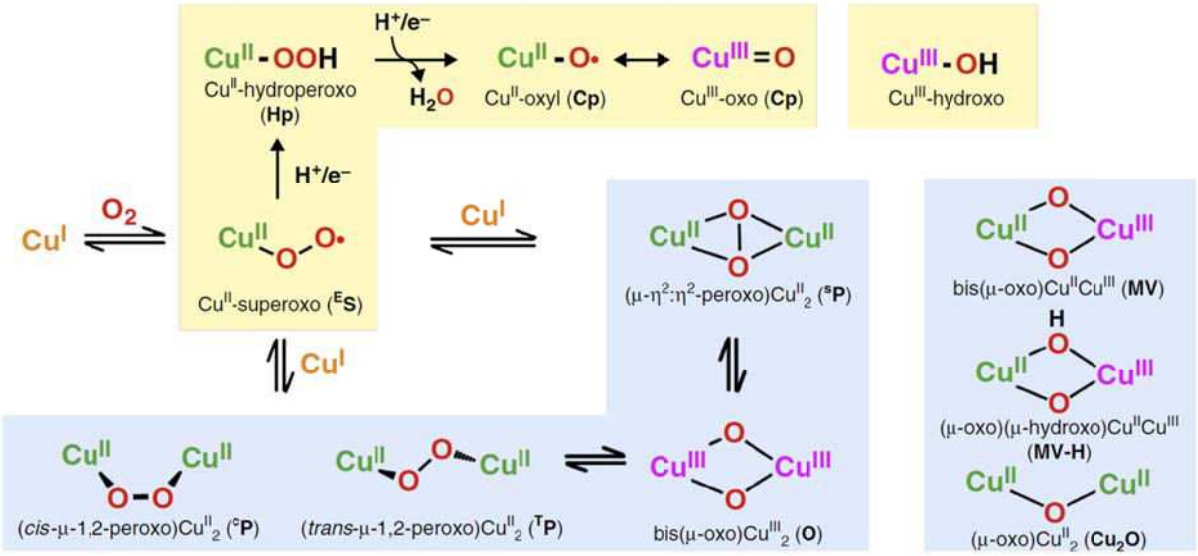

Figure VI.2. Principaux adduits cuivre-oxygène dans les enzymes à cuivre et dans leurs modèles synthétiques. [5]

La conception de systèmes bioinspirés et/ou biomimétiques capables de reproduire les propriétés des enzymes à cuivre est un défi majeur pour le développement de nouveaux dispositifs efficaces dans de nombreux domaines (catalyse, énergie, santé, industrie,...). Les modèles synthétiques de la pMMO sont particulièrement recherchés afin d'effectuer l'oxydation catalytique du méthane sous pression atmosphérique et à température ambiante à partir du dioxygène. Actuellement, la production industrielle de méthanol à partir du méthane est accomplie selon un procédé très coûteux en énergie et peu sélectif (reformage vapeur). Le mécanisme exact de l'activation C-H par la pMMO reste encore non élucidé, aucun intermédiaire réactionnel n'ayant pu être identifié. Différentes hypothèses de mécanismes ont été proposées sur la base de modèles expérimentaux et de calculs théoriques. Ainsi, plusieurs espèces intermédiaires cuivre-oxygène ont été suggérées pour l'oxydation du méthane en méthanol (Figure VI.2) : mononucléaire (oxo), dinucléaire (μ-oxo) ou (μ-η^2:η^2-peroxo) ou trinucléaires (μ-oxo).[4],[6],[7] Sur la base des données RX montrant la présence d'un site dinucléaire (Figure VI.1), Yoshizawa *et al.* ont réalisé des calculs théoriques sur la réactivité d'un site bis-cuivre vis-à-vis du méthane.[7] Les calculs indiquent clairement que l'espèce la plus probable pour l'activation C-H serait une espèce dinucléaire bis(μ-oxo) à valence mixte ($Cu^{III}Cu^{II}$) (Figure VI.2). La caractérisation par voies spectroscopiques et électrochimiques d'une telle espèce est donc primordiale pour le développement de catalyseurs efficaces. Au commencement de ces travaux de thèse (2014), un seul exemple d'espèce Cu^{II}-(μ-OH)-Cu^{III} avait été décrit par l'équipe de Tolman (Figure VI.3) sur la base d'études voltammétriques et spectroscopiques (UV-VIS-NIR) à basse température.[8] La

caractérisation de cet adduit cuivre-oxygène est en effet difficile du fait de son instabilité à température ambiante. De manière plus générale, il existe très peu de données sur les propriétés redox de ce type d'adduit. Des études récentes ont démontré la possibilité d'utiliser des agents chimiques pour estimer les potentiels redox des espèces, mais cette approche est une mesure indirecte, donc approximative. De plus, elle ne permet pas d'accéder à des données essentielles telles que la cinétique de transfert d'électron.[9]

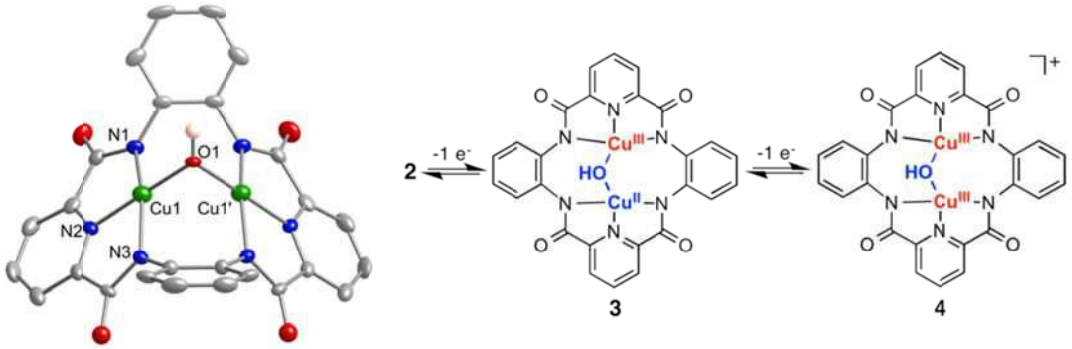

Figure VI.3. Structure RX et processus d'oxydations successives du complexe bis-cuivre hydroxo développé par Tolman *et al.*[8]

Dans ce cadre, l'objectif principal de la thèse a été de caractériser par voies électrochimiques et spectroscopiques des espèces à valence mixte $Cu_2^{III,II}$ bis(μ-O) ou bis(μ-O(H), μ-O(H)),qui sont considérées comme étant des espèces clés pour l'activation de la liaison C-H dans la pMMO.[4],[7] Comme notifié auparavant, de telles caractérisations nécessitent l'emploi de techniques particulières. Ainsi, un travail important de la thèse a consisté à développer des systèmes cryogéniques (-90 °C) permettant des études électrochimiques et spectroélectrochimiques à basse température. Tout particulièrement, les études réalisées se sont focalisées sur les techniques couplant électrochimie et spectroscopie UV-Vis-NIR ou RPE. En effet, les adduits cuivre-oxygène présentent des signatures typiques en spectroscopie UV-Vis. De plus, les spectroscopies RPE et proche-infrarouge permettent d'obtenir des informations sur la (dé)localisation de l'électron célibataire au sein du complexe à valence mixte.

Deux stratégies sont envisageables pour la préparation des espèces à valence mixte (Figure VI.4). La première (« Stratégie 1 ») est basée sur la réaction entre le dioxygène et un complexe de Cu^I, suivie d'une mono-réduction. Cette approche est intéressante car elle est analogue aux processus enzymatiques. Cependant, elle nécessite la préparation d'espèces cuivreuses qui peuvent se décomposer très rapidement. La seconde approche ("Stratégie 2") utilise une espèce (μ-hydroxo) ou bis(μ-hydroxo)$Cu_2^{II,II}$ qui est mono-oxydable en un intermédiaire à valence mixte $Cu^{III}Cu^{II}$. Cette stratégie a l'avantage d'utiliser des précurseurs stables (non sensibles au dioxygène) et conduit en une

seule étape au complexe à valence mixte désiré. Néanmoins, la question d'un simple transfert électronique ou bien d'un transfert couplé proton-électron (PCET) se pose, l'espèce finale pouvant être un cluster $Cu^{III}Cu^{II}$ bis(μ-OH), (μ-OH,μ-O), ou bis(μ-O). Ces trois intermédiaires possibles peuvent effectivement posséder des propriétés catalytiques tout à fait différentes pour l'activation de liaisons C-H. Ces deux stratégies générales peuvent être appliquées à la fois à des ligands mono- ou dinucléants. Du fait du grand nombre de possibilités, nous avons limité nos études à la stratégie 2 (oxydation d'une espèce (bis)μ-hydroxo) appliquée à des complexes dinucléaires pontés par un groupement organique coordinant (Figure VI.4).

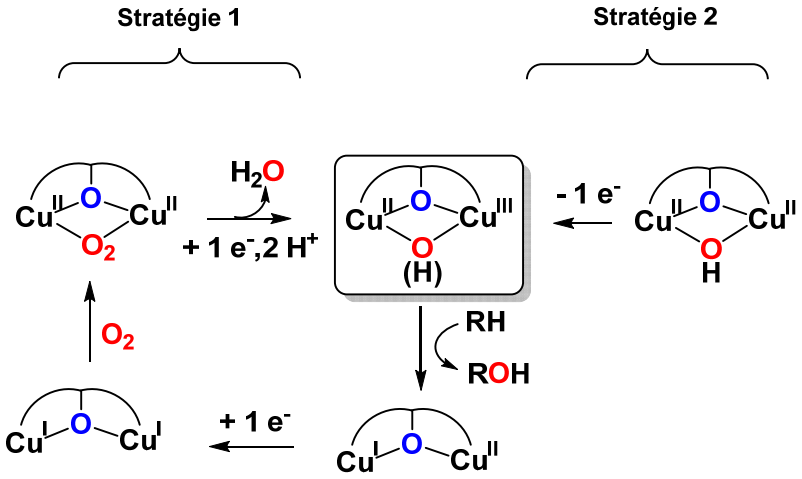

Figure VI.4. Stratégies 1 et 2 pour accéder à une espèce bis(μ-oxo)$Cu^{III}Cu^{II}$ à partir d'un ligand dinucléant.

L'étape suivante a consisté à définir l'identité du ligand pontant les ions cuivrique, ainsi que celle des groupements coordinants de chaque côté du pont. Sur la base structurale du site actif de la pMMO, la distance entre deux ions de cuivre doit avoisiner 2,6 Å idéalement, les ligands coordinants sur chaque bras devant reproduire le motif polyhistidine du site actif. Pour ces raisons, notre choix s'est porté essentiellement sur des ligands porteurs de ponts rigides afin de forcer une distance inter-cuivre optimale. Différents systèmes ont ainsi été envisagés. La Figure VI.5 présente les trois ponts qui ont été utilisées pour ce travail : phénoxo, alkoxo et naphthyridyle. Ces trois systèmes possèdent un ou plusieurs atomes coordinants pour les ions cuivriques, permettant de fixer potentiellement la distance Cu-Cu. D'autre part, deux familles de ligands coordinants, polypyridyle ou polyamide, sur chaque bras ont été considérées, l'intérêt étant de stabiliser l'état Cu^{III} par des groupements donneurs. La combinaison des différents espaceurs avec ces groupements donneurs a abouti à l'élaboration de divers ligands symétriques et dissymétriques.

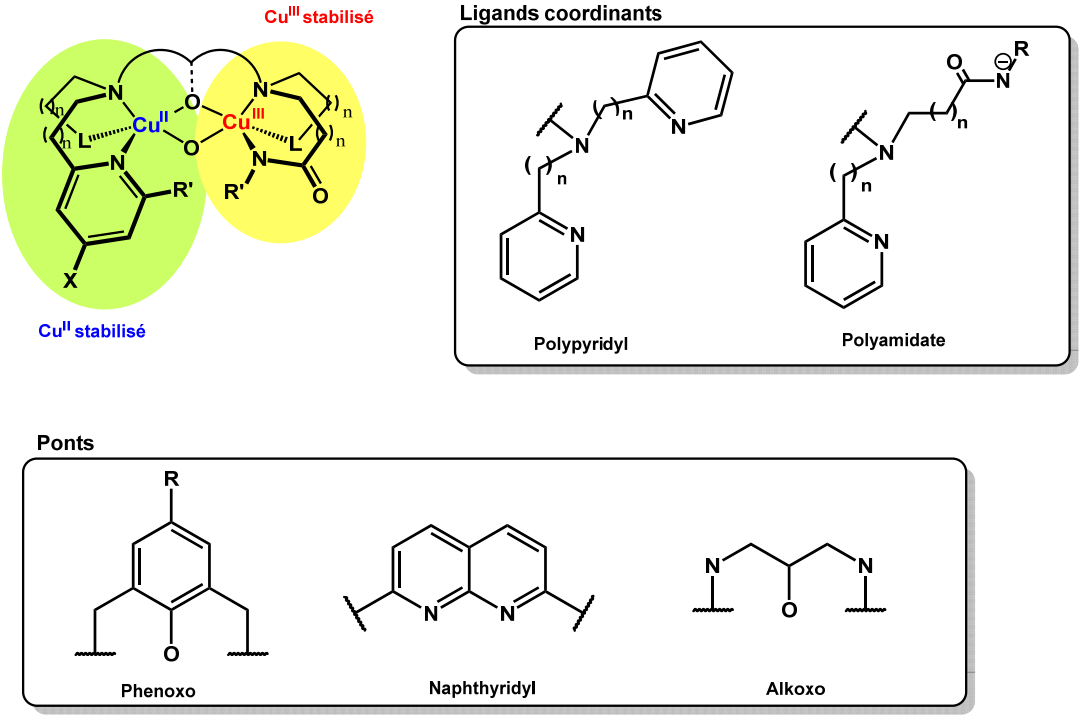

Figure IV.5. Différents ponts et ligands coordinants utilisés pendant la thèse pour la synthèse de complexes bis-cuivre.

Toutes les synthèses des ligands et complexes de cuivre rapportées dans ce manuscrit ont été réalisées par des équipes collaboratrices à Marseille (Dr M. Réglier, Dr J. Simaan) et Grenoble (Dr C. Belle, Dr A Thibon-Pourret). Les calculs théoriques ont été effectués par les Dr H. Jamet (Grenoble) et Dr. A. Kochem (Marseille). Ce manuscrit rapporte ainsi la études électrochimiques et spectroélectrochimiques à température ambiante et à basse température des différents complexes du cuivre décrits ci-dessus, ainsi que les études théoriques associées.

2. Etudes des complexes 1, 2 et 3, porteurs d'un pont phenoxo et de bras DPA

Les premières études ont été réalisées sur des complexes bis-cuivre(II) porteurs de ligands BPMP (**1a**$^{2+}$, **1b**$^{2+}$, **1c**$^{2+}$), BPEP (**2a**$^{2+}$) et BPMEP (**3a**$^{2+}$) (Figure VI.6). Les différentes synthèses des ligands et complexes ont été préalablement décrites, ainsi que l'étude électrochimique dans l'acétonitrile des complexes **1a**$^{2+}$, **1b**$^{2+}$ et **1c**$^{2+}$. Les objectifs de ces études ont donc été les suivants:

(i) Étudier les effets de la topologie du ligand (symétrie/dissymétrie) sur les propriétés redox et corréler les résultats expérimentaux aux données théoriques.

(ii) Explorer les propriétés d'oxydation des complexes vis-à-vis de substrats externes. Plus précisément, il est bien connu que l'oxydation d'un groupement phénoxo mène à la formation d'un radical phénoxyle, pouvant aboutir à l'oxydation de l'alcool benzylique ou au clivage de l'ADN.

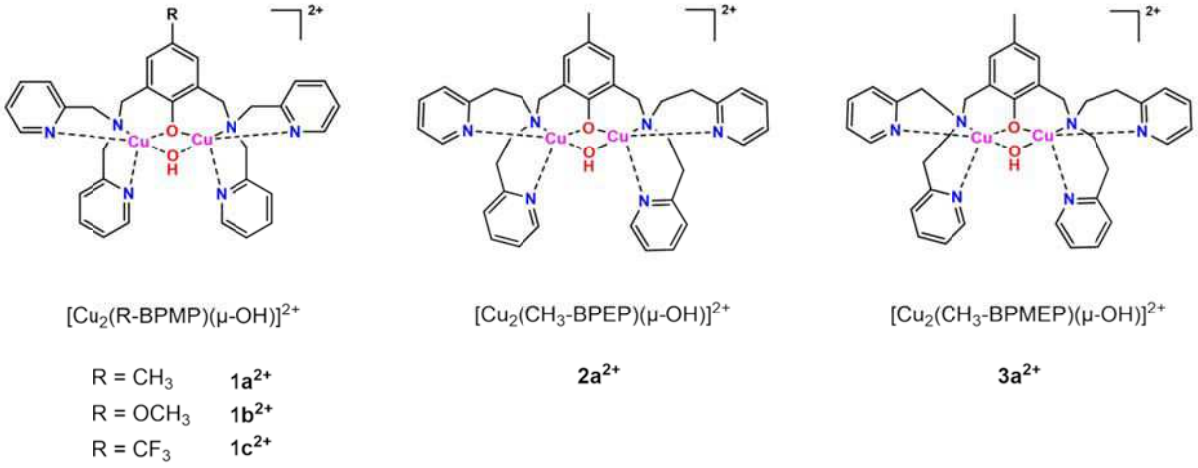

Figure VI.6. Représentation schématique des complexes [**1-3**]$^{2+}$ étudiés.

Les études électrochimiques et théoriques que nous avons réalisées dans différents solvants sur ces complexes dinucléaires démontrent que les propriétés redox en oxydation et en réduction peuvent être régulées par légère modification de la topologie de ligand. Ainsi, la variation du groupement R pour les complexes **1a**$^{2+}$, **1b**$^{2+}$ et **1c**$^{2+}$ induit un changement notable du potentiel d'oxydation (Tableau VI.1). D'autre part, en corrélation avec les calculs DFT, l'augmentation de la longueur de l'espaceur amine-pyridyle dans les motifs pyridylamine (DPA), ou bien la rupture de la symétrie de la molécule induit un déplacement du potentiel d'oxydation vers des valeurs positives, en accord avec une légère distorsion géométrique du motif phénoxo vis-à-vis du plan Cu_2O_2.

Tableau VI.1. Données électrochimiques [E^0/ V *vs* Fc (ΔE_p / mV)] des complexes **1a**$^{2+}$, **1b**$^{2+}$, **1c**$^{2+}$, **2a**$^{2+}$ et **3a**$^{2+}$ dans différent solvants /NBu_4PF_6 0,1 M (Solvant = MeCN, THF, PC).

	Solvent	**1a**$^{2+}$	**1b**$^{2+}$	**1c**$^{2+}$	**2a**$^{2+}$	**3a**$^{2+}$
Oxyd.	MeCN	0,71 (170)	0,51 (70)	1,20[a]	1,04[a]	0,90[a]
	THF	0,60 (280)	0,45 (90)	1,05[a]	1,01[a]	0,84[a]
	PC	0,67 (150)	0,49 (100)	1,22[a]	1,05[a]	0,93[a]
Reduct. I	MeCN	-1,03 (110)	-1,02 (105)	-0,95 (90)	-1,09[a]	-0,91 (140)
	THF	-1,11 (130)	-1,09 (130)	-1,03 (100)	-1,08[a]	-1,04 (140)
	PC	-1,03 (105)	-1,03 (100)	-0,95 (100)	-1,11[a]	-0,96[a]
Reduct. II	MeCN	-1,34[c]	-1,39[a]	-1,29[a]	[b]	-1,32[a]
	THF	-1,44 (130)	-1,41 (140)	-1,31 (140)	[b]	-1,41[a]
	PC	-1,38[a]	-1,38[a]	-1,27[a]	[b]	-1,36[a]

[a] Pic irréversible. [b] Pas de second pic de réduction observé.

De manière intéressante, les études spectroélectrochimiques à température ambiante montrent que la longueur de l'espaceur sur chaque bras DPA joue sur la nature de l'espèce formée par oxydation. Les complexes **1a**$^{2+}$, **1b**$^{2+}$ et **1c**$^{2+}$ présentent ainsi un signal caractéristique d'un radical phénoxyle par oxydation, en conformité avec une oxydation centrée sur le pont phénoxo (Figure VI.7). A contrario, les deux complexes **2a**$^{2+}$ et **3a**$^{2+}$ aboutissent à la formation d'une espèce à valence mixte $Cu_2^{III,II}$ avant d'évoluer vers un radical phénoxyle. Tout particulièrement pour le complexe **3a**$^{2+}$, l'espèce à valence mixte présente une bande d'absorption à λ = 518 nm (Figure VI.8). D'après les calculs DFT, cette bande correspondrait à un transfert de charge du phénoxo vers l'ion Cu(III).

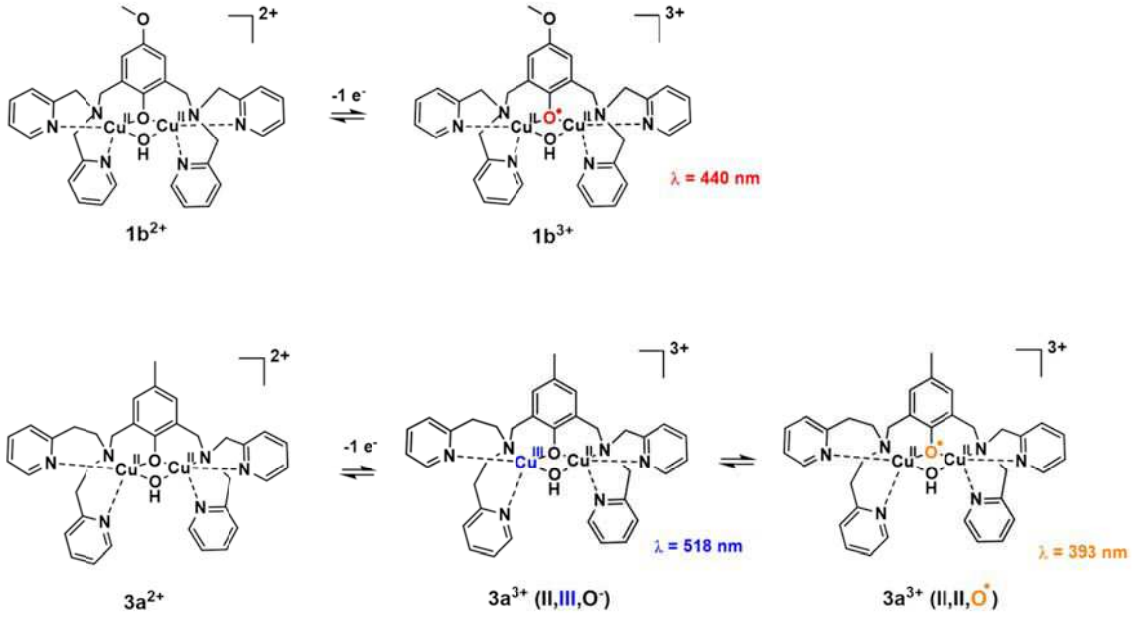

Figure VI.7. Espèces détectées par spectroélectrochimie pour l'oxydation de **1b**$^{2+}$ (haut) et **3a**$^{2+}$ (bas).

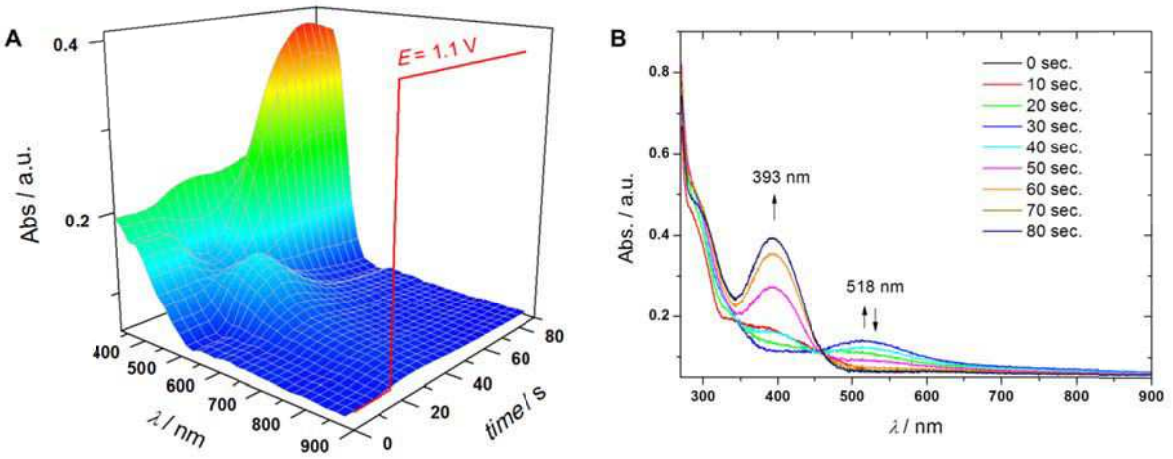

Figure VI.8. A) Représentation 3D du suivi spectroélectrochimique de l'oxydation du complexe $\mathbf{3a}^{2+}$ à 1,10 V *vs* Fc dans CH_3CN/NBu_4PF_6 (conditions : couche mince, trajet optique 0,2 mm, C = 4 mM) à 293 K. B) Suivi 2D des spectres UV-Vis.

Suite à ces résultats, nous nous sommes intéressés à la réactivité potentielle du radical phénoxyle $\mathbf{1b}^{3+}$, formé par oxydation électrochimique de $\mathbf{1b}^{2+}$, vis-à-vis de substrats organiques. Le complexe n'a démontré aucune activité électrocatalytique pour l'oxydation d'alcool benzylique dans l'acétonitrile. Cependant, l'accessibilité du substrat au radical phénoxyle et la réactivité vis-à-vis d'une amine primaire aliphatique ont été clairement mises en évidence par voltammétrie cyclique (Figure VI.9). Par utilisation d'un complexe analogue non porteur d'un groupement μ-OH (complexe $\mathbf{1d}^{4+}$), les études ont également suggéré que la réaction avec le radical phénoxyle se déroule selon un mécanisme de sphère externe (pas de coordination du substrat nécessaire pour un transfert d'électron).

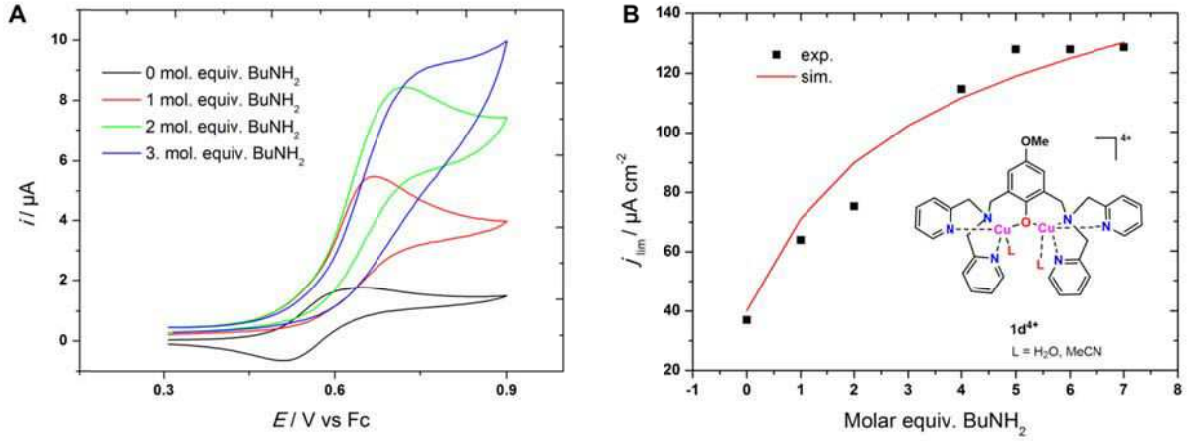

Figure VI.9. A) Voltammogrammes cycliques (v = 0,005 V/s) du complexe $\mathbf{1d}^{4+}$ dans CH_3CN/NBu_4PF_6 0.1 M sous ajout progressif de butylamine. B) Variation de la densité de courant avec la concentration en butylamine (courbe rouge : simulation selon un processus catalytique).

3. Etude du complexe 4 porteur d'un pont naphthyridyle

Suite aux résultats obtenus sur les complexes dinucléaires à pont phenoxo montrant essentiellement que l'espèce formée par oxydation aboutit à un radical phénoxyle, un nouveau complexe porteur d'un pont naphthyridyle a été synthétisé et étudié par voies électrochimique et spectroscopique. Ce groupement pontant est intéressant car sa rigidité le rend apte à forcer une distance Cu-Cu de l'ordre de 3 Å. Il est d'autre part non électroactif dans la zone de potentiel d'intérêt lorsque lié à un métal. Le complexe bis(μ-OH) **4** synthétisé présente ainsi une distance Cu^{II}-Cu^{II} de 2,75 Å (Figure VI.10). Il est oxydé électrochimiquement à 1,26 V *vs* Fc dans l'acétonitrile (confirmé à 1,36 V par DFT). La voltammétrie cyclique à différentes vitesses de balayage indique que l'espèce oxydée n'est pas très stable à température ambiante, et évolue selon un mécanisme de type ECE (E= Electrochimie, C = Chimique) (Figure VI.11).

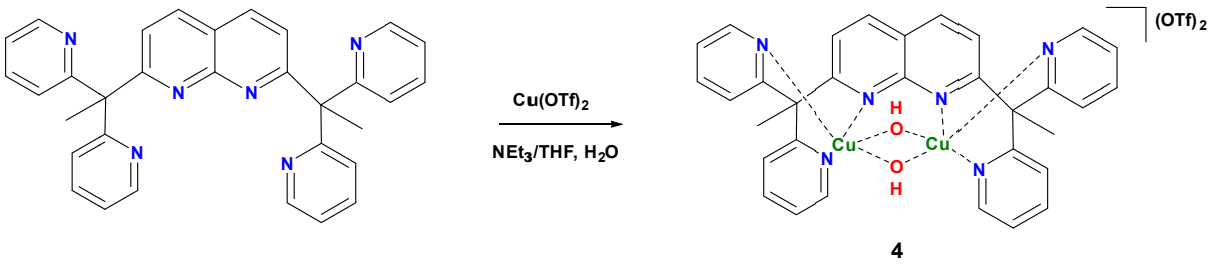

Figure VI.10. Synthèse du complexe **4**.

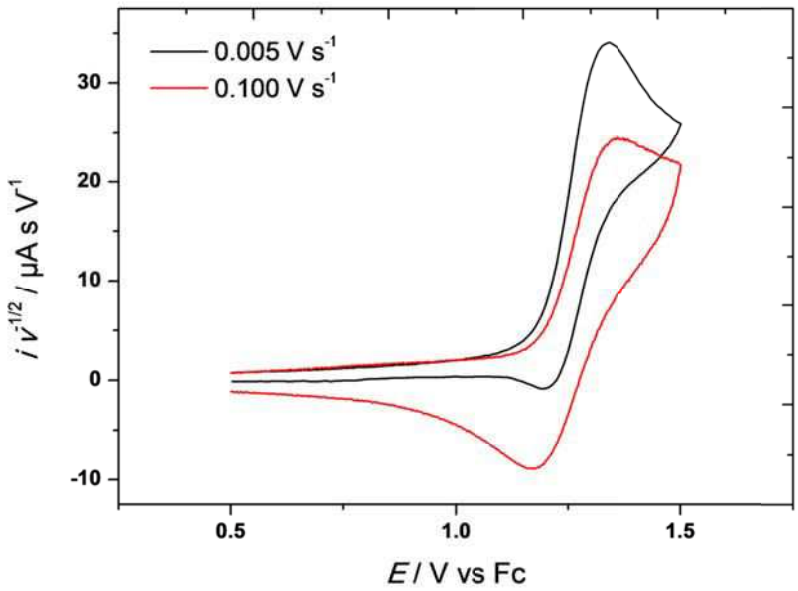

Figure VI.11. Voltammogrammes cycliques normalisés sur la racine carrée de la vitesse de balayage du complexe $\mathbf{4}^{2+}$ (C = 1 mM) dans 0,1 M Bu_4PF_6/CH_3CN (v = 0,005 V/s (noir) et v = 0,1 V/s (rouge)).

L'analyse des données électrochimiques montre que l'oxydation du complexe $\mathbf{4}^{2+}$ est mono-électronique, conduisant probablement à un complexe à valence mixte bis(μ-OH) $Cu_2^{III,II}$. L'utilisation de la spectroélectrochimie à température ambiante et à basse températures a permis de caractériser l'espèce oxydée générée. Celle-ci présente une bande d'absorption à λ_{max} = 424 nm (Figure VI.12), correspondant, d'après les calculs TD-DFT, à un transfert de charge d'une pyridine vers un ion Cu^{III} (Figure IV.13). Dans le proche-infra-rouge, une bande faible à λ_{max} = 1344 nm a été également observée, suggérant une faible délocalisation de la charge (Figure VI.14). L'analyse des spectres indique que cette espèce est de type II dans la classification de Robin−Day pour les espèces à valence mixte. La spectroscopie RPE du complexe formé par oxydation de $\mathbf{4}^{2+}$ par électrolyse à froid montre une signature typique d'un centre Cu^{II} mononucléaire. L'analyse par DFT des différentes espèces oxydées probables (bis(μ-O), bis(μ-OH), (μ-OH, μ-O)) converge vers la formation d'une espèce bis-μ-hydroxo) $Cu_2^{III,II}$.

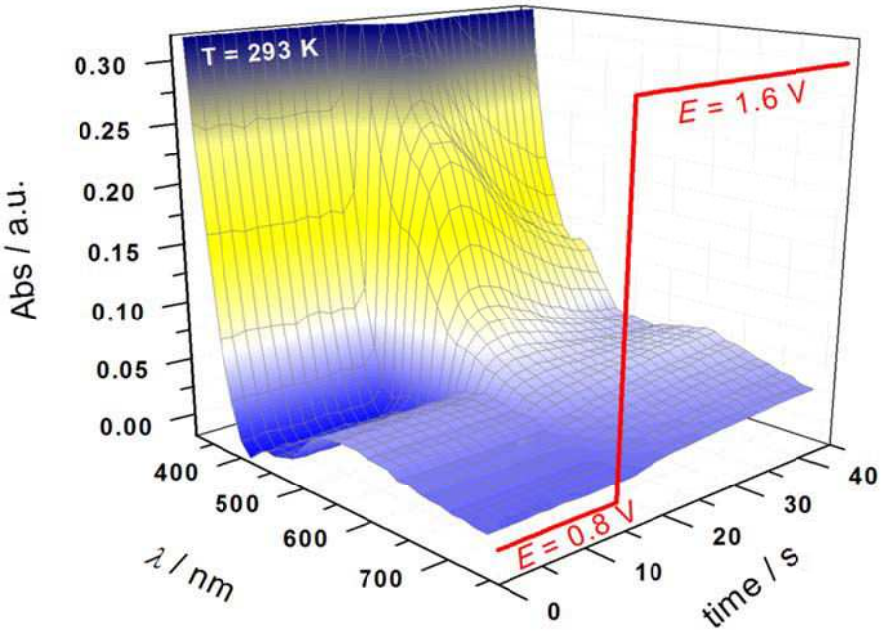

Figure VI.12. Représentation 3D du suivi spectroélectrochimique de l'oxydation du complexe $\mathbf{4}^{2+}$ à 1,6 V *vs* Fc dans CH_3CN/NBu_4PF_6 (conditions couche mince, trajet optique 0,2 mm, C = 10 mM) à 293 K.

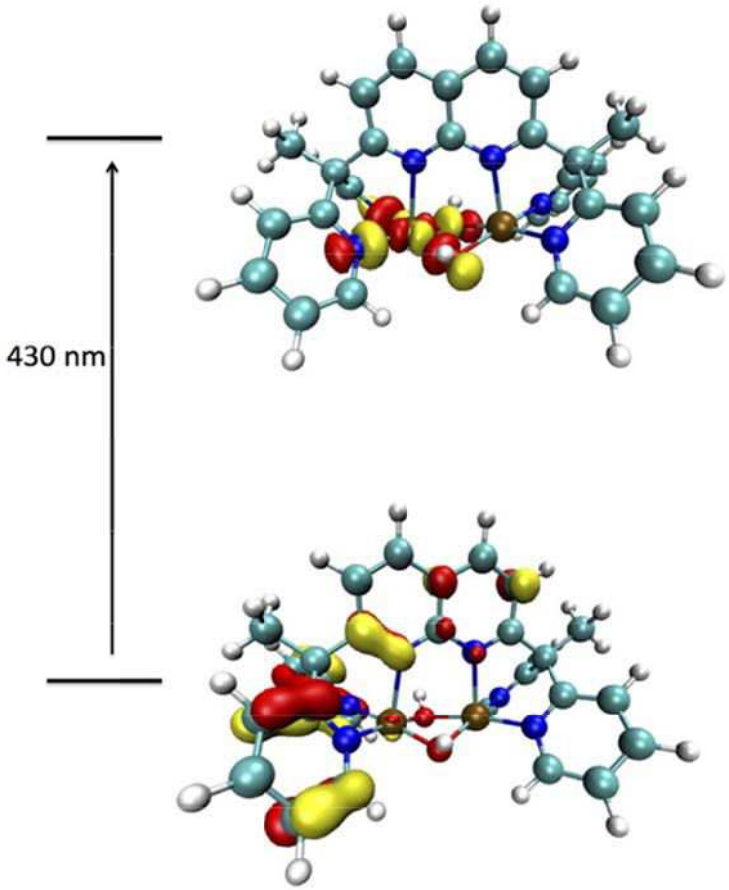

Figure VI.13. Transfert de charge Pyridine vers Cu^{III} calculé par TD-DFT, associé à la bande d'absorption détectée expérimentalement à 424 nm.

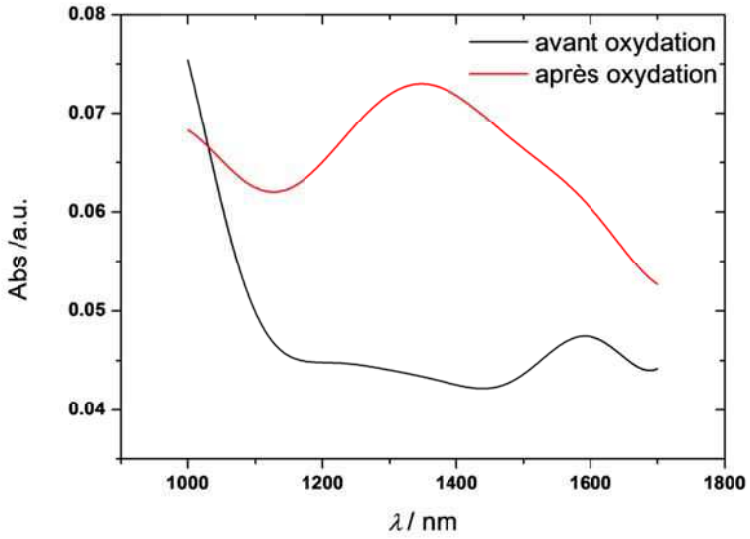

Figure VI.14. Spectre proche-infrarouge (T = 223 K, trajet optique 0,2 mm) du complexe $\mathbf{4}^{2+}$ dans CH_3CN/NBu_4PF_6 avant (noir) et après (rouge) oxydation à E = 1,6 V *vs* Fc.

4. Etude des complexes 5 et 6, porteurs de bras bis-amide.

Les études électrochimiques et spectroélectrochimiques sur les complexes **1-4** ont démontré que l'oxydation mono-électronique sur un des deux ions métalliques est favorisée si le groupement pontant est faiblement oxydable (tel que pour **4**), et/ou lorsque le ligand présente une dissymétrie structurale (telle que pour **3a**). Même lorsqu'une de ces conditions est remplie, nous avons observé que le potentiel d'oxydation pour accéder à l'espèce valence mixte est très élevé (1,3 V *vs* Fc pour **4**), ou bien le complexe évolue rapidement vers une nouvelle espèce par transfert électronique interne avec le pont phénoxo (complexe **3a**). Puisque notre objectif est de caractériser une espèce $Cu^{III}Cu^{II}$ (μ-O(H)), nous avons poursuivi nos travaux en mettant l'accent sur le développement de ligands qui pourrait stabiliser un état redox de Cu^{III} afin de réduire le potentiel d'oxydation. Sur la base d'une étude bibliographique, l'état redox Cu^{III} peut être stabilisé par l'emploi de groupements amide ou bis-amide. Ainsi, notre objectif a été d'accéder à des espèces à valence mixte de bas degré d'oxydation en incorporant un ou deux groupements bis-amide à la place des motifs DPA. Deux complexes différents ont été préparés, selon la nature du pont (alkoxo pour **5**, phénoxo pour **6**), et le nombre (1 ou 2) de groupements bis-amide (Figure VI.15).

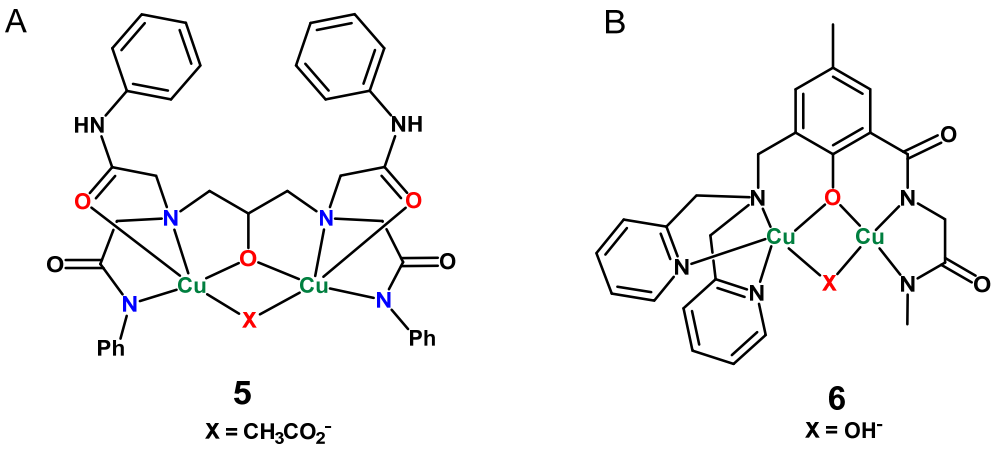

Figure VI.15. Complexes bis-cuivre **5** and **6** porteurs de groupements bis-amide.

L'analyse par diffraction aux rayons X de cristaux de complexe **5** montre que les deux ions Cu^{II} sont chacun dans un environnement bis-amide, et reliés par deux ponts (μ-alkoxo et μ-acetato). Le complexe **6** présente une structure dissymétrique liée à la topologie du ligand porteur d'un bras bis-amide d'un côté, et d'un bras DPA de l'autre côté. Les deux ions Cu^{II} dans **6** sont reliés par un pont phénoxo, ainsi qu'un groupement μ-OH. La distance inter-cuivre pour ces deux complexes est respectivement 3,4 et 3,0 Å. L'analyse voltammétrique à température ambiante dans le DMF de ces deux complexes suggère une oxydation mono-électronique ayant lieu sur un ion Cu^{II} dans l'environnement bis-amide. Le potentiel redox est sensiblement diffèrent selon le complexe (E_{pa} = 0,63 V *vs* Fc et $E_{1/2}$ = 0,12 V *vs* Fc pour **5** et **6**, respectivement). Dans les deux cas, le processus d'oxydation est suivi d'une réaction chimique.

Concernant le complexe **5,** l'analyse spectroélectrochimique (Figure VI.16) montre que l'espèce formée présente une bande d'absorption à λ_{max} = 463 nm. Les calculs DFT suggèrent la formation d'un complexe $Cu_2^{III,II}$ à valence mixte où l'ion acétate est décoordiné d'un ou des deux centres cuivre (Figure VI.17). D'autre part, la substitution du pont acétato par un ligand methoxo aboutit à la formation d'une nouvelle espèce attribuée par les calculs DFT à un complexe bis-cuivre(II) porteur d'un ligand methoxo coordiné de manière monodentate au Cu^{II} (Figure VI.17). Ce nouveau complexe s'oxyde électrochimiquement à 1 électron à E_{pa} = 0,40 V *vs* Fc, c'est-à-dire à une valeur de potentiel inférieure à celle de **5**.

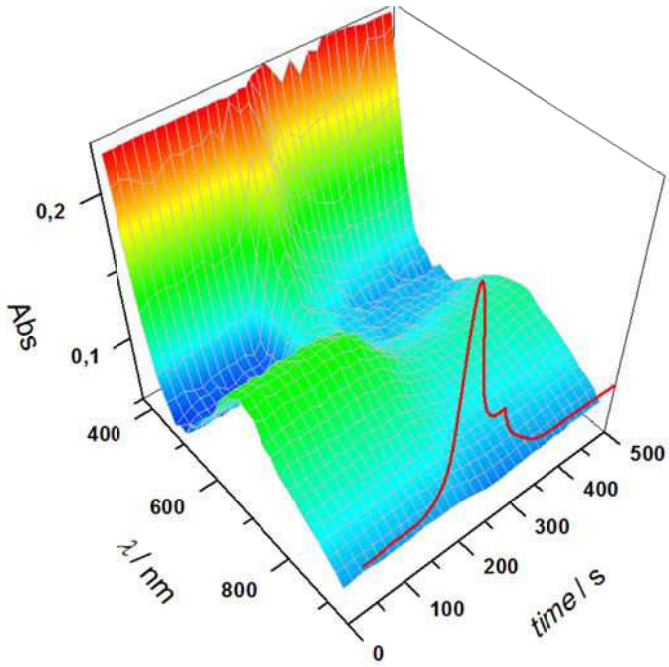

Figure VI.16. Représentation 3D du suivi spectroélectrochimique à T = 293 K de l'oxydation du complexe **5** dans DMF/NBu_4PF_6 (0,1 M) (trajet optique 0.2 mm) ; courbe rouge: voltammogramme cyclique en couche mince (v = 0,005 V/s).

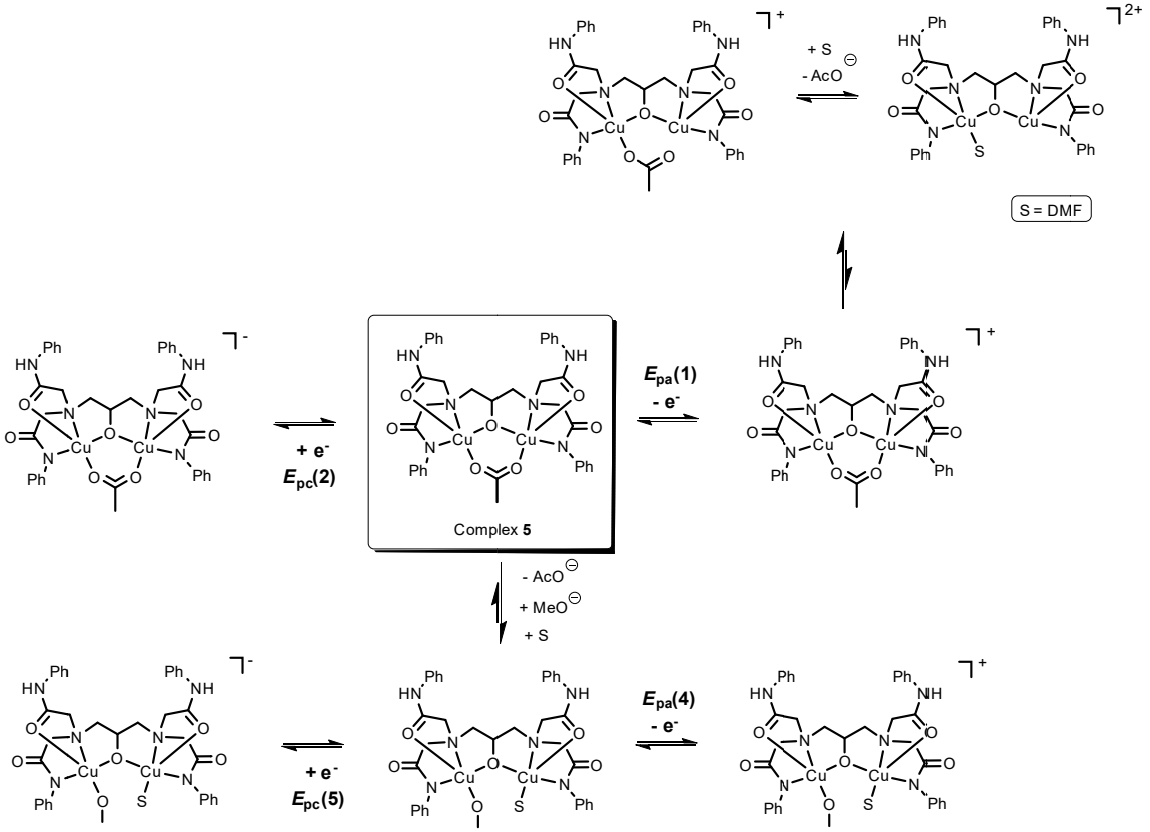

Figure VI.17. Proposition de mécanisme d'échange de ligand et d'oxydoréduction pour le complexe **5** sur la base des résultats électrochimiques, spectroélectrochimiques et théoriques.

Pour le complexe **6**, l'oxydation électrochimique conduit à une espèce instable à température ambiante. Cette espèce a pu néanmoins être stabilisée pendant plusieurs minutes à basse température dans le DMF (213 K). En effet, à cette température, le complexe démontre un comportement réversible électrochimiquement par voltammétrie cyclique (Figure VI.18).

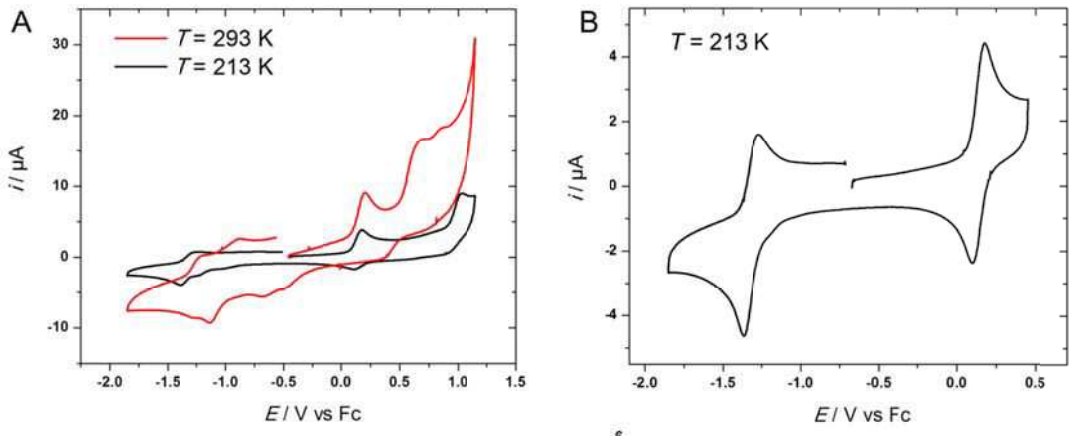

Figure VI.18. Voltammogrammes cycliques (v = 0,1 V/s) du complexe **6** dans DMF/NBu_4ClO_4 0.1 M, A) à deux températures différentes (T = 293 K and 213 K); B) à T = 213 K sur les premiers processus redox en oxydation et réduction.

Ce résultat suggère que l'espèce $\mathbf{6}^{+}$ formée par oxydation électrochimique est probablement similaire d'un point de vue structural au complexe **6**, l'ion cuivre(III) étant certainement dans l'environnement bis-amide (Figure VI.19).

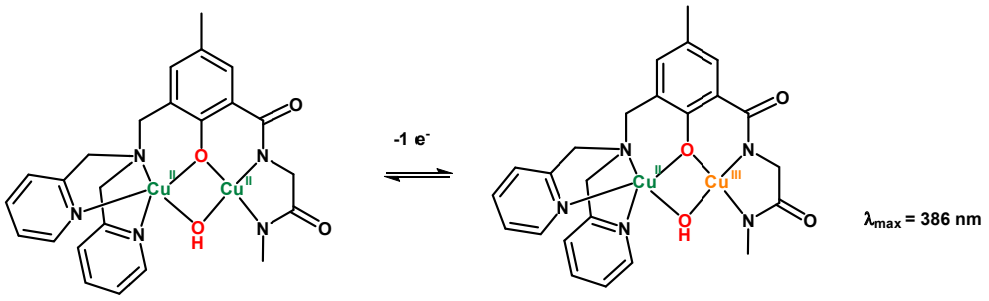

Figure VI.19. Structures proposées pour la mono-oxydation du complexe **6**.

Les études cryo-spectroélectrochimiques montrent l'émergence d'une bande d'absorption à λ_{max} = 386 nm (Figure VI.20). Cette bande pourrait ainsi correspondre, par analogie aux complexes précédents, à un transfert de charge du ligand (phénoxo ou amido) vers Cu^{III}. Des calculs TD-DFT sont actuellement en cours pour infirmer cette hypothèse.

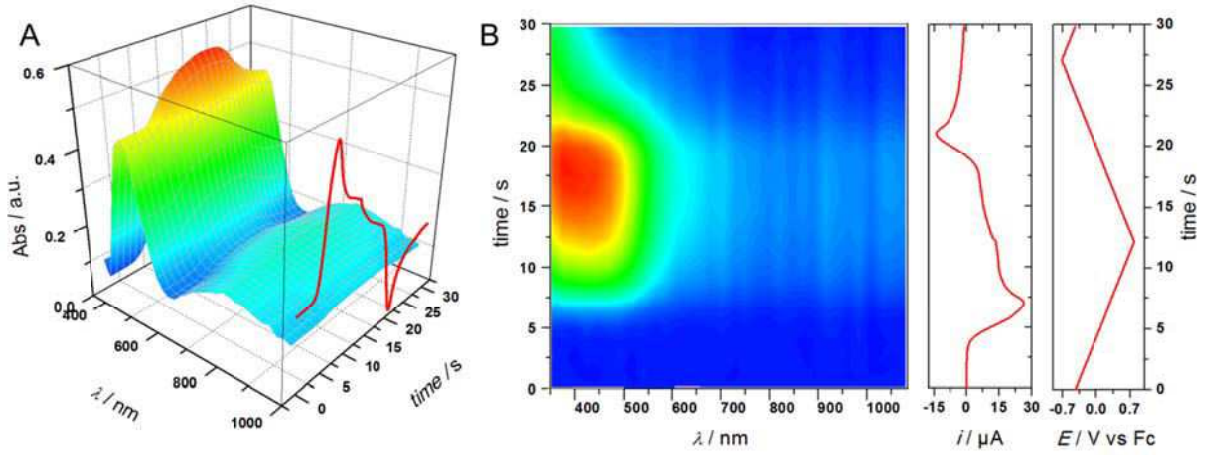

Figure VI.20. A) Représentation 3D du suivi spectroélectrochimique à T = 213 K de l'oxydation du complexe **6** dans DMF/NBu_4ClO_4 (0,1 M) (trajet optique 0,2 mm) ; courbe rouge: voltammogramme cyclique en couche mince (v = 0.1 V/s). B) Représentation 2D du spectre différentiel obtenu par rapport au spectre initial pour l'oxydation électrochimique du complexe **6**. Les courbes rouges sur les panneaux de droite représentent la variation de l'intensité du courant (i) et du potentiel appliqué (E) avec le temps.

5. Conclusions

L'objectif principal de ce projet de thèse était de développer et de caractériser des complexes modèles du site actif de l'enzyme pMMO. En particulier, les travaux ont porté sur l'étude de différents complexes porteurs de ligands dinucléants afin de générer des espèces à valence mixte de type $Cu_2^{III,II}$ bis(μ-OH), qui ont été suggérées pour être des intermédiaires clés pour l'oxydation du méthane en méthanol dans la pMMO. Par conséquent, plusieurs ligands ont été synthétisés en faisant varier les motifs coordinant chacun des ions cuivre (polypyridyl, bis-amide) ainsi que le pont (phénoxo, alkoxo, naphtyridine) reliant les groupements coordinants. Ces études, essentiellement électrochimiques et spectroscopiques, ont nécessité le développement de montages spécifiques de cryo-électrochimie et cryo-spectroélectrochimie afin de caractériser les espèces cuivre-oxygène (Figure VI.21, Tableau 2).

Les études ont débuté avec une famille de complexes à pont phénoxo porteurs de groupements faiblement donneurs DPA. L'oxydation monoélectronique de ces complexes suggère une oxydation centrée essentiellement sur le groupement phénoxo pontant, sauf lorsqu'une certaine flexibilité est apportée sur les groupements DPA. Tout particulièrement le complexe dissymétrique $\mathbf{3a}^{2+}$ s'oxyde en une espèce transitoire à valence-mixte (III,II) présentant une bande d'absorption à λ_{max} = 518 nm. La substitution du pont phénoxo par un pont naphthyridyle aboutit à la formation d'un nouveau complexe bis(μ-OH) **4** dont l'oxydation est principalement centrée sur le métal. L'espèce à valence mixte est stable quelques secondes à température ambiante et présente une bande d'absorption à λ_{max} = 424 nm, attribué à un transfert de charge d'une pyridine vers Cu^{III} d'après les calculs DFT. Cependant, la valeur élevée du potentiel redox (1,26 V *vs* Fc) pour l'oxydation est problématique pour une potentielle utilisation en électrocatalyse. Suite à ces résultats, deux types de complexes ont été synthétisés en utilisant un ou deux groupements donneurs bis-amide en substitution d'un ou deux motifs DPA, afin de diminuer le potentiel redox. Les complexes **5** et **6** obtenus, différenciés par le pont (phénoxo ou alkoxo) et le nombre de groupements bis-amide, présentent un potentiel redox plus bas que **4**, mais leur oxydation conduit à des espèces instables à température ambiante. Cependant, pour le complexe dissymétrique **6**, l'utilisation de la basse température a permis de générer une espèce à valence mixte $Cu^{III}Cu^{II}$ (μ-OH,μ-O) qui absorbe à 386 nm.

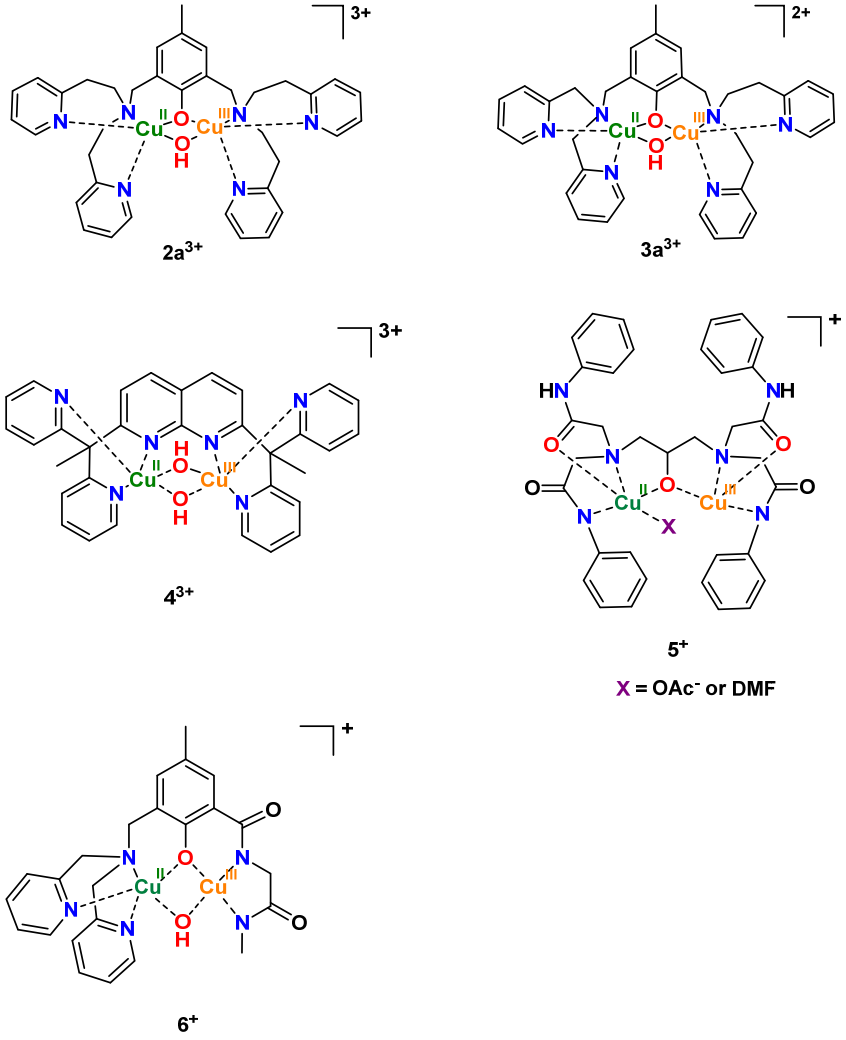

Figure VI.21. Complexes à valence mixte $Cu_2^{III,II}$ caractérisés dans ces études.

Tableau VI.2. Potentiel redox des différents complexes **1-6** étudiés et données spectroscopiques des espèces transitoires à valence mixte $Cu_2^{III,II}$.

Complexe	Solvant	E^0 /V vs Fc (ΔE_p /mV)	λ_{max} (nm) $Cu_2^{III,II}$
1a	CH_3CN	0.71 (170)	b
1b	CH_3CN	0.51 (70)	b
1c	CH_3CN	1.20[a]	b
2a	CH_3CN	1.04[a]	532
3a	CH_3CN	0.90[a]	520
4	CH_3CN	1.26 (190)	424
5	DMF	0.63[a]	463
6	DMF	0.124 (75)	386

[a]Pic irréversible ; [b]Non déterminé.

En conclusion, ce travail a démontré la caractérisation possible de complexes à valence mixte Cu^{III}-[μ-O(H)]$_n$-Cu^{II} par une combinaison de méthodes électrochimiques, spectroscopiques et théoriques. Ces systèmes restent les seuls décrits jusqu'à présent depuis le complexe (μ-OH) décrit par Tolman *et al*.[8] L'identification de ces intermédiaires instables n'a été possible que grâce à une approche cryo-spectroélectrochimique mis en place au cours de la thèse.

Ces études préliminaires ouvrent la voie à plusieurs perspectives. La première concerne des études catalytiques qui peuvent être réalisées avec ces complexes pour des réactions d'abstraction d'atome d'hydrogène sur des substrats classiques, tels que dihydroanthracène, le cyclohexane, le toluène... En particulier, il serait intéressant de corréler l'enthalpie de dissociation de la liaison C-H (BDE) aux propriétés redox et acido-basiques des complexes bis-cuivre. Un autre point d'intérêt serait la conception de nouveaux ligands qui pourrait permettre la stabilisation et la caractérisation (transitoire) d'une espèce à valence-mixte à température ambiante. Nos études ont montré que le complexe **6** présentait les propriétés les plus intéressantes (dissymétrie, faible potentiel redox). La compréhension du phénomène de décomposition de ce complexe pourrait permettre d'aboutir à des espèces $Cu_2^{III,II}$ plus stables. Enfin, l'approche cryo-spectroélectrochimie pourrait être utilisée pour détecter d'autres espèces réactives. Par exemple, l'espèce Cu^{III}-OH a été suggérée comme étant une espèce clé dans le mécanisme catalytique de la LPMO (polysaccharide lytique monooxygénase).[10],[11],[12],[13],[14],[15],[16],[17],[18],[19] A partir des résultats obtenus pendant la thèse sur la stabilisation de l'état redox Cu^{III}, de nouveaux complexes de cuivre(II)-hydroxo mononucléaires facilement oxydables pourraient être synthétisés à l'avenir. Les techniques cryo-spectroélectrochimiques (UV-Vis et proches-infrarouge) pourraient être utilisées pour la détection des différents intermédiaires réactionnels vis-à-vis de substrats organiques.

Références

[1] W. B. Tolman, *J. Biol. Inorg. Chem.* **2006**, *11*, 261-271.
[2] A. Messerschmidt, R. Huber, T. Poulas, K. Wieghardt, *Handbook of metalloproteins*, **2006**.
[3] S. Sirajuddin, A. C. Rosenzweig, *Biochemistry* **2015**, *54*, 2283-2294.
[4] E. I. Solomon, D. E. Heppner, E. M. Johnston, J. W. Ginsbach, J. Cirera, M. Qayyum, M. T. Kieber-Emmons, C. H. Kjaergaard, R. G. Hadt, L. Tian, *Chem. Rev.* **2014**, *114*, 3659-3853.
[5] R. A. Himes, K. D. Karlin, *Curr. Opin. Chem. Biol.* **2009**, *13*, 119-131.
[6] P. P. Y. Chen, S. I. Chan, *J. Inorg. Biochem.* **2006**, *100*, 801-809.
[7] Y. Shiota, K. Yoshizawa, *Inorg. Chem.* **2009**, *48*, 838-845.
[8] M. R. Halvagar, P. V. Solntsev, H. Lim, B. Hedman, K. O. Hodgson, E. I. Solomon, C. J. Cramer, W. B. Tolman, *J. Am. Chem. Soc.* **2014**, *136*, 7269-7272.
[9] R. Cao, C. Saracini, J. W. Ginsbach, M. T. Kieber-Emmons, M. A. Siegler, E. I. Solomon, S. Fukuzumi, K. D. Karlin, *J. Am. Chem. Soc.* **2016**, *138*, 7055-7066.
[10] P. Chen, E. I. Solomon, *J. Am. Chem. Soc.* **2004**, *126*, 4991-5000.
[11] A. Decker, E. I. Solomon, *Curr. Opin. Chem. Biol.* **2005**, *9*, 152-163.
[12] K. Yoshizawa, N. Kihara, T. Kamachi, Y. Shiota, *Inorg. Chem.* **2006**, *45*, 3034-3041.
[13] A. Crespo, M. A. Martí, A. E. Roitberg, L. M. Amzel, D. A. Estrin, *J. Am. Chem. Soc.* **2006**, *128*, 12817-12828.
[14] B. F. Gherman, D. E. Heppner, W. B. Tolman, C. J. Cramer, *J. Biol. Inorg. Chem.* **2006**, *11*, 197-205.
[15] S. M. Huber, M. Z. Ertem, F. Aquilante, L. Gagliardi, W. B. Tolman, C. J. Cramer, *Chem. Eur. J.* **2009**, *15*, 4886-4895.
[16] N. Dietl, C. van der Linde, M. Schlangen, M. K. Beyer, H. Schwarz, *Angew. Chem. Int. Ed. Eng.* **2011**, *50*, 4966-4969.
[17] S. Kim, J. Ståhlberg, M. Sandgren, R. S. Paton, G. T. Beckham, *Proc. Ntl. Acad. Sci. USA* **2014**, *111*, 149-154.
[18] A. Conde, L. Vilella, D. Balcells, M. M. Díaz-Requejo, A. Lledós, P. J. Pérez, *J. Am. Chem. Soc.* **2013**, *135*, 3887-3896.
[19] D. Dhar, W. B. Tolman, *J. Am. Chem. Soc.* **2015**, *137*, 1322-1329.

Dioxygen reactivity of new models of copper oxygenases: electrochemical and spectroscopic studies

Methane has the strongest C-H bond of any hydrocarbon (BDE = 104 kcal mol^{-1}); its oxidation under mild conditions remains a great challenge. The particulate Methane Monooxygenase (pMMO) is a copper enzyme that oxides methane (CH_4) to methanol (CH_3OH). In the active site of the enzyme, two copper ions are located at a short distance (2.6 Å). Recent researches have suggested a mixed-valent $Cu_2^{III,II}/O_2$ cluster as a key intermediate in the catalytic cycle. The main objective of this work was the synthesis and characterization of new mixed-valent $Cu^{III}Cu^{II}$ bis(μ-oxo) and (μ-OH, μ-O) dinuclear complexes. For this purpose we designed promising symmetrical and unsymmetrical complexes based on specific and distinct scaffolds for each side of the structure. Two families of coordination pattern have been used, polypyridyle or polyamide; the two sites are shortly and rigidly bridged by phenoxo, alkoxo or naphthyridine linkers. New complexes have been characterized by electrochemistry, UV-vis and EPR spectroscopies, and by theoretical calculations. A new cryo-UV-Vis-NIR spectroelectrochemical set up, developed in parallel during this work, has allowed the spectroscopic identification of these transient intermediate species, known to be unstable at room temperature. New mixed-valence $Cu_2^{III,II}$(μ-OH, μ-O) and $Cu_2^{III,II}$bis(μ-OH) complexes have been characterized. These results expand the recent knowledge on the only mixed valent Cu^{III}(μ-OH)Cu^{II} species described so far.

Keyword: pMMO, C-H activation, mixed-valent $Cu_2^{II,III}/O_2$ species, cryo-UV-Vis-NIR spectroelectrochemistry, symmetrical and unsymmetrical ligands

Réactivité vis-à-vis de l'oxygène des nouveaux modèles dinucléaires au cuivre: études électrochimiques et spectroscopiques

La molécule de méthane possède la liaison C-H la plus forte parmi les hydrocarbures (BDE = 104 kcal mol^{-1}) : son oxydation en conditions douces représente un challenge d'importance. La Méthane Monoxygénase particulaire (pMMO) est une enzyme à cuivre qui catalyse l'oxydation du méthane (CH_4) en méthanol (CH_3OH). Le site actif de l'enzyme est composé d'atomes de cuivre séparés par 2.6 Å. Des recherches récentes suggèrent qu'un cluster $Cu_2^{III,II}/O_2$ à valence mixte soit un intermédiaire-clé du cycle catalytique. L'objectif de ce travail vise à la synthèse et caractérisation de nouveaux complexes dinucléaires à valence mixte de type bis(μ-oxo)$Cu_2^{III,II}$ ou (μ-OH, μ-O)$Cu_2^{III,II}$. Deux familles de motifs coordinants ont été mises en œuvre, polypyridyle ou polyamide ; les deux sites sont assemblés par des ponts courts et rigides, phenoxo, naphthyridine ou alkoxo. De nouveaux complexes ont été caractérisés par électrochimie, spectroscopies UV-visible et RPE, et par des calculs théoriques. Un dispositif original de cryo-spectroélectrochimie UV-vis-NIR a été développé en parallèle de cette étude : il permet l'identification spectroscopique d'intermédiaires transitoires, réputés très instables à température ambiante. De nouveaux composés à valence mixte, $Cu_2^{III,II}$(μ-OH, μ-O) et $Cu_2^{III,II}$bis(μ-OH) ont été identifiés. Ces résultats élargissent le champ des données de cette famille d'intermédiaires instables limitée jusqu'ici à un seul exemple.

Mot-clé: pMMO, activation C-H, espèces à valence mixte $Cu_2^{II,III}/O_2$, cryo-UV-Vis-NIR spectroélectrochimie, ligands symétrique et asymétrique